Geologic and anthropogenic influences on rockfall and liquefaction in the 2010-2011 Canterbury earthquakes and their prehistoric predecessors

A thesis submitted in partial fulfillment of the requirements for the degree of Doctor of Philosophy in Geology at the University of Canterbury by

Josh W. Borella

March 2017

ABSTRACT

Geologic phenomena produced by earthquake shaking, including rockfalls and liquefaction features, provide important information on the intensity and spatiotemporal distribution of earthquake ground motions. The study of rockfall and liquefaction features produced in contemporary well-instrumented earthquakes increases our knowledge of how natural and anthropogenic environments respond to earthquakes and improves our ability to deduce seismologic information from analogous pre-contemporary (paleo-) geologic features. The study of contemporary and paleo- rockfall and liquefaction features enables improved forecasting of environmental responses to future earthquakes. In this thesis I utilize a combination of field and imagery-based mapping, trenching, stratigraphy, and numerical dating techniques to understand the nature and timing of rockfalls (and hillslope sedimentation) and liquefaction in the eastern South Island of New Zealand, and to examine the influence that anthropogenic activity has had on the geologic expressions of earthquake phenomena.

At Rapaki (Banks Peninsula, NZ), field and imagery-based mapping, statistical analysis and numerical modeling was conducted on rockfall boulders triggered by the fatal 2011 Christchurch earthquakes (*n=285*) and compared with newly identified prehistoric (Holocene and Pleistocene) boulders (*n=1049*) deposited on the same hillslope. A significant population of modern boulders (*n=26*) travelled farther downslope (>150 m) than their most-travelled prehistoric counterparts, causing extensive damage to residential dwellings at the foot of the hillslope. Replication of prehistoric boulder distributions using 3-dimensional rigid body numerical models requires the application of a drag-coefficient, attributed to moderate to dense slope vegetation, to account for their spatial distribution. Radiocarbon dating provides evidence for 17th to early 20th century deforestation at the study site during Polynesian and European colonization and after emplacement of prehistoric rockfalls. Anthropocene deforestation enabled modern rockfalls to exceed the limits of their prehistoric predecessors, highlighting a shift in the geologic expression of rockfalls due to anthropogenic activity.

Optical and radiocarbon dating of loessic hillslope sediments in New Zealand's South Island is used to constrain the timing of prehistoric rockfalls and associated seismic events, and quantify spatial and temporal patterns of hillslope sedimentation including responses to seismic and anthropogenic forcing. Luminescence ages from loessic sediments constrain timing of boulder emplacement to between ~3.0 and ~12.5 ka, well before the arrival of Polynesians (ca AD 1280) and Europeans (ca AD 1800) in New Zealand, and suggest loess accumulation was continuing at the study site until 12-13 ka. Large (>5 m^3) prehistoric rockfall boulders preserve an important record of Holocene hillslope sedimentation by creating local traps for sediment aggradation and upbuilding soil

formation. Sediment accumulation rates increased considerably (>~10 factor increase) following human arrival and associated anthropogenic burning of hillslope vegetation. New numerical ages are presented to place the evolution of loess-mantled hillslopes in New Zealand's South Island into a longer temporal framework and highlight the roles of earthquakes and humans on hillslope surface process.

Extensive field mapping and characterization for 1733 individual prehistoric rockfall boulders was conducted at Rapaki and another Banks Peninsula site, Purau, to understand their origin, frequency, and spatial and volumetric distributions. Boulder characteristics and distributions were compared to 421 boulders deposited at the same sites during the 2010-2011 Canterbury earthquake sequence. Prehistoric boulders at Rapaki and Purau are comprised of two dominant lithofacies types: volcanic breccia and massive (coherent) lava basalt. Volcanic breccia boulders are found in greatest abundance (64-73% of total mapped rockfall) and volume (~90-96% of total rockfall) at both locations and exclusively comprise the largest boulders with the longest runout distances that pose the greatest hazard to life and property. This study highlights the primary influence that volcanic lithofacies architecture has on rockfall hazard.

The influence of anthropogenic modifications on the surface and subsurface geologic expression of contemporary liquefaction created during the 2010-2011 Canterbury earthquake sequence (CES) in eastern Christchurch is examined. Trench observations indicate that anthropogenic fill layer boundaries and the composition/texture of discretely placed fill layers play an important role in absorbing fluidized sand/silt and controlling the subsurface architecture of preserved liquefaction features. Surface liquefaction morphologies (i.e. sand blows and linear sand blow arrays) display alignment with existing utility lines and utility excavations (and perforated pipes) provided conduits for liquefaction ejecta during the CES. No evidence of pre-CES liquefaction was identified within the anthropogenic fill layers or underlying native sediment. Radiocarbon dating of charcoal within the youngest native sediment suggests liquefaction has not occurred at the study site for at least the past 750-800 years. The importance of systematically examining the impact of buried infrastructure on channelizing and influencing surface and subsurface liquefaction morphologies is demonstrated.

This thesis highlights the importance of using a multi-technique approach for understanding prehistoric and contemporary earthquake phenomena and emphasizes the critical role that humans play in shaping the geologic record and Earth's surface processes.

CONTENTS

LIST OF FIGURES

LIST OF TABLES

ACKNOWLEDGEMENTS

During my Ph.D. I was supported financially by the EQC Scholarship for the study of earthquake hazards in New Zealand.

I thank my supervisory team for their guidance, friendship, and reviews of my research. Mark Quigley provided the important seed ideas for the projects presented within this thesis and offered valuable field assistance, as well as critical reviews and modifications during publication phases and for final stages in thesis writing. Mark, it has been a pleasure working with you over the past ~3 years and I hope we can continue to share ideas and collaborate in the years to come.

Darren Gravely has been a steady presence throughout my thesis, assuming a 'fatherly' role and fielding numerous important questions as well as accompanying me in the field on multiple occasions.

This thesis and any associated publications have benefitted greatly from thoughtful discussions I've had with Jarg Pettinga, David Bell, Ben Mackey, Max Borella, Sam Hampton, Sarah Bastin, Louise Vick, Phil Tonkin, Simon Brocklehurst, Brendan Duffy, Jonathan Davidson (including field assistance), Travis Horton, David Bell, Greg De Pascale, Narges Khajavi, and Sjoerd van Ballegooy.

I would like to offer a special thank you to Peter Almond. I found our discussions inspiring and transformative. Your input and careful review of publications was also essential to the overall integrity and quality of this thesis and any resulting publications.

The technical and secretarial staff at UC, including Pat Roberts, Janet Warburton, Rebekah Hunt, Cathy Higgins, Sacha Baldwin-Cunningham, Rob Spiers, Sarah Pope, and Chris Grimshaw, are wonderful and facilitated a smooth Ph.D. run. A sincere thank you for accommodating my requests at every turn. I would also like to say a special heartfelt thank you to Margaret Safi-Gorman, a cherished member of the department cleaning staff, whom recently passed. I will remember our wonderful chance meetings in the morning and your presence and bright smile.

The landowners at Rapaki have been incredibly receptive and generous, and I thank them for allowing me access onto their lands. In particular, Henry Couch, Rewi Couch, and Gavin Odering (farmer) have been gracious in allowing me to trench and perform other field duties, as well as provide UC and Frontiers Abroad undergraduate students the opportunity to experience Rapaki and its geologic hazards. It has been a pleasure to be involved with people so passionate about their land.

I thank Rafter Radiocarbon Laboratory at GNS Science for their efforts in dating my charcoal samples and Fugro Geotechnical (NZ) for conducting seismic cone penetration testing at Avondale Park.

The editorial staff and reviewers of three articles submitted for publication at Science Advances and Journal of Quaternary Science greatly improved the quality of the submitted papers (two of which are included as chapters within this thesis).

A very special thanks is offered to my brother, Max Borella, and lifetime friend (Darren Gravley, also advisor). Traveling to New Zealand to earn a PhD wasn't even a possibility until the two of you presented the idea and helped to make it a reality. Thank you for your continuous support and financial assistance through Frontiers Abroad Inc. You two are the absolute best!

As always, I am so appreciative of the love and support my mother and father have provided my family and I throughout the entire process. There is no way to truly express the gratitude I feel for having you in my life.

To Karyn, Cuinn, and Brea – I love you. Thanks for checking in all of the time and keeping a smile on my face.

Last, but certainly not least, I would like to thank my wife, Johanna, and my two amazing boys, Jack and Wyatt. I dedicate this thesis to the three of you. You and your love are the most precious things I have in this life. I hope I've done you proud!

THESIS PROLOGUE

Aims

To those living in or studying the geology of the Canterbury region, the 2010-2011 Canterbury earthquake sequence (CES) opened our eyes to a landscape that is tectonically active and prone to numerous hazards (e.g. liquefaction, rockfalls) as a result of strong earthquake-induced ground shaking. The most damaging ground shaking occurred from rupture on blind faults and thus no direct observations (e.g. fault scarps, surface traces) are available for determining the magnitude or recurrence interval for such shaking events. As a result, secondary or off-fault earthquake phenomena, such as liquefaction and rockfalls, offer a primary means for understanding the timing and conditions of prehistoric shaking in the region.

During and shortly after the earthquakes, GNS science and others (including the University of Canterbury) began mapping and characterizing modern rockfall boulders and documenting areas of extensive cliff collapse throughout the Port Hills of southern Christchurch. To no one's surprise, but not thoroughly considered prior to the CES, prehistoric rockfall boulders of similar-to-often greater size and comparable spatial distributions were observed in the same locations, suggesting that rupture on blind faults (and possibly other seismic sources) in the region had probably generated extensive rockfall in the recent geologic past (i.e. late Pleistocene to Holocene). Thus, it was logically concluded that if a method (or methods) for dating the timing of prehistoric rockfall emplacement was established, then the temporal distribution of past shaking events with similar ground shaking intensity to the 2011 Christchurch earthquakes could be determined and provide valuable information for contemporary rockfall hazard risk assessment, mitigation strategies, and response planning. Preliminary work was initiated by Mackey and Quigley (2014), who used CN surface exposure dating of prehistoric boulders to estimate the recurrence interval for strong prehistoric shaking in the region. This work featured in discussions of revisions to the Christchurch District plan and was entered into evidence during land use planning hearings. However, the number of data points (n=19) was limited and the efficacy and accuracy of the technique had not, up until the writing of this thesis, been cross-validated using other independent and complimentary dating techniques. As a result, the stage was set for using other forms of numerical dating (e.g. luminescence, radiocarbon) to advance our temporal understanding of prehistoric rockfall events and place the evolution of loess-mantled hillslopes in New Zealand's South Island into a longer temporal framework.

Following each of the major CES earthquakes (i.e. 4 September 2010, 22 February 2011, 13 June 2011, 22 December 2011), a similar ground reconnaissance strategy was employed throughout

Christchurch to understand the magnitude and spatial extent of liquefaction-induced ground damage. Several locations showing the most severe ground damage (i.e. lateral spreading cracks, extensive sand blow linear arrays) have been subsequently targeted to characterize modern liquefaction features (e.g. Quigley et al., 2013), and paleoliquefaction studies have been conducted (e.g. Bastin et al., 2015; Bastin et al., 2016) to estimate the timing and conditions of prehistoric ground shaking in Christchurch. However, these study sites occupy land that has been determined to be economically unbuildable (i.e. red zones) and thus the results from these investigations provide only a worst-case or most conservative scenario for purposes of future development in Christchurch. As a result, there remains an urgent need to examine and document modern (CES) and prehistoric liquefaction features in sections of Christchurch where damage may still have occurred but residential and commercial building continues (e.g. Technical Category 3 [TC3] land). Understanding the history and magnitude of modern and prehistoric ground shaking at these buildable sites would provide valuable data to be used in refining the expected ground accelerations at buildable sites and could also contribute to our geologic understanding of a how a site's soil profile behaves over time scales of 10^2-10^3 years under conditions of episodic liquefaction-inducing ground shaking.

As the rate and scale of anthropogenic interactions with the Earth system have intensified in recent decades, understanding human-induced alterations in the past and present is critical to our ability to anticipate, mitigate, and adapt to changes in the future. New Zealand's history of rapid anthropogenic deforestation and extensive modifications to low-elevation coastal plains (e.g. Christchurch) make it an optimal laboratory for evaluating anthropogenic influences on earthquake phenomena. Quantitative data comparing the distribution and behavior of geologic phenomena before and after human arrival is urgently required to evaluate the impact that human beings have on the geologic record and how these alterations may profoundly affect human society.

My thesis was fueled by several key questions that were developed prior to conducting fieldwork and further refined once preliminary field observations were made:

Can OSL dating of loessic hillslope sediments be successfully used to constrain the timing of boulder emplacement and reveal temporal patterns of prehistoric seismic activity, hillslope sedimentation and evolution?

How extensive is prehistoric rockfall in southern Christchurch and the greater Banks Peninsula area? What is the primary cause of prehistoric rockfall and can we determine its frequency and spatial and volumetric distributions?

What effect do humans have on the expression of rockfall and liquefaction hazard and can this signature (if present) be adequately quantified?

How has the rapid deforestation of hillslopes affected the rockfall hazard in New Zealand's South Island?

How are modern liquefaction features manifested in TC3 land (that is - land not in worst-affected liquefaction areas, but still located in moderate to severely damaged zones where in-depth geotechnical investigations are required)?

Do we observe paleoliquefaction at locations (i.e. Avondale) considered less vulnerable to liquefaction? If so, can we determine the timing for the causal earthquake(s) and derive an understanding for the conditions of shaking from liquefaction features (e.g. dike width, sand blow thickness)?

As a consequence of questions listed above, this thesis is centered on understanding the contemporary and prehistoric expression of secondary earthquake phenomena in New Zealand's South Island, with a special emphasis on examining the impact that human modifications have on rockfall and liquefaction hazard. Our investigations utilize the natural laboratory of southern Christchurch and western Banks Peninsula to explore prehistoric and contemporary rockfalls and eastern Christchurch to examine liquefaction. I present several important and novel contributions including (i) quantifying the impact of anthropogenic deforestation on rockfall boulder travel distance, (ii) the use of OSL dating of loessic hillslope sediments to constrain the timing of prehistoric rockfall emplacement and place the evolution of loess-mantled hillslopes in New Zealand's South Island into a longer temporal framework, (iii) extensive investigation of prehistoric rockfall in Banks Peninsula, and (iv) documenting the influence of anthropogenic modifications on the surface and subsurface expression of liquefaction.

Lastly, I propose potential directions that future research could be oriented, including the quantification of boulder surface roughness using photogrammetry and Sfm (structure-from-motion) software to derive a correlation between boulder surface roughness and CN surface exposure age. Under the right conditions this could provide a time-efficient and cost-effective method for deriving shaking recurrence intervals for prehistoric earthquakes in the Canterbury region with implications for global (even planetary) application.

Scientific Context

There has been limited research on prehistoric rockfalls in southern Christchurch and the greater Banks Peninsula area. This is, perhaps, not surprising given the challenges in determining the potential causes/triggers of prehistoric rockfalls and understanding possible complexities associated with post-emplacement mobility (e.g. movement resulting from debris/mud flows). Furthermore, prior to the CES rockfall as a potential hazard was considered a relatively low risk. It is my opinion, however, that prehistoric rockfalls are an under-valued data set and could be important in revealing regional shaking patterns in the Canterbury region and potentially identifying significant climatic, seismogenic, or anthropogenic forcing events in the recent geologic past. The cause of any studied rockfall deposits will need to be systematically researched and the influence of its topographic location (related to post-emplacement mobility) fully considered. However, in areas such as the Port Hills of southern Christchurch, where earthquakes are the most likely cause of rockfalls, the potential value in investigating prehistoric rockfall is high.

With regards to liquefaction, the geotechnical engineering and engineering geology fields have thoroughly considered and implemented specific anthropogenic structures (e.g. piles, gravel-mat slab foundations) to mitigate the effects of liquefaction, but research addressing the impact that anthropogenic modifications have on the expression of liquefaction in the geologic record, particularly in the subsurface, is limited. This, in addition to a lack of published studies investigating the geologic expression of contemporary and prehistoric liquefaction in areas of lower liquefaction susceptibility (as described above), represent key research topics addressed within this thesis.

Thesis Format

Chapter 1 investigates the impact of anthropogenic deforestation on contemporary rockfall hazard. Spatial distribution for rockfall boulders emplaced during the 2011 Christchurch earthquakes is compared with the same characteristics for their prehistoric counterparts. The runout distance for a large population of modern boulders (n=26) exceeds maximum travel distance for prehistoric boulders (n = 1049). The hypothesis that removal of the native forest at the Rapaki study site enabled the modern boulders to travel further (in some cases by more than ~150-175 meters) is tested. The increase in modern boulder travel distance meant impact and significant damage occurred within the Rapaki village and underscores the important mitigative properties of slope vegetation on rockfall hazard. RAMMS rockfall modeling is used to show that the application of moderate to dense vegetation on the Rapaki hillslope replicates the spatial distribution of prehistoric boulders. It is demonstrated that the rockfall hazard was enhanced throughout the Port Hills of southern

Christchurch during the CES. The planting of mature native forest is proposed as an effective method for mitigating rockfall hazard.

Chapter 1 was published in Science Advances (AAAS) in September of 2016 and is presented in its original published form. Per the required Science Advances manuscript format, the Material and Methods section is presented last. Below is the reference for the published article:

Borella, J. Quigley, M., Vick, L. (2016). Anthropocene rockfalls travel farther than prehistoric predecessors. *Science Advances* 2: e1600969.

Chapter 2 presents an in-depth study of the chronology and processes of late Quaternary hillslope sedimentation in the eastern South Island of New Zealand. OSL and radiocarbon dating of loessic hillslope sediments are used to constrain the timing of prehistoric rockfalls and associated seismic events, and quantify spatial and temporal patterns of hillslope sedimentation including responses to seismic and anthropogenic forcing. Trenches adjacent to prehistoric boulders enabled a stratigraphic analysis of loess and loess-colluvium that pre- and post-dates boulder emplacement. It is demonstrated that large prehistoric boulders preserve an important record of Holocene hillslope sedimentation (as colluvial wedges immediately upslope of the boulders). The study presents new numerical ages to place the evolution of loess-mantled hillslopes in New Zealand's South Island into a longer temporal framework.

Chapter 2 was published in the Journal of Quaternary Science (JQS) in October of 2016. This paper is presented as a companion paper to the Sohbati et al. article (of which the writer of this thesis is 2nd author) entitled "Optical dating of loessic hillslope sediments constrains timing of prehistoric rockfalls, Christchurch, New Zealand". The references for both of the published JQS papers are presented below:

Borella, J., Quigley, M., Sohbati, R., Almond, P., Gravley, D.M., Murray, A. (2016). Chronology and processes of late Quaternary hillslope sedimentation in the eastern South Island, New Zealand. *Journal of Quaternary Science* 31: 691-712.

Sohbati, R., Borella, J., Murray, A., Quigley, M., Buylaert, J. (2016). Optical dating of loessic hillslope sediments constrains timing of prehistoric rockfalls, Christchurch, New Zealand. *Journal of Quaternary Science* 31: 678-690.

Chapter 3 presents a detailed study of contemporary and prehistoric rockfalls in Banks Peninsula, New Zealand. I target two study locations – Rapaki and Purau – in Banks Peninsula to analyze prehistoric and modern (2011) rockfall boulder populations. Mapping and characterization of more than 1700 individual prehistoric rockfall boulders is conducted to understand their origin,

frequency, and spatial and volumetric distributions. Boulder characteristics and distributions are compared with ~421 rockfall boulders deposited at the same sites during the 2010-2011 CES. It is proposed that episodic earthquakes, with similar strong ground-shaking characteristics to the 2011 Christchurch earthquakes (i.e. 22 February and 13 June events) are probably the primary cause of rockfall in Banks Peninsula. This chapter highlights the strong influence that volcanic lithofacies architecture has on rockfall hazard.

Chapter 3 is intended as a comprehensive study of prehistoric and contemporary rockfalls at two study locales in Banks Peninsula, New Zealand. My intention is to refine and shorten the chapter and submit to *Geomorphology* or *New Zealand Journal of Geology and Geophysics (NZJGG)* for publication.

In **Chapter 4** I examine the influence of anthropogenic modifications on the surface and subsurface geologic expression of contemporary liquefaction created during the 2010-2011 Canterbury earthquake sequence (CES) in eastern Christchurch, New Zealand. Trenching and high-resolution aerial photography are used to document modern liquefaction features in Technical Category 3 land (i.e. land displaying moderate to severe liquefaction but not located in the worst-affected 'red zone' areas). Radiocarbon dating of charcoal (in native sediments) is used to determine a minimum age for the last occurrence of liquefaction at the study site. This chapter demonstrates the importance of systematically examining the impact of buried infrastructure on channelizing and influencing surface and subsurface liquefaction morphologies and presents one the first studies to document the influence of anthropogenic modifications on liquefaction in the geologic record.

Chapter 4 has been written in publication format and will be submitted (in shortened and refined form) to either *Anthropocene* or *Engineering Geology* for publication.

As a final note, I have presented the thesis chapters so the order is consistent with the natural progression of fieldwork and manuscript writing. Further explanation for the thesis structure is presented below.

Logistical explanation for thesis structure

This thesis began with a site visit to Rapaki (NZ) where numerous contemporary rockfall boulders, detached during the 2010-2011 CES, could be observed and subsequently studied. Equally noticeable were the abundant prehistoric boulders (comparable in spatial distribution and size) scattered across the Rapaki landscape. Previous work by Mackey and Quigley (2014) had used CN surface exposure dating of prehistoric boulder surfaces to estimate the last time a major rockfall event

(and presumed causative earthquake) had occurred in the area and to determine the probable recurrence interval for shaking events strong enough to create rockfall at the Rapaki study site. The results of this study can be found in Mackey and Quigley (2014). Our initial idea was to use radiocarbon and OSL dating of hillslope sediments present below the boulders and accumulated upslope of the boulders (i.e. behind as colluvial wedges) as an independent method for constraining the timing of boulder emplacement and for evaluating the accuracy of the CN-surface exposure ages. This, in fact, was performed on five (5) of the large prehistoric boulders and comprises Chapter 2 of this thesis.

However, after trenching behind the prehistoric boulders it became apparent to us that mapping and a detailed characterization of the prehistoric boulders was necessary to provide a more holistic context for the boulders (and adjacent/subjacent loessic sediments) chosen for OSL/radiocarbon dating and to reveal potential differences in spatial and volumetric distributions between the modern and prehistoric boulder sets. As a result, I conducted extensive mapping of more than ~1500 prehistoric boulders and with the help of Frontiers Abroad undergraduate students performed additional mapping of modern (2011) boulders at the Rapaki study site. Chapter 1 resulted from a relatively simple (but important) observation once mapping of prehistoric boulders was completed, and that was that maximum travel distance for modern rockfall boulders significantly exceeded runout for prehistoric boulders at the Rapaki study site. Further, this trend could be observed throughout the Port Hills of southern Christchurch, suggesting its effect was relatively widespread (i.e. not specific to Rapaki). This led to the next logical question: *Why have the modern boulders travelled further downslope than their prehistoric counterparts?* After some thought, I proposed that the removal of slope vegetation (that is, native podocarp/hardwood forest) by the Maori and/or Europeans may be the primary factor. As a result, in Chapter 1, we systematically evaluate a number of potential factors that could have enabled modern rockfall to travel further than the prehistoric boulders and impact the Rapaki village. We were aware that studies documenting and quantifying the impact of humans on earthquake hazards, such as rockfall, are rare but becoming increasingly important in the current geologic era now loosely but commonly defined as the 'Anthropocene'. The editors at *Science Advances* recognized the importance of the research and accepted our paper for publication.

Neither Chapter 1 nor Chapter 2 presents a sufficient overview of prehistoric rockfall in Banks Peninsula (which includes the Port Hills of southern Christchurch), which has remained largely unexplored. Consequently, I decided to extend the scope of research by performing additional mapping of prehistoric rockfall in Purau, where similar source rock characteristics are evident and both prehistoric and modern (2011) rockfall are observable. Chapter 3 presents a comprehensive study of prehistoric and contemporary rockfall boulders at Rapaki and Purau to understand their

origin, frequency, and spatial and volumetric distributions. The research highlights the importance of mapping and analyzing prehistoric rockfalls to develop a robust data set for informing paleoseismic studies and understanding contemporary rockfall hazard under known anthropogenically modified landscape conditions. Prehistoric rockfall potentially provides a record of major seismic, climatic, and/or anthropogenic events.

Although Chapter 4 (on liquefaction) is a departure from the study of rockfall, it remains focused on the documentation of off-fault earthquake phenomena (i.e. liquefaction), and specifically on site-specific anthropogenic modifications to the surface and subsurface geologic expression of liquefaction phenomena. It is worth pointing out here that my apparent focus on the 'Anthropocene' within this thesis is something that came about organically. As the research progressed and key observations were made, it was clear that the human impact on geologic hazards (i.e. rockfall and liquefaction) formed a major component of the study and represented a novel current of research. The original intention for research at Avondale Park was to document modern and paleoliquefaction features (carrying on the work of Bastin and Quigley, as well as others), with the aim of continuing to understand the distribution and magnitude of liquefaction features generated during the 2010-2011 CES and to compare with pre-CES liquefaction morphologies, particularly in TC3 land. The presence of thick anthropogenic fills (~1.5 meter thickness) at Avondale Park was unexpected, and although it limited our ability to observe paleoliquefaction with the native sediment profile, it provided a unique opportunity to study and document the influence of anthropogenic fills and other human modifications on the surface and subsurface expression of liquefaction. We are aware of no published studies that focus on examining the impact of anthropogenic modifications on the expression of liquefaction in the geologic record, especially those linking subsurface and surface patterns.

Scientific contributions arising from this PhD and related work

At the time of submitting this thesis, Chapters 1 and 2 have been published in peer-reviewed journals (Borella et al., 2016a, Borella et al., 2016b). The contents of the chapters have been presented at conferences, seminars, and undergraduate lectures/laboratory sessions. I also contributed to a third publication by Sohbati et al. (2016) as second author in which the methodology for the OSL dating (quartz and feldspar) of loessic sediments at Rapaki is presented in detail.

Originality

The material presented in this thesis has benefitted from discussions and contributions from my supervisors, co-authors and collaborators. In **Chapter 1**, Louise Vick performed the RAMMS rockfall modeling and utilized components of ArcGIS to analyze rockfall spatial distributions. Mark Quigley helped in the writing of the submitted manuscript (to Science Advances) and was instrumental in developing the strategy for testing our key hypothesis (i.e. removal of native forest enabled modern boulders to runout farther than prehistoric predecessors). In **Chapter 2**, Reza Sohbati and Andrew Murray performed OSL dating of the loessic sediment samples (see Sohbati et al., 2016). Peter Almond conducted Bayesian modeling of the OSL and radiocarbon ages and was influential in advancing key concepts within the manuscript, particularly those related to rockfall emplacement timing scenarios and hillslope soil development and process. Darren Gravley assisted with fieldwork and provided important insights related to the volcanic source rock (i.e. rockfall source) and native slope vegetation. In **Chapter 3**, several supervisors, colleagues, and UC students, including Max Borella, Samuel Hampton, Jonathan Davidson, and David Jacobson helped with the mapping and characterization of prehistoric and modern rockfall boulders at the Rapaki study site. At Purau, I was assisted by three Frontiers Abroad undergraduate students - Laura Stamp, Henry Lanman, and Sarah Trutner – who contributed greatly to the mapping/characterization of contemporary/prehistoric rockfall and were instrumental in expanding the breadth of rockfall investigation in Banks Peninsula. In **Chapter 4**, Max Borella and Sarah Trutner provided valuable field assistance, primarily during logging of the exploratory trenches. Sjoerd van Ballegooy performed the liquefaction susceptibility analysis and provided important insights on liquefaction process and related geotechnical issues.

My primary supervisors, Mark Quigley and Darren Gravley, engaged in scientific discussions and provided editorial assistance for all of the thesis chapters. Apart from these exceptions, the creation of the research questions, field data collection and processing, interpretations, presentation of data, and writing constitutes my own personal research.

Deputy Vice-Chancellor's Office
Postgraduate Office

UNIVERSITY OF CANTERBURY
Te Whare Wānanga o Waitaha
CHRISTCHURCH NEW ZEALAND

Co-Authorship Form

This form is to accompany the submission of any thesis that contains research reported in co-authored work that has been published, accepted for publication, or submitted for publication. A copy of this form should be included for each co-authored work that is included in the thesis. Completed forms should be included at the front (after the thesis abstract) of each copy of the thesis submitted for examination and library deposit.

Please indicate the chapter/section/pages of this thesis that are extracted from co-authored work and provide details of the publication or submission from the extract comes:

Chapter 1: Anthropocene rockfalls travel farther than prehistoric predecessors; Publication of same name in Science Advances (AAAS), 2016.

Please detail the nature and extent (%) of contribution by the candidate:

Research was performed under the guidance of Mark Quigley. Writing and scope benefitted from revisions with Mark Quigley and Louise Vick. Louise Vick performed RAMMS rockfall modeling and provided methodology section related to RAMMS. All ideas, execution of research, text and figures are those of the candidate, with input from co-authors. Estimated candidate contribution 85%.

Certification by Co-authors:

If there is more than one co-author then a single co-author can sign on behalf of all
The undersigned certifies that:

- The above statement correctly reflects the nature and extent of the PhD candidate's contribution to this co-authored work
- In cases where the candidate was the lead author of the co-authored work he or she wrote the text

Name: **Mark Quigley** Signature: 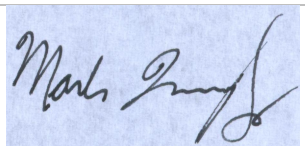 Date: **06 March 2017**

Deputy Vice-Chancellor's Office
Postgraduate Office

UNIVERSITY OF CANTERBURY
Te Whare Wānanga o Waitaha
CHRISTCHURCH NEW ZEALAND

Co-Authorship Form

This form is to accompany the submission of any thesis that contains research reported in co-authored work that has been published, accepted for publication, or submitted for publication. A copy of this form should be included for each co-authored work that is included in the thesis. Completed forms should be included at the front (after the thesis abstract) of each copy of the thesis submitted for examination and library deposit.

Please indicate the chapter/section/pages of this thesis that are extracted from co-authored work and provide details of the publication or submission from the extract comes:

Chapter 2: Chronology and processes of late Quaternary hillslope sedimentation in the eastern South Island, New Zealand; Publication of same name in Journal of Quaternary Science (JQS), 2016.

Please detail the nature and extent (%) of contribution by the candidate:

Research was performed under the guidance of Mark Quigley and Darren Gravley. Writing and scope benefitted from revisions with Mark Quigley, Darren Gravely, Peter Almond, and Reza Sohbati. Peter Almond performed Bayesian modeling of the OSL and radiocarbon ages. Reza Sohbati and Andrew Murray conducted OSL laboratory dating of loessic sediment samples. All ideas, execution of research, text and figures are those of the candidate, with input from co-authors.

Estimated contributions in components of research:

Field Work (planning, project aims, scope, execution): 100%
Analysis: 90%
Writing, literature review, formatting, revising: 90%

Certification by Co-authors:

If there is more than one co-author then a single co-author can sign on behalf of all
The undersigned certifies that:

- The above statement correctly reflects the nature and extent of the PhD candidate's contribution to this co-authored work
- In cases where the candidate was the lead author of the co-authored work he or she wrote the text

Name: **Darren Gravley** Signature: 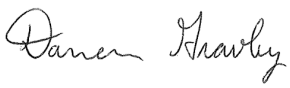 Date: **06 March 2017**

CHAPTER 1.

ANTHROPOCENE ROCKFALLS TRAVEL FARTHER THAN PREHISTORIC PREDECESSORS

1.1 Abstract

Human modification of natural landscapes has influenced surface processes in many settings on Earth. Quantitative data comparing the distribution and behavior of geologic phenomena prior to and after human arrival are sparse, but urgently required to evaluate possible anthropogenic influences on geologic hazards. Here we conduct field and imagery-based mapping, statistical analysis and numerical modeling of rockfall boulders triggered by the fatal 2011 Christchurch earthquakes (*n=285*) and newly identified prehistoric (Holocene and Pleistocene) boulders (*n=1049*) deposited on the same hillslope. Prehistoric and modern boulders are lithologically equivalent, derived from the same source cliff, and yield consistent power-law frequency-volume distributions. However, a significant population of modern boulders (*n=26*) travelled farther downslope (>150 m) than their most-travelled prehistoric counterparts, causing extensive damage to residential dwellings at the foot of the hillslope. Replication of prehistoric boulder distributions using 3-dimensional rigid body numerical models that incorporate lidar-derived digital topography and realistic boulder trajectories and volumes requires the application of a drag-coefficient, attributed to moderate to dense slope vegetation, to account for their spatial distribution. Incorporating a spatially variable native forest into the models successfully predicts prehistoric rockfall distributions. Radiocarbon dating provides evidence for 17th to early 20th century deforestation at the study site during Polynesian and European colonization and after emplacement of prehistoric rockfall. Anthropocene deforestation enabled modern rockfalls to exceed the limits of their prehistoric predecessors, highlighting a shift in the geologic expression of rockfalls due to anthropogenic activity. Reforestation of hillslopes by mature native vegetation could help to reduce future rockfall hazard.

1.2 Introduction

The detachment of large rock particles from source cliffs and subsequent downslope displacement by bouncing and rolling (i.e. rockfall) defines a major geologic hazard to humans and infrastructure in areas of steep topography (Evans and Hungr, 1993; Selby, 1993). Rockfall spatial distributions are commonly mapped as part of geologic hazard assessments (Guzzetti et al., 2003; Jaboyedoff and Labiouse, 2011; Stock et al., 2014) and are often used to delineate areas of comparably high hazard on the premise that the past is the key to the future. However, deforestation of hillslopes can induce rapid landscape transformation (Lambin et al., 2001; McWethy et al., 2010) and may increase the exposure of humans, dwellings, and critical infrastructure to slope hazards including rockfalls, landslides, and debris flows (Glade, 2003; Guns and Vanacker, 2014). Understanding the impact of changing land cover conditions on rockfall distributions and hazard requires a thorough understanding of landscape evolutionary chronology, boulder distribution statistics and depositional age, and boulder trajectory from source-to-resting position. In this study we conduct these analyses in unprecedented detail.

Severe deforestation has accompanied anthropogenic colonization of natural landscapes in many settings globally (McWethy et al., 2010; Achard et al., 2002) including New Zealand, where rapid deforestation began with Polynesian (Maori) settlement c. AD 1280 and continued with European colonisation from c. AD 1800 (Harding, 2003; McGlone, 1983; Fuller et al., 2015). By AD 1900, more than 98% of indigenous forest had been removed for urban and agricultural development in Banks Peninsula on the eastern coast of the South Island (Johnston, 1961; Wilson, 2013) (Fig. 1a,b,c,d). Human activity was accompanied by dramatic floral and faunal changes (Harding, 2003; Burrows, 1994), increased catchment erosion and alluvial sedimentation, and changes in river dynamics, marking the progressive emergence of the Anthropocene era (Waters et al., 2016; Zalasiewicz et al., 2015; Zalasiewicz et al., 2011; Lewis and Maslin, 2015).

Previous studies (McWethy et al., 2010; Glade et al., 2003; Guns and Vanacker, 2014) have examined the influence of anthropogenic deforestation on increasing landslide frequency, but none specifically address its impact on rockfall hazard as attributed to strong seismic-induced ground shaking. We are aware of no data that compares pre- with post-human arrival geologic phenomena with the resolution that we present in this study.

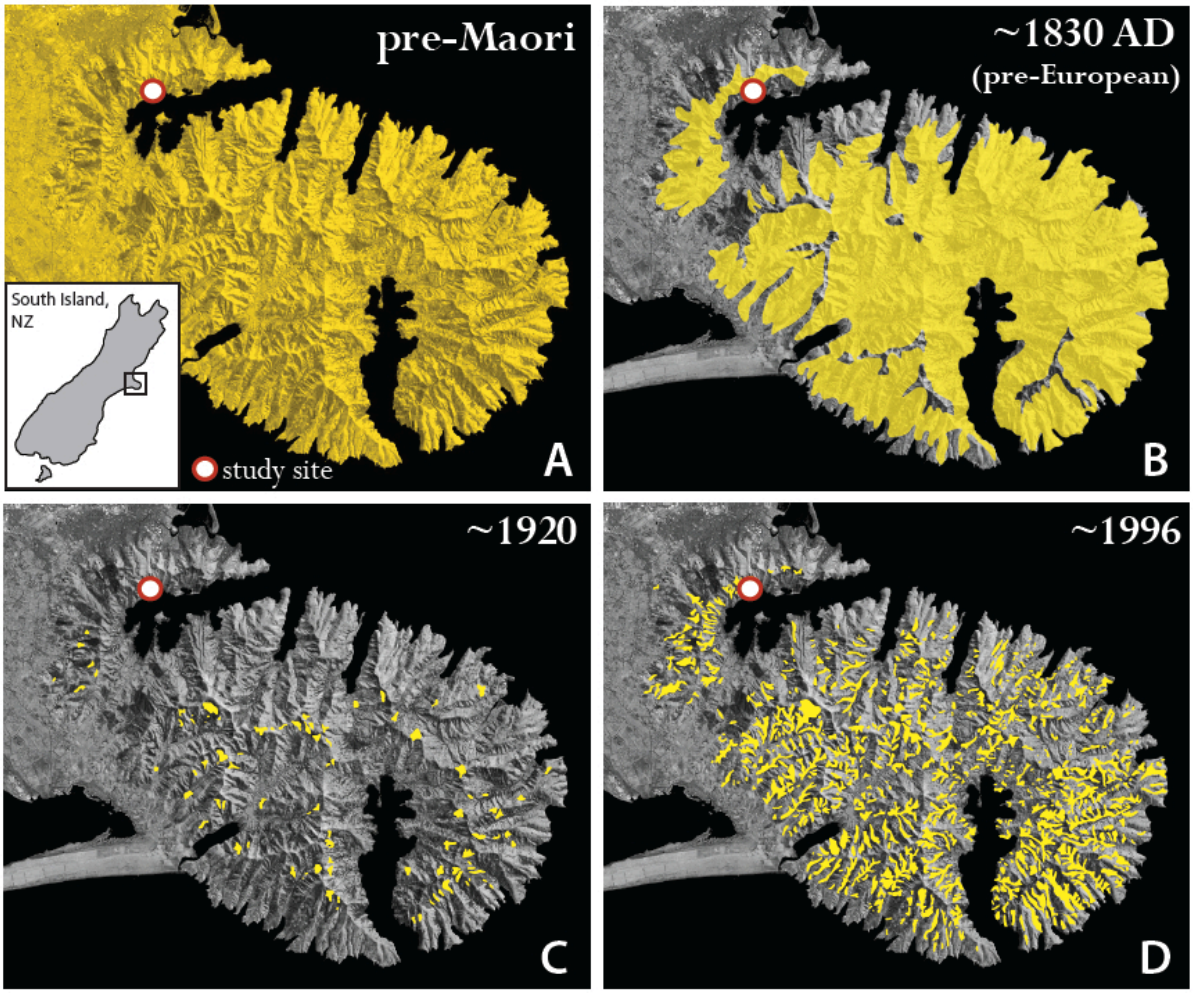

Figure 1. Anthropogenic Deforestation of Banks Peninsula. Removal of native forest (yellow) occurred rapidly in Banks Peninsula (BP) with the arrival of Polynesians (c. AD 1280) then Europeans (c. AD 1830). **(A)** Before arrival of the Polynesians (Maori), extensive native forest was present throughout BP. **(B)** Prior to European settlement, minor to moderate removal of indigenous forest by Maori had occurred in BP. Burning was the primary tool for clearance. **(C)** By 1920 Europeans had removed >98% of the native forest in BP, leaving slopes barren and low-lying areas vulnerable to slope hazards. **(D)** Minor re-establishment of old-growth native forest has occurred but slopes in BP and the Port Hills (including Rapaki) remain largely unvegetated (data from Johnston, 1961; Wilson, 2013; Burrows, 1994).

1.3 Results

Here we compare modern rockfall distributions and characteristics with their prehistoric counterparts at Rapaki in the Port Hills of southern Christchurch, New Zealand (Figs. 2a-e). During the 22 February 2011 moment magnitude (Mw) 6.2 Christchurch earthquake (Massey et al., 2014) more than 6,000 rockfall boulders were dislodged from source cliffs and deposited downslope, resulting in 5 fatalities, impacts to over 200 homes, and widespread evacuations in the Port Hills (Heron et al., 2014). More than 400 individual rocks (285 within the study area) were dislodged from the volcanic source rock near the top of Mount Rapaki (Fig. 2a and Fig. 3) in the 22 February and 13 June 2011 earthquakes. Twenty-six (26) of these rocks, ranging in volume from ~0.25 m^3 to ~28.0 m^3, impacted Rapaki village. Boulders travelled up to 770±15 m downslope from the source cliff (Fig. 2a,c).

During field mapping of modern rockfall at the Rapaki study site, abundant prehistoric rockfall boulders were discovered. The GPS location, elevation, volume, and lithology type were determined for 1049 individual prehistoric boulders with volume $\geq$ 0.1 m^3 (Fig. 2b). Prehistoric boulders are partially buried in colluvium and exhibit a high degree of surface roughness and lichen cover (Fig. 4), indicating long hillslope residence time. The absence of remobilization during the CES and the accumulation of thick colluvial wedges behind sampled prehistoric boulders implies boulders remained static after deposition. ^{3}He cosmogenic nuclide exposure ages (Mackey and Quigley, 2014) and preliminary optically stimulated luminescence dating (Sohbati et al., 2015; Sohbati et al., 2016; Borella et al., 2016) indicate prehistoric rockfall was emplaced no earlier than ~3-6 ka, long before arrival of Polynesians (Maori) and Europeans.

The prehistoric rockfall is attributed to a strong proximal earthquake at ca. 6-8 ka (Mackey and Quigley, 2014). The lack of any significant rockfall created at Rapaki during the 4 September 2010 main shock, 23 December 2011 after shock, recent (14 February 2016) Mw 5.7 Valentines Day earthquake, or during the estimated 1:100-year intensity storms in April 2014, suggests that most of the source rock is not 'waiting to fall', but rather, requires a significant stress for detachment of rock bodies (Mackey and Quigley, 2014). This is further supported by the absence of any prehistoric rockfall dated prior to ~3-6 ka (Mackey and Quigley, 2014; Sohbati et al., 2015; Sohbati et al., 2016; Borella et al., 2016), implying higher frequency precipitation events do not generate extensive rockfall. The Rapaki source rock is not (and would not have been for at least the past ~30 ka) located directly adjacent to any rivers or the harbour coastline, thereby eliminating natural undercutting as a potential triggering mechanism, and even during the last glacial maximum (~24-18 ka) would have obtained an elevation of only ~500-520 meters above sea level, precluding it from sustained freeze-thaw conditions (i.e. high precipitation and temperature fluctuations), typical in high-mountainous elevations (e.g. southern Alps).

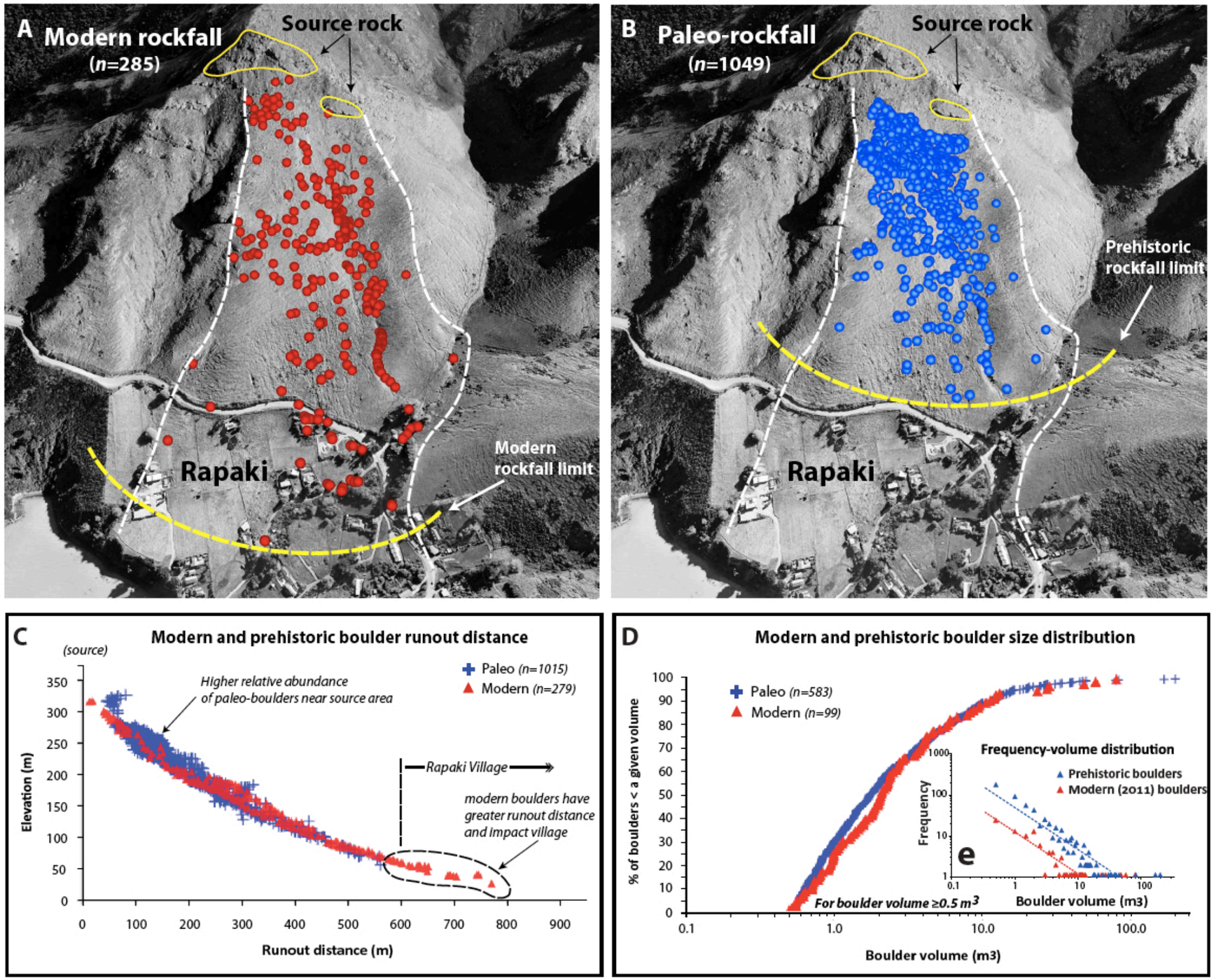

Figure 2. Spatial distribution and size comparison of modern and prehistoric rockfall at Rapaki. (A) Spatial distribution for mapped modern rockfall (n=285) generated during the 2011 Christchurch earthquakes (22 February and 13 June events). Twenty-six (26) modern boulders impacted the Rapaki village and caused severe damage to residential properties. Maximum run-out distance (map length) for modern boulders is ~770 meters. **(B)** Spatial distribution for mapped paleo-boulders (n=1049). No evidence for prehistoric boulders in area now occupied by the Rapaki village. Maximum travel distance for prehistoric boulders is ~560 meters. **(C)** Modern and prehistoric rockfall runout distance plotted as function of elevation. Travel distance for modern rockfalls exceeds limit of prehistoric predecessors. **(D)** Comparison of boulder size distribution for modern and prehistoric boulders indicates strong similarity. **(E)** The frequency-volume distributions for prehistoric and modern rockfall at Rapaki show a similar power-law trend.

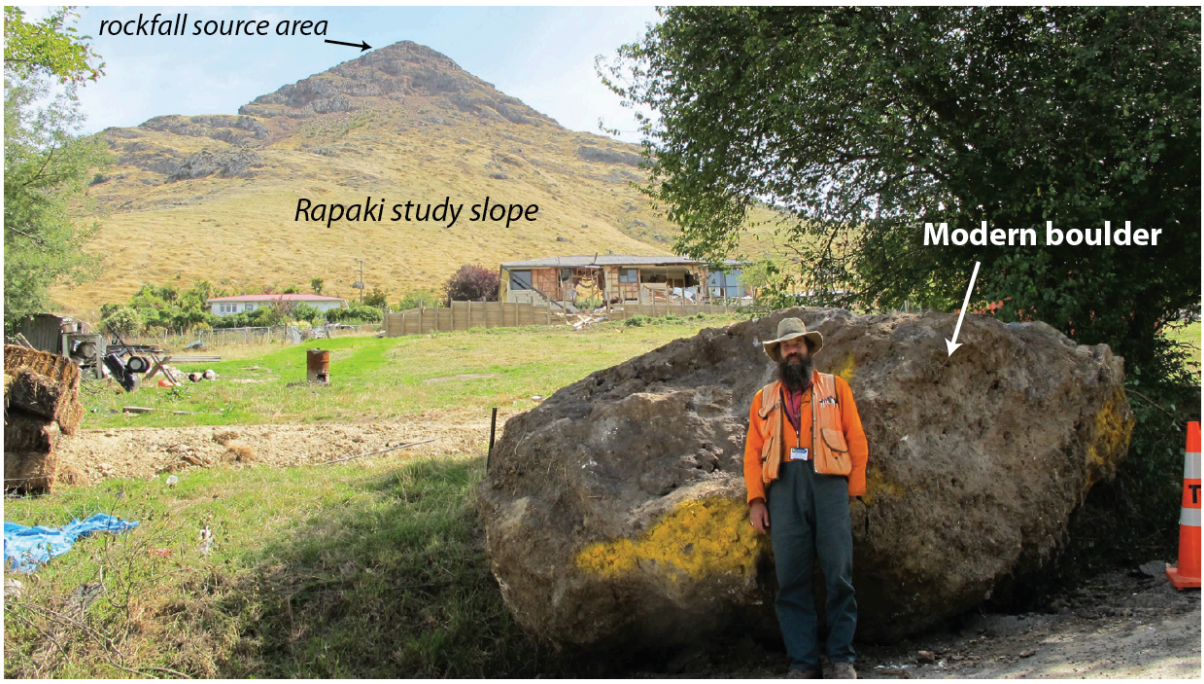

Figure 3. Modern boulder at Rapaki study site. Photo of large modern boulder (~28 m^3) detached from Mount Rapaki and emplaced in the Rapaki village during the 22 February 2011 earthquake (photo courtesy of D.J.A. Barrell, GNS Science). The boulder traveled through the center of the residential home located in background (center). Boulder runout distance from source was ~700 meters. Runout distance for furthest traveled modern boulders is significantly greater (~150-175 meters) than travel distance for prehistoric boulders.

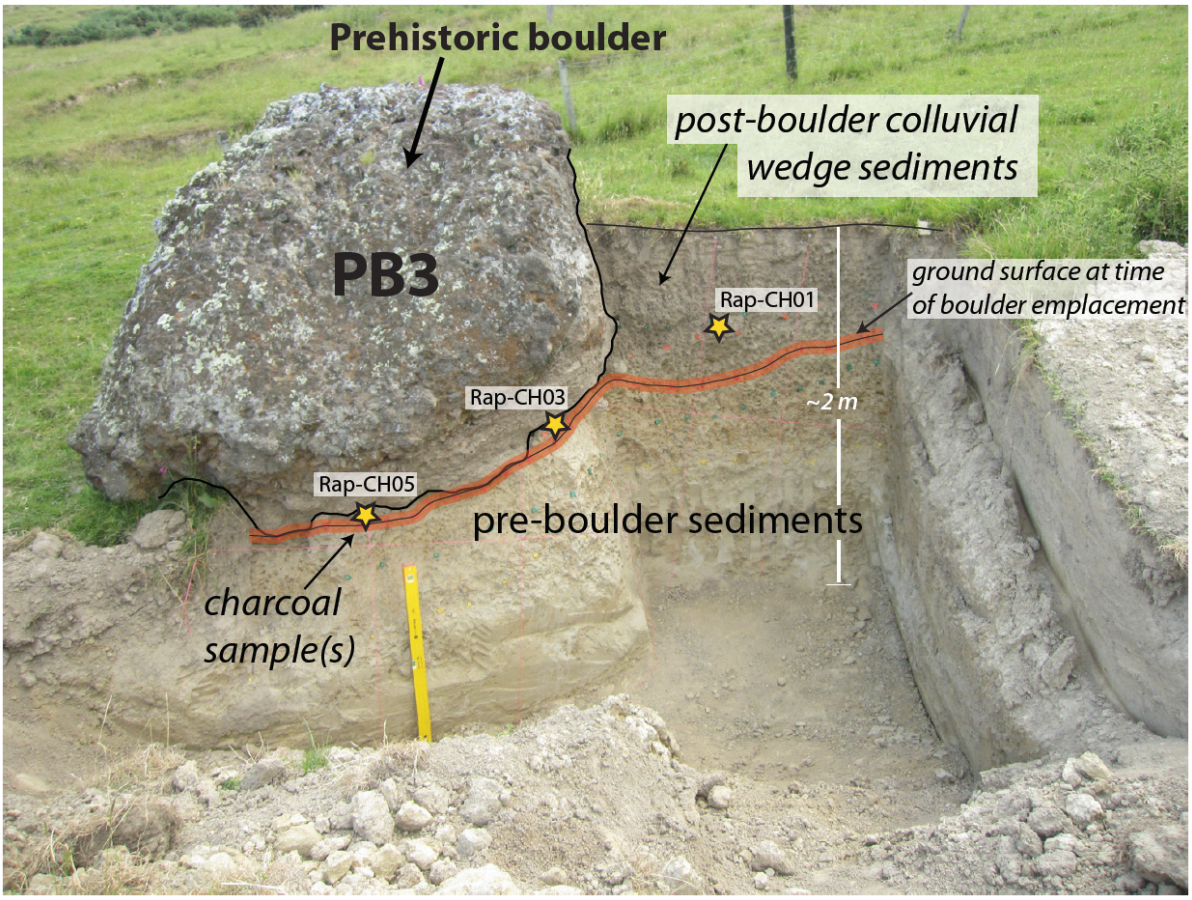

Fig. 4. Prehistoric boulder at Rapaki study site. Photo of exploratory trench excavated adjacent to Paleo-Boulder 3 (PB3), exposing hillslope sediments deposited before and after boulder emplacement. Locations for charcoal samples (yellow) Rap-CH01, Rap-CH03, and Rap-CH05 are shown. All samples were collected near the base of the most recent loess-colluvial wedge sediments and yield similar conventional radiocarbon ages (203±18, 197±17, 222±17 yr B.P.), respectively. 2-sigma calibrated ages suggest a probable burning event occurred at Rapaki sometime between AD 1661 and AD 1950, with highest 2-sigma sub-interval probability between AD 1722 and AD 1810. PB3 is deposited in footslope position and volume is ~14.5 m3. Total travel distance for PB3 is ~560 meters.

Comparison of modern and prehistoric boulder spatial distributions (Fig. 2a,b) indicate that (i) both have increased concentrations in topographic lows, (ii) both have decreased concentrations on interfluves, (iii) prehistoric boulders have shorter maximum runout distances (560 ± 15 m) compared to modern, and (iv) prehistoric rockfall is more concentrated near the source area compared to modern (Fig. 2c). A Kolmogorov-Smirnov (K-S) comparison test confirms the lack of similarity between modern and prehistoric boulder spatial distributions and indicates the maximum difference between cumulative distributions is 0.636 with a corresponding low P-value of 0.012 (see Materials and Methods for details of K-S test and Supplementary Data 1). No prehistoric boulders were identified on the surface or in the shallow subsurface in the area now occupied by Rapaki Village from field mapping and inspection of historical aerial photographs dating back to 1926. In interviews with the local Maori, they indicated, based upon a review of their recorded oral history, that there are no accounts of large boulders being removed or repositioned by their ancestors in the Rapaki village area.

Modern and prehistoric boulders are lithologically equivalent and maintain consistent frequency volume distributions (Fig. 2d,e). Statistical coherence is observed at 25th percentile (modern=1.01 m^3, prehistoric=0.89 m^3), median (modern=2.05 m^3, prehistoric=1.70 m^3), and 75th percentile (modern=4.16 m^3, prehistoric=4.53 m^3) boulder sizes. K-S analysis indicates a maximum difference between cumulative distributions of 0.102 with a corresponding P-value of 0.326 (see Supplementary Data 2). Similarities in boulder shape and size exist because the prehistoric and modern rockfalls at Rapaki are sourced from the same parent rock, where jointing in the source rock, predominantly from early cooling of the lava flows, imparts a first order control on boulder size and shape. Given its probable early formation and the persistent nature of jointing within the volcanic source rock, it is reasonable to assume that joint-control on boulder size and shape has remained constant over time (i.e. during multiple rockfall events). The abundance of both modern and prehistoric boulders in the same topographic lows suggests slope characteristics have also remained relatively constant with time and that from a landscape evolution perspective, the time between rockfall events (~3-7 ky) and that recorded by all observable rockfall (both prehistoric and modern) (estimate ~25 ky) at Rapaki, is relatively short. It is difficult to determine the influence that previous boulders might have had on changing the runout path for subsequent rockfall deposits. We expect impacts could be common near the source cliff, but much less so at midslope and footslope positions, because the frequency of boulders declines rapidly (power law reduction) and diffusion increases with increasing distance from the source area. If accumulated debris was an important limit on rockfall extents, we would predict a reduction of modern boulder runout distances with increasing time rather than the observed increase, due to an increased likelihood of boulder impacts with increasing hillslope debris. Additionally, we cannot dismiss outright that potential collisions of travelling boulders with other mobile rockfall debris could have influenced rockfall runout distances in some cases (Okura et al., 2000), but assume the impact of

this effect would be of similar extent during all major rockfall events and relatively unimportant given the steep slopes and rapid boulder velocities during transport (Fig. 5a,c).

Given the similarities in lithology and morphology but differences in runout distances between the modern and prehistoric boulder data sets, the abundance of evidence suggesting the presence of dense native forest on BP hillslopes during prehistoric times, and the observation that contemporary boulder impacts with trees were observed frequently in other (forested) parts of the landscape after the Christchurch earthquakes, it is sensible to reason that prehistoric boulder runouts may have been impeded by natural vegetation at the study site prior to deforestation. To test this hypothesis we used rapid mass movement simulation (RAMMS) software (Bartelt et al., 2013; Christen et al., 2007) and a 3-m DEM derived from post-earthquake LIDAR surveys to model modern and prehistoric rockfall distributions. Boulder trajectories and bounce positions were reconstructed using ground mapping and 10 cm resolution aerial photography. A total of 700 boulders with power-law frequency-volume distributions were released from three separate source rock areas (Fig. 5a,c) (see Materials and Methods); rockfall source areas and partitioning of boulder volumetric flux was informed by field observations from the 2011 Christchurch earthquakes.

RAMMS 1 (modern unvegetated landscape model) yields spatial distributions and maximum runout distances (700-770 meters) for simulated boulders that overlap tightly with empirical modern rockfall distributions (Fig. 5b and Fig. 6). The percentage of RAMMS 1 boulders deposited near the source rock (shadow angles 32° and 33°) is <25%. K-S analysis indicates high correlation (P-value=0.736) between RAMMS 1 simulated boulders and empirical data (see Supplementary Data 3), highlighting the ability of RAMMS to successfully replicate rockfall trajectories and runouts. RAMMS 1 significantly overpredicts prehistoric rockfall runout distance and underpredicts near-source prehistoric rockfall relative frequency. K-S analysis between RAMMS 1 and prehistoric boulders yields a low P-value of 0.012 (see Supplementary Data 4). Given the probable middle Holocene age of prehistoric rockfalls, we explored whether changes in the impact of slope vegetation between modern and prehistoric rockfalls could account for differences in respective boulder spatial distributions. Hillslope vegetation (e.g. forest stands) is widely recognized as an effective method of rockfall protection. The influence and effectiveness of variable tree sizes, spacing between trunks, and species has been thoroughly researched (Dorren, 2004; Dorren et al., 2005; Jancke et al., 2009; Vacchiano et al., 2008, Woltjer et al., 2008; Vick, 2015). Vick (2015) has demonstrated that vegetation reduces the number of CES boulders traveling to the lower shadow angles (i.e. vegetation reduces rockfall runout).

We implemented spatially variable, moderate to dense native hillslope vegetation (modeled using a forest drag-coefficient) into RAMMS simulations (RAMMS 2) to test whether more accurate replication of prehistoric boulders could be achieved with forest cover. Prior to Polynesian and

European settlement Banks Peninsula was almost completely covered by a richly varied native forest (Wilson, 2013; Wilson, 1993; Shulmeister et al., 1999; Soons et al., 2002) (Fig. 1a). Warm temperate and frost sensitive species like nikau palm and akeake grew in coastal gully forest, while valley floors and lower slopes were covered by tall podocarp forest dominated by kahikatea, lowland totara, and matai (Wilson, 2013; Wilson, 1993). Pollen and phytolith analyses from core samples taken in Banks Peninsula (Gebbies Pass) are consistent with the presence of podocarp forest during the Holocene and persistent woody conditions even in cooler glacial periods (Shulmeister et al., 1999; Soons et al., 2002). It is therefore reasonable to assume that similar forest conditions existed on the Rapaki hillslope prior to deforestation.

RAMMS 2 boulders show highest volumetric proportions (~62-64% of total population) near the source rock at steep (33°) shadow angles (i.e., angle from the horizontal of a line projected from the source area base to top of runout boulder) and increased volumes in the northern drainage gulley, consistent with distributions of mapped prehistoric boulders (Fig. 5d and Fig. 6). Boulder frequency decreases with increasing distance from the source rock and on the southern middle to lower-slope interfluve. Maximum modeled boulder runout distance is ~560-600 meters. No RAMMS 2 boulders reach Rapaki village. A K-S comparison test between prehistoric rockfall and RAMMS 2 boulders indicates high correlation, with a P-value of 0.736 (see Supplementary Data 5). We conclude that dense native forest cover increased the frequency of boulder-forest impacts and increased frictional drag on boulders during rockfall events, thereby limiting runout distances.

Radiocarbon dating of charcoal found within loess-colluvium sediments at the study site suggests removal of native forest by burning occurred sometime between AD 1661 and AD 1950 (2-sigma calibrated age), marking its occurrence well after deposition of prehistoric rockfall (Table 1, Fig. 4) (Lambin et al., 2001; McWethy et al., 2010; Glade, 2003) and sometime during Maori and subsequent European occupation. While we cannot exclude natural fire as a mechanism for deforestation, the onset of increased colluvial sedimentation during the period of local human colonization, widespread evidence for anthropogenic deforestation elsewhere in the region, and absence of modern forest cover suggests anthropogenic sustainment of an unforested landscape since the 17th to earliest 20th century. Anthropogenic landscape modification between successive rockfall triggering events enabled modern rockfall runout distances to exceed the identified limits of their prehistoric predecessors, providing geologic evidence for the emergence of the Anthropocene (Fig. 7).

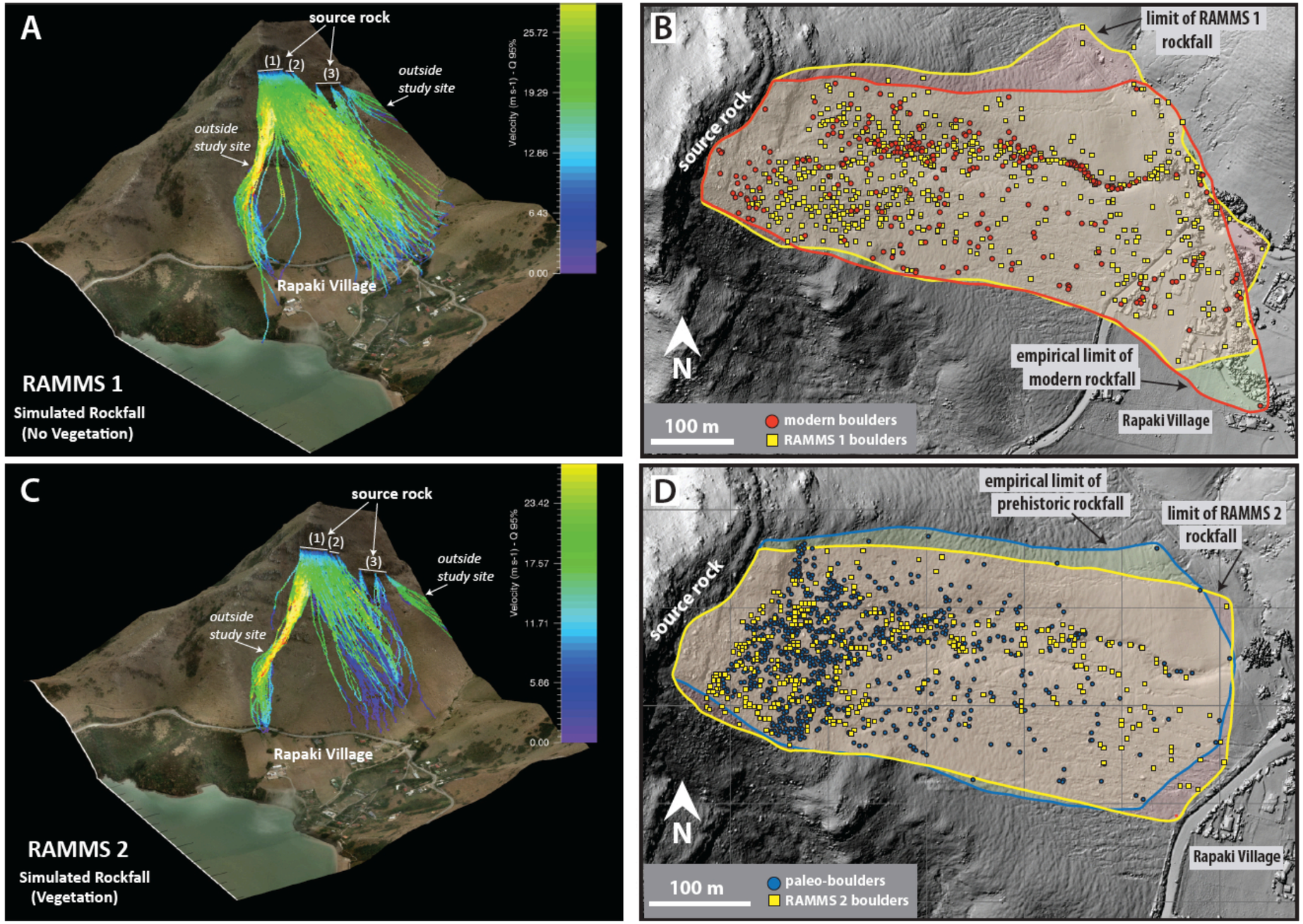

Figure 5. RAMMS rockfall modeling. (A) Simulated rockfall assuming no hillslope vegetation (RAMMS 1). Source areas, rockfall trajectories, boulder velocities, and final resting positions are shown. **(B)** RAMMS 1 successfully predicts modern boulder distributions, highlighting effectiveness of RAMMS in replicating modern rockfall distribution. **(C)** Simulated rockfall assuming moderate to dense vegetation on the hillslope (RAMMS 2). Vegetation is modeled in RAMMS as forest drag; a resisting force that acts on the rock's centre of mass when located below the drag layer height. The forest is parameterized by the effective height of the vegetation layer (10 meters) and a drag coefficient (moderate=3000 kgs-1 and dense=6000 kgs-1). **(D)** Prehistoric and RAMMS 2 boulder distributions display strong correlation, suggesting that a moderate to dense forest likely existed on the Rapaki hillslope during prehistoric boulder deposition.

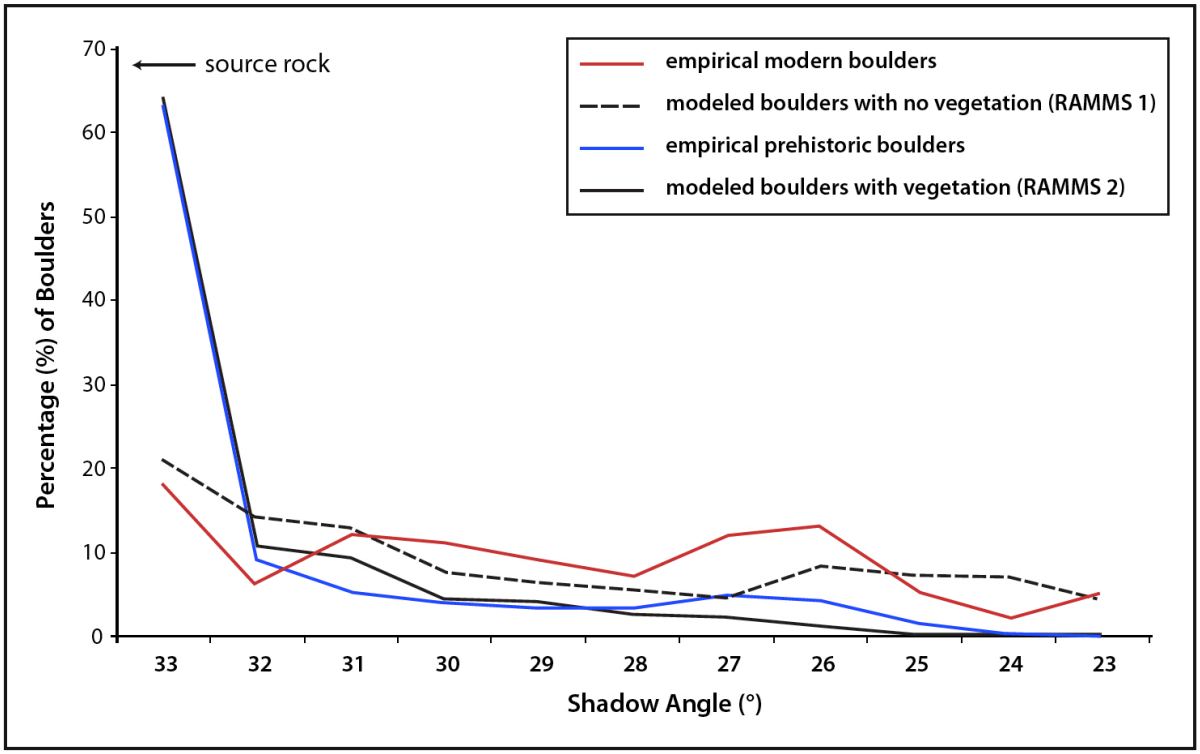

Figure 6. Comparison of empirical and modeled rockfall spatial distributions. Empirical prehistoric and RAMMS 2 boulders (vegetation) display a strong similarity (P=0.736) with the highest frequency (~62-64%) of boulders near the source rock (shadow angle 33°). Empirical modern and RAMMS 1 boulders (no vegetation) show an equivalently high correlation (P=0.736). In contrast, mapped prehistoric and modern boulders display a poor fit (P=0.012). ArcGIS has been utilized to determine percentage of boulders within each shadow angle.

Sample ID	Exposure Unit	NZA laboratory number	$\delta^{13}C$	Radiocarbon age	Calibrated age 2σ	Probability for each 2σ range	Materials and Significance
				(^{14}C yr B.P.)	(Calendar yr A.D.)	(%)	
Rap-CH01	loess-colluvium	56801	-28.6±0.2	203±18	A.D. 1664-1698, **1724-1809**, 1870-1876	22.8, **70.4**, 1.0	Charcoal in colluvial wedge sediment. Dates probable burning event at Rapaki.
Rap-CH03	loess-colluvium	56802	-29.1±0.2	197±17	A.D. 1666-1700, **1722-1810**, 1838-1845, 1867-1878, 1933-1938, 1946-1950	25.8, **63.8**, 1.3, 2.4, 0.6, 1.1	Charcoal in colluvial wedge sediment. Dates probable burning event at Rapaki.
Rap-CH05	loess-colluvium	56803	-27.9±0.2	222±17	A.D. 1661-1680, **1732-1802**	15.8, **79.0**	Charcoal in colluvial wedge sediment. Dates probable burning event at Rapaki.

Table 1. Results from radiocarbon dating of charcoal within loess colluvium sediments at Rapaki, New Zealand. NZA, Rafter Radiocarbon Laboratory; 14C yr B.P., radiocarbon years before the present.

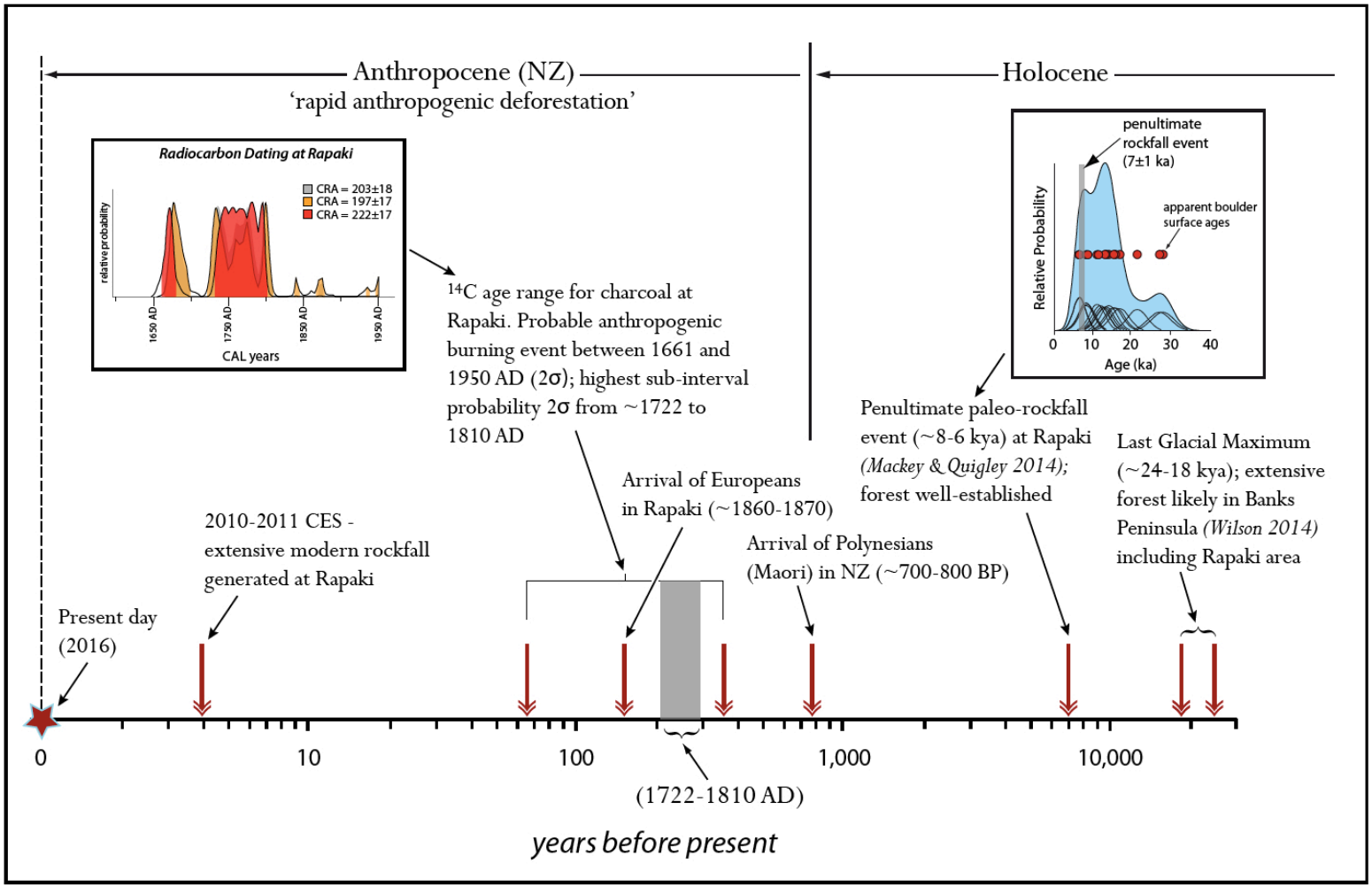

Figure 7. Rockfall and Anthropocene chronology for Rapaki study site. Native forest likely persisted during the LGM and thrived during the Holocene in Banks Peninsula and at Rapaki. The penultimate paleo-rockfall event at Rapaki occurred approximately 8-6 ka (Mackey & Quigley 2014) when a dense variable forest cover would have existed on the hillslope. Radiocarbon dating of charcoal at Rapaki suggests a probable burning event occurred sometime between AD 1661 and AD 1950, with highest sub-interval probability between AD 1722 and AD 1810. Slope deforestation by Maori and later Europeans allowed modern rockfall generated during the 2011 Christchurch earthquakes to travel further than their prehistoric predecessors and impact the Rapaki village

1.4 Discussion

The 2011 Christchurch earthquakes provide the rare opportunity to map the distribution and trajectory of modern rockfall deposits and compare them to prehistoric predecessors. We attribute the discrepancy between spatial distributions of modern and prehistoric rockfall deposits identified in this study to intervening landscape change in the form of Anthropocene deforestation sometime between AD 1661 and AD 1950. Field mapping (Fig. 8a-c) suggests increased modern rockfall runout distance occurred in other deforested areas of the Port Hills (Banks Peninsula), highlighting the widespread impact that removal of native forest has on increasing rockfall hazard. Deforestation allowed modern boulders to travel further than their geologic predecessors and damage infrastructure in downslope areas at source distances beyond what would be predicted from the distribution of past rockfall deposits (see Figs. 2a-c and Figs. 8a-c). Increases in hillslope substrate wetness relating to climate change or short-term weather fluctuations could theoretically reduce hillslope frictional properties and increase rockfall runout distances due to elevated substrate pore-pressures. However, this potential effect seems unimportant in this area because paleoclimate models (Ackerley et al., 2013) suggest cooler and wetter mid-Holocene (ca. 6000 yr B.P.) climates in eastern New Zealand relative to present, which should have favored longer prehistoric rockfall runout distances relative to modern distances, in opposition to what we observe. Conversely, Vick (2015) shows that there is greater scarring depth relative to length from boulder impacts during the winter when soil is moist (compared to dryer soil conditions during summer months). When a rockfall block impacts softer ground, much of the block's kinetic energy is dissipated as the soil deforms (Bozzolo and Pamini, 1986). Tests from loess derived soils show a decreasing strength with increasing water content (McDowell, 1989). At Rapaki, we would expect rockfall runout distance to be reduced when soil moisture content is high, although the magnitude of that reduction is unlikely to be as significant as that attributed to the removal of hillslope vegetation. Additional RAMMS rockfall modeling to determine the influence of soil moisture content on boulder runout distance needs to be performed.

Assessments of rockfall hazard must consider the potential for future effects to surpass prehistoric geologic analogues in severity and extent particularly where intervening anthropogenic activity has modified the landscape (see Figs. 2a-c and Figs. 8a,b). However, a positive implication of this study is that naturally regenerating native forest or exotic plantation forest (see Fig. 8b) cover may provide an effective and time-resilient method for mitigating rockfall hazard. Paleo-forest cover at Rapaki was presumably able to regenerate and dynamically stabilize itself through several high-impact rockfall events and a changing climate (Borella et al., 2016; Sohbati et al., 2016) (i.e. glacial to inter-glacial); essential capacities for any protective forest. Local and global discussions on the efficacy of forest cover (Dorren et al., 2004; Brauner et al., 2005) for mitigating rockfall hazard are becoming

increasingly important as human settlement continues to expand into hilly and mountainous regions throughout the world.

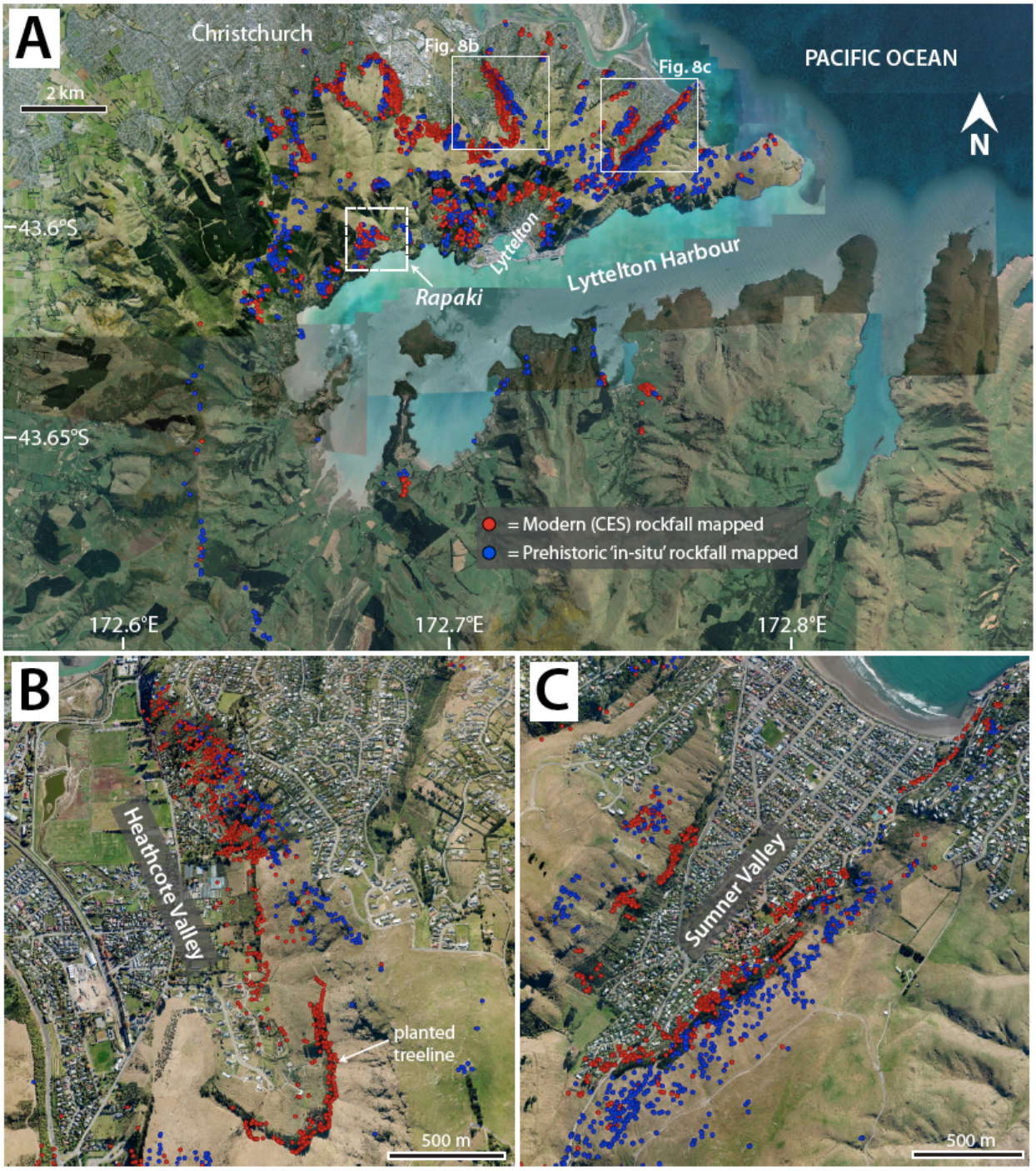

Figure 8. Comparison of spatial distribution for modern (CES) and prehistoric rockfall in Port Hills of Southern Christchurch. (A) Mapped modern (red) and prehistoric (blue) 'in-situ' rockfall. Rockfall data shown has been provided by the Christchurch City Council and was mapped in the field by GNS Science. [Prehistoric rockfall was only partially mapped in certain areas, such as upslope of the planted treeline shown in (B). Burial of pre-existing boulders by colluvial and alluvial sediments is possible, particularly in the footslope position, and would limit the number of observable prehistoric rockfalls.] Slopes in the Port Hills have been stripped of native vegetation. **(B)** Comparison of CES-generated and prehistoric 'in-situ' rockfall in Heathcote Valley reveals longer runout distances for CES rockfall boulders. Modern rockfall affected numerous residential dwellings. The southern planted treeline was effective in capturing modern rockfall, highlighting the importance of slope vegetation in mitigating rockfall hazard. **(C)** Modern rockfall boulders on the northwestern and southeastern sides of Sumner Valley display further runout distances (~50-100 m) than 'in-situ' [we recognize the possibility that, in rare cases, isolated exposures of intact volcanic bedrock may be mapped as in situ (prehistoric) boulders] or pre-existing rockfall. *Special note*: The 'in-situ' designation was originally used for rocks that showed some evidence of movement within their original setting (e.g. evidence of cracking, shifting, or rotation). However, some of the mapped 'in-situ' boulders have been deposited a significant distance from the source rock and thus likely represent displaced prehistoric rockfall boulders. As a result, it is safe to assume that the 'in-situ' boulders represent a mosaic of precarious rock masses on the slopes and boulders that have already fallen (i.e. pre-CES rockfall boulders). Therefore, although the 'in-situ' data set as a whole should be viewed cautiously, in certain areas (e.g. Sumner Valley), these boulders represent prehistoric rockfalls and their comparison with CES boulders effectively highlights the increased travel distance for modern (2011) rockfalls.

1.5 Materials and Methods

1.5.1. Mapping and characterization of prehistoric and modern rockfall boulders

We mapped 1,543 individual prehistoric rockfall boulders at the Rapaki study site. Location (i.e. latitude/longitude) and elevation (meters above sea level) were recorded for each rockfall deposit using a hand-held Garmin GPSMap 62s device. Boulder dimensions (i.e. height, length, width) were tape measured in the field. For prehistoric boulders partially buried to the degree that only two dimensions were adequately measurable, the shorter of the two measured lengths was used for the 3rd dimension, thus insuring a conservative boulder size estimate. No rounding factor has been applied to volumetric estimations of prehistoric boulders. Mapped prehistoric rockfall size (volume) ranges from 0.001 m^3 to >100 m^3. However, a negative sample bias exists for rockfall deposits with volume <0.1 m^3. At lower and mid-slope elevations, prehistoric rockfall deposits were mapped and recorded for the full size range (0.001 m^3 to >100 m^3). At higher elevations small rockfall populations (<0.1 m^3) were too high to be accurately mapped within a reasonable time frame. Consequently, the data set used for statistical analysis within our study is comprised of prehistoric boulders with a volume ≥ 0.1 m^3 (n=1049), thus insuring no sample bias within the analyzed boulder volume data set. Due to safety concerns, prehistoric boulder volumes were not recorded within ~100 meters of the source rock. Lithology type was determined for each prehistoric boulder and was based primarily upon the observed dominant rock 'texture'. Boulders were designated as either (1) volcanic breccia basalt (Vb) or (2) massive finely crystalline basalt (Fb). Transitional textures were occasionally observed in the field but are rare and represent outliers.

Collection of modern rockfall data reflects the combined efforts of Vick (co-author), Aurecon, and GNS. 307 individual modern boulders were identified in Rapaki. Due to safety concerns, 189 of the boulders were mapped via a GIS desktop study using post-earthquake high-resolution (10 cm) aerial photographs and therefore provided no boulder size data. Of the 118 modern boulders mapped in the field, 99 contain x-y-z length dimensions, thus providing a boulder volume. For comparison of modern and prehistoric boulder size distributions all 99 of the recorded modern boulder volumes have been utilized. Modern boulder volumes were calculated by the lead author using Microsoft Excel. No rounding factor has been applied to the modern boulder sizes. Vick employed a similar criterion for description of the boulder lithology types, designating each as either (1) volcanic breccia basalt or (2) massive lava.

1.5.2 Measuring runout distance for prehistoric and modern rockfall boulders

Boulder runout distance was analyzed by examining the distance from the nearest potential source area to their final resting position. Map and ground-length runout distances were measured using Google Earth Pro along a best-estimated local fall line projected downslope perpendicular to the local contour line. Runout distance was calculated for 1,049 prehistoric boulders and 279 modern boulders within the Rapaki study site. We report map-length runout distance.

1.5.3 Details and application of RAMMS rockfall model

RAMMS is a rigid-body three-dimensional rockfall simulation programs (Bartelt et al., 2013; Leine et al., 2013). Terrain is modeled using a high resolution DEM and rocks are modeled as rigid polyhedra. The user imports rocks as point clouds or selects pre-defined rock shapes from the model library. The RAMMS boulder library contains three shapes: equant (equi-dimensional), flat (one short axis and two long axes), and long (two short axes and one long axis). Boulder shapes are generated from lasers scans of real rocks, so that natural irregularity and angularity is incorporated. The rigid-body element of the model allows the influence of rock shape to affect the outcomes of the hazard assessment by incorporating natural variability in slope-block interactions (Bartelt et al., 2013). Rock interaction with the substrate in RAMMS is a function of 'slippage' through near-surface material, defined by the user as a function of Coulomb friction and drag force (Bartelt et al., 2013). RAMMS developers argue that rockfall impacts with soil are not simple point rebounds (Bartelt et al., 2013; Leine et al., 2013), as usually described in rockfall models and quantified by COR (coefficient of restitution). Instead, they are complex three-dimensional interactions with the substrate that include sliding a block through material until maximum frictional resistance is reached and angular momentum generated by contact forces cause the block to be launched from the ground (Bartelt et al., 2013; Leine et al., 2013; Paronuzzi, 2008). The slippage can be parameterised for hard surfaces (e.g. rock) by decreasing the distance and time spent during impact, to better reflect the instantaneous rebound observed in rock-rock interactions.

The source area was delineated as a polyline shapefile in ArcGIS from desktop study of orthophotography and satellite imagery. As it is not known from exactly which section of the source cliff the prehistoric boulders were released, the entire source cliff was delineated. Three separate source rock areas are utilized (Figures 2a,b) and have been weighted differently based upon our field observations of the source rock conditions and relative frequency of modern rockfalls detached from each source area during the 2011 Christchurch earthquakes. For every ~9 boulders released from Area 1, a single boulder is released from Areas 2 and 3. A reduction in the number of boulders released from Areas 2 and 3 was accomplished by creating less release points along these source lines. The number of release points is 35, with 20 boulders released from each source (seeder) point, making the initial total boulder count 700.

Boulder shape and size are highly influential in the dynamics and run-out of a rockfall event (Leine et al., 2013; Volkwein et al., 2011). Boulder shapes and sizes used in the model simulations are representative of the true boulder geometries. In this study, a virtual boulder population was created, using the RAMMS 'rock builder' tool, which creates boulder point clouds based on a user-defined shape and size. The sizes in this case were chosen from statistical analysis of the paleo-boulder inventory, which includes volume estimated from axis proportions. We assume a power law distribution for the frequency-volume of simulated boulders, consistent with prehistoric boulders at Rapaki (power-law equation: $y=83.607x^{-1.242}$, $R^2=0.86$). The following percentages have attributed to each boulder size range within RAMMS: ~60% for 0.1-10 m^3, ~35% for 1-10 m^3, and ~5% for 10-100 m^3. For each size class of boulder, varying shapes were selected, which are simplified to equant, flat and long. Twenty boulders were created, with varying shapes, sizes and densities (relative proportions of volcanic breccia and massive lava densities were applied).

Vegetation is modeled in RAMMS as forest drag, a resisting force that acts on the rock's centre of mass when located below the drag layer height. The forest is parameterized by the effective height of the vegetation layer and a drag coefficient. Typical values for this coefficient range between 1000 kgs^{-1} and 10,000 kgs^{-1} (Bartelt et al., 2013; Leine et al., 2013). A variable forest density was applied to account for presumed denser vegetation within the northern drainage valley at the Rapaki study site. We assume more surface and subsurface water would be focused into the northern drainage gully and would therefore promote denser tree growth. Within the drainage gulley, a uniform drag force of 6000 kg/sec was applied to each of the simulated boulders. Elsewhere on the hillslope, a drag force of 3000 kg/sec was applied. As evidence by modern native forest analogues, tree growth is extended upward to the base of the source rock and an average tree height of 10 meters is utilized within the RAMMS model.

Simulation results were analysed as ArcGIS shapefiles and boulder numbers within each rockfall shadow zone were summed for comparison to the mapped modern and prehistoric boulder distributions. For each shadow zone (23- >30°) the percentage of deposited simulated boulders was compared to the percentage of empirical boulders (i.e. modern or prehistoric) within the zone for quantitative analysis of the down-slope distribution. Shadow zones were created based on Evans and Hungr (1993) rockfall shadow angle (i.e., the angle from the horizontal of a line projected from the base of the source area to the top of the runout boulder). By combining this concept and the viewshed tool in ArcGIS, a series of shadow angle contours can be created, with 23° being the maximum runout distance achieved locally during the 2010-2011 Canterbury Earthquake Sequence.

1.5.4 Kolmogorov-Smirnov (K-S) Test

We use the Kolmogorov-Smirnov (K-S) test to quantify the 'goodness of fit' between two data sets (Kirkman, 1996). The two-sample K–S test is a non-parametric, distribution free method that uses the maximum vertical deviation between the empirical distribution functions (D) of two samples (e.g. curves) to generate a corresponding P-value. If the P-value is >0.05, then the null hypothesis of no significant difference between two measured phenomena is not rejected. A P-value equal to 1 reflects identical data sets. See Supplementary Data 1-4 for individual K-S tests performed on Rapaki rockfall data.

1.5.5 Radiocarbon Dating

Charcoal samples for radiocarbon dating were retrieved from colluvial wedge sediments accumulated at the backside of Paleo-Boulder #3 (Supplementary Fig. 2). Samples were dried at 40 °C for 1 week and then sorted to separate the organic material from the host sediment. Between 70 and 500 mg samples of charcoal were submitted to the Rafter Radiocarbon Laboratory in Wellington, New Zealand, for accelerator mass spectrometry (AMS) radiocarbon analysis. Samples were further cut and scraped with scalpel at the Rafter Laboratory to remove any remaining surface dirt. Chemical pretreatment was by repeated acid and alkali treatment. Weight obtained after chemical pretreatment ranged between 21.9 and 45.2 mg. Carbon dioxide was generated by elemental analyzer combustion and 1 mgC was obtained. Sample carbon dioxide was converted to graphite by reduction with hydrogen over iron catalyst. Conventional Radiocarbon Age (years BP) is reported as defined by Stuiver and Polach (1977). Ages were calibrated using the Southern Hemisphere calibration curve (SHCal13) (Hogg et al., 2013). Radiocarbon ages referred to in the text are reported as 2σ calendar calibrated age ranges (Millard, 2014). Detailed age range distributions of the calendar-calibrated ages are presented in Table 1.

1.6 Appendix 1: Supplementary Figures and Data

Rafter Radiocarbon
Calibration Report

NZA 56801
R 40527/1
Report issued: 29 Jun 2014

CONVENTIONAL RADIOCARBON AGE 203 ± 18 years BP

Calibrated with SHCal13 (Hogg et al., Radiocarbon 55(4):1889-1902, 2013).

CALIBRATED AGE in terms of confidence intervals

1 sigma interval is	1671 AD to 1684 AD	279 BP to 266 BP (14.0% of area)
	1730 AD to 1747 AD	220 BP to 203 BP (18.3% of area)
	1756 AD to 1783 AD	194 BP to 167 BP (27.3% of area)
	1796 AD to 1803 AD	154 BP to 147 BP (7.9% of area)
2 sigma interval is	1664 AD to 1698 AD	286 BP to 252 BP (22.8% of area)
	1724 AD to 1809 AD	226 BP to 141 BP (70.4% of area)
	1870 AD to 1876 AD	80 BP to 74 BP (1.0% of area)

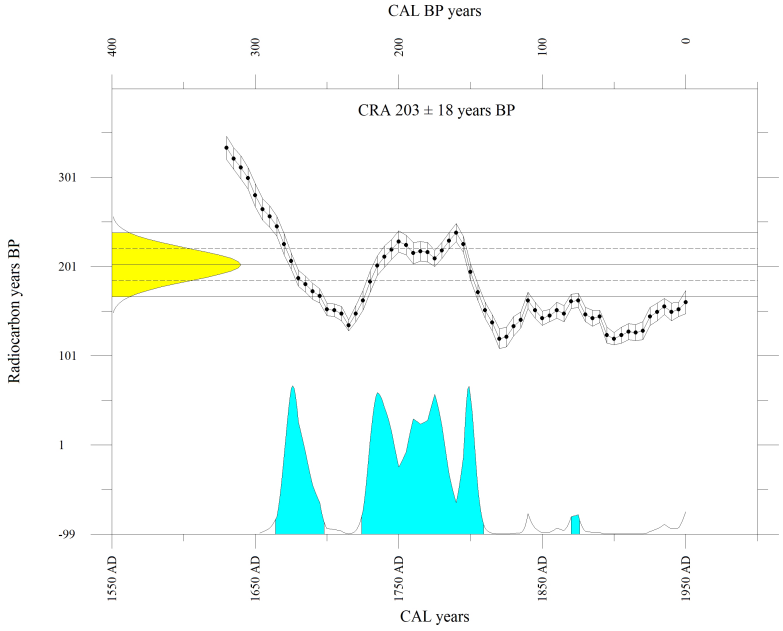

Calibration performed using Winscal v. 6.0 adapted from: Stuiver and Reimer (*Radiocarbon 35*(1): 215-230, 1993).

National Isotope Centre, GNS Science
PO Box 31-312 Lower Hutt, New Zealand Phone +64 4 570 4644
Email radiocarbon@gns.cri.nz Website www.RafterRadiocarbon.co.nz

Supplementary Figure 1 | Radiocarbon Calibration Report for Charcoal Sample RapCH-01

Rafter Radiocarbon
Calibration Report

NZA 56802

R 40527/2

Report issued: 29 Jun 2014

CONVENTIONAL RADIOCARBON AGE 197 ± 17 years BP

Calibrated with SHCal13 (Hogg et al., Radiocarbon 55(4):1889-1902, 2013).

CALIBRATED AGE in terms of confidence intervals

1 sigma interval is	1672 AD to 1690 AD	278 BP to 260 BP (19.6% of area)
	1728 AD to 1746 AD	222 BP to 204 BP (19.0% of area)
	1758 AD to 1781 AD	192 BP to 169 BP (20.0% of area)
	1796 AD to 1805 AD	154 BP to 145 BP (10.0% of area)
2 sigma interval is	1666 AD to 1700 AD	284 BP to 250 BP (25.8% of area)
	1722 AD to 1810 AD	228 BP to 140 BP (63.8% of area)
	1838 AD to 1845 AD	112 BP to 105 BP (1.3% of area)
	1867 AD to 1878 AD	83 BP to 72 BP (2.4% of area)
	1933 AD to 1938 AD	17 BP to 12 BP (0.6% of area)
	1946 AD to 1950 AD	4 BP to 0 BP (1.1% of area)

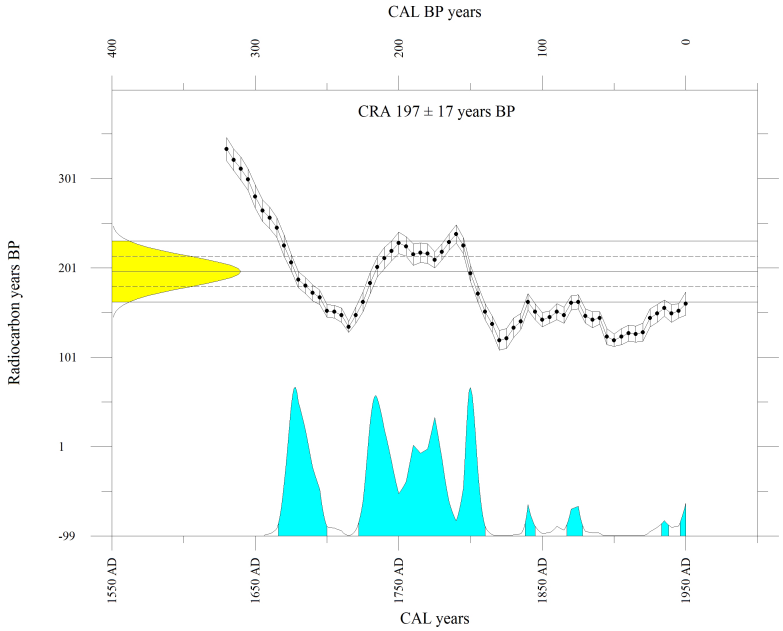

Calibration performed using Winscal v. 6.0 adapted from: Stuiver and Reimer (*Radiocarbon 35*(1): 215-230, 1993).

National Isotope Centre, GNS Science
PO Box 31-312 Lower Hutt, New Zealand Phone +64 4 570 4644
Email radiocarbon@gns.cri.nz Website www.RafterRadiocarbon.co.nz

Supplementary Figure 2 | Radiocarbon Calibration Report for Charcoal Sample RapCH-03

Rafter Radiocarbon
Calibration Report

NZA 56803

R 40527/3

Report issued: 29 Jun 2014

CONVENTIONAL RADIOCARBON AGE 222 ± 17 years BP

Calibrated with SHCal13 (Hogg et al., Radiocarbon 55(4):1889-1902, 2013).

CALIBRATED AGE in terms of confidence intervals

1 sigma interval is	1669 AD to 1674 AD	281 BP to 276 BP (6.1% of area)
	1741 AD to 1787 AD	209 BP to 163 BP (55.5% of area)
	1793 AD to 1798 AD	157 BP to 152 BP (6.3% of area)
2 sigma interval is	1661 AD to 1680 AD	289 BP to 270 BP (15.8% of area)
	1732 AD to 1802 AD	218 BP to 148 BP (79.0% of area)

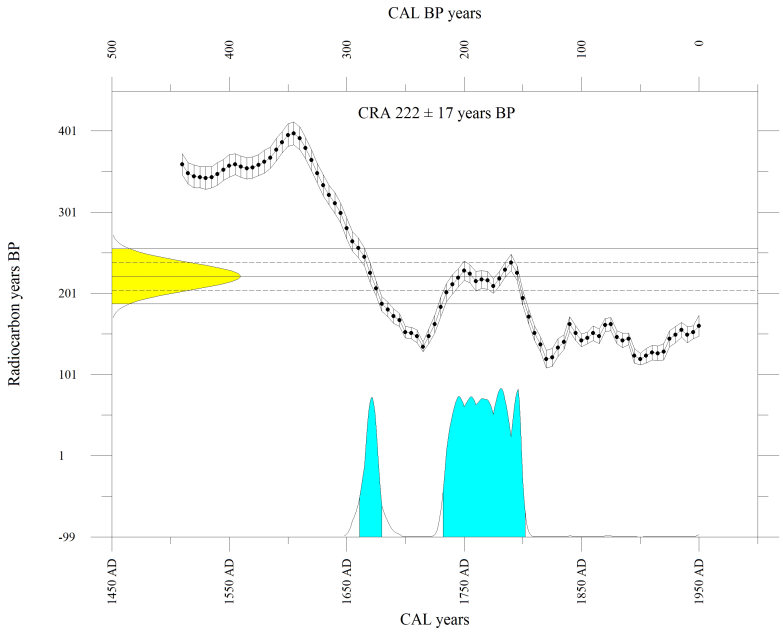

Calibration performed using Winscal v. 6.0 adapted from: Stuiver and Reimer (*Radiocarbon 35*(1): 215-230, 1993).

National Isotope Centre, GNS Science
PO Box 31-312 Lower Hutt, New Zealand Phone +64 4 570 4644
Email radiocarbon@gns.cri.nz Website www.RafterRadiocarbon.co.nz

Supplementary Figure 3 | Radiocarbon Calibration Report for Charcoal Sample RapCH-05

Supplementary Data 1 | K-S comparison test of empirical prehistoric and modern boulders

KS Test: Results
Kolmogorov-Smirnov Comparison of Two Data Sets

The results of a Kolmogorov-Smirnov test performed at 21:43 on 19-AUG-2015
The maximum difference between the cumulative distributions, *D*, is: 0.6364 with a corresponding *P* of: 0.012

Data Set 1:

11 data points were entered
Mean = 9.091
95% confidence interval for actual Mean: -3.425 thru 21.61
Standard Deviation = 18.6
High = 64.2 Low = 0.200
Third Quartile = 9.50 First Quartile = 0.200
Median = 2.700
Average Absolute Deviation from Median = 8.08
John Tukey defined data points as *outliers* if they are 1.5*IQR above the third quartile or below the first quartile. Following Tukey, the following data points are outliers: 64.2
KS says it's unlikely this data is normally distributed: *P*= 0.01 where the normal distribution has mean= 17.14 and sdev= 28.49
KS finds the data is consistent with a log normal distribution: *P*= 0.92 where the log normal distribution has geometric mean= 2.451 and multiplicative sdev= 9.090

Items in Data Set 1:

0.200 0.200 0.200 1.30 2.30 2.70 4.20 4.40 9.50 10.8 64.2

Data Set 2:

11 data points were entered
Mean = 9.091
95% confidence interval for actual Mean: 6.030 thru 12.15
Standard Deviation = 4.56
High = 18.0 Low = 2.30
Third Quartile = 12.3 First Quartile = 5.40
Median = 8.800
Average Absolute Deviation from Median = 3.69
KS finds the data is consistent with a normal distribution: *P*= 0.83 where the normal distribution has mean= 9.303 and sdev= 5.420
KS finds the data is consistent with a log normal distribution: *P*= 0.87 where the log normal distribution has geometric mean= 7.719 and multiplicative sdev= 2.154

Items in Data Set 2:

2.30 4.60 5.40 6.10 6.90 8.80 11.1 11.9 12.3 12.6 18.0
Data Reference: 0382

http://www.physics.csbsju.edu/stats/KS-test.n.plot_form.html

Supplementary Data 2 | K-S comparison test of frequency-volume distributions for modern and prehistoric boulders

KS Test: Results
Kolmogorov-Smirnov Comparison of Two Data Sets

The results of a Kolmogorov-Smirnov test performed at 18:39 on 8-JUN-2015
The maximum difference between the cumulative distributions, *D*, is: 0.1020 with a corresponding *P* of: 0.326

Data Set 1:

99 data points were entered
Mean = 5.504
95% confidence interval for actual Mean: 3.219 thru 7.789
Standard Deviation = 11.5
High = 80.0 Low = 0.500
Third Quartile = 4.21 First Quartile = 1.01
Median = 2.050
Average Absolute Deviation from Median = 4.37
John Tukey defined data points as *outliers* if they are 1.5*IQR above the third quartile or below the first quartile. Following Tukey, the following data points are outliers: 80.0 58.0 48.4 28.4 27.3 23.5 13.1 12.3 12.0 11.3 10.5 9.58 9.34
KS says it's unlikely this data is normally distributed: *P*= 0.00 where the normal distribution has mean= 19.68 and sdev= 19.10
KS says it's unlikely this data is log normally distributed: *P*= 0.00 where the log normal distribution has geometric mean= 3.401 and multiplicative sdev= 3.090

Items in Data Set 1:

0.500 0.500 0.530 0.560 0.560 0.570 0.600 0.630 0.630 0.650 0.720 0.720 0.730 0.740 0.790 0.810 0.820 0.850 0.920 0.940 0.960 0.970 0.990 1.00 1.01 1.01 1.06 1.08 1.10 1.13 1.16 1.26 1.30 1.35 1.39 1.45 1.50 1.57 1.57 1.63 1.73 1.80 1.82 1.84 1.87 1.98 2.00 2.02 2.03 2.05 2.09 2.10 2.18 2.25 2.30 2.31 2.34 2.38 2.38 2.50 2.62 2.67 2.74 2.75 2.90 3.00 3.47 3.60 3.74 3.80 3.92 4.05 4.06 4.12 4.21 4.52 4.68 5.15 5.63 5.80 6.00 6.08 6.73 7.84 8.25 8.72 9.34 9.58 10.5 11.3 12.0 12.3 13.1 23.5 27.3 28.4 48.4 58.0 80.0

Data Set 2:

583 data points were entered
Mean = 4.991
95% confidence interval for actual Mean: 3.920 thru 6.061
Standard Deviation = 13.2
High = 201. Low = 0.500
Third Quartile = 4.55 First Quartile = 0.891
Median = 1.700
Average Absolute Deviation from Median = 4.03
John Tukey defined data points as *outliers* if they are 1.5*IQR above the third quartile or below the first quartile. Following Tukey, the following data points are outliers: 201. 168. 82.8 79.0 49.9 47.3 45.4 40.6 39.9 39.2 34.4 33.3 30.8 27.4 26.7 26.2 25.9 24.8 24.1 22.0 20.6 20.5 20.3 19.8 19.7 18.9 17.8 16.3 16.1 15.9 15.6 15.5 15.3 15.2 15.2 14.5 14.5 14.4 14.4 13.8 13.5 13.2 13.1 13.0 12.9 12.9 12.8 12.8 12.7 12.4 12.1 12.0 12.0 11.6 11.6 11.5 11.3 10.6
KS says it's unlikely this data is normally distributed: *P*= 0.00 where the normal distribution has mean= 44.58 and sdev= 38.10
KS says it's unlikely this data is log normally distributed: *P*= 0.00 where the log normal distribution has geometric mean= 3.951 and multiplicative sdev= 2.894

Items in Data Set 2:

0.500 0.504 0.504 0.510 0.512 0.514 0.520 0.522 0.522 0.530 0.533 0.536 0.536 0.536 0.539 0.540 0.540 0.544 0.549 0.549 0.554 0.554 0.563 0.563 0.563 0.565 0.568 0.574 0.574 0.576 0.576 0.576 0.578 0.585 0.588 0.588 0.588 0.590 0.590 0.591 0.591 0.592 0.600 0.600 0.600 0.602 0.607 0.608 0.608 0.612 0.613 0.616 0.619 0.619 0.619 0.619 0.633 0.637 0.639 0.640 0.640 0.647 0.647 0.648 0.650 0.650 0.650 0.655 0.656 0.656 0.660 0.666

0.669 0.672 0.672 0.672 0.672 0.673 0.676 0.682 0.683 0.684 0.686 0.686 0.686 0.693 0.702 0.704 0.704 0.711
0.717 0.720 0.720 0.722 0.731 0.735 0.735 0.736 0.738 0.756 0.760 0.760 0.768 0.768 0.768 0.768 0.768 0.768
0.768 0.770 0.770 0.770 0.780 0.784 0.784 0.788 0.788 0.795 0.798 0.800 0.800 0.800 0.806 0.810 0.816 0.819
0.819 0.821 0.822 0.832 0.832 0.832 0.833 0.833 0.840 0.840 0.842 0.844 0.844 0.844 0.850 0.851 0.851 0.855
0.864 0.891 0.891 0.896 0.896 0.897 0.900 0.900 0.903 0.903 0.903 0.910 0.910 0.914 0.924 0.929 0.935 0.936
0.945 0.960 0.960 0.960 0.961 0.972 0.972 0.972 0.972 0.982 0.986 0.998 1.00 1.00 1.00 1.00 1.01 1.01 1.01
1.02 1.02 1.03 1.04 1.04 1.05 1.05 1.06 1.06 1.07 1.07 1.10 1.10 1.10 1.10 1.11 1.12 1.12 1.12 1.13 1.13 1.13
1.13 1.14 1.15 1.15 1.16 1.17 1.18 1.18 1.18 1.18 1.20 1.20 1.20 1.20 1.22 1.22 1.22 1.24 1.24 1.24 1.24 1.25
1.25 1.26 1.26 1.26 1.27 1.28 1.30 1.30 1.30 1.30 1.30 1.31 1.34 1.34 1.35 1.35 1.35 1.35 1.36 1.36 1.38 1.38
1.39 1.39 1.40 1.40 1.40 1.40 1.40 1.40 1.40 1.41 1.42 1.43 1.43 1.45 1.46 1.46 1.49 1.49 1.50 1.51 1.51 1.52
1.54 1.55 1.55 1.56 1.57 1.57 1.59 1.60 1.62 1.63 1.63 1.65 1.65 1.66 1.68 1.68 1.68 1.68 1.68 1.69 1.69 1.70
1.70 1.73 1.73 1.73 1.73 1.74 1.75 1.76 1.80 1.80 1.82 1.83 1.84 1.85 1.85 1.85 1.86 1.87 1.87 1.90 1.90 1.90
1.92 1.92 1.93 1.94 1.98 1.98 1.98 2.00 2.00 2.01 2.02 2.03 2.05 2.07 2.07 2.07 2.08 2.09 2.09 2.09 2.09 2.10
2.10 2.10 2.11 2.15 2.17 2.18 2.19 2.21 2.21 2.24 2.25 2.26 2.27 2.30 2.31 2.33 2.34 2.36 2.38 2.39 2.39 2.40
2.40 2.40 2.45 2.45 2.45 2.49 2.50 2.58 2.60 2.60 2.62 2.65 2.69 2.70 2.80 2.82 2.84 2.85 2.88 2.88 2.90 2.94
2.94 2.97 2.99 3.02 3.02 3.05 3.07 3.10 3.12 3.14 3.17 3.19 3.24 3.26 3.30 3.31 3.32 3.33 3.36 3.36 3.36 3.36
3.37 3.38 3.38 3.39 3.44 3.46 3.51 3.57 3.58 3.60 3.60 3.67 3.70 3.71 3.71 3.74 3.74 3.75 3.79 3.80 3.85 3.87
3.87 3.96 3.96 3.99 4.07 4.12 4.22 4.29 4.37 4.41 4.41 4.44 4.46 4.51 4.55 4.55 4.58 4.68 4.70 4.70 4.72 4.75
4.79 4.80 4.84 4.88 4.90 4.90 5.00 5.04 5.06 5.10 5.25 5.40 5.47 5.48 5.49 5.57 5.57 5.61 5.62 5.67 5.70 5.82
5.83 5.85 5.86 5.92 5.92 5.94 5.98 6.02 6.14 6.14 6.40 6.50 6.55 6.59 6.66 6.67 6.72 6.84 6.86 6.97 7.14 7.22
7.31 7.49 7.53 7.58 7.64 7.85 7.87 7.92 7.94 8.00 8.10 8.10 8.12 8.32 8.37 8.37 8.38 8.48 8.48 8.60 8.61 8.82
8.95 9.04 9.13 9.15 9.21 9.38 9.50 9.55 9.70 9.72 9.80 9.86 9.90 10.0 10.6 11.3 11.5 11.6 11.6 12.0 12.0 12.1
12.4 12.7 12.8 12.8 12.9 12.9 13.0 13.1 13.2 13.5 13.8 14.4 14.4 14.5 14.5 15.2 15.2 15.3 15.5 15.6 15.9 16.1
16.3 17.8 18.9 19.7 19.8 20.3 20.5 20.6 22.0 24.1 24.8 25.9 26.2 26.7 27.4 30.8 33.3 34.4 39.2 39.9 40.6 45.4
47.3 49.9 79.0 82.8 168. 201.

Data Reference: 0717

http://www.physics.csbsju.edu/stats/KS-test.n.plot_form.html

Supplementary Data 3 | K-S comparison test of empirical modern and RAMMS 1 boulders

KS Test: Results
Kolmogorov-Smirnov Comparison of Two Data Sets

The results of a Kolmogorov-Smirnov test performed at 21:13 on 19-AUG-2015
The maximum difference between the cumulative distributions, *D*, is: 0.2727 with a corresponding *P* of: 0.736

Data Set 1:

11 data points were entered
Mean = 9.091
95% confidence interval for actual Mean: 6.030 thru 12.15
Standard Deviation = 4.56
High = 18.0 Low = 2.30
Third Quartile = 12.3 First Quartile = 5.40
Median = 8.800
Average Absolute Deviation from Median = 3.69
KS finds the data is consistent with a normal distribution: *P*= 0.83 where the normal distribution has mean= 9.303 and sdev= 5.420
KS finds the data is consistent with a log normal distribution: *P*= 0.87 where the log normal distribution has geometric mean= 7.719 and multiplicative sdev= 2.154

Items in Data Set 1:

2.30 4.60 5.40 6.10 6.90 8.80 11.1 11.9 12.3 12.6 18.0

Data Set 2:

11 data points were entered
Mean = 9.091
95% confidence interval for actual Mean: 5.691 thru 12.49
Standard Deviation = 5.06
High = 21.1 Low = 4.40
Third Quartile = 13.0 First Quartile = 5.60
Median = 7.300
Average Absolute Deviation from Median = 3.30
KS is not particularly happy calling this data normally distributed: *P*= 0.13 where the normal distribution has mean= 10.10 and sdev= 6.155
KS finds the data is consistent with a log normal distribution: *P*= 0.55 where the log normal distribution has geometric mean= 8.437 and multiplicative sdev= 1.766

Items in Data Set 2:

4.40 4.60 5.60 6.40 7.20 7.30 7.80 8.40 13.0 14.2 21.1
Data Reference: 65BA

http://www.physics.csbsju.edu/stats/KS-test.n.plot_form.html

Supplementary Data 4 | K-S comparison test of empirical prehistoric and RAMMS 1

KS Test: Results
Kolmogorov-Smirnov Comparison of Two Data Sets

The results of a Kolmogorov-Smirnov test performed at 18:23 on 8-JUN-2015
The maximum difference between the cumulative distributions, *D*, is: 0.6364 with a corresponding *P* of: 0.012

Data Set 1:

11 data points were entered
Mean = 9.089
95% confidence interval for actual Mean: -3.431 thru 21.61
Standard Deviation = 18.6
High = 64.2 Low = 0.190
Third Quartile = 9.45 First Quartile = 0.190
Median = 2.700
Average Absolute Deviation from Median = 8.09
John Tukey defined data points as *outliers* if they are 1.5*IQR above the third quartile or below the first quartile. Following Tukey, the following data points are outliers: 64.2
KS says it's unlikely this data is normally distributed: *P*= 0.01 where the normal distribution has mean= 17.14 and sdev= 28.50
KS finds the data is consistent with a log normal distribution: *P*= 0.92 where the log normal distribution has geometric mean= 2.405 and multiplicative sdev= 9.323

Items in Data Set 1:

0.190 0.190 0.190 1.25 2.31 2.70 4.24 4.44 9.45 10.8 64.2

Data Set 2:

11 data points were entered
Mean = 9.093
95% confidence interval for actual Mean: 5.702 thru 12.48
Standard Deviation = 5.05
High = 21.1 Low = 4.43
Third Quartile = 13.0 First Quartile = 5.65
Median = 7.330
Average Absolute Deviation from Median = 3.29
KS is not particularly happy calling this data normally distributed: *P*= 0.13 where the normal distribution has mean= 10.10 and sdev= 6.139
KS finds the data is consistent with a log normal distribution: *P*= 0.54 where the log normal distribution has geometric mean= 8.448 and multiplicative sdev= 1.763

Items in Data Set 2:

4.43 4.58 5.65 6.41 7.18 7.33 7.79 8.40 13.0 14.2 21.1

Data Reference: 7639

http://www.physics.csbsju.edu/stats/KS-test.n.plot_form.html

Supplementary Data 5 | K-S comparison test of empirical prehistoric and RAMMS 2 boulders

KS Test: Results
Kolmogorov-Smirnov Comparison of Two Data Sets

The results of a Kolmogorov-Smirnov test performed at 17:25 on 20-AUG-2015
The maximum difference between the cumulative distributions, *D*, is: 0.2727 with a corresponding *P* of: 0.736

Data Set 1:

11 data points were entered
Mean = 9.091
95% confidence interval for actual Mean: -3.425 thru 21.61
Standard Deviation = 18.6
High = 64.2 Low = 0.200
Third Quartile = 9.50 First Quartile = 0.200
Median = 2.700
Average Absolute Deviation from Median = 8.08
John Tukey defined data points as *outliers* if they are 1.5*IQR above the third quartile or below the first quartile. Following Tukey, the following data points are outliers: 64.2
KS says it's unlikely this data is normally distributed: *P*= 0.01 where the normal distribution has mean= 17.14 and sdev= 28.49
KS finds the data is consistent with a log normal distribution: *P*= 0.92 where the log normal distribution has geometric mean= 2.451 and multiplicative sdev= 9.090

Items in Data Set 1:

0.200 0.200 0.200 1.30 2.30 2.70 4.20 4.40 9.50 10.8 64.2

Data Set 2:

11 data points were entered
Mean = 9.100
95% confidence interval for actual Mean: -3.095 thru 21.30
Standard Deviation = 18.2
High = 63.3 Low = 0.00
Third Quartile = 5.40 First Quartile = 1.70
Median = 4.000
Average Absolute Deviation from Median = 7.14
John Tukey defined data points as *outliers* if they are 1.5*IQR above the third quartile or below the first quartile. Following Tukey, the following data points are outliers: 63.3
KS says it's unlikely this data is normally distributed: *P*= 0.00 where the normal distribution has mean= 17.12 and sdev= 28.37

Items in Data Set 2:

0.00 0.300 1.70 3.40 3.40 4.00 4.40 5.10 5.40 9.10 63.3
Data Reference: 0CD7

http://www.physics.csbsju.edu/stats/KS-test.n.plot_form.html

CHAPTER 2.

CHRONOLOGY AND PROCESSES OF LATE QUATERNARY HILLSLOPE SEDIMENTATION IN THE EASTERN SOUTH ISLAND, NEW ZEALAND

2.1 Abstract

Optical and radiocarbon dating of loessic hillslope sediments in New Zealand's South Island is used to constrain the timing of prehistoric rockfalls and associated seismic events, and quantify spatial and temporal patterns of hillslope sedimentation including responses to seismic and anthropogenic forcing. Exploratory trenches adjacent to prehistoric boulders enable stratigraphic analysis of loess and loess-colluvium pre- and post-dating boulder emplacement, respectively. Luminescence ages from loessic sediments constrain timing of boulder emplacement to between ~3.0 and ~12.5 ka, well before the arrival of Polynesians (ca AD 1280) and Europeans (ca AD 1800) in New Zealand, and suggest loess accumulation was continuing at the study site until 12-13 ka. Large (>5 m^3) prehistoric rockfall boulders preserve an important record of Holocene hillslope sedimentation by creating local traps (i.e. accommodation space) for sediment aggradation (i.e. colluvial wedges) and upbuilding soil formation. Sediment accumulation rates increased considerably (>~10 factor increase) following human arrival and associated anthropogenic burning of hillslope vegetation. Our study presents new numerical ages to place the evolution of loess-mantled hillslopes in New Zealand's South Island into a longer temporal framework and highlights the roles of earthquakes and humans on hillslope surface process.

2.2 Introduction

Hillslope sediments provide a potentially valuable archive of contemporary and paleo-landscape processes (e.g. Fuchs and Lang, 2009; Fuchs et al., 2010). Dating of slope sediments has been extensively used for understanding landscape response to local and global climate change (e.g. Hanson et al., 2004), anthropogenic influences on hillslope sediment erosion and accumulation (e.g. Roering et al., 2002, 2004; Fuchs et al., 2004, 2010; Almond et al., 2008; Hughes et al., 2010; Borella et al., 2016), and tectonic activity (e.g. Fattahi et al., 2006). Additionally, hillslope sediment chronologies have been used to determine the timing of mass wasting events, such as landslides and rockfalls (Becker and Davenport, 2003; Matmon et al., 2005; Kanari, 2008; Chapot et al., 2012; Mackey and Quigley, 2014; Rinat et al., 2014).

Various methods have been used to date hillslope sediments (e.g. Jibson, 1996; Lang et al., 1999), including radiocarbon dating (^{14}C) (e.g. Stout, 1969; Becker and Davenport, 2003; Bertolini, 2007), lichenometry (e.g. Bull et al., 1994; Luckman and Fiske, 1995; Andre, 1997; McCarroll et al., 2001), dendrochronology (e.g. Stoffel, 2006), and optically stimulated luminescence (OSL) dating (e.g. Matmon et al., 2005; Balescu et al., 2007; Chapot et al., 2012). Cosmogenic nuclide (CN) surface exposure dating has also been implemented to determine the emplacement time for boulders entrenched within hillslope sediments (e.g. Cordes et al., 2013; Mackey and Quigley, 2014; Rinat et al., 2014; Stock et al. 2014a, b) and estimate production rates and residence times of colluvial hillslope soils (e.g. Heimsath et al. 2002). Increased confidence in hillslope sediment chronologies can be obtained by combining OSL, ^{14}C and CN (e.g. Lang and Wagner, 1996; Rinat, 2014) dating methods.

New Zealand's South Island provides a variety of important opportunities for investigating the spatiotemporal behavior of surface processes and their response to climatic, seismic, and anthropogenic forcing (Glade, 2003; Woodward and Shulmeister, 2005; Almond et al., 2008; Hughes et al., 2010; Rowan et al., 2012; Fuller et al., 2015). Prehistoric rockfall boulders at Rapaki (NZ) preserve an important record of Holocene hillslope soil transport. In this paper we examine the influence of large (>~5 m^3) rockfall boulders on local hillslope morphology and soil evolution. We perform detailed analysis (e.g. stratigraphic logging, grain-size analysis, sediment bulk density) and OSL and ^{14}C dating of loessic hillslope sediments to constrain the timing of prehistoric rockfall and associated earthquakes, and quantify spatial and temporal patterns of hillslope sedimentation including responses to seismic and human activity.

In combination with Sohbati et al. (2016) we present the first successful (i.e. reliable luminescence ages) optical dating of coarse-grained (i.e. >11 μm) loess and loess-colluvium hillslope sediments in New Zealand using the SAR protocol for quartz and $pIRIR_{290}$ protocol for K-rich feldspar.

Our numerical (luminescence and radiocarbon) ages provide a uniquely detailed chronology for understanding the evolution of loess-mantled hillslopes in New Zealand's South Island through the late Pleistocene and Holocene epochs. This study highlights the roles of earthquakes and humans on hillslope surface process, and demonstrates the value of rockfall-emplaced boulders on hillslopes for creating archives of past hillslope responses.

2.3 Geologic Setting

2.3.1 Geology of Banks Peninsula and the Port Hills

Banks Peninsula (Fig. 1) comprises three main volcanoes active between ~11.0 and 5.8 Ma (Hampton and Cole, 2009). The study site is located within the dissected Lyttelton Volcanic complex (~11.0-9.7 Ma) on the western side of Banks Peninsula (Fig. 1). Bedrock of the Lyttelton Volcanic complex is composed of subaerial basaltic and trachytic lava flows interlayered with ash and/or paleosol packages (Forsyth et al. 2008; Hampton and Cole, 2009). The volcanic rocks are mantled by four principal regolith materials: loess, loess-colluvium, mixed loess-volcanic colluvium, and volcanic colluvium, as defined by Bell and Trangmar (1987).

The initiation and timing of regionally sourced (Southern Alps and Canterbury Plains, see Fig. 1) loess accumulation on Banks Peninsula has been the subject of previous studies at multiple locations (e.g. Griffiths, 1973; Ives, 1973). Results from Almond et al. (2007b) indicate the last major phase of loess accumulation on the lower flanks of Banks Peninsula in Canterbury began before ca 35k cal a BP. In South Canterbury (Timaru) and based upon radiocarbon ages presented by Runge et al. (1973), Tonkin et al. (1974) proposed that loess accumulation ceased around ~10,000 cal a BP, with the last major accumulation phase between 9,900 and 11,800 cal a BP (Goh et al., 1977, 1978). On Banks Peninsula, Griffiths (1973) reports an age of 17,450±2070 cal a BP (radiocarbon age from humic acid) from the top of the first paleosol at Barrys Bay. However, Goh et al. (1977, 1978) demonstrated that these ages were underestimates due to contamination. At Ahuriri Quarry, Banks Peninsula, Almond et al. (2007b) report a carbonate radiocarbon age range of 9,927-10,235 cal a BP for youngest loess sediments, but warn that pedogenic carbonate is a post-depositional precipitate, and thus ages derived from carbonate-containing loess must be considered minimum loess ages. Several luminescence ages of ca 17 ka are generated within the upper loess unit (see Almond et al., 2007b – Unit 1a) but also show inconsistency with the position and accepted age of ~25.4k cal a BP for Kawakawa/Oruanui tephra (Vandergoes et al., 2013), bringing into question their reliability.

Almond et al. (2008) investigated hillslope response at Ahuriri Quarry on the western flank of Banks Peninsula and concluded that most erosion occurred in the Holocene after the primary loess accumulation phase (~35-17 ka), consistent with an increase in soil flux rates with Holocene climate amelioration and recolonization by forest. Their results suggest a complex interaction between climate, vegetation, land management and soil transport on soil mantled hillslopes. Bell and Trangmar (1987) present an in-depth study of regolith materials and erosion processes for slopes in the Port Hills of

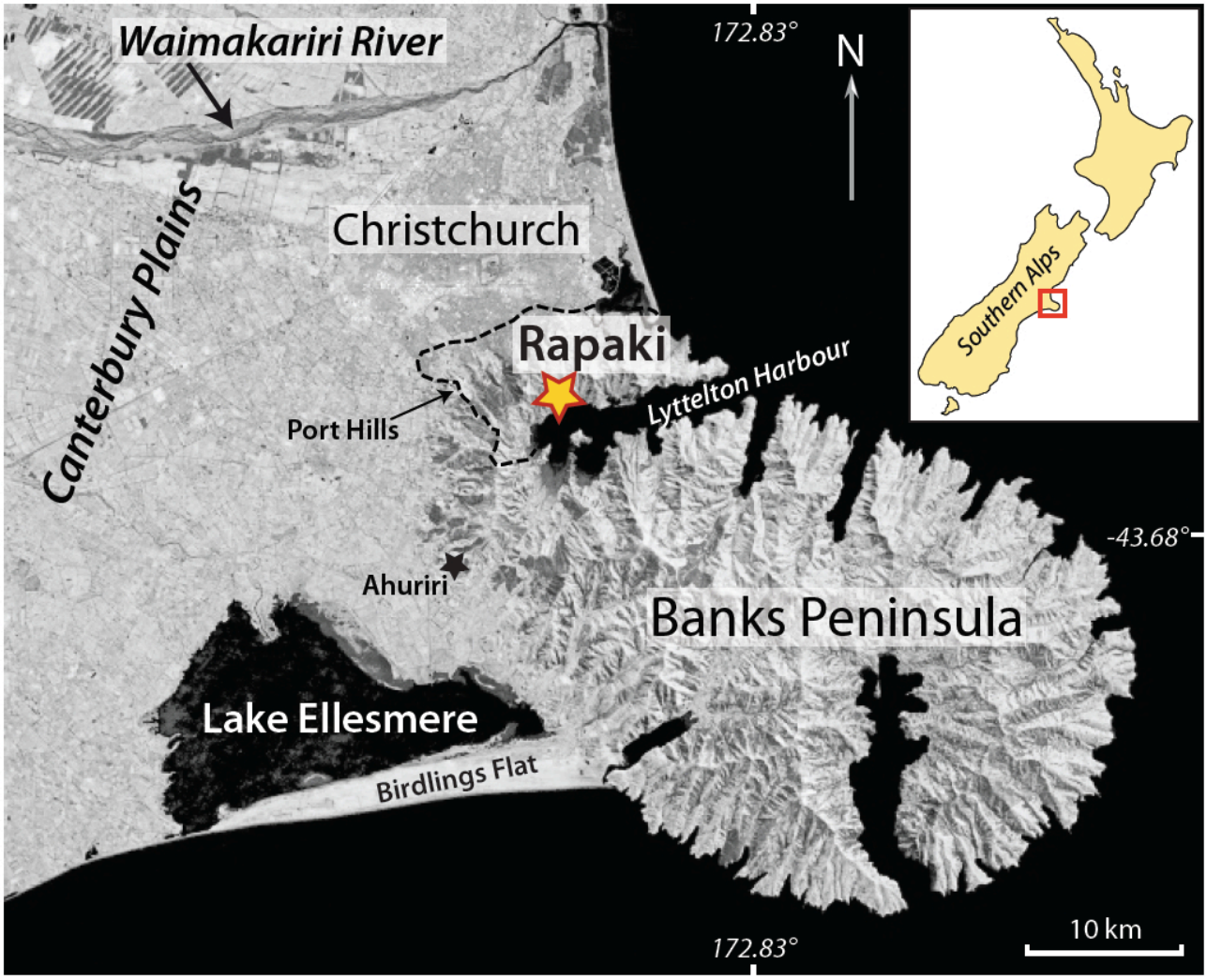

Figure 1. Location map showing Rapaki study site and surrounding Port Hills and greater Banks Peninsula.

Banks Peninsula (western side) but no temporal constraint (i.e. absolute dating) is provided for colluvial sediments, emplacement of prehistoric rockfall, or removal of slope vegetation. The general effects of meteorological phenomena on slope process are considered but the impact of earthquakes and humans on hillslope evolution were not examined.

2.3.2 Paleoclimate and paleovegetation of Banks Peninsula

The understanding of past climate and vegetation in Banks Peninsula is increasing (e.g. Wilson, 1993; Shulmeister et al. 1999; Soons et al., 2002), but establishing temporal bounds for local and regional climate/vegetation changes remains a primary challenge. Shulmeister et al. (1999) employed a multi-technique approach (e.g. radiocarbon dating, thermoluminescence) supported by proxy data (diatoms, phytoliths, pollen) to show that pre-European flora of Banks Peninsula was dominated by mixed podocarp broadleaf forests during interglacial periods and replaced by tall shrubland of mixed montane and coastal affinities during cooler glacial phases. Pollen diagrams from South Island consistently show a transition from grassland to shrubland (during Late Glacial) to forest (i.e. podocarp/hardwood) around the Holocene boundary (Markgraf et al., 1992; McGlone et al., 1993, McGlone, 1995; Shulmeister et al., 1999; Woodward and Shulmeister, 2005). Native forest in Banks Peninsula was modified by two separate phases of human activity, beginning with the Polynesians (Maori) 700-800 cal a BP and continuing with the Europeans, who settled the area approximately 150 a (McGlone 1989; Harding, 2003; McWethy, 2010). By 1900, Europeans had removed >98% of the indigenous forest (Harding, 2003; Wilson, 2008, 2013), leaving slopes vulnerable to accelerated erosion and mass wasting (Glade, 2003). Borella et al. (2016) demonstrate that anthropogenic deforestation in Banks Peninsula has increased the rockfall hazard by enabling modern boulders to travel further downslope than their prehistoric predecessors.

2.3.3 Rapaki Study Site

The Rapaki study site (Figs. 1-4) occupies the northern half of the southeastern slope of Mount Rapaki (Te Poho o Tamatea), situated above Rapaki village in Banks Peninsula. The hillslope is slightly concave in profile with a total area of approximately 0.21 km^2, and bounded in its upper part by steep to subvertical bedrock cliffs comprising distinct sub-horizontal packages of coherent, vertically to irregularly jointed basaltic lava flows separated by indurated volcanic breccias. The bedrock cliffs are ~60 meters tall and ~300 meters wide. A ~23° sloping grassy hillslope underlain by loess, loess and volcanic (i.e. sourced from volcanic bedrock) colluvium, and overlying prehistoric and modern rockfall boulders is subjacent to the bedrock cliffs. Rapaki village lies at the hillslope base, from approximately 70 meters (asl) to sea level. The removal of slope vegetation (i.e. native forest) has left the existing

hillslope vulnerable to erosion, such as surficial landsliding (i.e. debris and mudflow) and tunnel gulley erosion (Fig. 3).

Rockfall deposits sourced from the upslope bedrock cliffs are a prominent surface feature at Rapaki (Fig. 3). More than 650 individual modern (2011) boulders ranging in diameter from <15 cm to >3 m were dislodged from the bedrock source cliffs near the top of Mount Rapaki in the 22 February and 13 June 2011 Canterbury earthquakes (Massey et al., 2014; Heron et al., 2014; Mackey and Quigley, 2014; Borella et al, 2016). Twenty-six of these boulders, ranging in volume from ~0.25 m^3 to ~28.0 m^3, reached Rapaki village. Individual boulders (Fig. 1d) travelled up to 770±15 m downslope from the source cliff. Prehistoric fallen boulders are found interspersed with modern rockfall and are more abundant than their 2011 counterparts at Rapaki, where we mapped and characterized 1543 rocks ranging in volume from 0.001 m^3 to >100 m^3 (Borella et al., 2016) (Figs. 2 and 3). Mackey and Quigley (2014) used cosmogenic ^{3}He surface-exposure dating on 19 paleo-boulder surfaces to estimate the emplacement time of prehistoric rockfall at Rapaki. Rockfall was attributed to a strong proximal earthquake at 6-8 ka, with another potential prehistoric rockfall event occurring 13-14 ka.

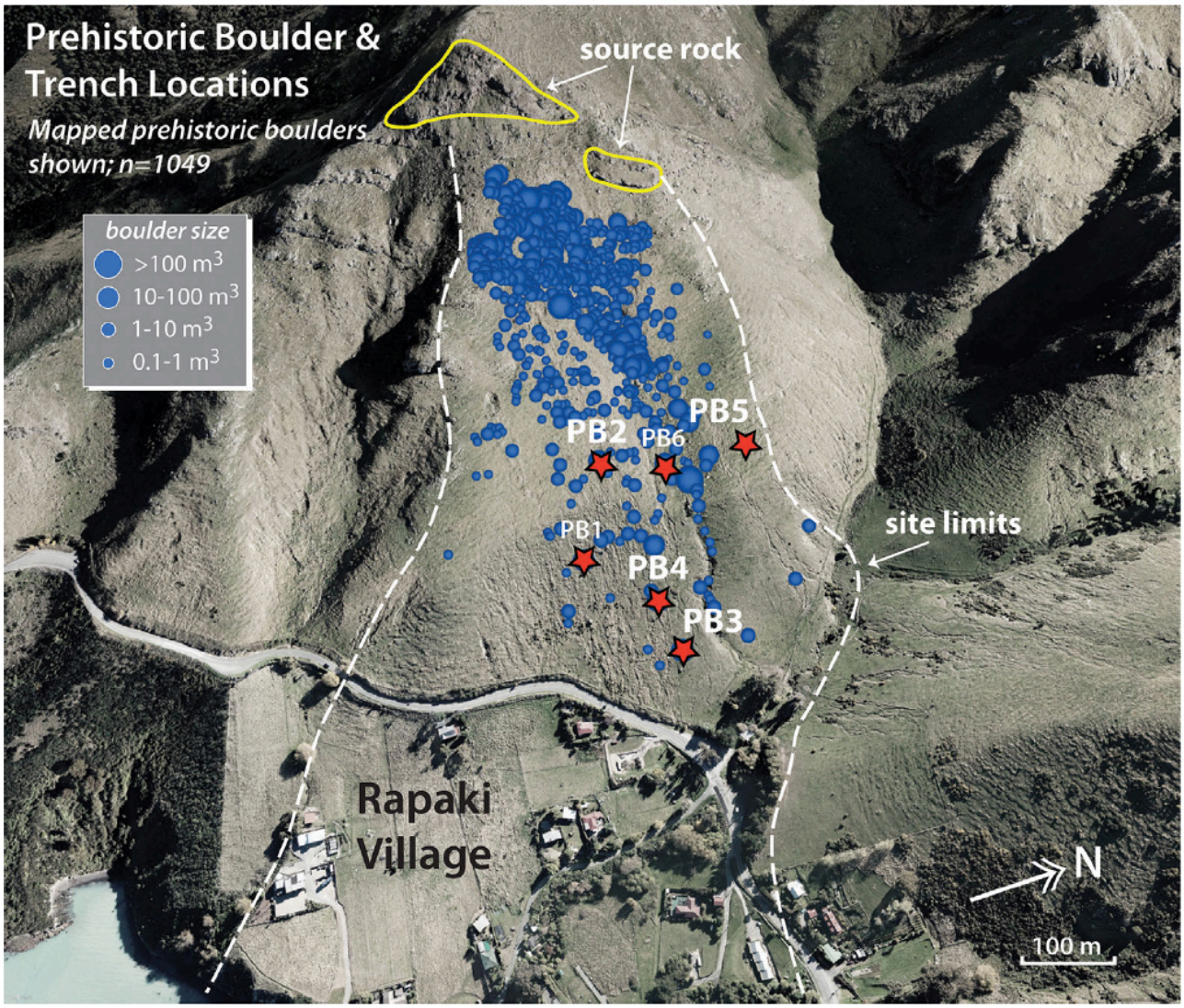

Figure 2. Rapaki study slope with prehistoric boulder and trench locations. Detailed logging was performed for PB2, PB3, PB4, and PB5 trenches. Mapped prehistoric boulders reflect boulder volume ≥0.1 m^3.

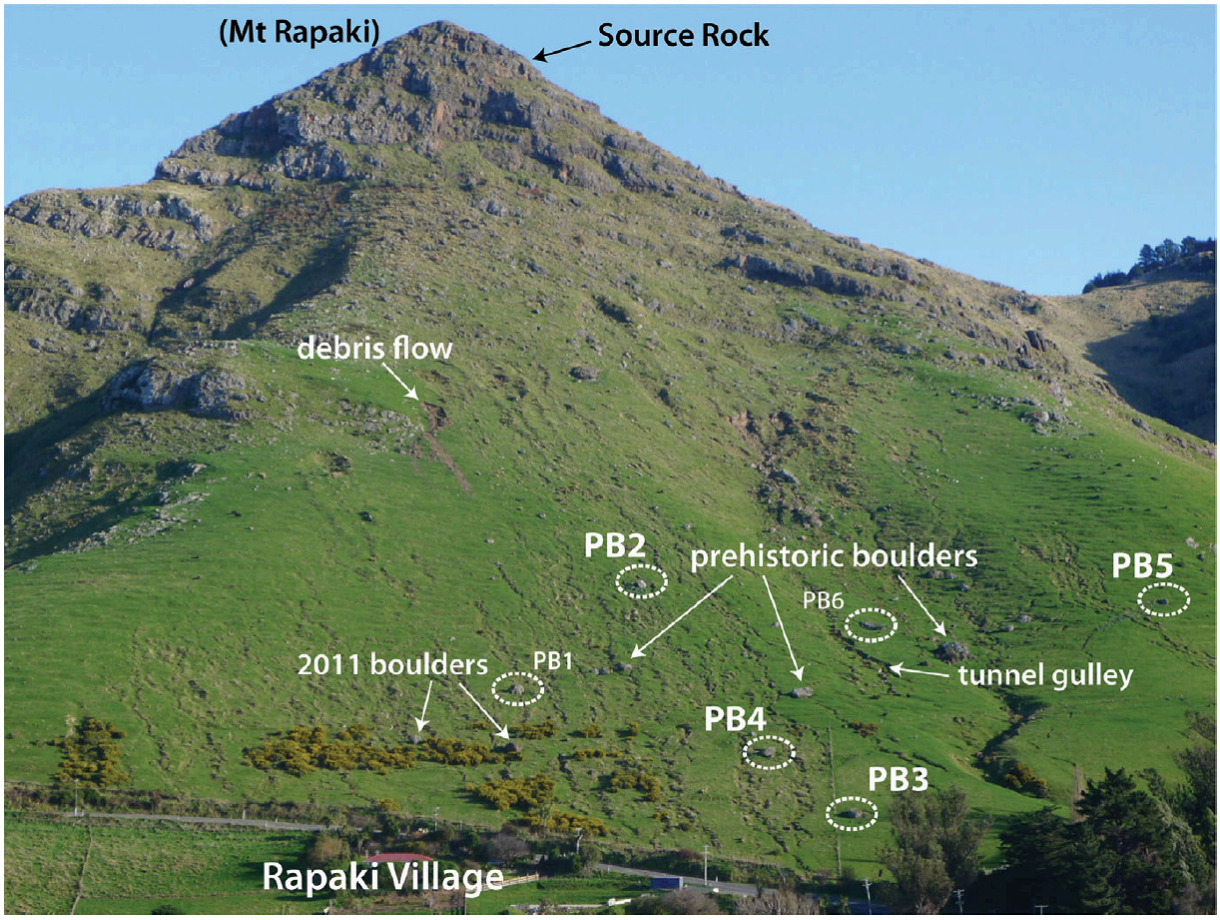

Figure 3. Prehistoric and modern (2011) boulders at the Rapaki study site. Prehistoric boulders are distinguishable from modern rockfall deposits because they are partially embedded in hillslope colluvium and are visible in pre-Canterbury earthquake sequence imagery. Surficial landslides (e.g. debris and mud flows) and extensive tunnel gulley formation and erosion are extensive on the modern deforested landscape. Locations for studied prehistoric boulders PB1-PB6 shown. Detailed trench logging was performed for PB2-PB5.

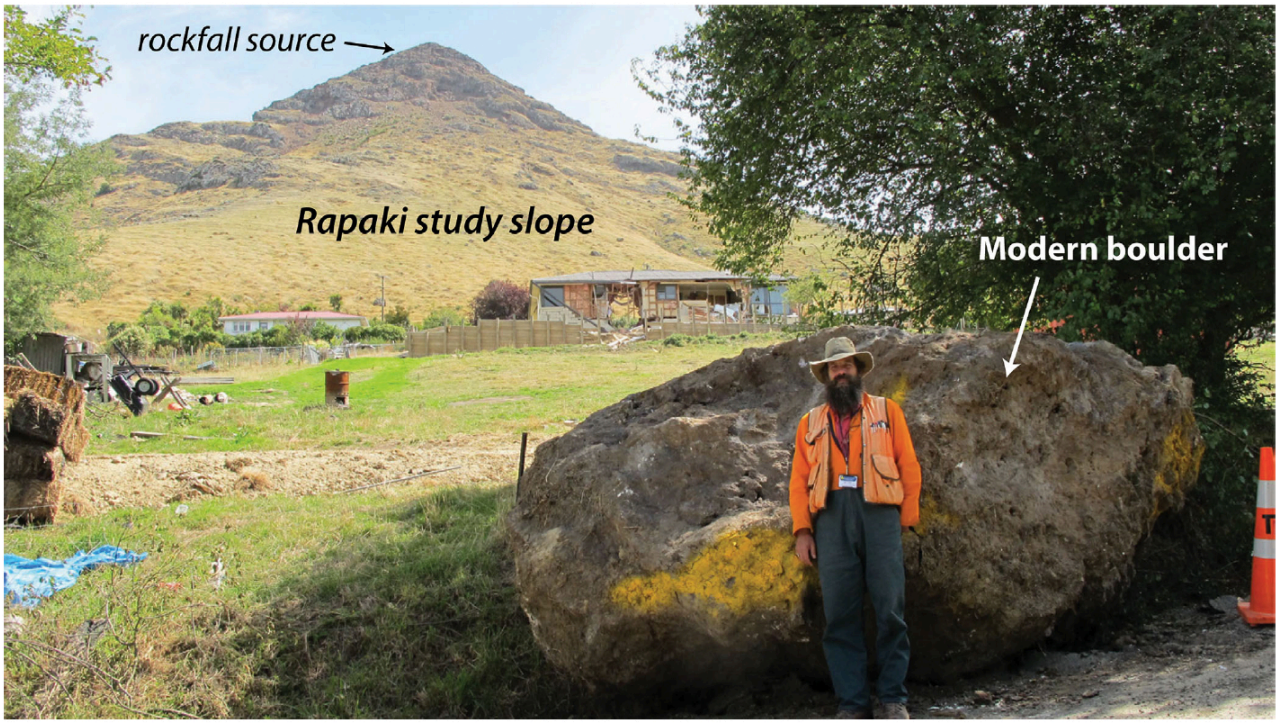

Figure 4. Large modern boulder (~28 m^3) detached from Mount Rapaki and emplaced in the Rapaki village during the 22 February 2011 earthquake. The boulder traveled through the center of the residential home located in background (center). Photo courtesy of D.J.A. Barrell, GNS Science.

2.4 Methods

2.4.1 Stratigraphic analysis and sampling

Prehistoric boulders and adjacent trench locations for stratigraphic analysis and sampling were selected based upon the following criteria: The prehistoric boulder should (1) be large enough (>5.0 m^3) to ensure subaerial exposure and sufficiently buried to ensure post-emplacement stability; (2) be located away from drainage valleys to limit post-emplacement mobility and sediment depositional complexities; (3) have a thick colluvial wedge developed upslope with no evidence of pervasive late-stage tunnel gulley erosion or anthropogenic and livestock modification; and (4) have a surface exposure age (Mackey and Quigley, 2014) so that cross-validation between luminescence and CN surface exposure dating methods could be performed. Four prehistoric boulders (PB2-PB5) were chosen for detailed investigation (Figs. 2 and 3; Supp. Table 1) and two (see Supp. Figs. 1 and 2 - PB1 and PB6) for more cursory description.

2.4.2 Dating Methods

We use luminescence and radiocarbon dating techniques to constrain the age of hillslope sediments and CN (cosmogenic nuclide) concentrations for prehistoric boulders (Mackey and Quigley, 2014). Luminescence dating provides a numerical age estimate of the last exposure to daylight of minerals such as quartz and feldspar (Aitken, 1998), while radiocarbon dating estimates the time elapsed since the death of an animal or plant. We use charcoal ages as a proxy for timing of sediment deposition, assuming charcoal originated from young wood, and that erosion, transport, and deposition of the charcoal-containing sediment occurred shortly after burning. Cosmogenic exposure ages estimate the length of time that a rock surface has been subaerially exposed, and rely on a simple exposure history for their accuracy (Heyman et al., 2011).

2.4.2.1 Luminescence Dating

Thirteen samples were collected for luminescence dating in (i) loess deposits underlying the prehistoric boulders and (ii) loess-colluvium accumulated upslope (i.e. colluvial wedge) of the boulders after emplacement on the hillside (Sohbati et al., 2016). Sampling involved pushing 5 cm-diameter stainless-steel tubes (with 15 cm length) into cleaned sections of the trench walls. To constrain emplacement timing for each of the prehistoric boulders, samples were collected within sediments lying directly below (maximum age) and above (minimum age) the geomorphic surface the boulder rested on.

Luminescence samples were analyzed at The Nordic Centre for Luminescence Research in Roskilde, Denmark. Luminescence sample preparation and analytical details are provided in Sohbati et al. (2016). Optical ages are labeled on corresponding trench logs (Figs. 5c, 6c, 7c, 9c, 10b) and presented in Table 1.

2.4.2.2 Radiocarbon Dating

Radiocarbon assays were performed on four individual pieces of charcoal to constrain the depositional age of the post-boulder emplacement colluvial sediments. Charcoal was retrieved near the base of the youngest colluvial sediments (LC_R) in PB3 and PB4. Charcoal samples ranging between 70 and 500 mg were submitted to the Rafter Radiocarbon Laboratory in Wellington, New Zealand, for accelerator mass spectrometry (AMS) radiocarbon analysis. Ages were calibrated using the Southern Hemisphere calibration curve (SHCal13; Hogg et al., 2013). We report both 2σ and 1σ calendar-calibrated ^{14}C age ranges in the text and both calibrated and conventional radiocarbon ages in Table 2 (see also Supp. Figs. 3-6).

2.5 Results

2.5.1 Trench stratigraphy

2.5.1.1 *In-situ* Loess

Putative *in-situ* loess beneath the boulders comprises the oldest sediment in each of the trenches (Figs. 5-10). It consists of a light yellowish brown to light olive brown, massive, hard, and dry silt to fine sandy loam and contains essentially no (≤0.2%) sediment derived from the proximal volcanic source rock (i.e. basalt) (Table 3a-d and Supp. Table 2). The loess exhibits characteristic gammate structure with grey fissures/veins and desiccation cracks with infilling translocated clay, as pedogenic carbonate rhizomorphs.

2.5.1.2 Preboulder Soil Stratigraphic Unit (PB-SSU)

The PB-SSU is a buried soil formed in ~13-44 cm of colluvium above the *in-situ* loess and below the boulders. The PB-SSU comprises a morphological B horizon that likely includes a former A horizon, characterized by a light olive brown to grayish brown to light yellowish brown, massive to very poorly layered, hard, dry to occasionally damp, silt loam with minor (≤1%) gravel, pebble, and cobble-sized basalt clasts (Table 3a-d and Supp. Table 2).

Development of PB-SSU is most advanced within PB2, PB4, and PB5 (maximum thickness ~44 cm) trenches, and displays abundant mottling, clay coatings/worm casts, mm-scale voids (burrows, dissolved roots), and calcite-filled desiccation cracks (see Table 3a-d and Supp. Table 2). PB-SSU thickness is generally consistent adjacent to and beneath the boulders, with the exception of PB2, where it thins beneath the boulder (perhaps due to compaction from the overlying boulder).

An irregular disconformity is observed at the top of the PB-SSU within each of the trenches. This surface marks the boundary between sediments that pre-date boulder emplacement (i.e. loess and colluvium) and those accumulating after boulder deposition (i.e. colluvium only).

2.5.1.3 Loess Colluvium (LC)

A 50-130 cm-thick wedge of loess colluvium has accumulated upslope of PB2-PB5 and must post-date these boulders. We define this lithostratigraphic unit as LC (Figs. 5-10). Differences in texture, density,

color, and relative moisture content were used to distinguish between the older loess (including PB-SSU) sediments and younger loess colluvium (LC) deposits (Table 3a-d). LC consists of a brown to dark grayish brown, massive to poorly layered, soft to firm, damp to semi-moist, silt loam (Table 3a-d). Gravel-sized clasts (3-6 mm diameter) are commonly encountered within the predominantly silty matrix. We observed a marked increase in volcanic-derived (basaltic) material within LC (see Supp. Table 2), ranging in size from medium to coarse-grained sand and gravel to pebble and small boulder sized volcanic rocks. Maximum abundance of volcanic clasts is ~17%. LC contains abundant small rootlets and pervasive yellowish brown to brownish yellow mottling.

2.5.1.4 Loess Colluvium – Recent (LC_R)

LC_R post-dates boulder emplacement and accumulation of LC. It is observable within the PB3 trench and possibly the PB4 trench (Figs. 3b,c; 4b,c), and represents the most recent phase of colluviation. In PB3, LC_R is comprises a grayish brown to very dark gray, poorly to moderately layered, soft, dry to slightly damp, silt loam with minor gravel (Table 3b and 3c). Charcoal was observed within the lower 30 cm and within sediment deposited around the sides of PB3 (at base). Radiocarbon dates for the charcoal fragments are presented in Table 2 and Supplementary Figures 3-5. At approximately 52 cm depth from the ground surface, charcoal is mixed with small fragments (mm to cm scale) of orange to reddish orange baked volcanic rock or brick/pottery, the latter indicating possible later European burning and suggesting that colluvium above this level occurred during European settlement. For PB4, we propose the upper ~35-50 cm of LC may be roughly time equivalent to the LC_R sediments observed in PB3. A 1-2 mm fragment of charcoal has been logged at a depth of ~33 cm from the existing ground surface. Radiocarbon dating of the charcoal fragment has been performed and results are presented in Table 2 (also see Supp. Fig. 6).

2.5.1.5 Infill Events

Infill events post-date boulder emplacement and deposition of adjacent LC and, in some cases, LC_R colluvial sediments. Two separate infill events (IF-1 and IF-2) were observed at the boundary between the PB2 boulder and loess colluvial wedge sediments (see Fig. 5c and Table 3a). We propose that space created at the back of PB2 for infilling may have resulted from several processes including (1) minor shifting of the boulder during earthquake-induced shaking, (2) desiccation and subsequent contraction of sediment adjacent to PB2, and/or (3) erosion of pre-existing sediment at the boulder-sediment boundary. A single infill (IF-1) event is observed adjacent to PB4 (Fig. 8) and consists of dark gray sandy silt (Table 3c). The sediment appears recent and has filled in space created adjacent (and partially beneath) to the upslope side

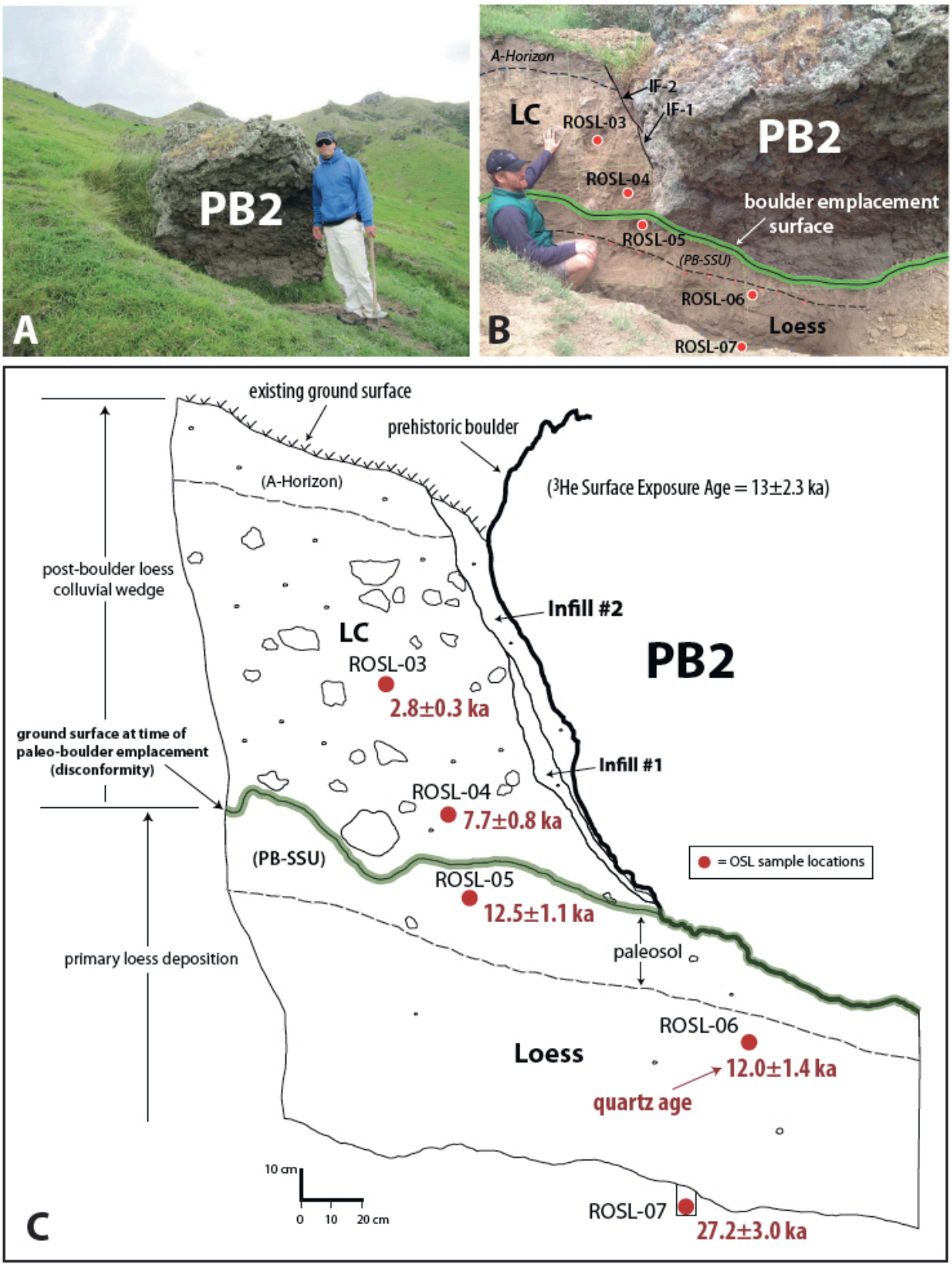

Figure 5. Prehistoric Boulder #2. **(A)** Photo of PB2 and surrounding hillslope sediment prior to exploratory trenching. **(B)** Photo of PB2 with pre-boulder (loess) and post-boulder (loess-colluvium) emplacement hillslope sediments exposed. **(C)** Detailed stratigraphic log of PB2 and surrounding loess and loess-colluvium (LC) sediments. PB-SSU (Preboulder Soil Stratigraphic Unit) is present at top of loess. OSL sample locations and quartz luminescence ages are shown. Mackey and Quigley (2014) ^{3}He CN surface exposure age for PB2 is shown.

Sample Name	Boulder/Trench Location	Sample Depth	Quartz OSL age	K-feldspar $pIRIR_{290}$ age
		(cm)	(ka) mean ± SE	(ka) mean ± SE
ROSL-02	PB1	247	29.3±2.5	28.5±1.6
ROSL-03	PB2	70	2.8±0.3	2.46±0.2
ROSL-04	PB2	99	7.7±0.8	6.9±0.4
ROSL-05	PB2	116	12.5±1.1	10.8±0.6
ROSL-06	PB2	87	12.0±1.4	10.2±0.6
ROSL-07	PB2	171	27.2±3.0	21.8±1.4
ROSL-08	PB3	81	2.9±0.3	2.6±0.2
ROSL-09	PB3	170	5.8±0.5	6.5±0.4
ROSL-10	PB4	93	4.2±0.4	3.8±0.2
ROSL-11	PB4	120	10.3±1.0	10.4±0.7
ROSL-12	PB4	131	13.4±1.2	12.7±0.7
ROSL-13	PB5	31	1.7±0.2	1.94±0.1
ROSL-14	PB5	110	10.2±0.8	12.6±0.8

Table 1. Summary of Rapaki (NZ) sample name, boulder/trench location, burial depth, quartz OSL and K-feldspar $pIRIR_{290}$ ages (Modified from Sobhati et al., 2016).

Sample ID	Boulder location	Exposure unit	NZA laboratory number	$\delta^{13}C$	Radiocarbon age (^{14}C yr B.P.)	Calibrated age 2σ (calendar yr A.D.)	Probability for each 2σ range (%)	Material
Rap-CH01	PB3	LC_R	56801	28.6±0.2	203±18	A.D. 1664-1698, **1724-1809**, 1870-1876	22.8, **70.4**, 1.0	Charcoal
Rap-CH03	PB3	LC_R	56802	29.1±0.2	197±17	A.D. 1666-1700, **1722-1810**, 1838-1845, 1867-1878, 1933-1938, 1946-1950	25.8, **63.8**, 1.3, 2.4, 0.6, 1.1	Charcoal
Rap-CH05	PB3	LC_R	56803	27.9±0.2	222±17	A.D. 1661-1680, **1732-1802**	15.8, **79.0**	Charcoal
Rap-CH06	PB4	LC_R	60079	26.9±0.2	162±22	A.D. 1667-1736, **1799-1950**	29.4, **65.7**	Charcoal

Note: NZA-Rafter Radiocarbon Laboratory; B.P. – before present

Table 2. Summary results from radiocarbon dating of charcoal within PB3 and PB4 loess-colluvium wedge sediments at the Rapaki study site.

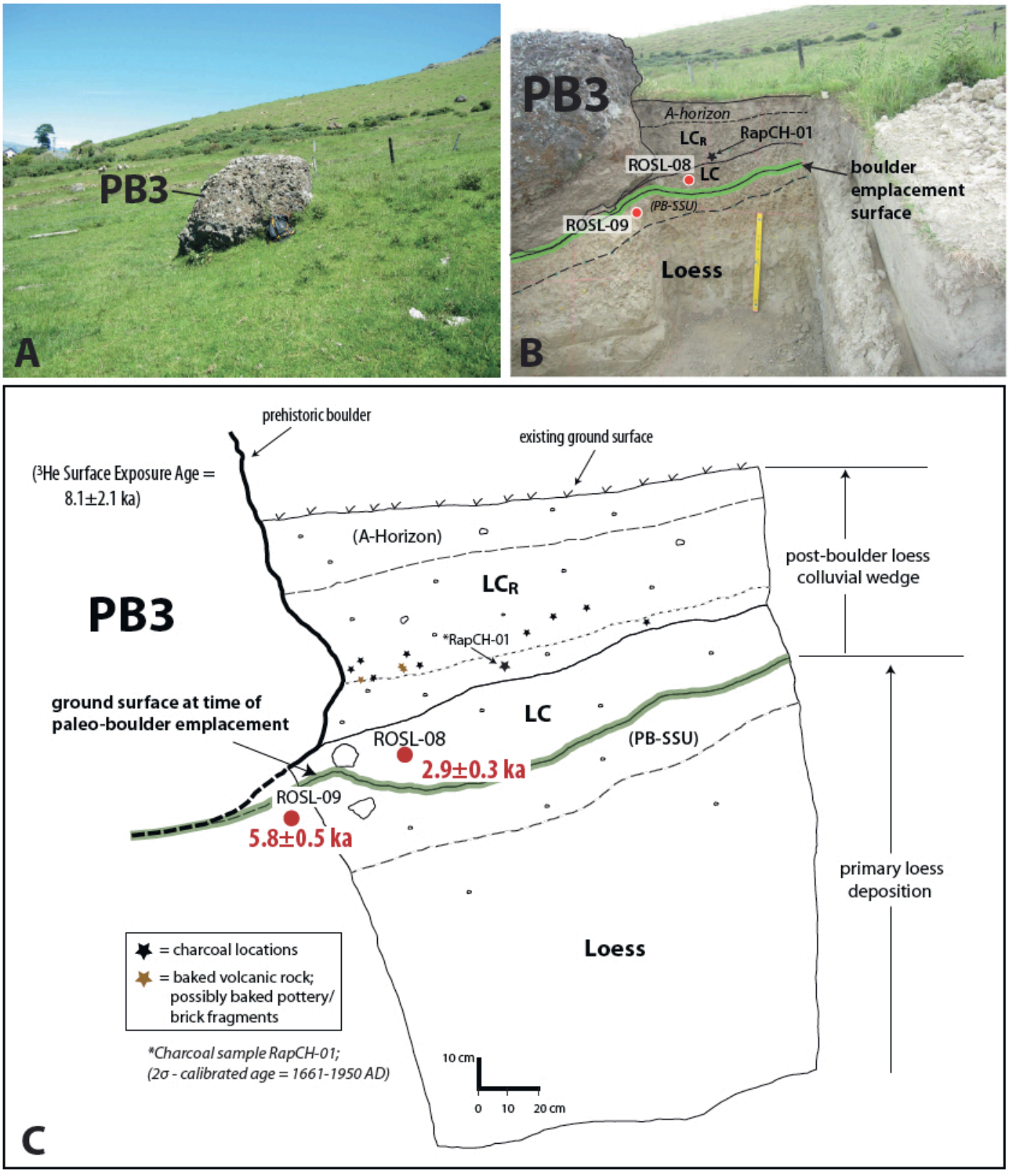

Figure 6. Prehistoric Boulder #3. **(A)** Photo of PB3 and surrounding hillslope sediment prior to exploratory trenching. **(B)** Photo of PB3 exploratory trench with pre-boulder and post-boulder emplacement hillslope sediments exposed. **(C)** Detailed stratigraphic log of PB3 and surrounding loess and loess-colluvium sediments. OSL (red) and radiocarbon sample location and ages shown. Mackey and Quigley (2014) ^{3}He surface exposure age for PB3 also displayed.

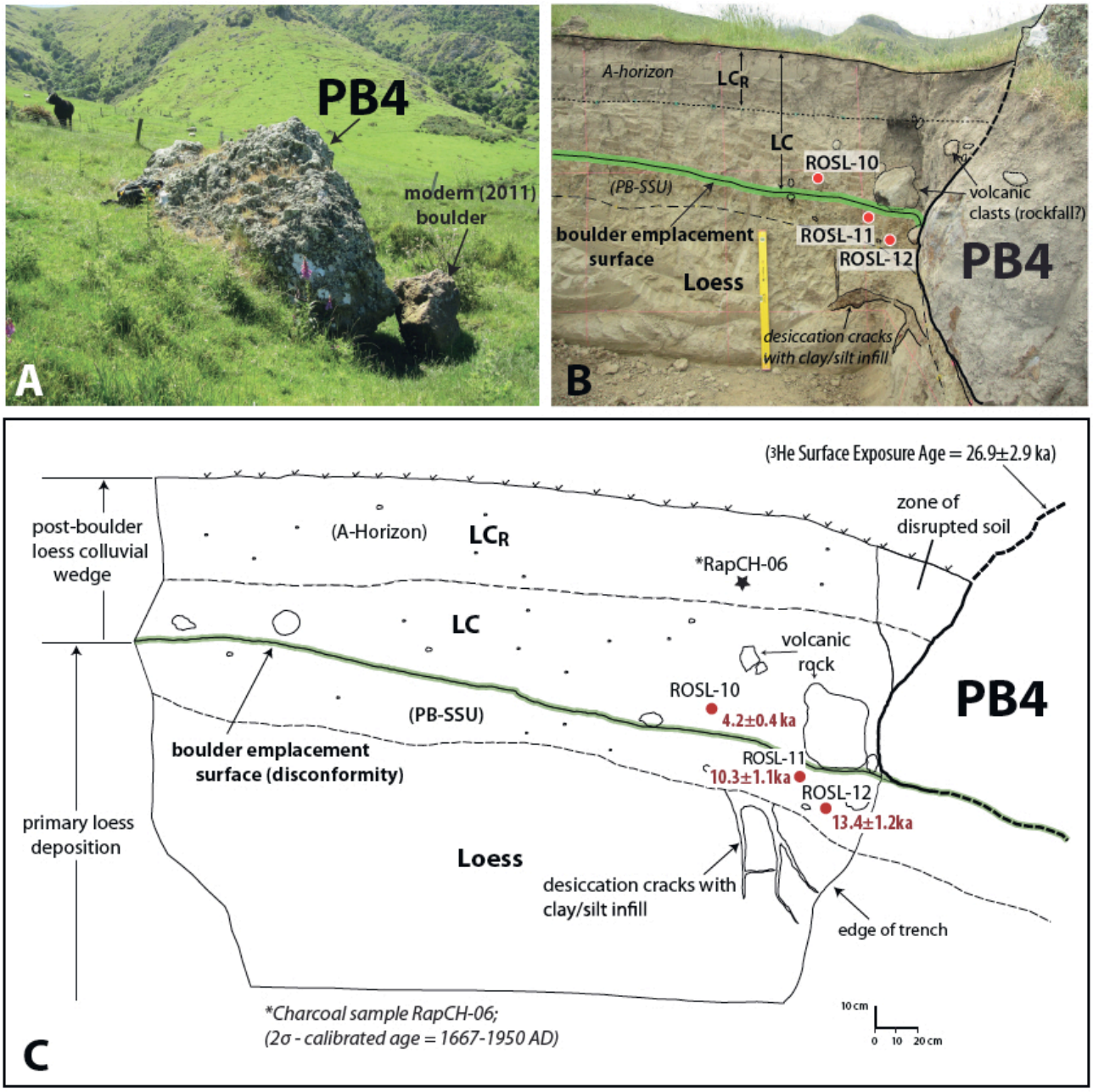

Figure 7. Prehistoric Boulder #4. **(A)** Photo of PB4 and surrounding hillslope sediment prior to exploratory trenching. **(B)** Photo of PB4 and exploratory trench with pre-boulder and post-boulder emplacement hillslope sediments exposed. Meter-stick shown for scale. **(C)** Stratigraphic log of PB4 and surrounding loess and loess-colluvium sediments. Note the truncation of infilled desiccation cracks at base of Preboulder Soil Stratigraphic Unit (PB-SSU). Quartz OSL and radiocarbon sample locations and ages shown. Mackey and Quigley (2014) ^{3}He surface exposure age for PB4 also displayed.

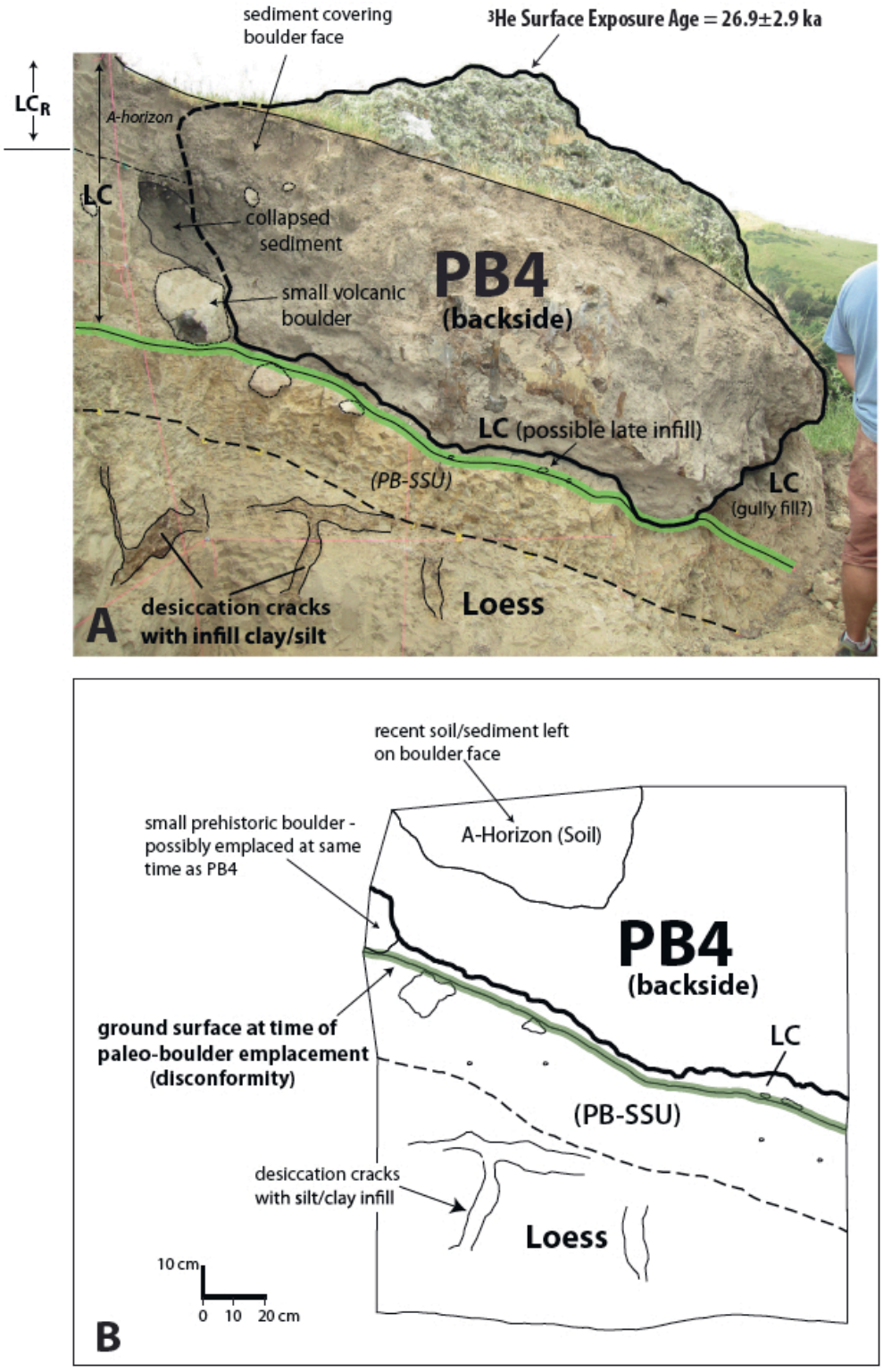

Figure 8. Prehistoric Boulder #4 (PB4). **(A)** Photo of PB4 backside (upslope) and exploratory trench with pre-boulder and post-boulder emplacement hillslope sediments exposed. Mackey and Quigley (2014) ^{3}He surface exposure age for PB4 also displayed. **(B)** Partial stratigraphic log of PB4 (upslope side) and surrounding loess and loess-colluvium sediments.

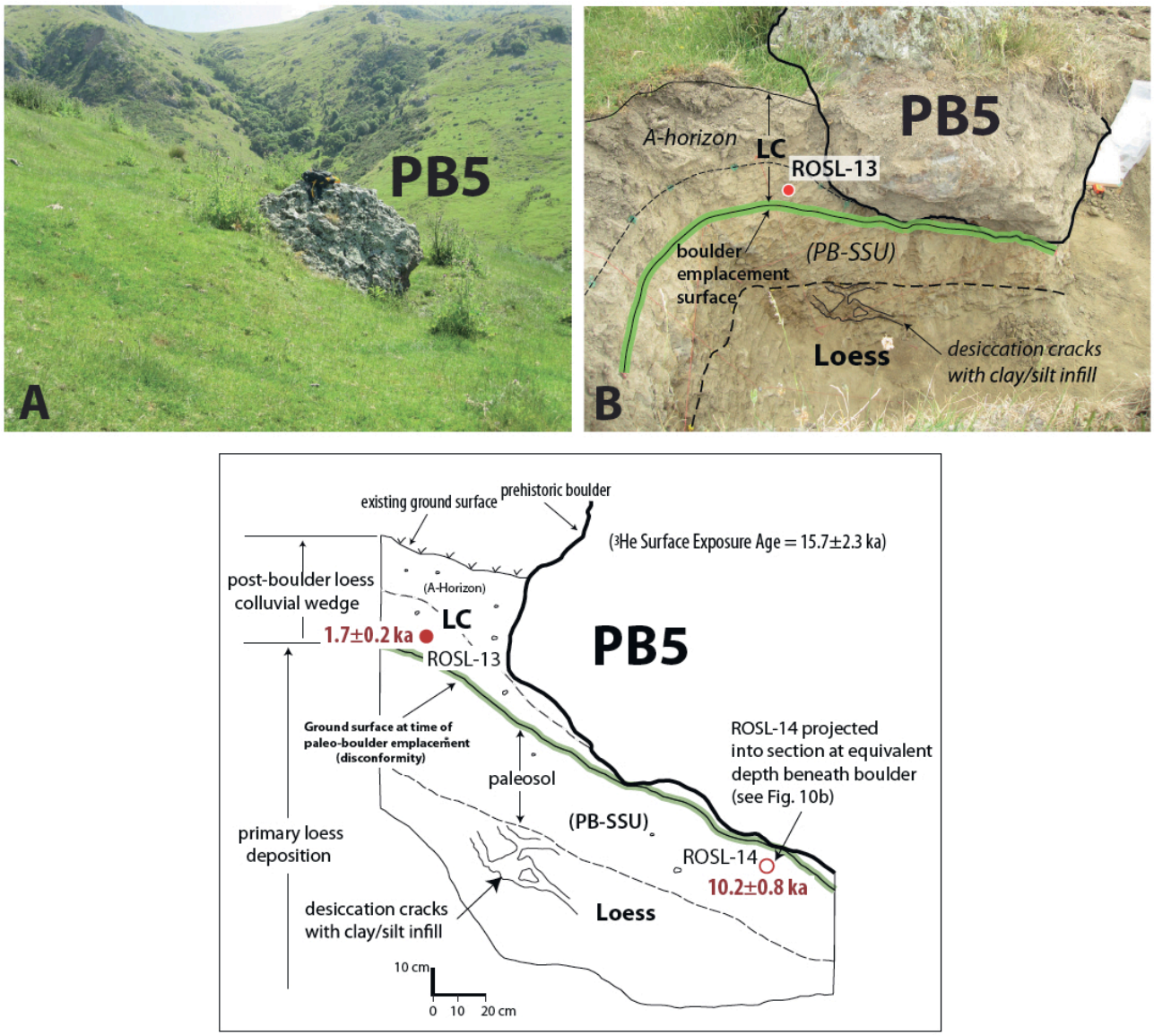

Figure 9. Prehistoric Boulder #5 (PB5). **(A)** Photo of PB5 and surrounding hillslope sediment prior to exploratory trenching. **(B)** Photo PB5 exploratory trench with pre-boulder and post-boulder emplacement hillslope sediments exposed. Note apparent truncation of infilled desiccation cracks at base of PB-SSU zone. **(C)** Stratigraphic log of PB5 with surrounding loess and loess-colluvium sediments. Quartz OSL sample locations and ages shown. Mackey and Quigley (2014) ^{3}He surface exposure age for PB5 displayed at top.

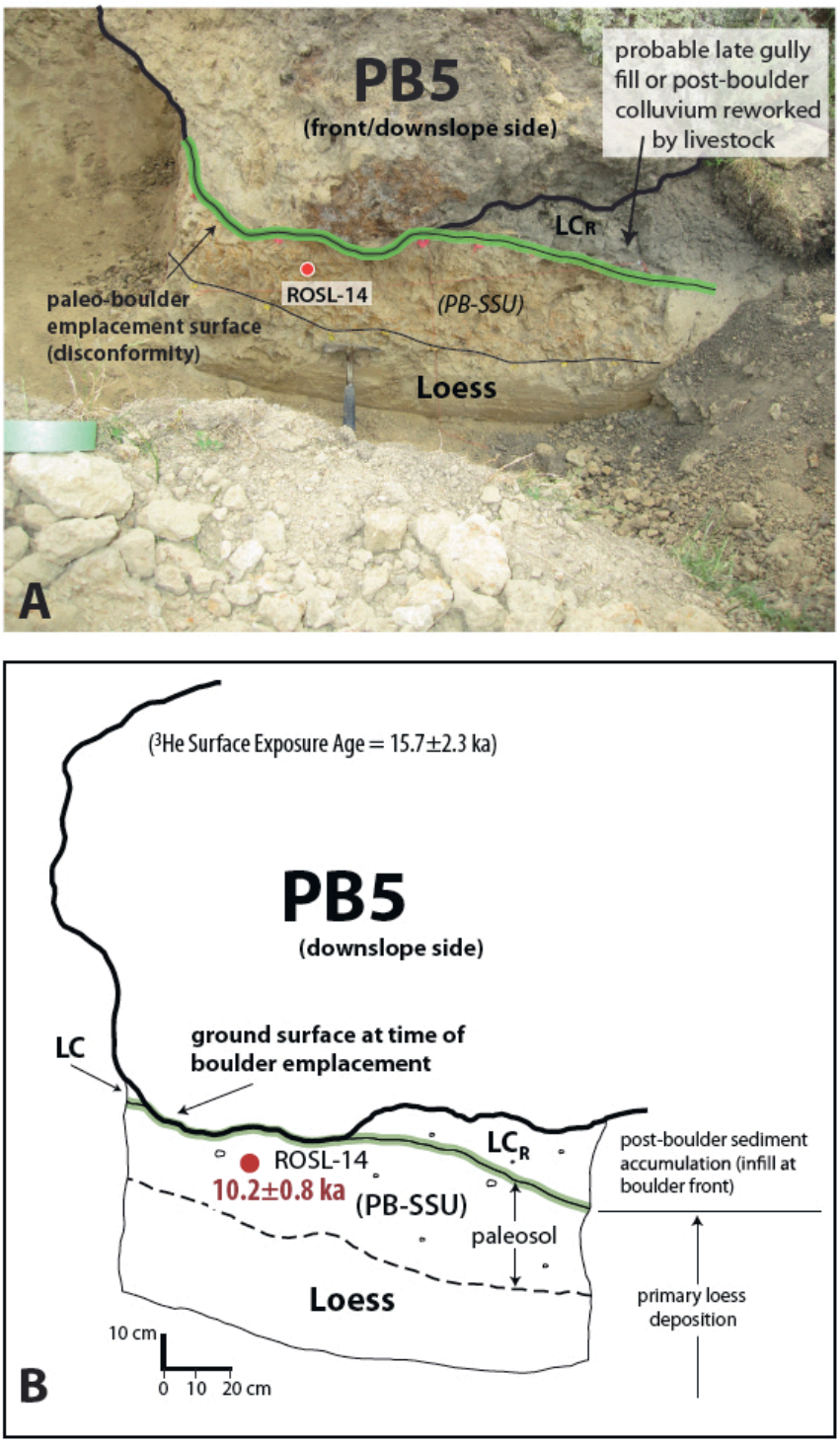

Figure 10. Prehistoric Boulder #5. **(A)** Photo of PB5 (downslope side of boulder) exploratory trench with pre-boulder and post-boulder emplacement hillslope sediments exposed. **(B)** Stratigraphic log of PB5 with surrounding loess and loess-colluvium sediments. Quartz OSL sample location and age shown. Mackey and Quigley (2014) ^{3}He surface exposure age for PB5 displayed at top.

Sediment Unit	Relative Timing	Colour	Texture	Relative Moisture	Sediment Strength	Bulk Density (cm^3)	Thickness (cm)	Structures
Loess	Predates PB2 emplacement	Light yellowish brown (2.5Y 6/4)	Silty loam comprised of ~30% sand, 60% silt, 10% clay, very little to no sediment derived from volcanic source rock	Dry	Hard	N/A	97 (min.)	Massive, characteristic gammate structure with grey fissures/veins from desiccation/shrinkage, calcite-filled tubular root structures
PB-SSU	Predates PB2 emplacement	Light olive brown (2.5Y 5/3.5) with dark yellowish brown mottling (10YR 4/6)	Silty loam with minor gravel comprised of ~19% sand, 65% silt, 16% clay, slight but notable increase in coarser-grained sediment derived from proximal volcanic source rock, occasional pebble to cobble-sized clasts of basalt, maximum cobble diameter is ~23 cm)	Dry	Hard	1.93-2.04	13-34	Massive, abundant subvertical to vertical cracks with infilling calcite, contains clay coatings (worm castings), intense and pervasive mottling and abundant desiccation cracks, top of PB-SSU marked by disconformity
LC	Postdates PB2 emplacement	Grayish brown (10YR 5/2) with yellowish brown mottling (10YR 5/2) A horizon soil is very dark gray (2.5YR 3/1)	Silty loam with gravel to small boulder-sized fragments of volcanic rock (basalt), lower half of LC comprised of ~13% gravel, 20% sand, 50% silt, 17% clay, upper half comprised of ~2% gravel, 26% sand, 59% silt, 13% clay (% gravel is conservative), significant increase in volcanic derived material, maximum diameter for volcanic rock is 18.87 cm	Damp to semi-moist	Soft to firm	1.59-1.92	110-128	Massive to very poorly layered, A-horizon soil (16-25 cm thick) is intensely altered and bioturbated, abundant small voids (dissolved roots, burrows)
IF-1	Postdates PB2 emplacement	Light gray (2.5Y 7/2) to light olive brown (2.5Y 5/4) with dark yellowish brown mottling (10YR 4/6)	Silty loam	Damp to dry	Stiff to very stiff	N/A	N/A	Laminations to thin layering (mm to cm scale) parallel to rear surface of PB2, minor rootlets and small mm-scale voids from burrowing
IF-2	Postdates PB2 emplacement	Very dark gray (2.5Y 3/1)	Silty loam	Damp to semi-moist	Soft to firm	N/A	N/A	No obvious layering, less oxidized than IF-1, small rootlets and mm-scale voids

*PB-SSU is 'Preboulder Soil Stratigraphic Unit' developed in top section of loess

Table 3. (A) Summary of trench stratigraphy and related field and laboratory measurements for PB2.

Sediment Unit	Relative Timing	Colour	Texture	Relative Moisture	Sediment Strength	Bulk Density (cm^3)	Thickness (cm)	Structures
Loess	Predates PB3 emplacement	Light yellowish brown (2.5Y 6/3) to light olive brown (2.5Y 5/4)	Silty loam comprised of ~36% sand, 51% silt, 13% clay, very little to no sediment derived from volcanic source rock	Dry	Hard	N/A	133 (min.)	Massive, small vertical to subvertical desiccation cracks observed but not abundant, calcite filled tubular root structures, some mottling (iron oxidation)
PB-SSU	Predates PB3 emplacement	Grayish brown (2.5Y 5/2) to light olive brown (2.5Y 5/3) with yellowish brown mottling (10YR 5/8	Silty loam with minor gravel comprised of ~28% sand, 58% silt, 14% clay, slight but notable increase in coarser-grained sediment derived from proximal volcanic source rock, occasional pebble to cobble-sized clasts of basalt, maximum cobble diameter is ~8.8 cm	Dry	Hard	1.9-2.01	17-34	Massive, tiny mm-scale voids (e.g. burrows, dissolved roots), paleosol development not as advanced compared with PB2/PB4/PB5, occasional old worm burrows with clay coatings and desiccation cracks observed, top of PB-SSU is marked by disconformity
LC	Postdates PB2 emplacement	Brown to grayish brown (10YR 5/2) with brownish yellow (10YR 6/8) mottling	Silty loam with minor gravel, slight increase in coarse-grained sand and gravel, occasional pebbles/small cobbles of basalt, LC sediment significantly less dense than underlying loess	Damp to semi-moist	Soft to firm	1.27 -1.59	24 LC compara-tively thin	Massive to very poorly layered, abundant mottling, tiny rootlets pervasive
LC_R	Postdates PB2 emplacement	Grayish brown (2.5Y 5/2) to very dark gray (2.5Y 4/1) A horizon soil is very dark gray (2.5Y 3/1)	Silty loam comprised of ~24% sand, 64% silt, 12% clay with minor gravel, charcoal abundant, small fragments of charred brick/pottery	Dry to slightly damp	Soft	1.27	70	Moderately to poorly layered, abundant roots and other organic matter (e.g. wood, charcoal), charcoal primarily observed within the lower 30 cm of LC_R, no infill episodes observed adjacent to PB3

Table 3. (Continued) (B) Summary of trench stratigraphy and related field and laboratory measurements for PB3.

Sediment Unit	Relative Timing	Color	Texture	Relative Moisture	Sediment Strength	Bulk Density (cm^3)	Thickness (cm)	Structures
Loess	Predates PB4 emplacement	Light yellowish brown (2.5Y 6/3) to light olive brown (2.5Y 5/3)	Sandy loam comprised of ~53% sand, 35% silt, 12% clay, we note increased sand % for PB4 loess	Dry	Hard	N/A	155 (min.)	Massive, desiccation cracks infilled with dark brown translocated clay, infilled cracks are part of prismatic structure and taper (i.e. become thinner) with depth, cracks are vertical to subvertical and horizontal to subhorizontal, maximum width for desiccation cracks is ~3.5 cm, calcite-filled root structures, tiny rootlets
PB-SSU	Predates PB4 emplacement	Olive brown (2.5Y 4/3) with dark yellowish brown (10YR 4/6) mottling	Silty loam comprised of ~35% sand, 49% silt, 16% clay with minor gravel, observe increase in coarse-grained sand and gravel sized material derived from the volcanic source rock, several subangular to subrounded, pebble to small cobble-sized basalt clasts, maximum cobble diameter is ~11 cm.	Dry to damp	Hard	2.17	18-39	Massive, well developed paleosol with pervasive mottling (iron oxidation), clay coatings with worm castings abundant, top of PB-SSU is marked by a disconformity
LC	Postdates PB4 emplacement	Grayish brown (10YR 5/2) to dark grayish brown (2.5YR 4/2) with dark yellowish brown (10YR 3/6) mottling	Silty loam comprised of ~24% sand, 57% silt, 19% clay with minor gravel, gravel-sized 'stones' (3-6 mm diameter) are commonly encountered within the predominantly silty matrix Upward grades into silty loam consisting of ~19% sand, 66% silt, 15% clay with minor gravel	Damp to semi-moist	Soft to firm	1.63-1.94	100	Massive to very poorly layered, abundant mottling, small rootlets pervasive, thin white lamination layer (~2-3 mm thick) is observed at depth of ~50 1-2 mm fragment of charcoal logged at depth of ~33 cm Upper 35-52 cm of LC may be time equivalent PB3 LC_R sediments
IF-1	Postdates PB4 emplacement	Dark gray (2.5 YR 3/1)	Silty loam, similar in character to PB2 IF-2	Damp to semi-moist	Soft to firm	N/A	N/A	No obvious layering, small rootlets and mm-scale voids

Table 3. (Continued) (C) Summary of trench stratigraphy and related field and laboratory measurements for PB4.

Sediment Unit	Relative Timing	Colour	Texture	Relative Moisture	Sediment Strength	Bulk Density (cm^3)	Thickness (cm)	Structures
Loess	Predates PB2 emplacement	Light yellowish brown (2.5YR 6/3) to light olive brown (2.5YR 5/4)	Silty loam comprised of ~39% sand, 50% silt, 11% clay	Dry	Hard	N/A	83 (min.)	Massive, desiccation cracks near top infilled with clay/silt, burrowing, calcite filled root structures
PB-SSU	Predates PB2 emplacement	Light yellowish brown (2.5YR 6/3) with yellowish brown mottling (10YR 4/6)	Silty loam comprised of ~26% sand, 62% silt, 12% clay; small increase (relative to in-situ loess) in volcanic derived subangular to subrounded, coarse-grained sand and gravel	Dry	Hard	1.83	29-44	Massive, subvertical to vertical desiccation cracks commonly filled with calcite, well developed paleosol with abundant mottling (iron oxidation), contains clay coated worm casts, top of PB-SSU marked by disconformity
LC	Postdates PB2 emplacement	Grayish brown (10YR 5/2), within A-horizon very dark gray (2.5YR 3/1)	Silty loam with minor gravel comprised of (~32% sand, 55% silt, 13% clay); relative increase in coarse-grained sand and gravel A-horizon soil is silty loam comprised of ~31% sand, 58% silt, 11% clay	Dry to damp	Soft to firm	1.30	37-47 A-horizon is 17-34 cm	Massive to very poorly layered, A-horizon soil intensely altered and bioturbated, abundant small voids (dissolved roots, burrows)

Table 3. (Continued) (D) Summary of trench stratigraphy and related field and laboratory measurements for PB5.

of the boulder. PB4 infill is similar in character (i.e. texture, composition) to IF-2 observed in PB2 trench sediments (see Figs. 5b,c). PB4 records only a single infill event and may reflect a higher in-situ stability or younger boulder emplacement age compared with PB2. No late infilling events are observed at the boundary between the loess colluvial wedge sediments and upslope side of PB3 and PB4.

2.5.2 OSL and Radiocarbon Chronology

The luminescence samples were dated using the single-aliquot regenerative-dose (SAR) protocol (Murray and Wintle, 2003) for blue-light stimulated luminescence of quartz (quartz OSL) and post-infrared stimulated luminescence of potassium-rich feldspar (K-rich feldspar $pIRIR_{290}$) (Buylaert et al., 2012) grains (i.e. 40-63 μm). Details of luminescence characteristics, equivalent doses, dose rates and ages are given in Sohbati et al. (2016). Despite the excellent agreement between the quartz OSL and K-feldspar $pIRIR_{290}$ ages, which assures the overall reliability of the optical ages (Sohbati et al., 2016), we base our geological interpretation on quartz OSL ages because the quartz signal does not suffer from the complications usually associated with the K-feldspar signals such as stability and complete resetting in nature (Sohbati et al., 2016).

2.5.2.1 PB2

The OSL age for ROSL-07 indicates loess accumulation 27.2±3.0 ka and agrees well with the quartz OSL age from ROSL-02 (29.3±2.5 ka) (Table 1 and Supp Fig. 1). The luminescence age for ROSL-06 suggests that loess accumulation at Rapaki may have occurred as late as 12.0±1.4 ka. The OSL age within the PB-SSU (ROSL-05) indicates a statistically similar age of 12.5±1.1 ka (Fig. 2c), suggesting that there was no re-bleaching during the colluviation and pedogenesis associated with the PB-SSU. The significant time interval (~4.8 ky) separating formation of the PB-SSU and earliest accumulation of LC (Figs. 5c and 11) suggests the boundary represents a disconformity. The ROSL-04 age indicates earliest accumulation of LC behind PB2 occurred 7.7±0.8 ka (Fig. 5c). An age of 2.8±0.3 ka for ROSL-03 (located above) suggests that sediment accumulation upslope of PB2 did not occur as a single event (i.e. landslide).

2.5.2.2 PB3

ROSL-09 (5.8±0.5 ka) (Fig. 6c) is the youngest luminescence age within the PB-SSU among the four studied prehistoric boulders. The OSL age for ROSL-08 suggests earliest accumulation of LC behind (i.e.

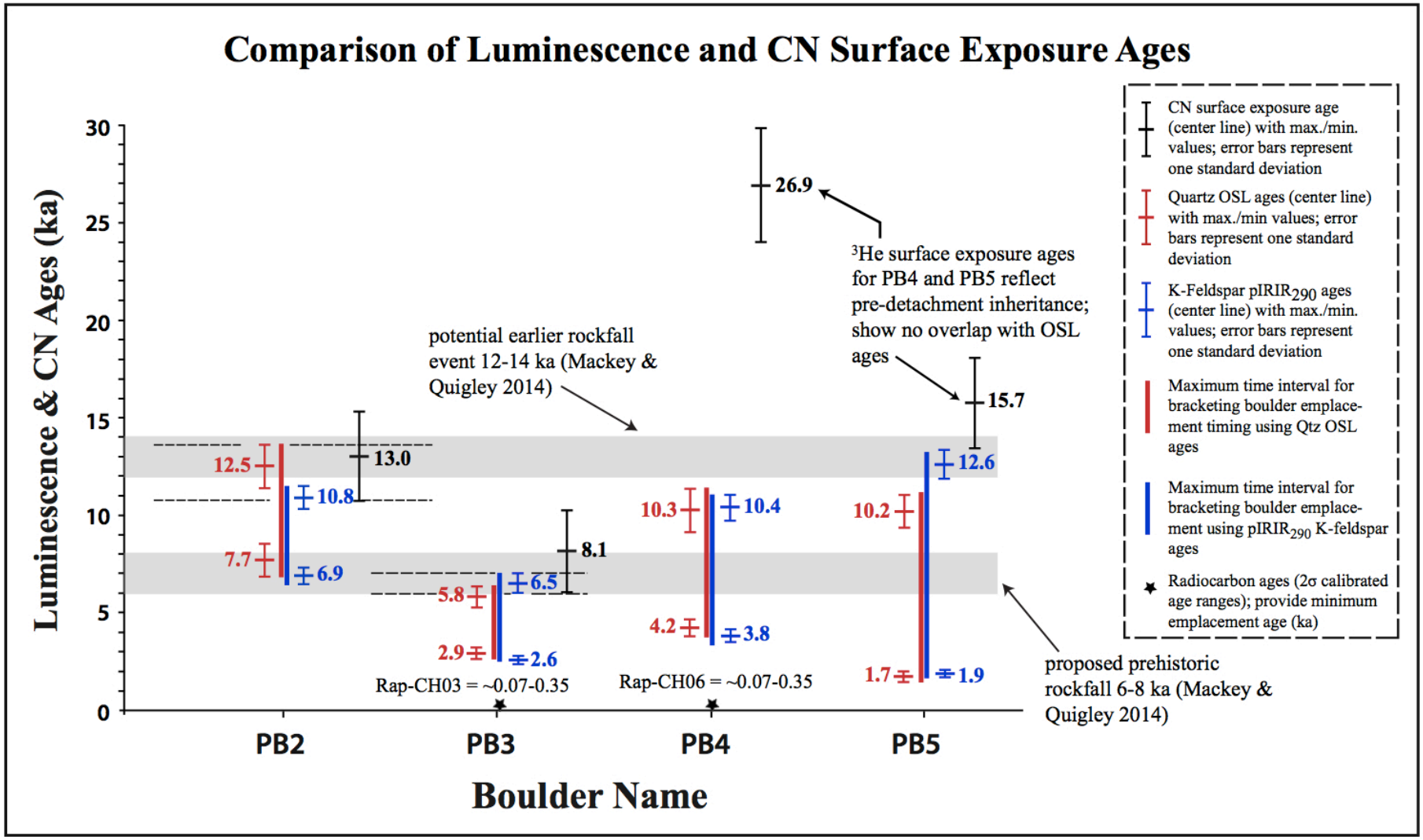

Figure 11. Luminescence ages are compared with CN surface exposure ages from the top surface of the prehistoric boulders (Mackey and Quigley, 2014). Both Quartz OSL and K-feldspar $pIRIR_{290}$ maximum and minimum emplacement ages are shown for each of the prehistoric boulders. Radiocarbon ages (calibrated 2σ range) for PB3 and PB4 also shown for comparison.

upslope) PB3 occurred 2.9±0.3 ka (Fig. 6c). Radiocarbon dates come from three charcoal samples from the lowest horizon of LC_R (Fig. 6c, Table 2 and Supp. Figs. 3-5). The 2σ calibrated ages (calendar yr A.D.) range from AD 1661 to AD 1950, with the highest sub-interval probability from AD 1724 to AD 1809 for Rap-CH01 (70.4% of area), AD 1722 to AD 1810 for Rap-CH03 (63.8%), and AD 1732 to AD 1802 for Rap-CH05 (79%). A fire event (or sequence of events) occurring sometime between ~1722 AD and 1810 AD predates European settlement and is consistent with localized burning during the late Maori Period (~AD 1600–1840) as proposed by McWethy et al. (2010). Assuming sediment deposition occurred shortly after burning (and death) of slope vegetation, earliest LC_R accumulation occurred between ~200 and 300 a. Charcoal stratigraphically above the dated samples was associated with fragments of baked volcanic rock or possibly brick/pottery mixed with charcoal, potentially indicative of a later phase of European burning (Fig. 6c).

2.5.2.3 PB4

Quartz OSL ages in PB4 PB-SSU are 13.4±1.2 ka (ROSL-12) and 10.3±1.1 ka (ROSL-11) (Fig. 7c). We interpret these ages as representing primary loess accumulation, but cannot preclude the possibility that the ROSL-11 age reflects bleaching during post-accumulation reworking within PB-SSU. Luminescence ages obtained above and below the PB-SSU/LC boundary suggest a depositional hiatus of ~6 ky (Fig. 11). Luminescence dating indicates earliest LC accumulation occurred 4.2±0.4 ka (Fig. 7c). The radiocarbon age from charcoal sample Rap-CH06 suggests LC_R sedimentation occurred sometime between AD 1677 and AD 1950, with the highest 1σ confidence interval occurring between AD 1799 and AD 1950 (see Supp. Fig. 6).

2.5.2.4 PB5

The quartz OSL age at the top of the PB-SSU (ROSL-14) establishes a maximum age of loess accumulation of 10.2±0.8 ka (Figs. 8c, 9b). Similar to ROSL-11, we cannot eliminate the possibility that ROSL-14 age is influenced by bleaching during colluviation and pedogenesis. Initiation of LC deposition upslope of PB5 began 1.7±0.2 ka. Ages from above and below the PB-SSU/LC contact suggest a depositional hiatus of ~8.5 ky at the PB5 location, the longest of the studied boulders (Fig. 11).

2.5.3 Sediment accumulation rates

Table 4 presents estimates of accumulation rates for PB2-PB5 colluvial wedge sediments. Optical and radiocarbon sample names and ages are shown, as well as the measured stratigraphic thickness between the bracketing ages. Temporal distributions may reflect differences in rates and processes of deposition between near-instantaneous debris and mud flow deposits and more gradual overland flow erosion and deposition. In consideration of this, the deposition rates represent only a first-order linear approximation, but serve to highlight changes in sediment accumulation through time. Our results suggest an overall increase in sediment accumulation rates within loess colluvium moving stratigraphically upward, with a dramatic increase in depositional rate during deposition of LC_R.

2.5.4 OSL constraints on timing of boulder emplacement

Quartz OSL ages suggest PB2 was emplaced after 12.5±1.1 ka and before 7.7±0.8 ka (Fig. 11). The top surface of PB2 yielded a surface exposure age of 13.0±2.3 ka (Fig. 5c and Fig. 10) (Mackey and Quigley, 2014). Assuming the calculated experimental uncertainty for both methods, the CN age and optical overlap can be used to further constrain the emplacement timing of PB2. Combining CN and quartz OSL ages suggests emplacement of PB2 after ~13.6 ka and before ~10.7 ka (Fig. 11). Quartz OSL ages constrain timing of PB3 to after 5.8±0.5 and before 2.9±0.3 ka (Fig. 11). The top surface of PB3 has a CN surface exposure age of 8.1±2.1 ka (Fig. 6c and Fig. 11). Again, the CN age and luminescence ages show statistical overlap. Combining CN and quartz OSL ages suggests emplacement of PB3 after ~6.3 ka and before ~6.0 ka (Fig. 11). Quartz OSL ages suggest PB4 was emplaced after 10.3±1.1 and before 4.2±0.4 ka (Fig. 11). The top surface of PB4 has a CN surface exposure age of 26.9±2.9 ka (Fig. 7c and Fig. 11). The OSL ages are inconsistent with the surface exposure age and strongly suggest that PB4 CN surface exposure age reflects pre-detachment inheritance (Mackey and Quigley, 2014) (Fig. 11). In middle and footslope positions it is likely that any boulder emplaced before ~27 ka would be partially or completely buried beneath loessic sediments. The quartz OSL ages constrain timing of PB5 to after 10.2±0.8 and before 1.7±0.2 ka (Fig. 11). The top surface of PB5 has a CN surface exposure age of 15.7±2.3 ka (Fig. 9c and Fig. 11). Similar to PB4, the optical ages are inconsistent with the surface exposure age and indicate that the PB5 CN surface exposure age reflects pre-detachment inheritance (Fig. 11).

We used the Bayesian modeling facility of OxCal (v 4.2) (Ramsey, 2009) to combine OSL and CN ages with stratigraphic information and refine our chronologies (Fig. 12 and Table 5). Figure 12 shows the probability distributions for the OSL and CN boulder ages. CN ages for PB4 and PB5 have been excluded from the analysis because their ages represent clear outliers. Boundaries on rockfall events have been

Boulder/ Trench	Unit	Sediment accumulation rate	Luminescence and radiocarbon samples used for rate determination	Time between bracketing samples	Measured stratigraphic thickness between samples
		(mm/a)		*(a)*	*(mm)*
PB2	LC	*Upper LC* 0.23±0.02	ROSL-03; Existing ground surface (t=0)	2800±300	640
		Lower LC 0.07±0.02	ROSL-04; ROSL-03	4900±1100	360
PB3	LC_R	2.21±0.39	RAP-CH01; Existing ground surface (t=0)	~249±44*	532
	LC	0.05±0.01	ROSL-08; RAP-CH01	2651±344	128
PB4	LC_R (?)	3.26±1.76	RAP-CH06; Existing ground surface (t=0)	~141±76*	326
	LC	0.12±0.015	ROSL-10; RAP-CH06	4059±476	497
	LC (assuming no LC_R deposition)	0.22±0.02	ROSL-10; Existing ground surface (t=0)	4200±400	926
PB5	LC	0.18±0.02	ROSL-13 & Existing ground surface (t=0)	1700±200	304

Quartz luminescence ages used to determine sediment accumulation rate; *ages from radiocarbon dating of charcoal samples

Table 4. Summary of sediment accumulation rates in post-boulder emplacement colluvial sediments, including sample name and ages used for rate determination, and measured stratigraphic thickness between samples. Quartz OSL ages used to determine approximate sediment accumulation rates. 2σ calibrated highest probability ranges (Table 2) used to estimate age and determine sediment accumulation rates for RAP-CH01 and RAP-CH06.

identified using the priors that the upper and lower boundaries must encapsulate the CN age of the boulder (where it is not an outlier); and be less than and greater than the overlying and underlying OSL sediment ages, respectively. PB2 and PB3 rockfall event minimum and maximum boundary 2σ ages do not overlap and define two distinct rockfall events at 7.0-13.5 ka (Red = E1) and 2.7-6.7 ka (Blue = E2), respectively (Fig. 12). PB4 and PB5 rockfall event boundary distributions are similar and display statistical overlap with E1 and E2, but show slightly stronger agreement with E2, suggesting PB3, PB4, and PB5 could have been emplaced at the same time. We are unable to more accurately constrain the emplacement timing of PB4 and PB5 based upon the OSL ages.

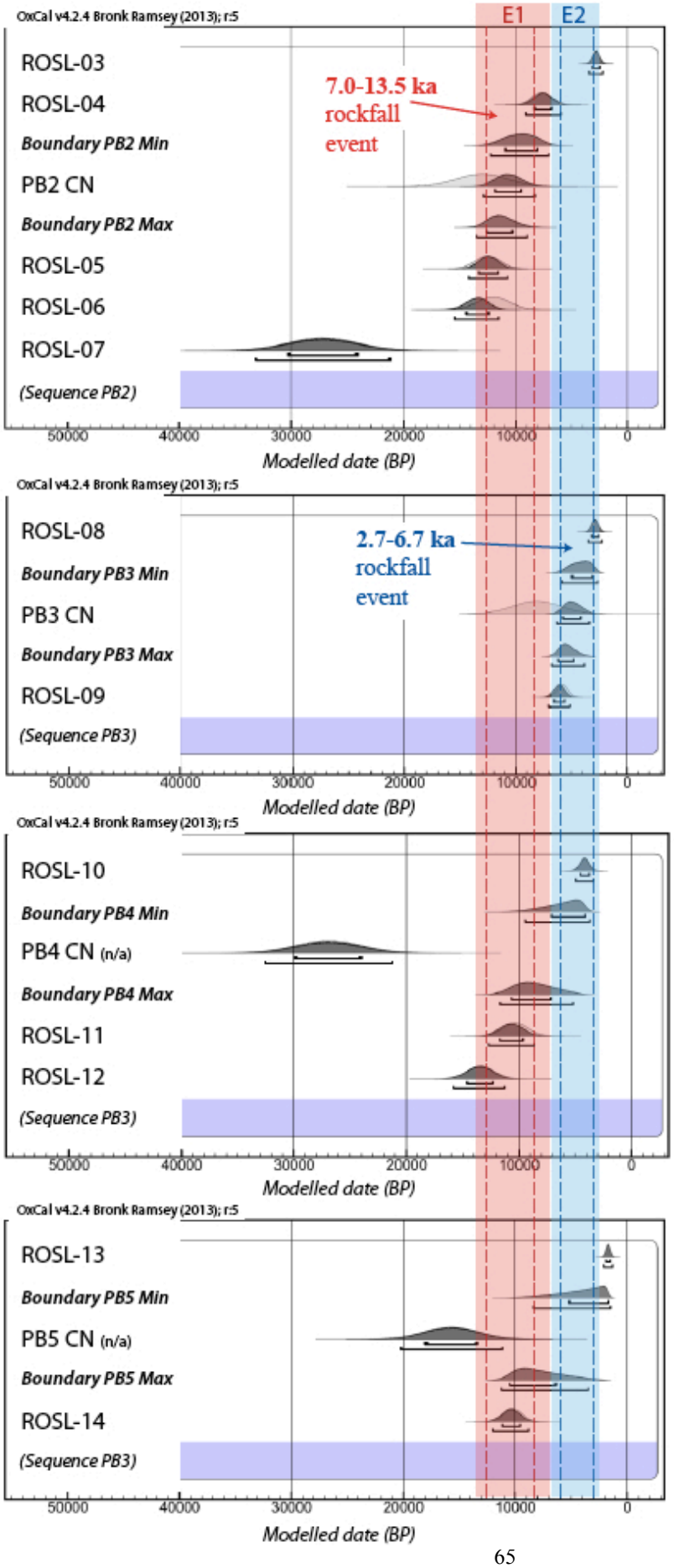

Figure 12. Bayesian modeled probability distributions (using OxCal) for luminescence and CN ages. PB2 and PB3 2σ minimum and maximum boundary ages do not overlap and define two distinct rockfall events at 7.0-13.5 ka (Red = E1) and 2.7-6.7 ka (Blue = E2), respectively. Vertical red and blue dashed lines represent 1σ PB2 and PB3 minimum and maximum boundary ages, respectively. PB4 and PB5 boundary distributions are similar and display statistical overlap with both events, but show slightly stronger agreement with E2, suggesting PB3, PB4, and PB5 could have been emplaced at the same time.

Name	Unmodeled (BP)						Modeled (BP)					
	from	to	%	from	to	%	from	to	%	from	to	%
Sequence PB2												
ROSL-03	3101	2500	68.2	3400	2200	95.4	3103	2503	68.2	3402	2205	95.4
ROSL-04	8500	6900	68.2	9296	6104	95.4	8324	6734	68.1	9087	5974	95.4
Boundary PB2_min							10943	8072	68.2	***12206***	***7023***	***95.4***
PB2CN	15300	10701	68.2	17590	8410	95.4	11858	9514	68.2	12864	8302	95.4
Boundary PB2_max							12583	10288	68.2	***13511***	***8964***	***95.4***
ROSL-05	13600	11400	68.2	14695	10305	95.4	13332	11595	68.2	14170	10719	95.4
ROSL-06	13400	10600	68.2	14795	9205	95.4	14427	12363	68.1	15476	11554	95.4
ROSL-07	30198	24203	68.2	33186	21215	95.4	30273	24115	68.2	33156	21218	95.4
Sequence PB3												
ROSL-08	3201	2600	68.2	3500	2300	95.4	3166	2557	68.2	3455	2265	95.4
Boundary PB3_min							4989	3085	68.1	***5850***	***2663***	***95.4***
PB3CN	10200	6000	68.2	12290	3910	95.4	5768	4165	68.3	6327	3362	95.4
Boundary PB3_max							6210	4749	68.2	***6726***	***3808***	***95.4***
ROSL-09	6300	5300	68.2	6799	4802	95.4	6574	5598	68.3	7040	5110	95.4
Sequence PB4												
ROSL-10	4600	3800	68.2	5000	3401	95.4	4542	3739	68.2	4930	3341	95.4
Boundary PB4_min							7063	4117	68.2	***9424***	***3695***	***95.4***
PB4CN	29798	24002	68.2	32687	21114	95.4	29896	23969	68.2	32559	21224	95.4
Boundary PB4_max							10642	7109	68.2	***11698***	***5165***	***95.4***
ROSL-11	11400	9200	68.2	12495	8105	95.4	11723	9643	68.1	12684	8616	95.4
ROSL-12	14600	12200	68.2	15795	11005	95.4	14616	12279	68.2	15783	11279	95.4
Sequence PB5												
ROSL-13	1901	1500	68.2	2100	1300	95.4	1889	1489	68.2	2089	1285	95.4
Boundary PB5_min							5196	1666	68.2	***8333***	***1468***	***95.4***
PB5CN	18000	13401	68.2	20290	11110	95.4	18088	13372	68.3	20267	11153	95.4
Boundary PB5_max							10475	6323	68.2	***11251***	***3475***	***95.4***
ROSL-14	11000	9400	68.2	11796	8604	95.4	11174	9587	68.2	11970	8804	95.4

Table 5. Summary of unmodeled and modeled ages for luminescence and CN surface exposure ages using Bayesian modeling facility of OxCal (v 4.2) (Ramsey, 2009). 2σ age ranges are highlighted (bold) for boundary minimum and maximum ages. Modeled CN ages for PB4 and PB5 have been excluded from the analysis (see Fig. 12) because they are inconsistent with the stratigraphy/OSL chronologies.

2.6 Discussion

2.6.1 Influence of prehistoric rockfall boulders on hillslope process and evolution

Our investigation suggests that the emplacement of large prehistoric boulders on the Rapaki hillslope has locally influenced sediment transport and soil development. We are unaware of any published study in New Zealand or elsewhere that examines this process in the level of detail presented within our study.

At the time loess accumulation ceased or dramatically slowed at ca 13 ka (see below), the hillslope at Rapaki shifted from being net aggradational to erosional. Coincident with this transition, soil evolution shifted from upbuilding during loess accumulation (Johnson and Watson-stegner, 1987; Johnson et al., 1987) to topdown (Almond and Tonkin, 1999) during downwasting (Fig. 13a). The (buried) soil in the top of the loess beneath each of the studied prehistoric boulders (PB-SSU) preserves the mobile colluvial biomantle (Johnson, 1990; Heimsath et al., 2001; Heimsath et al., 2002; Johnson et al., 2005) by which downwasting was achieved (Fig. 12a). Its morphology suggests a soil residence time (Almond et al., 2007a) in the order of many hundreds of years to millennia, and hence relative slope stability. We propose that the small percentage of coarser-grained volcanic sediment observed within PB-SSU was incorporated into the loess through a variety of surface hillslope transport processes (e.g. bioturbation, shallow debris and mud flows, local overland flow transport). Reworking of infilled desiccation cracks within the upper loess section for PB4 and PB5 supports our assertion that the PB-SSU was an active soil layer which underwent vigorous pedoturbation (Figs. 7c and 9b, c).

The emplacement of large prehistoric boulders on the Rapaki hillslope facilitated a return to localized aggradational hillslope process, by (1) creating accommodation space (i.e. sediment barrier/trap) for sediment accumulation and (2) effectively 'locking-in' or 'immobilizing' sections of the previously mobile soil layer (i.e. PB-SSU) lying directly below and upslope of the boulder (Fig. 13b). Once the boulder is emplaced and the underlying mobile soil layer 'fixed', sediment deposition may begin, with the rate of sediment accumulation depending on the boulder's topographic position, amount of available sediment, and the mechanism of deposition (e.g. mass wasting, creep, overland flow) (Fig. 13b). Soil evolution once again becomes upbuilding in character, although depositional events are more discrete and stochastic than the earlier loess upbuilding phase. The soil in colluvial wedge sediments upslope of the boulders is characterized by a series of stacked A-horizons with small rootlets and worm burrows evident throughout.

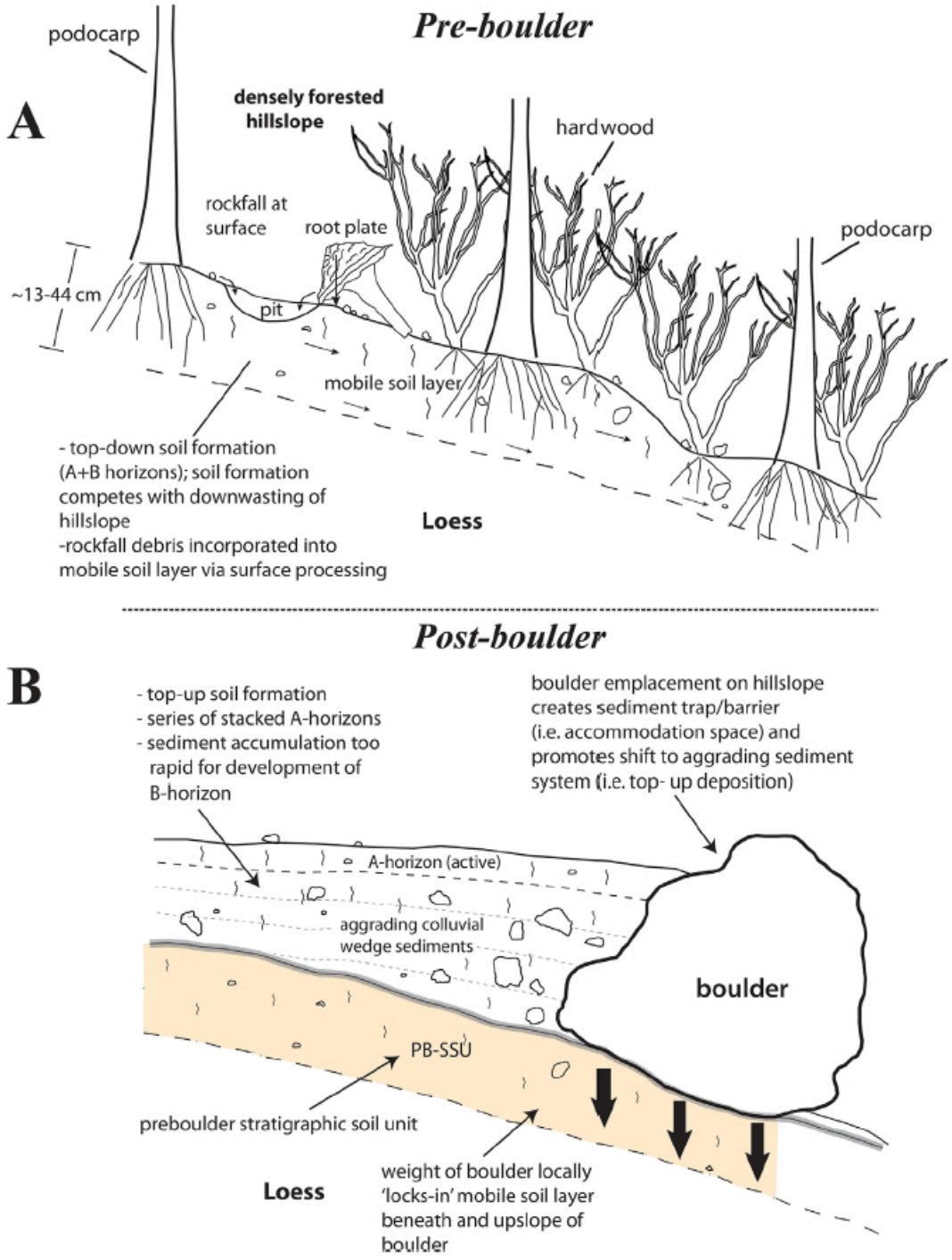

Figure 13. **(A)** Conceptual diagram for mobile soil layer before emplacement of large prehistoric boulder on Rapaki hillslope. Prior to boulder deposition, the local sediment system is degradational (i.e. dominated by creep and erosion). Top-down soil formation competes with hillslope downwasting. Soil flux and incorporation of coarse-grained volcanic rock into the physically disturbed soil layer presumably results from surface/subsurface processing including tree-throw, root growth, shallow mass wasting, and local overland flow process. **(B)** Conceptual diagram of post-boulder emplacement sedimentation and soil formation. Boulder emplacement on the hillslope creates two important conditions for accumulation (and preservation) of colluvial wedge sediments: (i) sediment trap/barrier (i.e. accommodation space) and (ii) locally 'locks-in' underlying mobile soil layer beneath and upslope of boulder. Locally, deposition of large boulder changes sediment system to aggradational. Soil development in PB-SSU stops with accumulation of the sediment behind the boulder. Soil formation behind the boulder is 'top-up' and consists of a series of stacked A-horizon. Sediment accumulation is rapid enough to inhibit B-horizon development.

The absence of B horizons indicates a relatively rapid rate of accumulation so that upbuilding was effectively retardant (Johnson and Watson-stegner, 1987).

We propose that the combined influence of boulders (and associated smaller sized rockfall debris) on hillslope process and resulting surface morphology may be underestimated, particularly in middle to upper slope positions, where spatial density of rockfall is high. Field observations reveal hummocky terrain in middle and upper slope positions that could be attributed to a combination of surficial landsliding and creep. However, we speculate that this geomorphic signature may be at least partially influenced by abundant prehistoric boulders lying beneath and at the surface. Build-up of sediment behind boulders and erosion adjacent to boulders could conceivably create a similar morphological pattern. Further surface and subsurface investigation is required to determine the influence that boulders have on hillslope process and geomorphic pattern.

2.6.2 Summary of landscape evolution at Rapaki

Based on a synthesis of the OSL age distributions from loessic sediments, our favored hypothesis is that loess accumulation occurred in at least some areas of the study site until ca 12-13 ka at the earliest. ROSL-06 is located within the in-situ loess at a depth of ~30 cm below the paleo-ground surface and yields an age of 12.0±1.4 ka (Figure 5). ROSL-05 is located near the top of the loess section (above ROSL-06) within PB-SSU and yields a statistically overlapping age of 12.5±1.1 ka (Figure 5). ROSL-12 within PB4 PB-SSU yields a statistically overlapping age of 13.4±1.2 ka. How much later loess accumulation continued is indeterminate from our work because the resulting deposits may have been eroded. Although Almond et al. (2007b) report an IRSL age of 1,860 years in the upper 40 cm of loess at Ahuriri Quarry, this age is likely to be much younger than the depositional age because of post-depositional bleaching during bioturbation and hillslope soil transport. The sources for the loess of Banks Peninsula are the outwash plains of the major rivers to the west that flow across the Canterbury Plains. The closest currently is the Rakaia River, which began its incision about 13 ka. The timing of incision comes from a thermoluminescence age from the base of loess above outwash gravels (Berger et al., 1996). This loess thins rapidly away from the Rakaia River to the south (Ives, 1973) forming a local loess wedge. The incision of the Rakaia River, if synchronous with the other glacially fed rivers of the plains, is therefore likely to mark the beginning of a period of much reduced loess flux.

It is possible the younger luminescence ages within PB-SSU (e.g. ~10 ka ages – ROSL-11, ROSL-14) reflect loess depositional ages or near surface reworking (e.g. bioturbation, tree throw, pedogenic

mixing) of the ~12-13 ka and older loess. Although the consistency between quartz and feldspar suggests (see Table 1, Fig. 11, and Sohbati et al., in press) these may reflect *in-situ* accumulation ages, we cannot dismiss the possibility that they result from resetting of the luminescence signal during near surface mixing. Further investigations involving single grain luminescence methods would be required to resolve whether these reflect deposition ages or not. With regard to ROSL-09 (5.8±0.5 ka), there are 3-dimensional stratigraphic complexities (i.e. a possible undulating PB-SSU/LC contact) that mean we cannot exclude the possibility that sampling punctured through the PB-SSU layer into LC. Hence, we cannot dismiss the possibility that OSL sampling represents a mixture of PB-SSU and LC sediments, and as a result we cannot be confident that this age is a meaningful loess depositional age.

Latest loess accumulation and earliest deposition of loess colluvium (LC) is separated by a depositional hiatus (disconformity) ranging from ~3 to 9 ky, suggesting multi millennial-scale time periods of non-deposition and/or erosion on the Rapaki landscape. Earliest onset of loess colluvium deposition behind the studied prehistoric boulders ranges from ~7.7 to ~1.7 ka (mid-Holocene), with accumulation and preservation contingent upon boulder presence.

We observe a significant pulse of sedimentation (behind PB3 and PB4) that occurs synchronously with human arrival and residence in the study area. We attribute this sediment increase to anthropogenic deforestation sometime between AD 1661 and AD 1950 (2σ calibrated age ranges), which destabilized the land surface and facilitated more hillslope erosion and re-deposition of sediment. Although we cannot rule out natural fire as cause of deforestation, the onset of increased colluvial sedimentation during the period of local human colonization, widespread evidence for anthropogenic deforestation elsewhere in the region, and absence of modern forest cover suggests human sustainment of an unforested landscape since the 17th to earliest 20th century (Borella et al., 2016). Similar responses to deforestation have been observed at other sites in New Zealand (e.g. Kettner et al., 2007; Kasai, 2005) and globally (e.g. Syvitski et al., 2005).

2.6.3 Temporal constraint of boulder emplacement using OSL method

Optical dating of loessic hillslope sediments can be used to successfully constrain timing of prehistoric boulder emplacement (Sohbati et al., in press), which, under certain circumstances may be used as a proxy for timing of prehistoric earthquakes (Mackey and Quigley, 2014). We are aware of only a handful of published studies globally (e.g. Chapot et al., 2012; Matmon et al., 2005; Rinat et al., 2014) that use OSL dating of hillslope sediments to date prehistoric rockfall events. These studies focus on OSL dating of sediments either below or behind the rockfall boulders (in support of other dating techniques; e.g.

radiocarbon, CN exposure dating), but do not combine OSL dating of both pre- and post-boulder fall sediments (for a single boulder) to constrain emplacement timing. At Rapaki, the influx of loessic sediments into the hillslope system (primarily during the Pleistocene) provides a significant volume of sediment for remobilization and eventual deposition behind rockfall boulders. At Rapaki, temporal constraints using the OSL method are controlled by two primary factors: (1) The timing of boulder emplacement and (2) the episodic and spatially irregular nature of hillslope sedimentation.

Luminescence ages within PB-SSU provide estimates of maximum boulder emplacement age. Determining the amount of time elapsed between PB-SSU deposition and boulder emplacement on top of PB-SSU (i.e. paleo-ground surface) is difficult. Sediments accumulated upslope of the boulder provide a minimum age for boulder emplacement because their deposition (and preservation) can occur only once the boulder is present. However, sediment accumulation may significantly postdate boulder emplacement. If sediment accumulation occurs during or shortly after boulder emplacement, then luminescence ages within the lowest LC sediments provide the best estimate of the timing of boulder emplacement. At Rapaki, maximum and minimum bounding OSL ages suggest there are long periods of non-deposition and erosion on the hillslope, ranging from ~3-9 ky in the boulder locations.

The temporal resolution for boulder emplacement timing could possibly be improved by sampling sediments closer to the PB-SSU contact (i.e. prehistoric boulder emplacement surface), although sampling near a former surface may be problematic because of bioturbation. Our results indicate areas that are topographically high (i.e. divergent zones) and receive low sediment input, are less desirable (e.g. PB5 location) for using luminescence dating to constrain the timing of boulder emplacement. Boulders located in drainage valleys/gullies (i.e. convergent zones) should be avoided because of potential boulder mobility issues and depositional complexities (i.e. frequent deposition and removal of sediment behind boulders).

We note that OSL dating of infill sediments behind prehistoric boulders could provide an independent method for constraining major prehistoric shaking events, as it is difficult to envisage a cause other than earthquakes (Khajavi et al., 2012) for episodic displacement (albeit small) of such large boulders. Assuming each of the infills is related to a seismically induced displacement, PB2 (see Fig. 5b, c) may potentially record two separate shaking events (i.e. 2011 and a previous prehistoric shaking episode).

2.6.4 Summary and comparison of OSL and CN ages

When the entire suite of OSL ages across the study site are considered and compared to the corresponding suite of CN ^{3}He boulder exposure ages, several general interpretations can be drawn. PB2, PB4, and PB5 overlie loessic sediment that yields OSL ages of ~10.2-12.5 ka, suggesting that boulder emplacement occurred during or after this time. The development and disturbance of a paleosol at the top of the loessic sediments (and beneath the boulders) favors the interpretation that boulder deposition occurred *after* loessic sediment aggradation had ceased on the hillslope; we cautiously infer that 100s to 1000s of yrs would have been required to develop the paleosol in the PB-SSU unit before the boulders were emplaced. Given our lack of confidence in the interpretation of the ROSL-09 sample age (see above) we are reluctant to constrain the maximum emplacement age of PB3 using the ~5.8 ka OSL age. We are similarly cautious about using the OSL age from beneath PB1 alone to constrain the timing of boulder emplacement beyond the conclusion that PB1 was emplaced after 29.3 ka. OSL ages of sediment accumulated upslope of the boulders range from ~7.7 to 1.7 ka; when considered collectively, these data imply that boulders were emplaced before this time.

The corresponding CN ^{3}He ages from all boulders are significantly older than all of the OSL ages for underlying sediment with the exception of PB2, where CN and OSL ages are within error, and PB1. This relationship of older CN ^{3}He-derived emplacement ages for boulders sitting above younger OSL ages is inconsistent with stratigraphic superposition and requires either that the OSL ages are younger than the true depositional age of the loessic sediment (e.g. Grapes, 2010a, b; Almond, 2007b), that the CN ages are older than the true timing of boulder emplacement (e.g. Mackey and Quigley, 2014), or both. Our confidence that the majority of OSL ages are robust representations of the depositional ages of the sampled sediment is increased by the inter-site age consistency for stratigraphically equivalent sediments, the intra-site adherence of OSL ages to stratigraphic position, and the consistency between quartz OSL and K-feldspar $pIRIR_{290}$ ages (Sohbati et al., in press). Conversely, in consideration of the entire suite (n=19 boulders) of CN ages from the study site, Mackey and Quigley (2014) concluded that a major rockfall event occurred between ca. 6 to 8 ka, with a possible precursor event at ca. 13 to 14 ka, and that older CN ages were interpreted to reflect inherited CN concentrations that accumulated in boulder surfaces prior to boulder emplacement.

In consideration of these data, we favor the interpretation that PB4 (CN age ~26.9 ka) and PB5 (~15.7 ka) contain significant inherited CN ^{3}He, and that the best temporal constraints on boulder emplacement age are provided by Bayesian modeling of OSL ages from the bounding sediments (Fig. 12). We favor an emplacement age closer to the central *PB4 Min* (~5 to 7 ka) and *PB5 Min* (~2-6 ka) estimates

(Fig. 12) for the reasons described above, however we cannot absolutely resolve these emplacement ages to this temporal resolution, and boulder emplacement any time after ~10 ka and before 2-4 ka is permissible.

CN ^{3}He ages from PB1 (~11.8 ka) and PB2 (~13 ka) are consistent with OSL ages of the bounding strata. Although ^{3}He inheritance cannot be excluded as influencing age distributions, particularly in the case of PB2 (where the central ^{3}He age is slightly older than the central ages of the underlying loess) we have no evidence to explicitly discredit the CN ages as a proxy for the timing of boulder emplacement. These ages were recorded elsewhere on the study slope and provide tentative evidence for boulder emplacement at ~12-14 ka (Mackey and Quigley, 2014).

Since we are uncertain about the meaningfulness of the ROSL-09 age, we are unable to evaluate the ~8 ka CN ^{3}He age for inheritance. If the ROSL-09 age represents the depositional age of the sediments underlying PB3, then PB3 is likely to have some ^{3}He inheritance, and if the ROSL-09 age underestimates the depositional age of this sediment, then the PB3 age could represent the timing of boulder emplacement age (or not). The occurrence of other ~6 to 8 ka CN ages at the study site suggests that the PB3 ^{3}He age could provide a reasonable estimate for the timing of boulder emplacement.

The proposed ~6-8 ka and possible 13-14 ka timings of major rockfall events at the study site (Mackey and Quigley, 2014) are not invalidated by the OSL ages. In some cases the OSL dating and stratigraphic mapping supports the proposed timing of these rockfall events. Further coupled analyses of rockfalls and hosting sedimentary sequences throughout this region would be required to further test the validity of this hypothesis. Clearly, this study illustrates both the opportunities and challenges of constraining the timing of rockfall events and hillslope sedimentation in this setting. Similar challenges will exist in analogous settings elsewhere.

2.7 Conclusions

Optical and radiocarbon dating of loessic hillslope sediments enables evaluation of the timing of prehistoric rockfall and provides a reliable temporal framework for the evolution of loess mantled hillslopes at Rapaki (NZ). Under certain circumstances, our approach may be used to date earthquake-triggered rockfalls and hillslope responses to seismic and anthropogenic influence elsewhere in New Zealand and globally. Rockfall boulders preserve an important record of Holocene hillslope soil transport, and influence local hillslope morphology and soil evolution. In this instance, stratigraphic analysis and OSL dating have provided greater confidence in some previously obtained boulder emplacement ages (derived from CN ^{3}He) and have helped to recognize which CN ^{3}He ages are most likely to overestimate boulder emplacement timing due to CN inheritance. Sediment accumulation rates increased (>~10x) following human arrival and associated anthropogenic burning of slope vegetation. Field observations and luminescence ages suggest boulder emplacement and deposition of loess colluvium did not occur concurrently and probably result from different causal mechanisms, implying that seismologic and meteorological phenomena play different roles in shaping the modern landscape. Our study highlights the importance of understanding the roles of earthquakes and humans on surface processes.

2.8 Acknowledgements

Financial support for the project came from the EQC (Earthquake Commission) capability fund for South Island geohazards research. JB thanks Jarg Pettinga, David Bell, Sam Hampton, Maxwell Borella, and Simon Brocklehurst for field assistance and/or insightful discussions related to Banks Peninsula geology. RS thanks the Carlsberg Foundation for financial support (Grant no. 2012_01_0838) during the project. The authors declare that they have no competing interests.

2.9 Appendix 1: Supplementary Figures and Tables

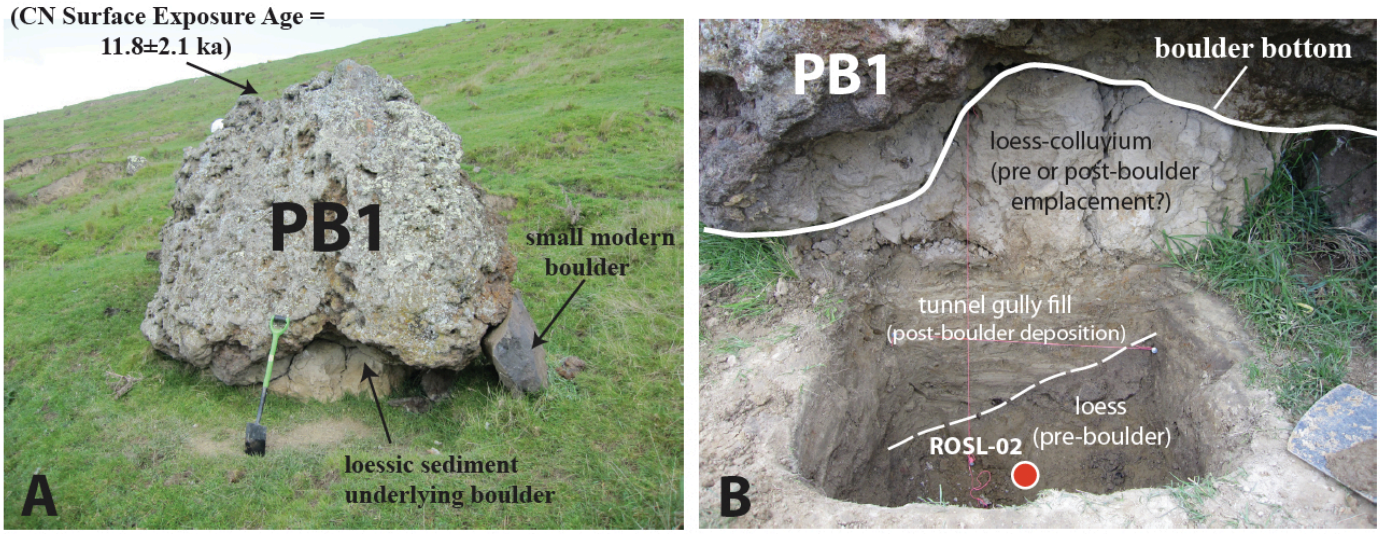

Supplementary Figure 1. (A) Photo of PB1 prior to exploratory trenching. **(B)** Photo of PB1 with underlying loessic sediments exposed. An OSL sample (shown) was retrieved within the *in-situ* loess and yields a quartz OSL age of 29.3±2.5 ka (see Table 1). PB1 is located in an area of active tunnel gully erosion and deposition, and highlights the potential depositional complexities associated with prehistoric boulders on the Rapaki hillslope. Recent tunnel gully fill is found underlying PB1 and older loess deposits.

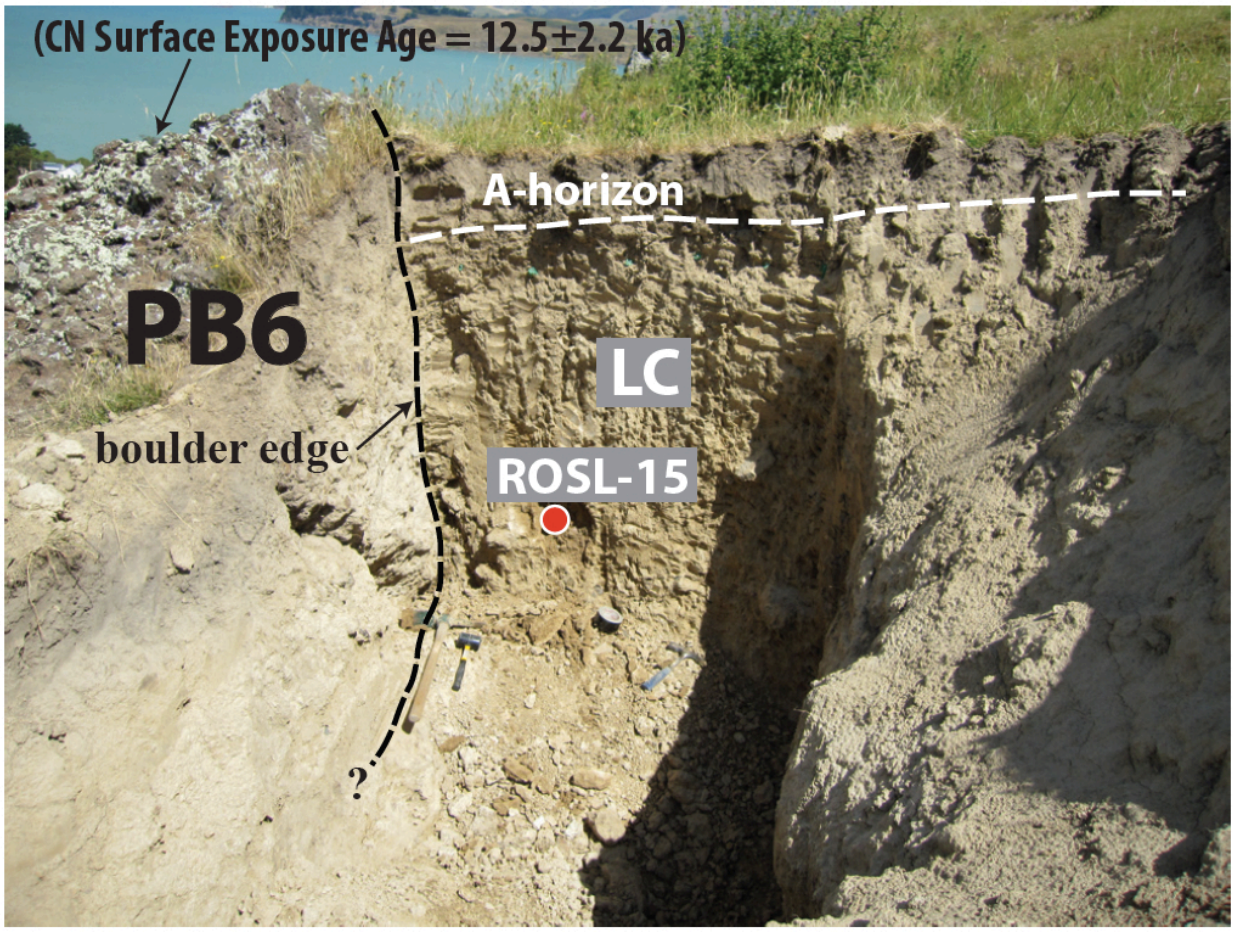

Supplementary Figure 2. Photo of PB6 and adjacent (upslope) exploratory trench. Due to safety concerns, we were unable to expose the boulder base and identify the boulder emplacement surface. OSL sample location (ROSL-15; red circle) shown - sample not dated. PB6 is located within the axis of a drainage valley (see Figs. 2 and 3) - a zone of active erosion and sediment (and potentially boulder) remobilization. Large volcanic clasts are observed to bottom of trench, indicating deposition by possible debris and mudflow and/or high velocity water flow. PB6 CN surface exposure age shown at top.

Supplementary Figure 3 | Radiocarbon Calibration Report for Charcoal Sample RapCH-01

Rafter Radiocarbon
Calibration Report

NZA 56801
R 40527/1
Report issued: 29 Jun 2014

CONVENTIONAL RADIOCARBON AGE 203 ± 18 years BP

Calibrated with SHCal13 (Hogg et al., Radiocarbon 55(4):1889-1902, 2013).

CALIBRATED AGE in terms of confidence intervals

1 sigma interval is	1671 AD to 1684 AD	279 BP to 266 BP (14.0% of area)
	1730 AD to 1747 AD	220 BP to 203 BP (18.3% of area)
	1756 AD to 1783 AD	194 BP to 167 BP (27.3% of area)
	1796 AD to 1803 AD	154 BP to 147 BP (7.9% of area)
2 sigma interval is	1664 AD to 1698 AD	286 BP to 252 BP (22.8% of area)
	1724 AD to 1809 AD	226 BP to 141 BP (70.4% of area)
	1870 AD to 1876 AD	80 BP to 74 BP (1.0% of area)

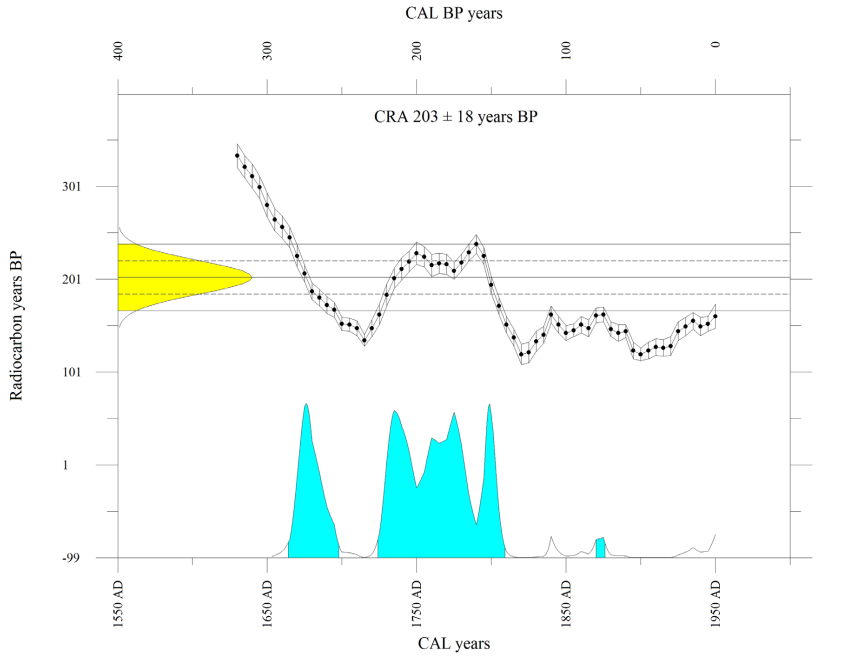

Calibration performed using Winscal v. 6.0 adapted from: Stuiver and Reimer (*Radiocarbon 35*(1): 215-230, 1993).

National Isotope Centre, GNS Science
PO Box 31-312 Lower Hutt, New Zealand Phone +64 4 570 4644
Email radiocarbon@gns.cri.nz Website www.RafterRadiocarbon.co.nz

Supplementary Figure 3. Radiocarbon calibration report for charcoal sample RapCH-01.

Supplementary Figure 4 | Radiocarbon Calibration Report for Charcoal Sample RapCH-03

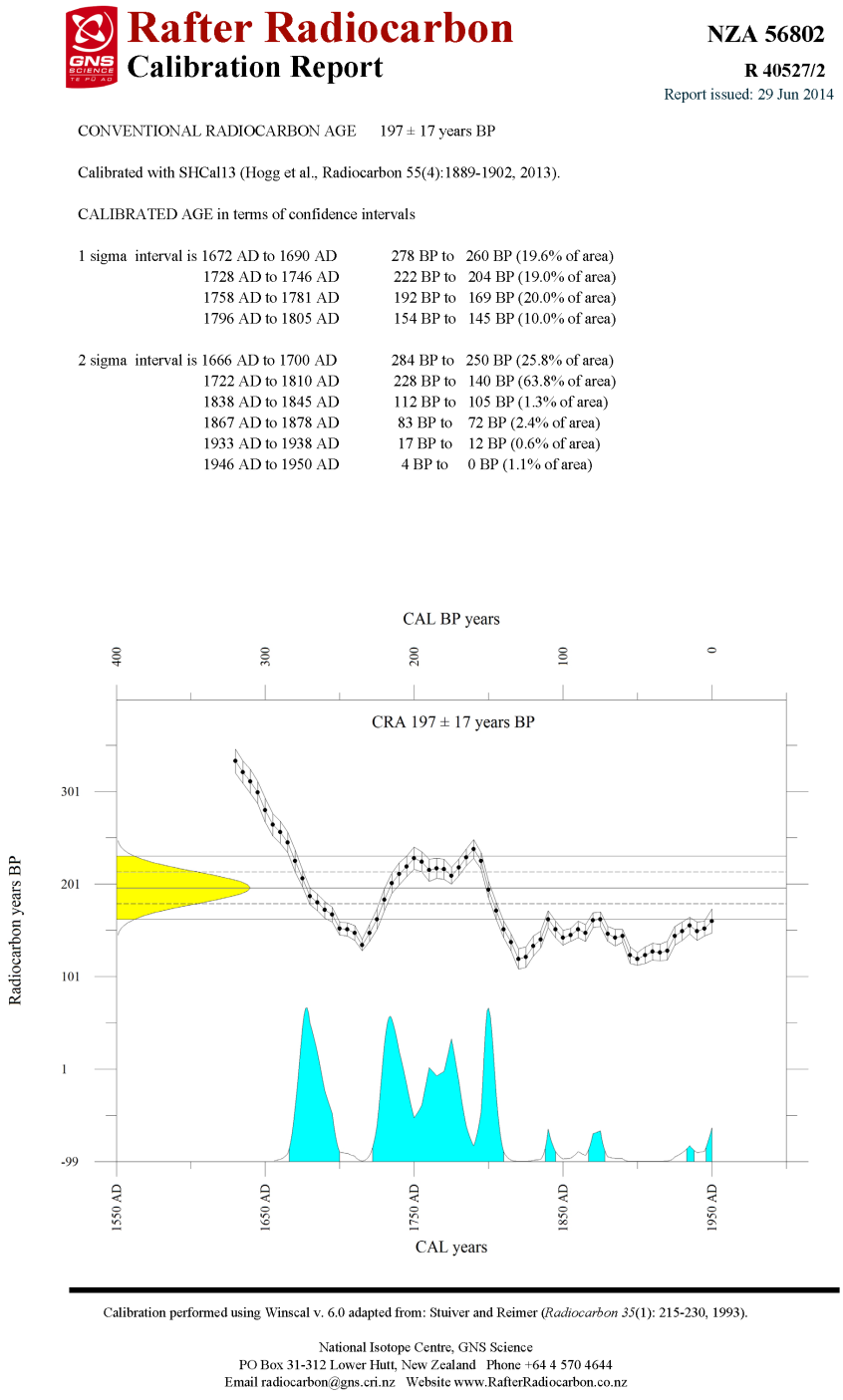

Rafter Radiocarbon
Calibration Report

NZA 56802
R 40527/2
Report issued: 29 Jun 2014

CONVENTIONAL RADIOCARBON AGE 197 ± 17 years BP

Calibrated with SHCal13 (Hogg et al., Radiocarbon 55(4):1889-1902, 2013).

CALIBRATED AGE in terms of confidence intervals

1 sigma interval is	1672 AD to 1690 AD	278 BP to 260 BP (19.6% of area)
	1728 AD to 1746 AD	222 BP to 204 BP (19.0% of area)
	1758 AD to 1781 AD	192 BP to 169 BP (20.0% of area)
	1796 AD to 1805 AD	154 BP to 145 BP (10.0% of area)
2 sigma interval is	1666 AD to 1700 AD	284 BP to 250 BP (25.8% of area)
	1722 AD to 1810 AD	228 BP to 140 BP (63.8% of area)
	1838 AD to 1845 AD	112 BP to 105 BP (1.3% of area)
	1867 AD to 1878 AD	83 BP to 72 BP (2.4% of area)
	1933 AD to 1938 AD	17 BP to 12 BP (0.6% of area)
	1946 AD to 1950 AD	4 BP to 0 BP (1.1% of area)

Calibration performed using Winscal v. 6.0 adapted from: Stuiver and Reimer (*Radiocarbon 35*(1): 215-230, 1993).

National Isotope Centre, GNS Science
PO Box 31-312 Lower Hutt, New Zealand Phone +64 4 570 4644
Email radiocarbon@gns.cri.nz Website www.RafterRadiocarbon.co.nz

Supplementary Figure 4. Radiocarbon calibration report for charcoal sample RapCH-03.

Supplementary Figure 5 | Radiocarbon Calibration Report for Charcoal Sample RapCH-05

Rafter Radiocarbon
Calibration Report

NZA 56803
R 40527/3
Report issued: 29 Jun 2014

CONVENTIONAL RADIOCARBON AGE 222 ± 17 years BP

Calibrated with SHCal13 (Hogg et al., Radiocarbon 55(4):1889-1902, 2013).

CALIBRATED AGE in terms of confidence intervals

1 sigma interval is	1669 AD to 1674 AD	281 BP to 276 BP (6.1% of area)
	1741 AD to 1787 AD	209 BP to 163 BP (55.5% of area)
	1793 AD to 1798 AD	157 BP to 152 BP (6.3% of area)
2 sigma interval is	1661 AD to 1680 AD	289 BP to 270 BP (15.8% of area)
	1732 AD to 1802 AD	218 BP to 148 BP (79.0% of area)

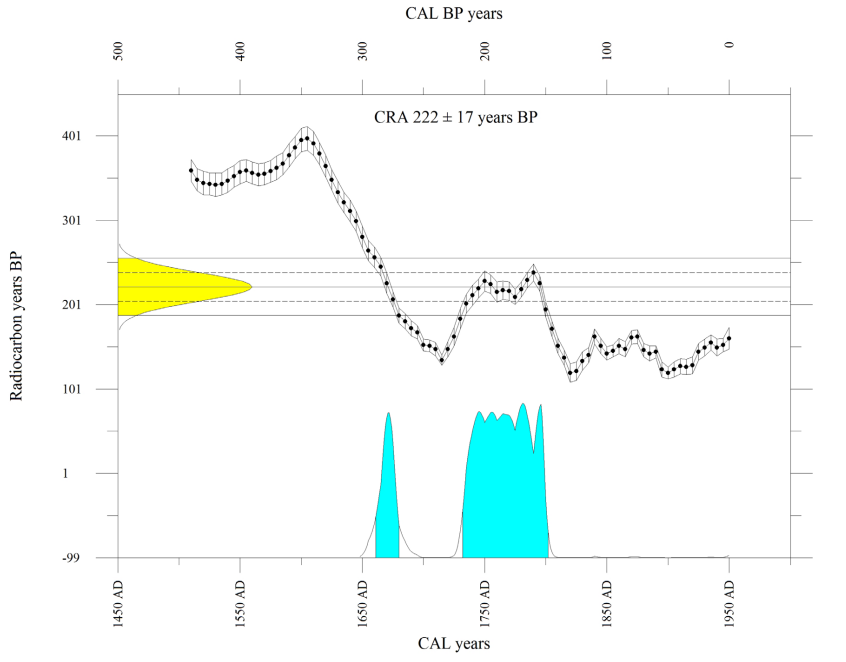

Calibration performed using Winscal v. 6.0 adapted from: Stuiver and Reimer (*Radiocarbon 35*(1): 215-230, 1993).

National Isotope Centre, GNS Science
PO Box 31-312 Lower Hutt, New Zealand Phone +64 4 570 4644
Email radiocarbon@gns.cri.nz Website www.RafterRadiocarbon.co.nz

Supplementary Figure 5. Radiocarbon calibration report for charcoal sample RapCH-05.

Supplementary Figure 6 | Radiocarbon Calibration Report for Charcoal Sample RapCH-06

Rafter Radiocarbon
Calibration Report

NZA 60079
R 40797/1
Report issued: 20 Oct 2015

CONVENTIONAL RADIOCARBON AGE 162 ± 22 years BP

Calibrated with SHCal13 (Hogg et al., Radiocarbon 55(4):1889-1902, 2013).

CALIBRATED AGE in terms of confidence intervals

1 sigma interval is	1687 AD to 1712 AD	263 BP to 238 BP (14.8% of area)
	1719 AD to 1729 AD	231 BP to 221 BP (5.8% of area)
	1804 AD to 1813 AD	146 BP to 137 BP (5.3% of area)
	1836 AD to 1884 AD	114 BP to 66 BP (26.2% of area)
	1889 AD to 1891 AD	61 BP to 59 BP (1.0% of area)
	1925 AD to 1950 AD	25 BP to 0 BP (15.1% of area)
2 sigma interval is	1677 AD to 1736 AD	273 BP to 214 BP (29.4% of area)
	1799 AD to 1950 AD	151 BP to 0 BP (65.7% of area)

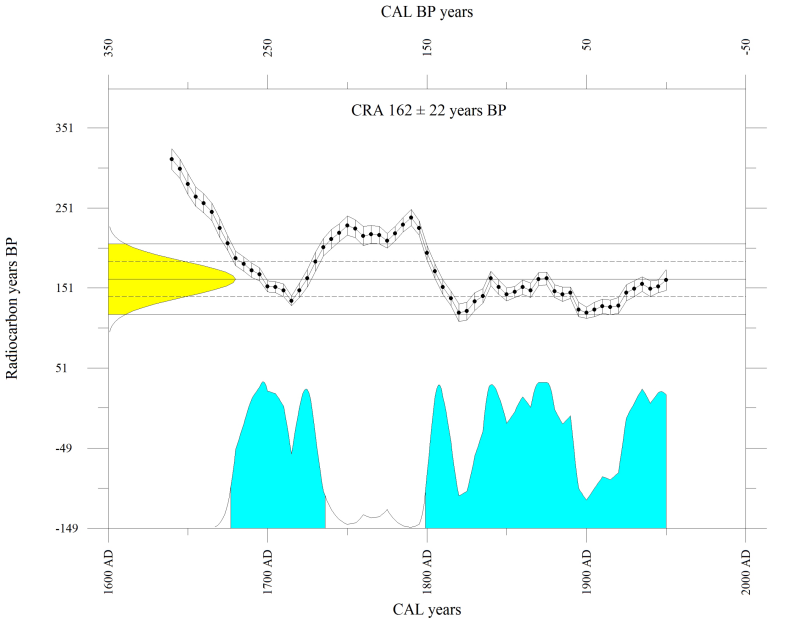

Calibration performed using Winscal v. 6.0 adapted from: Stuiver and Reimer (*Radiocarbon 35*(1): 215-230, 1993).

National Isotope Centre, GNS Science
PO Box 31-312 Lower Hutt, New Zealand Phone +64 4 570 4644
Email radiocarbon@gns.cri.nz Website www.RafterRadiocarbon.co.nz

Supplementary Figure 6. Radiocarbon calibration report for charcoal sample RapCH-06.

Boulder Name	Volume	Location	Elevation	Lithology	Rounding/ Shape	Lichen Cover	Colluvial wedge thickness
	(m^3)	(lat/long)	(m asl)				(cm)
PB2	12.7	-43.604/172.675	134	volcanic breccia basalt	subangular to subrounded/blocky equant	dense	125
PB3	14.5	-43.604/172.678	66	volcanic breccia basalt	subangular to subrounded/blocky equant	moderate to dense	70
PB4	24.8	-43.604/172.677	81	volcanic breccia basalt	subangular to subrounded/elongate to irregular	dense	107
PB5	7.3	-43.602/172.676	135	volcanic breccia basalt	subangular to subrounded/equant to slightly elongate	dense	50

Supplementary Table 1. Summary of boulder name, volume, elevation, lithology, rounding/shape, lichen cover (moderate to dense = 50-75% cover; dense = >75% cover), surface roughness (low, moderate, high reflects average surface amplitudes of ~<3 cm, ~3-6 cm, and ~>6 cm, respectively), and colluvial wedge thickness.

Unit	Granule (>2 mm) (%)	Sand (>63μm) (%)	Silt (>3.9μm) (%)	Clay (<3.9μm) (%)	% >106 μm (%)	% >212 μm (%)
PB2						
Loess	0	30	60	10	1	0.2
[1](PDP)	1	18	65	16	2-3	1-2
LC	[*]13	20	50	17	7-18	6-17
PB3						
Loess	0	36	51	13	1	0.2
(PDP)	1	27	57	14	2	1
LC	1	30	54	14	2	1
LC_R	1	23	63	12	2-3	1
PB4						
Loess	0	53	35	12	2	0.1
(PDP)	1	34	49	16	2	1
LC	2	22	57	19	3	1.5
PB5						
Loess	0	39	50	11	1	0.1
(PDP)	0	26	62	12	1	0.15
LC-2	0	32	55	13	4	3

*maximum % value reported; [1]PDP (physically disturbed paleosol) is a subunit of loess.

Supplementary Table 2. Summary of grain size distribution for PB2-PB5 Rapaki hillslope sediments.

Sample	Unit Name	Depth below ground surface	Cylinder Weight	Cylinder Height	Inner Radius of Cylinder	Cylinder + sample weight	Sample Weight	Cylinder Volume	Bulk Density
		(cm)	(g)	(cm)	(cm)	(g)	(g)	(cm^3)	(g/cm^3)
D01	LC	30	26.379	2.491	1.784	66.061	39.682	24.92	1.59
D02	LC	60	28.277	2.542	1.781	69.720	41.443	25.32	1.64
D03	LC	90	26.269	2.504	1.820	76.376	50.107	26.04	1.92
D04	*PDP	120	27.933	2.562	1.791	80.643	52.710	25.82	2.04
D05	Loess	150	27.361	2.510	1.784	75.827	48.466	25.10	1.93
D07	LC_R	26	26.336	2.495	1.786	58.035	31.699	25.00	1.27
D08	LC	57	27.797	2.513	1.783	64.905	37.108	25.08	1.48
D09	LC	72	26.145	2.489	1.783	65.720	39.575	24.84	1.59
D10	PDP	97	27.771	2.492	1.779	74.943	47.172	24.76	1.90
D11	Loess	120	27.465	2.523	1.788	78.294	50.829	25.33	2.01
D12	LC_R	30	28.039	2.552	1.742	67.594	39.555	24.32	1.63
D13	LC	57	27.526	2.469	1.780	67.930	40.404	24.56	1.64
D14	LC	85	27.771	2.520	1.775	76.122	48.351	24.93	1.94
D15	PDP	113	27.844	2.505	1.770	81.229	53.385	24.64	2.17
D17	LC	28	27.521	2.498	1.789	60.173	32.652	25.10	1.30
D18	PDP	56	27.771	2.220	1.776	67.999	40.228	22.00	1.83

*PDP = 'physically disturbed paleosol' developed in top section of loess

Supplementary Table 3. Bulk density for loess and loess-colluvial sediments at Rapaki, New Zealand.

CHAPTER 3.

CONTEMPORARY AND PREHISTORIC ROCKFALLS IN BANKS PENINSULA, NEW ZEALAND

3.1 Abstract

I performed extensive field mapping and characterization of 1733 individual prehistoric rockfall boulders at two study sites (Rapaki and Purau) in Banks Peninsula, New Zealand, to understand their origin, frequency, and spatial and volumetric distributions. Boulder characteristics and distributions are compared to 421 boulders deposited at the same sites during the 2010-2011 Canterbury earthquake sequence. The prehistoric boulders at both study sites are comprised of two dominant lithofacies types: volcanic breccia and massive (coherent) lava basalt. Volcanic breccia boulders are found in greatest abundance (64-73% of total mapped rockfall) and volume (~90-96% of total rockfall) at both locations and exclusively comprise the largest boulders with the longest runout distances that pose the greatest hazard to life and property. A comparison of maximum runout distance for modern and prehistoric boulders at Rapaki suggest a ~37% increase (modern=770 m; prehistoric=561 m) for modern boulder travel distance, while at Purau the difference is as high as ~420% (modern 344 m; prehistoric=66 m). The differences in runout distance are primarily attributed to anthropogenic deforestation, occurring coincident with Maori and/or subsequent European occupation sometime between AD 1661 and AD 1950, which enabled modern rockfall boulders to travel further than their prehistoric counterparts by reducing slope impedances. We propose that episodic earthquakes with similar strong ground-shaking characteristics to the 2011 Christchurch earthquakes (i.e. 22 February and 13 June events) are probably the main driver for rockfall flux in Banks Peninsula. Our study highlights the strong influence that volcanic lithofacies architecture has on rockfall hazard. Lava flow emplacement and cooling mechanics play a primary role in controlling the size and shape of rockfall boulders by creating texturally distinct volcanic lithofacies with variable rock strength properties and discontinuity patterns.

3.2 Introduction

Rockfall is a ubiquitous feature in mountainous and hilly regions worldwide (Evans and Hungr, 1993; Varnes, 1978; Guzzetti et al., 2003; Porter and Orombelli, 1981; Wieczorek, 2002; Wieczorek et al., 1999) and may provide a record of major seismic, climatic, and/or anthropogenic events (Keefer, 1984, 1994, 2002; Allen et al., 2011; Stock et al., 2014a, b; Borella et al., 2016). Many rockfall studies have focused primarily on historical (e.g. Wieczorek et al., 2004) and modern rockfall deposits (e.g. Massey et al., 2012, 2014) but the investigations of prehistoric rockfall (Bull and Brandon, 1998; Bull et al., 1994; Cordes et al., 2013; Costa and Gonzalez Diaz, 2007; Schuster et al., 1992) may also assist in characterizing the mechanisms and spatiotemporal distributions of rockfall to inform future rockfall hazard (Jibson, 1996; Solonenko, 1997a, 1977b; Nikonov, 1988; Mackey and Quigley, 2014).

In New Zealand's South Island, prehistoric rockfall studies have been conducted primarily in the Southern Alps (Bull and Brandon, 1998; Bull et al., 1994; Speight, 1929; Burrows, 1975; Whitehouse, 1981; Whitehouse, 1983; Whitehouse and Griffiths, 1983) where evidence of landsliding, including large rock avalanches, is extensive. However, surprisingly little research has been published on prehistoric rockfall elsewhere on the South Island (Mackey and Quigley, 2014; Townsend and Rosser, 2012; Borella et al., 2016a, b; Sohbati et al., 2016), including Banks Peninsula (Figs. 1 and 2), despite the presence of prehistoric rockfall and vulnerable source rock within and adjacent to cities and residential developments throughout the area (e.g. Massey et al., 2014; Heron et al., 2014).

The 2010-2011 Canterbury Earthquake Sequence (CES) dramatically highlighted the importance of mapping and characterizing prehistoric rockfall (Massey et al., 2014; Heron et al., 2014). During the CES, widespread rockfall and cliff collapse occurred in Banks Peninsula (Fig. 2), primarily in the Port Hills of southern Christchurch, causing 5 fatalities and extensive damage to homes and critical infrastructure (Massey et al., 2012; Massey et al., 2014). The majority of rockfall near Christchurch was caused by strong ground shaking from rupture on proximal blind faults. Mackey and Quigley (2014) proposed a strong (peak ground velocity >20 cm s^{-1}) shaking recurrence interval of ~7±2 ka for such events. Recent studies by Borella et al. (2016b) and Sohbati et al. (2016) using OSL and radiocarbon dating of hillslope sediments to constrain timing of rockfall events and associated shaking events are in general agreement and suggest a recurrence interval of ~3-7 ka. As a consequence of the long shaking recurrence interval, historical records provided no evidence of similar magnitude (i.e. size and spatial distribution) rockfall events to the 2011 Christchurch earthquakes (22 Feb and 13 June 2011) (Lundy, 1995). Historical records of rockfall in Christchurch indicate only small isolated events, with its occurrence primarily along the coast and attributed to storms, blasting by humans, or lower intensity earthquake-induced shaking episodes.

The geologic record provides clear evidence of large and abundant prehistoric boulders with similar characteristics and distributions to those deposited in the 2010-2011 CES. I propose that field mapping and detailed characterization of prehistoric rockfall can provide valuable site-specific data (i.e. range of boulder sizes and minimum runout distances) for understanding the potential rockfall hazard in these areas. Given the considerable damage to the city during the 2011 Christchurch earthquakes (e.g. Bannister and Gledhill, 2012), understanding the conditions of ground shaking and establishing recurrence intervals for shaking episodes of this magnitude represent a top priority.

Preliminary studies by Mackey and Quigley (2014), Borella et al. (2016b), and Sohbati et al. (2016) indicate that prehistoric rockfall (and associated seismic events) may be constrained temporally to provide important information on the likely causative process for rockfall deposition. However, the research is limited to a single study site (i.e. Rapaki, NZ). More extensive mapping of prehistoric rockfall (and source rock geology) in Banks Peninsula is required to understand the full extent of generated rockfall sizes and spatial distribution, evaluate seismicity as a primary cause of rockfall, and identify potential shaking epicenters (and possible fault sources). Continued mapping of prehistoric rockfall will also help identify boulders suitable for numerical dating (e.g. CN surface exposure, ^{14}C, OSL).

Here I investigate the origin, frequency, and volumetric and spatial distribution of prehistoric rockfalls (n=1733) at two locations (Rapaki and Purau) in Banks Peninsula, New Zealand (Figs. 3 and 4) and compare them with additionally mapped 2011 modern rockfalls (n=421) at these sites. This research provides the first regional investigation of prehistoric rockfall distributions in Banks Peninsula and outlines a methodology for establishing a robust paleo-rockfall data set for use in evaluating future rockfall hazard, establishing a regional shaking history, and revealing major tectonic and climatic events in the region. My study highlights the primary role that lava flow emplacement and cooling mechanics plays in controlling rockfall hazard (i.e. size and shape of rockfall boulders) by influencing the spatial distribution and density of structural discontinuities (i.e. joints) and creating distinct layer boundaries in the source rock.

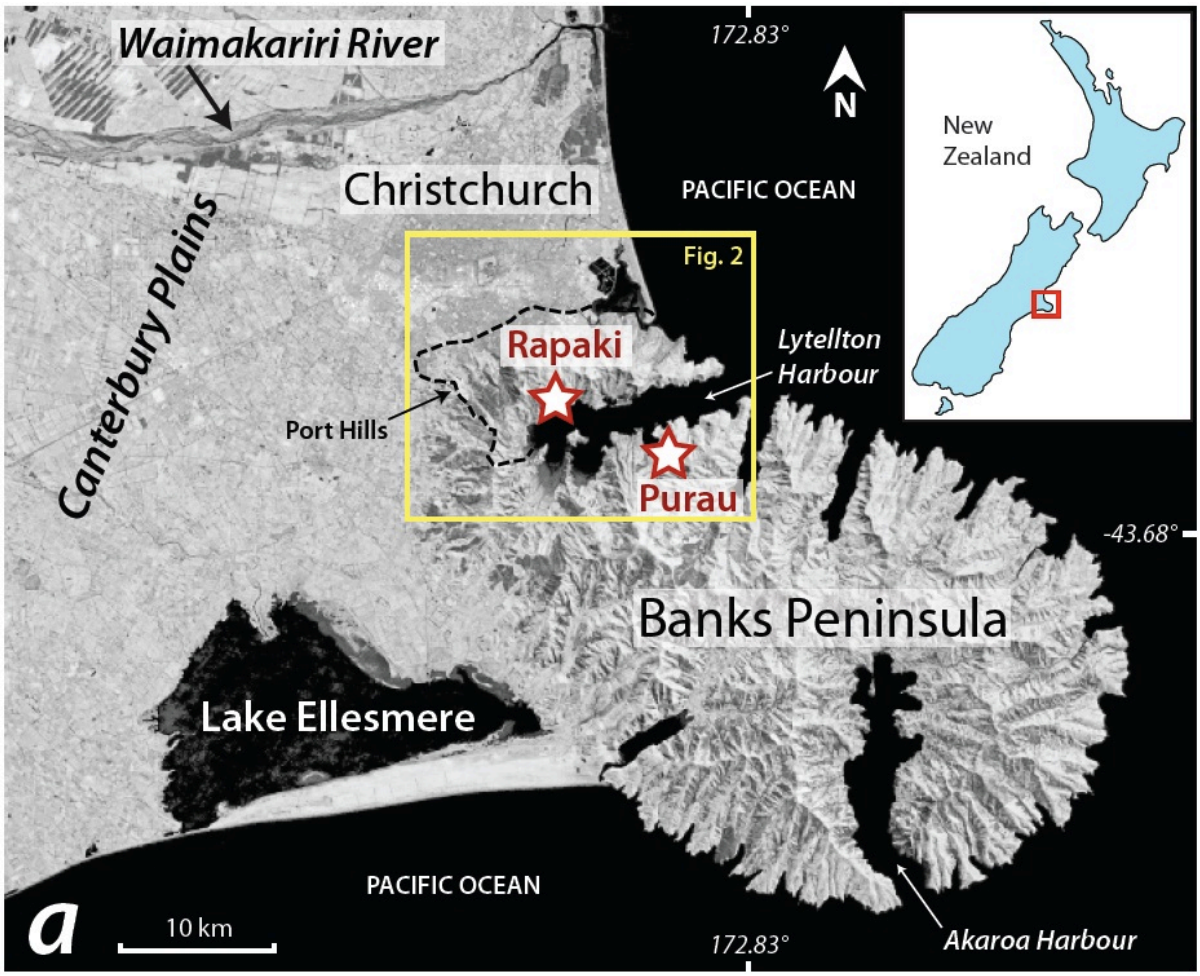

Figure 1. Location map showing Rapaki and Purau study sites and surrounding Port Hills and greater Banks Peninsula. Inset map of New Zealand shows area encompassing Christchurch and Banks Peninsula.

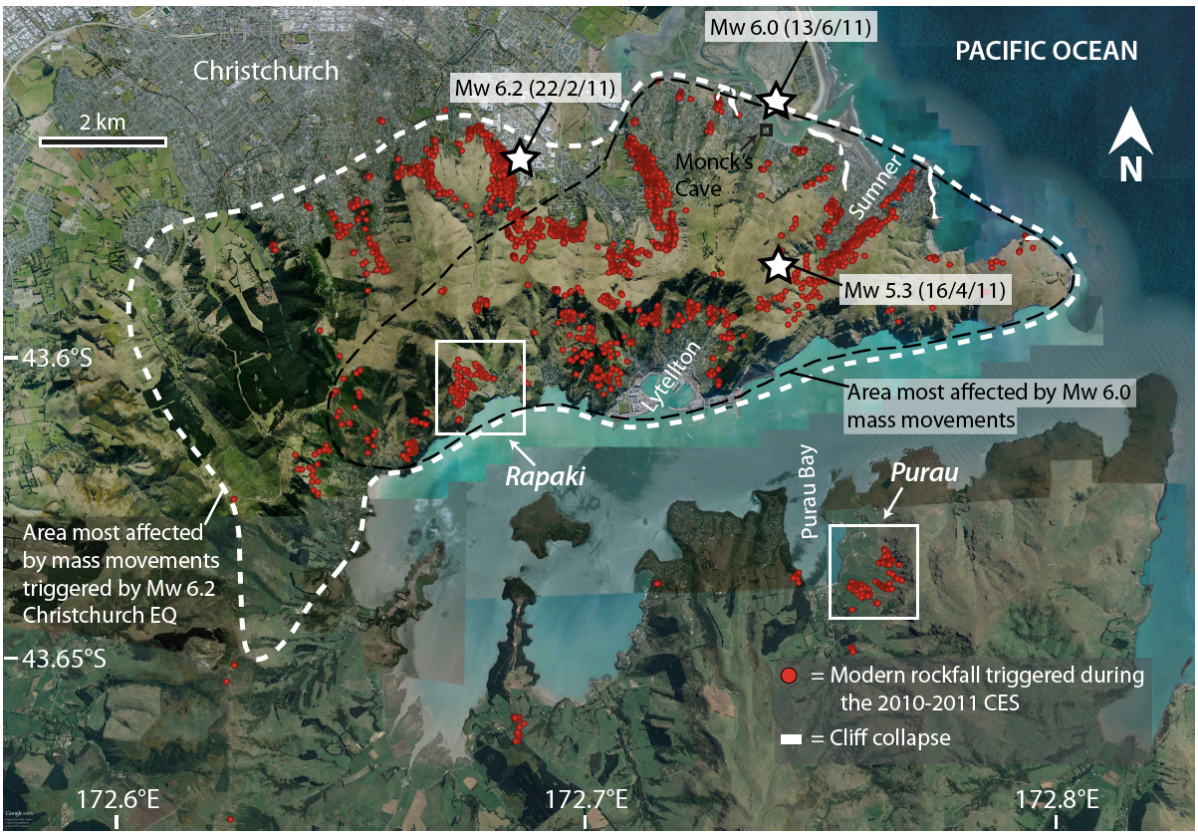

Figure 2. Google Earth image showing Rapaki and Purau study sites. Modern rockfall as mapped by GNS Science and the author (at Rapaki and Purau) is shown (red). White dashed line depicts the area most strongly affected by mass movements triggered by Mw 6.2 Christchurch EQ. Black dashed line shows area most strongly affected by Mw 6.0 mass movements. Epicenter locations for 22 February, 13 June, and 16 April 2011 events are displayed. Modified from Massey et al. (2014).

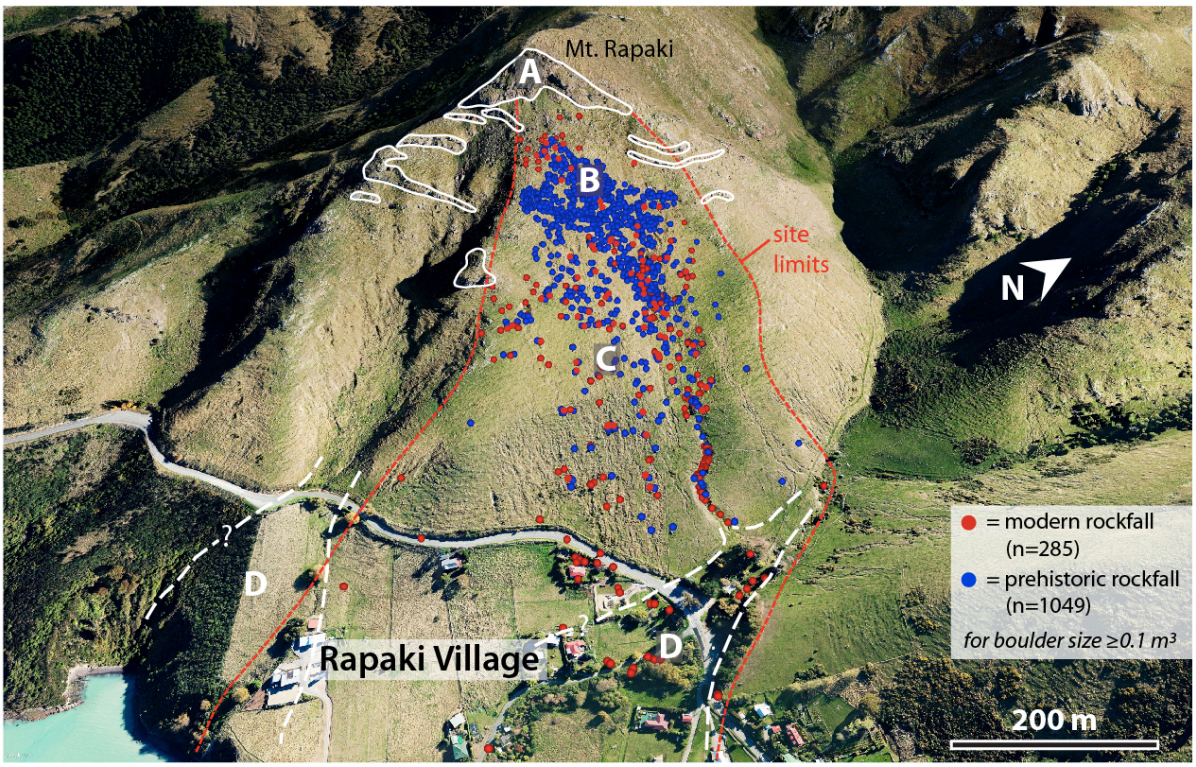

Figure 3. Rapaki study hillslope with mapped modern (n=285) (red) and prehistoric (n=1049) (blue) rockfall boulders. Boulders shown are for size ≥0.1 m^3. A=volcanic source rock; B=dominated by volcanic boulder colluvium and volcanic loess colluvium; C=loess colluvium underlain by in-situ loess and volcanic rock; D=alluvial sediments overlying loess and bedrock.

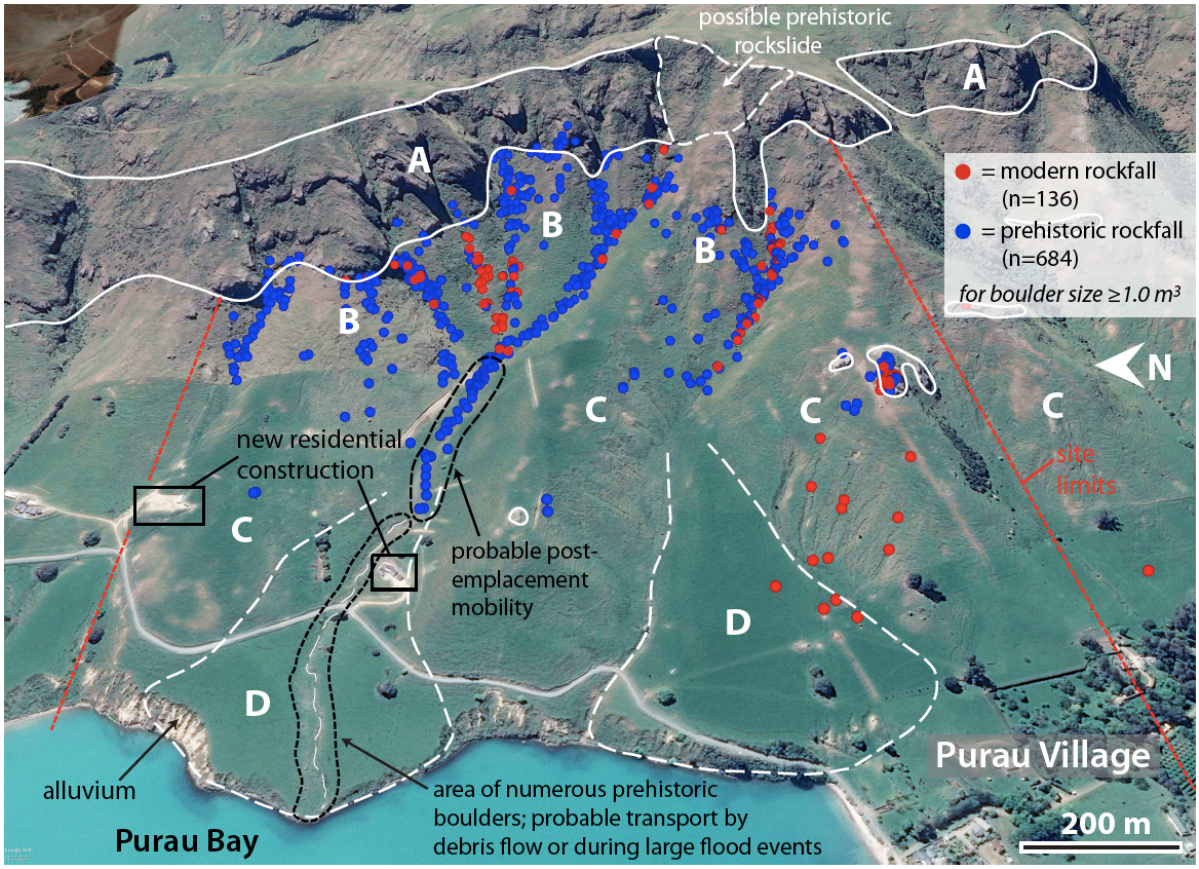

Figure 4. Purau study site with mapped modern (n=136) and prehistoric (n=684) rockfall boulders. Boulders shown are for size ≥1.0 m^3. A=volcanic source rock; B=dominated by volcanic boulder colluvium and volcanic loess colluvium; C=loess colluvium underlain by in-situ loess and volcanic rock; D=alluvial sediments overlying loess and bedrock.

3.3 Geologic Setting

Banks Peninsula, located on the east coast of New Zealand's South Island, is comprised of three main volcanoes (Lyttelton, Akaroa, and Mt. Herbert) active between 11.0 and 5.8 Ma (Hampton and Cole, 2009) (Fig. 1). The two study sites are located within the inner crater rim of the Lyttelton Volcanic complex (Figs. 1 and 2), the oldest of the volcanic centers and thought to be active from 11.0 to 9.7 Ma (Hampton and Cole, 2009). The Rapaki location is situated within the Port Hills of southern Christchurch, while the Purau study location is located approximately 5 kilometers to the southeast, across Lyttelton Harbour (Figs. 1 and 2).

Source rock at both sites is classified by Sewell (1988) and Sewell et al. (1992) as part of the Lyttelton Volcanic Group (LVG) and consists of basaltic to trachytic lava flows interbedded with breccia and tuff (Mvl). Numerous dikes and minor domes are observed within the LVG. Our field observations support the reported lithologic equivalence for the two study locales. The inferred strike and dip for lava flows nearest to the Rapaki and Purau study sites indicates a shallow inclination in a predominantly northerly direction for measurements nearest the Rapaki and Purau study sites (Hampton and Cole, 2009). Sewell et al. (1992) reports a similar shallow northerly to northwesterly dip of 12° for lava flows nearest Rapaki.

The study sites were selected because both have abundant prehistoric and modern (2011) rockfall boulders derived from lithologically equivalent volcanic source rocks. Rapaki represents a case study location proximal (epicenters <3 km) to the 2011 Christchurch earthquakes, while Purau lies further away, approximately ~7.5 km to the southeast.

3.3.1 Rapaki study site

The Rapaki study site is situated within the Port Hills of southern Christchurch (Figs. 2 and 3) on the southeastern slope of Mount Rapaki (Te Poho o Tamatea), which has a summit height of ~400 meters. The study hillslope is slightly concave to planar with a total area of ~0.21 km^2 and faces to the east-southeast. The source zone consists of steep to subvertical bedrock cliffs composed of stratified basaltic lava and indurated auto-breccia or pyroclastic flow deposits (Fig. 3). Breccia layers are thicker (~3-10 meters) and jointing is more widely spaced (often >10 m). Massive (or coherent) lava layers are comparably thin (<3 meters) and joints are more closely spaced (generally <1 meter). Total height and length of the source rock are ~60 meters and ~300 meters, respectively. Below the source area is a ~23°, grassy hillslope composed of windblown sediment deposits (loess), loess and volcanic colluvium, and overlying rockfall boulders (both modern and prehistoric) (Bell and Trangmar, 1987). Rapaki village lies at the hillslope base, at elevations ranging from ~70 meters (asl) to sea level (Fig. 3). Anthropogenic

deforestation has exposed a hillslope that is currently experiencing accelerated erosion (Borella et al., 2016b) in the form of mass wasting and tunnel gully formation. Shallow landslides, including debris and earth flows, are most prevalent in upper to mid-slope positions, while rill and gulley erosion predominate in lower slope positions.

Rockfall is a dominant surface feature at the Rapaki study site (Mackey and Quigley, 2014; Vick, 2015). Reflective of source rock conditions, prehistoric and modern rockfall boulders at the study site can be divided into two dominant lithology types: volcanic breccia (VB) and massive lava (ML) basalt (see Results section). During the 22 February and 13 June 2011 earthquakes, more than 650 individual modern boulders ranging in diameter from <15 cm to >3m were dislodged from the volcanic source rock near the top of Mount Rapaki, many impacting and destroying residential homes.

Ring and Hampton (2012) map the NE-SW striking Gebbies Pass fault system (consisting of the Gebbies Pass Fault with two minor subparallel faults) in proximity (within ~1 km) to the Rapaki study site. The lack of offset within the overlying loess deposits suggests this fault (and others nearby, including the Mt. Herbert Fault) has been inactive for ~50-60 ka, although Ring and Hampton (2012) propose that analogous faults may have provided a major anisotropy along which the recent (2011) faults ruptured. Sewell et al. (1992) depict a single approximate fault trace in the same area.

3.3.1.1 Geomorphic zones at Rapaki

I classify the Rapaki study site into six (6) main zones based upon the dominant surface morphology feature(s) (Fig. 5). Zone 1 consists of the subvertical to steeply dipping volcanic source rock. The parent volcanic rock is layered and lava flows dip gently to the North. The source rock is highly jointed. Zone 2 marks the zone of maximum boulder accumulation (boulder colluvium) and extends downslope from the source rock base for a distance of ~100 meters (map length). Zone 3 is dominated by shallow landslides, including small debris and earth flows. Headscarps are commonly observed, both old and new. Based upon our field observations and measurements, the depth of the slide base is relatively shallow, generally measuring 1-2 meters and commonly occurring at the boundary between loess-colluvium and *in-situ* loess or the contact between loess-colluvium or *in-situ* loess with bedrock. This area exhibits hummocky terrain indicative of landslides and possibly creep. It is within Zone 3 that widening of the northern drainage canyon (Area 'B', see below) is greatest (Fig. 5). Zone 4 marks the transition from mass wasting to rill and gully erosion. Only a few landslides are observed in this zone, primarily within the northern drainage canyon where water is most abundant/concentrated. Presently, erosion by flowing water (from rainfall) dominates in Zone 4. Slope angle is lower than in Zone 3, limiting slope failure. Zone 5 comprises the lower footslope and is dominated by tunnel-gully erosion. I observed numerous holes at the surface extending downward to

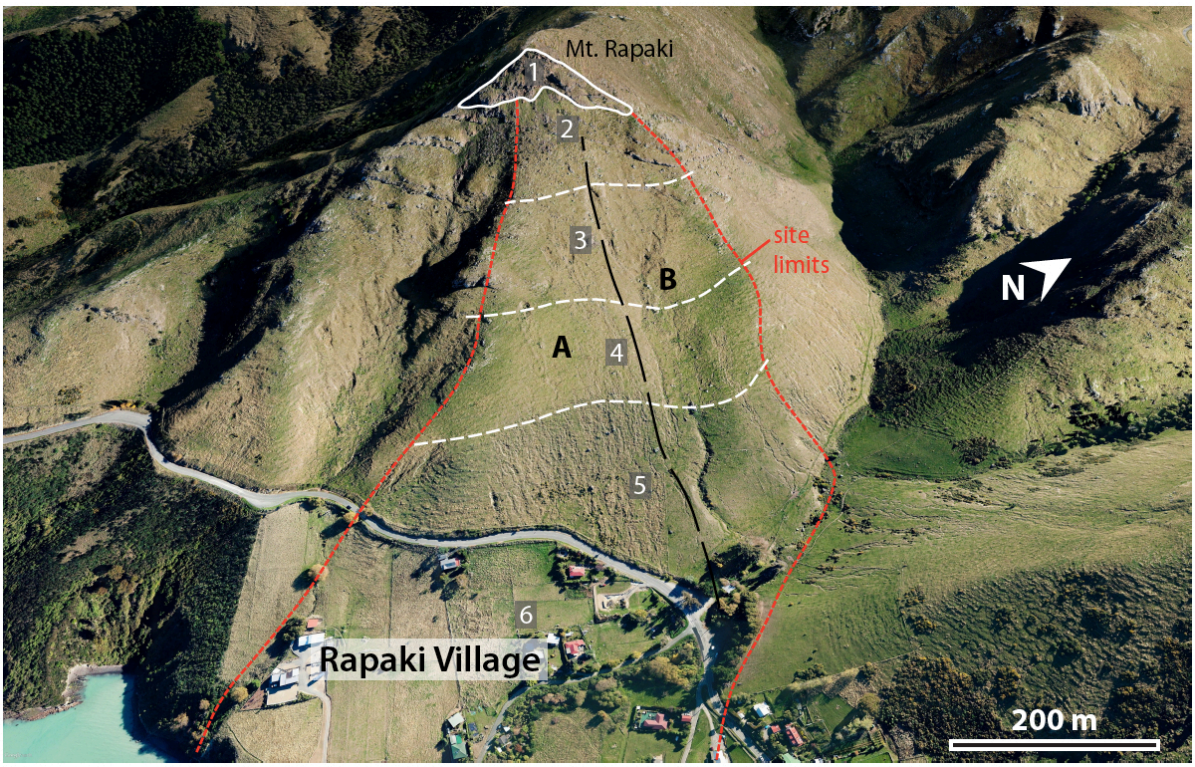

Figure 5. Rapaki geomorphic zones. 1=volcanic source rock; 2=zone of maximum boulder accumulation; 3=shallow, primarily recent debris/mud flows and hummocky topography; 4=transition from mass wasting to rill and gully erosion; 5=dominated by tunnel gully formation and erosion; 6=developed land within Rapaki village.

existing tunnels. Additionally, widespread roof collapse of former tunnels was evident throughout this area of the field site. Maximum depth for observed tunnel gullies is ~1.0 to 1.5 meters. Zone 6 is occupied by developed land within the Rapaki village. Slope gradient is lowest in Zone 6.

Across strike, the study hillslope can be roughly separated into two areas (Fig. 5). Area 'A' consists of a relatively planar (and laterally convex) interfluvial slope. Erosion and mass wasting on this section of the hillside are far less prevalent than is observed to the North in Area 'B' (see below). Area 'A' represents a zone of divergence and captures less water (surface and subsurface) than Area 'B'. At middle and lower slope positions, Area 'A' contains significantly fewer boulders than Area 'B'. Area 'B' is occupied by a large drainage canyon/gully (i.e. convergent topography) that is continuing to deepen and widen through the ongoing process of mass wasting (e.g. landslides and debris/earth flow) and to a lesser extent, rill and gully erosion. This area exhibits abundant water with seepage at the surface common. Area 'B' contains the highest number of prehistoric and modern rockfall boulders.

3.3.2 Purau study site

In contrast to the study of a single hillslope at Rapaki, research at Purau involved mapping of prehistoric and modern rockfall on and within several interfluves (spurs) and bounding valleys, respectively (Fig. 4). Purau is located on the southern side of Lyttelton Harbour, approximately 5 kilometers southeast of Rapaki (Figs. 1 and 2). Slopes at Purau have a west to northwest aspect, the opposite of the Rapaki study hillslope.

Source rock geology at Purau, including lithology and structure, is equivalent to that observed at Rapaki. Sewell (1988) and Sewell et al. (1992) characterize the geology of Purau as LVG and describe the site as being underlain by dark grey to black hawaiite with minor basalt, mugearite, and grey-green trachyte lava flows. Interbedded pyroclastic and epiclastic deposits including lahars are described, as are numerous basalt to trachyte radial dykes, some feeding endogenous domes.

The ridgeline (i.e. volcanic source rock) to the east obtains a maximum elevation of ~440 meters. Total combined vertical thickness of the source rock is variable but is on average ~100 meters. Locally, individual vertical to subvertical bluff faces are estimated to be ~30 meters in height. From the base of the volcanic source rock, slopes extend downward toward Purau Bay at angles ranging from ~30° to near flat. Spurs (or interfluves) extending downward from the source rock have slopes ranging from 20° to 30°. Slopes typically have a maximum length of ~300 meters before flattening out (<5°) quickly. Total length for slopes at Purau is generally less than ~300 meters (ground length), making them significantly shorter than the hillslope studied at Rapaki.

Field observations indicate the volcanic rock is overlain by loess, loess- and volcanic-colluvium, and prehistoric and modern rockfall boulders of small (e.g. <1 m^3) to extremely large size (e.g. >100 m^3). Similar to Rapaki, prehistoric and modern boulders can be separated into two distinct lithologies: volcanic breccia (VB) and massive (or coherent) lava (ML) basalt. Purau boulders display a similar range of boulder shapes and sizes to that observed at Rapaki.

Deforestation of Purau slopes has left the hillside covered primarily in low-lying grass and bush. Shallow slips are abundant and are commonly observed on steep slopes, including valley flanks. Similar to Rapaki, maximum landslide depth is typically ~1-1.5 meters and often exposes volcanic bedrock at bottom, indicating the overlying sediment is relatively thin. Tunnel gulley erosion predominates on canyon flanks and at lower elevations.

Sewell et al. (1992) map a buried (i.e. concealed) fault in the general area of the Purau study site. Its location coincides approximately with the Mt. Herbert fault system as mapped by Ring and Hampton (2012).

3.4 Methods

3.4.1 Field mapping and characterization of rockfall boulders

3.4.1.1 Rapaki

I mapped 1,543 individual prehistoric rockfall deposits at the Rapaki study site. Location (latitude/longitude) and elevation (meters above sea level) were recorded for each rockfall deposit using a hand-held Garmin GPSMap 62s device. Boulder dimensions (i.e. height, length, width) were tape measured in the field. For prehistoric boulders partially buried to the degree that only two dimensions were adequately measurable, the shorter of the two measured lengths was used for the 3rd dimension, thus insuring a conservative boulder size estimate. No rounding factor was applied to volumetric estimations of paleo-boulders. Paleo-rockall volumes range from 0.001 m^3 to >100 m^3. At lower and mid-slope elevations, prehistoric rockfall deposits were mapped and recorded for the full size range (0.001 m^3 to >100 m^3). At higher elevations small rockfall populations (<0.1 m^3) were too numerous to be accurately mapped within a reasonable time frame. Consequently, the data set used for statistical analysis within our study is comprised of prehistoric boulders with a volume ≥0.1 m^3 (n=1049), thus insuring no sample bias within the analyzed boulder volume data set. Due to safety concerns, prehistoric rockfall volumes were not recorded within ~100 meters of the source rock.

Lithology type was determined for each prehistoric boulder and was based primarily upon the observed dominant rock 'texture'. Boulders were designated as either (1) volcanic breccia (VB) or (2) massive (coherent) lava (ML) basalt. Transitional textures were occasionally observed in the field but are rare and represent outliers.

Collection of modern rockfall data at Rapaki reflects the combined efforts of Dr. Louise Vick (University of Canterbury), Aurecon, CCC, and GNS Science. Field measurements and description of modern rockfall was provided to the lead author by Louise Vick within an excel spreadsheet for comparative analysis with prehistoric rockfall. 307 individual modern boulders were identified in Rapaki. Due to safety concerns, 189 of the boulders were mapped via a GIS desktop study using post-earthquake high-resolution (10 cm) aerial photographs and therefore provided no boulder size data. Of the 118 modern boulders mapped in the field, 99 contain x-y-z length dimensions, thus providing a boulder volume. For comparison of modern and paleo-boulder size distributions at Rapaki all 99 of the recorded modern boulder volumes have been utilized. Modern boulder volumes were calculated by the lead author using Microsoft Excel. No rounding factor has been applied to the modern boulder sizes. Vick (2015) employed a similar criterion for description of boulder lithology types, designating each as either (1) volcanic breccia basalt or (2) massive lava.

3.4.1.2 Purau

The same field mapping and rockfall characterization techniques employed at Rapaki were used for prehistoric and modern rockfall at Purau. I (with the help of several Frontiers Abroad Inc. students) mapped 820 individual rockfall boulders at the Purau study site in Banks Peninsula with volume ≥1.0 m^3. 684 of the rockfall boulders were prehistoric and 136 were modern rockfall boulders (generated during the 2010-2011 CES). Total area mapped is ~1.1 km^2 and includes several interfluves and bounding valleys.

3.4.2 Boulder runout distance

Boulder runout distance was analyzed by examining the distance from the nearest potential source area to their final resting position. Map and ground-length runout distances were measured using Google Earth Pro along a best-estimated local fall line projected downslope perpendicular to the local contour line. Runout distance was calculated for 1,049 prehistoric boulders and 279 modern boulders within the Rapaki study site. I generally report map-length runout distance within this paper. Due to safety concerns I was unable to record locations for all boulders ≥0.1 m^3 within ~100 meters (map-length) of the volcanic source rock. However, boulder frequency counts were field collected within a 300 m^2 area at distances of 0-10 meters (n=31), 30-40 meters (n=35), 60-70 meters (n=77), and 100-110 (n=24) meters from the volcanic source rock (see Supplementary Fig. 1). The boulder frequency counts at these distances were used to extrapolate the number of boulders across remaining sections of the study site. Reductions (i.e. 2 or 3) were applied in areas where the number of individual prehistoric boulders was observed to be low (Supplementary Fig. 1 – see areas ‘b’ and ‘c’), primarily due to a lack of nearby, higher-elevation, susceptible volcanic source rock.

Due to the high number of boulders captured within bounding valleys, I did not calculate runout distance for the entire Purau rockfall data set. However, for purposes of comparison with the Rapaki rockfall data set I do report maximum runout distance for furthest traveled prehistoric and modern boulders at Purau.

3.5 Results

3.5.1 Rapaki prehistoric boulders

3.5.1.1 Volcanic breccia (VB) rockfall boulders

VB boulders (Figs. 6a-c) contain small to large porphyritic volcanic clasts that exhibit minor to moderate vesicularity (up to ~10%) and are embedded within a finer crystalline and ash-bearing matrix (Figs. 6d,e). They exhibit a wide range of shapes, from blocky to elongate to irregular, and typically have subangular to subrounded to rounded edges. VB boulders are found in greater abundance and size than ML boulders and range in color from brown to greenish brown to dark gray to light gray, with color strongly influenced by the amount of lichen covering the boulder surfaces. Boulder surfaces are covered in lichen to varying degree, although instances occur where surfaces shielded from sunlight contain very little to no lichen. The lichen exhibits variable color but is dominantly brown to light green to light gray to white. Minor patches of yellow and red growth are also observed.

VB prehistoric boulder surfaces show a high degree of weathering and surface roughness (Fig. 6a-d). Surface roughness results from in-situ differential weathering between the finer crystalline host matrix and more resistant embedded volcanic clasts. Surfaces show deep pitting, with amplitudes often exceeding 5-10 centimeters in height. In boulder surfaces with the highest degree of surface roughness, removal of matrix material is so advanced as to partially remove material below the clasts and leave volcanic clasts precariously isolated and easily plucked from the boulder by hand (although plucking was avoided). In general, VB boulder surfaces with the lightest color (i.e. light gray to white) contain the densest lichen cover and highest degree of surface roughness. Sediment can often be found deposited within the topographic lows (pockets) on the VB prehistoric boulder surfaces. In some instances, up to 5.0 to 6.0 centimeters of sediment can be observed infilling depressions on boulder surfaces, as well as growing grass and small bushes.

3.5.1.2 Massive lava (ML) rockfall boulders

ML prehistoric boulders are tabular to blocky to slightly irregular in shape and exhibit sharper edges and clear boundaries between individual boulder surfaces (Fig. 7). Compared with VB boulders they are texturally homogenous, contain significantly fewer vesicles (estimated ~ <1%) and exhibit a higher relative density. ML boulders are less abundant and significantly smaller in size compared with VB boulders. Massive lava prehistoric boulders are typically lighter in color, ranging from light orange to pink to light gray and show less lichen colonization (compared with VB boulders), both old and new.

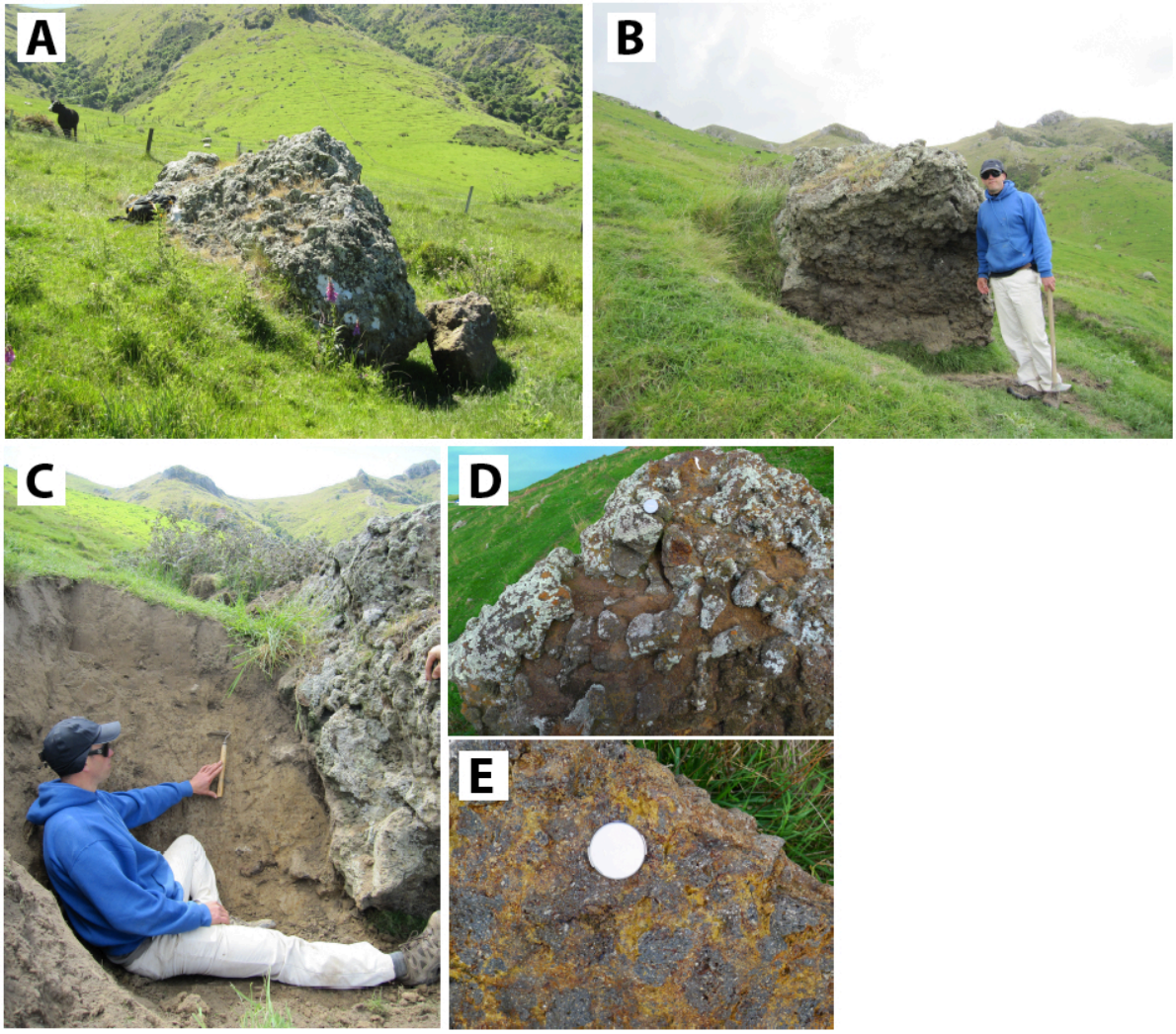

Figure 6. Photos of prehistoric boulders at Rapaki study site. **(A)** Prehistoric boulder in footslope position with smaller modern (2011) boulder at right bottom. Prehistoric boulders commonly exhibit a colluvial sediment wedge behind the upslope boulder side. **(B)** Prehistoric boulder from midslope position with sediment wedge at backside. Prehistoric boulders comprised of volcanic breccia exhibit the largest size, contain the thickest sediment wedges and display the highest amount of surface roughness. **(C)** Exploratory trenching exposes the colluvial sediment wedge at the backside of boulder depicted in Fig. 4b. **(D)** Photo showing advanced surface roughness and abundant lichen growth on prehistoric boulder surface. Prehistoric boulders with greatest surface roughness show deep and connected pitting and expose precarious volcanic clasts. **(E)** Freshly exposed prehistoric boulder surface highlighting the porphyritic texture of the volcanic breccia boulders. Embedded volcanic clasts are surrounded by a more finely and often highly oxidized crystalline host matrix. Camera lid is shown for scale (diameter is 5 cm).

Figure 7. Massive lava (ML) prehistoric boulder. ML prehistoric boulders are more angular to tabular in shape and are on average significantly smaller than VB prehistoric boulders. Smaller VB boulder is positioned to bottom right and exhibits subrounded shape and higher degree of surface roughness.

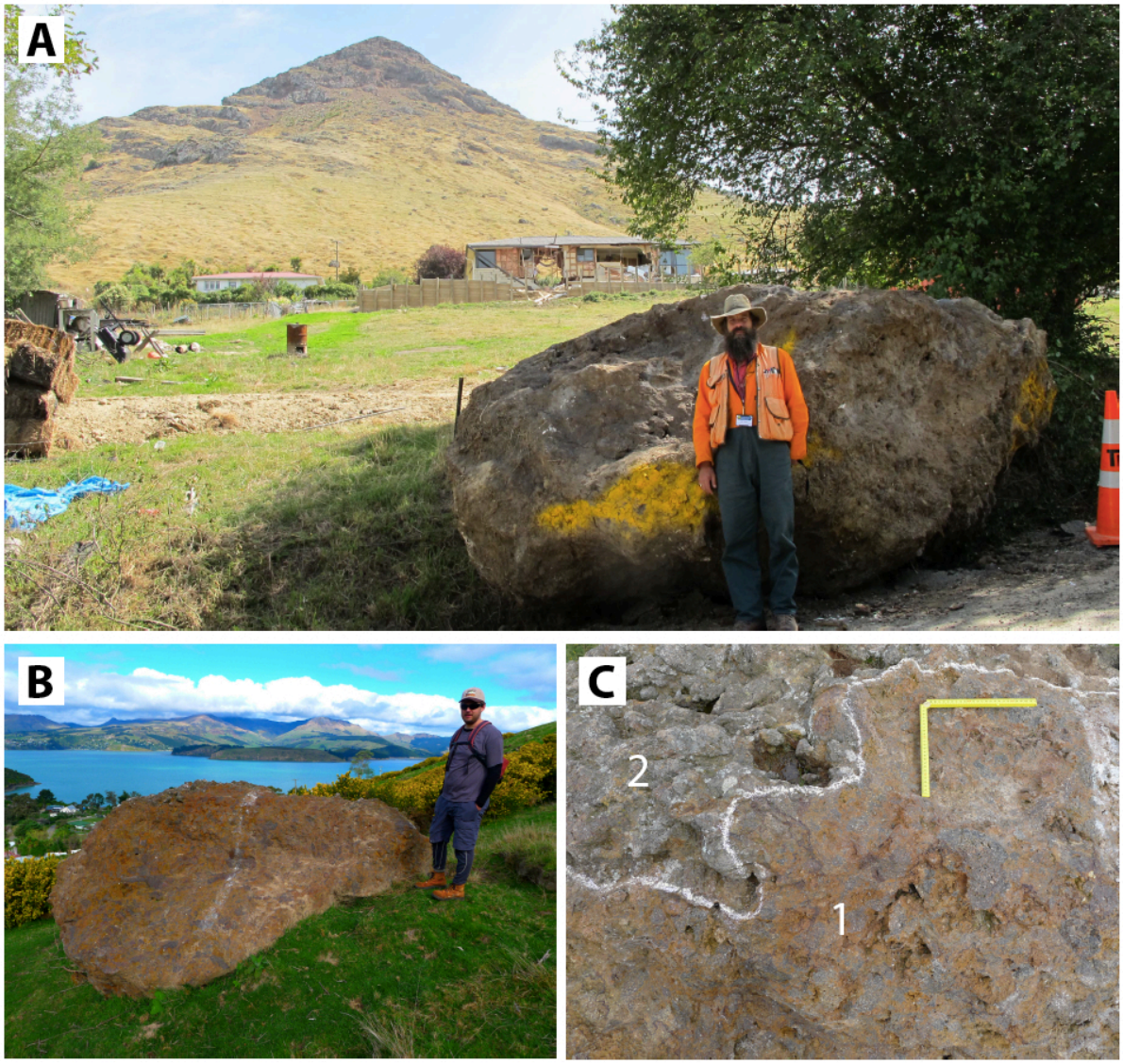

Figure 8. **(A)** Photo of large modern boulder (~28 m^3) detached from Mount Rapaki and emplaced in the Rapaki village during the 22 February 2011 earthquake (photo courtesy of D.J.A. Barrell, GNS Science). Boulder runout distance from source was ~700 meters, exceeding maximum travel distance for prehistoric boulders by ~150-175 meters. **(B)** Modern boulder deposited with detached face upward. Surface exhibits characteristic orange to reddish orange color, low surface roughness, and no lichen growth. **(C)** Modern boulder showing 2011 detachment surface (1) and adjacent non-detached surface (2). Surface roughness is significantly lower in modern detachment surface, reflecting conditions of detachment from the volcanic source rock and subsequent fragmentation during descent. The difference in color and lack of lichen on the modern surface is apparent.

Where present, lichen is typically light gray to white in color and commonly occurs as a circular or radial pattern. ML boulder surfaces exhibit very low surface roughness (i.e. smooth).

3.5.1.3 Hillslope sediment-boulder interaction

Both VB and ML prehistoric boulders can be observed partially to nearly completely buried by loess-colluvium. Instances do occur, however, where no sediment is built-up at the boulder backside, suggesting a location of minimal sediment accumulation and/or a dominance of erosional processes over sedimentation. Burial in hillslope sediment is most common for boulders located on midslope and footslope positions, rather than those located on upper slope elevations, where erosion dominates. Prehistoric boulders located in drainage canyons are subject to rapid deposition and erosion, and therefore can be found without any sediment pile-up or preserving large colluvial wedges. Deposition of sediment is primarily found behind and to a lesser degree around the sides of prehistoric boulders. Due to their larger size and greater subaerial exposure, VB boulders preserve the thickest colluvial wedge sediments (Fig. 6c) that have been stratigraphically analyzed and dated using the radiocarbon and OSL methods (Borella et al., 2016b).

3.5.1.4 Boulder size distribution

The total number of prehistoric boulders mapped in Rapaki with volume ≥0.1 m^3 is 1049, and corresponds with a total volume of 3025.62 m^3. Data presented below reflects only those boulders with volumes ≥0.1 m^3, as a sample bias exists against boulders below this size.

Rapaki Prehistoric Rockfall – Boulder Size Statistics (for volume ≥0.1 m^3)

Prehistoric Rockfall Boulders	All (n=1049) (m^3)	VB (n=779) (m^3)	ML (n=270) (m^3)
25th (Q1)	0.25	0.36	0.1
Median	0.638	1.00	0.25
75th (Q3)	1.995	3.11	0.456
95th	11.96	14.49	1.22
Maximum	200.56	200.56	10.00
Mean	2.882	3.74	0.415
Total Volume	3025.62	2913.49	111.98
% of total volume	100	96	4
% of mapped boulders	100	74	26

Table 1. Statistical size distribution for Rapaki Prehistoric boulders.

Table 1 shows the statistical size distribution for prehistoric boulders at the Rapaki field site, including a comparison between VB and ML boulders. ML boulders have a significantly smaller size range than VB boulders, with 7% of ML boulders ≥1.0 m^3, while 50% of VB boulders are ≥1.0 m^3. ~74% of the mapped boulders are comprised of volcanic breccia, while the remaining ~26% consist of

massive lava. Volcanic breccia comprises ~96% of the total mapped rockfall volume, while the remaining ~4% consists of massive lava. The ML/VB boulder frequency ratio is 0.35.

Boulder size distribution graphs (Fig. 9) and histograms (Fig. 10) for the combined boulder population (n = 1049) and separately for VB and ML boulders show a 'strongly skewed to the right' boulder size distribution, consistent with the mean (2.88 m^3) being greater than the median (0.64 m^3) boulder sizes. Figure 10 shows a steep drop in boulder frequency with increasing volume, with the highest rate of decrease occurring for ML boulders.

The rockfall frequency-volume distribution (Fig. 11) can be modeled using a power law ($R^2 = 0.86$) over the range of boulder sizes. Bin size is 0.5 m^3.

Power law equation: $B\# = 83.607(BV)^{-1.242}$ (1)

Where B# = number of boulders of given volume, BV = boulder volume.

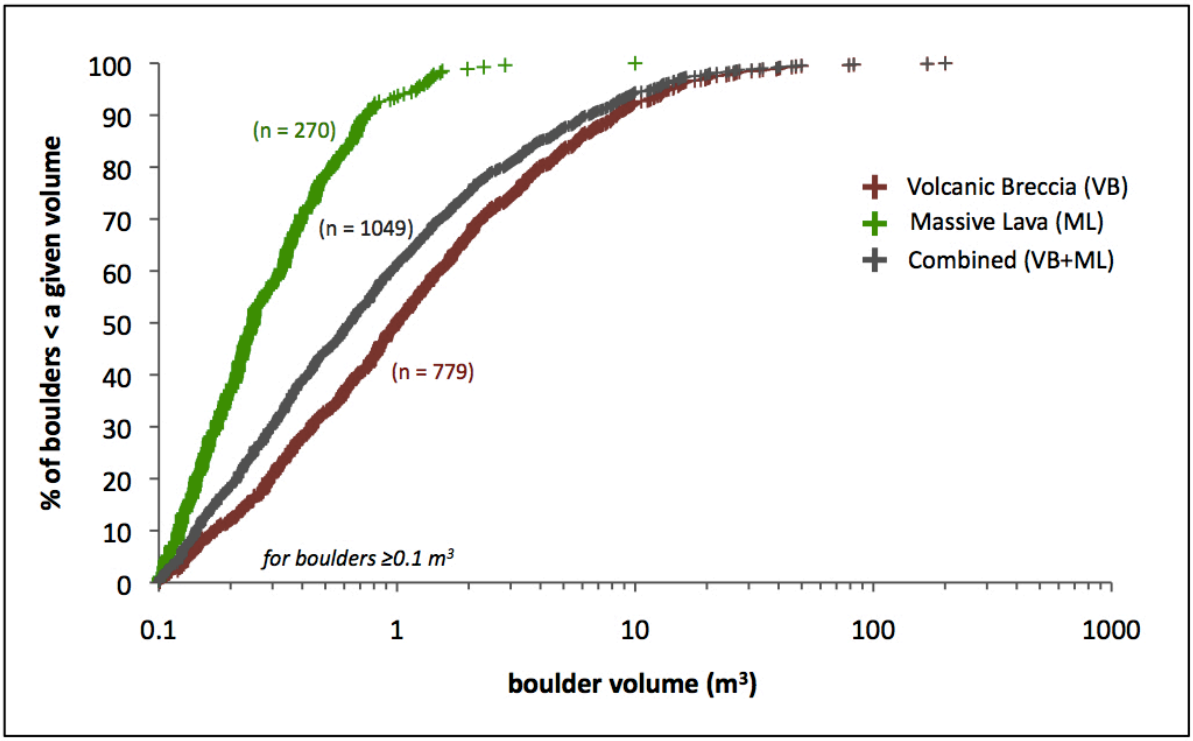

Figure 9. Boulder size distribution graph for combined Rapaki boulder population and separately for VB and ML boulders.

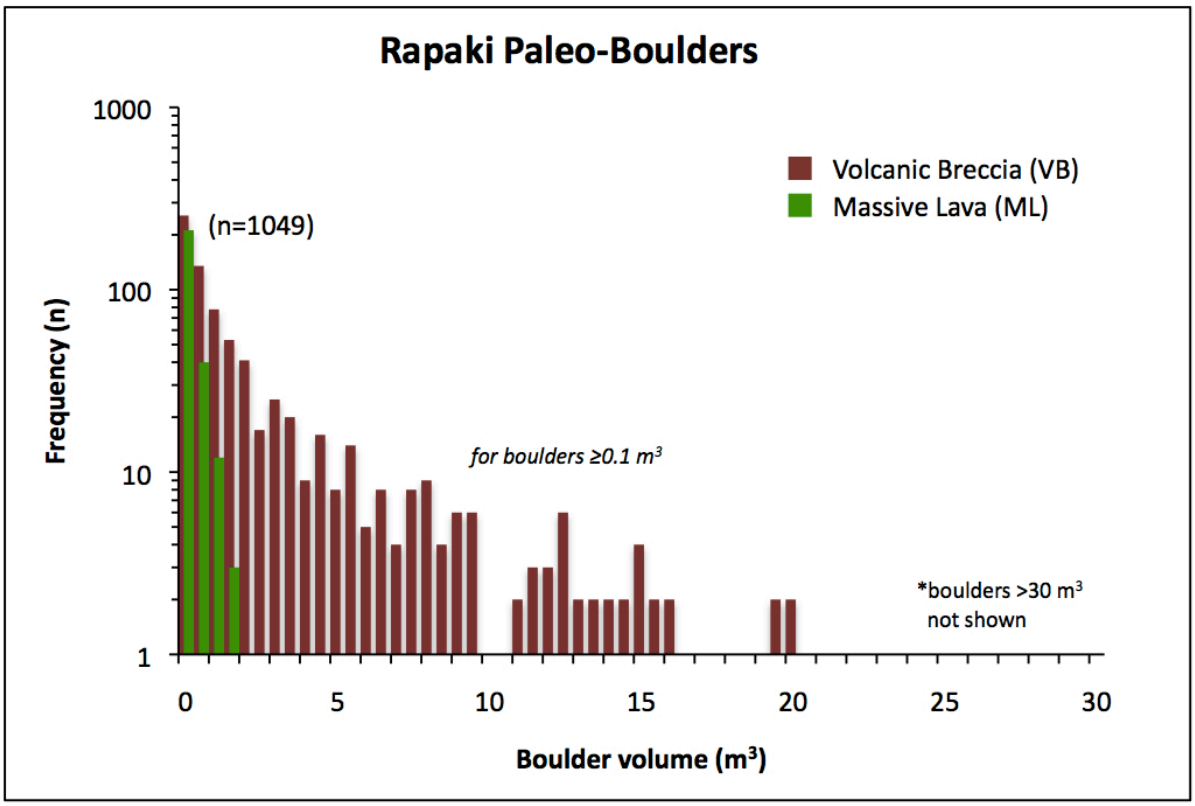

Figure 10. Histogram showing boulder frequency as function of volume for Rapaki VB and ML rockfall boulders.

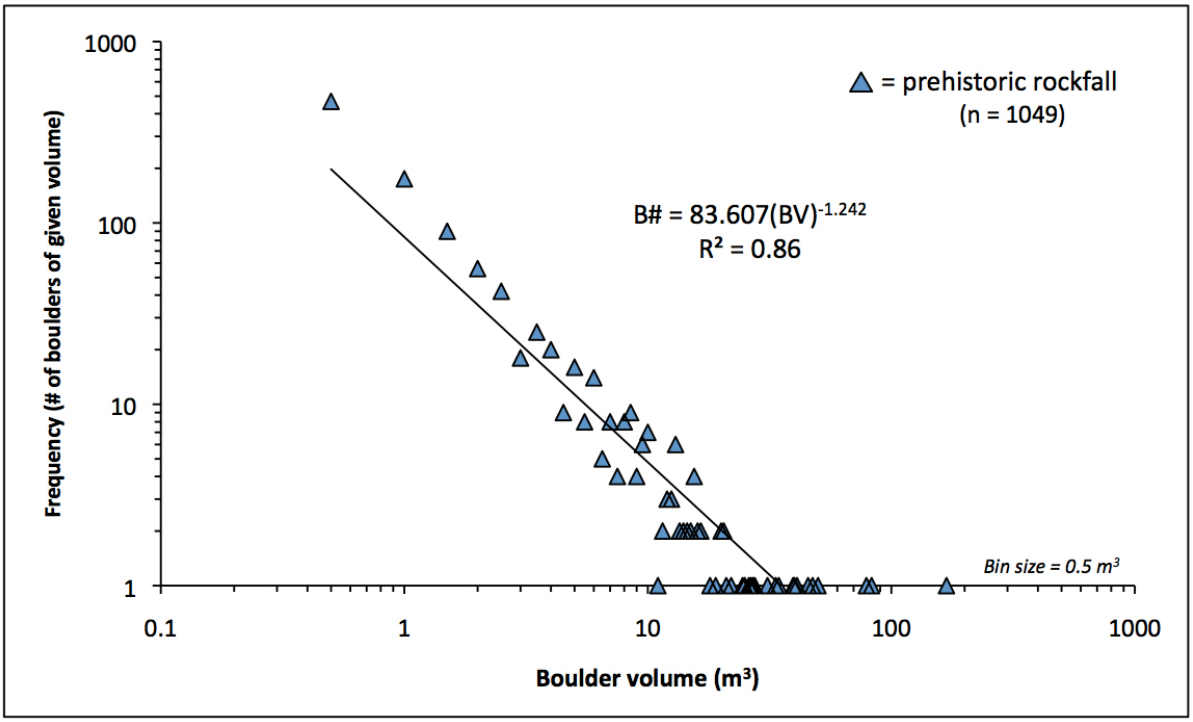

Fig. 11. Power law rockfall frequency-volume distribution for Rapaki prehistoric boulders.

3.5.2 Source rock geology and influence on boulder size and shape

All prehistoric rockfall at Rapaki is derived from the same source cliff, located at or near the top of Mount Rapaki (Fig. 12). The source cliff is comprised of interlayered VB and ML layers. The breccia layers comprise the bottom and top of discrete lava flows, while the massive lava generally occupies the center of the lava flow where cooling was not as rapid and there was less interaction with the substrate and/or cooling interface.

3.5.2.1 Jointing

Jointing is pervasive within the volcanic source rock, but to varying degree depending upon layer composition and corresponding texture. Safety concerns (i.e. rockfall threat) precluded us from making direct measurements within the source rock (i.e. joint orientations, spacing between joints). However, I present the following estimates based upon field observations made approximately 10 meters from the source rock. Layers comprised of ML exhibit the highest fracture density. Joints within the massive lava were formed during primary cooling of the lava flow, producing a columnar-style pattern. The massive lava layers contain numerous intersecting subvertical to vertical, to curvilinear joint sets, with spacing rarely exceeding ~1 meter. The small joint spacing imparts a first-order control on ML prehistoric boulder size and is reflective in the small size range for ML prehistoric boulders. Only 18 individual ML prehistoric rockfall boulders with size $\geq$1.0 m^3 were mapped at the Rapaki study site, reflecting ~7% of total number of ML boulders.

Layers consisting of volcanic breccia exhibit a lower fracture density. Joints within VB layers are widely spaced, often 5-10 meter or greater apart. Surprisingly, observable joints within VB layers are more regular and planar than those observed in exposed sections of the ML layers. Regularly spaced subvertical joints within VB layers suggests primary cooling of lava as a mechanism for joint formation. The wider spacing for joints within VB layers promotes greater boulder size, reflective in size distribution for VB prehistoric boulders (Table 1). Approximately 50% of VB boulders have a volume $\geq$1.0 m^3 and ~8% contain a size $\geq$10.0 m^3.

3.5.2.2 Volcanic layer boundaries and thickness

Field observations and a review of high-resolution aerial photography of the Rapaki source rock suggest layer boundaries influenced the spatial distribution and size of modern rockfall detachment sites. The contact between ML and VB layers represent discontinuities and planes of preferential detachment.

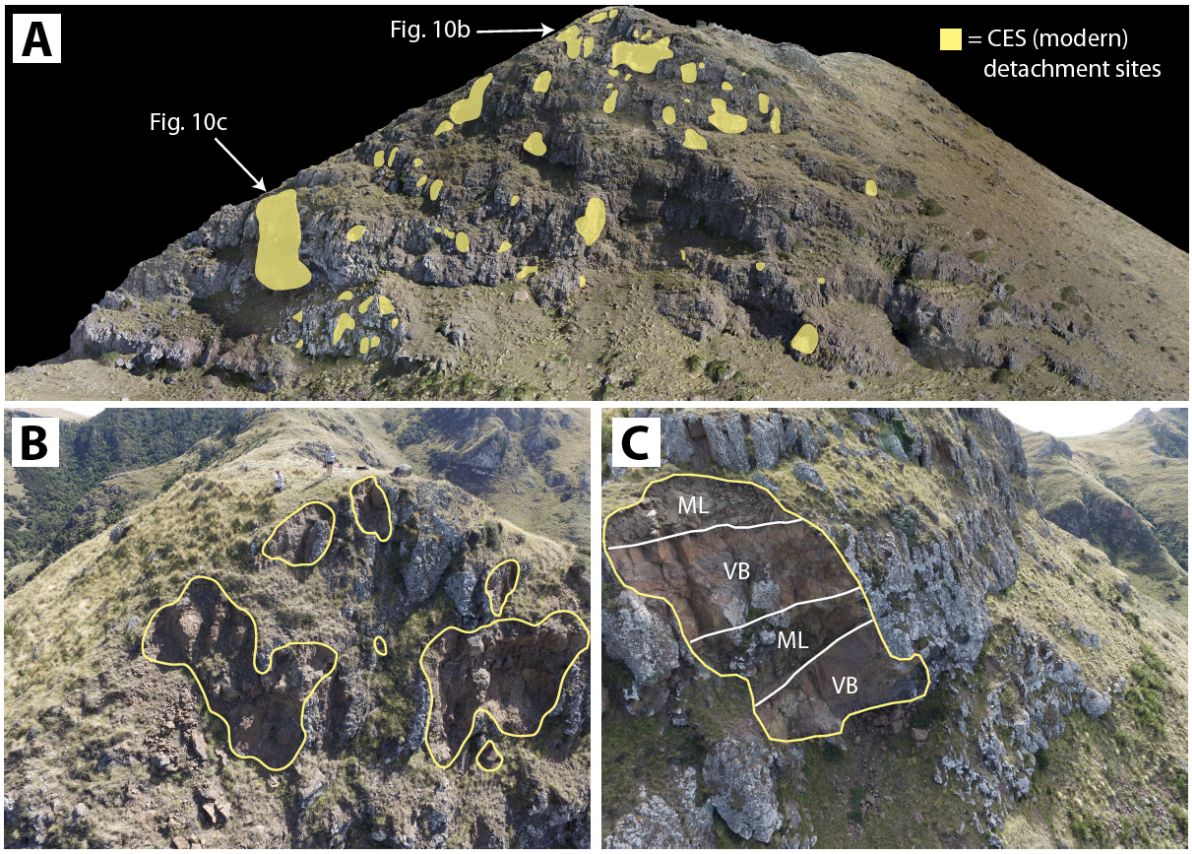

Figure 12. Photos of Rapaki volcanic source rock. **(A)** Rapaki source rock showing spatial distribution of modern (2011) rockfall detachments sites (yellow). During the 2011 Christchurch earthquakes (i.e. 22 February and 13 June events) approximately 9% of the available rock mass (by area) failed. We identify a minimum of ~55 detachment sites of variable size. **(B)** Close up of source rock and modern detachment sites near the top of Mount Rapaki. Rockfall detachment sites display irregular geometries and are primarily controlled by pre-existing joints and volcanic layer boundaries in the source rock. **(C)** Photo of large rockfall detachment site showing volcanic layers comprised of VB and ML. Largest rockfall detachments span across layer boundaries.

Volcanic layer thickness may also play a role (in some instances) by limiting maximum size for prehistoric boulders at Rapaki. Maximum thickness for ML layers is typically ~1-2 meters, while maximum thickness for VB layers may exceed ~10 meters.

3.5.2.3 Fragmentation

Fragmentation during descent (i.e. sliding, rolling, bouncing) influences boulder size to varying degree depending on the intrinsic properties of the boulder. Impacts with the ground surface (including pre-existing boulders) may reduce the initial boulder size. Boulder roll experiments (Vick, 2015) near Rapaki suggest that fragmentation is greatest within VB boulders due to its lower density and internal strength. Laboratory tests conducted by Carey et al. (2014) showed an unconfined compressive strength of 100-243 (average 180) MPa for the massive lava (ML) and 0.9-15.8 (average 3.5) MPa for the volcanic lava breccias (VB). Vick (2015) found that although breccia blocks were released as large boulders, fragmentation occurred within the first few impacts with the loess and volcanic colluvium. Boulders consisting of massive lava tended to stay intact and retain their initial shape unless they impacted existing boulders during run out. I expect that fragmentation is greatest near the source rock where impact with existing boulders and exposed bedrock is common and decreases further down slope where the ground surface is composed of softer loess colluvium and spatial density of pre-existing boulders is significantly less.

3.5.3 Spatial distribution

Spatial distribution of prehistoric boulders is strongly influenced by surface morphology (including roughness and pre-existing boulders), boulder size and shape, and presumably, the presence of a dense podocarp/hardwood forest existing on the hillslope during emplacement of the prehistoric rockfall. The presence of dense vegetation on the study hillslope would have significantly impacted boulder distribution by reducing spatial extent, including boulder runout distance.

The highest accumulation of paleo-rockfall is found near the source rock (within ~175 meter run out distance and above ~220-meter elevation) and upper sections of the northern drainage canyon (Fig. 13). A high percentage of both prehistoric and modern (i.e. 2011) boulders are deposited in the northern canyon, implying that the canyon feature has persisted at the study site for deposition of both modern and observed prehistoric rockfall. Lateral distribution of Rapaki prehistoric boulders is

controlled by two resistant ridges/spurs marking the northern and southern limits of the study area. Bedrock exposures are present on both of these topographic highs.

A comparison of spatial distribution for prehistoric VB and ML boulders (all sizes ≥0.1 m^3) on the hillside, irrespective of size, indicates similar lateral distribution and runout distance from the source (Fig. 14). Boulder dispersion (outward from the source) is similar and increases dramatically with distance from the source area. However, important differences in prehistoric boulder behavior (i.e. lateral extent and runout distance) are revealed when considering boulder spatial distribution as a function of boulder volume for the two lithologies (i.e. VB and ML). The following is a systematic evaluation of boulder spatial distribution as a function of prehistoric boulder volume and lithology type.

3.5.3.1 Boulder volume = >100 m^3

Three prehistoric VB boulders with size >100 m^3 were mapped at the Rapaki study site (Fig. 15a). Boulders of this size are strongly influenced by surface topography and are clearly being directed from the source area downslope and into the northern drainage valley (Area 1; see Fig. 5). Runout distance is apparently limited due to the extreme size of the boulders. We expect the primary means of transport for boulders of this size would be sliding and rolling (e.g. Quigley et al., 2016 – see photo of fallen rock mass at Rapaki). No boulders >100 m^3 are found below an elevation of 115 meters (asl), equating to a maximum map length runout distance of ~401 meters from the source area. ML boulders do not obtain sizes >100.0 m^3.

3.5.3.2 Boulder volume = 10-100 m^3

There is a significant increase (factor of ~19) in the number of VB prehistoric boulders (n=56) with size between 10.0 and 100.0 m^3 (Fig. 15b). Surface topography strongly influences boulder distribution for this size range. Boulder frequency is highest near the source area but accumulation also favors the central axis of the northern drainage canyon (Area 1), primarily in the middle to upper sections of the valley. Maximum boulder runout distance increases compared with the largest boulders (>100.0 m^3), with several large boulders (n=4) deposited on the footslope in Area 2. In Area 1 (northern drainage canyon), boulders are more numerous due to the presence of the valley, but maximum runout distances are shorter. This may result from the increased number of large boulders within the valley, creating a high degree of surface roughness (i.e. land surface obstructions) that impacts on subsequent rolling/bouncing boulders. Additionally, more water is conducted into the valley making the ground softer and promoting denser tree growth, both of which could reduce boulder rolling energy and runout distance. The southern interfluve (Area 2) reveals a different scenario, with boulders apparently passing over the midslope area before depositing on the footslope. The slope in Area 2 is more planar, the

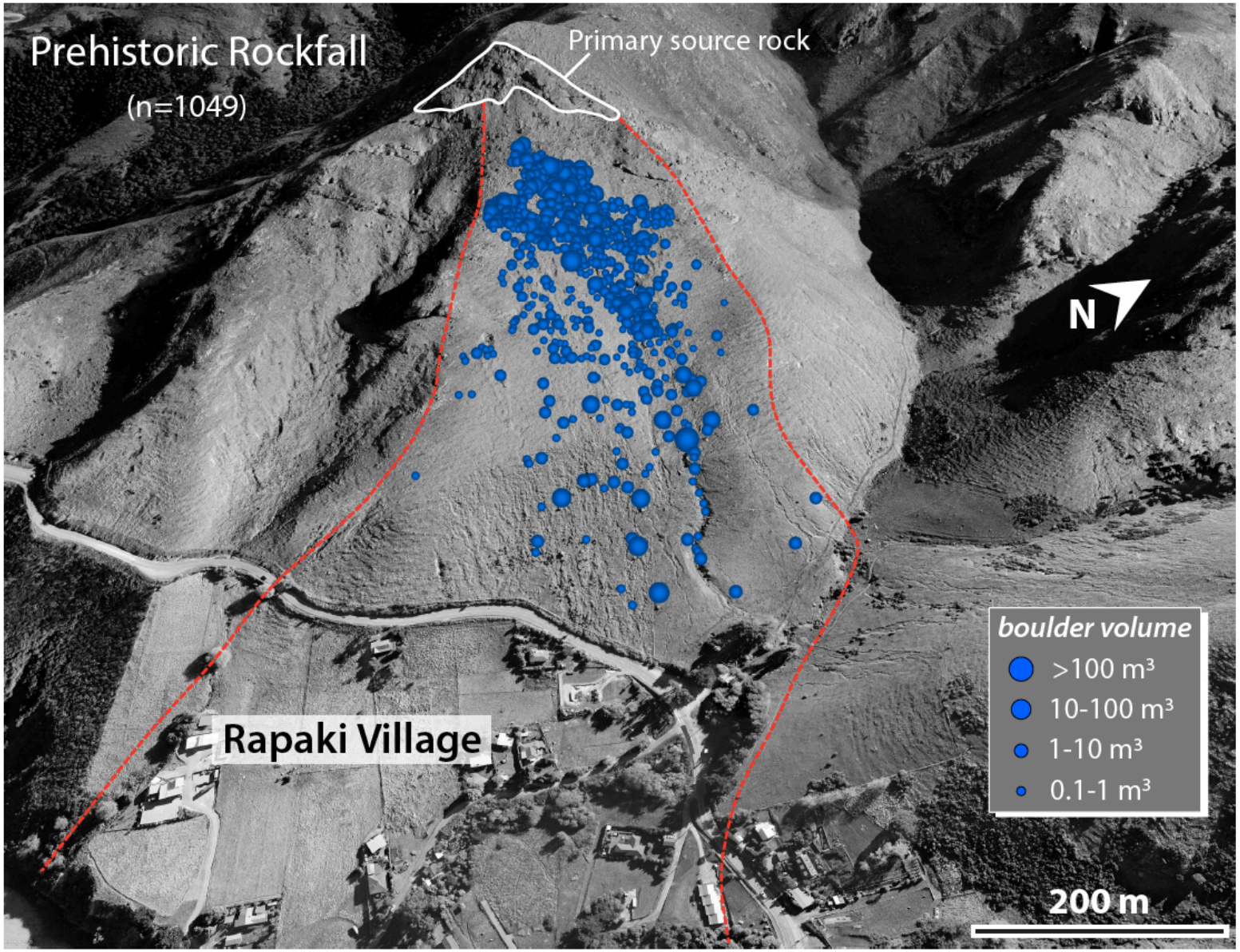

Figure 13. Mapped prehistoric rockfall (n=1049) at Rapaki study site. All mapped prehistoric rockfall boulders originate from the same source volcanic source rock, located near and at the top of Mount Rapaki. Boulder volume has been grouped into the following four size bins: 0.1-1 m^3, 1-10 m^3, 10-100 m^3, >100 m^3.

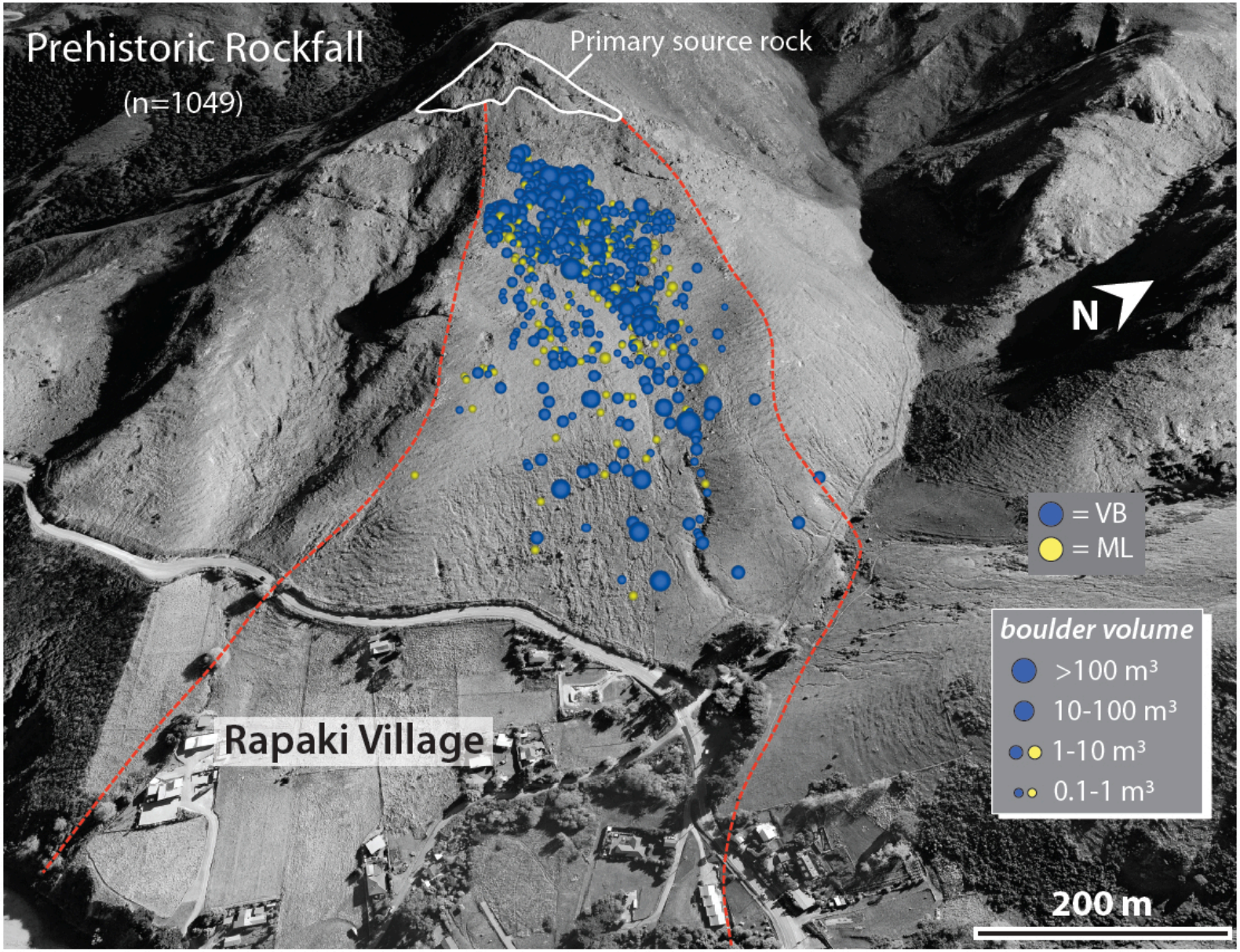

Figure 14. VB and ML prehistoric rockfall boulders at Rapaki study site. ML boulders are smaller than VB boulders and ML boulders ≥1.0 m^3 have significantly smaller maximum runout distances than VB counterparts of equivalent size.

ground surface is comparatively drier (and harder), and the number of boulders on the southern slope is significantly less, all contributing to increased boulder travel distance. ML boulders do not obtain sizes between 10.0 and 100.0 m^3.

3.5.3.3 Boulder volume = 1-10 m^3

The number of VB boulders (n=333) with size between 1.0 and 10.0 m^3 increases dramatically (relative to boulders with volume ≥10 m^3) within the field site (Fig. 15c). Boulder density is highest near the source area and within the northern drainage canyon (Area 1). However, there is an increase in lateral distribution and dispersion, and paleo-boulders of this size are deposited on the midslope in Area 1 (southern divergent zone) (Fig. 15c). Maximum runout distances are similar (~600-650 meters) to those with volumes between 10.0-100.0 m^3, with several boulders reaching the footslope position. Surface topography continues to impart a strong influence on boulder distribution for this size range.

Very few ML boulders (n=18) of this size range are mapped at the Rapaki study site. Where present, ML boulders of this size are observed near the source area and within the Area 1 drainage canyon (Fig. 15c). Only a single (and largest ML boulder) boulder of this size is found on the midslope of Area 1. Runout distance for ML boulders ≥1.0 m^3 is significantly less than those for VB boulders. No ML boulders of this size are found below an elevation of 140 meters above sea level (maximum map length runout distance = 328 meters). VB boulders with similar volumes have longer runout distances (~230 meters) than ML boulders, suggesting that the shape (tabular and blocky) and higher density of ML boulders could have reduced boulder runout distance.

3.5.3.4 Boulder volume = 0.1-1 m^3

I observed an increase (n=389) in the number of VB prehistoric boulders with size between 0.1 and 1 m^3. Lateral dispersion is similar (compared with boulder size 1-10 m^3) on upper and midslope positions but decreases significantly on the lower footslope, perhaps reflecting lower boulder velocities (Fig. 15d). Average boulder runout distance is less compared with larger boulder sizes (1-100 m^3). Only three VB boulders of this size are deposited on the lower slope within Area 2, indicating that the smaller and less dense VB boulders have shorter runout distances than ML. The majority of VB boulders for this size have shorter runout distances than those for larger volume boulders (excluding boulder volumes >100 m^3) (Fig. 15d). The possibility exists that footslope boulders of this size were transported downslope as part of a larger boulder, before fragmenting at lower elevations. However, it is probable that the majority of fragmentation occurs nearest the source rock where the surface consists of dense boulder colluvium rather than further downslope where the ground is comprised of softer loess-colluvium sediment.

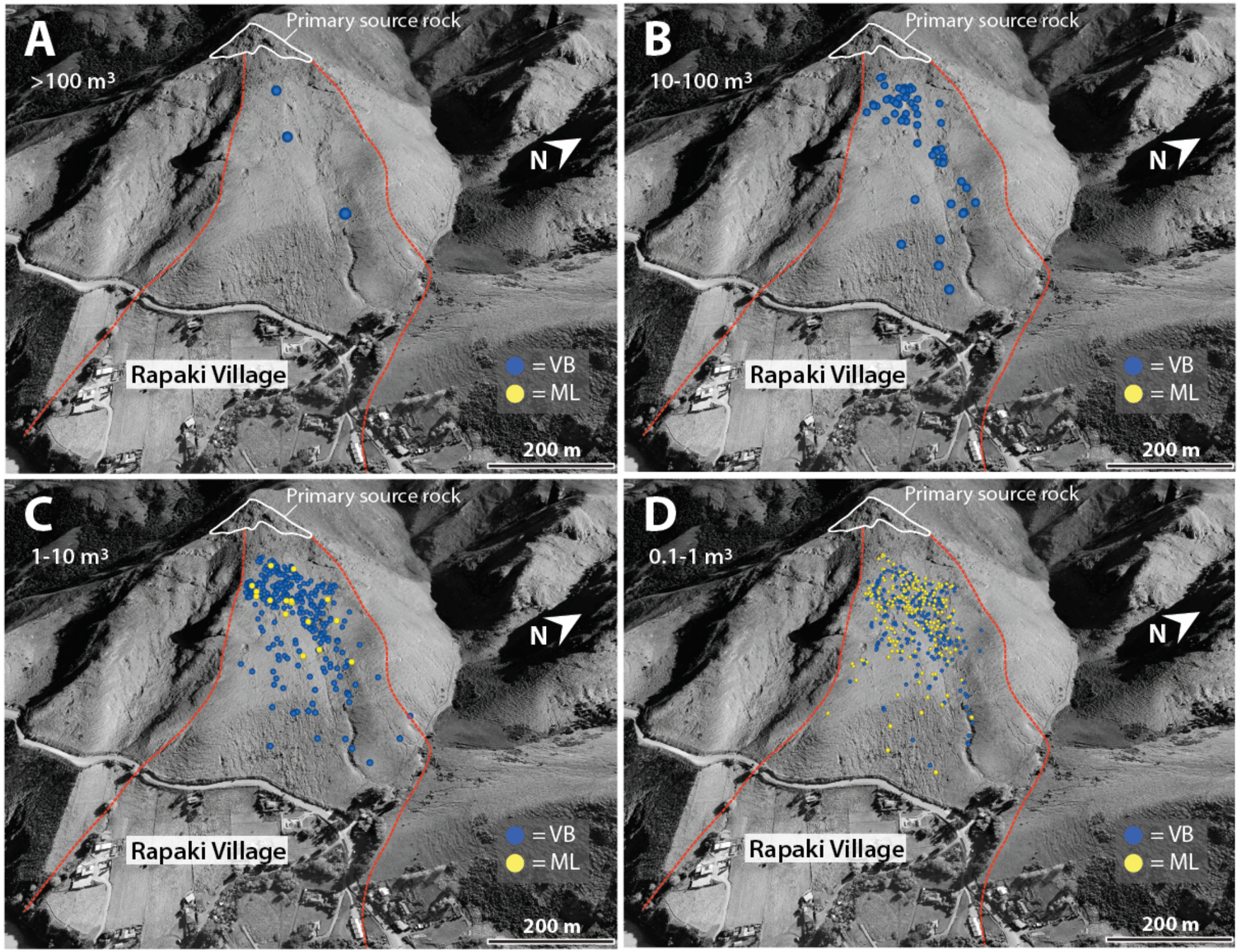

Figure 15. Spatial distribution for mapped VB and ML prehistoric boulders. **(A)** Prehistoric boulders with size >100 m^3 display shortest maximum runout distance and are deposited on upper slope and within the northern drainage canyon. No ML boulders of this size exist. **(B)** Prehistoric boulders with size between 10-100 m^3 are deposited primarily near the volcanic source rock and within northern drainage canyon. Several boulders have long runout distances (~500-550 meters). No ML boulders exist within this size range. **(C)** Prehistoric boulders with size between 1-10 m^3. ML boulders of this size have comparatively shorter maximum runout distances. **(D)** Prehistoric boulders with size between 0.1-1 m^3. Number of ML boulders with volume ≤1.0 m^3 increases significantly (compared with number of ML boulders with volume >1.0 m^3) and obtain furthest boulder runout distances.

The number of ML boulders (n=252) for this size range increases dramatically compared to ML boulders with volume >1.0 m^3 (Fig. 15d) and decreases rapidly with distance from the source. Lateral distribution and runout distance increase relative to the larger ML boulders (compare with Fig. 15c). Maximum runout distance for ML boulders of this size is ~561 meters, representing the furthest travel distance for all mapped prehistoric boulders. Numerous boulders are observed deposited on the Area 2 midslope, and six ML boulders of this size range are observed in the Area 2 footslope. Average, median, and maximum boulder size for these six boulders is 0.28, 0.23, and 0.465 m^3, indicating that maximum runout distance for ML boulders favors a smaller boulder size.

3.5.4 Boulder runout distance

The frequency-runout distribution for Rapaki prehistoric boulders can be modeled by a power law ($R^2 = 0.86$) over the range of boulder sizes where runout distance is ≥ ~60-70 meters (from volcanic source rock) (Fig. 16 – see power law fit A). Because of safety concerns, limited mapping of prehistoric boulders was performed closer to the source rock (within ~140 meters) to extrapolate the number of boulders with ground-length runout distances between 0-10, 30-40, 60-70, and 100-110 meters. Power law fit B includes all data points and highlights the importance of slope and initial impact velocity at the cliff base, which causes more boulders to be deposited at greater distances and creates a deviation in the power law fit (Fig. 16 – see power law fit B with lower R^2=0.60).

Power law equation A: $B\# = 4E+07(RD)^{-2.623}$ (2)

Power law equation B: $B\# = 51709(RD)^{-1.481}$ (3)

Where B# = number of fallen boulders, RD = ground length runout distance.

When considering all data points, the boulder frequency-runout distribution is best modeled using an exponential function and has an $R^2 = 0.88$ (Fig. 17).

Exponential equation: $B\# = 202.02e^{-0.008(RD)}$ (4)

Where B# = number of fallen boulders, RD = ground length runout distance.

Beyond a distance of approximately 200 meters from the source rock, the frequency-runout distribution plots (Figs. 16, 17, and 18) show the number of rockfall boulders decreasing rapidly with increasing distance from source. The number of rockfall boulders increases dramatically beginning approximately 200 meters from the source rock and continues to increase until ~30-40 meters from the

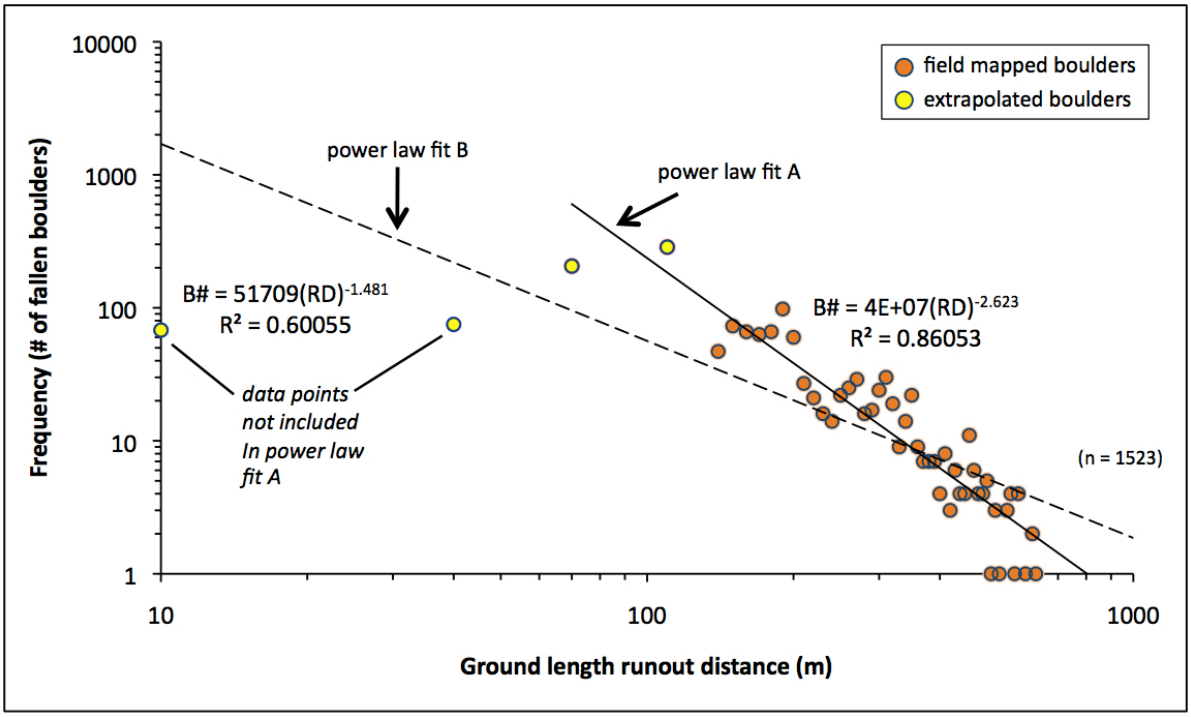

Figure 16. Rapaki prehistoric boulder frequency-runout distribution plot modeled using a power law. Power law fit A includes data points where ground length runout distance is ≥ ~60-70 meters. Power law fit B includes all data points.

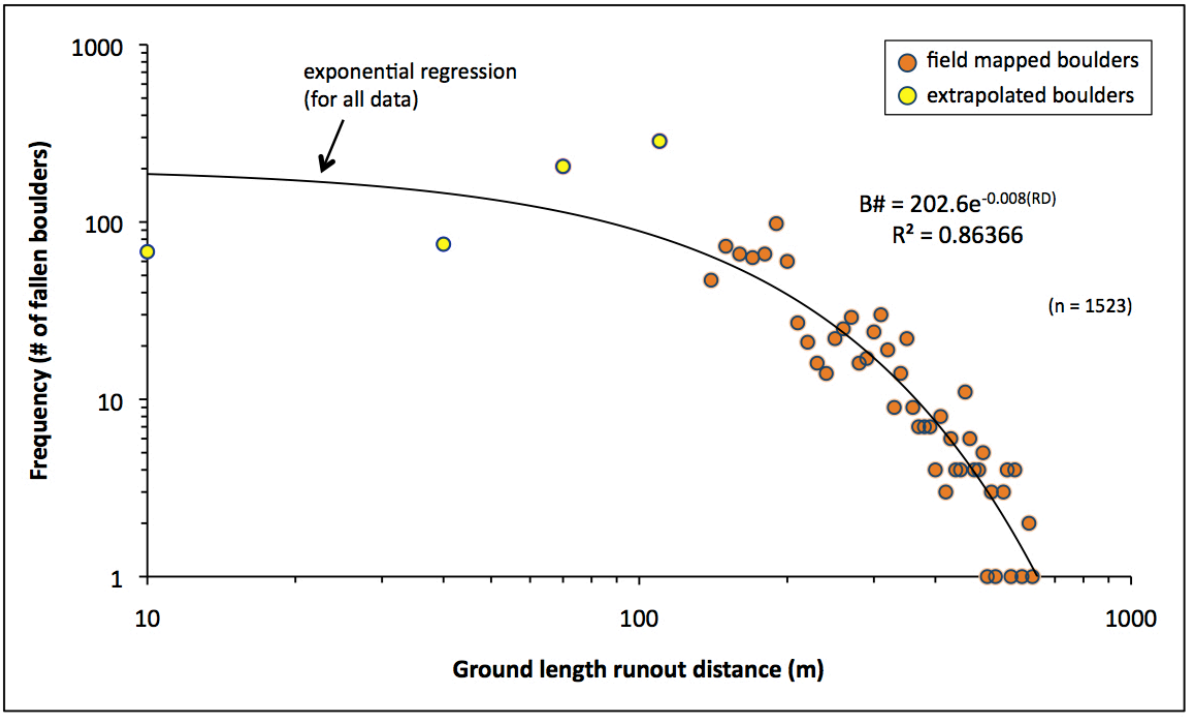

Figure 17. Rapaki prehistoric boulder frequency-runout distribution (with extrapolated boulder frequencies near the source rock [i.e. 0-10 and 30-40 meter runout distances] included) using exponential regression fit.

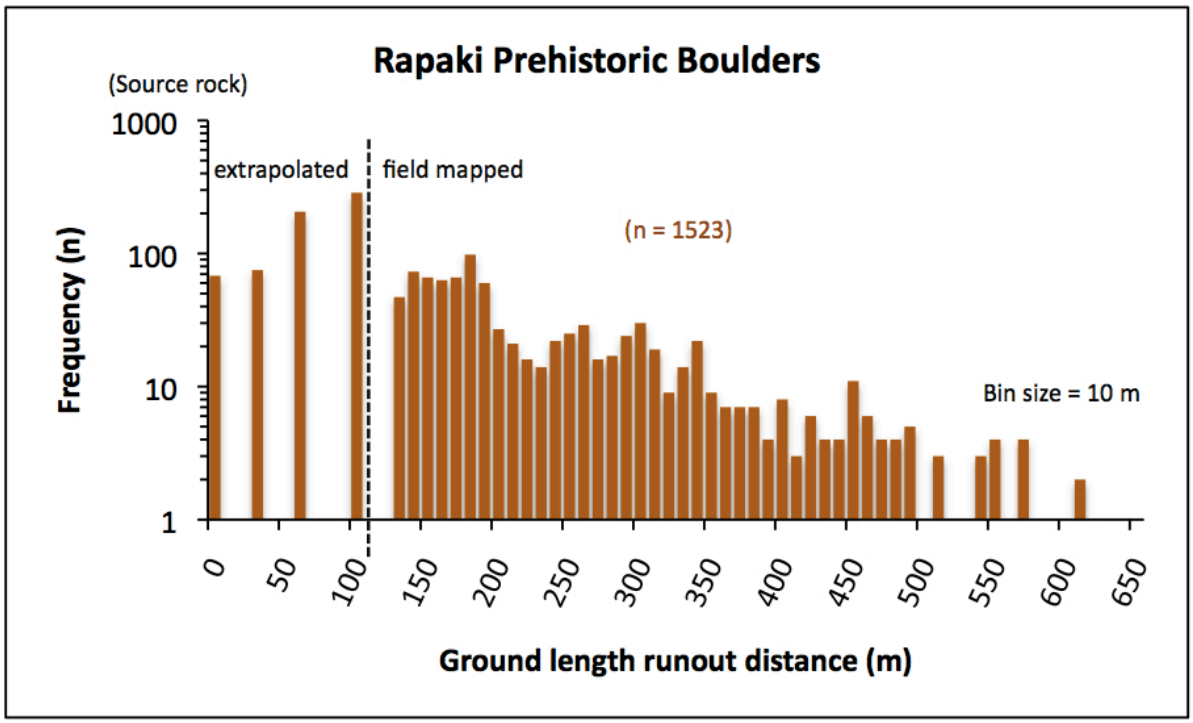

Figure 18. Histogram plot showing frequency distribution for Rapaki prehistoric boulder runout distances. The maximum ground-length runout distance for the Rapaki prehistoric boulders is ~621 meters (~561 meter map-length distance).

source, where the frequency of boulders is reduced towards the base of the source cliff. The highest abundance for mapped prehistoric boulders is found between 180-190 meters (n=98) from the source area, with smaller boulder frequency highs located between 260-270 (n=29), 300-310 (n=30), and 340-350 (n=22) meters from the source rock (Fig. 18). The reduction in number of boulders within ~40 meters of the source rock may reflect several factors including: (1) Smaller depositional area for boulders near the source rock; (2) The majority of detached boulders will impact the ground and travel a minimum distance before deposition.

3.5.5 Boulder volume vs. runout Distance

No clear correlation exists between prehistoric boulder size and runout distance at Rapaki (Fig. 19), although there is a slight increase in the percentage of boulders with long runout distances for rockfall size between 1-10 m^3 and >10 m^3 (Figs. 20 and 21). In contrast, smaller prehistoric boulders with size between 0.1-1 m^3 display a decrease in percentage of boulders as distance increases from the source, suggesting that smaller rockfall (on average) does not travel as far as their larger counterparts. For VB prehistoric boulders, a wide range of boulder volumes is generated for all runout distances (Fig. 19). However, of the 21 paleo-boulders exceeding a map length runout distance of 450 meters, ~81% (n = 17) are comprised of volcanic breccia and have an average size of 8.24 m^3, highlighting the considerable size for some of the furthest traveled VB boulders and their potential danger. For ML boulders (Fig. 19) a small range of boulder volumes are generated for all runout distances, although we do observe that the number of larger boulders decreases with increasing distance from the source, revealing that smaller ML boulders have greater success traveling further from the parent rock. ML boulders with map-length runout distance exceeding 450 meters (n=4) have an average size of 0.44 m^3, reflecting their comparatively smaller size.

3.5.6 Boulder elevation vs. runout distance

I plot boulder elevation as function of runout distance to highlight frequency-runout distribution and total runout distances for Rapaki paleo-boulders (Fig. 22). The western (upslope) limit of the Rapaki village is shown. The boulder data points reveal a slightly concave (average) slope. The best fit is an exponential decay (R^2=0.96) with distance from the source, although a linear fit also yields R^2=0.94. The highest accumulation of boulders is present at elevations ranging from ~200 to 275 meters (asl) and between runout distances of ~100-175 meters (map-length) from the source rock. Maximum runout distance for Rapaki prehistoric boulders is ~561 meters. Mapping suggests that prehistoric boulders were not deposited in the low-lying area now occupied by the Rapaki village.

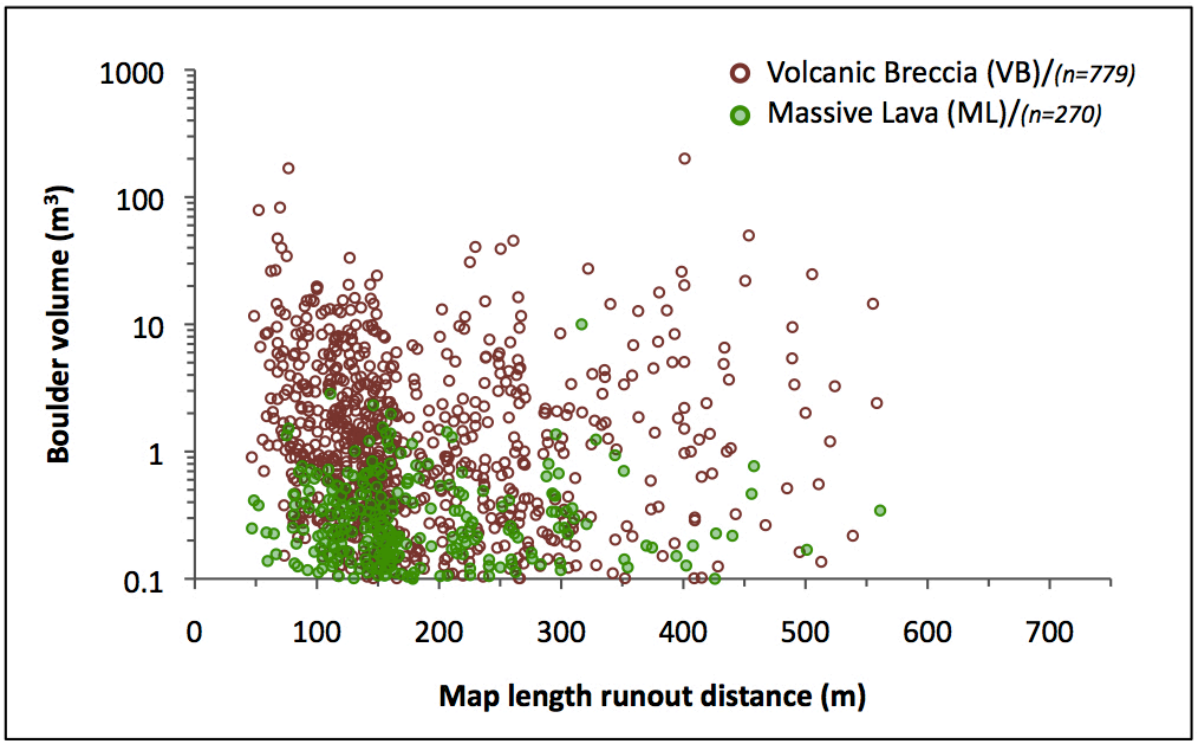

Figure 19. Runout distance for Rapaki prehistoric rockfall boulders plotted as a function of boulder volume (m^3).

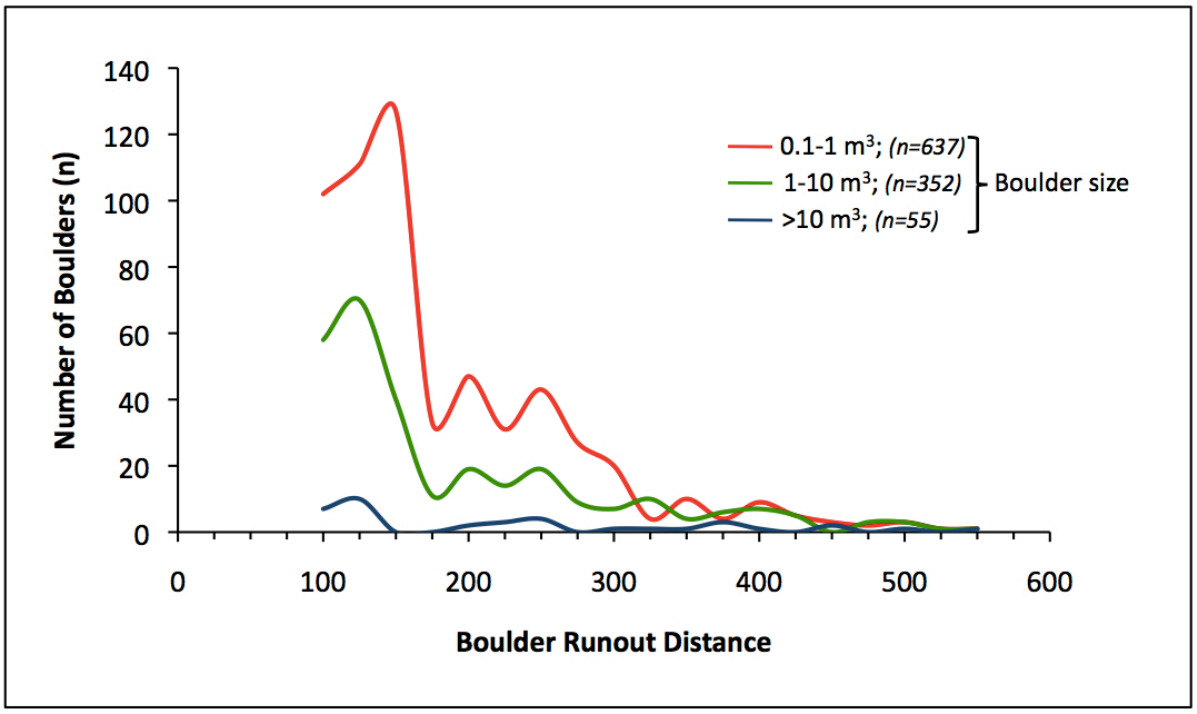

Figure 20. Frequency-runout distribution for boulder sizes 0.1-1 m^3, 1-10 m^3, and >10 m^3. Data includes VB and ML rockfall boulders. Due to safety concerns, volumes were not recorded for prehistoric rockfall boulders within 100 meters of the source cliff.

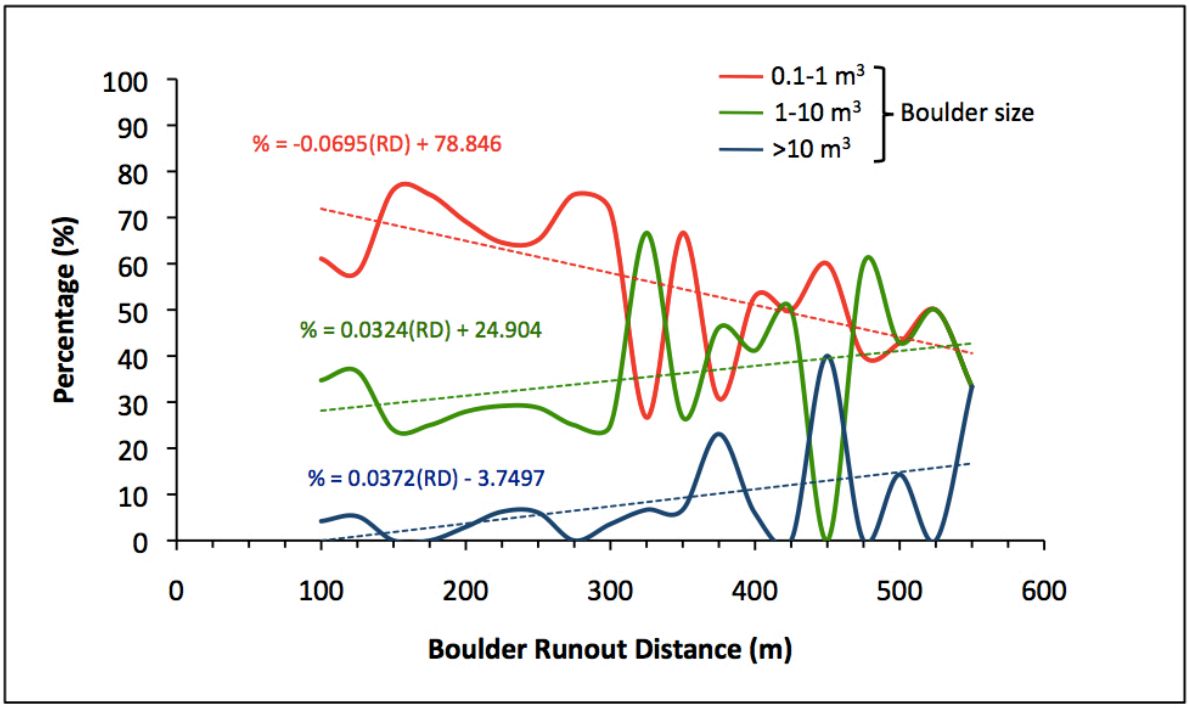

Figure 21. Relative percentage of rockfall boulders (with volume = 0.1-1 m^3, 1-10 m^3, or >10 m^3) for a given runout distance. Moderate and large boulders show gradual increase while smaller size boulders show overall decline with increasing distance from the source rock.

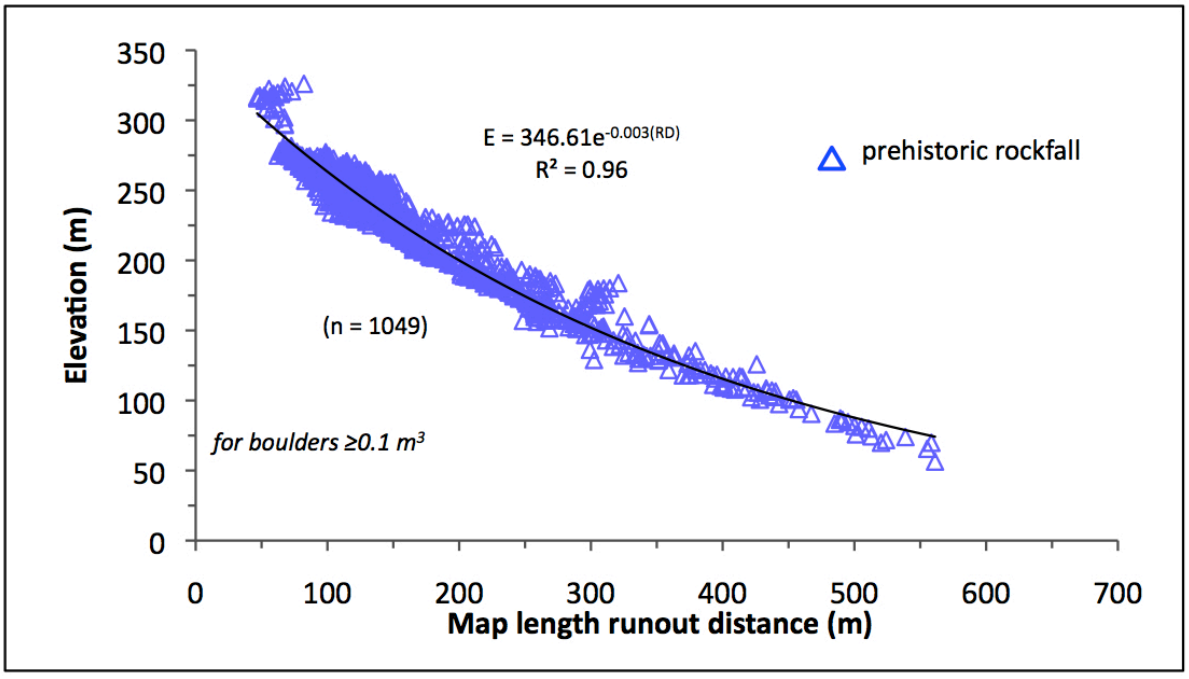

Figure 22. Rapaki prehistoric boulder runout distance plotted as a function of elevation. Exponential regression line is shown (where E is elevation, RD is map length runout distance).

3.5.7 Boulder elevation vs. volume

Figure 23a shows elevation plotted as a function of boulder volume for both VB and ML boulder lithologies. No prehistoric boulders are deposited below an elevation of ~56 meters (asl). ML boulders rarely exceed ~2 m^3 in size and the number of ML boulders decreases significantly below an elevation of ~150 meters (asl). Clustering for both VB and ML boulders is observed at elevations above ~210 meters (asl) and between ~150-200 meters (asl). Figure 23b incorporates boulder size and highlights the reduction of boulder frequency moving downward in elevation and with increasing boulder size.

3.5.8 Comparison of prehistoric and modern rockfall at Rapaki

Modern (2011 CES-generated) and prehistoric rockfall boulders at Rapaki are lithologically equivalent and exhibit a similar range of shapes and sizes (Borella et al., 2016a). In contrast to the Rapaki paleo-boulders, modern boulders (deposited during the CES) exhibit fresh, bright colored faces, ranging in color from reddish brown to orange brown to light reddish brown (Figs. 8a,b). Modern boulder surfaces (i.e. those created during detachment and subsequent fragmentation) do not contain lichen and exhibit a relatively low degree of surface roughness (Fig. 8b,c). For modern VB boulders, surface roughness is apparent (albeit less) but clearly reflects conditions of fracturing during detachment and subsequent descent rather than in-situ differential weathering between host matrix and more resistant volcanic clasts. At a scale of ~5-10 cm, VB modern boulder surfaces exhibit significantly less sinuosity and shallower micro-slope angles compared with their VB prehistoric rockfall counterparts. The deep pitting and grooves created in the VB prehistoric boulders are not observed in the modern boulder surfaces. ML modern boulders show similar smooth surfaces (compared with prehistoric ML boulders) with very little surface roughness. Modern boulders do not have upslope sedimentary wedge accumulations.

3.5.8.1 Boulder frequency

During the 2011 Christchurch earthquakes (22 February and 13 June events) approximately 285 rockfall boulders with size ≥0.5 m^3 were emplaced within the Rapaki study site boundaries (Fig. 24). In comparison, I mapped 583 prehistoric boulders with size ≥0.5 m^3 (Fig. 24). However, this represents only a fraction of the entire data set for prehistoric boulders at Rapaki. As a result, boulder frequency counts at specific distances from the source cliff (see Section 3.2) were recorded and used to extrapolate the total number of prehistoric boulders (for volume ≥0.1 m^3) for the remaining (i.e. unmapped) areas of the study site (Supplementary Fig. 1). I estimate the total number of boulders with size ≥0.1 m^3 at Rapaki to be ~2,406. This equates to 1,337 boulders for size ≥0.5 m^3 within the entire study site

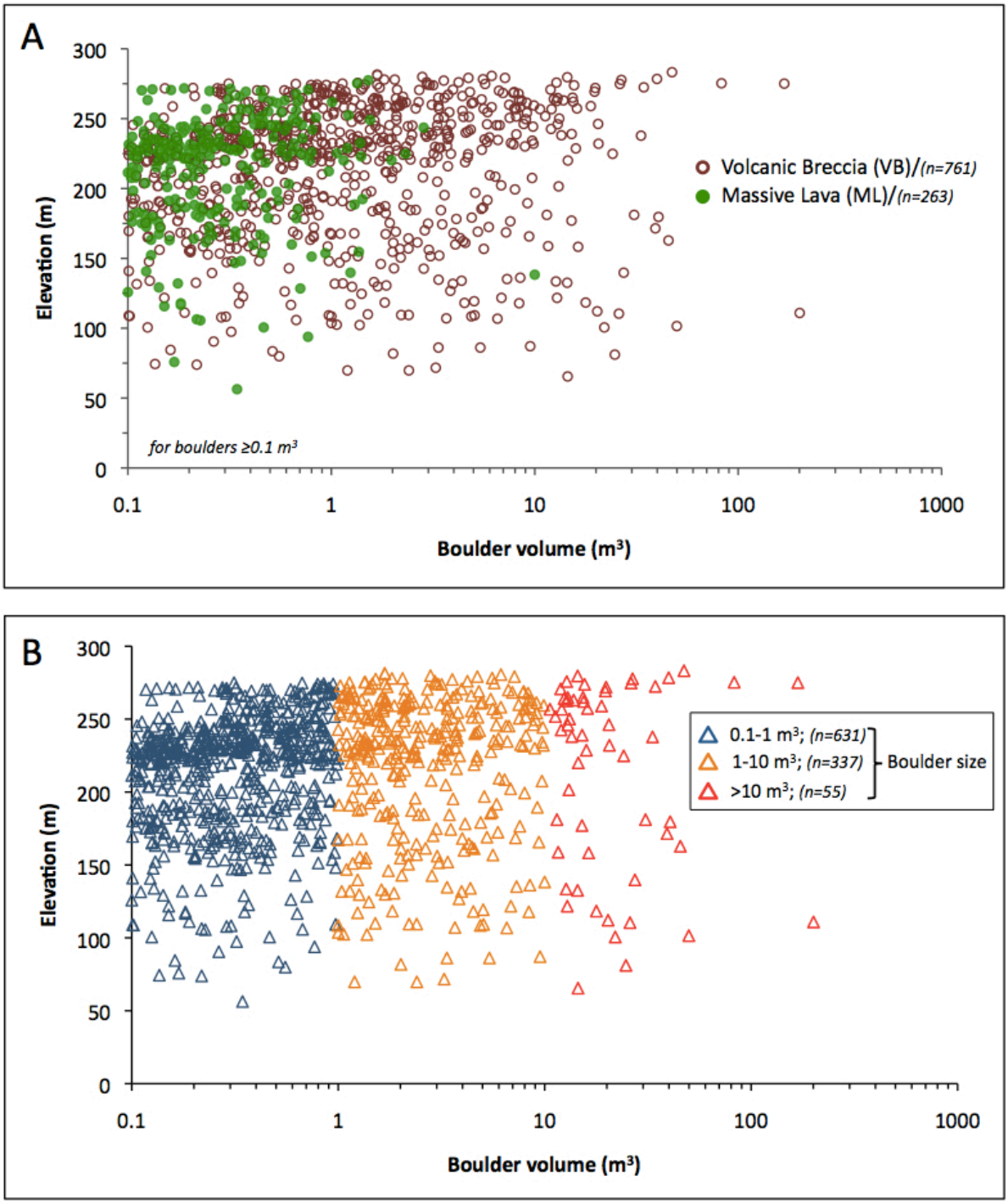

Figure 23. **(A)** Prehistoric boulder volume plotted as a function of elevation, highlighting the larger size range for VB boulders and the absence of prehistoric boulders deposited below ~50 meters asl. **(B)** Prehistoric boulder volume plotted as a function of elevation with boulder volume (categories = 0.1-1 m^3; 1-10 m^3; >10 m^3) shown.

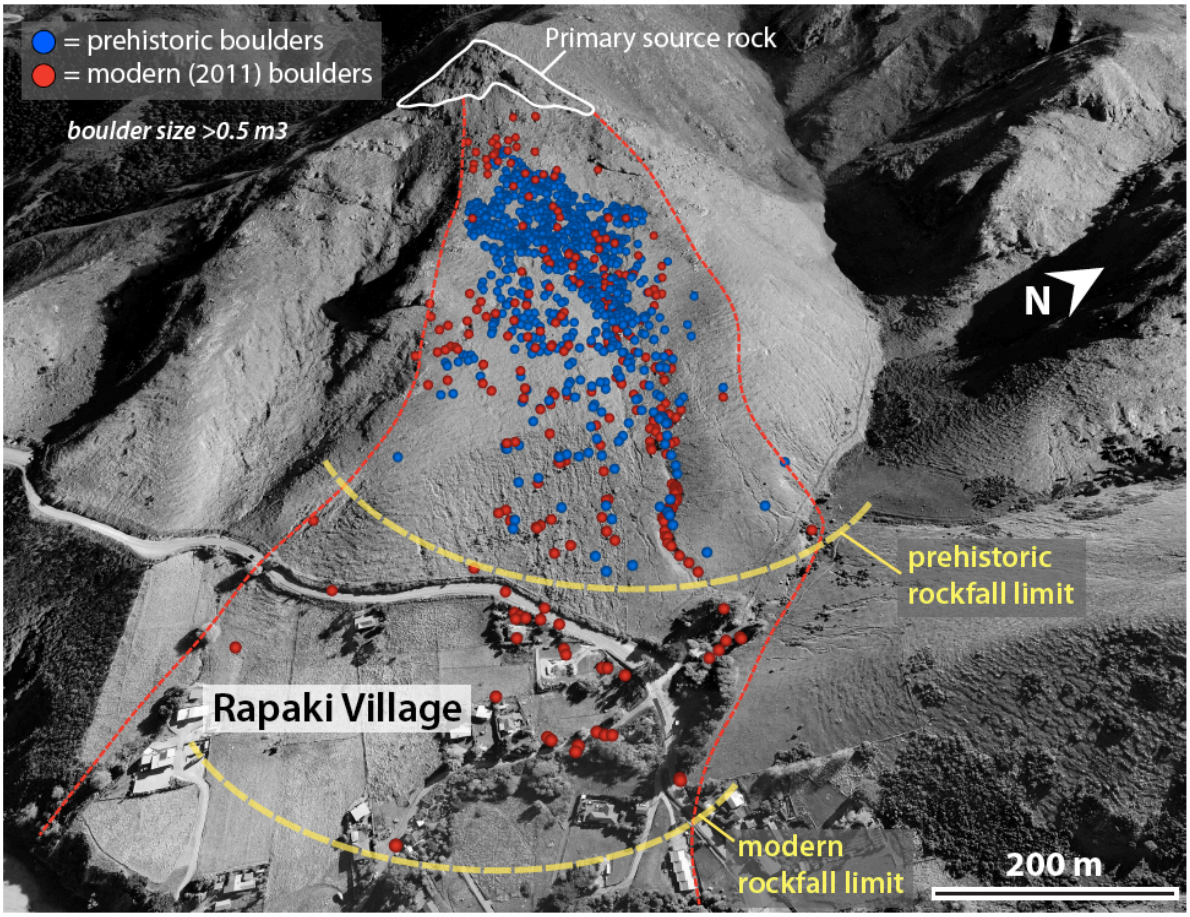

Figure 24. Comparison of spatial distribution for mapped prehistoric and modern (2011) rockfall boulders. Maximum travel distance for modern rockfall boulders exceeds maximum runout distance for prehistoric boulders by ~150-175 meters, and would have likely been further if roads and homes were absent. ~26 modern boulders reached the Rapaki village and caused major destruction to residential homes and properties. The increase in maximum travel distance for modern boulders is attributed to anthropogenic deforestation of the study hillslope, occurring sometime between AD 1661 and AD 1950 (Borella et al., 2016a,b).

(including mapped and extrapolated areas) and indicates that modern rockfall represents approximately 1/5th of the total observable prehistoric rockfall at Rapaki. Assuming a coseismic origin with ground shaking intensity similar to that experienced during the 22 February and 13 June 2011 Christchurch earthquakes, this would suggest ~5 previous rockfall events have occurred to account for the observable prehistoric rockfall at Rapaki. It is, however, probably more reasonable to assume 3 or 4 prehistoric rockfall events at the Rapaki study site from our dataset of mapped boulders because the potential to expose prehistoric boulders that were emplaced during even earlier rockfall events is high near the source rock where erosion dominates.

3.5.8.2 Boulder size distribution

Size and frequency-volume distributions for modern and prehistoric boulders (size ≥0.5 m^3) at Rapaki show a strong similarity (Fig. 25). For modern boulders (n = 112) median size (50%) is 2.05 m^3, with 25% (Q1) of boulders lying below 1.01 m^3, 75% (Q3) of boulders lying below 4.16 m^3, and 95% of boulders lying below 23.48 m^3 (Table 2). Average (mean) boulder size is 5.50 m^3. For the combined prehistoric boulder population (n = 583, boulder volume ≥ 0.5 m^3), median size is 1.70 m^3, with 25% (Q1) of boulders lying below 0.89 m^3, 75% (Q3) of boulders lying below 4.53 m^3, and 95% of boulders lying below 15.93 m^3 (Table 2). Average (mean) boulder size is 4.99 m^3. The ratio of prehistoric to modern rockfall boulders is ~5:1.

	Modern Rockfall Boulders (n=112)	*Prehistoric Rockfall Boulders (n=583)*
	(m^3)	(m^3)
25th (Q1)	1.01	0.89
Median	2.05	1.70
75th (Q3)	4.16	4.53
95th	23.48	15.93
Maximum	80.00	200.56
Mean	5.50	4.99

Table 2. Volumetric comparison of prehistoric and modern boulders at Rapaki.

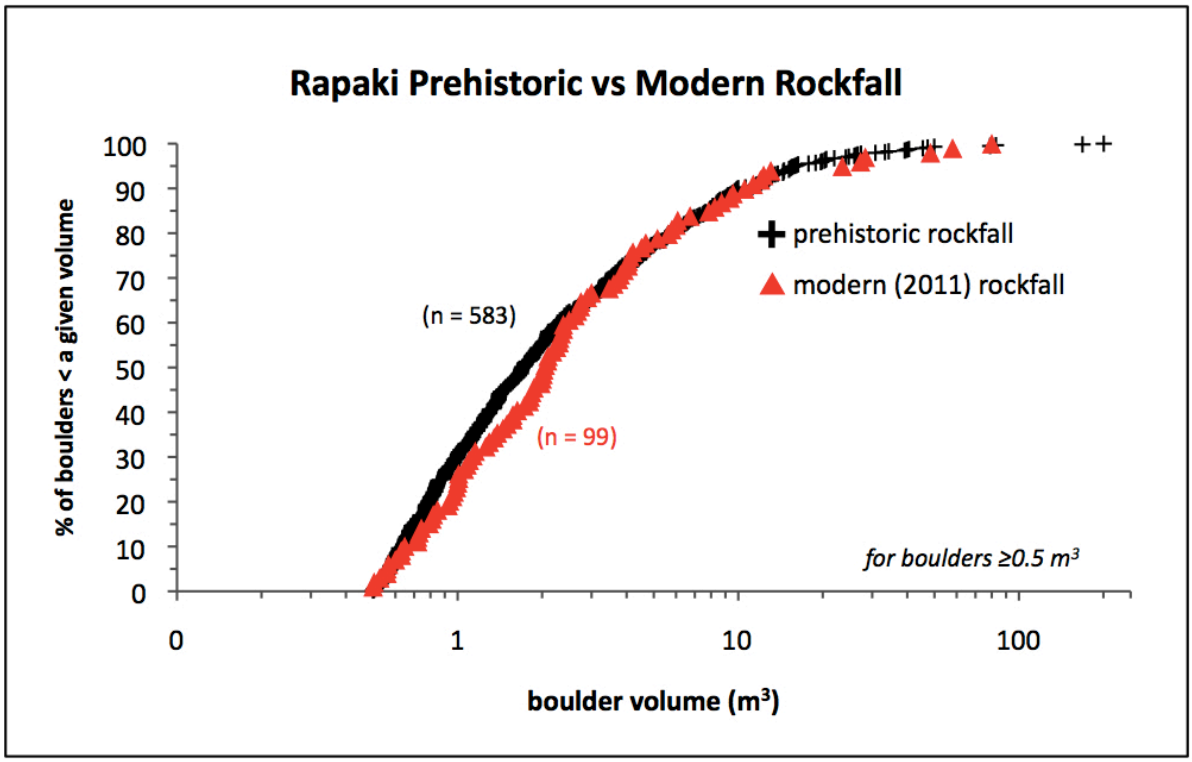

Figure 25. Rockfall size distribution for prehistoric (n=583) and modern (n=99) boulders at Rapaki as a proportion (percent) of boulders less than a given size.

3.5.8.3 Spatial distribution

A comparison of spatial distribution for prehistoric and modern boulders at Rapaki reveals two primary differences:

(1) Of the total mapped boulder population (modern + prehistoric), the prehistoric boulders have a higher relative percentage deposited close to the source cliff, with the increase most pronounced above an elevation of ~220 meters (asl) (Figs. 24 and 26). In contrast, the highest density for modern boulders is found at elevations ranging from ~125-200 meters (asl).

(2) Maximum runout distance for Rapaki modern boulders is significantly greater than for prehistoric boulders. Maximum travel distance for modern boulders is ~770 meters (boulder volume=8.72 m^3), compared with ~561 meters for Rapaki prehistoric boulders (boulders volume=14.5 m^3), highlighting a maximum runout difference of ~210 meters (~680 feet) (Figs. 24, 26, 27). As a result of the increased runout distance, numerous modern boulders (n=26) impacted and severely damaged homes within the Rapaki village during the 2011 Christchurch earthquakes (Figs. 24 and 26).

The discrepancy between spatial distributions of modern and prehistoric rockfall deposits identified in this study is primarily attributed to intervening landscape change in the form of anthropogenic deforestation sometime between AD 1661 and AD 1950 (Borella et al., 2016a). The presence of a dense podocarp/hardwood forest on the Rapaki hillslope during emplacement of prehistoric boulders would have promoted deposition of rockfall on the upper slope. Its subsequent removal enabled 2011 modern boulders to travel further and impact the low-lying Rapaki village (Borella et al., 2016a).

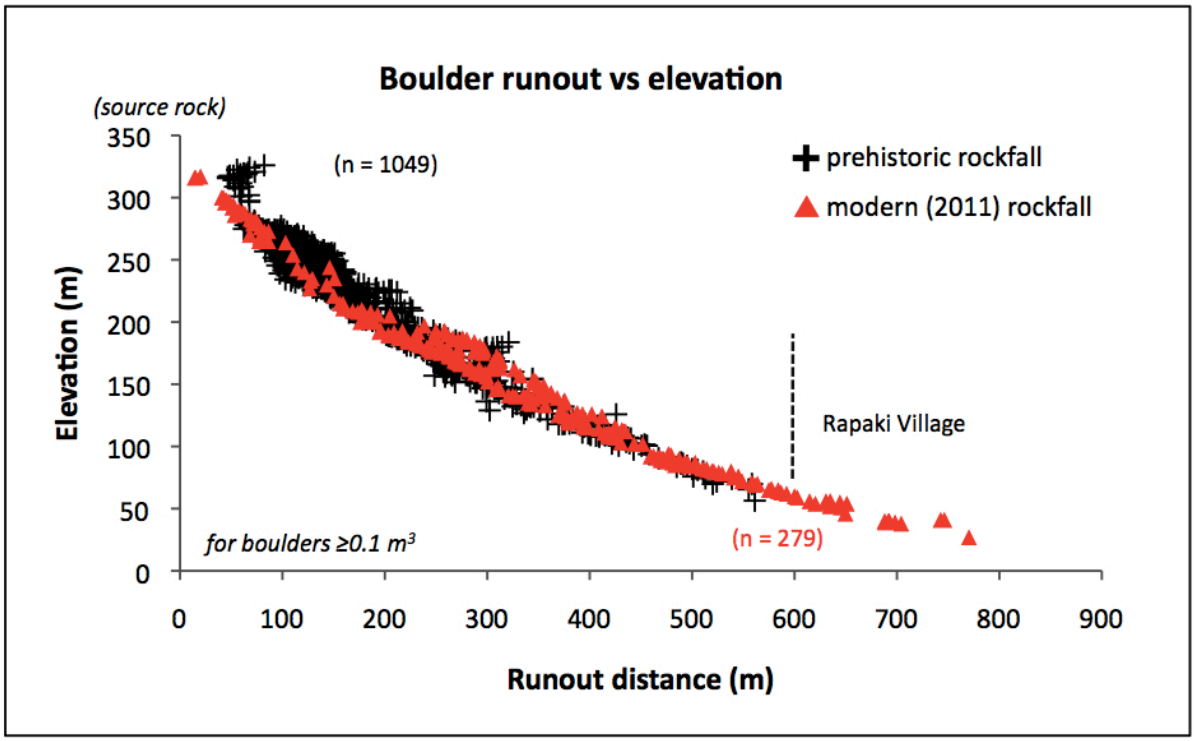

Figure 26. Prehistoric and modern boulder runout distance plotted as a function of elevation (asl). Maximum runout distance for modern boulders exceeds travel distance for prehistoric boulders with ~26 modern boulders (~9% of 2011 rockfall boulders) impacting the Rapaki village.

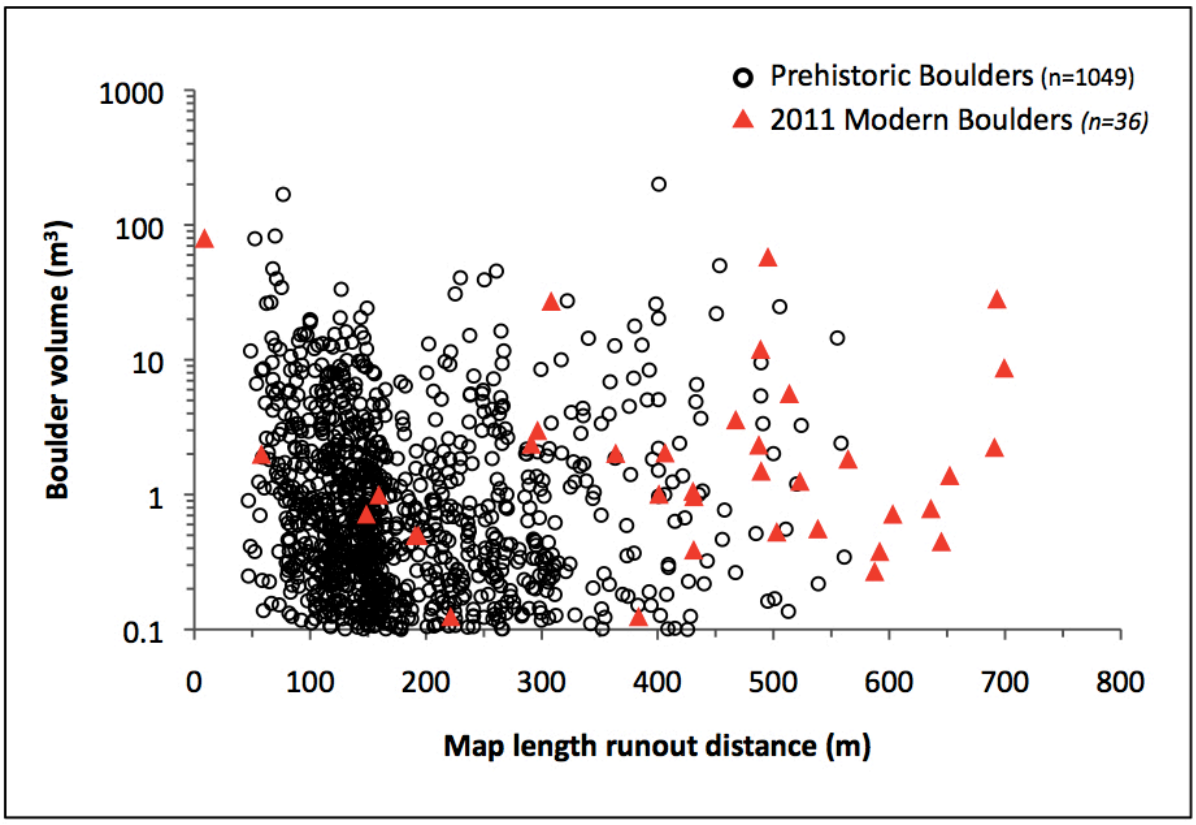

Figure 27. Runout distance plotted as a function of boulder volume for modern and prehistoric rockfall boulders.

3.5.9 Purau rockfall boulders

Purau prehistoric and modern boulders are lithologically equivalent to Rapaki rockfall boulders and consist of two primary lithology types: volcanic breccia (VB) and massive lava (ML) basalt. Purau rockfall was characterized and mapped primarily for a comparative analysis with Rapaki rockfall.

3.5.9.1 Size distribution for prehistoric rockfall boulders

Of the 684 mapped prehistoric rockfall boulders at the Purau study site with size ≥1.0 m^3, ~64% of the mapped prehistoric boulders are comprised of volcanic breccia (n=436), while the remaining ~36% consist of massive lava (n=248). ML/VB frequency ratio is 0.57 and total volume of mapped prehistoric rockfall is 5,539.39 m^3. ML boulders exhibit a significantly smaller range of boulder sizes than VB boulders. Total volume for mapped VB boulders is 4938.76 m^3, representing ~90% of the total boulder volume. Volume for mapped ML boulders is 555.63 m^3, comprising the remaining ~10% of the total boulder volume (Table 3).

Prehistoric Rockfall Boulders	All (n=684) (m^3)	VB (n=436) (m^3)	ML (n=248) (m^3)
25th (Q1)	1.42	1.70	1.20
Median	2.20	3.21	1.56
75th (Q3)	5.08	7.65	2.30
95th	27.06	40.91	5.26
Maximum	616.00	616.00	26.21
Mean	8.10	11.43	2.24
Total volume	5539.39	4938.76	555.63
% of total volume	100	89	11
% of mapped boulders	100	64	36

Table 3. Boulder size statistics for Purau prehistoric rockfall, including comparison of VB and ML lithologies (volume ≥1.0 m^3).

The rockfall frequency-volume distribution (Fig. 28) for Purau prehistoric rockfall can be modeled using a power law ($R^2 = 0.89$). Bin size is 0.5 m^3. The trendline is fit to boulder volumes with frequency greater than 2.

Power law equation: $B\# = 204.76(BV)^{-1.512}$ (5)

Where B# = number of boulders, BV = boulder volume

Figures 28 and 29 show a steep drop in the number of boulders with increasing boulder volume.

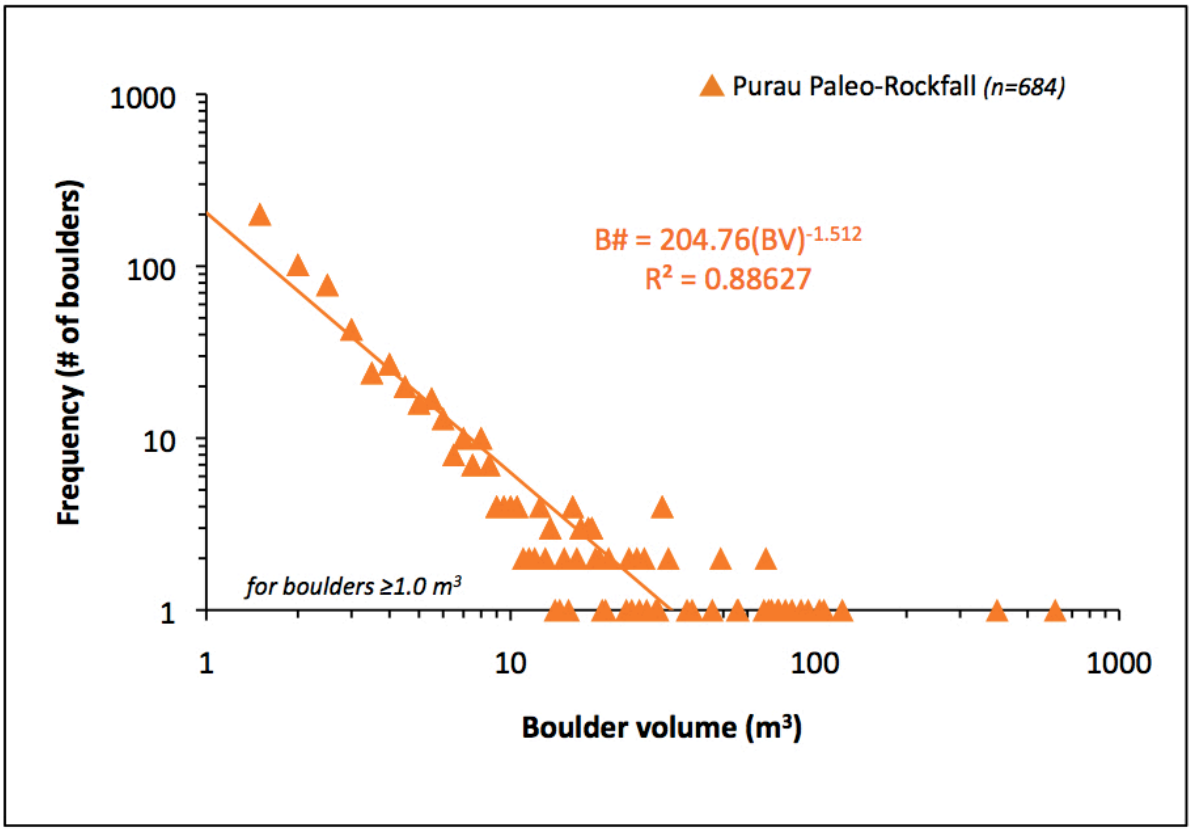

Figure 28. Boulder frequency-volume distributions for Purau prehistoric boulders can be modeled using a power law. The trendline is fit to boulder volumes with frequency (N) greater than 2.

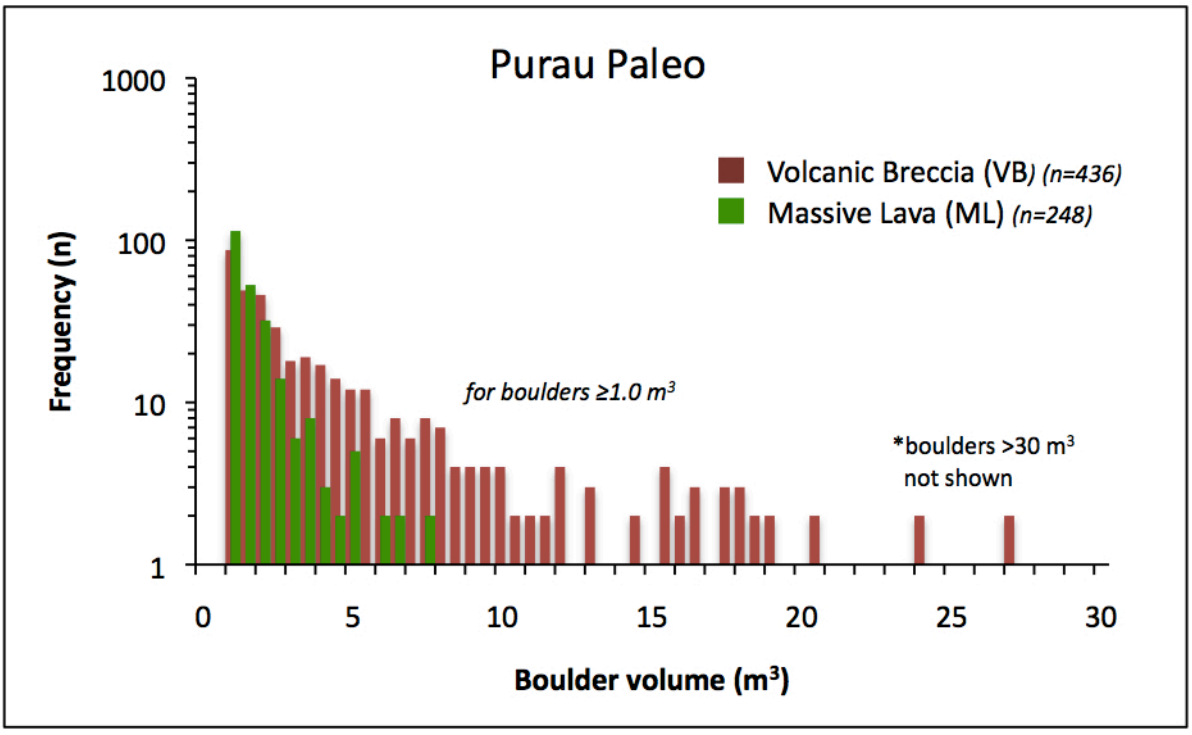

Figure 29. Histogram comparing boulder volume frequency for Purau prehistoric VB and ML boulders.

3.5.9.2 Size distribution for modern rockfall boulders

I mapped 136 modern rockfall boulders (generated during 2010-2011 CES) at the Purau study site with volume ≥1.0 m^3 (Table 4). ~93% of the mapped modern boulders are comprised of volcanic breccia (n=127), while the remaining ~7% consist of massive lava (n=9). ML/VB frequency ratio is 0.07. Total volume of mapped modern rockfall is 723.35 m^3.

Modern Rockfall Boulders	All (n=136) (m^3)	VB (n=127) (m^3)	ML (n=9) (m^3)
25th (Q1)	1.34	1.36	1.13
Median	2.01	2.04	1.68
75th (Q3)	4.46	4.87	2.14
95th	17.66	17.78	2.48
Maximum	79.97	79.97	2.64
Mean	5.32	5.58	1.67
Total volume	723.35	708.34	15.00
% of total volume	100	98	2
% of mapped boulders	100	93	7

Table 4. Boulder size statistics for Purau modern rockfall (volume ≥1.0 m^3).

ML boulders exhibit a significantly smaller range of boulder sizes than VB boulders. The total volume for mapped modern VB boulders is 708.34 m^3, representing ~98% of the total boulder volume (723.35 m^3) identified (Table 4). The total volume of the mapped modern ML boulders is 15.00 m^3, representing the remaining ~2% of the total boulder volume (723.35 m^3). VB and ML boulders comprise ~93% and ~7% of total mapped modern rockfall, respectively, highlighting a greater differential than mapped VB and ML prehistoric boulders (Table 4).

The rockfall frequency-volume distribution (Fig. 30) for Purau modern rockfall can be modeled using a power law ($R^2 = 0.91$). Bin size is 0.5 m^3. The trendline is fit to boulder volumes with frequency (N) greater than 2.

Power law equation: $B\# = 70.325(BV)^{-1.754}$ (6)

Where B# = number of boulders, BV = boulder volume

Similar to Purau prehistoric rockfall, the number of modern rockfall boulders decreases rapidly with increasing boulder volume.

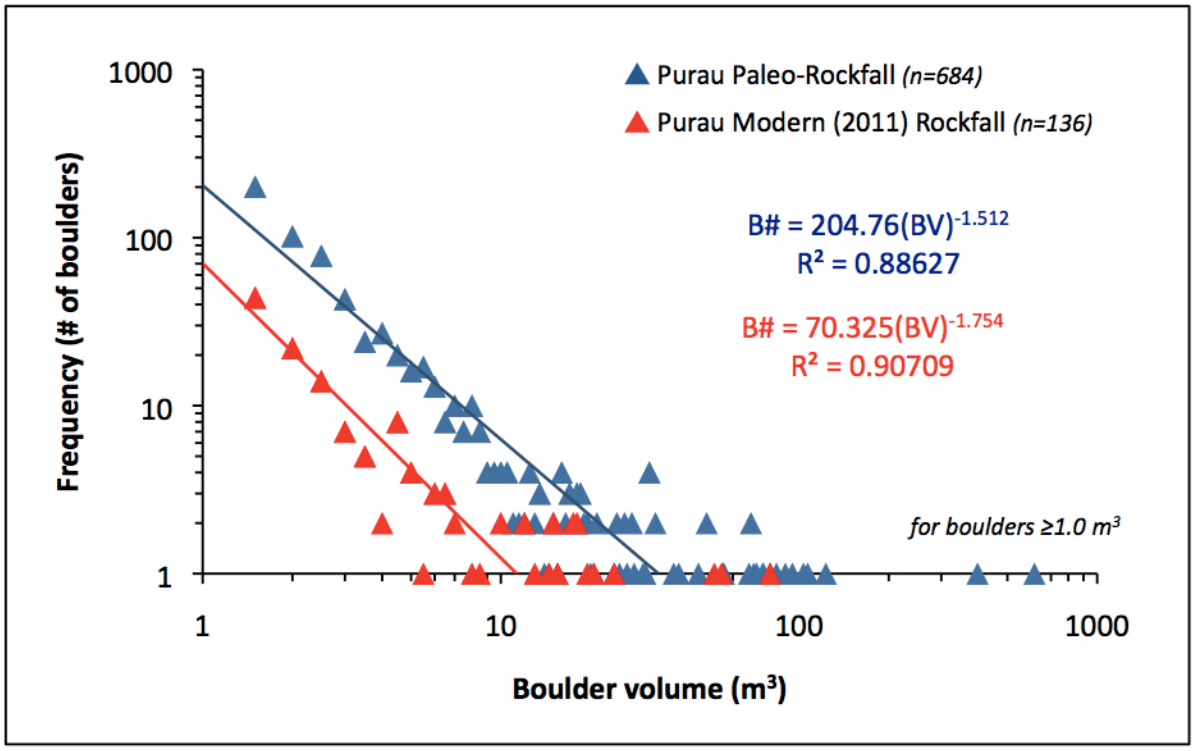

Figure 30. Purau modern rockfall boulders can be modeled using a power law and show similar fit to their prehistoric counterparts. The trendline is fit to boulder volumes with frequency (N) greater than 2.

3.5.9.3 Comparison of size distribution for prehistoric and modern rockfalls

A statistical comparison of boulder size distribution suggests prehistoric boulders at Purau obtain slightly larger sizes than their modern rockfall counterparts (Tables 3 and 4). Notable increases are the 95th percentile (prehistoric=27.06 m^3; modern=17.66 m^3) and maximum (prehistoric=616.00 m^3; modern=79.97 m^3) boulder sizes.

Figure 31 shows prehistoric and modern rockfall size distributions as a proportion of boulders less than a given size. The comparison suggests the modern boulder data set fits nicely as a subset of the prehistoric boulder population, but also reveals a higher number of large prehistoric rockfall boulders.

3.5.9.4 Comparison of boulder frequency for prehistoric and modern rockfalls

The total number of mapped prehistoric rockfall boulders at Purau with size ≥1.0 m^3 is 684. In comparison, the total number of mapped modern rockfall at Purau with size ≥1.0 m^3 is 136. The frequency ratio of prehistoric to modern rockfall is ~5:1.

Assuming that prehistoric rockfall production at Purau is dominated by rare strong earthquakes with similar ground-shaking characteristics to that observed in 2011, then five prehistoric rockfall events of equivalent volume to the 2011 events could account for the total number of prehistoric rockfall at Purau. If prehistoric rockfall events were more (less) voluminous (i.e. ground-shaking intensity was lower or higher) than the 2011 events, then fewer (more) events may have occurred over the duration of time represented by the cumulative rockfall volumes identified.

3.5.9.5 Comparison of total boulder volume for prehistoric and modern rockfalls

The total volume of the Purau prehistoric and modern rockfall is 5,539.39 m^3 and 723.35 m^3, respectively (Table 4). The ratio of prehistoric to modern boulder volume is ~7.5:1. I attribute the discrepancy in prehistoric/modern volume ratios compared with the boulder frequency ratio to the extreme size for several of the prehistoric boulders at Purau. Normalizing maximum prehistoric boulder size to that of modern boulders (i.e. eliminating boulders with volume greater than ~80 m^3 [size of largest modern boulder]) reduces total prehistoric volume to ~3750 m^3 and generates a prehistoric to modern boulder volume ratio of ~5:1, similar to that derived from the relative number of mapped boulders.

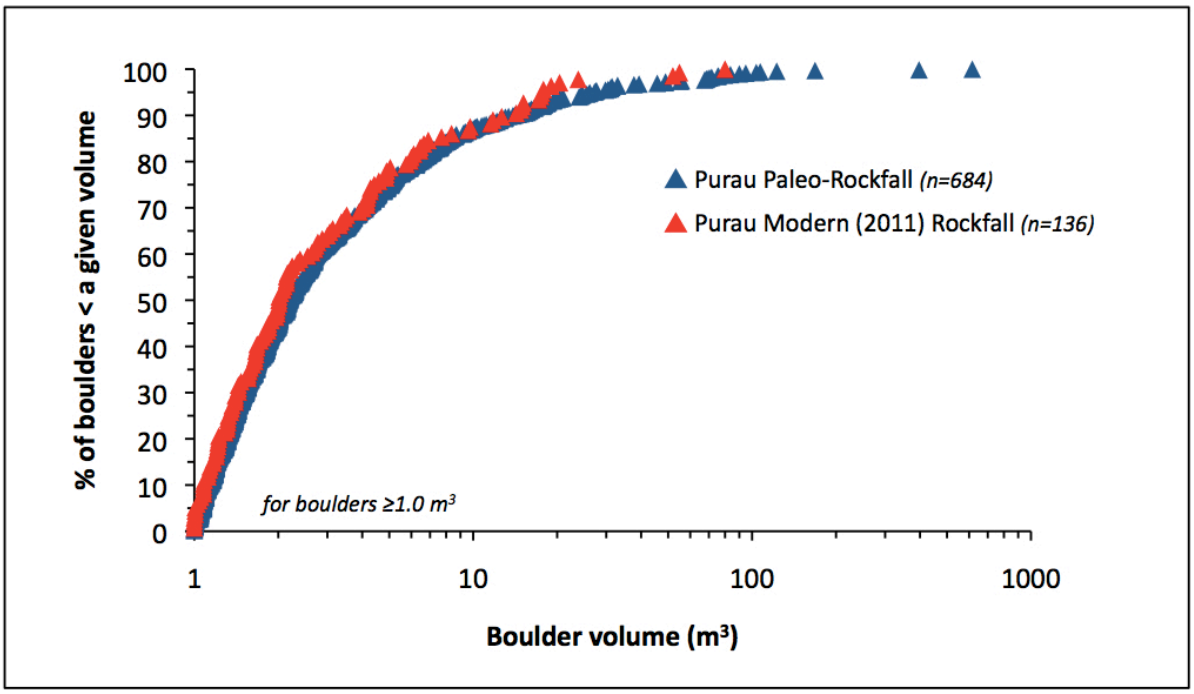

Figure 31. Purau prehistoric and modern rockfall size distributions as a proportion of boulders less than a given size.

3.5.9.6 Comparison of prehistoric and modern VB boulders

Prehistoric VB boulders display consistently larger sizes than modern VB boulders (Tables 3 and 4). Median (prehistoric=3.21 m^3; modern=2.04 m^3), mean (prehistoric=11.43 m^3; modern=5.58 m^3), and 95th percentile (prehistoric=40.91 m^3; modern=17.78 m^3) boulder sizes are all significantly higher. The larger prehistoric boulder size may reflect detachment from source rock locations with wider joint spacing and/or bed thickness during prehistoric rockfall events.

3.5.9.7 Comparison of prehistoric and modern ML boulders

The number of mapped ML boulders is significantly higher (paleo=248 vs. modern=9) within the prehistoric boulder data set. Mapped prehistoric ML boulders comprise ~36% of the total data set, while mapped contemporary (2010-2011) ML boulders comprise a mere ~7% of the entire modern data set (Tables 4 and 5). ML/VB ratio is 0.57 for prehistoric rockfall and 0.07 for modern rockfall.

Prehistoric ML boulders comprise ~10% of the total paleo-boulder volume, while modern ML boulders comprise only ~2% of the entire modern boulder volume (Table 4). Prehistoric ML boulders obtain larger sizes than their modern counterparts, with 95th percentile (prehistoric=5.26 m^3; modern=2.48 m^3) and maximum (prehistoric=26.12 m^3; modern=2.64 m^3) boulder sizes for prehistoric boulders displaying significantly higher values (Tables 4 and 5). This may indicate variability in joint density and spacing and layer thickness within the massive lava source rock. The possibility exists that prehistoric boulders were sourced from thicker massive lava layers with more widely spaced joint networks. I do note that the majority of ML paleo-boulders are deposited near and within a single drainage canyon suggesting a common proximal source. Field observations suggest this section of the source rock is currently less susceptible (i.e. smooth lower gradient slope) to rockfall and thus during the 2011 earthquakes did not produce rockfall. Further, this section of the source rock displays surface morphologies consistent with a possible prehistoric rockslide, thus providing a high volume of massive lava boulders into the nearby canyon.

3.5.9.8 Source rock geology and influence on boulder size and shape

Field observations suggest source rock conditions, including texture and structure, at Purau are similar to Rapaki, although a detailed structural analysis of the source rock is required at both study locations for verification. The source rock is comprised of the same two primary lithologies: volcanic breccia (VB) and massive lava (ML) basalt. Jointing is pervasive within the volcanic source rock, with layers comprised of ML exhibiting the highest fracture density and smallest spacing between individual joints. In contrast, layers consisting of volcanic breccia are thicker and contain irregular to regular joint

patterns with wider spacing (often >10 meters). Prehistoric and modern boulders at Purau exhibit a similar range of shapes compared to their counterparts at the Rapaki study site. ML boulders are blocky to tabular to angular, while boulders comprised of volcanic breccia range from blocky to elongate, with subrounded to subangular boundaries.

3.5.9.9 Spatial distribution for Purau prehistoric and modern boulders

Spatial distribution of prehistoric rockfall boulders at Purau is strongly influenced by surface topography. The study site is dominated by several small interfluves/spurs with bounding valleys. The majority of prehistoric rockfall has been captured in drainage gullies and larger canyons (Fig. 32), within ~100-115 meters (i.e. upper slope) of the source rock. The largest prehistoric boulders are deposited near the source rock, but some large prehistoric rockfall boulders (~20-90 m^3) have been emplaced further downslope (maximum map length runout distances between ~260 and 295 meters). Maximum runout distance for prehistoric boulders emplaced on interfluves is ~355 meters (map length). Prehistoric boulders are deposited at elevations ranging between ~50 and ~300 meters above sea level (Fig. 33).

Deposition of modern rockfall boulders is also primarily influenced by surface topography. With the exception of modern boulders furthest to the south, the majority of contemporary (2011) rockfall boulders have been emplaced into drainage canyons (Fig. 32). Several canyons and interfluves, which contain prehistoric rockfalls, show no modern rockfall deposition, reflecting the absence of source rock detachment in these areas during the 2011 Christchurch earthquakes. It is reasonable to assume that modern rockfall boulders have experienced very little to no remobilization, and thus runout distances within canyons can be included. Maximum runout distance for contemporary rockfall boulders ranges from ~250 to 400 meters. The majority of modern boulders are deposited within an elevation range of ~40 to ~250 meters (asl) (Fig. 34).

3.5.9.10 Comparison of VB and ML prehistoric boulders

Prehistoric VB boulders are widely distributed throughout the Purau field site, while deposition of prehistoric ML boulders is primarily focused within the southern section of the field site (Fig. 35). The relatively small percentage of ML boulders in the northern sections of the field site reflects a lack of ML source rock in these areas. The largest ML boulders are typically observed nearest the source at elevations ranging from ~200-250 meters (asl). The large VB boulders (>10 m^3) are found in greatest abundance nearest the source rock, but have also been emplaced further downslope at a minimum elevation of ~75 meters (asl) (Fig. 33). The contrast in boulder travel distance for the largest ML and VB boulders can likely be attributed to differences in shape, as the VB boulders are typically more

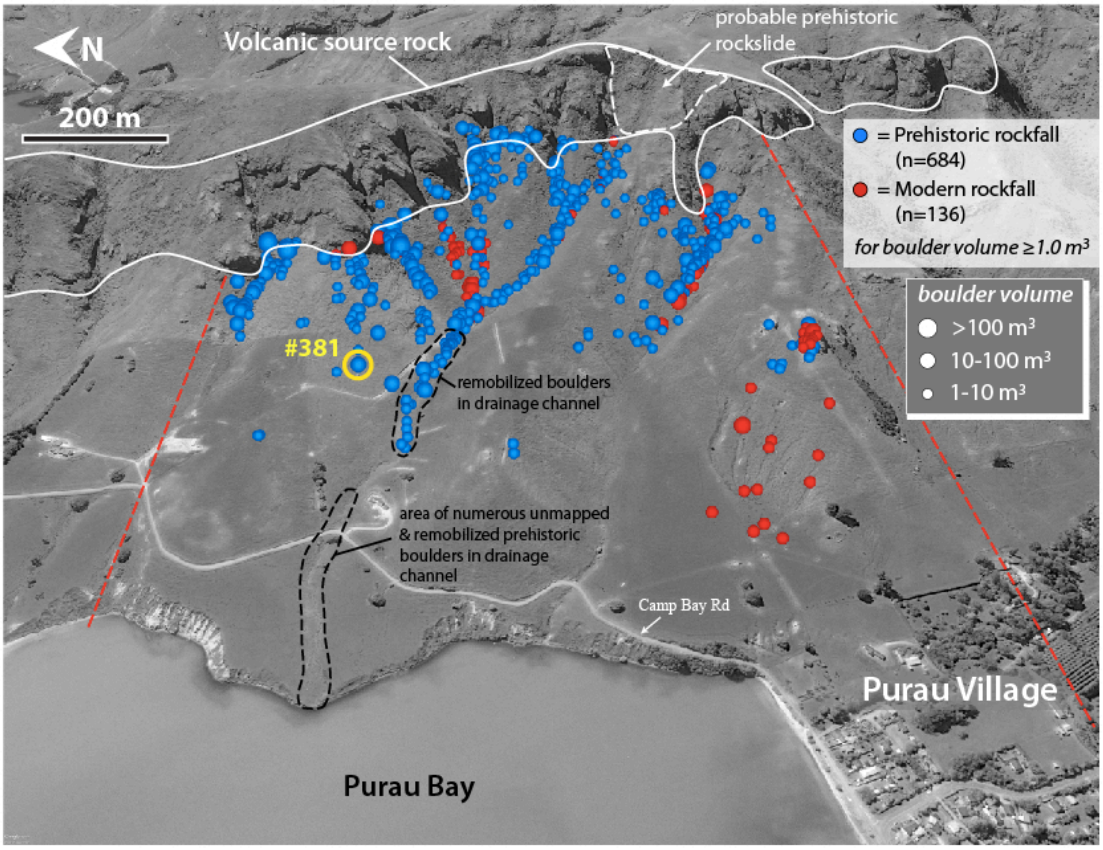

Figure 32. Mapped prehistoric and modern rockfall boulders at Purau study site. Displayed rockfall locations are for boulder size ≥1.0 m^3. Rockfall boulders have been separated into three size bins: 1-10 m^3, 10-100 m^3, and >100 m^3. Near the village of Purau, maximum runout distance for modern boulders exceeds that of prehistoric rockfall.

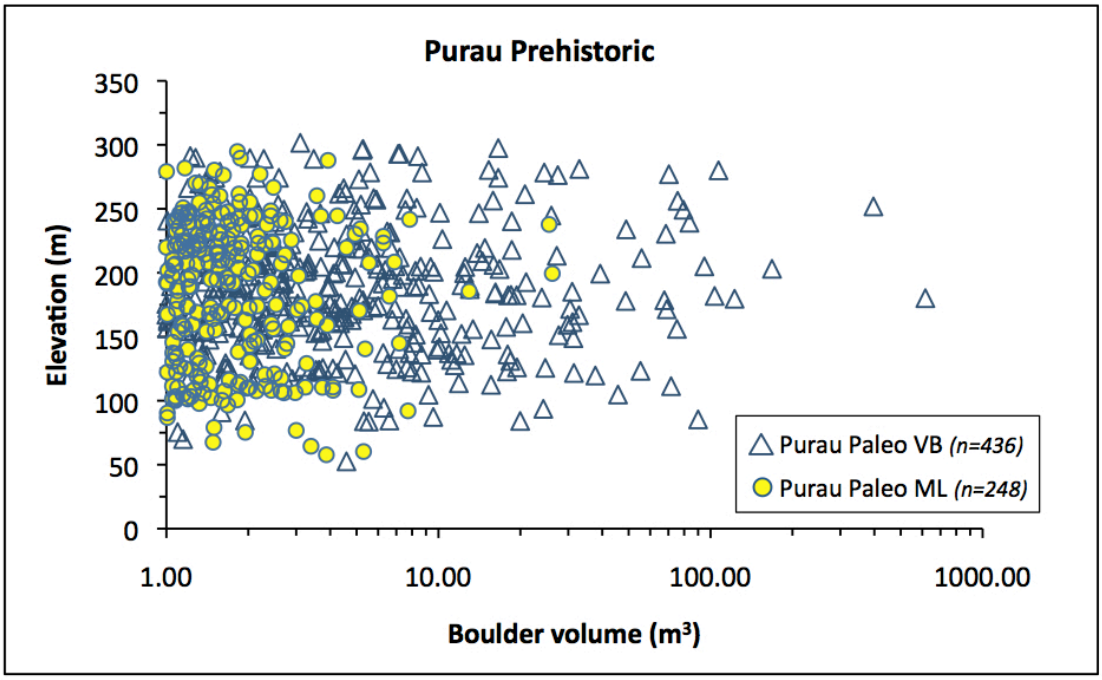

Figure 33. Prehistoric boulder volume plotted as a function of elevation. Mapped prehistoric rockfall boulders are deposited at elevations ranging from ~50-300 meters above sea level. VB and ML boulders are delineated.

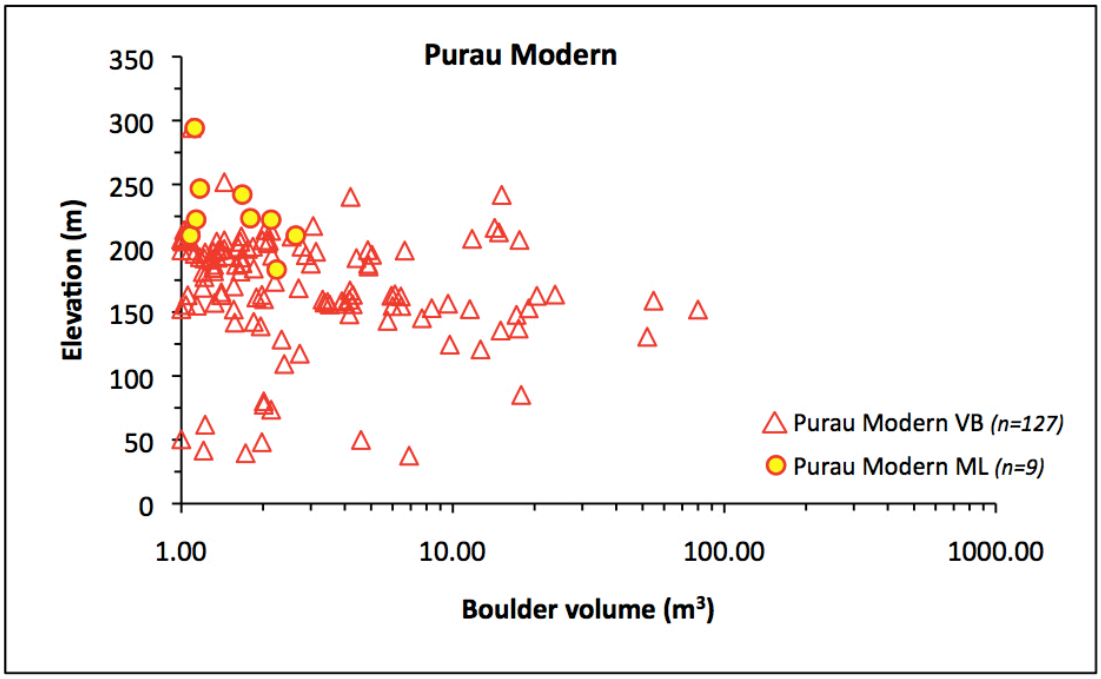

Figure 34. Modern (2011) boulder volume plotted as a function of elevation. Modern boulders are primarily deposited beneath at elevation of ~250 meters (asl). Emplacement of modern rockfall boulders extends downward to ~35 meters (asl).

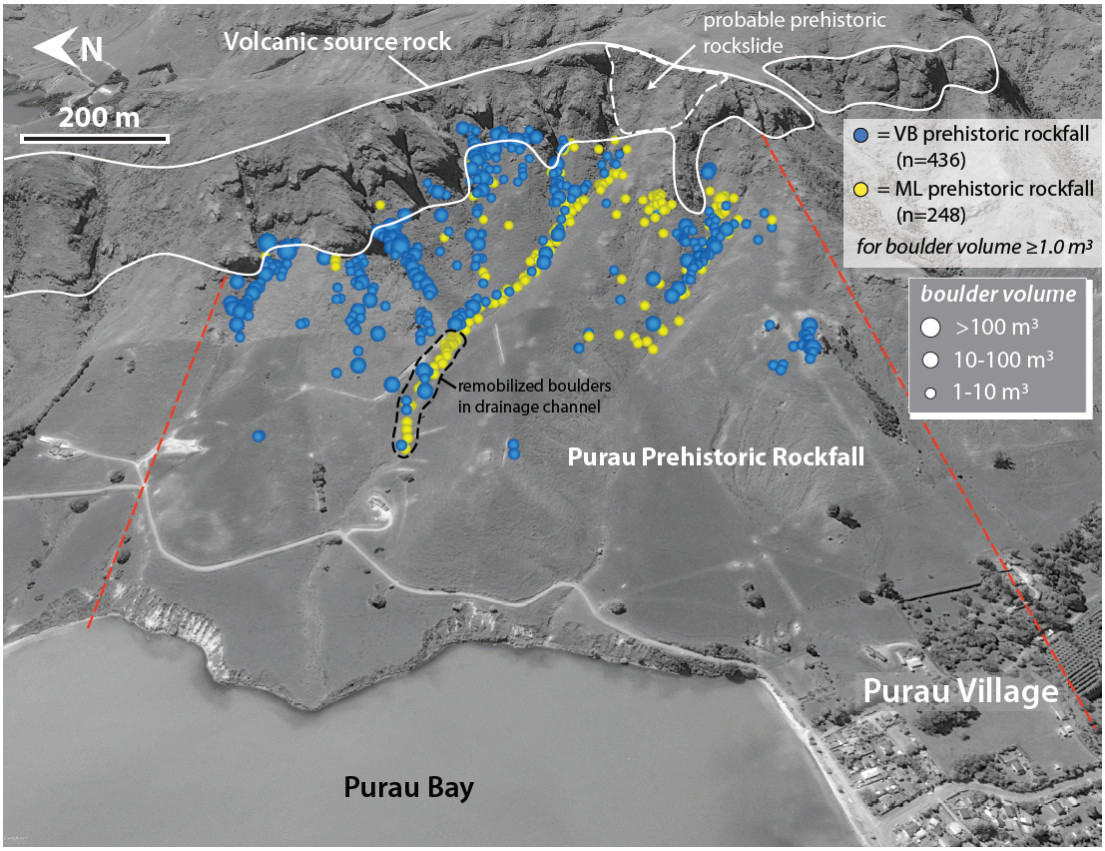

Figure 35. Mapped prehistoric VB and ML rockfall boulders at Purau study site. Prehistoric VB boulders show a wider spatial distribution. The majority of prehistoric ML boulders are located to the south, primarily within valleys.

subangular to subrounded (promoting travel), while the ML boulders are generally blocky and tabular in form (limiting transport distance).

3.5.9.11 Comparison of VB and ML modern boulders

Very few (n=9) ML boulders were generated within the Purau study site (Fig. 36) during the 2011 Christchurch earthquakes, reflecting less ML in the source rock. The high number and relative percentage of ML prehistoric boulders suggests ML layers have been highly susceptible and prone to detachment in the past, but are currently more stable. Modern ML boulders are emplaced at higher elevations (i.e. closer to the source rock) compared with modern VB boulders. Deposition of ML boulders occurs at elevations ranging from ~175 to ~300 meters (asl), while emplacement of VB boulders occurs at elevations of ~40 to ~300 meters (asl). I hypothesize that the angular shape and relatively small size for modern ML boulders promotes short travel distance, but may also reflect detachment close to the base of the source rock (i.e. low potential energy). The highest concentration of modern boulders occurs between an elevation of ~150 and ~225 meters (asl) (Fig. 34).

3.5.9.12 Purau modern (CES) vs prehistoric boulder runouts and the influence of vegetation on boulder spatial distribution

At Purau, the deposition of modern boulders is rare above an elevation of ~250 meters (asl). In contrast, abundant prehistoric boulders are deposited between elevations of ~250 and ~300 meters (asl). The low number of modern boulders deposited at higher elevations (>~250 meters asl) partially reflects the lack of detachment within higher elevation source areas during the 2011 Christchurch earthquakes. However, several locations that contain both prehistoric and modern rockfall show modern rockfall is deposited at further minimum distances from the source rock. I attribute the higher concentration of paleo-rockfall near the source rock to the presence of dense vegetation (i.e. podocarp/hardwood forest) on the hillslope during deposition of prehistoric rockfall boulders. The probable influence of slope vegetation on boulder spatial distribution is dramatically highlighted by the observed differences in runout distance for prehistoric and modern rockfall furthest to the south, near the town on Purau (Figs. 32 and 36). In this area, a single common source is evident and is comprised of VB basalt. Prehistoric rockfall boulders obtain a maximum runout distance of ~66 meters (map length) with the majority of rockfall boulders deposited within 10-15 meters of the volcanic source rock. In contrast, modern boulders of equivalent lithology and size obtain maximum travel distances of ~344 meters, reflecting a runout increase of ~278 meters (~420% increase). Locally (i.e. southern section of field site), I attribute the extreme difference between prehistoric and modern boulder travel distance to intervening anthropogenic deforestation, likely occurring during Maori or subsequent European occupation.

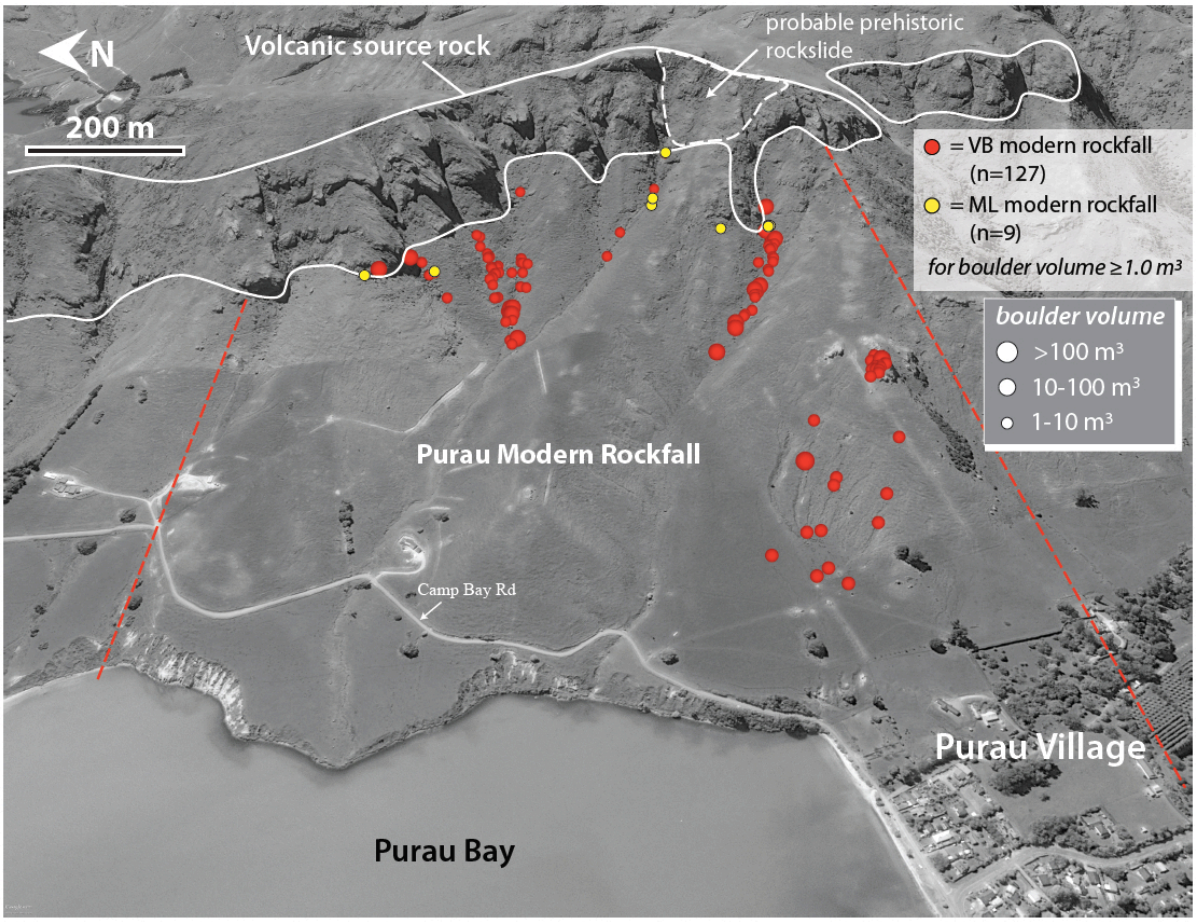

Figure 36. Mapped modern VB and ML rockfall boulders at Purau study site. Very few (n=9) ML boulders were created during the CES. Runout distance is strongly controlled by topography, with the majority of modern rockfall being captured in nearby canyons.

The furthest traveled modern rockfall boulder came to within ~185 meters of the nearest Purau residential home. Similar differences in maximum runout distance (between modern and prehistoric boulders) are not observed elsewhere at the study site, because detachment within the source rock during the 2011 Christchurch earthquakes generally did not occur in sections overlying interfluves and was limited primarily to areas positioned above drainage channels. Furthermore, remobilization of prehistoric boulders within the drainage canyons is probable, as evidenced by the increased distance from source for prehistoric boulders within the central canyon (compared with CES boulders) and the presence of numerous prehistoric boulders near the shoreline. As a result, a perfunctory comparison of spatial distributions for modern and prehistoric rockfalls would suggest, that in many locations, prehistoric rockfalls have travelled farther than the CES boulders. However, had modern rockfall detachment occurred within source areas overlying interfluves, then it is highly probable that runout distance would have increased. For instance, prehistoric boulder #381 (volume=45.7 m^3) has a runout distance of ~210 meters (map length) (Figs. 32 and 36). Should large rock bodies be detached from the same source area during future episodes of strong ground shaking, then rockfall boulders would likely travel significantly further than their prehistoric counterparts, primarily due to the absence of slope vegetation. Only a 250-meter increase in maximum travel distance is required to potentially impact the relatively new residential home (see Fig. 4) located further downslope, adjacent to Camp Bay Road. Numerical modeling for Purau rockfalls could potentially determine the expected resting locations for prehistoric boulders, and thus also help reveal boulders that have experienced post-emplacement remobilization. Furthermore, numerical models that account for the influence of hillslope vegetation on boulder deposition are required to validate our proposal that anthropogenic deforestation and its subsequent removal has influenced prehistoric and modern (2011) boulder depositional patterns.

Modern field analogs indicate that slope vegetation (i.e. trees, shrubs) had a considerable influence on limiting runout distance for rockfall detached during the 2010-2011 CES (Borella et al., 2016a). Figure 37 shows several examples from the Port Hills where trees arrested modern rockfall boulders.

Figure 37. Photos from the Port Hills showing modern rockfall boulders arrested by existing trees. Slope vegetation helped to mitigate rockfall hazard in the Port Hills during the 2010-2011 CES.

3.5.10 Comparison of Rapaki and Purau rockfall

3.5.10.1 Rockfall frequency ratio

The prehistoric to modern boulder frequency ratio (for boulder size ≥1.0 m^3) for the Purau study site is 5.03, while the same frequency ratio (for boulder size ≥0.5 m^3) for the Rapaki study site is 4.69. This suggests modern rockfall at both sites comprises ~1/5th of the total prehistoric rockfall.

3.5.10.2 Boulder size

Rapaki and Purau prehistoric boulder populations show similar but slightly variant boulder frequency-volume power-law distribution fits (Fig. 38).

Rapaki power law equation: $B\# = 121.26(BV)^{-1.384}$, $R^2 = 0.86$ (7)

Purau power law equation: $B\# = 205.72(BV)^{-1.517}$, $R^2 = 0.89$ (8)

Where B# = number of boulders, BV = boulder volume

Rapaki and Purau prehistoric boulders are statistically close, with Rapaki boulders showing slightly higher 25th, median, and 75th percentile sizes, but Purau paleo-boulders displaying higher mean, 95th percentile, and maximum boulder sizes (Table 5 and Fig. 39). A comparison of VB prehistoric boulders shows a very strong agreement between 25th, median, and 75th percentile boulder sizes (only slightly higher at Purau), but slightly greater size for Purau boulders in all size categories (Table 5 and Fig. 40). ML prehistoric boulders remain similar but vary slightly, with Purau ML boulders typically exhibiting a greater size (Table 5 and Fig. 40). I attribute the high number of large ML prehistoric boulders (> 2 m^3) at Purau to wider joint spacing and possibly greater bed thickness within the massive lava layers. Field observations also suggest that a large rockslide may have occurred above the primary canyon where abundant ML boulders are deposited (Fig. 32).

Given the similarities in composition (i.e. basalt), texture (i.e. VB and ML), and structure (jointing) between the two source rocks, it is not surprising that prehistoric rockfall boulder statistics are in relatively strong agreement.

Size of modern rockfall at Rapaki is consistently higher than contemporary (2011) rockfall at Purau (Table 6), representing a reversal compared with size trends within the prehistoric boulder

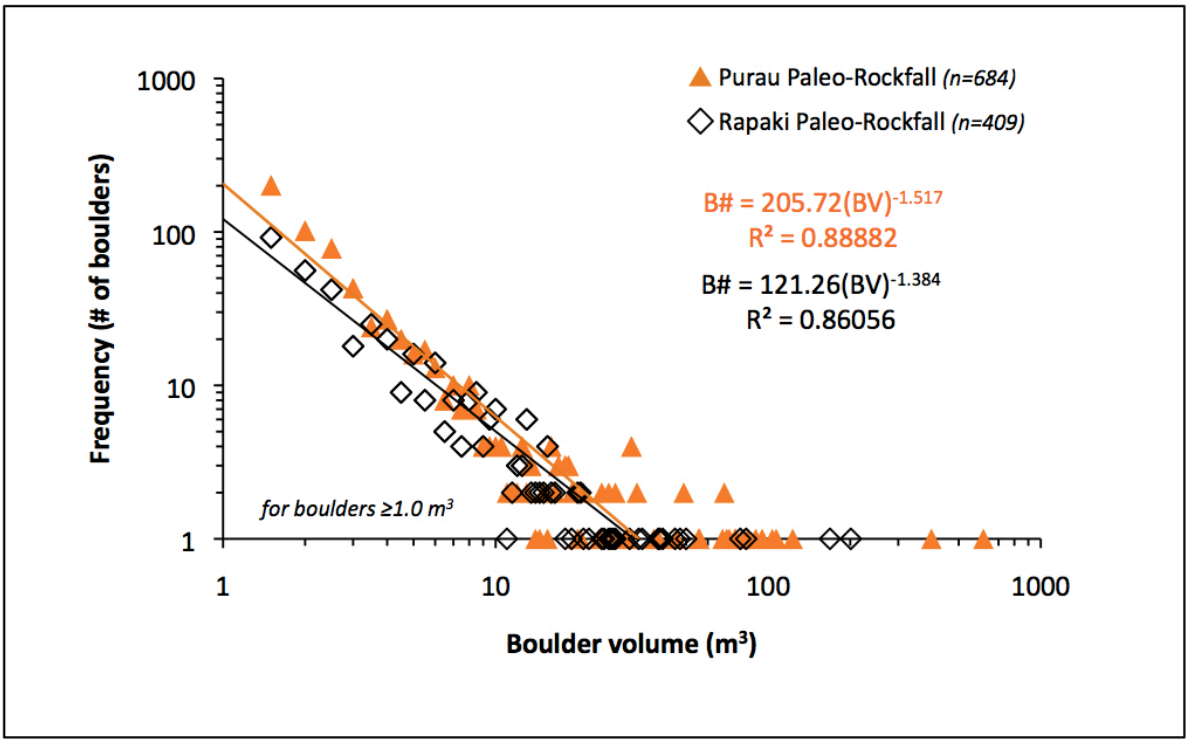

Figure 38. Boulder frequency-volume distributions for Purau and Rapaki prehistoric rockfall can be modeled using a power law. The trendline is fit to boulder volumes with frequency greater than 2.

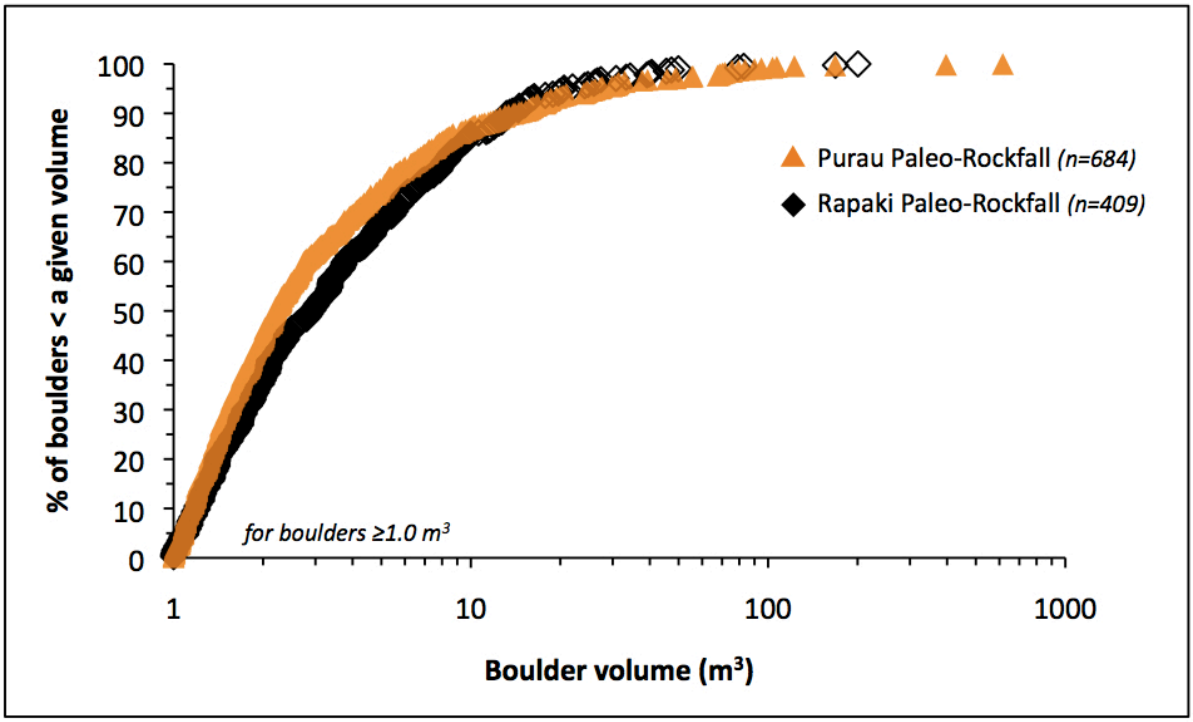

Figure 39. Comparison of Purau and Rapaki prehistoric rockfall size distributions as a proportion of boulders less than a given size.

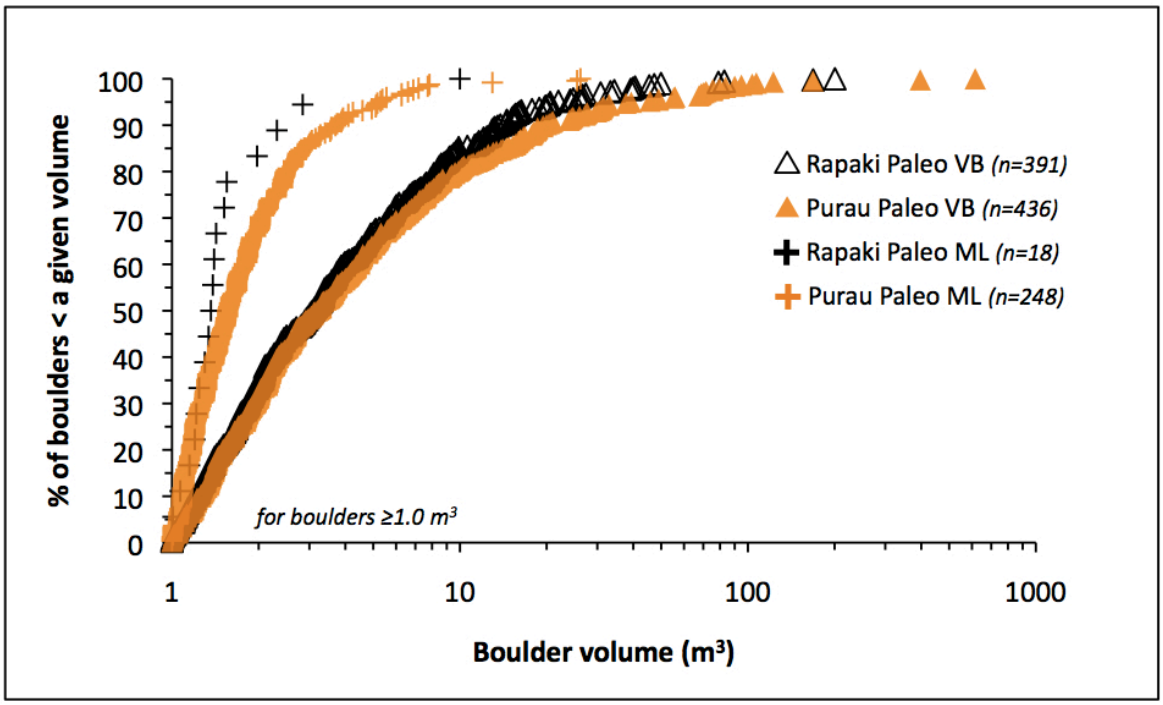

Figure 40. Comparison of Purau and Rapaki prehistoric rockfall size distributions as a proportion of boulders less than a given size for VB and ML boulders.

Prehistoric Rockfall	Purau All	*Rapaki All*	Purau VB	*Rapaki VB*	Purau ML	*Rapaki ML*
	(m^3)	(m^3)	(m^3)	(m^3)	(m^3)	(m^3)
25th (Q1)	1.42	*1.60*	1.70	*1.68*	1.20	*1.22*
Median	2.20	*2.94*	3.21	*3.10*	1.56	*1.38*
75th (Q3)	5.08	*6.59*	7.65	*6.78*	2.30	*1.54*
95th	27.06	*20.54*	40.91	*21.28*	5.26	*3.92*
Maximum	616.00	*200.56*	616.00	*200.56*	26.21	*10.00*
Mean	8.10	*6.81*	11.43	*7.03*	2.24	*1.96*

Table 5. Comparison of Purau and Rapaki prehistoric boulder size statistics (for volume ≥1.0 m^3).

Modern Rockfall	Purau All	Rapaki All
	(m^3)	(m^3)
25th (Q1)	1.34	1.81
Median	2.01	2.65
75th (Q3)	4.46	5.85
95th	17.66	27.53
Maximum	79.97	80.00
Mean	5.32	6.95

Table 6. Comparison of Purau and Rapaki modern (2011) boulder size statistics (for volume ≥1.0 m^3. Modern Rapaki rockfall exhibits higher values for all size categories.

populations. The greater size for Rapaki modern boulders could reflect the closer proximity of Rapaki to the 2011 earthquake fault sources. The Rapaki site experienced stronger ground shaking than Purau, and consequently, may have been a factor in creating comparatively larger detached rock bodies. I expect this would occur predominantly within the relatively weaker VB lithology and less so within the massive lava.

3.5.10.3 Boulder spatial distribution

The Rapaki study site reflects rockfall boulder deposition on a single hillslope, while emplacement of boulders at Purau occurs on a landscape consisting of several small and large valleys with intervening interfluves. Rockfall spatial distribution is strongly influenced by surface topography at both study locations. Maximum runout distance for prehistoric boulders at Rapaki is ~561 meters, while maximum travel distance for Purau paleo-boulders is ~273 meters. Maximum runout distance for modern boulders at Rapaki is ~770 meters, while maximum travel distance for Purau modern rockfall is ~344 meters. Both sites provide evidence that deforestation of the landscape has increased the rockfall hazard by allowing modern (2011) boulders to runout further than their prehistoric counterparts.

3.5.11 Origin of Rapaki and Purau rockfall

Modern rockfall at the Rapaki site was triggered by strong intensity ground shaking from rupture on proximal blind faults, primarily during the 22 February and 13 June 2011 earthquakes. A comparison of boulder size and frequency-volume distribution for the modern and prehistoric rockfall data sets show strong similarity, with the contemporary rockfalls fitting nicely as a subset of the larger paleo-rockfall data collection. Given the active seismicity in the area and similarities in size and depositional extent between the Rapaki prehistoric and contemporary rockfall, it is probable that the majority of observed prehistoric rockfall at Rapaki was also created during episodes of strong earthquake-induced ground shaking. I am not dismissing the idea that some prehistoric rockfall at Rapaki and Purau may have been caused by non-seismic causes/triggers. However, I do propose that episodic earthquakes are probably the most important driver for the flux of rockfall boulders from cliffs in the Port Hills.

During the 2011 Christchurch earthquakes, rocks fell from the source cliff only in earthquakes with interpolated peak ground velocities exceeding ~10-20 cm/s (Mackey and Quigley, 2014). Rockfall was rare in the 4 September (2010) mainshock and 23 December (2011) aftershock. No rockfall was observed at the study sites in hundreds of smaller earthquakes, implying the Rapaki source rock is generally competent and not highly susceptible to rockfall detachment. Mackey and Quigley (2014) further establish that higher frequency-lower magnitude shaking episodes from distal sources such as

the Alpine and Porters Pass faults are unlikely to have generated rockfall at the Rapaki study site over the Holocene. This is supported by absence of prehistoric boulders younger than ~7-3 ka. I also note that there was no rockfall observed/reported at the study sites (or in other areas of Christchurch) during the recent large M_w 7.8 Kaikoura earthquake. Below, I consider potential non-seismic rockfall triggers.

3.5.11.1 Potential non-seismic triggers

Rockfall may be caused by a variety of processes, including intense or prolonged precipitation, temperature fluctuations (i.e. freeze-thaw), fires, floral and faunal activity, undercutting of cliffs by natural or man-made processes, groundwater changes, anthropogenic activity, and residual weathering (e.g. Tatard et al., 2010; Varnes, 1978).

Freeze-thaw has the potential to cause detachment of large rockfall blocks (e.g. Guzzetti et al., 2003; Wieczorek, 2002) but predominates in high-elevation mountainous areas, where precipitation and temperature fluctuations are high. The Rapaki area is presently located within the lower cool to maritime cool temperate (montane) bioclimatic zone and experiences an average rainfall of less than 750 mm/year. Hales and Roering (2007) investigated climatic controls on frost cracking and predict that rock temperatures need to be between -3 and -8°C for frost cracking to occur in bedrock. This temperature range is unlikely to have occurred in Banks Peninsula during the time period represented by observable prehistoric rockfall at Rapaki. Current mean annual temperature (MAT) in Banks Peninsula is ~12°C, and even during the LGM (~18-24 ka) mean annual temperature probably only dropped ~4.5° (Soons, 1979) from present day MAT, above the threshold for frost cracking.

Undercutting of cliffs by natural or man-made processes can be eliminated as a cause of Rapaki and Purau prehistoric rockfall. Neither source area is positioned adjacent to any nearby river or within ~750 meters of the Rapaki bay coastline (where erosion and undercutting can be observed), nor is there any evidence suggesting it has been in the past.

Residual weathering of the source rock may cause minor rockfall, but does not provide an efficient mechanism for 'popping/throwing' large detachment blocks off the cliff face and generating the high frequency of large paleo-rockfall at both study sites within a period of ~15 ky. Generation of high-volume rockfall from residual weathering would presumably require vast amounts of time (i.e. 10^4-10^6 years). Mackey and Quigley (2014) report an erosion rate of ~7 mm/ky (assuming steady state) for the volcanic cliff exposure at Rapaki - a rate that is too low to account for the abundance of large rockfall boulders at the study site.

Earliest human occupation of New Zealand occurred ~800-700 years ago, thus eliminating human influence as a potential triggering mechanism for the prehistoric rockfall at Rapaki and Purau. Evidence from surface exposure (Mackey and Quigley, 2014) boulders and optical dating of hillslope sediments to constrain rockfall emplacement timing at Rapaki suggests boulder deposition before ~3-6 ka. Results from Borella et al. (2016b) and Sohbati et al. (2016) are in general agreement and use OSL dating of loessic hillslope sediments to demonstrate that prehistoric boulders were not emplaced on the Rapaki hillslope within at least the last ~3 ky.

Intense or prolonged precipitation may loosen highly susceptible rock bodies and generate rockfall, and can mobilize rocks in drainage channels (Fig. 41), but is unlikely as a primary mechanism for generating rockfall (in the source cliff) at Rapaki and elsewhere, such as Purau, where equivalent lithologies exist. During the recent 100-year storm (April of 2014) I performed periodic monitoring of the Rapaki source rock and underlying hillslope. Numerous landslides were evident throughout the Port Hills and greater Banks Peninsula during this extreme storm episode, including a few small debris/mud flows at Rapaki. However, there was no evidence of rockfall generated during this time, nor was any reported by the local villagers.

Massey et al. (2012) estimate rockfall boulder frequencies from 'other' non-seismic triggers throughout the Port Hills, including the Rapaki study site. The number of rockfalls at each location is estimated using historical records, mainly: (1) the GNS Science landslide database – complete only since 1996; (2) insurance claims made to the Earthquake Commission (EQC) – complete only since 1996; and (3) information from local consultants covering the period from 1992 to 2009. Their study suggests there are on average about 8 claims made to the EQC for rockfalls per year in the Port Hills and knowledge held by other local geotechnical consultants indicates that rockfalls have occurred in the Port Hills over the past 30 years or more. No specific historical observations are cited at the Rapaki study site. Massey et al. (2012) estimate the number of boulders leaving the Rapaki source area over a given period of time. They conclude 5 boulders for <1-15 years, 50 boulders during 15-100 years; 259 for 100-1,000 years; and 518 boulder for >>1,000 years. I am uncertain what boulder size is utilized within the study, but assume a minimum boulder size of at least 0.1 m^3 based upon the reported boulder size ranges. It appears that a sample bias (few reported sizes) exists below this size range.

I am surprised by the high frequency of potential boulders attributed to non-seismic triggers for the Rapaki study site. I recognize that high-intensity or long-duration rainfall may cause small rockfall to unravel and fall from the source rock, but it is unlikely as a mechanism for generating the total volume and high number of large (e.g. >1 m^3) rockfall boulders at the study site. Intense rain primarily erodes material around rock blocks, making them more unstable, but does not provide a force capable of 'throwing' rocks off of slopes and generating new cracks (as experienced during episodes of

Figure 41. Photo of debris flow occurring during the April 2014 100-year storm near the Gondola in Heathcote Valley, Christchurch. Mud and debris flows were observed occurring within existing drainage gullies and have the potential to remobilize pre-existing (e.g. prehistoric) boulders.

earthquake-induced strong ground shaking), unless significant water is retained within the fractures and pressure builds. During the April 2014 rain events, water could be observed flowing out from the base of the volcanic source rock, suggesting that water is being transmitted through the rock body and not collecting within existing joints. The lack of any prehistoric boulders emplaced after ~7-3 ka implies that higher frequency rainstorms (and other short recurrence interval non-seismic triggers) and smaller shaking intensity earthquakes are not generating significant rockfall at Rapaki, at least for larger boulders (≥1.0 m^3) targeted as part of the Rapaki studies.

Numerous conversations with the resident Maori at Rapaki suggest rockfall during rainstorm events and higher-frequency lower magnitude shaking events is uncommon. Throughout the history of their Rapaki settlement, the local Iwi record only a single rockfall boulder being released approximately 300 years ago from the source rock. The cause of this released boulder is unknown, and may have been triggered by an earthquake (e.g. Alpine fault rupture) or other non-seismic triggers. In summary, it is probable that minor amounts of smaller-size rockfall have been generated at Rapaki as a result of smaller shaking intensity earthquakes and non-seismic triggers, but we expect the geologic rockfall record to be dominated by rare, infrequent strong shaking events.

3.5.12 Historical overview of rockfall in the Port Hills and Banks Peninsula

Lundy (1995) provides a record of historic rockfall events in the Port Hills and greater Banks Peninsula prior to 1992 (see Supplementary Table 1). Historical accounts suggest rockfalls created in the past have predominantly occurred within coastal cliffs where slopes are subvertical to overhanging, primarily from the erosive action of ocean waters, but also anthropogenic influence (i.e. creation of roadways). The rockfalls have resulted primarily from blasting (i.e. road/tunnel work), shaking from earthquakes, and/or intense or prolonged storm events. I note that there are very few reports of rockfalls occurring in hilly areas further away from the coastline. This may reflect the lack of settlement (and humans) in these areas or the higher susceptibility of coastal source rock to rockfall.

3.5.13 Potential prehistoric rockfall events

Massey et al. (2012) cite archaeological evidence for substantial rockfalls in the Sumner-Redcliffs area some 500 years ago (e.g. Trotter, 1975) and further suggest a possible local earthquake trigger for the rockfall. I presume this is based upon radiocarbon ages for marine shells within the cave, suggesting the bulk of the occupation at Moncks Cave occurred sometime between the late 14th to early 15th centuries, and that settlement time was very short and probably close to the beginning of the 15th century (Jacomb, 2008). Based upon the results, Jacomb (2008) speculates that it is possible the slip blocking the cave's entrance occurred at about the same time. However, it is also plausible that the

rockfall event occurred much later. Furthermore, given their location near the coastline and in areas of cave formation and overhanging rock, the rockfalls could have been also created during high-intensity or prolonged rainfall.

3.6 Discussion

The CES has provided a unique opportunity to analyze rockfall origin, frequency, and volumetric and spatial distributions during well-recorded seismic events (e.g. Mercalli intensity, moment magnitude, peak ground acceleration) and under known geomorphic conditions (e.g. Massey et al., 2014; Heron et al., 2014; Mackey and Quigley, 2014; Vick, 2015; Quigley et al., 2016). The 2011 Christchurch earthquakes demonstrated that strong earthquake-induced ground shaking has the capacity to generate large volumes of rockfall within the Port Hills and wider Banks Peninsula area. The strong similarity between frequency-volume characteristics and depositional extent for modern and prehistoric boulders, and the absence of emplaced prehistoric boulders younger than ~3-7 ka, support a seismogenic origin for the majority of Rapaki and Purau prehistoric rockfalls. Consequently, prehistoric rockfall at these two sites and elsewhere throughout Banks Peninsula potentially provides a sensitive recorder of strong prehistoric ground shaking in the region. It is important to note that I cannot resolutely distinguish between purely episodic rockfall deposition, where rockfall detachment and deposition occurs in distinct events separated by 1000s of yrs, versus a more temporally steady accumulation of boulders with shorter inter-depositional periods. An episodic model is favored on the basis of preliminary dating of boulder deposition at Rapaki, and supported by historical observational records, which suggest interseismic rockfall deposition is rare. However, it may be possible that rocks were detached and deposited at different frequencies in the geologic past. More dating and analysis would be required to further test my episodic, seismically-driven rockfall deposition model vs mixed modes of deposition.

Prior to the CES, rockfall hazard was not considered a high threat in Banks Peninsula and surrounding areas, including the Port Hills of southern Christchurch, where damage was most critical and 5 fatalities occurred (Massey et al., 2014). I assume this was primarily because there were few records of historical rockfall occurrence, and of those described, none hinted at the potential for future widespread cliff collapse and rockfall in the region. However, the geologic record clearly provides evidence, in the form of abundant and large prehistoric rockfall boulders (many located on developed properties in the Port Hills), that rockfall events of similar ground shaking intensity to the 2011 Christchurch earthquakes have probably occurred in the past.

CN surface exposure dating of boulders and luminescence ages for loess-colluvium pre- and post-dating boulder emplacement suggests observable prehistoric boulders at Rapaki were emplaced between ~3 and 13 ka (Mackey and Quigley, 2014; Borella et al., 2016b; Sohbati et al., 2016), implying the production of a high volume of prehistoric rockfall within a geologically short time period (i.e. ~10 ky). Given this temporal condition, I propose that earthquake-induced ground shaking is the most viable mechanism for generating rockfall of this size and frequency-magnitude, although other factors, including hillslope erosion and burial processes need to be considered. In reality, I would expect that

rockfalls older than ~13 ka (perhaps dating back ~30 ky or more) would be exposed on sections of the hillslope nearest the source cliff because erosion predominates.

The study of prehistoric rockfall provides important boulder volume and runout statistics to be used in contemporary hazard analyses, including predictive rockfall modeling (e.g. Vick, 2015). I consider maximum runout distance for prehistoric boulders to be a minimum proxy for future rockfall boulders because emplacement of the prehistoric boulders occurred before deforestation in Banks Peninsula. Comparison of maximum runout distance for modern and prehistoric boulders at Rapaki suggest a ~37% increase (modern=770 m; prehistoric=561 m) for modern boulder travel distance, while at Purau the difference is as high as ~420% (modern 344 m; prehistoric=66 m), suggesting removal of vegetation has a variable but significant impact on boulder travel distance.

My research indicates that source rock geology and structure (i.e. volcanic lithofacies architecture) play a particularly important role in influencing rockfall hazard in Banks Peninsula (including the Port Hills). I find that boulders consisting of massive lava are significantly smaller and runout distance for largest ML boulders is comparatively short relative to equivalently sized VB boulders. The apparent higher joint density within the ML source rock layers effectively mitigates the rockfall hazard for ML boulders by reducing its size and creating a more angular and tabular boulder shape, which has more difficulty traveling downslope. This comparison highlights the importance of studying variability in source rock geology and boulder composition, texture, and shape to understand the potential impact (i.e. boulder size and runout distance) from rockfall. Developed areas located downslope of source rock comprised of thick volcanic breccia layers should be given highest priority.

There remain vulnerable sections of volcanic source rock in the Port Hills and throughout Banks Peninsula that did not experience detachment during the 2010-2011 CES. In these areas, the study of prehistoric rockfall and source rock geology (if safe) is particularly critical to understanding future rockfall hazard and evaluating local risk. In regions devoid of historical or contemporary rockfall, prehistoric boulders provide the only empirical proxy for evaluating local rockfall behavior, including the influence of surface morphology on boulder spatial distribution. Combining this knowledge with an understanding of local landscape evolution (e.g. history of anthropogenic deforestation) will provide valuable input for rockfall modeling and risk assessment.

Comparison of boulder frequency and total rockfall volume for modern and prehistoric rockfalls at Rapaki and Purau indicates that modern rockfall represents approximately $1/5^{th}$ of the total prehistoric rockfall. The similarity in prehistoric to modern boulder frequency ratios (~5) suggests that the rockfall production mechanism is likely to be regional in extent (e.g. regional shaking or storms), rather than local causes related to differences in slope aspect, lithology, or rock mass susceptibility to

residual weathering processes. Assuming the majority of prehistoric rockfall at the study sites is created during high-intensity ground shaking (i.e. earthquakes) equivalent to the 2011 Christchurch blind faults, this would imply approximately five (5) prehistoric shaking events are responsible for the observed prehistoric rockfall at the Rapaki and Purau study locations. It is, however, probably more reasonable to assume 3 or 4 prehistoric rockfall events at the Rapaki study site from our dataset of mapped boulders because the potential to expose prehistoric boulders that were emplaced during even earlier rockfall events is high near the source rock where erosion dominates. Further, I recognize it is improbable that prehistoric ground-shaking intensities on the Rapaki and Purau hillslopes were the same as those experienced during the 2011 Christchurch earthquakes, and thus my assumption of equivalent earthquake-induced ground-shaking characteristics should be viewed cautiously. I am not able to establish a linear relationship between the number of earthquakes and the amount of rockfall debris (i.e. boulders) produced at the study sites. CN surface exposure (Mackey and Quigley, 2014) and OSL dating of hillslope sediment bounding several of the rockfall boulders (Sohbati et al., 2016; Borella et al., 2016b) at Rapaki suggests at least two previous rockfall events at Rapaki. The major challenges are reconciling the timing of observed rockfall boulders near the source rock (where erosion predominates) versus those emplaced on middle and lower slope positions (where burial by loess and loess colluvium occurs), and also the potential contribution of paleoboulders resulting from other causes/triggers (e.g. prolonged rainfall).

A statistical comparison of Rapaki and Purau prehistoric boulder size distributions shows agreement, although Purau shows significantly higher 95th percentile and maximum boulder sizes (Tables 7 and 8). Interestingly, prehistoric rockfalls at both sites are statistically larger than their modern rockfall counterparts. This may reflect changes in source rock geology (including joint pattern and persistency) through time, or could suggest that higher ground shaking intensities were experienced at the Rapaki and Purau study sites during prehistoric rockfall events, resulting in larger rockfall detachment bodies. I expect that the formation of new joints would occur primarily within layers comprised of volcanic breccia, due to its lower density and rock strength properties. Stronger ground shaking may have resulted from higher magnitude rupture on the same 2011 blind fault sources and/or movement on unidentified fault sources. Although I can only speculate, the higher number of large prehistoric boulders at Purau may indicate that prehistoric rupture occurred on unidentified faults closer to Purau (compared with 2011 faults), where shaking was of higher intensity and able to detach larger rockfall bodies within the volcanic breccia lithology.

Modern boulders at Rapaki exhibit larger median and maximum sizes than contemporary boulders at Purau. Assuming equivalent source rock geology (including joint spacing) at the study sites, it is probable the larger boulder size is a result of stronger ground shaking intensity at the Rapaki location. The Rapaki site is located within ~1 km of the 22 February and ~3 km of the 13 June 2011

Christchurch earthquakes. The Purau study site is located further away, approximately 5 km from the 22 February and 6 km from the 13 June 2011 Christchurch earthquakes. Peak ground accelerations were lower at Purau and thus the frequency and size of rockfall boulders may have been reduced, suggesting decreased distance from the earthquake focus may result in larger rockfall detachment. This assumes that the strong ground accelerations are exploiting pre-existing discontinuities (e.g. joints, layer boundaries) to greater depth within the source rock and/or new cracks are being created within the volcanic source rock. A detailed source rock investigation at Purau and Rapaki needs to be performed to assess how the relative volume of ML and VB (i.e. lithofacies architecture) at Purau compare to the Rapaki field site.

A primary goal of paleoseismic studies is to understand fault behavior or shaking history for a particular region with the aim of evaluating earthquake hazards and their potential impact on humans, dwellings, and critical infrastructure (Jibson, 1996). The occurrence of the 2011 Christchurch earthquakes on previously unidentified blind faults and the abundance of prehistoric rockfall boulders in the area point to the potential role of these faults in past rockfall activity in the region and into the future. Rockfall boulders of probable seismogenic origin are abundant in Banks Peninsula (including the Port Hills) and provide a sensitive recorder of prehistoric shaking episodes. However, this data set has been largely unexplored. This study presents the first robust investigation (i.e. mapping, characterization) and interpretation of prehistoric rockfalls in Banks Peninsula, NZ. As demonstrated by previous studies (Mackey and Quigley, 2014; Borella et al., 2016a,b; Sohbati et al., 2016), prehistoric rockfall can provide a wealth of information to be implemented within paleoseismic and earthquake hazard investigations. At Rapaki, prehistoric rockfall has been used to determine temporal distribution for prehistoric shaking episodes and infer probable fault source locations (Mackey and Quigley, 2014), and stratigraphy and chronology of late Quaternary loessic hillslope sediments have been used to reveal seismic, climatic, and anthropogenic influences on surface processes (Sobhati et al., 2016; Borella et al., 2016a,b). These studies, however, have been performed on relatively few boulders (n=20) and more ages are required to support our preliminary conclusions and reveal regional patterns of strong ground shaking and landscape evolution.

Lacking is a proper regional geologic and spatial context for the prehistoric and modern boulder populations in Banks Peninsula. GNS Science has performed thorough mapping of modern rockfall - and partial mapping of prehistoric rockfall (Townsend and Rosser, 2012) - in the Port Hills of southern Christchurch, but elsewhere in Banks Peninsula, including Birdlings Flat and the Akaroa region, rockfall has not been mapped and characterized. Interviews with residents in Akaroa and surrounding regions indicate the September main shock was responsible for the majority of rockfall created at these more distal locations, highlighting the role of rockfall in defining and understanding the limits of hazard under known and variable seismic conditions (Hancox et al., 1997; Keefer, 1984, 1992, 2002). Mapping

and detailed field characterization of rockfall will also help identify prehistoric boulders that are optimal for CN surface exposure, and OSL and radiocarbon dating. For example, at Purau I have identified prehistoric boulders with thick colluvial wedge sediments, essential for constraining boulder emplacement timing using optical dating of hillslope sediments (see Borella et al., 2016b). Several such boulders have also been identified at Goat Rock (Banks Peninsula) for future evaluation (Fig. 42). Additionally, the use of drones/UAV and photogrammetry, combined with field data measurements, may allow for detailed characterization of source rock geology, which could help identify rockfall deposits of non-seismic origin that are unsuitable for use in temporal constraint of prehistoric shaking events, but may yield important information about major prehistoric climatic events.

Systematic geologic mapping of volcanics in Banks Peninsula has been initiated by Frontiers Abroad Inc. (2013-present), and in many locations coincides with source rock that has generated prehistoric and/or modern (2010-2011) rockfall. I propose the continued detailed mapping and characterization of prehistoric rockfall throughout the Port Hills and Banks Peninsula area to establish a robust prehistoric rockfall data inventory for use in paleoseismic and contemporary earthquake hazard investigations. Mapping and characterization of prehistoric rockfall in Banks Peninsula could serve as a global standard for paleoseismic rockfall studies, incorporating multiple dating techniques with geologic and geomorphic mapping.

Figure 42. Prehistoric rockfall boulders (1) at Goat Rock, Banks Peninsula. Thick colluvial wedge deposits (2) have developed behind the paleo-boulders. OSL and radiocarbon dating of bounding sediments can be used to constrain boulder fall timing and potentially infer prehistoric shaking events. Extensive field mapping of prehistoric boulders and study of source rock geology is required to identify candidate rockfall boulders and understand conditions of formation. Backpack (black) located at the top of each colluvial wedge shown for scale.

3.7 Conclusions

I mapped and characterized more than 1500 prehistoric rockfall boulders at two study sites in Banks Peninsula to understand their origin, frequency, and spatial and volumetric distributions. Prehistoric boulders at both sites show two distinct textural lithofacies: volcanic breccia (VB) and massive lava (ML) basalt. Rockall boulder frequency-volume (at both sites) and frequency-runout distributions (at the Rapaki study site) can be modeled using a power law, with the number of boulders decreasing rapidly with increasing size and distance from the source rock, respectively. VB boulders comprise ~64% (Rap) and 73% (Purau study site) of the total mapped rockfall and ~90% (Rap) and 96% (Purau) of the total boulder volume, reflecting the predominance of volcanic breccia lithologic facies within the source rock. At Rapaki, median and 95th percentile ML boulder sizes are 0.25 m^3 and ~1.2 m^3, respectively (for boulders ≥0.1 m^3). Median and 95th percentile VB boulder sizes are 1.0 m^3 and ~14.5 m^3, respectively, reflecting the significantly greater size and comparatively high number of large VB rockfall boulders. The largest boulders with the longest runout distances that pose the greatest hazard to life and property are comprised exclusively of volcanic breccia.

Boulder characteristics and distributions are compared to 421 boulders deposited at the same sites during the 2010-2011 Canterbury earthquake sequence. A comparison of the spatial distribution of Rapaki and Purau prehistoric and modern rockfall boulders reveals significantly longer runout distance (~25-400% increase) for modern boulder populations. I primarily attribute the increase in modern boulder travel distance to anthropogenic deforestation by Maori and/or Europeans sometime between AD 1661 and AD 1950 and after emplacement of the prehistoric boulders.

I propose that the majority of prehistoric rockfall at the two study locations has resulted from episodic earthquakes with strong ground shaking intensities similar to the 2011 Christchurch earthquakes (i.e. 22 February and 13 June events). The frequency and volume of rockfall generated at the two study sites during the 2011 Christchurch earthquakes represents ~1/5th of the total prehistoric rockfall, suggesting the rockfall production mechanism is likely to be regional in extent (e.g. regional shaking or possibly storms).

This study highlights the primary role that lava flow emplacement and cooling mechanics play in controlling rockfall hazard and demonstrates the importance of mapping and analyzing prehistoric rockfall to develop a robust data set for informing paleoseismic studies and understanding contemporary rockfall hazard under known anthropogenically modified landscape conditions. Prehistoric rockfall remains largely unexplored in Banks Peninsula and potentially provides a record of major seismic, climatic, and/or anthropogenic events.

3.8 Appendix 1: Supplementary Figures and Data

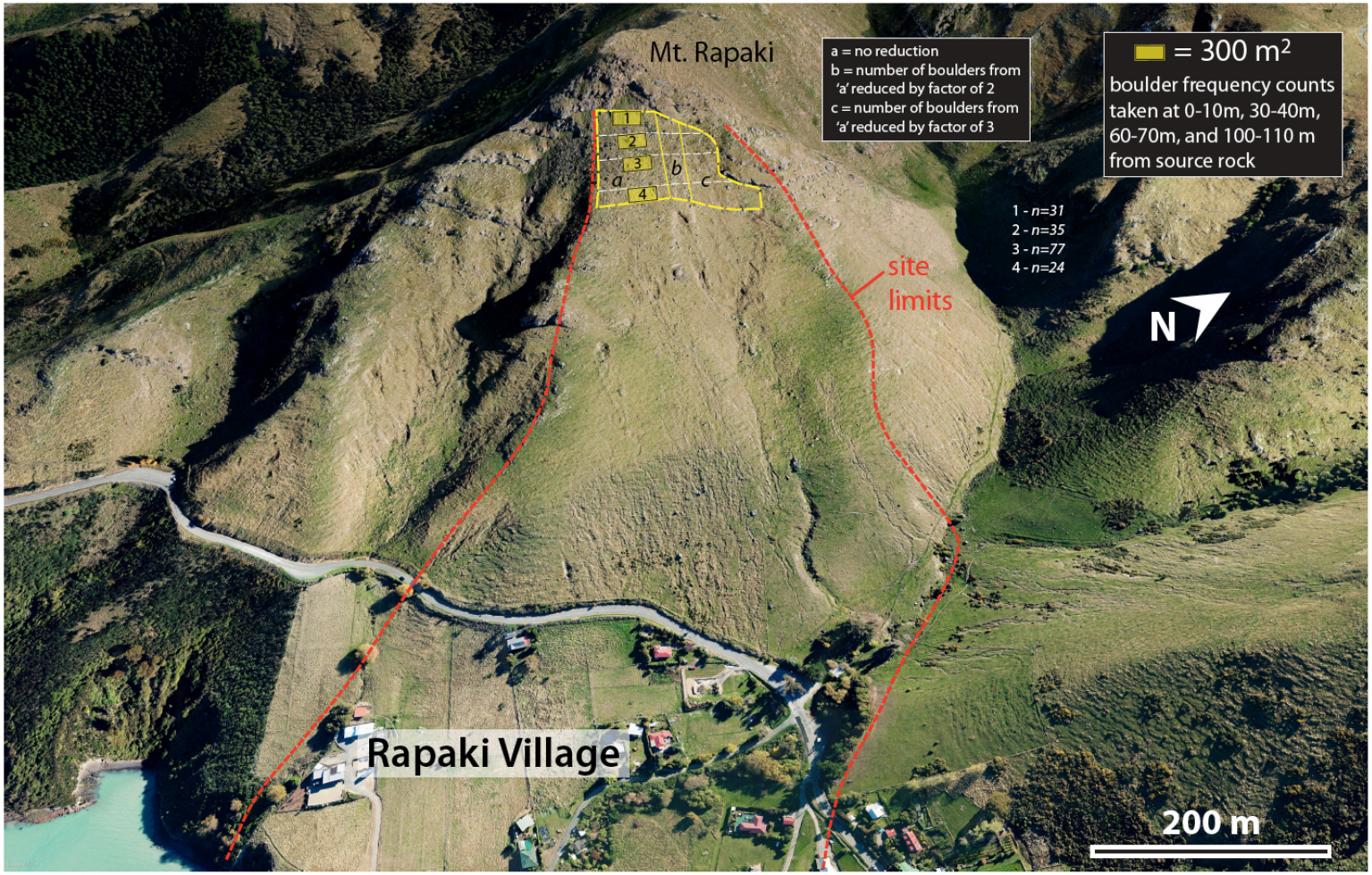

Supplementary Figure 1. The total number of boulders with volume ≥ 0.1 m^3 were taken at runout distances of 1-10 m (yellow polygon 1), 30-40 m (yellow polygon 2), 60-70 m (yellow polygon 3), and 100-110 m (yellow polygon 4) from the volcanic source rock to estimate the total number of boulders in areas near the source cliff where conditions were unsafe for continuous mapping. The number of boulders in areas 'b' and 'c' were reduced by factors of 2 and 3, respectively, based upon field observations.

Appendix 2: Rapaki and Purau Rockfall Boulder Data

Rapaki Prehistoric Rockfall

ID	Latitude	Longitude	Elevation	Length	Width	Height	Volume	Type
			(m - asl)	*(m)*	*(m)*	*(m)*	*(m^3)*	
1	-43.60375875	172.677831	65.49511719	3.1	2.6	1.8	14.508	VB
2	-43.60374408	172.6771894	81.11633301	2.5	4.5	2.2	24.75	VB
3	-43.60374215	172.677004	86.16320801	1.6	1.75	1.2	3.36	VB
4	-43.60444372	172.6767742	87.12451172	2.7	1.6	2.2	9.5	VB
5	-43.60415538	172.6763716	100.5828857	3.7	2.2	3.7	21.978	VB
6	-43.60431313	172.6763346	100.5828857	0.95	0.7	0.7	0.465	ML
7	-43.60393376	172.6762162	107.0716553	1.4	1.25	2.1	3.675	VB
8	-43.60393577	172.6762029	106.8312988	3	1.15	1.9	6.555	VB
9	-43.60386888	172.6762135	108.5137939	3.1	1.05	1.5	4.88	VB
10	-43.60378607	172.6762965	106.350708	1.45	0.5	0.3	0.218	ML
11	-43.60355054	172.6765768	101.5441895	7.1	3.7	1.9	49.913	VB
12	-43.60360393	172.676366	102.5054932	1.1	1.4	0.69	1.063	VB
13	-43.60369915	172.6762862	103.7071533	1.1	1.3	0.7	1.001	VB
14	-43.60358398	172.6761265	109.4750977	1.2	1.6	1.25	2.4	VB
15	-43.60344468	172.6757711	119.3284912	1.97	1.55	1.65	5.038	VB
16	-43.60349748	172.6756765	121.7316895	0.55	0.55	0.5	0.151	VB
17	-43.60347359	172.6756417	122.6929932	0.87	0.65	0.65	0.368	VB
18	-43.60342573	172.6753687	131.8254395	2	1.8	1.1	3.96	VB
19	-43.603658	172.6753721	133.5078125	2	3.1	2.05	12.71	VB
20	-43.60383091	172.6754266	126.2979736	0.9	0.82	0.8	0.59	VB
21	-43.60392613	172.6754895	124.6157227	1.5	0.92	1.02	1.408	VB
22	-43.60404164	172.6753078	130.6239014	1.35	1.2	1.15	1.863	VB
23	-43.60396997	172.6751642	134.7094727	1.87	1.2	1.5	3.366	VB
24	-43.60397114	172.6749411	142.6402588	2.25	1.15	1.1	2.846	VB
25	-43.60380342	172.6746661	152.0130615	1.95	1.45	1.2	3.393	VB
26	-43.60373436	172.6746747	152.7340088	0.65	0.76	0.5	0.247	VB
27	-43.60368515	172.6746015	155.3775635	1.73	1.05	0.7	1.272	VB
28	-43.60365733	172.6746901	150.5710449	2.05	1.15	0.93	2.192	VB

29	-43.6035699	172.6746752	148.1678467	0.85	0.65	0.65	0.359	ML
30	-43.60351458	172.6746435	148.1678467	1.26	0.78	0.45	0.442	VB
31	-43.60347234	172.674676	147.6871338	0.46	0.55	0.5	0.127	VB
32	-43.60340143	172.6745236	151.0516357	1.2	0.98	1	1.176	VB
33	-43.60337108	172.6747299	138.3143311	3	1.7	1.96	9.996	ML
34	-43.6032353	172.6746377	128.9416504	1	1	0.35	0.35	VB
35	-43.60323479	172.6745664	133.5078125	0.75	0.45	0.2	0.068	ML
36	-43.60339338	172.6742517	151.5323486	1.97	1.56	1	3.073	VB
37	-43.60337519	172.6741444	156.0986328	2.03	1.27	1.17	3.016	VB
38	-43.6033762	172.6741491	158.9825439	1.2	0.87	0.45	0.47	VB
39	-43.60337569	172.6741495	157.7810059	0.5	0.55	0.32	0.088	VB
40	-43.60338575	172.674094	159.7036133	1.15	0.6	0.6	0.414	ML
41	-43.60344283	172.6740716	161.6262207	0.83	0.55	0.53	0.242	ML
42	-43.6034596	172.6740713	162.5874023	1	0.63	0.5	0.315	VB
43	-43.60348684	172.6740433	165.7116699	0.7	0.75	0.54	0.284	VB
44	-43.60362405	172.6740041	166.1923828	1.2	0.8	0.85	0.816	VB
45	-43.6036818	172.6739908	172.440918	2.2	2	1.35	5.94	VB
46	-43.60367258	172.6741045	164.0294189	0.71	0.54	0.55	0.211	ML
47	-43.60365112	172.6741718	162.347168	2.44	1.4	1.3	4.44	VB
48	-43.60378641	172.6741512	167.6342773	1.45	0.85	0.9	1.11	VB
49	-43.60388733	172.6742084	161.3858643	1.86	1.5	0.95	2.65	VB
50	-43.60383075	172.6743626	159.9438477	1.55	0.75	0.55	0.639	ML
51	-43.60395673	172.6777879	56.36254883	0.82	0.7	0.6	0.344	ML
52	-43.60398305	172.6775625	73.90649414	0.58	0.5	0.75	0.218	VB
53	-43.60420131	172.675868	117.1655273	1.44	1.15	0.75	1.242	VB
54	-43.60430131	172.6758567	116.6848145	1.1	1.1	0.5	0.633	VB
55	-43.60517479	172.6755705	125.8173828	0.44	0.65	0.35	0.1	ML
56	-43.60466357	172.6747605	154.4162598	1	0.45	0.45	0.203	VB
57	-43.60456165	172.6748129	153.6953125	1.3	0.9	0.8	0.936	ML
58	-43.60429318	172.6747118	159.9438477	2.7	1.16	0.936	4.072	VB
59	-43.60378699	172.6745372	169.0762939	1.35	1.92	0.8	2.074	VB
60	-43.6039253	172.6744971	169.3166504	0.75	1	0.45	0.338	ML
61	-43.60404273	172.6740808	185.1782227	1.4	0.95	0.6	0.798	VB
62	-43.60406226	172.6741233	183.2556152	1.4	0.85	0.36	0.428	VB
63	-43.60402437	172.67399	186.6202393	1	0.8	0.6	0.48	VB
64	-43.60399445	172.6739623	186.8604736	0.5	0.6	0.4	0.12	VB

65	-43.60400735	172.6739614	188.7832031	1	0.85	0.6	0.51	VB
66	-43.60398011	172.67392	189.9848633	0.56	0.65	0.5	0.182	VB
67	-43.60390199	172.673863	193.1091309	1.2	0.9	0.7	0.756	VB
68	-43.60359538	172.6734401	210.1723633	1	1	0.9	0.9	VB
69	-43.60359161	172.6733965	211.3740234	1.3	1.25	1.15	1.869	VB
70	-43.60340629	172.6733159	212.815918	0.6	0.5	0.5	0.15	ML
71	-43.60332121	172.6731816	220.0258789	1.25	1.15	0.8	1.15	ML
72	-43.6032182	172.673223	219.5450439	1.93	0.93	0.5	0.897	VB
73	-43.60322583	172.6732132	219.7854004	1.3	0.75	0.8	0.78	ML
74	-43.60322507	172.6732616	216.6611328	1.15	0.75	0.75	0.647	VB
75	-43.6032296	172.6732576	216.180542	0.6	0.7	0.2	0.084	ML
76	-43.60317864	172.6732921	214.9788818	1	0.75	0.75	0.563	VB
77	-43.60318182	172.6732888	214.4981689	0.9	0.58	0.4	0.209	ML
78	-43.60315575	172.6734677	204.8851318	1	0.7	0.7	0.49	VB
79	-43.60314905	172.6735402	201.5205078	3.9	1.6	2.1	13.104	VB
80	-43.60309917	172.6735245	201.5205078	1.1	0.7	0.35	0.27	VB
81	-43.60307763	172.6736098	196.9543457	2.4	1.7	1.25	5.1	VB
82	-43.60316455	172.6736598	196.4736328	0.9	0.71	0.71	0.454	ML
83	-43.60340763	172.6736628	197.4349365	1.3	1.4	0.45	0.819	VB
84	-43.60345951	172.6737286	195.993042	0.6	0.45	0.75	0.203	ML
85	-43.60364492	172.6737904	193.5897217	1.2	0.7	0.5	0.42	VB
86	-43.6033622	172.6744564	165.7116699	0.4	0.45	0.7	0.126	VB
87	-43.60349547	172.6749426	147.2064209	0.65	0.47	1	0.306	VB
88	-43.60353596	172.6749751	146.0048828	1.66	1.1	0.96	1.75	VB
89	-43.60314528	172.6753136	131.8254395	1.3	0.8	1	1.04	VB
90	-43.60313874	172.6751991	133.9884033	2.4	1.4	1.3	4.368	VB
91	-43.60301536	172.6749274	142.8806152	2.15	1.35	0.7	2.032	VB
92	-43.60299901	172.6749292	142.8806152	1.1	0.75	0.75	0.619	VB
93	-43.60306322	172.6747812	148.1678467	1.2	0.9	0.9	0.972	VB
94	-43.60304645	172.6747228	153.6953125	1.4	0.65	0.6	0.546	ML
95	-43.60304226	172.6746119	155.137207	1.05	1	0.4	0.42	VB
96	-43.60304243	172.6746155	154.6566162	1.3	1.05	1	1.365	ML
97	-43.60307378	172.6745973	155.3775635	0.8	0.5	0.5	0.2	VB
98	-43.60306925	172.6745955	154.6566162	2	1	1	2	VB
99	-43.60305584	172.674598	156.8195801	2.1	1.15	0.9	2.174	VB
100	-43.60305819	172.6745552	156.3389893	0.85	0.6	0.4	0.204	VB

101	-43.60315391	172.6744999	158.5019531	1.5	0.8	0.8	0.96	VB
102	-43.6030089	172.6741661	156.8195801	2.6	1.6	1.35	5.616	VB
103	-43.60292248	172.6743751	157.300293	0.75	0.65	0.65	0.317	VB
104	-43.60287462	172.6744642	158.5019531	0.85	0.55	0.5	0.234	VB
105	-43.60287152	172.6745985	152.2532959	0.65	0.4	0.5	0.13	ML
106	-43.60274454	172.6746708	151.5323486	1.8	1	0.75	1.35	VB
107	-43.60272459	172.6746919	151.2919922	1.25	0.8	0.8	0.8	ML
108	-43.60284495	172.6747613	146.7258301	0.7	0.6	0.8	0.336	ML
109	-43.60266709	172.6748089	146.9661865	1.65	0.95	0.7	1.097	VB
110	-43.6026691	172.674806	147.9274902	0.9	0.6	0.6	0.324	VB
111	-43.60273641	172.6750883	139.7562256	4.25	2.8	2.3	27.37	VB
112	-43.60260037	172.6751857	139.7562256	1.2	1.15	0.9	1.242	ML
113	-43.6026655	172.6751219	136.1513672	1.95	1.5	2.9	8.483	VB
114	-43.60270749	172.6753111	132.5465088	3	2.75	1.75	14.438	VB
115	-43.60275644	172.6752813	129.6625977	1.4	0.95	0.95	1.264	VB
116	-43.60272895	172.6752643	129.902832	1.4	1.1	1.1	1.69	VB
117	-43.60290681	172.6752805	126.7786865	2.7	1.5	0.95	3.848	VB
118	-43.60298669	172.675108	132.0657959	1.15	0.9	1.1	1.139	VB
119	-43.60301661	172.6751103	133.9884033	0.8	0.4	0.4	0.128	VB
120	-43.60329313	172.6753483	128.4609375	1.1	0.8	0.8	0.704	ML
121	-43.60333563	172.6753339	129.1818848	0.7	0.45	0.45	0.142	ML
122	-43.60293145	172.6755311	121.7316895	1.9	1.9	1.9	6.859	VB
123	-43.60269617	172.6758059	121.7316895	2.6	1.5	3.3	12.87	VB
124	-43.60275233	172.6758672	117.8864746	2.7	2.3	1.35	8.384	VB
125	-43.60288653	172.6757256	117.8864746	0.7	0.67	0.75	0.352	VB
126	-43.60290622	172.6756809	117.8864746	0.52	0.7	0.5	0.182	ML
127	-43.60308518	172.6756871	118.1268311	2.15	2.1	1	4.515	VB
128	-43.60310764	172.6756966	118.3670654	4.1	3.1	1.4	17.794	VB
129	-43.60301276	172.6759319	111.1573486	0.85	0.56	0.4	0.19	VB
130	-43.60296909	172.6760125	110.4364014	4.4	1.9	3.1	25.916	VB
131	-43.60299465	172.6760347	112.1186523	4.2	2.1	2.3	20.286	VB
132	-43.60299113	172.6760468	110.9169922	10.9	4.6	4	200.56	VB
133	-43.60295266	172.6760311	109.9556885	2.8	0.9	0.6	1.512	VB
134	-43.60296138	172.6760645	109.4750977	2	1.05	1.05	2.205	VB
135	-43.60295769	172.6760535	109.2347412	2.3	2.2	1	5.06	VB
136	-43.60295777	172.6760542	109.2347412	1.2	0.9	0.9	0.972	VB

137	-43.60294604	172.6761153	108.5137939	1.25	0.8	1	1	VB
138	-43.6029478	172.6761319	107.7927246	0.6	0.8	0.6	0.288	VB
139	-43.60295886	172.6761326	108.2734375	1	0.55	0.55	0.303	VB
140	-43.60300119	172.6763015	102.2651367	1.05	1.25	1.05	1.378	VB
141	-43.60336346	172.67617	105.8701172	1.05	0.8	0.8	0.672	VB
142	-43.60341576	172.6762277	105.6297607	0.75	0.55	0.55	0.227	ML
143	-43.60305416	172.6764129	100.5828857	0.5	0.125	0.5	0.125	VB
144	-43.60305039	172.6765784	97.45861816	1.15	0.7	0.4	0.322	VB
145	-43.60305727	172.6767263	93.85375977	1.2	0.8	0.8	0.768	ML
146	-43.6030783	172.6768397	90.48913574	0.8	0.6	0.55	0.264	VB
147	-43.6032332	172.6770586	84.96154785	0.45	0.5	0.4	0.09	ML
148	-43.60323278	172.6771355	84.48095703	0.8	0.45	0.45	0.162	VB
149	-43.60334116	172.6771993	81.83728027	1.33	1.23	1.23	2.012	VB
150	-43.60330495	172.6773	79.91467285	1.04	0.73	0.73	0.554	VB
151	-43.60318894	172.6779633	69.82092285	2.6	1.85	0.5	2.405	VB
152	-43.6043827	172.6774532	63.09179688	0.55	0.38	0.35	0.073	VB
153	-43.6046018	172.6771459	69.82092285	0.3	0.2	0.2	0.012	VB
154	-43.60447984	172.6768653	75.82910156	0.75	0.45	0.5	0.169	ML
155	-43.60475946	172.676787	79.43408203	0.4	0.3	0.3	0.036	VB
156	-43.60545952	172.6769549	76.79052734	0.2	0.25	0.18	0.009	ML
157	-43.60423157	172.6766543	87.84545898	0.8	0.3	0.45	0.041	VB
158	-43.6042221	172.6766374	86.6439209	0.26	0.2	0.35	0.0182	VB
159	-43.60422252	172.6766304	88.08581543	0.27	0.31	0.2	0.017	ML
160	-43.60421699	172.6766184	87.60510254	0.12	0.12	0.12	0.002	ML
161	-43.60421279	172.6766032	87.60510254	0.3	0.25	0.2	0.015	VB
162	-43.60432746	172.6766664	83.7598877	0.2	0.12	0.12	0.003	VB
163	-43.60442268	172.6767252	82.79870605	0.35	0.25	0.28	0.025	ML
164	-43.60446014	172.6767757	81.11633301	0.35	0.3	0.3	0.032	VB
165	-43.60446802	172.6767769	82.31799316	0.65	0.48	0.25	0.078	VB
166	-43.60453307	172.6765487	89.76806641	0.15	0.22	0.15	0.005	ML
167	-43.60446132	172.6765452	89.76806641	0.33	0.29	0.2	0.019	VB
168	-43.60445453	172.6765749	89.28747559	0.17	0.17	0.15	0.004	VB
169	-43.60439611	172.6764856	92.17150879	0.46	0.28	0.2	0.026	ML
170	-43.60445118	172.6765163	91.45031738	0.15	0.16	0.1	0.0024	VB
171	-43.6044402	172.6766267	89.28747559	0.2	0.25	0.05	0.003	ML
172	-43.60431011	172.6765964	89.76806641	0.2	0.13	0.13	0.003	VB

173	-43.60431531	172.6765885	89.04711914	0.17	0.17	0.15	0.004	ML
174	-43.60432327	172.6765807	88.08581543	0.18	0.1	0.1	0.002	VB
175	-43.60436317	172.6766586	85.44226074	0.17	0.17	0.1	0.003	VB
176	-43.60431522	172.6766516	86.16320801	0.2	0.1	0.1	0.002	VB
177	-43.60407089	172.6768309	83.51965332	1.05	0.7	0.7	0.514	VB
178	-43.60323597	172.6780612	62.61108398	0.4	0.15	0.15	0.009	VB
179	-43.6025624	172.6775975	71.74353027	1.45	1.5	1.5	3.26	VB
180	-43.60257673	172.6775856	71.02258301	0.25	0.3	0.3	0.022	VB
181	-43.60261898	172.6772274	85.68249512	0.7	0.3	0.3	0.063	VB
182	-43.60280212	172.6771612	88.56652832	0.3	0.15	0.2	0.009	ML
183	-43.6028079	172.6771009	88.56652832	0.15	0.12	0.12	0.002	ML
184	-43.60217239	172.67705	86.16320801	3	1.8	1	5.4	VB
185	-43.60326815	172.6779279	66.45629883	0.14	0.13	0.13	0.002	VB
186	-43.60332088	172.6778406	64.77404785	0.35	0.2	0.2	0.014	VB
187	-43.60332373	172.677839	65.73535156	0.28	0.2	0.26	0.019	VB
188	-43.60326136	172.6776445	69.09997559	0.5	0.35	0.35	0.0613	VB
189	-43.60332146	172.6774893	69.82092285	1.2	1	1	1.2	VB
190	-43.60328408	172.6773727	73.18554688	0.7	0.3	0.3	0.063	VB
191	-43.60328559	172.6773722	73.18554688	0.42	0.45	0.42	0.079	VB
192	-43.60328509	172.6773713	73.90649414	0.25	0.2	0.2	0.01	VB
193	-43.60328601	172.6773673	73.90649414	0.5	0.35	0.35	0.0613	VB
194	-43.60328542	172.6773639	74.14672852	0.2	0.11	0.11	0.0024	VB
195	-43.6032855	172.6773514	75.1081543	0.15	0.15	0.15	0.0034	VB
196	-43.60329766	172.6773246	74.62744141	0.45	0.2	0.2	0.018	VB
197	-43.60330462	172.677348	74.38708496	0.85	0.4	0.4	0.136	VB
198	-43.60330344	172.6773418	76.06945801	0.35	0.3	0.35	0.037	VB
199	-43.60331601	172.6773239	76.06945801	0.3	0.15	0.15	0.007	VB
200	-43.60330914	172.6773199	75.58874512	0.35	0.4	0.35	0.049	VB
201	-43.60329405	172.6772632	77.99206543	0.41	0.22	0.21	0.019	VB
202	-43.60322692	172.6770611	83.51965332	0.13	0.13	0.13	0.002	VB
203	-43.60318953	172.6770549	83.51965332	0.31	0.3	0.15	0.014	ML
204	-43.60315584	172.6770107	85.2019043	0.5	0.3	0.2	0.045	VB
205	-43.6031529	172.6770094	86.16320801	0.25	0.2	0.2	0.01	VB
206	-43.60315877	172.6769958	85.92285156	0.27	0.23	0.23	0.014	VB
207	-43.60307721	172.6769134	91.93103027	0.25	0.13	0.13	0.004	ML
208	-43.60308954	172.6767957	92.17150879	0.25	0.25	0.25	0.016	ML

209	-43.60309356	172.6767921	93.85375977	0.18	0.1	0.1	0.002	VB
210	-43.60310798	172.6767071	96.97802734	0.3	0.2	0.15	0.009	VB
211	-43.60308543	172.6766753	95.2956543	0.21	0.12	0.12	0.003	VB
212	-43.60307763	172.676679	95.77636719	0.3	0.2	0.2	0.012	VB
213	-43.60307914	172.6766361	97.69897461	0.3	0.27	0.1	0.008	VB
214	-43.60308618	172.6766368	97.21826172	0.17	0.15	0.15	0.004	VB
215	-43.60308903	172.6766389	97.45861816	0.13	0.1	0.1	0.001	VB
216	-43.60308719	172.6765916	98.1796875	0.35	0.4	0.25	0.035	ML
217	-43.60308769	172.6766076	98.66027832	0.3	0.2	0.25	0.015	VB
218	-43.60308426	172.676609	99.86193848	0.36	0.17	0.17	0.01	VB
219	-43.60307654	172.6766024	99.62158203	0.32	0.2	0.2	0.013	ML
220	-43.60306389	172.6766515	97.69897461	0.58	0.35	0.35	0.071	VB
221	-43.60307562	172.6765631	100.3425293	0.15	0.12	0.12	0.002	VB
222	-43.60306523	172.6765594	101.303833	0.36	0.3	0.3	0.032	VB
223	-43.60302919	172.6765448	102.5054932	0.23	0.1	0.1	0.002	VB
224	-43.60305626	172.6764664	103.4667969	0.39	0.1	0.1	0.004	ML
225	-43.60302558	172.6765216	103.2264404	0.27	0.25	0.25	0.017	ML
226	-43.60309683	172.676461	102.5054932	0.15	0.1	0.12	0.002	ML
227	-43.60310446	172.6764437	102.0249023	0.18	0.1	0.1	0.002	VB
228	-43.60309842	172.6764414	105.3894043	0.28	0.2	0.2	0.011	VB
229	-43.60309406	172.6764362	104.1877441	0.17	0.07	0.07	0.008	VB
230	-43.60309658	172.6764303	104.4281006	0.17	0.13	0.13	0.003	VB
231	-43.60307277	172.676393	103.4667969	0.45	0.45	0.45	0.091	ML
232	-43.60313857	172.6763449	105.6297607	0.38	0.2	0.2	0.015	VB
233	-43.60301427	172.6762966	105.8701172	0.33	0.3	0.15	0.015	VB
234	-43.60306825	172.6762792	106.350708	0.15	0.15	0.15	0.003	VB
235	-43.60303497	172.6763309	105.1490479	0.22	0.13	0.1	0.003	VB
236	-43.60303245	172.676323	105.3894043	0.2	0.1	0.14	0.003	VB
237	-43.60298996	172.67628	107.0716553	0.35	0.35	0.35	0.043	VB
238	-43.60298032	172.6762736	106.8312988	0.4	0.25	0.2	0.02	VB
239	-43.6029887	172.6762561	106.350708	0.5	0.4	0.4	0.08	VB
240	-43.602969	172.6761232	110.4364014	0.5	0.25	0.2	0.025	VB
241	-43.60293489	172.6761011	111.6380615	0.33	0.18	0.17	0.01	VB
242	-43.60290061	172.676096	112.3590088	0.5	0.5	0.25	0.0625	VB
243	-43.602897	172.6760907	112.5992432	0.25	0.2	0.16	0.008	ML
244	-43.60293682	172.6759898	113.3203125	0.45	0.22	0.2	0.0198	VB

245	-43.60280774	172.6759583	116.2042236	0.6	0.3	0.3	0.054	ML
246	-43.60273523	172.675941	117.8864746	0.43	0.42	0.42	0.0758	ML
247	-43.60295995	172.6759506	115.4832764	0.64	0.2	0.2	0.0256	VB
248	-43.6029203	172.6759179	116.9251709	0.5	0.26	0.25	0.0325	ML
249	-43.60295165	172.6758684	119.0881348	0.25	0.32	0.3	0.072	VB
250	-43.60305634	172.6759639	115.4832764	0.57	0.29	0.29	0.0479	ML
251	-43.6030716	172.6759604	116.444458	0.15	0.13	0.15	0.003	ML
252	-43.60310504	172.6758701	118.3670654	1.83	1	1	1.83	VB
253	-43.60310169	172.6758337	118.6074219	0.1	0.13	0.1	0.001	VB
254	-43.60306037	172.6757987	120.0494385	0.33	0.33	0.33	0.036	VB
255	-43.60313731	172.6757457	120.0494385	0.64	0.46	0.23	0.068	ML
256	-43.60303698	172.6757667	119.809082	0.3	0.2	0.2	0.012	VB
257	-43.60303354	172.6757437	120.2896729	0.4	0.32	0.22	0.0281	ML
258	-43.60298996	172.6757511	120.0494385	0.2	0.2	0.2	0.008	VB
259	-43.60329858	172.6755794	123.8946533	0.35	0.25	0.25	0.022	ML
260	-43.60322767	172.6755117	126.5383301	0.4	0.4	0.22	0.035	ML
261	-43.60298292	172.6755391	124.1350098	0.56	0.5	0.2	0.056	VB
262	-43.60293196	172.6756286	122.6929932	0.21	0.13	0.12	0.003	ML
263	-43.60294973	172.6756183	121.0107422	0.5	0.3	0.3	0.045	VB
264	-43.60291477	172.6756742	121.2510986	0.35	0.17	0.2	0.012	ML
265	-43.6028846	172.6756864	123.1737061	0.28	0.23	0.15	0.0097	ML
266	-43.60288753	172.6756789	122.2122803	0.25	0.2	0.2	0.01	ML
267	-43.60289114	172.675668	123.6542969	0.25	0.25	0.25	0.0156	VB
268	-43.60289591	172.6756625	121.9720459	0.22	0.1	0.1	0.0022	ML
269	-43.60289566	172.6756661	121.491333	0.18	0.13	0.13	0.003	VB
270	-43.60289181	172.6756691	123.1737061	0.2	0.11	0.1	0.0022	ML
271	-43.60281897	172.6756536	122.9333496	0.23	0.17	0.17	0.0066	ML
272	-43.60285761	172.67561	123.8946533	0.22	0.26	0.2	0.0119	ML
273	-43.60275627	172.6755604	128.4609375	0.32	0.24	0.24	0.018	ML
274	-43.60276088	172.6754533	131.5852051	0.36	0.25	0.2	0.018	VB
275	-43.60278871	172.6754576	128.7012939	0.38	0.38	0.42	0.06	VB
276	-43.6028271	172.6755368	125.3366699	0.26	0.15	0.12	0.005	VB
277	-43.60286658	172.6755457	124.1350098	0.65	0.15	0.15	0.015	VB
278	-43.60293338	172.6754876	125.0964355	0.24	0.24	0.38	0.023	ML
279	-43.60293204	172.6754885	126.0576172	0.3	0.18	0.18	0.0097	VB
280	-43.60294981	172.675484	126.5383301	0.31	0.22	0.22	0.015	VB

281	-43.60294704	172.6754777	125.8173828	0.35	0.22	0.22	0.0169	VB
282	-43.60315072	172.6752593	131.5852051	0.48	0.48	0.48	0.1105	VB
283	-43.60310387	172.6752178	132.0657959	0.34	0.25	0.15	0.0129	VB
284	-43.60311049	172.6751891	131.8254395	0.22	0.1	0.1	0.0022	VB
285	-43.60310052	172.6751895	133.2674561	0.59	0.28	0.28	0.046	VB
286	-43.60309582	172.6751916	133.0270996	0.25	0.15	0.15	0.0056	VB
287	-43.60301267	172.6752048	133.0270996	2	0.9	0.9	1.62	VB
288	-43.60290606	172.6753715	130.3835449	0.3	0.14	0.14	0.0059	ML
289	-43.60286557	172.6753815	129.1818848	0.3	0.2	0.27	0.0162	VB
290	-43.60287395	172.6753774	128.4609375	0.4	0.25	0.25	0.025	VB
291	-43.60287102	172.6753781	129.6625977	0.47	0.22	0.22	0.0227	VB
292	-43.6028737	172.6753753	128.9416504	0.43	0.41	0.41	0.072	ML
293	-43.60287513	172.6753551	130.1431885	0.25	0.2	0.2	0.01	ML
294	-43.60283716	172.6753201	128.7012939	0.32	0.24	0.24	0.018	ML
295	-43.60284034	172.6753205	129.6625977	0.2	0.2	0.2	0.008	ML
296	-43.60286239	172.6753157	129.1818848	0.5	0.5	0.2	0.05	VB
297	-43.60285878	172.6754274	127.4996338	0.31	0.18	0.18	0.01	ML
298	-43.60286021	172.6754261	127.2592773	0.27	0.12	0.12	0.004	ML
299	-43.60285878	172.6754171	127.9802246	0.12	0.1	0.1	0.001	ML
300	-43.60289063	172.6754079	127.7399902	0.22	0.15	0.15	0.005	ML
301	-43.60327553	172.6759891	185.1782227	0.73	0.35	0.35	0.089	ML
302	-43.60326489	172.676009	177.9683838	0.67	0.63	0.3	0.127	ML
303	-43.60323144	172.6757726	176.5264893	0.45	0.35	0.35	0.055	VB
304	-43.60304997	172.6751305	186.1395264	0.17	0.28	0.15	0.007	ML
305	-43.60297462	172.675035	183.7362061	0.63	0.57	0.75	0.269	ML
306	-43.60287588	172.6749802	180.1313477	0.95	0.82	0.4	0.3116	VB
307	-43.60287915	172.6749888	178.4490967	0.5	0.4	0.45	0.09	VB
308	-43.60286247	172.6750414	174.3635254	0.53	0.33	0.3	0.052	ML
309	-43.6028986	172.6749984	171.4794922	0.3	0.23	0.2	0.0138	ML
310	-43.60302382	172.6747978	175.0845947	0.65	0.45	0.4	0.117	ML
311	-43.60307151	172.6748114	172.440918	0.45	0.25	0.25	0.028	VB
312	-43.60309104	172.6748213	170.7585449	0.95	0.5	0.5	0.2375	VB
313	-43.60317763	172.6748575	168.3552246	0.6	0.55	0.55	0.1815	VB
314	-43.60316925	172.6748477	166.9133301	0.24	0.13	0.13	0.004	VB
315	-43.60314569	172.6749103	164.0294189	0.3	0.24	0.5	0.036	ML
316	-43.60320026	172.6747704	168.1149902	0.88	0.47	0.47	0.194	VB

317	-43.60312457	172.6746888	171.7198486	0.4	0.16	0.16	0.01	ML
318	-43.60317738	172.6746381	171.2392578	0.2	0.13	0.13	0.003	VB
319	-43.60315324	172.674658	170.7585449	0.24	0.15	0.15	0.005	VB
320	-43.60315466	172.6746551	169.7972412	0.22	0.15	0.15	0.005	VB
321	-43.60315047	172.6746589	170.0375977	0.25	0.17	0.15	0.006	VB
322	-43.60308803	172.6745455	168.3552246	0.75	0.33	0.33	0.082	ML
323	-43.60315961	172.6745184	164.2697754	1.3	0.6	0.6	0.468	ML
324	-43.60313731	172.6744727	162.8277588	0.38	0.4	0.26	0.0395	ML
325	-43.60309607	172.6745313	160.4245605	0.2	0.15	0.15	0.0045	VB
326	-43.60303748	172.6745554	162.347168	0.27	0.15	0.1	0.004	ML
327	-43.60303991	172.6745653	161.6262207	0.55	0.23	0.23	0.029	ML
328	-43.60300764	172.6745978	159.9438477	0.3	0.15	0.15	0.0067	VB
329	-43.60303899	172.6744383	163.0681152	1	0.4	0.4	0.16	ML
330	-43.60314628	172.6743439	165.9520264	0.47	0.32	0.3	0.045	ML
331	-43.60313497	172.6743548	168.1149902	0.6	0.27	0.27	0.0437	VB
332	-43.60304184	172.6742966	166.6729736	0.7	0.26	0.26	0.047	VB
333	-43.60304318	172.6742941	166.1923828	0.3	0.2	0.2	0.012	ML
334	-43.60262342	172.674372	170.0375977	2.4	1.2	1	2.88	VB
335	-43.60264814	172.6743785	169.0762939	3	1.25	1.4	5.25	VB
336	-43.60264597	172.6744196	167.1536865	0.93	1.16	0.93	1.003	VB
337	-43.60262753	172.6743887	168.1149902	1.9	1.45	1.45	3.99	VB
338	-43.60261646	172.6743785	168.8359375	0.65	0.65	0.65	0.275	VB
339	-43.60261789	172.6743735	169.5568848	0.5	0.45	0.45	0.101	VB
340	-43.60275577	172.67435	165.2310791	1.28	0.8	0.8	0.819	VB
341	-43.60273691	172.6743166	167.1536865	0.7	0.45	1	0.315	VB
342	-43.6027375	172.6743113	166.6729736	0.5	0.3	0.3	0.045	ML
343	-43.60276021	172.6742458	166.9133301	1.5	0.77	0.77	0.682	VB
344	-43.60277421	172.6742493	167.8746338	0.9	1.6	0.9	1.296	VB
345	-43.60275099	172.6742775	167.394043	0.45	0.7	0.45	0.142	ML
346	-43.60283716	172.6742356	167.394043	1.4	1.15	1.15	1.85	VB
347	-43.60283087	172.6742374	168.1149902	1.1	1.1	0.8	0.986	VB
348	-43.60283179	172.6742285	168.3552246	0.43	0.32	0.32	0.044	ML
349	-43.60280447	172.6742135	167.6342773	1.15	0.78	0.4	0.3588	VB
350	-43.60279466	172.6742148	167.6342773	0.45	0.28	0.28	0.035	VB
351	-43.60278829	172.6742119	167.394043	0.5	0.3	0.3	0.045	ML
352	-43.60280346	172.6742262	168.5955811	2.5	1.7	1.7	7.225	VB

353	-43.60281226	172.6741647	169.0762939	0.9	0.85	0.85	0.65	VB
354	-43.60281712	172.6741921	171.4794922	6.8	2.4	2.4	39.168	VB
355	-43.60280598	172.6741551	170.5181885	1	0.8	0.35	0.28	VB
356	-43.60282006	172.6741191	172.2005615	0.93	0.95	0.93	0.821	VB
357	-43.60280824	172.6740874	172.6812744	0.5	0.5	1	0.25	VB
358	-43.60284545	172.674075	174.8442383	2.3	1.3	1	2.99	VB
359	-43.60283674	172.6740086	174.3635254	0.9	0.65	0.65	0.38	VB
360	-43.6028395	172.6739995	175.805542	0.46	0.67	0.46	0.141	ML
361	-43.60278795	172.6740181	176.5264893	2.1	1.9	1.9	7.58	VB
362	-43.60278611	172.6740563	174.6038818	0.36	0.33	0.33	0.039	ML
363	-43.60277991	172.6739901	177.487793	0.65	0.34	0.34	0.075	ML
364	-43.6027157	172.6740079	177.9683838	0.77	0.9	0.77	0.533	VB
365	-43.60269844	172.6739992	178.9298096	1.16	0.65	0.65	0.49	ML
366	-43.60267924	172.673922	181.3330078	1.14	0.4	0.4	0.18	VB
367	-43.60272945	172.6738063	183.7362061	1.1	1.45	1	1.595	VB
368	-43.60272383	172.6738046	184.4572754	1.7	1.2	1.2	2.448	VB
369	-43.60268913	172.6737836	186.3798828	0.85	0.75	0.75	0.478	ML
370	-43.60268016	172.6737863	186.1395264	0.32	0.3	0.3	0.029	ML
371	-43.60272911	172.6738215	185.4185791	1.4	0.7	0.7	0.686	VB
372	-43.6027561	172.6737966	184.6976318	0.84	1.1	0.84	0.77	VB
373	-43.60276893	172.6737565	184.2169189	0.4	0.15	0.15	0.009	ML
374	-43.60274957	172.6738632	181.5733643	0.72	0.67	0.25	0.1206	ML
375	-43.60275258	172.6738647	181.8135986	0.53	0.45	0.45	0.107	ML
376	-43.60274412	172.673856	181.8135986	0.8	0.8	0.4	0.256	ML
377	-43.60276859	172.6738786	181.0926514	2.6	2.1	2.1	11.466	VB
378	-43.60294067	172.6737888	184.4572754	2.4	2.4	0.6	3.456	VB
379	-43.60293665	172.6737899	185.8991699	0.5	0.8	0.7	0.28	ML
380	-43.60299163	172.6737867	187.3411865	2.1	1.2	0.9	2.268	VB
381	-43.60299474	172.6738194	185.4185791	3.8	1.2	1.2	5.47	VB
382	-43.60301276	172.673821	184.6976318	1.3	1.15	1.15	1.7	VB
383	-43.60301577	172.6738195	185.4185791	0.32	0.4	0.4	0.051	VB
384	-43.60308216	172.6738936	183.7362061	1	0.6	0.6	0.36	VB
385	-43.60308141	172.6738894	184.6976318	0.36	0.36	0.2	0.026	ML
386	-43.60307126	172.6739096	184.4572754	0.4	0.25	0.3	0.03	ML
387	-43.60307453	172.6739067	184.4572754	0.35	0.2	0.2	0.014	ML
388	-43.60307344	172.673905	184.9378662	0.38	0.38	0.38	0.055	ML

389	-43.60307395	172.673899	185.4185791	0.7	0.35	0.35	0.086	VB
390	-43.60301686	172.6738759	185.8991699	0.68	0.68	0.37	0.171	VB
391	-43.60291922	172.6738715	186.3798828	2.25	2.25	1.1	5.569	VB
392	-43.60292441	172.6738943	184.4572754	0.4	0.2	0.2	0.016	ML
393	-43.60288133	172.6739975	180.852417	1.6	0.6	0.9	0.864	VB
394	-43.60286322	172.6740124	179.4104004	0.42	0.4	0.4	0.067	ML
395	-43.60285015	172.674016	179.1700439	1.8	1.65	1.65	4.9	VB
396	-43.6029856	172.674049	177.0072021	3.8	2.1	1.9	15.16	VB
397	-43.6030079	172.6739959	176.2861328	0.7	0.3	0.5	0.105	ML
398	-43.6030053	172.6739984	176.5264893	0.63	0.32	0.32	0.065	ML
399	-43.60300228	172.6739998	176.2861328	0.78	0.8	0.2	0.125	ML
400	-43.60299105	172.6739899	176.2861328	0.25	0.25	0.25	0.016	ML
401	-43.60298811	172.6739274	178.2087402	2.1	1.4	1.4	4.116	VB
402	-43.60304218	172.674044	176.7668457	0.6	0.54	0.54	0.175	VB
403	-43.60305475	172.6740165	176.5264893	0.43	0.3	0.3	0.039	VB
404	-43.60305802	172.6739565	175.805542	0.3	0.2	0.2	0.012	ML
405	-43.60301309	172.6740901	170.7585449	1	0.6	0.5	0.3	VB
406	-43.60302541	172.6741699	166.4326172	0.32	0.3	0.3	0.029	ML
407	-43.60301343	172.6741639	165.7116699	0.45	0.35	0.35	0.055	VB
408	-43.60306573	172.6742157	164.9907227	0.5	0.5	0.5	0.125	VB
409	-43.60302047	172.6746332	149.1290283	0.7	0.35	0.4	0.098	VB
410	-43.60302114	172.6746315	149.8500977	0.5	0.4	0.4	0.08	ML
411	-43.60302818	172.6746587	149.3693848	0.46	0.2	0.06	0.0055	ML
412	-43.60305634	172.6746799	150.5710449	0.48	0.32	0.32	0.049	VB
413	-43.60302977	172.6752096	134.949707	0.22	0.15	0.15	0.005	VB
414	-43.60303262	172.675201	134.7094727	0.25	0.1	0.1	0.0025	VB
415	-43.60290924	172.6753516	130.1431885	0.6	0.3	0.3	0.054	VB
416	-43.60230616	172.6757897	135.1900635	2.9	1.8	1.4	7.308	VB
417	-43.60265745	172.674917	143.1209717	0.17	0.17	0.17	0.005	ML
418	-43.60267656	172.6749882	141.1983643	0.5	0.32	0.32	0.051	VB
419	-43.60256935	172.6750941	141.9193115	0.7	0.31	0.31	0.067	VB
420	-43.60264395	172.6749414	140.9580078	0.4	0.43	0.4	0.069	VB
421	-43.60240842	172.6751681	141.9193115	0.43	0.34	0.34	0.05	ML
422	-43.60240222	172.6751545	141.1983643	0.43	0.26	0.26	0.029	ML
423	-43.60255955	172.6749401	144.3226318	0.3	0.24	0.24	0.017	ML
424	-43.60231253	172.674864	153.4549561	1.01	0.7	0.4	0.283	VB

425	-43.60227699	172.6747249	158.7421875	0.45	0.42	0.42	0.079	VB
426	-43.60228244	172.6746505	161.1455078	1.4	1.2	1.2	2.016	VB
427	-43.60235671	172.674575	161.8664551	0.22	0.22	0.22	0.011	ML
428	-43.60252024	172.6746765	156.0986328	0.57	0.5	0.5	0.143	VB
429	-43.60253289	172.6746719	155.8582764	0.23	0.13	0.13	0.004	VB
430	-43.60255058	172.6746035	157.5406494	0.37	0.25	0.25	0.023	VB
431	-43.60264144	172.6745524	157.0599365	0.95	0.6	0.6	0.342	VB
432	-43.60266776	172.6745962	155.137207	0.55	0.35	0.35	0.067	VB
433	-43.60269542	172.674549	154.6566162	0.5	0.4	0.4	0.08	VB
434	-43.60269081	172.6745553	154.8968506	0.64	0.35	0.35	0.078	ML
435	-43.60269223	172.6745536	154.1759033	0.45	0.2	0.2	0.018	VB
436	-43.60217188	172.6746832	162.1068115	0.25	0.18	0.18	0.008	ML
437	-43.60245855	172.6744824	163.3084717	0.47	0.26	0.26	0.032	VB
438	-43.60249945	172.6744452	163.3084717	1.4	0.75	0.75	0.788	VB
439	-43.60251202	172.6744233	164.5100098	0.3	0.2	0.2	0.012	VB
440	-43.60251412	172.6744168	165.2310791	0.24	0.21	0.21	0.011	VB
441	-43.60254195	172.6743093	166.4326172	1.04	0.5	0.5	0.26	ML
442	-43.60249945	172.6743641	166.6729736	0.46	0.3	0.3	0.041	ML
443	-43.60248679	172.6743165	166.4326172	0.25	0.2	0.2	0.01	ML
444	-43.60248428	172.6742894	167.394043	0.82	0.3	0.26	0.064	ML
445	-43.60246559	172.6743784	166.4326172	0.46	0.35	0.35	0.056	VB
446	-43.60246492	172.6743711	167.1536865	0.4	0.2	0.2	0.016	VB
447	-43.60246626	172.6743501	168.1149902	0.5	0.23	0.23	0.026	VB
448	-43.60222477	172.6743864	170.277832	0.65	0.28	0.28	0.051	ML
449	-43.60227758	172.674317	170.9989014	0.4	0.2	0.2	0.016	ML
450	-43.60227624	172.6742947	171.4794922	0.35	0.2	0.2	0.014	ML
451	-43.60239535	172.6743118	171.2392578	0.32	0.32	0.32	0.033	VB
452	-43.60226383	172.6742394	174.1231689	0.22	0.22	0.27	0.013	ML
453	-43.60216132	172.6743088	174.6038818	0.4	0.42	0.4	0.067	VB
454	-43.60214297	172.6742983	175.0845947	0.5	0.38	0.38	0.0722	VB
455	-43.60201464	172.6744838	174.3635254	0.68	0.22	0.22	0.033	ML
456	-43.60205353	172.6741568	182.2943115	1.2	0.5	0.5	0.3	VB
457	-43.60209133	172.6739901	185.6588135	0.36	0.34	0.34	0.042	ML
458	-43.60227339	172.6741191	176.5264893	0.22	0.13	0.13	0.0037	ML
459	-43.60229133	172.6740938	178.6894531	0.25	0.12	0.12	0.0036	ML
460	-43.60236391	172.6739564	181.5733643	0.42	0.2	0.2	0.017	VB

461	-43.60240432	172.6739319	182.2943115	1.85	1	1	1.85	VB
462	-43.60247774	172.6739503	181.0926514	1.3	1	0.5	0.65	VB
463	-43.6024184	172.6740295	178.2087402	1.5	0.7	0.7	0.735	VB
464	-43.60244488	172.6740423	178.2087402	0.4	0.3	0.3	0.036	VB
465	-43.60229577	172.6737233	191.1865234	1.2	1.05	0.8	1.008	VB
466	-43.60243642	172.6736954	192.3881836	1.85	1.1	0.7	1.423	ML
467	-43.60247489	172.673623	194.310791	0.6	0.45	0.33	0.089	VB
468	-43.60253298	172.6736092	194.5510254	1.25	0.86	0.85	0.914	VB
469	-43.60252837	172.6736146	194.0704346	0.4	0.2	0.2	0.016	VB
470	-43.60249191	172.6737544	187.3411865	0.7	0.7	0.7	0.343	ML
471	-43.60247246	172.6738012	187.1008301	0.2	0.17	0.17	0.006	VB
472	-43.60248059	172.6737855	186.3798828	0.4	0.32	0.32	0.041	VB
473	-43.60248218	172.6738902	183.7362061	0.25	0.27	0.25	0.017	ML
474	-43.60248067	172.6738916	183.7362061	0.26	0.15	0.15	0.006	ML
475	-43.60248327	172.6738812	185.6588135	0.5	0.25	0.25	0.0313	ML
476	-43.60253616	172.6738011	184.9378662	0.37	0.31	0.31	0.036	ML
477	-43.6025629	172.6738337	184.9378662	0.55	0.42	0.42	0.097	ML
478	-43.60259794	172.6738446	184.6976318	0.3	0.3	0.35	0.032	ML
479	-43.60266281	172.6737075	189.5041504	4.7	1.4	1.4	9.212	VB
480	-43.60252728	172.6735545	196.7139893	0.42	0.25	0.25	0.026	ML
481	-43.60252636	172.6735418	199.3575439	4.1	1.5	1.3	7.995	VB
482	-43.60252669	172.6735269	197.675293	1.1	0.7	0.7	0.539	ML
483	-43.60247162	172.6734836	198.6365967	1.1	0.57	0.57	0.357	ML
484	-43.60248403	172.6734219	201.7608643	0.4	0.26	0.26	0.027	VB
485	-43.6024241	172.6734119	202.9624023	1.55	0.7	0.7	0.76	VB
486	-43.6024189	172.6733948	203.2027588	0.93	0.67	0.67	0.417	VB
487	-43.60245151	172.6733649	203.6834717	0.21	0.18	0.18	0.007	ML
488	-43.60238621	172.673339	204.8851318	0.25	0.2	0.2	0.01	ML
489	-43.60239216	172.6733442	206.086792	0.3	0.15	0.15	0.007	ML
490	-43.60217641	172.673557	200.0786133	0.4	0.25	0.25	0.025	ML
491	-43.60209561	172.6734027	204.8851318	1.67	1.41	1.41	3.32	VB
492	-43.60240473	172.6735749	201.7608643	0.56	0.2	0.2	0.0224	ML
493	-43.60239996	172.6735535	202.0012207	0.3	0.15	0.15	0.007	ML
494	-43.60240063	172.6735474	202.4818115	0.34	0.27	0.27	0.025	VB
495	-43.60241001	172.6733655	208.0093994	0.24	0.15	0.15	0.0045	ML
496	-43.6026199	172.6733201	208.4901123	2.35	1.65	1.65	6.398	VB

497	-43.60245637	172.6733329	208.2497559	0.43	0.3	0.3	0.039	ML
498	-43.60246173	172.6733139	208.7303467	0.2	0.2	0.2	0.008	VB
499	-43.60236408	172.6724456	241.1746826	3.3	1	1	3.3	VB
500	-43.60239493	172.6724112	239.0117188	2.35	2.75	2.35	15.187	VB
501	-43.60237179	172.6724626	238.2907715	1.6	1.4	1.4	3.136	VB
502	-43.60236509	172.672519	237.5697021	1.2	0.75	0.6	0.54	VB
503	-43.60236123	172.6725156	237.5697021	1.3	0.5	0.5	0.325	VB
504	-43.60240817	172.6724789	235.4067383	3	0.8	0.8	1.92	VB
505	-43.60240993	172.6725339	235.4067383	2.5	1.15	1.3	3.74	VB
506	-43.60238311	172.6725125	235.4067383	1.1	0.6	0.6	0.396	ML
507	-43.60227272	172.6726087	233.003418	1.86	0.9	0.9	1.507	VB
508	-43.6022039	172.6725666	235.4067383	1.85	1.4	0.65	1.684	VB
509	-43.60220625	172.672555	237.3294678	1.05	0.55	0.4	0.23	ML
510	-43.6022112	172.6725428	237.5697021	0.65	0.35	0.35	0.08	ML
511	-43.60216551	172.6725054	238.050415	0.2	0.3	0.3	0.018	ML
512	-43.60215319	172.6725033	239.9730225	1.8	1.6	1.05	3.024	VB
513	-43.60213224	172.672557	239.2520752	2.2	2.4	0.7	3.696	VB
514	-43.60216199	172.6725842	239.4923096	1	0.75	0.3	0.225	VB
515	-43.60215311	172.6725319	240.6939697	1.07	0.75	0.75	0.602	VB
516	-43.60219158	172.6725172	242.1359863	1.25	0.5	0.5	0.313	VB
517	-43.6021941	172.6725138	242.8569336	0.55	0.42	0.42	0.097	ML
518	-43.60219527	172.6725092	241.414917	0.45	0.25	0.4	0.045	ML
519	-43.60218337	172.6725197	240.6939697	0.52	0.26	0.26	0.035	ML
520	-43.60215864	172.6725148	242.1359863	0.95	0.45	0.45	0.192	ML
521	-43.60215663	172.6725145	242.3763428	0.5	0.37	0.37	0.068	ML
522	-43.60216468	172.6726088	242.3763428	0.37	0.27	0.27	0.027	ML
523	-43.60212159	172.6725424	242.6165771	0.46	0.2	0.2	0.018	ML
524	-43.60226702	172.6724703	243.09729	0.75	0.45	0.45	0.152	ML
525	-43.60211615	172.6725907	242.1359863	1.3	0.75	0.6	0.585	VB
526	-43.60216241	172.6726903	241.6552734	0.65	0.65	0.65	0.275	VB
527	-43.60223819	172.6725254	242.1359863	1.55	1	1	1.55	VB
528	-43.60224011	172.6725547	240.2133789	0.5	0.4	0.25	0.05	ML
529	-43.60214431	172.6726262	240.9343262	0.3	0.45	0.3	0.041	ML
530	-43.60216233	172.6725417	243.09729	0.75	0.65	0.65	0.317	ML
531	-43.60227683	172.6726062	238.5311279	2.9	1	1	2.9	VB
532	-43.60225202	172.6727121	237.3294678	1.8	1.45	1.45	3.785	VB

533	-43.60222913	172.6726098	238.050415	0.6	0.25	0.25	0.0375	VB
534	-43.60234665	172.6725067	237.8100586	0.5	0.85	0.5	0.213	VB
535	-43.60239996	172.6725348	237.0891113	0.7	0.5	0.3	0.105	ML
536	-43.60239509	172.6726383	237.5697021	0.6	0.6	0.6	0.216	VB
537	-43.60243206	172.672582	233.4841309	0.4	0.3	0.35	0.042	ML
538	-43.60241597	172.6726296	233.7243652	0.4	0.4	0.4	0.064	ML
539	-43.60231429	172.6727031	233.2437744	2.8	1.3	1.6	5.824	VB
540	-43.60232242	172.6727132	233.4841309	0.7	0.55	0.55	0.212	VB
541	-43.60240532	172.6726879	232.5228271	3.9	1.4	1.4	7.644	VB
542	-43.602422	172.6726485	232.7631836	1.6	0.75	0.75	0.9	VB
543	-43.60243457	172.672671	231.0808105	1	0.6	0.6	0.36	VB
544	-43.602451	172.6726638	231.0808105	0.3	0.3	0.3	0.027	ML
545	-43.60249476	172.6724979	242.1359863	1.7	1.7	0.6	1.734	VB
546	-43.60254899	172.6726126	230.1195068	3.5	1.65	1.55	8.95	VB
547	-43.60257941	172.6726782	227.4759521	1.17	0.5	0.6	0.351	ML
548	-43.60257237	172.6726355	227.956543	1.5	0.65	0.55	0.536	VB
549	-43.60256542	172.6726377	227.4759521	1.15	0.75	0.75	0.647	ML
550	-43.60256684	172.6726047	229.8791504	1.3	1.1	1.1	1.573	VB
551	-43.60358273	172.6759147	118.3670654	0.5	0.3	0.3	0.045	ML
552	-43.60358851	172.6759446	116.6848145	0.9	0.45	0.45	0.182	ML
553	-43.60355398	172.6759349	117.4058838	0.17	0.15	0.15	0.004	ML
554	-43.60345951	172.675785	121.491333	0.45	0.41	0.41	0.076	VB
555	-43.60343244	172.6759526	116.9251709	0.4	0.25	0.25	0.025	VB
556	-43.6033762	172.6756374	124.8560791	0.4	0.27	0.27	0.029	VB
557	-43.60350922	172.6755862	129.1818848	0.2	0.25	0.25	0.013	ML
558	-43.60331761	172.6754499	132.5465088	0.6	0.6	0.6	0.216	VB
559	-43.60326757	172.6753715	133.7480469	0.4	0.15	0.15	0.009	ML
560	-43.6032762	172.6753753	133.0270996	0.7	0.35	0.35	0.086	ML
561	-43.60344308	172.675469	134.4691162	0.43	0.32	0.32	0.044	VB
562	-43.60340872	172.6754273	134.7094727	0.2	0.15	0.15	0.0045	ML
563	-43.60341827	172.6753577	136.8723145	0.53	0.4	0.4	0.084	VB
564	-43.60343973	172.6753356	138.7949219	0.5	0.4	0.4	0.08	VB
565	-43.60356077	172.6753137	138.5546875	0.25	0.13	0.13	0.004	ML
566	-43.60356286	172.6753074	139.7562256	0.2	0.12	0.12	0.003	ML
567	-43.60361458	172.6752773	139.5158691	0.72	0.6	0.6	0.259	VB
568	-43.60349815	172.6752432	140.7176514	1	0.35	0.35	0.123	ML

569	-43.60359186	172.6752427	140.9580078	0.45	0.5	0.45	0.101	VB
570	-43.60359387	172.6752298	140.9580078	0.3	0.23	0.23	0.015	VB
571	-43.603601	172.6752403	140.7176514	0.2	0.12	0.12	0.003	VB
572	-43.60343571	172.6752175	140.477417	0.31	0.2	0.2	0.012	ML
573	-43.60343127	172.6751562	142.6402588	0.7	0.35	0.35	0.086	VB
574	-43.60337662	172.6751654	142.159668	0.18	0.15	0.15	0.004	ML
575	-43.6033684	172.6748904	151.7727051	0.15	0.13	0.13	0.0025	VB
576	-43.60339321	172.674814	154.1759033	0.28	0.17	0.17	0.008	ML
577	-43.60321887	172.6746563	157.0599365	0.37	0.15	0.15	0.008	ML
578	-43.60332423	172.6747243	157.0599365	0.24	0.12	0.12	0.003	ML
579	-43.60335918	172.6747274	157.5406494	0.2	0.2	0.2	0.008	ML
580	-43.6033596	172.6747256	157.5406494	0.21	0.15	0.15	0.005	ML
581	-43.6033627	172.6747245	157.5406494	0.23	0.2	0.2	0.009	ML
582	-43.60336237	172.6747231	157.5406494	0.17	0.13	0.13	0.003	VB
583	-43.6034798	172.674728	157.7810059	0.42	0.25	0.25	0.026	VB
584	-43.60344015	172.6745215	167.8746338	0.6	0.7	0.6	0.252	ML
585	-43.60343487	172.6745176	169.0762939	0.66	0.35	0.35	0.08	VB
586	-43.60343177	172.6745115	170.277832	0.65	0.25	0.25	0.041	VB
587	-43.60323731	172.6743817	176.5264893	0.58	0.28	0.28	0.045	VB
588	-43.60330663	172.6742812	180.852417	0.65	0.45	0.45	0.132	VB
589	-43.60350285	172.6741906	180.1313477	0.5	0.45	0.45	0.101	VB
590	-43.60348734	172.6741953	178.6894531	0.53	0.3	0.15	0.024	VB
591	-43.60348349	172.674192	177.487793	0.3	0.3	0.15	0.014	VB
592	-43.60341031	172.6740068	185.4185791	0.5	0.3	0.3	0.045	ML
593	-43.60333236	172.6738972	187.8217773	0.7	0.6	0.3	0.126	VB
594	-43.60329875	172.6738813	187.3411865	1.13	0.7	0.7	0.554	VB
595	-43.60329397	172.6738829	185.8991699	0.7	0.3	0.3	0.063	ML
596	-43.60335013	172.6737904	188.0622559	1	0.5	0.5	0.25	VB
597	-43.60318316	172.6735469	198.3962402	0.85	0.5	0.5	0.213	ML
598	-43.60318643	172.6735428	198.8769531	0.67	0.35	0.35	0.082	ML
599	-43.60319666	172.6733997	205.1254883	0.56	0.3	0.3	0.05	ML
600	-43.60323035	172.6727077	234.685791	2.6	1.3	1.95	6.591	VB
601	-43.60330302	172.6727109	235.1663818	1.4	1.6	0.85	1.904	VB
602	-43.60329037	172.6727692	232.0421143	2.8	4.9	1.5	20.58	VB
603	-43.60319456	172.6727547	232.0421143	3.4	2.9	1	9.86	VB
604	-43.60319909	172.6728022	228.6776123	3.5	3.5	1.3	15.925	VB

605	-43.60321141	172.6728139	228.9179688	1	1.2	1	1.2	ML
606	-43.60321233	172.6728136	229.1582031	0.83	0.73	0.73	0.44	VB
607	-43.60321417	172.6728126	229.3985596	1	0.5	0.5	0.25	ML
608	-43.60320613	172.6728007	228.4372559	0.75	0.6	0.6	0.27	VB
609	-43.60321074	172.6728039	227.956543	0.35	0.5	0.35	0.061	ML
610	-43.60321317	172.6728084	227.4759521	0.4	0.35	0.35	0.049	VB
611	-43.60321744	172.6728075	229.1582031	0.85	0.6	0.6	0.306	VB
612	-43.60322658	172.6727841	229.3985596	1.3	0.45	0.45	0.263	ML
613	-43.60321241	172.6728494	226.9953613	0.65	0.35	0.35	0.0796	VB
614	-43.60323069	172.6728187	228.4372559	0.75	0.4	0.4	0.12	VB
615	-43.60318894	172.6728423	226.5146484	0.7	0.45	0.45	0.142	ML
616	-43.60313958	172.6728148	226.7550049	1.45	1.15	1.15	1.918	VB
617	-43.60315609	172.6728156	225.5533447	1.3	0.7	0.7	0.637	VB
618	-43.60315123	172.6728152	225.0727539	1.05	0.9	0.9	0.85	VB
619	-43.60315123	172.6728175	224.592041	1.1	1.15	1.1	1.392	VB
620	-43.603141	172.6728272	225.3129883	0.9	0.7	0.7	0.441	ML
621	-43.60319448	172.6728658	225.7937012	1.3	0.65	0.65	0.549	VB
622	-43.60316833	172.6729047	222.90979	0.7	0.46	0.46	0.148	ML
623	-43.60318853	172.6728798	223.6307373	0.45	0.25	0.25	0.028	ML
624	-43.60314494	172.6728355	223.1501465	1.1	0.45	0.45	0.223	ML
625	-43.60314603	172.672836	223.3903809	0.6	0.3	0.3	0.054	ML
626	-43.60313346	172.6728414	222.6694336	0.64	0.3	0.3	0.058	ML
627	-43.60313463	172.6728425	223.6307373	0.63	0.34	0.34	0.073	VB
628	-43.60313513	172.6728417	222.6694336	0.63	0.6	0.6	0.227	VB
629	-43.60313765	172.6728358	221.2275391	1	0.7	0.7	0.49	VB
630	-43.60313622	172.6728371	221.4677734	0.8	0.5	0.5	0.2	VB
631	-43.6031374	172.6728405	220.2661133	0.57	0.5	0.5	0.143	VB
632	-43.60313639	172.6728784	220.2661133	1.7	1.4	0.83	1.975	ML
633	-43.60312616	172.6728377	222.90979	1	2	0.7	1.4	ML
634	-43.6031415	172.6727959	224.3516846	0.36	0.36	0.36	0.047	VB
635	-43.60316866	172.6727278	228.1968994	0.8	0.7	0.6	0.336	ML
636	-43.6031819	172.6726501	235.4067383	1.25	0.75	0.7	0.656	VB
637	-43.60322138	172.6726595	233.2437744	1	0.95	0.95	0.903	VB
638	-43.60324477	172.6726525	230.3598633	0.8	0.9	1.7	1.224	VB
639	-43.6032363	172.6726643	230.3598633	0.9	0.5	0.4	0.18	ML
640	-43.60323303	172.6726682	232.2824707	1	0.3	0.3	0.09	VB

641	-43.6032301	172.6726698	231.321167	0.47	0.25	0.25	0.029	ML
642	-43.60322784	172.6726751	230.6002197	0.57	0.5	0.5	0.143	ML
643	-43.60315919	172.6726474	232.0421143	1.25	1.2	0.9	1.35	VB
644	-43.60315743	172.6726473	230.6002197	1.1	0.55	0.55	0.333	VB
645	-43.60315835	172.6726456	231.321167	0.65	0.43	0.43	0.12	ML
646	-43.60316061	172.6726457	231.8017578	0.45	0.45	0.45	0.091	ML
647	-43.60316455	172.6726442	231.321167	0.68	0.25	0.2	0.034	ML
648	-43.60316514	172.6726339	232.5228271	1.1	1	1	1.1	VB
649	-43.60317101	172.6725559	232.5228271	0.8	0.7	0.7	0.392	ML
650	-43.60316673	172.6725585	234.2050781	0.65	0.2	0.2	0.026	ML
651	-43.60327972	172.6727732	233.7243652	0.8	0.3	0.3	0.072	VB
652	-43.60328483	172.6727319	235.6469727	0.8	0.25	0.25	0.05	VB
653	-43.603285	172.6727252	233.4841309	0.5	0.25	0.25	0.031	ML
654	-43.60330068	172.6727075	235.4067383	0.82	0.4	0.4	0.131	ML
655	-43.60332347	172.672678	236.6085205	1.23	0.65	0.65	0.5196	ML
656	-43.60338617	172.6727122	235.8873291	0.6	0.45	0.45	0.122	ML
657	-43.60333898	172.6727511	234.685791	1	0.6	0.6	0.36	VB
658	-43.60336916	172.6727535	235.1663818	0.47	0.36	0.36	0.061	VB
659	-43.60336396	172.6727663	233.9647217	1.5	1	1	1.5	VB
660	-43.60337134	172.672669	238.7713623	0.4	0.4	0.25	0.04	ML
661	-43.60338248	172.6726605	239.0117188	1.15	0.8	0.8	0.736	VB
662	-43.6033767	172.672683	238.2907715	0.6	0.5	0.5	0.15	VB
663	-43.60337804	172.6726791	238.7713623	0.67	0.3	0.3	0.06	VB
664	-43.60340813	172.6726333	240.9343262	0.95	0.7	0.7	0.466	VB
665	-43.6035212	172.6726973	237.0891113	2.45	1.5	0.8	2.94	VB
666	-43.60350511	172.6727563	231.321167	0.75	0.4	0.4	0.12	ML
667	-43.60347477	172.672801	231.8017578	0.75	0.45	0.45	0.152	ML
668	-43.60347477	172.6727942	232.7631836	0.56	0.35	0.35	0.069	ML
669	-43.60350377	172.6727797	232.2824707	1.05	0.75	0.75	0.591	VB
670	-43.60347737	172.6728019	230.8405762	1.5	1.2	1.15	2.07	VB
671	-43.60349857	172.6727884	231.5615234	1.9	1.8	2.3	7.866	VB
672	-43.60348131	172.6727563	233.4841309	1.6	1.05	1.05	1.764	VB
673	-43.60345507	172.6727884	231.8017578	1	0.45	0.45	0.203	ML
674	-43.60344107	172.672773	230.6002197	0.7	0.3	0.3	0.063	ML
675	-43.6034373	172.6727956	230.1195068	0.5	0.3	0.3	0.045	ML
676	-43.60341961	172.6728123	231.5615234	0.5	0.5	0.5	0.125	VB

677	-43.60346613	172.672849	227.7163086	1.8	0.7	0.7	0.578	VB
678	-43.60347955	172.6728397	228.1968994	0.4	0.5	0.6	0.12	ML
679	-43.60346588	172.6728744	227.2355957	1	1.2	1	1.2	VB
680	-43.60346236	172.6728631	227.956543	0.65	0.45	0.45	0.132	VB
681	-43.60346035	172.6728612	227.7163086	3.25	1.3	1.3	5.493	VB
682	-43.60349287	172.6728463	229.1582031	0.5	0.5	0.5	0.125	VB
683	-43.60348089	172.6729051	226.5146484	0.7	0.5	0.4	0.14	ML
684	-43.60348474	172.6728946	225.3129883	0.7	0.5	0.5	0.175	ML
685	-43.60349078	172.6728771	224.8323975	0.7	0.3	0.3	0.063	ML
686	-43.60349271	172.6728795	224.592041	0.4	0.35	0.35	0.049	ML
687	-43.60348717	172.6729033	224.1113281	2.5	0.95	0.95	2.256	VB
688	-43.60343738	172.672934	224.592041	2.4	1.4	1.4	4.704	VB
689	-43.60342213	172.6729357	223.1501465	0.9	0.25	0.25	0.056	ML
690	-43.60341308	172.672937	222.4290771	0.5	0.4	0.4	0.08	ML
691	-43.60337972	172.6729627	222.1887207	0.55	0.5	0.5	0.138	VB
692	-43.60337259	172.6729445	224.1113281	0.42	0.3	0.3	0.038	ML
693	-43.60337033	172.6729513	223.8710938	0.5	0.45	0.45	0.101	VB
694	-43.60330319	172.6729735	224.8323975	1.5	1.72	1.5	3.87	VB
695	-43.603112	172.6728789	225.3129883	1.9	0.75	0.75	1.068	ML
696	-43.60317285	172.6730081	226.7550049	0.6	0.6	0.6	0.216	ML
697	-43.60325466	172.6729663	226.274292	0.7	0.7	0.5	0.245	ML
698	-43.60328257	172.6729991	227.7163086	0.64	0.33	0.33	0.07	VB
699	-43.60325709	172.6731271	226.7550049	1	0.75	0.75	0.563	ML
700	-43.60335063	172.673097	226.7550049	0.95	0.32	0.32	0.097	ML
701	-43.60215185	172.6741663	173.4022217	0.3	0.23	0.23	0.016	VB
702	-43.60234371	172.673284	207.5288086	0.5	0.34	0.34	0.104	ML
703	-43.60245268	172.6730928	215.2192383	0.86	0.4	0.52	0.138	ML
704	-43.60243667	172.6730942	216.4207764	0.5	0.33	0.33	0.054	VB
705	-43.60243097	172.6730185	218.5837402	0.36	0.17	0.17	0.01	ML
706	-43.6024935	172.6729785	218.5837402	2.3	1.12	1.12	2.885	VB
707	-43.60251538	172.6729553	220.0258789	2.75	2.3	2.3	14.548	VB
708	-43.60252728	172.6729539	219.5450439	0.6	0.6	0.6	0.216	VB
709	-43.60250532	172.6730243	219.0644531	1.44	0.45	0.7	0.454	VB
710	-43.60249903	172.6730303	220.0258789	0.7	0.35	0.3	0.074	ML
711	-43.60251856	172.6730585	218.3433838	0.65	0.65	0.65	0.275	VB
712	-43.60256843	172.6730629	218.8240967	2.5	1.4	1.3	4.55	VB

713	-43.60253507	172.6730141	220.5064697	0.8	0.5	0.4	0.16	ML
714	-43.60253423	172.6730151	220.0258789	0.5	0.5	0.5	0.125	VB
715	-43.60247355	172.6729529	223.1501465	0.6	0.35	0.35	0.074	VB
716	-43.60247422	172.672951	223.3903809	0.66	0.4	0.4	0.106	ML
717	-43.60239828	172.6729208	224.8323975	1.75	1.15	1.15	2.314	ML
718	-43.60240063	172.6729193	225.7937012	1.1	0.8	0.8	0.704	ML
719	-43.60245972	172.6729256	223.8710938	0.72	0.5	0.3	0.108	ML
720	-43.60230264	172.6730121	222.90979	1.42	1.65	1.42	3.327	VB
721	-43.60252493	172.6727467	226.7550049	0.52	0.42	0.42	0.092	ML
722	-43.60247791	172.6728931	227.4759521	0.85	0.63	0.6	0.321	ML
723	-43.60243449	172.6729088	228.6776123	0.47	0.45	0.5	0.106	ML
724	-43.60246299	172.6729671	227.7163086	0.94	0.46	0.46	0.199	ML
725	-43.60253063	172.6728308	228.6776123	0.7	0.5	0.5	0.175	VB
726	-43.60253122	172.6728249	229.1582031	0.36	0.4	0.4	0.058	VB
727	-43.6025251	172.6729295	229.8791504	2.25	1.2	1.2	3.24	VB
728	-43.60253843	172.6728706	230.3598633	1.15	0.5	0.5	0.288	VB
729	-43.60255083	172.6729042	230.8405762	0.82	0.45	0.45	0.166	VB
730	-43.6025691	172.6727902	231.0808105	0.42	0.25	0.25	0.026	ML
731	-43.60257782	172.6727824	231.5615234	0.3	0.22	0.22	0.015	ML
732	-43.60256734	172.672863	229.3985596	0.92	0.7	0.7	0.451	VB
733	-43.60262157	172.6727909	229.3985596	0.72	0.7	0.7	0.353	VB
734	-43.60267203	172.6726943	228.1968994	0.8	0.63	0.63	0.318	VB
735	-43.60263096	172.6728132	227.2355957	0.5	0.45	0.45	0.101	VB
736	-43.60260204	172.6729003	227.956543	0.46	0.22	0.22	0.022	ML
737	-43.60257204	172.6728552	225.3129883	1.4	0.8	0.8	0.896	VB
738	-43.60262359	172.6728874	226.5146484	0.78	0.4	0.4	0.125	ML
739	-43.60256885	172.6727484	225.7937012	0.53	0.33	0.33	0.058	VB
740	-43.60260422	172.6729168	224.1113281	1.05	0.65	0.65	0.444	VB
741	-43.60262359	172.6728333	222.1887207	0.47	0.4	0.4	0.075	ML
742	-43.60266189	172.6728835	222.1887207	0.56	0.4	0.4	0.0896	VB
743	-43.6026095	172.6729008	220.7468262	0.55	0.75	0.55	0.223	ML
744	-43.6026261	172.6729445	221.7081299	0.66	0.73	0.4	0.193	VB
745	-43.60263163	172.6729114	223.6307373	1.2	0.75	0.82	0.738	ML
746	-43.60261629	172.6728495	224.1113281	0.55	0.31	0.31	0.053	ML
747	-43.60262224	172.6728483	223.1501465	0.77	0.38	0.38	0.111	VB
748	-43.60262258	172.6728482	223.3903809	0.58	0.3	0.3	0.052	VB

749	-43.60262149	172.6727659	224.8323975	0.71	0.5	0.56	0.199	ML
750	-43.60261403	172.6727462	225.0727539	1.35	1.75	1.35	3.189	VB
751	-43.60262509	172.6727551	226.5146484	0.7	0.4	0.4	0.112	ML
752	-43.60241823	172.6724423	235.8873291	1.25	0.76	0.76	0.722	ML
753	-43.6024168	172.6724475	234.9260254	0.3	0.36	0.3	0.032	ML
754	-43.60244094	172.6724421	235.8873291	0.6	0.4	0.4	0.096	VB
755	-43.60243206	172.6724201	236.8487549	0.45	0.37	0.37	0.062	ML
756	-43.60242234	172.672517	235.6469727	0.55	0.5	0.5	0.138	ML
757	-43.60244052	172.6725142	235.8873291	0.5	0.4	0.4	0.08	ML
758	-43.60240683	172.672484	236.8487549	0.57	0.35	0.35	0.0698	ML
759	-43.60237204	172.6724549	237.5697021	0.35	0.35	0.35	0.043	ML
760	-43.60229191	172.6725063	237.3294678	0.75	0.36	0.36	0.097	ML
761	-43.60229233	172.6725099	237.3294678	0.55	0.25	0.25	0.034	ML
762	-43.60229384	172.6725187	237.5697021	0.42	0.29	0.29	0.035	VB
763	-43.60229317	172.6725202	237.0891113	0.3	0.3	0.3	0.027	VB
764	-43.60229359	172.6725211	235.6469727	0.64	0.6	0.6	0.23	VB
765	-43.60230281	172.6725203	236.3681641	0.8	0.65	0.65	0.338	VB
766	-43.6023262	172.6725366	235.1663818	0.6	0.3	0.3	0.054	VB
767	-43.60233299	172.6725343	238.2907715	0.4	0.27	0.27	0.029	VB
768	-43.60233441	172.6725243	231.321167	0.5	0.5	0.5	0.125	VB
769	-43.6023645	172.6724559	231.8017578	0.42	0.25	0.25	0.026	ML
770	-43.60235729	172.672487	231.8017578	0.5	0.5	0.5	0.125	ML
771	-43.6023728	172.6724796	232.7631836	0.42	0.39	0.39	0.064	ML
772	-43.60238319	172.6724848	233.2437744	0.4	0.3	0.3	0.036	ML
773	-43.60237573	172.6724501	233.4841309	0.5	0.3	0.3	0.045	ML
774	-43.60247933	172.6724895	232.7631836	0.47	0.4	0.4	0.075	ML
775	-43.6024945	172.6725382	231.8017578	0.32	0.32	0.32	0.033	ML
776	-43.60250833	172.6725727	229.3985596	0.78	0.46	0.46	0.165	ML
777	-43.60250808	172.672516	230.3598633	0.45	0.22	0.22	0.022	ML
778	-43.60250347	172.6725097	231.321167	0.4	0.2	0.2	0.016	ML
779	-43.60252904	172.6725286	230.3598633	0.62	0.4	0.4	0.099	VB
780	-43.60254488	172.6723858	233.2437744	1.2	0.7	0.7	0.588	VB
781	-43.60254865	172.6723907	234.4454346	0.75	0.65	0.65	0.317	VB
782	-43.60253298	172.672382	234.2050781	0.5	0.7	0.5	0.175	ML
783	-43.60258101	172.6724226	236.1278076	1.02	0.75	0.75	0.574	VB
784	-43.60257816	172.6724204	237.3294678	1.5	0.75	0.75	0.844	VB

785	-43.60257648	172.6724175	238.2907715	0.66	0.35	0.35	0.08	ML
786	-43.60259643	172.6723297	241.414917	2	2.1	0.5	2.1	VB
787	-43.60264965	172.6722569	245.5004883	1.12	0.8	0.8	0.717	ML
788	-43.60277303	172.6722188	251.508667	3	3	0.9	8.1	VB
789	-43.60280639	172.672231	251.7490234	3.2	2.2	1.6	11.264	VB
790	-43.6028354	172.6722015	255.1136475	1	0.7	0.7	0.49	ML
791	-43.60283699	172.6721968	256.3153076	1	0.6	0.6	0.36	ML
792	-43.60283908	172.6721928	255.5943604	1.5	0.54	0.54	0.437	VB
793	-43.60284185	172.6721945	253.6717529	1.15	0.5	0.5	0.288	VB
794	-43.60283908	172.6722051	249.1053467	1.2	1.45	1.2	2.088	VB
795	-43.60283716	172.6722407	250.5473633	0.6	0.5	0.5	0.15	VB
796	-43.60278955	172.6722241	250.3070068	0.82	0.6	0.6	0.295	VB
797	-43.6028452	172.6722221	250.3070068	0.55	0.4	0.3	0.066	ML
798	-43.60284638	172.6722118	250.0667725	0.4	0.25	0.25	0.025	VB
799	-43.60284998	172.6722084	249.3457031	0.8	0.6	0.6	0.288	VB
800	-43.60281679	172.6723038	248.3843994	0.6	0.6	0.6	0.216	ML
801	-43.60284185	172.6723066	248.144165	0.7	0.4	0.4	0.112	ML
802	-43.60284579	172.6722384	249.1053467	0.5	0.4	0.4	0.08	ML
803	-43.60285141	172.6722472	248.3843994	0.75	0.6	0.6	0.27	VB
804	-43.602853	172.6722501	248.144165	0.45	0.33	0.33	0.049	ML
805	-43.60285442	172.6722534	248.6247559	0.5	0.2	0.2	0.02	ML
806	-43.60285727	172.6722549	245.5004883	1.25	0.7	0.7	0.613	ML
807	-43.60285535	172.6722797	244.779541	0.7	0.36	0.36	0.09	ML
808	-43.60287739	172.6723477	242.6165771	0.8	0.65	0.65	0.338	ML
809	-43.60288569	172.6723139	242.8569336	0.45	0.5	0.25	0.056	ML
810	-43.60290279	172.6723684	243.09729	0.8	0.35	0.35	0.098	VB
811	-43.60289088	172.6724105	241.6552734	0.75	1.05	0.75	0.59	ML
812	-43.6029074	172.6723564	241.1746826	0.75	0.4	0.4	0.12	ML
813	-43.60284629	172.6724397	242.6165771	0.55	0.43	0.43	0.092	ML
814	-43.60286389	172.6724584	241.6552734	3.3	1.25	0.9	3.713	VB
815	-43.60276197	172.6724195	241.1746826	0.86	0.9	0.86	0.666	VB
816	-43.60267991	172.6724013	245.2601318	2.3	1.4	0.6	1.932	VB
817	-43.60268318	172.6723903	246.2215576	0.57	0.5	0.5	0.143	ML
818	-43.60275585	172.6723778	245.9812012	2.7	1.8	1.2	5.832	VB
819	-43.60264739	172.6724	242.3763428	1.24	0.7	0.7	0.607	VB
820	-43.60275409	172.6724798	241.414917	0.9	0.7	0.7	0.441	VB

821	-43.60277572	172.6724819	242.8569336	1.25	0.6	0.6	0.45	VB
822	-43.60276767	172.6724708	243.09729	0.9	0.3	0.3	0.081	ML
823	-43.60278653	172.6725649	241.1746826	0.9	0.6	0.3	0.162	ML
824	-43.60279164	172.6724868	239.2520752	0.94	0.6	0.43	0.243	ML
825	-43.60278712	172.672533	239.2520752	1	0.53	0.53	0.281	VB
826	-43.60275158	172.6725726	238.5311279	0.75	0.4	0.4	0.12	VB
827	-43.60279877	172.6725397	238.2907715	0.4	0.57	0.3	0.068	ML
828	-43.6028183	172.6726014	238.2907715	1.9	1.6	0.82	2.493	VB
829	-43.6028224	172.6725964	237.3294678	1.35	1	1	1.35	VB
830	-43.60282358	172.6726017	236.1278076	1.6	1	0.8	1.28	VB
831	-43.60282777	172.6726055	234.9260254	0.7	0.45	0.45	0.142	VB
832	-43.60281603	172.6726497	233.7243652	1.4	1	1	1.4	VB
833	-43.60282224	172.6726479	233.003418	0.7	0.3	0.3	0.063	VB
834	-43.60281209	172.6726387	233.7243652	0.37	0.4	0.37	0.055	ML
835	-43.60259626	172.6726109	232.0421143	0.8	0.55	0.55	0.242	VB
836	-43.602595	172.6726543	231.321167	0.85	0.62	0.4	0.211	VB
837	-43.6027447	172.6726115	233.003418	0.8	0.56	0.56	0.251	ML
838	-43.60274965	172.672637	233.2437744	0.65	0.5	0.5	0.1625	ML
839	-43.60274831	172.6726574	234.685791	0.47	0.47	0.6	0.133	VB
840	-43.60276884	172.672639	235.6469727	0.4	0.4	0.3	0.036	ML
841	-43.60277723	172.672676	234.2050781	0.6	0.4	0.4	0.096	VB
842	-43.60276138	172.6725859	234.4454346	0.6	0.5	0.5	0.15	VB
843	-43.60267664	172.6726679	232.5228271	1.4	0.85	0.85	1.012	VB
844	-43.60271051	172.6726967	231.0808105	0.63	0.52	0.52	0.164	VB
845	-43.60273054	172.6726848	231.5615234	0.7	0.38	0.38	0.101	ML
846	-43.6027582	172.672665	230.6002197	0.65	0.6	0.6	0.234	ML
847	-43.60275191	172.6725815	229.638916	0.6	0.6	0.6	0.216	ML
848	-43.60277303	172.6726216	229.1582031	0.75	0.35	0.35	0.092	ML
849	-43.60275602	172.6727544	229.1582031	2.6	1.15	1.15	3.439	VB
850	-43.60271855	172.672735	229.638916	0.65	0.4	0.4	0.104	VB
851	-43.603385	172.6719042	271.4559326	0.95	0.95	1	0.903	VB
852	-43.60338416	172.6719062	270.2542725	1.3	0.6	0.6	0.468	VB
853	-43.60334292	172.671942	269.0527344	2.4	1.6	1.25	4.8	VB
854	-43.60327628	172.6719233	269.2930908	1.3	0.95	0.95	1.173	VB
855	-43.60334284	172.6718941	274.8205566	3.8	2	0.75	5.7	VB
856	-43.6033948	172.6719523	274.3398438	1.6	1.5	0.7	1.68	VB

857	-43.60338793	172.6718228	272.8979492	1.3	1.05	0.75	1.024	VB
858	-43.60306129	172.671858	271.6962891	0.95	0.4	0.4	0.152	VB
859	-43.60340402	172.6719287	273.8592529	2.2	1.2	1.2	3.168	VB
860	-43.60342959	172.6719043	270.4946289	1.6	1.3	1.3	2.704	VB
861	-43.60343713	172.6719016	270.7349854	1.3	1.2	0.9	1.404	VB
862	-43.60344728	172.6719009	271.4559326	0.65	0.7	0.7	0.319	ML
863	-43.60343864	172.6719036	269.2930908	0.9	0.65	0.5	0.38	ML
864	-43.60343353	172.6719034	269.7736816	0.8	0.75	0.75	0.45	ML
865	-43.60343311	172.6719028	270.9753418	0.65	0.45	0.45	0.132	ML
866	-43.60340721	172.6718981	269.0527344	1.1	0.8	0.7	0.616	VB
867	-43.60340654	172.6718997	269.7736816	0.7	0.6	0.6	0.252	ML
868	-43.6034021	172.6719035	269.2930908	1.1	0.5	0.5	0.275	VB
869	-43.60332565	172.6719571	267.1300049	1.4	0.9	0.9	1.134	VB
870	-43.60332431	172.6719456	271.2156982	0.8	0.6	0.6	0.288	VB
871	-43.60333571	172.6719472	270.2542725	1.2	0.7	0.7	0.588	VB
872	-43.60326396	172.6719854	266.1687012	0.85	0.5	0.5	0.213	VB
873	-43.60329305	172.6720013	268.331665	1.55	0.3	1.5	6.975	VB
874	-43.60336765	172.6720488	264.967041	0.8	1.3	1	1.04	VB
875	-43.60341894	172.6719419	267.6105957	0.95	0.55	0.55	0.287	VB
876	-43.60342565	172.6719831	265.4477539	1.25	1.1	0.45	0.619	VB
877	-43.60318249	172.6720874	259.920166	1.6	1.5	1.3	3.12	VB
878	-43.60315232	172.6720978	261.1218262	1.1	1.15	0.65	0.822	VB
879	-43.6031602	172.6720859	261.3621826	1.05	0.9	0.9	0.851	VB
880	-43.60320202	172.6720463	263.7653809	2.9	2.1	0.9	5.48	VB
881	-43.60313748	172.6720498	263.0444336	2.7	2.9	1.1	8.613	VB
882	-43.60319012	172.6720227	265.6879883	1.7	1.15	1.15	2.248	VB
883	-43.60317285	172.6719868	265.9283447	1	1.05	1	1.05	VB
884	-43.60318886	172.6720126	264.2460938	0.85	0.6	0.6	0.306	VB
885	-43.60310286	172.6720502	262.0831299	0.7	0.8	0.7	0.392	VB
886	-43.6031156	172.6720136	263.28479	0.5	0.5	0.5	0.125	ML
887	-43.60308551	172.6720817	259.1992188	2.2	1.1	0.9	2.178	VB
888	-43.60313086	172.6720824	259.1992188	2.4	2	0.7	3.36	VB
889	-43.60311602	172.6720867	257.5169678	1.4	1	0.65	0.91	VB
890	-43.60311996	172.6721147	256.7958984	1.1	0.6	0.6	0.396	ML
891	-43.6030426	172.6721238	256.3153076	1.1	0.55	0.55	0.333	VB
892	-43.60301712	172.6721047	256.7958984	3.1	1.85	1.85	10.61	VB

893	-43.60307294	172.6721036	256.7958984	0.9	0.52	0.52	0.243	ML
894	-43.60297789	172.6720965	257.9975586	1	0.45	0.2	0.09	ML
895	-43.60291771	172.6722572	258.7185059	0.55	0.55	0.55	0.166	VB
896	-43.6031586	172.6720854	263.0444336	1.04	0.75	0.75	0.591	ML
897	-43.60310831	172.6722887	266.8896484	1.1	0.9	0.9	0.891	VB
898	-43.60319188	172.6721623	264.967041	4.25	1.9	1.9	15.342	VB
899	-43.60311929	172.6722809	264.7266846	1.35	1.1	1.1	1.63	VB
900	-43.60325231	172.6722039	267.3703613	1.25	0.75	0.7	0.656	VB
901	-43.60374081	172.674415	165.4714355	0.75	0.67	0.67	0.337	ML
902	-43.60370301	172.6744382	166.1923828	0.93	0.6	0.4	0.223	VB
903	-43.60373251	172.6744554	167.1536865	0.33	0.32	0.32	0.034	ML
904	-43.60366395	172.6744495	166.9133301	0.7	0.8	0.8	0.448	ML
905	-43.60373519	172.6742222	171.7198486	0.9	0.4	0.4	0.144	ML
906	-43.60376026	172.6742439	172.440918	0.5	0.3	0.3	0.045	ML
907	-43.60400601	172.6743898	169.3166504	0.6	0.4	0.4	0.096	VB
908	-43.60380543	172.6746196	152.7340088	0.5	0.37	0.37	0.068	VB
909	-43.6037528	172.6746993	152.4936523	0.42	0.4	0.4	0.067	VB
910	-43.60375456	172.6746133	153.9356689	0.5	0.35	0.35	0.061	ML
911	-43.60375648	172.6746468	151.5323486	0.41	0.34	0.34	0.047	ML
912	-43.60365054	172.6747129	149.6097412	0.8	0.3	0.3	0.072	VB
913	-43.60352028	172.6747819	147.9274902	0.3	0.3	0.7	0.063	ML
914	-43.60341081	172.6750199	137.1126709	0.43	0.3	0.3	0.039	VB
915	-43.60402144	172.6756252	115.7235107	0.7	0.6	0.36	0.151	ML
916	-43.60423551	172.6757364	111.6380615	0.38	0.38	0.5	0.072	ML
917	-43.60427767	172.675709	112.3590088	0.5	0.25	0.25	0.031	ML
918	-43.60430776	172.675799	109.7154541	0.54	0.3	0.3	0.049	VB
919	-43.60430835	172.6758032	108.9943848	0.5	0.45	0.45	0.101	VB
920	-43.60431145	172.6758498	108.7540283	0.58	0.42	0.42	0.102	VB
921	-43.60317369	172.6719522	326.0102539	2.9	1.7	1.2	5.916	VB
922	-43.60315969	172.6718423	324.0876465	1.9	1.6	0.85	2.584	VB
923	-43.60322432	172.6716615	322.4053955	1.6	1.55	0.5	1.24	VB
924	-43.60316657	172.671885	320.7231445	0.9	0.7	0.6	0.378	VB
925	-43.60319867	172.6717876	320.2424316	0.65	0.6	0.4	0.156	ML
926	-43.60319825	172.6717654	319.5214844	1.55	1.3	1.3	2.619	VB
927	-43.60318534	172.6717815	318.8005371	0.94	0.6	0.4	0.226	ML
928	-43.60320336	172.6717233	318.8005371	1.1	1.3	1.1	1.896	VB

929	-43.60331962	172.671527	317.1182861	0.75	1	0.55	0.413	ML
930	-43.60333982	172.671482	316.6375732	0.95	0.95	1	0.903	VB
931	-43.60326966	172.6716759	317.1182861	0.55	0.6	0.7	0.231	ML
932	-43.60327519	172.671621	316.8779297	1.3	0.9	0.6	0.702	VB
933	-43.60336513	172.6715458	317.598877	0.7	0.9	0.6	0.378	ML
934	-43.60334342	172.6714908	315.6761475	0.83	0.6	0.5	0.249	ML
935	-43.60327905	172.6716965	316.6375732	1.6	1.1	0.5	1.12	VB
936	-43.60337066	172.671534	317.598877	3.6	1.7	1.9	11.628	VB
937	-43.60343051	172.6715599	313.9938965	9.8	1.3	6.2	78.988	VB
938	-43.60345532	172.6716091	311.5906982	2	2.15	2	8.6	VB
939	-43.60347678	172.6716099	308.706665	1.9	2.1	1.2	4.788	VB
940	-43.60346194	172.6715834	307.2647705	1.3	2.3	2.8	8.372	VB
941	-43.60340151	172.6715631	308.706665	2.2	1.1	2.75	6.655	VB
944	-43.60345113	172.671607	301.0162354	0.5	0.5	0.55	0.138	ML
945	-43.603472	172.6717003	296.6903076	1.56	0.8	0.9	1.123	VB
946	-43.60347879	172.6716959	297.4112549	2.05	1.7	1.7	5.925	VB
947	-43.60351928	172.6716751	301.9776611	1.55	2.2	2.8	9.548	VB
948	-43.60283121	172.6719319	279.6270752	4.3	3.2	1.5	14.448	VB
949	-43.60290824	172.6719673	279.8673096	2.8	1.1	1	2.8	VB
950	-43.60288829	172.6719563	279.1463623	3.3	1.3	1.1	4.719	VB
951	-43.60284537	172.6719666	275.3011475	2	1	0.67	1.34	ML
952	-43.60290086	172.6719575	278.425415	4.4	4.9	1.85	39.886	VB
953	-43.60290865	172.6719404	280.5883789	2.4	1.6	1.6	6.144	VB
954	-43.60288619	172.6719003	279.1463623	3.4	2.1	1	7.14	VB
955	-43.60286867	172.6718631	274.8205566	2.4	3.9	2.8	26.208	VB
956	-43.60287488	172.6718648	277.9447021	1.4	1.3	1	1.82	VB
957	-43.6028856	172.6718604	277.9447021	1.15	1.55	1.15	2.05	VB
958	-43.6030037	172.6718735	277.7044678	2.8	2.8	3.4	26.656	VB
959	-43.60302407	172.6718666	276.0220947	1.3	2.5	1.3	4.225	VB
960	-43.60300446	172.6719467	274.0994873	1.45	1.45	1.45	3.049	VB
961	-43.60301251	172.6719341	274.8205566	0.88	0.95	0.8	0.669	VB
962	-43.60301502	172.6719271	275.0609131	0.85	0.8	0.46	0.313	VB
963	-43.60302994	172.6719078	275.7818604	2.9	2.1	2.1	12.789	VB
964	-43.60305785	172.6719623	272.4172363	4.7	4.3	1.7	34.357	VB
965	-43.60312331	172.6718756	275.3011475	9	4.6	2	82.8	VB
966	-43.60316455	172.6718718	274.3398438	0.95	1.4	1.1	1.463	VB

967	-43.60318132	172.6718751	275.5415039	1.35	1	1	1.35	VB
968	-43.60320428	172.6719407	275.0609131	9.4	6.4	2.8	168.448	VB
969	-43.60329355	172.6718166	278.1850586	2.4	2.9	0.8	5.568	VB
970	-43.60329045	172.671835	277.4641113	2.3	1.1	0.6	1.518	ML
971	-43.6032855	172.6718568	281.5496826	2.1	0.5	1.6	1.68	VB
972	-43.60328483	172.6718565	281.0689697	1.7	1.65	0.6	1.683	VB
973	-43.60339028	172.6717812	283.2319336	1.8	7.1	3.7	47.286	VB
974	-43.60306665	172.6721448	265.4477539	1.45	0.85	0.85	1.048	VB
975	-43.60305634	172.6721589	263.0444336	5.4	1.6	1.6	13.824	VB
976	-43.60296515	172.6720336	265.4477539	1.1	0.6	0.7	0.462	ML
977	-43.60288954	172.6720773	266.8896484	1.2	0.53	0.53	0.337	VB
978	-43.60295056	172.6720606	268.331665	1.5	1.6	0.4	0.96	VB
979	-43.60298476	172.6720011	268.5720215	1.6	0.8	0.7	0.896	VB
980	-43.60299591	172.6719553	270.7349854	2	2.6	2.3	11.96	VB
981	-43.60297764	172.6719772	270.9753418	1.28	1.15	0.75	1.104	VB
982	-43.60297797	172.6719755	272.1768799	1.6	1.2	0.9	1.728	VB
983	-43.6029882	172.6719789	270.7349854	0.9	1.1	4	3.96	VB
984	-43.60301167	172.6720426	271.6962891	0.54	0.5	0.7	0.189	ML
985	-43.60308853	172.6720974	271.9366455	0.87	0.6	0.4	0.209	VB
986	-43.60308434	172.6721003	270.7349854	1.2	0.8	0.8	0.768	ML
987	-43.60309205	172.6720371	271.9366455	0.95	0.9	1	0.855	VB
988	-43.60304243	172.672087	271.6962891	1.1	0.5	0.5	0.275	VB
989	-43.60306288	172.6721471	274.3398438	1.8	1.65	1	2.97	VB
990	-43.60325022	172.6721282	270.2542725	1.2	0.6	0.6	0.432	VB
991	-43.60327587	172.6721014	270.2542725	0.6	0.65	0.3	0.117	ML
992	-43.60331124	172.6721633	270.4946289	0.5	0.65	0.5	0.163	ML
993	-43.60332599	172.6722196	269.2930908	2.7	2.7	2.7	19.683	VB
994	-43.60338458	172.6721507	273.8592529	2.7	3.4	2.7	15.606	VB
995	-43.60344627	172.672175	271.9366455	4.08	3.2	1.55	19.84	VB
996	-43.6034637	172.672125	271.4559326	1.4	0.75	0.75	0.788	VB
997	-43.6034715	172.6721248	274.0994873	1.17	0.85	0.95	0.945	VB
998	-43.60347603	172.672117	274.3398438	0.9	1.05	0.9	0.851	VB
999	-43.60353361	172.672054	277.2237549	1	1.7	2.1	3.57	VB
1000	-43.60352665	172.6720521	276.0220947	1.5	1.4	1.4	2.94	VB
1001	-43.60351659	172.6720562	275.0609131	1.4	0.9	0.9	1.134	VB
1002	-43.60350796	172.6720605	274.0994873	1.1	0.85	0.85	0.795	VB

1003	-43.60345683	172.672119	272.1768799	1.05	1.3	1.05	1.43	VB
1004	-43.60348399	172.6721406	267.8509521	1.05	0.8	0.8	0.672	ML
1005	-43.60349438	172.6721502	267.8509521	3.7	1.5	1.5	8.325	VB
1006	-43.60347276	172.6721923	265.2073975	1.2	1	1	1.2	VB
1007	-43.60346924	172.6722056	265.9283447	0.7	0.82	0.6	0.354	ML
1008	-43.60371164	172.6755065	133.7480469	0.6	0.25	0.3	0.045	VB
1009	-43.60360871	172.675481	132.0657959	0.65	0.52	0.52	0.176	ML
1010	-43.60432402	172.6745555	168.1149902	0.45	0.4	0.4	0.072	VB
1011	-43.60436258	172.674528	168.8359375	0.73	0.3	0.3	0.066	VB
1012	-43.60433442	172.6744494	172.9216309	0.4	0.4	0.43	0.069	ML
1013	-43.60433282	172.674453	173.1619873	0.58	0.3	0.3	0.052	ML
1014	-43.60434012	172.6744025	175.3248291	0.6	0.45	0.45	0.122	VB
1015	-43.60436493	172.6742768	178.6894531	0.91	0.86	0.86	0.673	ML
1016	-43.60442528	172.6743673	175.3248291	1.6	1.1	1.1	1.936	VB
1017	-43.60452862	172.6743669	175.805542	0.95	0.55	0.57	0.298	ML
1018	-43.60452552	172.6743537	179.8909912	1.02	0.52	0.52	0.276	VB
1019	-43.60453265	172.674299	179.4104004	0.9	0.5	0.5	0.225	ML
1020	-43.60433718	172.6743201	177.487793	0.34	0.34	0.34	0.039	ML
1021	-43.60433785	172.6743175	179.6507568	0.5	0.53	0.5	0.133	ML
1022	-43.60433785	172.6743177	176.0457764	0.5	0.3	0.3	0.045	VB
1023	-43.60429988	172.6743357	172.440918	0.6	0.6	0.4	0.144	VB
1024	-43.60428949	172.6744044	172.440918	0.7	0.6	0.6	0.252	ML
1025	-43.60362983	172.6742582	176.7668457	0.87	0.45	0.45	0.176	VB
1026	-43.60382614	172.6741104	182.0539551	0.72	0.45	0.45	0.146	VB
1027	-43.60387299	172.6740814	183.9765625	0.5	0.4	0.4	0.08	ML
1028	-43.60374098	172.6740617	183.0152588	0.5	0.5	0.45	0.113	ML
1029	-43.6037771	172.6740466	186.6202393	0.75	0.55	0.55	0.227	ML
1030	-43.60377417	172.6740161	185.1782227	0.49	0.4	0.4	0.078	ML
1031	-43.6037621	172.673991	185.6588135	0.66	0.32	0.32	0.068	ML
1032	-43.60378071	172.6739249	187.8217773	1.1	0.58	0.58	0.37	ML
1033	-43.60382295	172.673979	186.3798828	0.4	0.3	0.3	0.036	ML
1034	-43.60382664	172.6740019	185.6588135	0.68	0.3	0.3	0.061	ML
1035	-43.60383251	172.6740116	184.9378662	0.42	0.45	0.2	0.038	ML
1036	-43.60374332	172.673969	184.9378662	0.7	0.3	0.3	0.063	ML
1037	-43.60370938	172.6739882	184.6976318	0.4	0.4	0.4	0.064	ML
1038	-43.60349656	172.674116	176.2861328	0.62	0.45	0.35	0.098	ML

1039	-43.60343127	172.6740377	180.3717041	0.64	0.36	0.36	0.083	ML
1040	-43.60383125	172.6737541	195.2719727	1.1	0.75	0.75	0.619	VB
1041	-43.60383762	172.6737404	192.628418	0.65	0.4	0.4	0.104	VB
1042	-43.60379244	172.6737086	195.5123291	0.64	0.6	0.6	0.23	VB
1043	-43.60369647	172.6736579	195.0317383	0.46	0.4	0.4	0.074	VB
1044	-43.60370167	172.6736491	195.993042	0.7	0.3	0.3	0.063	ML
1045	-43.60377149	172.6735581	200.7995605	0.55	0.37	0.37	0.068	VB
1046	-43.60373855	172.6735588	201.0397949	0.6	0.51	0.51	0.156	ML
1047	-43.60367342	172.6736156	199.8382568	0.85	0.6	0.6	0.306	ML
1048	-43.6033974	172.6735174	198.3962402	0.58	0.7	0.58	0.235	VB
1049	-43.60337452	172.6735084	198.3962402	0.66	0.4	0.4	0.106	ML
1050	-43.60332272	172.673699	200.7995605	0.73	0.25	0.25	0.046	VB
1051	-43.60348558	172.6734774	209.6917725	0.45	0.37	0.37	0.062	VB
1052	-43.60355146	172.6734991	209.2110596	0.9	0.35	0.35	0.11	VB
1053	-43.60354744	172.6734027	210.6529541	0.78	0.5	0.5	0.195	VB
1054	-43.60367493	172.673456	210.4127197	0.48	0.33	0.33	0.052	VB
1055	-43.60365607	172.6736474	211.3740234	0.5	0.68	0.4	0.136	VB
1056	-43.60371944	172.6735122	211.6143799	0.45	0.44	0.44	0.087	VB
1057	-43.6038631	172.6734606	214.9788818	1.75	1	1.2	2.1	VB
1058	-43.60385891	172.6736018	209.2110596	1.4	1.7	0.55	1.309	VB
1059	-43.60395052	172.6732059	224.3516846	1.45	0.7	0.7	0.711	VB
1060	-43.60397575	172.6733494	224.1113281	1.05	0.68	0.68	0.486	VB
1061	-43.60397835	172.6732765	225.5533447	1.1	1.7	0.45	0.842	VB
1062	-43.60380912	172.6733346	225.5533447	0.6	0.46	0.46	0.127	VB
1063	-43.60383234	172.6733284	224.8323975	0.38	0.45	0.38	0.065	VB
1064	-43.60385774	172.6731386	226.0339355	1	1	0.8	0.8	ML
1065	-43.60385103	172.6731426	227.2355957	2.1	0.8	1.25	2.1	VB
1066	-43.60390677	172.6730688	229.3985596	0.94	0.32	0.32	0.096	ML
1067	-43.60389378	172.6731144	228.9179688	0.53	0.33	0.33	0.058	ML
1068	-43.60394491	172.6730633	227.4759521	0.48	0.32	0.32	0.049	VB
1069	-43.60375321	172.6730241	230.3598633	2.05	1.3	1	3.705	VB
1070	-43.60375866	172.6729632	230.8405762	1.02	0.75	0.75	0.574	ML
1071	-43.60369865	172.6731334	226.9953613	1.02	0.4	0.4	0.163	VB
1072	-43.60375523	172.6732507	217.862793	0.36	0.5	0.36	0.065	ML
1073	-43.60372975	172.6733271	215.2192383	1.05	0.5	0.2	0.105	ML
1074	-43.60366797	172.6733441	219.7854004	0.76	0.3	0.3	0.068	ML

1075	-43.6037025	172.6731236	223.3903809	0.86	0.86	1.3	0.961	VB
1076	-43.60363	172.6731268	223.6307373	0.62	0.55	0.5	0.171	VB
1077	-43.60364794	172.6730878	222.1887207	0.5	0.6	0.5	0.15	VB
1078	-43.60363654	172.6730807	221.9484863	0.8	0.35	0.4	0.112	ML
1079	-43.60364718	172.673011	223.1501465	0.95	0.8	0.8	0.608	ML
1080	-43.60363922	172.6729954	223.1501465	0.95	0.75	0.6	0.428	ML
1081	-43.60363704	172.672999	222.90979	0.54	0.43	0.43	0.998	VB
1082	-43.60370125	172.6728938	225.5533447	0.9	1.2	0.9	0.972	VB
1083	-43.60369605	172.6729035	224.8323975	0.52	0.8	0.52	0.216	ML
1084	-43.60366956	172.6728811	224.592041	0.53	0.32	0.32	0.054	VB
1085	-43.60363377	172.6728949	225.3129883	1	1	0.6	0.6	VB
1086	-43.60365951	172.6728634	226.0339355	0.7	0.47	0.47	0.155	ML
1087	-43.60374475	172.6728267	226.9953613	0.95	0.6	0.6	0.342	ML
1088	-43.60376386	172.6728549	227.2355957	1.2	0.35	0.35	0.147	ML
1089	-43.60375204	172.6729123	227.956543	0.6	0.35	0.4	0.084	VB
1090	-43.60367635	172.6728724	230.3598633	1.4	0.7	0.7	0.686	VB
1091	-43.60361173	172.6729339	228.4372559	0.65	0.6	0.6	0.234	VB
1092	-43.60350796	172.6729252	229.8791504	1.6	0.9	0.9	1.296	VB
1093	-43.60348851	172.6729241	228.6776123	0.53	0.6	0.53	0.169	ML
1094	-43.60346689	172.6728852	230.6002197	0.75	0.55	0.55	0.227	ML
1095	-43.60347653	172.6728902	231.5615234	0.5	0.5	0.5	0.125	ML
1096	-43.60352296	172.6728292	232.7631836	0.8	0.3	0.3	0.072	ML
1097	-43.6035383	172.6728347	231.0808105	0.85	0.25	0.25	0.053	ML
1098	-43.60355523	172.6728336	232.0421143	0.57	0.52	0.52	0.154	ML
1099	-43.60354585	172.6728257	232.2824707	0.75	0.35	0.35	0.092	ML
1100	-43.60352908	172.6728296	232.5228271	0.95	0.6	0.6	0.342	VB
1101	-43.60352288	172.6728239	233.9647217	0.73	0.3	0.3	0.066	ML
1102	-43.60352154	172.6728167	233.003418	0.53	0.43	0.43	0.098	ML
1103	-43.60351165	172.6728407	233.2437744	0.63	0.2	0.2	0.025	ML
1104	-43.60352011	172.6728167	229.8791504	0.58	0.33	0.33	0.063	ML
1105	-43.60352565	172.6728111	233.7243652	1.1	0.7	0.5	0.385	VB
1106	-43.60352875	172.6728132	233.2437744	0.6	0.5	0.5	0.15	ML
1107	-43.60353168	172.672816	232.7631836	0.52	0.3	0.3	0.047	VB
1108	-43.60353478	172.6728158	232.5228271	0.41	0.28	0.28	0.032	ML
1109	-43.60360008	172.6728184	234.2050781	1.85	1.15	1.15	2.45	VB
1110	-43.6035865	172.6727831	234.2050781	0.7	0.5	0.5	0.175	VB

1111	-43.60358683	172.6727796	235.8873291	0.75	0.75	0.5	0.281	ML
1112	-43.60358574	172.6727772	234.685791	1.05	0.7	0.5	0.368	ML
1113	-43.60358415	172.6727757	235.1663818	0.87	0.7	0.7	0.426	VB
1114	-43.60360377	172.672774	236.6085205	0.85	0.45	0.45	0.172	VB
1115	-43.60352917	172.6727853	232.2824707	1.9	0.75	0.1	1.425	VB
1116	-43.60353185	172.6727858	232.2824707	1.55	0.65	0.65	0.655	ML
1117	-43.60352665	172.6727547	233.003418	0.57	0.75	0.65	0.278	VB
1118	-43.60352464	172.6727588	232.5228271	1.65	1.4	0.6	1.386	ML
1119	-43.60346572	172.6727103	234.4454346	1.4	1.6	0.6	1.344	VB
1120	-43.60344468	172.6727398	234.4454346	1.3	0.65	0.9	0.76	VB
1121	-43.60343898	172.6727887	234.9260254	0.85	1.3	0.55	0.608	VB
1122	-43.60349413	172.6727853	232.0421143	0.72	0.42	0.17	0.051	ML
1123	-43.60349555	172.6729082	223.6307373	0.85	0.46	0.46	0.18	ML
1124	-43.60347284	172.6731327	218.1031494	0.55	0.38	0.38	0.079	VB
1125	-43.60339824	172.6733014	208.2497559	0.6	0.37	0.37	0.082	VB
1126	-43.60302835	172.6744421	153.6953125	0.45	0.45	0.45	0.091	VB
1127	-43.60295325	172.674369	157.0599365	2.1	1.2	0.95	2.394	VB
1128	-43.60293933	172.6743317	158.2615967	5.5	1.65	1.8	16.335	VB
1129	-43.60296716	172.6743771	155.3775635	0.56	0.42	0.42	0.099	VB
1130	-43.60294889	172.6742594	161.6262207	0.75	0.7	0.7	0.368	VB
1131	-43.60287915	172.6742649	164.2697754	0.95	2.1	1.2	2.394	VB
1132	-43.60280396	172.6743471	161.1455078	2.2	1.8	1.15	4.554	VB
1133	-43.60287379	172.6743817	158.7421875	4.5	2.35	1.1	11.633	VB
1134	-43.60288979	172.6743195	162.8277588	1.9	4.6	5.2	45.448	VB
1135	-43.6028323	172.6742502	164.5100098	2.65	1.2	1.35	4.293	VB
1136	-43.60287907	172.6742632	165.7116699	3.4	2.3	1.2	9.384	VB
1137	-43.60282819	172.6742992	163.3084717	1	0.5	0.5	0.25	VB
1138	-43.60279801	172.6742828	164.2697754	0.5	0.31	0.31	0.048	VB
1139	-43.60281955	172.6742843	163.7890625	0.4	0.2	0.4	0.032	ML
1140	-43.6028613	172.6743856	158.9825439	0.35	0.4	0.35	0.049	VB
1141	-43.60285895	172.674504	156.3389893	0.35	0.46	0.35	0.056	VB
1142	-43.60285099	172.6744979	156.5793457	0.47	0.3	0.3	0.042	ML
1143	-43.60286205	172.6744843	157.0599365	0.5	0.21	0.25	0.026	ML
1144	-43.60286063	172.6744817	157.0599365	0.3	0.3	0.4	0.036	VB
1145	-43.60285509	172.6744789	158.2615967	0.43	0.38	0.15	0.025	ML
1146	-43.60285291	172.6744778	158.5019531	0.57	0.26	0.26	0.039	VB

1147	-43.60278485	172.6744672	158.5019531	0.8	0.7	0.7	0.392	VB
1148	-43.60278795	172.6744766	157.7810059	0.53	0.4	0.4	0.085	ML
1149	-43.60272509	172.6744146	161.3858643	1	0.44	0.44	0.194	VB
1150	-43.60299474	172.6742441	163.3084717	0.52	0.5	0.5	0.13	ML
1151	-43.60299759	172.6742479	164.0294189	0.46	0.3	0.3	0.041	VB
1152	-43.60295073	172.6742372	165.9520264	1	0.4	0.4	0.16	VB
1153	-43.60295107	172.6742366	166.6729736	0.67	0.95	0.67	0.426	VB
1154	-43.60285887	172.6742762	166.9133301	0.42	0.54	0.42	0.095	VB
1155	-43.60288753	172.6741244	174.3635254	2.9	1.1	1.1	3.509	VB
1156	-43.60281453	172.6741785	172.440918	0.95	0.65	0.65	0.401	VB
1157	-43.60284428	172.6741357	172.9216309	0.6	0.32	0.32	0.061	VB
1158	-43.60284445	172.674136	172.6812744	0.6	0.45	0.45	0.123	ML
1159	-43.60284118	172.6740891	173.4022217	0.4	0.35	0.25	0.035	VB
1160	-43.60287052	172.674025	174.1231689	0.5	0.4	0.4	0.08	VB
1161	-43.60287881	172.6739522	179.6507568	4.3	3.7	2.55	40.57	VB
1162	-43.60288753	172.6738888	181.0926514	3.85	3.2	2.5	30.8	VB
1163	-43.60288267	172.6738913	181.0926514	0.74	0.54	0.54	0.216	ML
1164	-43.60286482	172.673864	178.6894531	0.53	0.32	0.32	0.054	VB
1165	-43.60286213	172.6738617	178.6894531	0.6	0.3	0.3	0.054	VB
1166	-43.60281419	172.673784	183.4959717	0.83	0.53	0.53	0.233	ML
1167	-43.60290673	172.6736859	184.6976318	2.15	1.1	1.1	2.6	VB
1168	-43.602997	172.6736275	187.3411865	1.13	0.6	0.6	0.407	VB
1169	-43.60298552	172.6736949	185.8991699	0.6	0.38	0.38	0.087	ML
1170	-43.60298971	172.6737488	183.9765625	0.74	0.35	0.35	0.091	VB
1171	-43.60305768	172.6737094	187.3411865	1.7	1.04	1.04	1.839	VB
1172	-43.60307956	172.6737396	185.6588135	0.94	0.5	0.5	0.235	VB
1173	-43.60307956	172.6737377	185.8991699	0.5	0.35	0.35	0.061	VB
1174	-43.60307026	172.6737983	184.4572754	0.6	0.4	0.4	0.096	VB
1175	-43.60304587	172.6737764	184.6976318	0.9	0.42	0.42	0.159	VB
1176	-43.60308928	172.6737601	184.9378662	0.44	0.4	0.4	0.07	VB
1177	-43.60310228	172.6737996	184.9378662	0.65	0.65	0.65	0.275	ML
1178	-43.60301871	172.6736751	189.0235596	0.9	0.95	0.9	0.77	VB
1179	-43.60299566	172.6736634	188.3026123	0.55	0.7	0.55	0.212	ML
1180	-43.60297269	172.6735789	188.5429688	1.3	1	1	1.3	ML
1181	-43.60297604	172.6735334	191.4267578	1.3	0.65	0.65	0.549	ML
1182	-43.60298594	172.6735436	192.3881836	0.95	0.6	0.3	0.171	ML

1183	-43.60304218	172.6735457	193.5897217	1.3	1	0.7	0.91	VB
1184	-43.60305475	172.6734468	196.2333984	1.1	1.5	1.9	1.485	VB
1185	-43.60299608	172.6734198	196.7139893	1.45	0.9	0.9	1.175	VB
1186	-43.60298946	172.6734305	195.993042	0.5	0.4	0.4	0.08	ML
1187	-43.60298677	172.6734301	195.0317383	0.57	0.4	0.4	0.091	ML
1188	-43.60290664	172.6734959	191.9074707	1	0.7	0.4	0.28	VB
1189	-43.60289491	172.6735113	191.6671143	2.6	1.5	1.5	5.85	VB
1190	-43.60290572	172.6735493	190.946167	1.8	0.7	0.9	1.134	VB
1191	-43.60292383	172.6735353	191.4267578	0.62	0.35	0.35	0.076	VB
1192	-43.60292944	172.6734975	189.7445068	1.4	0.6	0.6	0.504	VB
1193	-43.6029302	172.6735528	188.0622559	0.7	0.46	0.46	0.148	VB
1194	-43.6029276	172.6735714	188.7832031	0.7	0.6	0.6	0.252	VB
1195	-43.60294193	172.6735706	188.5429688	0.9	0.65	0.65	0.38	VB
1196	-43.60296289	172.6734683	190.7058105	0.77	0.43	0.43	0.142	VB
1197	-43.60290782	172.6735534	186.1395264	1.2	1.2	1.2	1.728	VB
1198	-43.60284772	172.6736359	186.6202393	0.5	0.62	0.62	0.192	ML
1199	-43.60291083	172.673566	186.1395264	0.6	0.4	0.4	0.096	ML
1200	-43.60290279	172.6735903	186.1395264	0.5	0.7	0.5	0.175	ML
1201	-43.60273247	172.6736996	187.5814209	1.6	1.2	0.65	1.248	VB
1202	-43.60275552	172.673779	185.1782227	0.7	0.7	1.4	0.686	ML
1203	-43.60267824	172.6737024	189.263916	0.6	0.42	0.42	0.106	VB
1204	-43.60266315	172.6736789	190.2252197	0.9	0.4	0.4	0.144	VB
1205	-43.60275451	172.6735951	191.1865234	0.7	0.5	0.42	0.159	ML
1206	-43.60273917	172.6735885	192.1478271	1.7	0.6	0.6	0.612	VB
1207	-43.60271855	172.6735766	192.628418	1.3	0.75	0.75	0.731	VB
1208	-43.60271922	172.6735821	192.628418	0.75	0.38	0.38	0.108	VB
1209	-43.60271419	172.6735815	192.3881836	0.7	0.7	0.7	0.343	ML
1210	-43.602551	172.6736194	195.2719727	2	1.5	1.2	3.6	VB
1211	-43.60256257	172.6736341	194.7913818	0.56	0.4	0.3	0.067	VB
1212	-43.6027722	172.6733847	197.9156494	1.4	1.6	0.7	1.568	VB
1213	-43.6027499	172.6733618	199.5979004	0.84	0.57	0.57	0.273	VB
1214	-43.60280187	172.6734953	195.7526855	1.35	2.5	0.7	2.36	VB
1215	-43.60289055	172.6734256	197.9156494	0.47	0.45	0.45	0.095	VB
1216	-43.60295635	172.673352	201.0397949	1.3	1.3	0.4	0.676	VB
1217	-43.60298811	172.6732881	203.9238281	1.3	0.7	0.65	0.592	VB
1218	-43.60298853	172.6732819	203.6834717	0.75	0.4	0.4	0.12	VB

1219	-43.60298208	172.6732844	203.9238281	0.53	0.48	0.48	0.122	ML
1220	-43.60297747	172.6732839	203.6834717	0.62	0.4	0.4	0.099	VB
1221	-43.60289742	172.6733019	201.7608643	0.7	0.5	0.4	0.14	VB
1222	-43.60288393	172.6732823	200.7995605	1.2	0.9	0.4	0.432	VB
1223	-43.60289759	172.6732504	201.7608643	0.55	0.33	0.33	0.06	VB
1224	-43.60284797	172.6732628	202.4818115	1.3	1	1	1.3	VB
1225	-43.60284856	172.6732573	201.7608643	0.8	0.42	0.42	0.141	VB
1226	-43.60265804	172.6732857	202.2414551	3.8	1.8	1	6.84	VB
1227	-43.6026686	172.6732742	203.2027588	1.1	0.75	0.75	0.619	ML
1228	-43.60266373	172.673268	203.2027588	0.45	0.48	0.45	0.097	VB
1229	-43.60266566	172.6732515	203.9238281	0.6	0.65	0.25	0.098	VB
1230	-43.60270347	172.6732292	202.722168	0.7	0.53	0.53	0.197	VB
1231	-43.60260582	172.6732683	201.0397949	0.77	0.34	0.34	0.089	VB
1232	-43.60258151	172.6732651	202.4818115	1.1	0.6	0.6	0.396	ML
1233	-43.60260062	172.6732438	203.4431152	0.53	0.64	0.53	0.178	VB
1234	-43.60260246	172.6732385	203.6834717	0.45	0.45	0.4	0.081	ML
1235	-43.60261244	172.6731926	205.8465576	0.83	0.7	0.7	0.407	VB
1236	-43.60261093	172.6731922	206.086792	0.6	0.5	0.5	0.15	VB
1237	-43.60260942	172.6731785	207.0480957	0.8	0.65	0.65	0.338	VB
1238	-43.60267639	172.6731267	207.5288086	2.2	0.9	1	1.98	VB
1239	-43.6026753	172.6731275	208.2497559	0.7	0.8	0.7	0.392	VB
1240	-43.6026753	172.6731258	208.0093994	0.7	0.7	0.75	0.368	VB
1241	-43.60267564	172.673124	209.2110596	0.85	0.4	0.45	0.153	ML
1242	-43.6026784	172.6731166	209.451416	2.35	1.6	1.6	6.016	VB
1243	-43.60270095	172.6731622	208.0093994	1.2	1.4	0.7	1.176	VB
1244	-43.6026981	172.6731101	208.7303467	0.56	0.75	0.5	0.21	ML
1245	-43.60267572	172.6731462	207.5288086	0.9	0.5	0.5	0.225	VB
1246	-43.60268855	172.6731484	207.769165	0.84	0.36	0.36	0.109	ML
1247	-43.60271612	172.6730582	212.0949707	2	1	1	2	VB
1248	-43.60290622	172.6731743	207.5288086	2.2	2.1	2.1	9.702	VB
1249	-43.60290983	172.6731773	204.8851318	0.42	0.7	0.25	0.074	ML
1250	-43.60292802	172.6731521	207.769165	0.47	0.57	0.5	0.134	VB
1251	-43.60296573	172.6731457	208.0093994	0.7	0.35	0.3	0.074	ML
1252	-43.6029892	172.6731915	209.2110596	1.1	1.2	1.1	1.452	VB
1253	-43.60297336	172.6731277	208.9707031	0.5	0.47	0.35	0.082	ML
1254	-43.60303137	172.6731776	207.2884521	1.2	0.75	0.4	0.36	VB

1255	-43.60304981	172.6731728	208.0093994	2.7	1.1	0.95	2.82	VB
1256	-43.60313203	172.6732562	204.6448975	1.1	1	0.7	0.77	VB
1257	-43.60317612	172.6731277	212.0949707	1.85	1	1	1.85	VB
1258	-43.60316489	172.6731707	211.3740234	0.4	0.5	0.5	0.1	ML
1259	-43.60313094	172.6731596	211.6143799	0.65	0.5	0.5	0.163	VB
1260	-43.60314553	172.6731518	211.3740234	0.65	0.4	0.4	0.104	ML
1261	-43.60314938	172.6729909	214.0175781	1.06	0.47	0.47	0.234	ML
1262	-43.60314913	172.6730568	214.0175781	0.7	0.4	0.4	0.112	ML
1263	-43.60318098	172.6730301	217.862793	0.75	0.35	0.35	0.092	ML
1264	-43.60319389	172.6730444	217.1418457	1	0.45	0.45	0.203	ML
1265	-43.60307621	172.6730999	212.3353271	0.9	1.2	0.9	0.972	ML
1266	-43.6030949	172.6731328	208.0093994	0.25	0.5	0.5	0.188	ML
1267	-43.60300262	172.6730308	214.0175781	0.8	0.8	0.9	0.576	VB
1268	-43.60297755	172.6730213	213.5369873	0.66	0.9	0.66	0.392	ML
1269	-43.60298342	172.6730349	216.4207764	1	0.6	0.6	0.36	VB
1270	-43.60299398	172.6730364	216.6611328	1.35	0.95	0.95	1.218	VB
1271	-43.60294478	172.6730818	218.5837402	1	0.95	0.5	0.475	ML
1272	-43.60299138	172.6729853	221.2275391	0.5	0.55	0.5	0.138	VB
1273	-43.60304897	172.6729607	221.4677734	0.9	0.8	0.8	0.576	VB
1274	-43.60298309	172.673047	223.1501465	2	1	0.95	1.9	VB
1275	-43.60302131	172.6730481	222.1887207	0.56	0.62	0.56	0.194	ML
1276	-43.60297931	172.6730695	220.9871826	0.45	0.55	0.55	0.111	VB
1277	-43.60298468	172.6730182	217.6224365	0.55	0.42	0.42	0.098	ML
1278	-43.60293522	172.6729553	221.9484863	1.4	1	0.6	0.84	VB
1279	-43.6029561	172.6729632	221.4677734	0.67	0.7	0.4	0.188	ML
1280	-43.60294688	172.6729726	219.7854004	0.64	0.7	0.3	0.134	VB
1281	-43.60289382	172.6729295	218.3433838	0.9	0.85	0.85	0.65	VB
1282	-43.6029193	172.6728937	220.9871826	1.1	1.5	0.9	1.485	VB
1283	-43.60291117	172.6728622	222.90979	1.2	2	0.75	1.8	VB
1284	-43.60293053	172.6728526	223.8710938	1.3	0.8	0.8	0.832	VB
1285	-43.60292768	172.672862	224.1113281	1	0.8	0.8	0.64	VB
1286	-43.60292617	172.6728697	221.7081299	0.8	0.42	0.42	0.141	VB
1287	-43.60293506	172.6729085	223.6307373	0.7	0.5	0.5	0.175	VB
1288	-43.60293481	172.672908	224.1113281	1.1	0.8	0.5	0.44	VB
1289	-43.60299298	172.6729305	224.8323975	4.6	3.5	1.5	24.15	VB
1290	-43.60303329	172.6727987	225.7937012	1.2	1.3	0.8	1.248	VB

1291	-43.60304201	172.6729085	226.274292	0.9	0.35	0.3	0.095	VB
1292	-43.60302525	172.6728552	226.274292	1.2	1.6	1.2	2.3	VB
1293	-43.60316464	172.6728726	227.7163086	1.3	2.2	0.9	1.404	VB
1294	-43.60312583	172.6728967	226.9953613	1	1	0.8	0.8	VB
1295	-43.60318777	172.6729576	227.7163086	1.4	0.9	0.9	1.134	VB
1296	-43.60318425	172.6729889	227.2355957	0.5	0.5	0.4	0.113	VB
1297	-43.60321627	172.6729701	229.638916	1.2	0.5	0.5	0.3	ML
1298	-43.60320806	172.6729016	229.638916	1.5	0.7	0.7	0.735	VB
1299	-43.60317939	172.6729036	229.638916	0.65	0.8	0.65	0.338	VB
1300	-43.60305835	172.6728459	231.8017578	1.1	1	0.85	0.935	VB
1301	-43.60306246	172.6728393	233.003418	1.05	0.65	0.55	0.375	VB
1302	-43.60306137	172.6728329	232.2824707	1.1	0.6	0.6	0.396	VB
1303	-43.60308627	172.6727742	233.2437744	1.4	1	1	1.4	VB
1304	-43.60308828	172.6727451	234.2050781	2	1.8	2.7	9.72	VB
1305	-43.60281402	172.6729611	219.0644531	1.36	0.85	0.85	0.982	VB
1306	-43.60276985	172.6729738	222.1887207	2.6	1.8	1	4.68	VB
1307	-43.60276113	172.6730059	220.7468262	1.7	1.2	1.2	2.45	VB
1308	-43.60271277	172.672986	220.5064697	1.2	0.5	0.5	0.3	VB
1309	-43.60270673	172.6729909	219.5450439	0.7	0.63	0.32	0.141	ML
1310	-43.60271713	172.6729935	219.7854004	2	1.15	0.75	1.725	VB
1311	-43.60273272	172.6729681	218.8240967	0.4	0.4	0.53	0.085	ML
1312	-43.60257464	172.6730147	215.9401855	1.2	1.3	2.4	3.74	VB
1313	-43.6026002	172.6729894	216.180542	0.7	1.05	0.5	0.368	ML
1314	-43.60261344	172.673002	215.2192383	0.85	0.7	0.7	0.417	VB
1315	-43.6026748	172.6730593	211.6143799	0.9	0.65	0.65	0.38	VB
1316	-43.60266759	172.6730565	212.0949707	1.4	0.4	0.4	0.224	VB
1317	-43.60268201	172.6730242	214.0175781	0.9	0.45	0.4	0.162	ML
1318	-43.60267748	172.6730325	213.0562744	0.5	0.55	0.27	0.074	ML
1319	-43.60268192	172.6729236	217.3822021	0.9	0.55	0.5	0.248	VB
1320	-43.60269726	172.6729322	218.8240967	1	0.9	0.9	0.81	VB
1321	-43.60273791	172.6728709	218.8240967	0.8	1.55	2.5	3.1	VB
1322	-43.60276658	172.6729685	219.7854004	1.2	0.5	0.5	0.3	ML
1323	-43.60276457	172.6729093	219.0644531	0.77	0.4	0.4	0.123	VB
1324	-43.60277832	172.6728429	222.6694336	1.56	0.7	0.55	0.6	VB
1325	-43.60277873	172.6727507	223.8710938	1.24	0.78	0.5	0.484	VB
1326	-43.60279173	172.672821	221.7081299	1	0.55	0.35	0.193	ML

1327	-43.60281562	172.6727845	223.6307373	0.8	0.45	0.45	0.162	ML
1328	-43.602926	172.6727728	224.3516846	2.4	1	1	2.4	VB
1329	-43.60291712	172.6727879	223.3903809	0.7	0.6	0.6	0.252	ML
1330	-43.60290488	172.6728132	225.3129883	0.75	0.7	0.7	0.368	VB
1331	-43.60281168	172.6728417	227.4759521	0.8	0.45	0.4	0.144	VB
1332	-43.60285669	172.6726676	230.1195068	1.25	1.1	1.7	2.34	VB
1333	-43.60291326	172.6727734	229.1582031	2	1.3	1.3	3.38	VB
1334	-43.6028815	172.6729495	230.3598633	0.9	0.64	0.47	0.27	ML
1335	-43.60283942	172.6728678	232.7631836	0.82	0.84	0.4	0.276	ML
1336	-43.60292726	172.6727568	235.6469727	1.9	1.6	0.65	1.976	VB
1337	-43.6029245	172.6727427	237.0891113	0.9	0.4	0.35	0.126	VB
1338	-43.60284135	172.6727671	238.2907715	0.8	0.8	0.6	0.384	ML
1339	-43.60292927	172.6727869	240.9343262	1.9	2.75	0.9	4.7	VB
1340	-43.60299155	172.672709	240.4537354	0.65	0.8	0.7	0.364	VB
1341	-43.60297613	172.6727267	240.2133789	0.76	0.44	0.44	0.147	VB
1342	-43.60292684	172.672733	241.1746826	1.4	0.5	0.5	0.35	VB
1343	-43.60296716	172.6726907	245.2601318	1.3	2.5	2	6.5	VB
1344	-43.60289826	172.6726813	239.4923096	1.2	0.9	0.5	0.54	VB
1345	-43.60287714	172.6726518	241.1746826	0.75	0.67	0.67	0.337	VB
1346	-43.60287873	172.6726148	242.1359863	2.3	1.45	1.45	4.84	VB
1347	-43.60291779	172.6726487	246.2215576	1.6	3.2	4	20.48	VB
1348	-43.60288368	172.6725449	244.2989502	0.7	0.6	0.45	0.189	ML
1349	-43.60293891	172.6724907	245.2601318	0.8	1	0.67	0.536	ML
1350	-43.60287228	172.6725653	247.6634521	0.95	0.55	0.55	0.287	ML
1351	-43.60291695	172.672504	245.2601318	0.6	0.6	0.9	0.324	ML
1352	-43.60292424	172.6725084	244.2989502	0.7	0.55	0.55	0.212	ML
1353	-43.6029566	172.6724879	246.2215576	0.67	0.67	0.1	0.45	ML
1354	-43.60291427	172.67249	245.0198975	0.8	0.4	0.4	0.128	VB
1355	-43.60291469	172.6724669	250.0667725	1.3	3.5	2.9	13.195	VB
1356	-43.60289432	172.672437	245.2601318	0.7	0.7	1	0.5	ML
1357	-43.60290027	172.6724565	242.6165771	0.6	0.5	0.5	0.15	VB
1358	-43.60290254	172.6724107	245.9812012	1.1	0.95	0.4	0.418	ML
1359	-43.60290312	172.6724053	243.09729	0.75	0.45	0.45	0.152	ML
1360	-43.60290044	172.6723976	244.2989502	0.64	0.82	0.64	0.336	VB
1361	-43.60291385	172.6723889	244.2989502	0.67	0.58	0.58	0.225	VB
1362	-43.60292165	172.6723829	244.779541	1.35	0.66	0.66	0.588	VB

1363	-43.60292676	172.6724112	244.0585938	0.57	0.8	0.4	0.182	ML
1364	-43.60292047	172.6724289	244.779541	0.97	0.97	0.6	0.565	VB
1365	-43.60292139	172.672419	243.5778809	1	0.5	0.5	0.25	VB
1366	-43.6030001	172.6723612	243.5778809	2.4	0.75	1.58	2.844	ML
1367	-43.60299499	172.67237	242.1359863	1.34	0.4	0.58	0.311	VB
1368	-43.60294403	172.6723818	242.1359863	1	0.5	0.5	0.25	ML
1369	-43.60291821	172.6723487	242.3763428	0.5	0.8	0.56	0.224	ML
1370	-43.60295601	172.6724232	239.9730225	0.66	0.64	0.44	0.186	ML
1371	-43.60295777	172.6724809	239.2520752	0.6	0.6	0.6	0.216	VB
1372	-43.60303522	172.6724214	241.8956299	0.9	1.25	0.75	0.844	VB
1373	-43.60302927	172.6727776	231.0808105	1.2	0.8	0.8	0.768	VB
1374	-43.60303489	172.672723	233.9647217	1	0.5	0.5	0.25	ML
1375	-43.60302868	172.6727084	235.4067383	0.5	1	0.5	0.25	VB
1376	-43.60303304	172.672708	234.4454346	1	0.4	0.2	0.08	ML
1377	-43.60303631	172.6727074	233.9647217	0.7	0.65	0.65	0.296	VB
1378	-43.60323622	172.6727186	238.050415	1.4	4.2	2.3	13.52	VB
1379	-43.60317897	172.6726833	236.6085205	1.7	3.2	1.1	5.98	VB
1380	-43.60316514	172.6726238	235.1663818	1.2	3.5	1.35	5.67	VB
1381	-43.60311644	172.6725618	238.2907715	1.45	1.2	0.3	0.522	VB
1382	-43.60315701	172.6725977	237.8100586	6.1	3.9	1.4	33.31	VB
1383	-43.60319389	172.6725772	238.5311279	0.7	1.25	1.42	1.243	VB
1384	-43.60317386	172.6725848	237.5697021	0.6	0.85	0.6	0.306	VB
1385	-43.60313949	172.6725493	235.4067383	0.8	0.4	0.42	0.134	ML
1386	-43.60307336	172.6724437	239.9730225	2.6	2.2	0.8	4.58	VB
1387	-43.60317285	172.6723885	238.050415	0.9	0.9	1.1	0.891	VB
1388	-43.60316263	172.6723688	236.3681641	0.7	0.5	0.5	0.175	ML
1389	-43.60303413	172.6724144	236.6085205	1.5	1.2	1	1.8	VB
1390	-43.60305794	172.6724936	237.0891113	1.06	0.6	0.6	0.382	ML
1391	-43.6030918	172.6725821	233.7243652	1.45	0.6	0.6	0.522	VB
1392	-43.60310638	172.672613	232.5228271	1	0.5	0.5	0.25	VB
1393	-43.60305031	172.672462	233.4841309	1.1	0.52	0.42	0.24	ML
1394	-43.60294411	172.6724908	231.321167	0.55	0.5	0.6	0.165	VB
1395	-43.60322306	172.6724878	245.2601318	2.8	2.4	1	6.72	VB
1396	-43.60319925	172.672489	245.0198975	0.9	1	0.5	0.45	VB
1397	-43.60314293	172.6724837	245.0198975	1.9	1.15	1.15	2.5	VB
1398	-43.60310965	172.6724279	245.5004883	0.55	0.55	0.35	0.106	VB

1399	-43.60314871	172.6724917	244.779541	0.68	1	0.68	0.462	VB
1400	-43.60315433	172.6725002	244.779541	1.3	0.5	0.5	0.325	ML
1401	-43.60312239	172.6723448	250.5473633	1.35	1.55	3.6	7.53	VB
1402	-43.60312407	172.6723592	250.0667725	0.56	0.56	1	0.314	VB
1403	-43.60306313	172.6723724	250.3070068	1.2	1.15	0.3	0.414	ML
1404	-43.60307629	172.672366	250.7877197	1.6	0.54	0.25	0.135	ML
1405	-43.60311694	172.6723121	254.1523438	2.2	1.6	2.6	9.152	VB
1406	-43.60306766	172.6722533	251.2683105	1.65	1.23	2.2	4.46	VB
1407	-43.60311745	172.6723087	254.6330566	1.55	2.1	1.8	5.86	VB
1408	-43.60337242	172.6725698	245.9812012	5.4	2.4	1	12.96	VB
1409	-43.60336781	172.6726013	245.2601318	0.85	3	1.3	3.315	VB
1410	-43.6033995	172.6725911	245.9812012	1.1	3.2	1.1	3.87	VB
1411	-43.60347234	172.672519	250.0667725	1.15	0.6	0.5	0.345	ML
1412	-43.60352539	172.6725472	249.5860596	1.7	1.1	0.75	1.403	VB
1413	-43.60354149	172.6724809	251.7490234	1.5	0.8	0.8	0.96	VB
1414	-43.60354241	172.6724429	255.5943604	1.1	0.7	0.5	0.385	VB
1415	-43.60357443	172.6724842	255.5943604	1.4	3.5	0.9	4.41	VB
1416	-43.6036642	172.6725355	249.826416	0.9	0.9	0.8	0.648	ML
1417	-43.60367057	172.672505	248.6247559	0.6	1.1	0.7	0.462	ML
1418	-43.60361818	172.6725694	249.3457031	0.7	0.6	0.9	0.378	VB
1419	-43.60366043	172.6725172	250.0667725	2.8	1.2	1	3.36	VB
1420	-43.60365489	172.6725289	250.7877197	1.9	1.1	0.65	1.359	VB
1421	-43.6037269	172.6724974	252.4700928	1.35	1	0.9	1.215	ML
1422	-43.60371868	172.6724988	253.19104	1.3	1.2	1	1.56	VB
1423	-43.60371441	172.6725027	252.4700928	1.2	0.8	0.8	0.768	VB
1424	-43.60374433	172.6724122	258.7185059	0.8	0.9	2.9	2.088	VB
1425	-43.60372757	172.672405	257.0362549	1	0.8	0.8	0.64	VB
1426	-43.60373737	172.6723869	257.9975586	0.8	1.6	0.9	1.152	VB
1427	-43.60372933	172.6723958	257.9975586	0.9	0.7	0.7	0.441	VB
1428	-43.6037186	172.6723749	258.4782715	1.45	4.5	1.3	8.48	VB
1429	-43.60366588	172.6723536	259.4395752	1.2	0.8	0.8	0.768	VB
1430	-43.60366487	172.6723532	260.1605225	1.7	0.7	0.7	0.833	VB
1431	-43.60366177	172.6723545	258.9588623	0.95	1.1	0.45	0.47	VB
1432	-43.60361315	172.6723941	262.0831299	1.3	0.7	0.75	0.683	ML
1433	-43.60358306	172.6723873	260.4008789	1.65	0.8	0.8	1.056	VB
1434	-43.60362296	172.6722855	262.3234863	1.25	1.7	0.8	1.7	VB

1435	-43.60362698	172.6723034	259.6799316	0.8	0.9	0.6	0.432	VB
1436	-43.60362975	172.6723063	262.3234863	1	0.7	0.7	0.49	VB
1437	-43.60367225	172.6723245	264.0057373	1.8	2.3	3	12.42	VB
1438	-43.60370829	172.672314	264.0057373	1.1	1.05	1	1.155	VB
1439	-43.60372094	172.6722955	263.28479	1.5	1.4	0.8	1.68	VB
1440	-43.60373025	172.6723122	262.3234863	0.8	0.8	0.8	0.512	ML
1441	-43.60373469	172.6723115	262.0831299	1.4	2.4	4.6	15.456	VB
1442	-43.60375129	172.6722718	264.967041	1.6	1.5	1.5	3.6	VB
1443	-43.60373109	172.6722662	264.7266846	3.7	2.5	1.4	12.95	VB
1444	-43.60361919	172.6722479	266.1687012	2.1	1.4	1.5	4.41	VB
1445	-43.60363687	172.6722638	264.7266846	1	0.9	0.8	0.72	VB
1446	-43.60363889	172.6722608	263.28479	1.6	0.9	0.9	1.298	VB
1447	-43.60356093	172.6723018	262.3234863	1.7	1	1.3	2.21	VB
1448	-43.6035487	172.6722815	260.1605225	1.65	1.3	1	2.145	VB
1449	-43.603601	172.6721926	267.6105957	1.4	1.1	0.6	0.924	VB
1450	-43.60357812	172.6722189	269.0527344	0.8	0.8	0.45	0.288	VB
1451	-43.60353596	172.6721308	272.6575928	0.8	1.6	0.65	0.832	VB
1452	-43.60378901	172.6721748	270.0140381	1.3	1.9	2.7	6.669	VB
1453	-43.60378691	172.6721873	268.8123779	1.3	1.1	0.65	0.929	VB
1454	-43.60378733	172.6721755	265.9283447	1.2	0.8	0.8	0.768	VB
1455	-43.60376906	172.6721764	270.7349854	2.6	0.9	0.9	2.106	VB
1456	-43.60384265	172.6721678	268.331665	1.7	1.4	3.3	7.854	VB
1457	-43.60378792	172.6722424	261.8427734	1.6	1.2	1.4	2.688	VB
1458	-43.60380979	172.6722634	259.4395752	1.4	1.55	0.8	1.736	VB
1459	-43.6038393	172.6721952	265.4477539	1.4	0.8	1	1.12	VB
1460	-43.60386008	172.6722174	269.0527344	3.3	1.6	1.5	7.92	VB
1461	-43.60387886	172.67225	264.4863281	1.6	1.3	1	2.08	VB
1462	-43.60383863	172.6722803	256.3153076	1.9	0.9	0.9	1.539	VB
1463	-43.60377601	172.6723221	261.8427734	1.2	0.7	1.2	1.008	ML
1464	-43.60388347	172.6723931	257.2766113	2.8	3.6	1.6	16.128	VB
1465	-43.60391591	172.6723936	251.7490234	1.2	1	1.15	1.38	VB
1466	-43.60391582	172.6725264	255.5943604	1.05	1.05	1.5	1.654	VB
1467	-43.60388858	172.6725236	254.6330566	1.9	2	1	3.8	VB
1468	-43.60388841	172.6725439	253.4313965	1.4	1.3	0.8	1.456	VB
1469	-43.60390015	172.6725783	255.1136475	0.85	0.9	0.6	0.46	VB
1470	-43.60383469	172.6724946	254.873291	1.2	0.95	0.9	1.026	VB

1471	-43.60382119	172.6724583	254.6330566	0.9	0.9	0.7	0.568	ML
1472	-43.60382463	172.6724587	257.5169678	2.3	0.9	1	2.07	VB
1473	-43.60383544	172.6723722	259.4395752	1.5	4.4	1.5	9.9	VB
1474	-43.60382262	172.6724096	257.5169678	2.3	0.8	0.9	1.656	VB
1475	-43.60381868	172.6724056	257.5169678	1	0.7	1.8	1.26	VB
1476	-43.60385003	172.6723578	257.2766113	1	1	2.6	2.6	VB
1477	-43.60381784	172.6723451	264.2460938	0.56	1	0.56	0.314	ML
1478	-43.60384868	172.6723223	261.6025391	3.4	1.05	1.4	4.998	VB
1479	-43.6039025	172.672436	255.5943604	1.05	0.8	0.8	0.672	ML
1480	-43.60390023	172.6724377	257.7573242	0.7	0.7	0.6	0.294	ML
1481	-43.60384055	172.6724931	252.2297363	1.35	1.25	0.7	1.18	VB
1482	-43.60376042	172.6725039	253.19104	1.6	0.8	0.8	1.024	VB
1483	-43.60376	172.6725041	251.0279541	1.2	0.8	0.8	0.768	VB
1484	-43.60374701	172.672561	248.6247559	0.8	0.7	0.5	0.28	VB
1485	-43.60374869	172.672561	250.7877197	1	0.5	0.7	0.35	VB
1486	-43.6038227	172.6725511	250.7877197	1.4	1.2	0.5	0.84	ML
1487	-43.60384349	172.6725338	255.1136475	1.2	0.8	0.6	0.576	VB
1488	-43.60385405	172.6725433	249.5860596	1.4	1.9	3.4	9.044	VB
1489	-43.60385908	172.6724754	251.7490234	1.3	0.7	0.5	0.455	ML
1490	-43.60382237	172.6725115	250.0667725	1.5	0.55	0.65	0.536	VB
1491	-43.60375321	172.6726118	249.1053467	1.35	1.15	1	1.55	ML
1492	-43.60378297	172.6725308	248.144165	1.7	1.15	0.35	0.684	ML
1493	-43.60378607	172.6725238	246.9425049	1.2	0.8	0.7	0.672	VB
1494	-43.60375523	172.6725256	246.2215576	1.7	0.7	0.7	0.833	VB
1495	-43.60375129	172.6725295	243.8182373	1	0.75	0.75	0.563	VB
1496	-43.60370192	172.6725907	244.5391846	1.5	0.75	0.75	0.844	VB
1497	-43.60367266	172.6726108	244.779541	1.1	0.75	2	1.65	VB
1498	-43.60359102	172.6726539	246.2215576	4.2	2.1	1	8.82	VB
1499	-43.60358231	172.6727262	242.6165771	1.25	3.7	2.6	12.025	VB
1500	-43.60354023	172.6726628	244.2989502	1.2	1.9	4.3	9.804	VB
1501	-43.60351056	172.672643	244.5391846	1.7	1.4	1	2.38	VB
1502	-43.60350301	172.6727751	238.7713623	2.9	2.8	1	8.12	VB
1503	-43.60368608	172.6726712	243.5778809	1.1	0.7	0.7	0.53	ML
1504	-43.60372966	172.672655	245.2601318	1.7	0.7	0.7	0.832	VB
1505	-43.60383142	172.672741	242.1359863	1.55	1.3	0.4	0.806	ML
1506	-43.60381868	172.6727705	240.2133789	1	1	1.1	1.1	VB

1507	-43.60375104	172.6728105	238.5311279	1.6	0.7	0.7	0.784	VB
1508	-43.60364676	172.6726782	251.0279541	3.2	1.4	0.8	3.58	VB
1509	-43.60362237	172.6726788	250.7877197	1.6	0.7	0.7	0.784	VB
1510	-43.60363285	172.6726971	247.6634521	2.1	1.2	0.5	1.26	VB
1511	-43.60324276	172.6728303	242.8569336	1.4	1.2	0.6	1	VB
1512	-43.60329062	172.6728164	243.8182373	1.1	1.2	0.5	0.66	VB
1513	-43.60329866	172.6727925	245.0198975	0.8	0.7	0.9	0.504	VB
1514	-43.60331878	172.6728198	244.0585938	1.2	1	0.5	0.6	VB
1515	-43.60332607	172.6725098	259.920166	2.7	1.5	1.85	7.49	VB
1516	-43.603342	172.6724906	259.6799316	1.4	1	1	1.4	VB
1517	-43.60334979	172.6724721	257.2766113	3.1	1.6	1.6	7.936	VB
1518	-43.60336865	172.6724488	257.0362549	0.9	0.4	1	0.36	ML
1519	-43.60338734	172.6723798	261.6025391	1.5	1.55	1	2.325	VB
1520	-43.60328978	172.6723532	259.1992188	1.1	1.7	1	1.87	VB
1521	-43.60334217	172.6723781	261.1218262	0.8	0.8	0.85	0.544	ML
1522	-43.60324041	172.6723885	257.0362549	1.3	3.45	1.25	5.606	VB
1523	-43.60323169	172.6724006	256.7958984	3.6	1.5	1.5	8.1	VB
1524	-43.60328877	172.6723351	258.237915	1.1	1.8	3.1	6.138	VB
1525	-43.60323823	172.6723306	262.5637207	3.8	2.5	1.35	12.825	VB
1526	-43.60322264	172.672296	260.8814697	1.2	3.4	1.2	4.896	VB
1527	-43.60328014	172.672291	256.7958984	3.9	3.1	1	12.09	VB
1528	-43.6031327	172.6722945	257.2766113	2.6	1.3	1	3.38	VB
1529	-43.60303254	172.6721577	261.3621826	1.3	5.4	1.3	9.126	VB
1530	-43.60305224	172.6721454	260.6411133	1.6	1.4	1	2.24	VB
1531	-43.60294579	172.672193	263.28479	1.6	1	1	1.6	VB
1532	-43.60284378	172.6720894	263.28479	3	3.1	0.9	8.37	VB
1533	-43.60285635	172.6721099	263.5251465	1.1	0.7	0.9	0.693	ML
1534	-43.60282416	172.6721575	264.967041	2.8	0.75	1.6	3.36	VB
1535	-43.60290295	172.6721914	264.2460938	1	1.3	1.3	1.69	VB
1536	-43.60285786	172.6721024	267.1300049	2.4	1.25	1.25	3.75	VB
1537	-43.60288988	172.67202	267.1300049	1.9	0.75	0.75	1.068	VB
1538	-43.60294973	172.6721956	259.4395752	1.8	1.45	0.8	2.088	VB
1539	-43.60286817	172.6721569	261.3621826	1.05	0.9	0.4	0.378	VB
1540	-43.60296733	172.6723198	258.9588623	4.6	4.1	1	18.86	VB
1541	-43.6028701	172.6722915	251.2683105	3.3	1.2	1.2	4.752	VB
1542	-43.60288938	172.6723491	251.508667	0.9	1	0.8	0.72	VB

1543	-43.60300161	172.6723736	248.6247559	0.75	1.5	1.45	1.63	VB
1544	-43.60312759	172.6724428	251.9893799	1.9	1.1	1	2.09	VB
1545	-43.60327746	172.6724087	251.9893799	0.9	0.7	0.7	0.441	VB

Purau Prehistoric and Modern (CES) Rockfall

ID	Latitude	Longitude	Elevation *(m - asl)*	Length *(m)*	Width *(m)*	Height *(m)*	Volume *(m^3)*	Type	Relative Age
1	-43.63090203	172.760487	84.49	2	2.2	1.5	6.60	VB	Prehistoric
2	-43.63037297	172.763151	104.62	3.8	2.2	1.1	9.20	VB	Prehistoric
4	-43.63031304	172.763369	111.38				71.59	VB	Prehistoric
5	-43.63030197	172.763462	112.63	2	1.25	1.25	3.13	VB	Prehistoric
6	-43.63034204	172.763674	119.71	2	4.6	4.1	37.72	VB	Prehistoric
7	-43.63161097	172.764854	199.71	3.7	2.4	1.4	12.43	VB	Prehistoric
8	-43.63114201	172.765386	199.47	2	1.3	1	2.60	VB	Prehistoric
9	-43.63112298	172.765321	198.22	0.75	3.4	2.9	7.40	VB	Prehistoric
10	-43.63100002	172.765392	195.34	1	1.5	0.7	1.05	VB	Prehistoric
12	-43.63069902	172.765492	192.17	1.6	1.1	1	1.76	FB	Prehistoric
13	-43.63094503	172.765354	188.25	1.75	1	0.85	1.49	VB	Prehistoric
14	-43.63101301	172.765016	179.70	9.5	4.3	3	122.55	VB	Prehistoric
15	-43.63101502	172.764861	170.60	0.65	2.2	3.7	5.29	VB	Prehistoric
16	-43.63099599	172.764878	170.34	3.2	1.6	0.75	3.84	VB	Prehistoric
17	-43.63068704	172.765259	181.88	7.5	3	4.6	103.50	VB	Prehistoric
18	-43.63065703	172.765065	169.06	1.3	1	1	1.30	FB	Prehistoric
19	-43.630681	172.764969	165.26	1.4	1.7	1.9	4.52	VB	Prehistoric
20	-43.63070204	172.764975	165.20	2.75	1.5	0.8	3.30	VB	Prehistoric
21	-43.63086297	172.764861	165.27	2.3	1.9	1	4.37	VB	Prehistoric
22	-43.63086096	172.764865	165.49	1.8	0.9	0.75	1.22	VB	Prehistoric
24	-43.63095199	172.764681	164.01	3.8	2	1	7.60	VB	Prehistoric
26	-43.63083003	172.764855	164.07	1.5	0.9	0.9	1.22	VB	Prehistoric
27	-43.63085702	172.764816	163.57	1.25	0.9	0.9	1.01	VB	Prehistoric
28	-43.63086096	172.764821	163.29	1.2	1.5	0.8	1.44	VB	Prehistoric
29	-43.63089298	172.764699	161.92	2.8	1.2	1.2	4.03	VB	Prehistoric
30	-43.63093397	172.764554	161.40	1.7	1.2	0.7	1.43	VB	Prehistoric
31	-43.63078804	172.764797	162.05	1.5	1.35	0.5	1.01	VB	Prehistoric
32	-43.63072501	172.764918	165.67	1.4	1.6	1.6	3.58	VB	Prehistoric
33	-43.63067396	172.76486	165.93	1.3	1.4	0.75	1.37	VB	Prehistoric

34	-43.63068804	172.764716	159.44	1.4	0.9	0.9	1.13	FB	Prehistoric
36	-43.63074403	172.764672	158.28	1.5	1.1	1	1.65	VB	Prehistoric
38	-43.63183997	172.764648	209.90	0.8	1.5	0.9	1.08	ML	CES
40	-43.63183502	172.764589	203.75	1.2	1.7	0.9	1.84	FB	Prehistoric
42	-43.63184198	172.764183	180.58	1.7	0.8	1.1	1.50	VB	Prehistoric
43	-43.63189604	172.763919	172.36	0.6	1.2	1.4	1.01	VB	Prehistoric
44	-43.63183301	172.763901	172.42	1.8	1.9	1	3.42	VB	Prehistoric
45	-43.63129204	172.763375	146.66	1.2	2.6	1.2	3.74	VB	Prehistoric
47	-43.63087697	172.760473	83.97	3.8	1.4	1	5.32	VB	Prehistoric
48	-43.63087898	172.760475	84.54	1.8	0.9	1.2	1.94	VB	Prehistoric
49	-43.63330303	172.76305	116.93	2.2	1.2	1.1	2.90	VB	Prehistoric
50	-43.633269	172.763237	120.73	2	1.9	1.3	4.94	VB	Prehistoric
51	-43.63317202	172.763027	118.09	1.6	1.3	1.3	2.70	VB	Prehistoric
52	-43.63314603	172.762977	118.04	1.5	0.9	0.9	1.22	VB	Prehistoric
53	-43.63314897	172.762842	116.62	1.8	0.9	1	1.62	VB	Prehistoric
55	-43.63322801	172.763302	121.89	3.2	2	1.35	8.64	VB	Prehistoric
56	-43.63314603	172.763333	121.72	1.4	1.6	1.9	4.26	VB	Prehistoric
57	-43.63320203	172.763432	123.64	2.6	1.4	1	3.64	VB	Prehistoric
58	-43.63325399	172.76342	124.20	2.6	1.4	1	3.64	VB	Prehistoric
59	-43.63317302	172.763521	124.66	2.8	2.5	1	7.00	VB	Prehistoric
60	-43.63314603	172.763502	125.08	3.1	1.2	1.1	4.09	VB	Prehistoric
61	-43.63330303	172.763949	136.18	4.5	1.9	2.1	17.96	VB	Prehistoric
62	-43.63329398	172.763933	137.16	2.9	2.7	1	7.83	VB	Prehistoric
63	-43.633356	172.764014	139.88	3.3	2.3	1.3	9.87	VB	Prehistoric
64	-43.63325098	172.764114	141.84	3.1	2.5	1.3	10.08	VB	Prehistoric
65	-43.63310404	172.764186	145.80	1.3	1.7	1	2.21	VB	Prehistoric
66	-43.63312701	172.764242	147.92	3.4	2	2.3	15.64	VB	Prehistoric
67	-43.63316699	172.764259	148.88	1.78	4.4	4	31.33	VB	Prehistoric
68	-43.63312298	172.764356	151.62	1.2	4.3	1.6	8.26	VB	Prehistoric
69	-43.63307102	172.764368	152.23	3.1	2.8	1.4	12.15	VB	Prehistoric
70	-43.63314796	172.764587	159.56	2.6	3	1	7.80	VB	Prehistoric
71	-43.63304696	172.764658	161.48	2.7	1.3	1.2	4.21	VB	Prehistoric
72	-43.63301301	172.764623	161.46	1.4	1.5	0.9	1.89	VB	CES
73	-43.63302399	172.764564	161.42	4	3.7	2.1	31.08	VB	Prehistoric
74	-43.63303497	172.764712	162.98	2.5	1.6	1.2	4.80	VB	Prehistoric
75	-43.63296398	172.764746	166.23	2	1.35	1	2.70	VB	Prehistoric

76	-43.63296004	172.764767	166.82	2.5	1.3	1.2	3.90	VB	Prehistoric
77	-43.63301301	172.764795	166.87	1.4	1.1	1.5	2.31	VB	Prehistoric
78	-43.63306599	172.764871	171.44	5	3	4.6	69.00	VB	Prehistoric
79	-43.63304696	172.764883	173.46	1.6	2.5	1.2	4.80	VB	Prehistoric
80	-43.632997	172.764921	173.99	2.4	2.5	1	6.00	VB	Prehistoric
81	-43.63294403	172.764917	172.70	2.5	2.3	1	5.75	VB	Prehistoric
82	-43.63297597	172.764854	171.53	1.4	1.6	1	2.24	VB	Prehistoric
83	-43.63291101	172.764778	168.65	2	1.7	1.1	3.74	VB	Prehistoric
84	-43.63284001	172.764991	180.16	11	5.6	10	616.00	VB	Prehistoric
85	-43.63279399	172.765021	182.69	3.5	2.2	2.4	18.48	VB	Prehistoric
86	-43.63274999	172.764946	183.29	2	2.2	2.1	9.24	VB	Prehistoric
87	-43.63281403	172.765071	183.24	2	1.3	1	2.60	VB	Prehistoric
88	-43.63278796	172.765089	187.22	2.3	2.7	2.1	13.04	VB	Prehistoric
89	-43.63274697	172.765113	188.18	2.1	0.8	1	1.68	VB	CES
90	-43.63269199	172.765078	189.61	2.3	2.7	2.1	13.04	VB	Prehistoric
91	-43.63265896	172.765087	195.12	2.9	1.8	1.3	6.79	VB	Prehistoric
92	-43.63264597	172.765113	193.94	1.1	1.6	1.5	2.64	VB	Prehistoric
93	-43.63247397	172.765338	206.48	1.6	4.4	2.5	17.60	VB	CES
94	-43.63246601	172.765464	209.03	3.7	2.8	1.4	14.50	VB	Prehistoric
95	-43.63254002	172.765428	205.05	3.4	1.7	1.2	6.94	VB	Prehistoric
96	-43.63254203	172.765415	204.60	2	1.1	1.5	3.30	VB	Prehistoric
97	-43.632579	172.765452	204.66	2.2	1.4	1.2	3.70	VB	Prehistoric
98	-43.632579	172.765463	204.67	1.5	1.2	0.7	1.26	VB	Prehistoric
99	-43.63256802	172.765502	204.70	2	1	1	2.00	VB	Prehistoric
100	-43.63258101	172.765505	204.82	2.3	2.2	1.7	8.60	VB	Prehistoric
101	-43.632565	172.765507	206.38	2.3	1.3	1.5	4.49	VB	Prehistoric
102	-43.63256299	172.765509	206.37	1.1	1.5	1.3	2.15	VB	Prehistoric
103	-43.63259903	172.765464	204.57	2.6	2	1.8	9.36	VB	Prehistoric
104	-43.63260498	172.76549	204.09	1.3	1.7	1.4	3.09	VB	Prehistoric
105	-43.63264002	172.765516	203.51	1.8	0.7	1.7	2.14	VB	Prehistoric
106	-43.63264304	172.765507	204.54	3	1.9	2.2	12.54	VB	Prehistoric
108	-43.63260398	172.765591	205.88	1.9	0.8	0.7	1.06	FB	Prehistoric
109	-43.63250297	172.76616	228.50	1.5	1.7	0.85	2.17	FB	Prehistoric
110	-43.63286398	172.765992	228.10	2.3	0.95	0.9	1.97	VB	Prehistoric
111	-43.63290799	172.765878	219.38	4.6	2.3	1.4	14.81	VB	Prehistoric
112	-43.63279601	172.765708	207.02	2.1	0.8	2.6	4.37	VB	Prehistoric

113	-43.63268998	172.765497	203.95	1	1.5	1.1	1.65	VB	Prehistoric
114	-43.63268704	172.765486	203.10	7.2	7.3	3.2	168.19	VB	Prehistoric
115	-43.63267497	172.765421	201.49	2.2	1.7	2.2	8.23	VB	Prehistoric
116	-43.63263097	172.765434	200.98	2.1	1.4	1.1	3.23	VB	Prehistoric
117	-43.63263499	172.765395	201.22	2.1	1.2	1.1	2.77	VB	CES
118	-43.63261999	172.765391	201.14	1.2	1.1	0.9	1.19	VB	Prehistoric
119	-43.63263901	172.765389	201.25	1.7	1.2	0.9	1.84	VB	CES
120	-43.63263398	172.765318	199.35	1.7	2.2	1.1	4.11	VB	Prehistoric
121	-43.63267296	172.765329	199.32	5.6	2.7	2.6	39.31	VB	Prehistoric
122	-43.63268201	172.765374	198.73	1	1	1.3	1.30	VB	Prehistoric
123	-43.63270397	172.76543	198.04	2.1	1	0.5	1.05	VB	Prehistoric
124	-43.63275401	172.765359	192.66	3.5	2.5	2.4	21.00	VB	Prehistoric
125	-43.63281403	172.765354	192.13	1.6	1.1	1	1.76	VB	Prehistoric
126	-43.63271001	172.765297	190.25	2.7	2.5	1.8	12.15	VB	Prehistoric
127	-43.63274203	172.76522	188.83	4.6	1.6	1.1	8.10	VB	Prehistoric
128	-43.63275896	172.765224	186.04	1.5	1.6	0.9	2.16	VB	Prehistoric
129	-43.63280296	172.765208	187.34	1.5	2	1	3.00	VB	Prehistoric
130	-43.63284303	172.765225	185.17	3.9	5.3	1.5	31.01	VB	Prehistoric
131	-43.63282098	172.765226	183.30	1.2	1.7	1.1	2.24	ML	CES
132	-43.63282501	172.765178	184.07	1.1	1.2	1.4	1.85	VB	CES
133	-43.63286499	172.765158	182.41	3.8	3.4	1.5	19.38	VB	Prehistoric
134	-43.63291101	172.765051	176.26	2.6	1.2	1.4	4.37	VB	Prehistoric
135	-43.63294202	172.765019	175.63	3.3	1.1	1.1	3.99	VB	Prehistoric
136	-43.63296004	172.765037	175.66	1.6	1.1	1	1.76	VB	Prehistoric
137	-43.63310597	172.765166	178.05	1.1	1.2	0.9	1.19	VB	Prehistoric
138	-43.63311804	172.765157	179.11	1.3	1.4	0.7	1.27	VB	Prehistoric
139	-43.63304797	172.765025	173.73	1.2	1.1	0.9	1.19	FB	Prehistoric
140	-43.63300002	172.765026	173.71	2.4	1.3	0.85	2.65	VB	Prehistoric
141	-43.63295702	172.764988	172.11	2.6	1.6	1	4.16	VB	Prehistoric
142	-43.63292702	172.764941	172.04	2.6	1.9	1.4	6.92	VB	Prehistoric
143	-43.63299801	172.764868	168.04	1.8	0.9	0.9	1.46	VB	Prehistoric
144	-43.63333002	172.764013	138.14	0.9	1.2	1	1.08	VB	Prehistoric
146	-43.63328802	172.766777	248.70	1.5	1.2	1.2	2.16	VB	Prehistoric
148	-43.63335801	172.766616	238.92	1.6	1.5	1.5	3.60	VB	Prehistoric
149	-43.63346002	172.766481	230.49	3.2	4.2	5.1	68.54	VB	Prehistoric
150	-43.63359799	172.766494	227.61	1.2	1.4	0.7	1.18	VB	Prehistoric

151	-43.63347201	172.766197	214.25	1.7	1.2	1	2.04	VB	CES
152	-43.63351903	172.766183	214.23	1.95	0.7	0.75	1.02	VB	CES
153	-43.63352196	172.766183	213.65	2.1	1.2	0.85	2.14	VB	CES
154	-43.63352104	172.765973	207.73	1.4	0.8	0.9	1.01	VB	CES
155	-43.63350797	172.765908	205.02	3.7	5.7	4.5	94.91	VB	Prehistoric
156	-43.63362799	172.765848	198.22	1.6	0.95	0.9	1.37	VB	CES
159	-43.63366102	172.765783	197.24	1.05	1	1.25	1.31	VB	CES
160	-43.63366001	172.765778	198.54	3.4	1.3	1.1	4.86	VB	CES
161	-43.63364702	172.765738	197.23	1.9	1.1	1.5	3.14	VB	CES
162	-43.63363202	172.765733	198.09	1	1.2	0.9	1.08	VB	CES
163	-43.63363998	172.765763	198.40	1.3	1.1	0.7	1.00	VB	CES
164	-43.63353797	172.765718	198.36	1.5	0.75	1.1	1.24	FB	Prehistoric
165	-43.63379002	172.765585	194.57	2.5	1	1.15	2.88	VB	CES
166	-43.63376898	172.76554	193.05	0.75	1.3	1.2	1.17	VB	CES
167	-43.63367803	172.765505	200.73	1.2	1.35	1	1.62	VB	CES
168	-43.63369597	172.765517	199.46	1.8	1	0.8	1.44	VB	CES
169	-43.63368901	172.765485	198.88	1.5	1.1	0.85	1.40	VB	CES
170	-43.63362296	172.765599	203.10	1.9	2.1	1.5	5.99	VB	Prehistoric
172	-43.63375003	172.765365	192.26	2.3	1.6	1.2	4.42	VB	CES
173	-43.63379697	172.76541	193.93	1.5	1.4	0.7	1.47	VB	CES
174	-43.63374601	172.765364	192.69	1.3	1.6	0.8	1.66	VB	CES
175	-43.63373403	172.765379	192.06	0.9	1.5	0.9	1.22	VB	CES
176	-43.63369203	172.765275	187.89	1.2	2	1.25	3.00	VB	CES
177	-43.63369899	172.765242	187.72	2.5	1.5	1.3	4.88	VB	CES
178	-43.63365398	172.765206	186.98	1.7	1.1	0.85	1.59	VB	CES
179	-43.63347301	172.765063	188.88	2.1	2.3	1.5	7.25	VB	Prehistoric
180	-43.63369698	172.765085	181.34	1.5	0.8	1	1.20	VB	CES
181	-43.63376998	172.764785	170.14	1.3	1.2	1	1.56	VB	CES
182	-43.63371802	172.764765	169.07	1	1.2	1	1.20	VB	CES
183	-43.63374299	172.764772	168.64	1.6	1.3	1.3	2.70	VB	CES
184	-43.633744	172.764697	167.73	2.3	1.9	1.1	4.81	VB	Prehistoric
185	-43.63403896	172.764677	161.21	2.1	1.3	0.9	2.46	VB	Prehistoric
186	-43.63389001	172.76443	156.57	2.5	1.6	2.4	9.60	VB	CES
187	-43.63395103	172.764419	152.93	4.1	1.6	2.9	19.02	VB	CES
188	-43.63397299	172.764391	151.97	0.8	1.5	1.3	1.56	VB	CES
189	-43.633989	172.764414	152.31	1.1	4.2	2.5	11.55	VB	CES

190	-43.63394802	172.764271	147.86	2	2.2	3.9	17.16	VB	CES
191	-43.63396998	172.764262	151.94	4.2	2.8	6.8	79.97	VB	CES
192	-43.633975	172.764182	145.21	1.9	2.7	1.5	7.70	VB	CES
193	-43.63387702	172.764151	143.17	2.3	2.5	1	5.75	VB	CES
194	-43.63415496	172.764217	145.26	2.2	1.3	0.7	2.00	VB	Prehistoric
196	-43.63419604	172.764631	153.90	1.6	0.6	1.15	1.10	FB	Prehistoric
197	-43.63415899	172.764797	156.19	1.9	1.3	1	2.47	FB	Prehistoric
198	-43.63415798	172.764891	156.50	1.25	1.15	0.7	1.01	VB	Prehistoric
199	-43.63420601	172.764956	162.22	1.1	3.9	1.5	6.44	VB	CES
200	-43.63414801	172.765765	196.67	1.7	0.9	0.8	1.22	VB	CES
201	-43.63415304	172.765754	194.12	2.4	0.9	1	2.16	VB	CES
203	-43.63414298	172.765661	192.58	1.7	0.8	1	1.36	VB	CES
204	-43.63416997	172.765634	191.11	1.3	1.5	0.66	1.29	VB	CES
205	-43.634175	172.765572	189.67	3.1	2.1	1.3	8.46	VB	Prehistoric
206	-43.63415002	172.765541	187.08	1.8	2.2	1.5	5.94	VB	Prehistoric
208	-43.63416201	172.765371	182.01	1.2	1	1.1	1.32	VB	CES
209	-43.63410803	172.765196	177.98	4.3	5.4	2.1	48.76	VB	Prehistoric
210	-43.63412202	172.765024	173.67	1.3	1.7	1	2.21	VB	CES
211	-43.63406402	172.764893	168.39	1.5	1.1	0.95	1.57	VB	Prehistoric
212	-43.63410702	172.764899	169.27	3.7	2.3	1.1	9.36	VB	Prehistoric
214	-43.634133	172.76618	191.53	1.7	3	0.53	2.70	VB	Prehistoric
215	-43.63409696	172.766144	191.59	2.4	2	1.3	6.24	VB	Prehistoric
216	-43.63410501	172.766072	189.11	2.6	1.8	0.85	3.98	VB	Prehistoric
217	-43.63420601	172.766304	194.77	1.7	0.95	0.95	1.53	FB	Prehistoric
218	-43.63411498	172.766579	200.57	1	1.05	1	1.05	VB	Prehistoric
219	-43.63415597	172.766588	202.06	2	1.5	1.1	3.30	VB	Prehistoric
220	-43.63419796	172.766606	204.18	1.1	1.4	1.3	2.00	VB	Prehistoric
221	-43.63422101	172.766579	202.90	4.3	2.6	1.5	16.77	VB	Prehistoric
222	-43.63435898	172.766472	204.77	1.8	1.05	1	1.89	VB	Prehistoric
223	-43.63414801	172.766656	206.40	1.8	1	1	1.80	VB	Prehistoric
224	-43.63425697	172.766627	207.01	2.3	0.75	0.75	1.29	VB	Prehistoric
225	-43.634003	172.76687	218.66	0.9	2.9	2	5.22	VB	Prehistoric
226	-43.63404701	172.766912	221.11	1.2	1.3	0.8	1.25	FB	Prehistoric
227	-43.63406201	172.766933	221.09	1.4	1.1	0.7	1.08	FB	Prehistoric
228	-43.63413502	172.76693	219.89	2.3	1.8	1	4.14	VB	Prehistoric
229	-43.63416603	172.766963	219.30	2.7	1.7	1	4.59	VB	Prehistoric

230	-43.63408204	172.766943	219.88	1	1	1	1.00	FB	Prehistoric
231	-43.63416804	172.766977	219.30	0.65	2.9	1	1.89	FB	Prehistoric
232	-43.63424499	172.766899	217.86	3.1	6	1	18.60	VB	Prehistoric
233	-43.63432302	172.766926	217.89	1.8	2.4	0.65	2.81	VB	Prehistoric
234	-43.63433098	172.766908	217.90	1.7	0.9	0.9	1.38	VB	Prehistoric
235	-43.63432998	172.766933	218.92	0.9	1.1	1.85	1.83	VB	Prehistoric
237	-43.634248	172.76708	225.21	1.6	2.3	1.3	4.78	VB	Prehistoric
238	-43.63415002	172.767092	224.88	1.4	1.15	1.05	1.69	VB	Prehistoric
239	-43.63405304	172.76712	226.29	0.9	2.8	4.1	10.33	VB	Prehistoric
240	-43.63402898	172.767228	231.57	1.75	2.6	0.65	2.96	VB	Prehistoric
241	-43.63405304	172.767186	232.22	4.5	1.2	1.2	6.48	VB	Prehistoric
242	-43.63406704	172.767261	232.23	1.2	1	1.2	1.44	VB	Prehistoric
243	-43.63414801	172.767343	233.96	3.6	8	1.7	48.96	VB	Prehistoric
245	-43.63433803	172.767206	230.12	2.6	1	1.9	4.94	FB	Prehistoric
246	-43.63438597	172.7672	230.08	2.3	0.85	0.7	1.37	FB	Prehistoric
247	-43.63435102	172.767198	230.02	2.3	2	1	4.60	VB	Prehistoric
248	-43.63429603	172.767268	231.32	1.2	1.2	0.75	1.08	VB	Prehistoric
249	-43.63411398	172.767436	239.12	3.8	7.1	3.1	83.64	VB	Prehistoric
250	-43.63418296	172.767427	240.22	1.4	2.5	1.2	4.20	VB	CES
251	-43.63418598	172.767431	240.23	2.4	2.5	3.1	18.60	VB	Prehistoric
252	-43.63425203	172.76749	242.26	1.8	1.6	1.15	3.31	VB	Prehistoric
253	-43.63432202	172.76755	242.69	1.5	1.2	1.1	1.98	VB	Prehistoric
254	-43.63410803	172.767583	249.27	3	6.8	3.9	79.56	VB	Prehistoric
255	-43.63410601	172.767616	249.11	3	1.8	1.4	7.56	VB	Prehistoric
256	-43.63429603	172.767716	249.34	1.4	2.5	1.4	4.90	VB	Prehistoric
257	-43.63432897	172.767713	249.34	1.3	1.3	1.6	2.70	VB	Prehistoric
259	-43.63442897	172.767566	251.88	7	9	6.3	396.90	VB	Prehistoric
260	-43.634477	172.767543	253.30	1.9	3.9	0.7	5.19	VB	Prehistoric
261	-43.63447901	172.767509	250.87	2.8	3.3	0.9	8.32	VB	Prehistoric
262	-43.63413904	172.767721	253.33	1.8	1.1	1.3	2.57	VB	Prehistoric
263	-43.63414097	172.767788	253.93	1.5	1.1	0.9	1.49	FB	Prehistoric
264	-43.63413401	172.767766	257.16	2.9	1.7	1.2	5.92	VB	Prehistoric
265	-43.63412102	172.767772	256.26	6.6	3.1	3.7	75.70	VB	Prehistoric
266	-43.63412999	172.767845	258.32	1.7	2	1.7	5.78	VB	Prehistoric
267	-43.63415698	172.767857	258.24	1.4	1	1	1.40	VB	Prehistoric
268	-43.63415102	172.767905	258.56	1.3	1.2	1.3	2.03	VB	Prehistoric

269	-43.63404902	172.767859	260.21	2.9	1.45	0.85	3.57	FB	Prehistoric
270	-43.63406704	172.76799	262.48	2.3	1.8	1.1	4.55	VB	Prehistoric
272	-43.63406301	172.768071	266.71	2.5	1.8	0.55	2.48	FB	Prehistoric
273	-43.63392203	172.768177	277.04	5.4	3.1	4.2	70.31	VB	Prehistoric
274	-43.63402798	172.768259	277.14	1.2	1.2	1	1.44	VB	Prehistoric
275	-43.63406997	172.768282	278.41	1.7	1.6	3.2	8.70	VB	Prehistoric
276	-43.63415203	172.76821	274.31	2.1	1.2	0.6	1.51	VB	Prehistoric
277	-43.63450499	172.768061	274.23	2.6	2.9	2.2	16.59	VB	Prehistoric
278	-43.63452704	172.768065	278.35	1.8	3.4	4	24.48	VB	Prehistoric
279	-43.63460197	172.768121	281.15	2.7	6.1	2	32.94	VB	Prehistoric
280	-43.63464396	172.767969	276.36	1.6	4.4	3.9	27.46	VB	Prehistoric
281	-43.63466903	172.767915	274.26	1.8	1.6	0.9	2.59	VB	Prehistoric
282	-43.63475896	172.767793	274.15	0.9	1.7	1.4	2.14	VB	Prehistoric
283	-43.63484203	172.767807	280.08	6.9	6.2	2.5	106.95	VB	Prehistoric
284	-43.63490196	172.767799	280.35	1.7	2	4.5	15.30	VB	Prehistoric
285	-43.63489601	172.767757	279.05	1.3	1.1	1.1	1.57	VB	Prehistoric
286	-43.635197	172.76793	297.45	1.1	2.6	5.8	16.59	VB	Prehistoric
287	-43.634923	172.767908	289.62	1.3	1.3	1.2	2.03	VB	Prehistoric
288	-43.63493398	172.767933	289.85	0.8	1.6	1	1.28	VB	Prehistoric
289	-43.63491604	172.767997	291.12	2.8	2	1.5	8.40	VB	Prehistoric
290	-43.63497002	172.768017	293.14	2	1.8	2	7.20	VB	Prehistoric
291	-43.63498502	172.767971	292.95	1.9	2.2	1.7	7.11	VB	Prehistoric
292	-43.63500598	172.767966	295.96	1.2	2.3	1.9	5.24	VB	Prehistoric
293	-43.63499802	172.768089	296.83	3.2	1.5	1.1	5.28	VB	Prehistoric
294	-43.63509198	172.768245	301.56	0.9	2.3	1.5	3.11	VB	Prehistoric
295	-43.635024	172.767969	291.23	0.9	1.7	0.8	1.22	VB	Prehistoric
296	-43.63495904	172.767906	289.03	1.9	1.2	1	2.28	VB	Prehistoric
297	-43.63496097	172.767901	289.00	2.9	1.2	1	3.48	VB	Prehistoric
299	-43.63505401	172.767495	273.06	0.75	3.4	2	5.10	VB	Prehistoric
300	-43.63493197	172.767306	266.08	1.3	2.3	1.5	4.49	VB	Prehistoric
301	-43.63491998	172.76719	258.09	1.9	3.1	1.3	7.66	VB	Prehistoric
302	-43.63492602	172.767076	253.80	1.9	1	0.95	1.81	VB	Prehistoric
304	-43.63482703	172.766911	244.00	0.9	1.25	1.8	2.03	VB	Prehistoric
306	-43.63447901	172.767212	240.75	1.8	1.4	0.4	1.01	VB	Prehistoric
307	-43.63441799	172.767123	235.87	0.9	0.95	1.3	1.11	FB	Prehistoric
308	-43.63458797	172.766963	233.53	1.1	1.2	0.85	1.12	VB	Prehistoric

309	-43.63462703	172.765927	207.38	1.2	1.8	0.55	1.19	FB	Prehistoric
310	-43.63400401	172.76544	184.71	4.5	1.8	2	16.20	VB	Prehistoric
311	-43.63399596	172.765436	184.52	1.2	0.95	1.15	1.31	VB	CES
312	-43.63424398	172.765553	177.40	1.6	0.95	0.8	1.22	VB	CES
313	-43.63628397	172.765997	231.50	2.6	1.6	1.6	6.66	VB	Prehistoric
314	-43.63660499	172.765979	241.11	0.85	1.5	0.85	1.08	FB	Prehistoric
315	-43.63638598	172.767118	254.11	1.8	1.4	0.65	1.64	VB	Prehistoric
316	-43.63632697	172.767025	251.73	1.6	0.9	1	1.44	VB	CES
318	-43.636276	172.766941	249.30	1.9	0.95	1	1.81	VB	Prehistoric
319	-43.63628598	172.766842	246.75	1.3	1	0.9	1.17	ML	CES
320	-43.63622697	172.76679	244.39	1.1	2.4	1.4	3.70	FB	Prehistoric
321	-43.63630199	172.766714	243.42	1.5	2.6	1.3	5.07	VB	Prehistoric
322	-43.63624902	172.766697	242.48	1.2	1.8	0.85	1.84	FB	Prehistoric
323	-43.63623904	172.766639	242.11	0.9	1.95	0.8	1.40	FB	Prehistoric
324	-43.63625103	172.766659	242.03	1.07	1.65	0.95	1.68	ML	CES
325	-43.63038202	172.76367	123.35	4.7	2.8	4.2	55.27	VB	Prehistoric
326	-43.63047497	172.763652	122.42	1.4	1.5	1.6	3.36	VB	Prehistoric
327	-43.63041999	172.763755	122.74	1.9	2	2.1	7.98	VB	Prehistoric
328	-43.63038998	172.763751	122.89	3.1	2.4	2.4	17.86	VB	Prehistoric
329	-43.630422	172.763806	126.04	4	1.8	2.7	19.44	VB	Prehistoric
330	-43.63041798	172.76389	126.24	1.9	1.4	1.2	3.19	VB	Prehistoric
331	-43.63022301	172.763763	121.67	3.5	2.9	3.1	31.47	VB	Prehistoric
332	-43.63020499	172.763859	124.05	2.1	1.3	1.3	3.55	VB	Prehistoric
333	-43.63018404	172.763895	127.72	2.6	2.1	2.1	11.47	VB	Prehistoric
334	-43.63028504	172.763949	125.98	2.5	1.7	1.8	7.65	VB	Prehistoric
335	-43.63044203	172.76405	128.55	1.8	2	1.8	6.48	VB	Prehistoric
336	-43.63051403	172.764096	131.07	3.5	2.1	2.5	18.38	VB	Prehistoric
337	-43.63054404	172.764213	135.55	3.2	1.5	2.6	12.48	VB	Prehistoric
338	-43.63051504	172.764203	136.07	2.4	1.9	1.9	8.66	VB	Prehistoric
339	-43.63054203	172.764255	137.28	2.9	1.2	1.8	6.26	VB	Prehistoric
340	-43.63061202	172.7643	140.40	1.6	1.6	2.8	7.17	VB	Prehistoric
341	-43.63061998	172.764437	143.66	1.8	1.1	1.1	2.18	VB	Prehistoric
342	-43.630609	172.764432	145.19	2.5	1.8	1.8	8.10	VB	Prehistoric
343	-43.63025	172.764412	156.13	9	4.4	1.9	75.24	VB	Prehistoric
344	-43.63068896	172.764548	152.68	2.9	2.2	1.6	10.21	VB	Prehistoric
345	-43.63204801	172.764712	212.51	1.6	4.4	2.1	14.78	VB	CES

346	-43.63202403	172.764709	209.42	1.1	1.5	1.4	2.31	VB	Prehistoric
347	-43.63212101	172.764778	211.40	1.5	1.1	1	1.65	VB	Prehistoric
348	-43.63221003	172.76487	212.39	1.4	1	1.2	1.68	VB	Prehistoric
349	-43.63225101	172.764751	207.27	2.6	1.6	0.8	3.33	VB	Prehistoric
350	-43.63217399	172.764667	206.83	1.2	1.2	1.5	2.16	VB	Prehistoric
351	-43.63214398	172.764634	206.88	1.7	0.6	1	1.02	VB	Prehistoric
352	-43.63204096	172.764561	202.23	2.5	1.5	1.7	6.38	VB	Prehistoric
353	-43.63214599	172.764572	202.82	1.4	1.1	1.7	2.62	VB	Prehistoric
354	-43.63220902	172.764495	198.76	1.4	1.3	0.8	1.46	VB	Prehistoric
355	-43.63217901	172.764483	197.32	1.6	1.4	0.9	2.02	VB	Prehistoric
357	-43.63182597	172.764526	197.79	0.75	1	1.4	1.05	FB	Prehistoric
358	-43.63182999	172.764433	191.50	1.4	0.9	0.8	1.01	FB	Prehistoric
360	-43.63212302	172.764283	187.94	1.2	2.2	0.7	1.85	VB	Prehistoric
361	-43.63217499	172.764315	189.46	1.6	1.3	0.5	1.04	VB	Prehistoric
362	-43.632234	172.764192	183.75	1.8	2.8	3.2	16.13	VB	Prehistoric
363	-43.63217901	172.764198	187.02	1.5	1.5	0.5	1.13	VB	Prehistoric
364	-43.63241597	172.764138	181.53	2.3	0.9	1.3	2.69	VB	Prehistoric
365	-43.63238898	172.764061	181.08	0.8	1.8	1.3	1.87	VB	Prehistoric
369	-43.632363	172.763758	166.83	4.6	3.4	2.1	32.84	VB	Prehistoric
370	-43.63260004	172.76369	161.75	1	1.9	1.5	2.85	VB	Prehistoric
371	-43.63218103	172.763518	160.56	1.2	5	3.4	20.40	VB	Prehistoric
372	-43.63221799	172.763434	157.64	2.2	1.4	1	3.08	VB	Prehistoric
373	-43.63209897	172.763493	156.99	1.4	1	0.8	1.12	VB	Prehistoric
374	-43.63205496	172.763377	156.62	1.8	1.7	2.5	7.65	VB	Prehistoric
375	-43.63213099	172.763274	154.45	1.5	1	0.9	1.35	VB	Prehistoric
376	-43.63211003	172.763238	150.00	1.7	0.7	1	1.19	VB	Prehistoric
377	-43.63216099	172.763161	147.68	1.6	1	0.9	1.44	VB	Prehistoric
378	-43.63135097	172.763395	148.66	1.7	1.6	1	2.72	VB	Prehistoric
379	-43.63249501	172.762969	136.96	1.2	1.8	5.4	11.66	VB	Prehistoric
380	-43.63219704	172.762658	125.28	1.1	1	1.5	1.65	VB	Prehistoric
381	-43.63222201	172.762131	104.83	2.8	3.2	5.1	45.70	VB	Prehistoric
382	-43.63189897	172.762061	101.29	2.6	1.7	1.3	5.75	VB	Prehistoric
383	-43.63290598	172.760038	52.60	1.7	1.5	1.8	4.59	VB	Prehistoric
384	-43.632953	172.76004	57.76	2.2	2.2	0.8	3.87	FB	Prehistoric
385	-43.632982	172.760312	60.26	1.2	1.3	3.4	5.30	FB	Prehistoric
386	-43.63296499	172.760542	64.42	1.7	2	1	3.40	FB	Prehistoric

388	-43.63296197	172.760749	67.53	1.5	1.1	0.9	1.49	FB	Prehistoric
390	-43.63296197	172.760938	69.95	1.2	1.2	0.8	1.15	VB	Prehistoric
391	-43.63301704	172.761201	76.79	2.5	1.2	1	3.00	FB	Prehistoric
392	-43.63298301	172.761195	75.29	1.5	1.3	1	1.95	FB	Prehistoric
393	-43.63295803	172.761176	75.47	1.1	1	1	1.10	VB	Prehistoric
394	-43.63293699	172.761276	79.08	1.7	1.1	0.8	1.50	FB	Prehistoric
395	-43.63274203	172.76154	84.17	3.1	2.8	2.3	19.96	VB	Prehistoric
396	-43.63323002	172.761309	85.40	2.5	7.2	5	90.00	VB	Prehistoric
397	-43.633126	172.76165	86.87	1.2	1.2	0.7	1.01	FB	Prehistoric
399	-43.63317898	172.761745	90.42	1.4	0.9	0.8	1.01	FB	Prehistoric
400	-43.63321996	172.761754	90.94	1.9	1.2	0.7	1.60	VB	Prehistoric
401	-43.63320303	172.761876	93.66	3.3	3.2	2.3	24.29	VB	Prehistoric
402	-43.63322097	172.761936	92.06	2.8	2.3	1.2	7.73	FB	Prehistoric
403	-43.63327101	172.761945	94.51	1.5	1.2	3.5	6.30	VB	Prehistoric
404	-43.63335399	172.761998	96.51	2	1.2	0.7	1.68	FB	Prehistoric
405	-43.63334804	172.762197	97.83	1.5	1.1	0.8	1.32	FB	Prehistoric
406	-43.63347997	172.762258	100.24	2	1	0.8	1.60	FB	Prehistoric
407	-43.63343496	172.762385	101.18	1.5	1.2	0.6	1.08	FB	Prehistoric
408	-43.633543	172.762466	100.60	1.4	1.3	1	1.82	FB	Prehistoric
410	-43.633542	172.762565	100.12	1.2	0.9	1	1.08	FB	Prehistoric
411	-43.63354996	172.762583	101.41	1.3	0.9	0.9	1.05	FB	Prehistoric
412	-43.63355398	172.762612	101.36	1.2	1	1	1.20	FB	Prehistoric
413	-43.63356496	172.762653	102.33	1.8	0.9	0.9	1.46	FB	Prehistoric
414	-43.633529	172.762677	102.32	1.3	1.3	0.7	1.18	FB	Prehistoric
415	-43.63354099	172.762703	103.20	1.4	1.1	0.8	1.23	FB	Prehistoric
416	-43.63354501	172.762698	103.22	1.2	1	0.9	1.08	FB	Prehistoric
417	-43.633601	172.762746	105.66	1.9	0.9	0.8	1.37	FB	Prehistoric
418	-43.63363897	172.762754	107.67	1.7	1.4	0.9	2.14	FB	Prehistoric
419	-43.63363202	172.76277	108.14	1.6	1.6	1.6	4.10	FB	Prehistoric
420	-43.633614	172.762788	108.10	1.7	1.3	1.1	2.43	FB	Prehistoric
422	-43.633586	172.762768	105.04	1.6	0.9	0.8	1.15	FB	Prehistoric
424	-43.63351501	172.762816	106.15	1.6	1.3	1.3	2.70	FB	Prehistoric
425	-43.63363797	172.762863	108.71	2.5	1.2	1.7	5.10	FB	Prehistoric
426	-43.63363998	172.762791	107.18	1.6	1.5	1.1	2.64	FB	Prehistoric
427	-43.63366102	172.76281	108.22	1.4	1.5	0.6	1.26	FB	Prehistoric
428	-43.63360796	172.762906	106.26	2.5	0.7	1.7	2.98	FB	Prehistoric

429	-43.63362196	172.762935	107.60	1.7	1.2	0.8	1.63	FB	Prehistoric
430	-43.63361802	172.762995	109.76	2.2	0.9	1	1.98	FB	Prehistoric
431	-43.63367602	172.762988	110.23	1.1	1	1	1.10	FB	Prehistoric
432	-43.63366798	172.762995	110.20	1.4	1.2	1.2	2.02	FB	Prehistoric
433	-43.63371198	172.762936	110.56	2.7	1.2	1	3.24	FB	Prehistoric
434	-43.63370201	172.762877	110.45	1.8	1.6	1.3	3.74	FB	Prehistoric
435	-43.63369899	172.763051	110.68	2.1	1.5	1.3	4.10	FB	Prehistoric
436	-43.63368801	172.7631	112.45	2.6	2.5	2.4	15.60	VB	Prehistoric
437	-43.63369304	172.763139	112.87	1.5	1.2	0.8	1.44	FB	Prehistoric
438	-43.633716	172.76316	114.41	1.7	1.1	1	1.87	FB	Prehistoric
439	-43.63371802	172.763168	114.49	1.1	1.1	1.1	1.33	FB	Prehistoric
440	-43.63378197	172.763181	113.53	2	1.3	0.8	2.08	VB	Prehistoric
441	-43.63384802	172.763187	116.17	1.7	1	1	1.70	FB	Prehistoric
442	-43.63375196	172.763314	116.64	1.4	1.5	1.1	2.31	VB	Prehistoric
443	-43.63378004	172.763383	118.79	1.8	0.8	0.9	1.30	FB	Prehistoric
444	-43.63380301	172.763386	118.94	1.8	1.2	1	2.16	VB	Prehistoric
445	-43.63372397	172.763413	118.54	1.6	1	1	1.60	VB	Prehistoric
446	-43.633787	172.763465	122.47	1.8	1.4	1.1	2.77	VB	Prehistoric
448	-43.63389898	172.76342	122.40	1.1	1.1	0.9	1.09	FB	Prehistoric
449	-43.63390099	172.76349	122.34	1.4	0.8	0.9	1.01	FB	Prehistoric
451	-43.63391901	172.76345	124.09	1.4	1.2	0.8	1.34	VB	Prehistoric
453	-43.63395799	172.763528	124.51	2.9	2.8	1.2	9.74	VB	CES
454	-43.63396696	172.763541	125.27	1.3	1	0.9	1.17	FB	Prehistoric
455	-43.63398104	172.763518	125.67	4.2	2.8	2.1	24.70	VB	Prehistoric
457	-43.63404198	172.763558	130.66	4	5	2.6	52.00	VB	CES
458	-43.63404902	172.763486	126.93	1.4	1	1	1.40	FB	Prehistoric
459	-43.633959	172.763571	126.94	1.4	1	0.8	1.12	FB	Prehistoric
460	-43.63393201	172.763638	128.51	1.8	1.3	1	2.34	VB	CES
461	-43.63392798	172.763644	129.41	1	1.2	1.1	1.32	FB	Prehistoric
462	-43.63392304	172.76366	129.33	1.5	1.1	1	1.65	VB	Prehistoric
463	-43.63393502	172.763704	130.71	1.2	1.1	0.8	1.06	FB	Prehistoric
464	-43.63396302	172.763697	130.59	1.2	1.3	1.3	2.03	FB	Prehistoric
465	-43.63403804	172.763809	133.66	1.1	1.1	0.9	1.09	FB	Prehistoric
466	-43.63404097	172.763815	135.69	2.2	0.8	0.8	1.41	VB	Prehistoric
467	-43.63409101	172.763818	133.23	1.3	1	1	1.30	FB	Prehistoric
469	-43.63417902	172.763728	132.14	2.3	2.2	0.9	4.55	VB	Prehistoric

471	-43.63426502	172.763865	136.75	1.5	0.9	0.8	1.08	FB	Prehistoric
472	-43.63432696	172.763845	137.29	0.8	1.2	1.1	1.06	FB	Prehistoric
473	-43.63435797	172.76388	140.08	1.2	1	1	1.20	FB	Prehistoric
474	-43.63436099	172.763905	140.55	1.5	1.3	1.3	2.54	VB	Prehistoric
475	-43.634449	172.763859	143.19	1.5	1.5	0.9	2.03	FB	Prehistoric
476	-43.63448303	172.764	144.96	2.1	1.8	1.9	7.18	FB	Prehistoric
477	-43.63445596	172.764048	145.66	1.2	1.1	0.8	1.06	FB	Prehistoric
478	-43.63451597	172.764051	146.25	1.4	1	1.5	2.10	FB	Prehistoric
479	-43.634564	172.763984	148.98	1.4	1.6	2	4.48	VB	Prehistoric
480	-43.63453701	172.76418	147.47	1.5	1.2	1.2	2.16	FB	Prehistoric
482	-43.63469803	172.764207	155.14	1.4	1.2	0.9	1.51	FB	Prehistoric
483	-43.63471496	172.764251	156.10	1.3	1	0.9	1.17	FB	Prehistoric
484	-43.63483298	172.764397	158.93	2	1.3	1.5	3.90	FB	Prehistoric
485	-43.63484404	172.764412	159.34	0.8	1.3	1.2	1.25	FB	Prehistoric
486	-43.63481504	172.764501	160.20	1.7	1.3	1.1	2.43	FB	Prehistoric
487	-43.63489299	172.764561	163.89	1.7	1.5	1.4	3.57	FB	Prehistoric
488	-43.634952	172.76453	163.32	1.2	1.1	0.8	1.06	VB	Prehistoric
489	-43.63502299	172.764585	164.17	1.5	1.1	0.9	1.49	FB	Prehistoric
491	-43.63515803	172.764636	170.62	2.1	1.7	3	10.71	VB	Prehistoric
492	-43.63520304	172.764875	171.74	3.2	3.4	2.8	30.46	VB	Prehistoric
493	-43.63520597	172.764972	170.29	1.6	2	1.6	5.12	FB	Prehistoric
494	-43.63508703	172.764907	167.99	0.9	1.6	1	1.44	FB	Prehistoric
495	-43.63506499	172.764887	167.38	0.7	0.9	1.6	1.01	FB	Prehistoric
496	-43.63494001	172.764868	169.48	1.4	1.1	1	1.54	FB	Prehistoric
497	-43.63501604	172.764945	170.97	2.1	1.2	1.2	3.02	FB	Prehistoric
498	-43.63504898	172.765042	174.50	1.1	1.4	1.1	1.69	FB	Prehistoric
499	-43.63517303	172.765099	173.55	1.2	1	1	1.20	FB	Prehistoric
500	-43.635196	172.765086	172.68	1.8	1.1	0.9	1.78	FB	Prehistoric
501	-43.63523397	172.765062	171.50	1.1	1.1	0.9	1.09	FB	Prehistoric
502	-43.63522701	172.7651	172.49	1.4	1.2	1.2	2.02	FB	Prehistoric
503	-43.63521603	172.765113	173.07	1.4	1.3	0.8	1.46	FB	Prehistoric
504	-43.63524201	172.765141	174.04	2.5	1.4	0.9	3.15	FB	Prehistoric
505	-43.63529499	172.765097	174.99	1.1	2.3	1	2.53	FB	Prehistoric
506	-43.63527001	172.765307	173.99	1.8	1.2	1	2.16	FB	Prehistoric
508	-43.63517898	172.765361	180.35	1.8	1.9	1.5	5.13	VB	Prehistoric
509	-43.635384	172.765396	177.60	2.3	1.1	1.4	3.54	FB	Prehistoric

510	-43.63542097	172.7654	178.58	1.5	2.2	1.6	5.28	VB	Prehistoric
511	-43.63540999	172.765382	178.04	1.1	1	1	1.10	FB	Prehistoric
512	-43.63543597	172.765366	180.66	3.7	2.4	2.7	23.98	VB	Prehistoric
513	-43.63543698	172.76542	181.91	2	1.3	0.7	1.82	VB	Prehistoric
514	-43.63539498	172.76544	181.17	1.3	1.2	1	1.56	VB	Prehistoric
515	-43.635398	172.765406	181.19	1.3	1.6	1.3	2.70	VB	Prehistoric
516	-43.63546497	172.765435	183.65	1.4	1.4	1.2	2.35	VB	Prehistoric
517	-43.63546296	172.765555	185.88	1	1.1	1	1.10	FB	Prehistoric
519	-43.63547998	172.765554	186.27	1.6	1.8	0.8	2.30	FB	Prehistoric
520	-43.63547998	172.765526	186.86	1.5	1.1	0.8	1.32	VB	CES
521	-43.63547201	172.765601	188.33	2	1.3	1.5	3.90	VB	Prehistoric
522	-43.63542298	172.765629	189.09	1.6	1.1	0.7	1.23	FB	Prehistoric
523	-43.63544997	172.765641	189.22	1.1	1.1	1	1.21	FB	Prehistoric
524	-43.63540404	172.765735	192.72	1	1	1	1.00	FB	Prehistoric
525	-43.63537998	172.765743	192.67	2.2	1.1	1	2.42	FB	Prehistoric
526	-43.63543698	172.765852	195.16	1.2	1	1	1.20	FB	Prehistoric
527	-43.63542298	172.765831	196.36	1.6	1.3	0.8	1.66	FB	Prehistoric
528	-43.63551401	172.765821	196.38	2	1.9	1.3	4.94	VB	Prehistoric
529	-43.63551401	172.76584	195.93	1.2	1.4	1	1.68	FB	Prehistoric
530	-43.63558399	172.766015	200.77	1.9	2.2	2.3	9.61	VB	Prehistoric
531	-43.63561199	172.765985	199.43	4.8	2.6	2.1	26.21	FB	Prehistoric
533	-43.63567502	172.765959	202.14	1.6	1.3	1	2.08	FB	Prehistoric
534	-43.63572196	172.766134	205.35	1.2	1.2	0.7	1.01	VB	CES
536	-43.63560403	172.766223	207.03	1.6	1.5	1.1	2.64	FB	Prehistoric
537	-43.63557603	172.766203	206.95	1.5	0.8	0.9	1.08	FB	Prehistoric
538	-43.63550202	172.766274	211.46	4.5	4	3.1	55.80	VB	Prehistoric
539	-43.63550303	172.766343	211.47	1.4	1.1	0.9	1.39	VB	Prehistoric
540	-43.63540102	172.766259	212.04	2	2	1.8	7.20	VB	Prehistoric
541	-43.63545902	172.766245	208.96	1.6	1.4	1.3	2.91	VB	Prehistoric
543	-43.63572397	172.76623	208.09	1.3	1.1	1	1.43	FB	Prehistoric
544	-43.635714	172.766266	209.26	1.4	1.3	1	1.82	VB	Prehistoric
545	-43.63570997	172.766274	209.82	1.6	1	1	1.60	FB	Prehistoric
546	-43.63577401	172.766344	213.31	4.2	3.6	1.8	27.22	VB	Prehistoric
547	-43.63582204	172.766314	213.63	1.4	1.3	1	1.82	FB	Prehistoric
548	-43.63582799	172.766364	214.00	2.1	1.3	1	2.73	FB	Prehistoric
549	-43.63583503	172.766439	216.00	1.7	1	0.9	1.53	FB	Prehistoric

550	-43.635714	172.766493	215.91	1.2	1.3	1	1.56	FB	Prehistoric
551	-43.63563898	172.76643	214.36	1.5	1.2	1.2	2.16	FB	Prehistoric
552	-43.63562096	172.766432	214.36	1.1	1.4	0.9	1.39	FB	Prehistoric
553	-43.63560797	172.766434	214.33	2	1.1	0.7	1.54	FB	Prehistoric
554	-43.63560998	172.766467	216.27	1.9	1	0.9	1.71	FB	Prehistoric
555	-43.63563697	172.766497	219.11	1.1	1.2	0.9	1.19	FB	Prehistoric
556	-43.63563403	172.766503	219.00	1.4	1	0.9	1.26	FB	Prehistoric
557	-43.63553999	172.766561	219.51	1.8	1.1	0.9	1.78	FB	Prehistoric
559	-43.63552297	172.7666	220.08	1.6	1.2	0.8	1.54	FB	Prehistoric
560	-43.63543597	172.766547	218.83	2.2	2.3	1	5.06	VB	Prehistoric
561	-43.63543597	172.766581	219.76	1.6	1.5	1	2.40	VB	Prehistoric
562	-43.63551501	172.766645	222.25	1.5	1.1	1	1.65	VB	Prehistoric
563	-43.63556103	172.766651	222.26	1.6	1.5	1.2	2.88	VB	Prehistoric
564	-43.63555701	172.766652	223.30	1.6	1.4	1.1	2.46	FB	Prehistoric
565	-43.63554896	172.766685	225.53	1.6	1.2	1.5	2.88	FB	Prehistoric
566	-43.63580997	172.766579	222.80	1.9	1.1	0.9	1.88	FB	Prehistoric
567	-43.63593603	172.766436	219.41	2.1	1.5	1.8	5.67	VB	Prehistoric
568	-43.63593603	172.766451	221.12	1.4	0.9	0.9	1.13	FB	Prehistoric
569	-43.63593897	172.766468	221.50	1.5	1.1	0.8	1.32	FB	Prehistoric
570	-43.635944	172.766468	221.40	1.1	1	1	1.10	VB	Prehistoric
571	-43.63595297	172.766474	222.89	1.1	1	1	1.10	FB	Prehistoric
572	-43.63599496	172.766537	224.98	2	1.4	1.3	3.64	VB	Prehistoric
573	-43.63564904	172.766603	226.45	1.5	1	1	1.50	VB	Prehistoric
574	-43.63551501	172.766709	227.74	2	1.1	1	2.20	VB	Prehistoric
575	-43.63546497	172.766745	229.37	1.3	0.9	0.9	1.05	VB	Prehistoric
577	-43.63553999	172.766782	232.08	1.7	1.8	1.7	5.20	VB	Prehistoric
578	-43.63544402	172.766973	239.42	1.1	1.4	1	1.54	VB	Prehistoric
579	-43.63553898	172.766932	237.53	2	1.3	0.9	2.34	FB	Prehistoric
580	-43.63560403	172.766969	239.89	1.5	1	0.9	1.35	FB	Prehistoric
581	-43.63559104	172.766989	240.85	1.2	1.2	1.2	1.73	FB	Prehistoric
582	-43.63552499	172.767001	239.68	1.2	1.6	1.3	2.50	VB	Prehistoric
583	-43.63553002	172.767103	244.77	2.5	2.6	4	26.00	VB	Prehistoric
584	-43.63551401	172.767144	246.91	4.5	1.5	1.5	10.13	VB	Prehistoric
585	-43.63549397	172.767129	246.55	4.6	1.8	1.7	14.08	VB	Prehistoric
586	-43.63559003	172.767202	248.44	2	1.1	1.1	2.42	FB	Prehistoric
587	-43.63553002	172.767242	247.50	1.4	1.8	1.3	3.28	VB	Prehistoric

588	-43.63541904	172.767232	255.34	1.3	1.3	1.1	1.86	FB	Prehistoric
589	-43.63541502	172.767223	255.33	1.3	1.3	1.2	2.03	FB	Prehistoric
590	-43.63562096	172.767552	266.19	1.2	1	1	1.20	VB	Prehistoric
591	-43.63563504	172.767574	267.96	1.3	1.1	1	1.43	VB	Prehistoric
592	-43.63567703	172.767666	269.74	1.2	1.1	1	1.32	VB	Prehistoric
593	-43.63566597	172.767666	270.23	1.6	1	0.8	1.28	FB	Prehistoric
594	-43.63569296	172.767701	276.31	2	0.9	0.9	1.62	FB	Prehistoric
595	-43.63571199	172.767725	277.16	1.3	1.7	1	2.21	FB	Prehistoric
596	-43.635657	172.767772	278.46	1.5	2.2	1.7	5.61	VB	Prehistoric
597	-43.63578902	172.767754	279.12	1.1	1.3	0.7	1.00	FB	Prehistoric
598	-43.63580704	172.767786	281.85	1.3	1	0.9	1.17	FB	Prehistoric
599	-43.63585004	172.767679	280.23	1	1.5	1	1.50	FB	Prehistoric
600	-43.63627198	172.767571	289.58	1.3	1.2	1.2	1.87	FB	Prehistoric
601	-43.63656099	172.767752	294.14	1.4	1	0.8	1.12	ML	CES
602	-43.63655596	172.767723	294.09	1.7	0.8	0.8	1.09	VB	CES
603	-43.63657298	172.767761	294.76	1.9	1.2	0.8	1.82	FB	Prehistoric
604	-43.63675696	172.76743	287.83	2.1	1.1	1.7	3.93	FB	Prehistoric
605	-43.63658999	172.767094	269.99	1.2	1.3	0.9	1.40	VB	Prehistoric
606	-43.63655102	172.767008	266.21	2	0.8	0.9	1.44	FB	Prehistoric
608	-43.63662997	172.766744	269.55	1.1	1.1	1.1	1.33	FB	Prehistoric
609	-43.63652101	172.766871	261.84	1.4	1.4	2.2	4.31	VB	Prehistoric
610	-43.63652796	172.766901	261.60	2.4	1.1	0.7	1.85	FB	Prehistoric
611	-43.636491	172.766911	261.38	1.9	0.9	0.8	1.37	VB	Prehistoric
612	-43.63646803	172.76693	260.06	1.3	1.1	1.1	1.57	FB	Prehistoric
613	-43.63648798	172.766944	260.99	1.4	1.5	0.7	1.47	FB	Prehistoric
614	-43.63640098	172.766846	255.00	1.2	1.1	1	1.32	FB	Prehistoric
615	-43.63632998	172.766822	250.84	1.6	1.2	0.6	1.15	FB	Prehistoric
616	-43.63629	172.766785	248.89	1	1	1.4	1.40	FB	Prehistoric
617	-43.636246	172.766784	246.37	1.4	1	0.8	1.12	FB	Prehistoric
618	-43.63623099	172.766802	246.14	1.2	1.1	0.9	1.19	FB	Prehistoric
619	-43.63622303	172.766818	246.68	1.6	1	1	1.60	FB	Prehistoric
620	-43.63622798	172.76683	246.87	1.9	1	0.6	1.14	FB	Prehistoric
621	-43.63623904	172.766829	247.07	1	1.2	1	1.20	FB	Prehistoric
622	-43.63574702	172.762601	124.47	1.6	1.1	0.7	1.23	FB	Prehistoric
623	-43.63574602	172.762665	125.61	1.7	1.7	1.3	3.76	VB	Prehistoric
624	-43.63556899	172.762262	124.93	1	1	1.7	1.70	VB	Prehistoric

625	-43.63556698	172.762285	125.26	1.3	1.4	1.2	2.18	VB	Prehistoric
626	-43.63622496	172.762689	121.04	1.3	1.6	1.2	2.50	FB	Prehistoric
627	-43.636462	172.762589	117.67	1.5	1.6	1.1	2.64	FB	Prehistoric
628	-43.63649502	172.762428	112.57	1.7	0.9	1.2	1.84	FB	Prehistoric
629	-43.636635	172.762435	111.40	1.3	0.9	0.9	1.05	FB	Prehistoric
630	-43.63670398	172.762189	111.25	1.5	1.4	1.1	2.31	FB	Prehistoric
631	-43.63673701	172.762559	113.65	3.3	1.8	2	11.88	VB	Prehistoric
632	-43.63691102	172.762664	119.52	1.1	1.1	1.1	1.33	FB	Prehistoric
633	-43.63689501	172.762735	120.39	1.9	1.1	1.1	2.30	FB	Prehistoric
634	-43.63690197	172.76273	120.76	2.2	2.5	2.3	12.65	VB	CES
635	-43.63718301	172.762871	129.10	1.8	1.4	1.3	3.28	FB	Prehistoric
636	-43.63709601	172.763202	131.90	2.2	2.3	2.2	11.13	VB	Prehistoric
637	-43.63723598	172.763278	135.56	2.5	2.4	2.5	15.00	VB	CES
638	-43.63725199	172.763393	137.12	2.4	2.6	2.8	17.47	VB	CES
639	-43.63721997	172.763363	137.11	2	2.1	2.6	10.92	VB	Prehistoric
640	-43.63728703	172.763413	138.85	1.4	1.4	1	1.96	VB	CES
641	-43.63731503	172.763549	140.44	1.7	1.6	1	2.72	FB	Prehistoric
642	-43.63736498	172.763577	140.51	2.1	1.6	1.6	5.38	FB	Prehistoric
644	-43.63738996	172.763595	141.75	1.3	1.1	1.1	1.57	VB	CES
645	-43.63741301	172.763632	142.34	1.2	1.4	1.1	1.85	VB	CES
646	-43.63743396	172.763631	142.98	1.9	1	1	1.90	VB	Prehistoric
647	-43.63739801	172.76367	143.10	1.2	1.1	1	1.32	VB	Prehistoric
648	-43.63737797	172.763666	143.64	1.5	1.4	1.1	2.31	VB	Prehistoric
649	-43.63733103	172.76371	144.75	1.1	1.4	1.8	2.77	FB	Prehistoric
650	-43.636966	172.763776	151.86	1.2	1.3	1.3	2.03	FB	Prehistoric
651	-43.63685503	172.763716	151.20	2.6	2.8	3.8	27.66	VB	Prehistoric
652	-43.63745601	172.763759	145.74	1.7	1.1	1	1.87	VB	Prehistoric
653	-43.63752399	172.763694	148.23	2.1	1.1	1.8	4.16	VB	CES
654	-43.63748501	172.763922	152.76	1.3	1.2	1	1.56	VB	Prehistoric
655	-43.63751502	172.763922	152.80	1.4	1.8	1.4	3.53	VB	Prehistoric
656	-43.637527	172.763929	153.90	1.7	1.8	1.2	3.67	VB	Prehistoric
657	-43.63743698	172.76405	159.35	3.8	2.8	2.8	29.79	VB	Prehistoric
658	-43.63743799	172.764065	160.42	1.9	0.9	0.9	1.54	VB	Prehistoric
659	-43.63743003	172.764068	158.63	1.2	1.2	0.8	1.15	FB	Prehistoric
660	-43.63745299	172.76406	157.69	1.2	1	0.9	1.08	VB	Prehistoric
661	-43.63753497	172.764001	154.21	1.2	1.1	0.9	1.19	VB	Prehistoric

662	-43.63757797	172.764014	153.79	1.4	1.4	1	1.96	VB	Prehistoric
663	-43.63759398	172.76395	152.35	1	1	1	1.00	VB	CES
664	-43.63759196	172.764007	154.71	1.9	3.4	1	6.46	VB	CES
665	-43.637598	172.763984	154.79	1.4	1	0.9	1.26	VB	Prehistoric
666	-43.637612	172.764064	155.58	0.9	2.1	1.2	2.27	VB	Prehistoric
668	-43.63762599	172.764008	156.39	1.8	1.6	1.4	4.03	VB	CES
669	-43.63760303	172.764029	158.98	4.9	3.2	3.5	54.88	VB	CES
670	-43.63759699	172.764052	159.82	1.4	1.5	1	2.10	VB	Prehistoric
671	-43.63765097	172.764035	158.00	1.8	1.6	1.2	3.46	VB	CES
672	-43.63767997	172.76406	158.06	1.8	1.2	1.3	2.81	FB	Prehistoric
673	-43.63768701	172.764072	160.53	1.6	1.6	1.7	4.35	VB	Prehistoric
674	-43.63768802	172.764105	162.73	3.4	2.4	2.5	20.40	VB	CES
675	-43.63769003	172.764111	162.81	1.5	2.2	1.8	5.94	VB	CES
676	-43.63770604	172.764141	163.94	1.7	2	1.8	6.12	VB	CES
677	-43.63768802	172.764141	163.06	1.5	1	1.3	1.95	FB	Prehistoric
678	-43.63768802	172.764161	163.16	1.2	1.1	0.8	1.06	VB	CES
679	-43.637714	172.764144	163.19	1.3	1.2	0.9	1.40	VB	CES
680	-43.63770504	172.76414	163.24	2.1	1.4	2.3	6.76	VB	Prehistoric
682	-43.63770202	172.764241	165.87	1	1.2	0.9	1.08	VB	Prehistoric
683	-43.63769598	172.764239	165.89	1	1.4	0.8	1.12	VB	Prehistoric
685	-43.63771099	172.764228	167.27	1	1.3	1.1	1.43	VB	Prehistoric
686	-43.63775399	172.764241	167.96	1.2	1.1	1.2	1.58	FB	Prehistoric
687	-43.63772297	172.7642	166.91	1.9	1	1	1.90	VB	Prehistoric
688	-43.63774904	172.764242	168.41	1.1	1	1	1.10	VB	Prehistoric
689	-43.63767201	172.764272	170.05	1.4	1.4	1	1.96	VB	Prehistoric
690	-43.63766103	172.764236	168.73	2.5	1.1	1.2	3.30	VB	Prehistoric
691	-43.637641	172.764225	168.48	1.1	1	1	1.10	VB	Prehistoric
692	-43.63764502	172.764234	168.69	1.8	1.3	1.3	3.04	VB	Prehistoric
693	-43.63761803	172.764246	170.23	1.3	0.9	1	1.17	VB	Prehistoric
694	-43.63763404	172.764241	170.66	1.5	1.1	1.1	1.82	VB	Prehistoric
695	-43.63781702	172.764239	174.96	1.4	1.1	1.1	1.69	VB	Prehistoric
696	-43.637814	172.764293	175.63	1	1	1	1.00	VB	Prehistoric
697	-43.63783797	172.764365	178.44	2.1	0.8	1.2	2.02	VB	Prehistoric
698	-43.63792296	172.764328	182.31	2.8	2.8	2.3	18.03	VB	Prehistoric
699	-43.63786597	172.76446	181.62	1.5	2	2.2	6.60	FB	Prehistoric
700	-43.63785298	172.764452	181.73	1.5	1.1	1	1.65	VB	CES

701	-43.63784996	172.764498	185.75	1.6	1.8	1.7	4.90	VB	CES
702	-43.63785801	172.76454	185.60	3.6	1.8	2	12.96	FB	Prehistoric
703	-43.637871	172.764532	187.14	1.7	0.9	1	1.53	VB	Prehistoric
704	-43.63788097	172.764527	187.35	1.4	1.2	1.3	2.18	VB	Prehistoric
705	-43.63789103	172.764522	188.63	1	1.1	1	1.10	FB	Prehistoric
706	-43.63790402	172.764593	189.89	1.6	1.5	0.8	1.92	VB	Prehistoric
707	-43.63790997	172.764572	190.15	1.7	1.2	0.9	1.84	VB	Prehistoric
708	-43.63793503	172.7646	192.50	1.2	1	1.4	1.68	FB	Prehistoric
709	-43.63790503	172.764611	192.86	1.4	1.1	0.9	1.39	VB	Prehistoric
710	-43.63794702	172.764684	194.74	1.4	1.3	0.8	1.46	FB	Prehistoric
711	-43.637943	172.764663	195.55	1.4	0.8	1	1.12	VB	CES
712	-43.63792498	172.764748	197.54	1.7	1.8	1	3.06	FB	Prehistoric
713	-43.63795498	172.764788	198.17	1.9	2.5	1.4	6.65	VB	CES
714	-43.63797502	172.76479	200.29	2.5	1.4	1.2	4.20	VB	Prehistoric
715	-43.63798801	172.764811	200.43	1	1	1.2	1.20	VB	Prehistoric
716	-43.63796404	172.764747	199.53	1.6	1.1	1	1.76	VB	CES
717	-43.63799304	172.764738	199.37	2.5	1	0.8	2.00	FB	Prehistoric
718	-43.63803998	172.764666	201.06	1.3	1.1	2	2.86	VB	Prehistoric
719	-43.63815397	172.764735	206.09	3.3	2.3	2.1	15.94	VB	Prehistoric
720	-43.63819303	172.764753	206.81	1.2	1.2	0.9	1.30	FB	Prehistoric
721	-43.63803101	172.764895	204.68	1.3	1.2	1	1.56	FB	Prehistoric
722	-43.637986	172.764965	204.48	1.2	1.4	0.8	1.34	VB	Prehistoric
723	-43.63796798	172.764964	204.40	1.5	0.9	1	1.35	VB	Prehistoric
724	-43.63793696	172.764995	205.26	1.2	0.9	1	1.08	VB	CES
725	-43.637943	172.764993	205.21	1.5	1	0.9	1.35	VB	CES
726	-43.63793897	172.765006	205.06	1.5	1.1	1	1.65	VB	CES
727	-43.63792498	172.765082	206.18	1.3	1.7	0.9	1.99	VB	CES
728	-43.63793001	172.765088	206.71	1.7	1.1	0.8	1.50	VB	Prehistoric
729	-43.63791299	172.76511	208.87	2.5	1.1	1	2.75	VB	Prehistoric
730	-43.63792296	172.765126	209.96	1	1.2	1.3	1.56	FB	Prehistoric
731	-43.63792799	172.765145	209.96	1.7	1.1	0.9	1.68	FB	Prehistoric
732	-43.637958	172.765169	209.08	1.4	1.4	1.3	2.55	VB	CES
733	-43.63794903	172.765143	208.61	1.4	0.9	0.8	1.01	VB	CES
734	-43.63795498	172.765138	208.43	2.7	1.7	1.5	6.89	FB	Prehistoric
735	-43.63797703	172.765176	209.39	1.1	1.3	0.9	1.29	VB	Prehistoric
736	-43.63797803	172.765181	209.30	1.3	1.6	0.8	1.66	VB	CES

737	-43.63796999	172.765095	206.91	1	1	1	1.00	VB	CES
738	-43.63794903	172.765097	206.22	1.2	1.5	0.8	1.44	VB	CES
739	-43.63801902	172.765101	205.83	2.1	1	1	2.10	VB	CES
740	-43.63801902	172.765105	205.84	1.6	1.3	1.1	2.29	VB	Prehistoric
741	-43.63797996	172.765017	203.94	1.6	1.3	1	2.08	VB	CES
742	-43.63803604	172.76513	207.34	2.9	2.9	1.4	11.77	VB	CES
743	-43.638044	172.765172	210.42	1.1	0.8	1.2	1.06	FB	Prehistoric
744	-43.63806001	172.765151	209.92	1.1	1	2.4	2.64	ML	CES
745	-43.63793604	172.765331	215.26	1.4	1	1	1.40	VB	Prehistoric
746	-43.63792296	172.765374	215.98	2.7	2.2	2.4	14.26	VB	CES
747	-43.637929	172.765388	217.42	1.7	1.8	1	3.06	VB	CES
748	-43.63795599	172.765466	219.51	1.2	0.9	1	1.08	VB	CES
749	-43.63797996	172.765553	222.34	1.7	1.4	0.9	2.14	ML	CES
750	-43.638001	172.765553	222.44	0.9	0.7	1.8	1.13	ML	CES
751	-43.63812698	172.765406	223.21	1.1	1.8	1.1	2.18	FB	Prehistoric
752	-43.63816403	172.765356	223.26	2.2	1.9	1.5	6.27	FB	Prehistoric
753	-43.63821097	172.765368	224.40	1.7	1.2	1.2	2.45	FB	Prehistoric
754	-43.63820803	172.765368	225.11	1	1.1	1.2	1.32	FB	Prehistoric
755	-43.63817803	172.765386	226.26	1.3	1.3	1	1.69	FB	Prehistoric
756	-43.63817702	172.76539	225.93	1.6	1.1	0.9	1.58	FB	Prehistoric
757	-43.638217	172.765375	227.48	1.1	1.3	1	1.43	VB	Prehistoric
758	-43.63817099	172.765534	232.03	1.6	0.9	1	1.44	FB	Prehistoric
759	-43.63808197	172.765555	232.05	1	1.2	1.3	1.56	FB	Prehistoric
760	-43.63816998	172.765609	237.75	4.5	2.7	2.1	25.52	FB	Prehistoric
761	-43.63816202	172.76563	238.27	1.9	0.9	0.8	1.37	FB	Prehistoric
762	-43.638144	172.765651	239.34	1.4	1.2	1	1.68	FB	Prehistoric
763	-43.63816202	172.765654	239.97	1.9	1.2	1.2	2.74	FB	Prehistoric
764	-43.63797401	172.765845	241.76	2.9	2.9	1.8	15.14	VB	CES
765	-43.63801802	172.765898	244.47	2.2	1.1	1	2.42	FB	Prehistoric
766	-43.63822899	172.765672	247.66	1.4	1.2	1	1.68	FB	Prehistoric
767	-43.63823997	172.765716	247.72	1.5	0.9	0.9	1.22	FB	Prehistoric
768	-43.63830199	172.764937	216.82	1.3	0.9	1	1.17	FB	Prehistoric
769	-43.63827098	172.764963	218.13	1.5	1.1	0.8	1.32	FB	Prehistoric
770	-43.63829596	172.764917	216.83	1.7	0.9	0.8	1.22	VB	Prehistoric
771	-43.637038	172.757953	48.13	1.2	1.5	1.1	1.98	VB	CES
772	-43.63447398	172.759477	83.66	2.4	1.1	2.1	5.54	VB	Prehistoric

773	-43.63447197	172.7597	87.31	2.9	2.2	1.5	9.57	VB	Prehistoric
774	-43.63642504	172.765626	223.29	1.4	1.55	0.6	1.30	FB	Prehistoric
775	-43.637052	172.765772	241.00	1.55	1.3	1.3	2.62	FB	Prehistoric
776	-43.63703096	172.765763	239.63	1.35	1.05	0.85	1.20	FB	Prehistoric
777	-43.63710204	172.765712	241.71	3.3	1.9	1.25	7.84	FB	Prehistoric
779	-43.63714596	172.765779	244.56	1	2.5	1.7	4.25	FB	Prehistoric
780	-43.637124	172.765768	244.24	1.5	0.9	1.5	2.03	FB	Prehistoric
781	-43.63709701	172.765775	242.88	1.15	1.7	0.6	1.17	FB	Prehistoric
782	-43.63717396	172.765733	244.65	1.2	1.6	1.1	2.11	FB	Prehistoric
783	-43.63715703	172.76571	240.56	0.8	1.4	0.95	1.06	FB	Prehistoric
784	-43.63711797	172.765664	237.20	1.4	1.8	0.75	1.89	FB	Prehistoric
785	-43.63711101	172.765631	236.90	1.25	1.2	1.8	2.70	VB	Prehistoric
786	-43.63687296	172.765765	233.45	1.35	1.3	1	1.76	FB	Prehistoric
788	-43.63703096	172.765563	229.43	0.95	1.2	1	1.14	FB	Prehistoric
789	-43.637052	172.765573	229.38	0.75	1.2	1.45	1.31	FB	Prehistoric
790	-43.63708402	172.765574	230.78	1.1	1.9	0.75	1.57	FB	Prehistoric
792	-43.63716398	172.765577	232.60	1.15	0.9	1.05	1.09	FB	Prehistoric
793	-43.63732902	172.765521	234.40	1.9	1.7	1.6	5.17	FB	Prehistoric
796	-43.63694597	172.765504	224.91	1.9	1.05	0.6	1.20	FB	Prehistoric
797	-43.63703499	172.765307	219.60	1.6	1.55	1.85	4.59	FB	Prehistoric
798	-43.63717999	172.765404	221.81	1.2	1.6	1.2	2.30	FB	Prehistoric
799	-43.63721704	172.765409	223.42	0.7	0.9	1.85	1.17	FB	Prehistoric
800	-43.63720397	172.765379	223.48	0.9	2.1	0.95	1.80	ML	CES
801	-43.63685796	172.765272	207.74	1.9	1.3	2.25	5.56	FB	Prehistoric
803	-43.63713498	172.764931	201.74	1.6	1.15	0.55	1.01	FB	Prehistoric
805	-43.63735903	172.76492	206.42	2.2	2.7	1	5.94	VB	Prehistoric
806	-43.63626796	172.764198	164.97	1.1	1.2	3.4	4.49	VB	Prehistoric
807	-43.63638002	172.76403	154.19	1.2	1.8	0.65	1.40	FB	Prehistoric
808	-43.63668798	172.763339	138.19	1.7	1.2	0.9	1.84	FB	Prehistoric
809	-43.63630199	172.763389	136.85	0.95	0.95	1.5	1.35	VB	Prehistoric
810	-43.63771099	172.764328	176.00	1.2	2.3	1.1	3.04	VB	Prehistoric
811	-43.63763203	172.764428	181.75	1.05	1.8	0.9	1.70	VB	Prehistoric
812	-43.63760596	172.764595	191.95	0.55	2.8	1.7	2.62	VB	Prehistoric
813	-43.63747797	172.764645	198.08	1.2	0.8	2.3	2.21	VB	Prehistoric
814	-43.63746498	172.764714	198.50	1.7	1.25	0.7	1.49	VB	Prehistoric
815	-43.63745299	172.764701	199.58	1.8	0.6	1.6	1.73	VB	Prehistoric

816	-43.63745098	172.764654	197.27	0.9	1.5	0.8	1.08	VB	Prehistoric
817	-43.63774099	172.764625	191.69	1	1	1.2	1.20	VB	Prehistoric
818	-43.63772398	172.764678	194.90	1.8	1.4	2	5.04	VB	CES
819	-43.63746297	172.764774	204.15	1.6	1.6	0.55	1.41	VB	Prehistoric
820	-43.637454	172.76474	205.01	0.6	1.5	2	1.80	VB	Prehistoric
821	-43.63741402	172.764778	205.98	1.3	2	0.85	2.21	VB	Prehistoric
822	-43.63751602	172.764999	215.43	1.7	3.4	2.4	13.87	VB	Prehistoric
823	-43.63753798	172.764962	211.85	1.45	1.2	3.2	5.57	VB	Prehistoric
824	-43.63761996	172.764934	212.61	1.9	1.3	0.9	2.22	VB	Prehistoric
825	-43.63756397	172.765088	219.56	1.1	2	1	2.20	VB	Prehistoric
826	-43.63754896	172.765128	220.10	2.9	1.25	0.7	2.54	VB	Prehistoric
827	-43.63756799	172.76512	220.71	1.9	1.2	0.6	1.37	VB	Prehistoric
828	-43.63753304	172.765167	223.34	1.8	1	1.3	2.34	VB	Prehistoric
829	-43.63799497	172.766108	256.46	3.1	1.6	3.2	15.87	VB	Prehistoric
830	-43.63803201	172.766167	261.42	3.3	3	2.1	20.79	VB	Prehistoric
831	-43.63836897	172.765555	243.37	0.6	0.8	2.3	1.10	FB	Prehistoric
832	-43.63879804	172.765018	246.45	1.6	1	2.3	3.68	VB	Prehistoric
834	-43.63884799	172.764626	237.37	0.9	2.25	0.7	1.42	FB	Prehistoric
835	-43.63885503	172.764579	236.55	1.85	0.85	0.8	1.26	VB	Prehistoric
836	-43.63838104	172.765048	228.49	4.1	1.7	0.9	6.27	FB	Prehistoric
837	-43.63848204	172.764839	221.78	1.6	1.8	0.85	2.45	VB	Prehistoric
838	-43.63859997	172.764331	219.34	3	1.2	1.85	6.66	VB	Prehistoric
839	-43.63898504	172.761752	178.55	3.9	3.4	5.1	67.63	VB	Prehistoric
840	-43.63896199	172.761787	175.03	0.8	1.3	1.35	1.40	VB	Prehistoric
841	-43.63898504	172.761694	172.45	1.1	1.55	2.9	4.94	VB	Prehistoric
842	-43.63888102	172.761653	167.23	1	1	1	1.00	VB	Prehistoric
843	-43.63888797	172.761543	165.53	0.8	1.3	1.35	1.40	VB	CES
844	-43.638922	172.761529	166.82	2.6	1	0.9	2.34	VB	Prehistoric
845	-43.63894003	172.761524	167.98	1.8	0.9	0.8	1.30	VB	Prehistoric
846	-43.63898604	172.761341	166.90	1.9	2.2	1	4.18	VB	CES
847	-43.63895503	172.761339	163.72	3.1	3.2	2.4	23.81	VB	CES
848	-43.63901001	172.761327	163.57	1.7	2.8	0.9	4.28	VB	CES
849	-43.63899501	172.761338	163.47	1.2	1.5	1.1	1.98	VB	CES
850	-43.63898696	172.761286	162.96	3.2	2.6	1.2	9.98	VB	Prehistoric
851	-43.638993	172.761272	161.38	1.4	2.5	0.65	2.28	VB	Prehistoric
852	-43.63892804	172.761267	160.09	1.2	1.2	1.4	2.02	VB	CES

853	-43.63890097	172.761357	159.82	1.3	1.5	1.7	3.32	VB	CES
854	-43.63891798	172.761303	159.74	1.2	1.65	2.1	4.16	VB	CES
855	-43.63891203	172.761238	155.92	3.1	1.6	2.7	13.39	VB	Prehistoric
856	-43.63894396	172.76122	157.70	2.2	3.1	2.6	17.73	VB	Prehistoric
857	-43.63885503	172.76124	156.15	1.3	2.35	1.4	4.28	VB	CES
858	-43.63886199	172.761296	157.44	1.3	1.85	1.4	3.37	VB	CES
859	-43.638835	172.761262	155.95	1	1.6	2.2	3.52	VB	CES
860	-43.63884497	172.76125	154.69	2	2.5	1.2	6.00	VB	CES
861	-43.63882301	172.761425	158.51	1.3	1.5	2	3.90	VB	CES
862	-43.63881497	172.761416	157.87	2.7	1.1	0.85	2.52	VB	Prehistoric
863	-43.63881798	172.761414	156.76	0.8	2.3	1	1.84	VB	Prehistoric
864	-43.638921	172.761626	161.40	1.2	2.2	0.9	2.38	VB	Prehistoric
866	-43.63844298	172.76206	158.36	0.6	2.6	1.4	2.18	VB	Prehistoric
867	-43.63868999	172.761421	155.25	1.6	1.8	1.3	3.74	VB	Prehistoric
868	-43.63880298	172.761243	155.03	0.9	1.95	0.65	1.14	VB	CES
869	-43.63890197	172.761222	157.22	1.3	1.2	0.85	1.33	VB	CES
870	-43.63893701	172.761198	157.38	2	1.2	1	2.40	VB	Prehistoric
871	-43.63888596	172.761165	155.52	1	1.3	0.8	1.04	VB	CES
872	-43.63887498	172.76106	153.73	0.95	1.3	1.1	1.36	VB	Prehistoric
873	-43.63877096	172.76112	153.08	1.9	2	2.2	8.36	VB	CES
874	-43.63847299	172.76103	137.06	1.5	1.6	0.85	2.04	VB	Prehistoric
875	-43.63833996	172.761059	135.34	0.9	1.4	1.6	2.02	VB	Prehistoric
876	-43.63842504	172.760922	134.13	1.5	1.05	0.85	1.34	VB	Prehistoric
877	-43.63895	172.759894	117.46	1.5	1.4	1.3	2.73	VB	CES
878	-43.63794903	172.760571	109.33	1.4	1.8	0.95	2.39	VB	CES
880	-43.63771702	172.759724	85.10	3.1	1.8	3.2	17.86	VB	CES
881	-43.63806202	172.759365	77.45	1.15	1.75	1	2.01	VB	CES
882	-43.63800896	172.759226	73.56	0.9	1.4	1.7	2.14	VB	CES
883	-43.63861699	172.758873	80.09	1.15	1.75	1	2.01	VB	CES
884	-43.638433	172.758395	61.80	1.6	0.9	0.85	1.22	VB	CES
886	-43.63755098	172.758426	49.89	1.9	2.1	1.15	4.59	VB	CES
888	-43.63773404	172.758448	50.38	1	1	1	1.00	VB	CES
889	-43.63770604	172.7577	41.56	1	1.05	1.15	1.21	VB	CES
890	-43.63753396	172.757533	39.49	1.5	1.15	1	1.73	VB	CES
891	-43.63789002	172.757359	37.54	2.3	2	1.5	6.90	VB	CES

CHAPTER 4.

ANTHROPOGENIC INFLUENCES ON THE GEOLOGIC EXPRESSION OF LIQUEFACTION

4.1 Abstract

I examine the influence of anthropogenic modifications on the surface and subsurface geologic expression of contemporary liquefaction created during the 2010-2011 Canterbury earthquake sequence (CES) in eastern Christchurch, New Zealand. Trenching and aerial photography are used to document modern liquefaction features in Technical Category 3 land (i.e. land displaying moderate to severe liquefaction damage but not located in the worst-affected 'red zone' areas) and radiocarbon dating of charcoal (in native sediments) is used to determine a minimum age for the last occurrence of liquefaction at the study site.

Recurrent liquefaction is evident at Avondale Park, where surface manifestations (e.g. sand blows and linear arrays) of liquefaction were observed following the 22 February (area=~4190m^2), 13 June (area=~2839 m^2), and 23 December 2011 (area=~946 m^2) events. Surface manifestations of liquefaction were not evident following the 4 September 2010 main shock earthquake, despite the prediction of liquefaction triggering for the estimated September levels of ground shaking. June and December surface ejecta comprise ~68% and ~23% of the February output, respectively. Comparison of sand blow aerial extent with peak ground acceleration (PGA) and M_w 7.5-normalized peak ground accelerations ($PGA_{7.5}$) displays a positive correlation (R^2=0.58 for median PGA, R^2=0.69 for median $PGA_{7.5}$).

Trench observations indicate that anthropogenic fill layer boundaries and the composition/texture of discretely placed fill layers play an important role in absorbing fluidized sand/silt (thereby suppressing the total volume breaching the ground surface) and controlling the subsurface architecture (i.e. orientation, shape, size) of preserved liquefaction features. The spatial distribution of surface liquefaction morphologies (i.e. sand blows and linear sand blow arrays) displays alignment with park boundaries and existing utility lines (e.g. sprinkler and drainage pipes). I observed evidence in the trenches that utility excavations (and perforated pipes) provided conduits for liquefaction injecta during the CES.

No evidence of pre-CES liquefaction was identified within the anthropogenic fill layers or underlying native sediment. Radiocarbon dating of charcoal within the youngest native sediment yields a 2σ calibrated age range of 1209 AD to1274 AD, implying that liquefaction at the study site has probably not occurred for at least the past 750-800 years.

4.2 Introduction

Understanding the influence that humans are having on the geologic record and the nature of geologic processes has become an important problem in the 21st Century (Waters et al., 2016; Zalasiewicz et al., 2015, 2011; Lewis and Maslin, 2015; Price et al., 2011: Steffen et al., 2007). The impact of human beings on the atmosphere and oceans is well documented (e.g. Crutzen, 2002; Zalasiewicz, 2011; 2015) and human constructs, such as plastic, aluminum, and concrete are becoming fixtures in the modern geologic record (i.e. within sediment layers) (Zalasiewicz, 2016). However, published studies evaluating anthropogenic influences on geologic hazards, such as rockfalls (Borella et al., 2016a, b) and liquefaction, are relatively sparse, but urgently required if we are to continue expanding our understanding of the Anthropocene (e.g. Crutzen, 2002; Lewis and Maslin, 2015) and the crucial role humans play in influencing and shaping earth's surface processes.

The 2010-2011 Canterbury earthquake sequence (CES) provides us with a rare opportunity to observe and document the manifestation of surface and subsurface liquefaction phenomena formed during multiple distinct earthquakes (e.g. Quigley et al., 2013; Quigley et al., 2016; Cubrinovski et al., 2011a,b; Villamor et al., 2016) in areas strongly modified by humans. Surface mapping of liquefaction ejecta distributions resulting from the CES has been performed by Quigley et al. (2013), Bastin et al. (2015, 2016), Townsend et al. (2016), and Villamor et al. (2016), but these studies do not explicitly examine the impact that anthropogenic modifications have had upon the geologic expression of liquefaction in Christchurch and the greater Canterbury region. Similarly, we recognize that the engineering field has put considerable research into quantifying the impact that anthropogenic elements have on liquefaction hazard, such as how piers or gravel piles influence liquefaction mechanics, but there has been no emphasis on how these modifications affect the expression of liquefaction in the geologic record.

In this Chapter, I examine the impact of anthropogenic features (e.g. fill, utility trenches and pipes) on the surface and subsurface geologic expression (i.e. geometry and spatial distribution) of contemporary liquefaction (during the CES) at Avondale Park in eastern Christchurch, New Zealand. The study site is underlain by relatively thick (~1.5-2.0 m) and spatially extensive anthropogenic fills and is located in an area where ground damage from liquefaction (during the CES) was not as severe as in the worst affected 'red zone' sections of Christchurch. The location provided me with an opportunity to (i) document the magnitude and distribution of CES liquefaction morphologies, (ii) search for evidence of paleoliquefaction (in native sediments), and (iii) determine a minimum age for prehistoric liquefaction - at a Technical Category 3 (TC3) land site. [From this point forward, I use TC3 to describe land in Christchurch where liquefaction damage is possible in future large earthquakes and individual engineering assessment is required to select the appropriate foundation repair or rebuild

option (MBIE, 2002; van Ballegooy et al., 2014).] We note than in Christchurch the study of contemporary and/or prehistoric liquefaction has focused primarily in areas with the greatest amount of ground damage (i.e. 'red zone' land) (Quigley et al., 2013; Bastin et al., 2015; Bastin et al., 2016) because liquefaction features are most pronounced and the preservation potential for paleoliquefaction signatures in these worst affected areas is highest. However, studies within 'red zone' areas provide us with only an understanding of liquefaction process for locations with the highest vulnerability to liquefaction, and do not offer any specific understanding of processes in areas of slightly to significantly less liquefaction-induced damage, such as TC3 land, where mitigation to existing buildings/foundations or new construction of residential and commercial structures is on-going.

I am not aware of any prior studies that document the subsurface interactions between anthropogenic modifications and liquefaction injecta to the level of detail presented within this chapter. Pradel et al. (2014) examined the impact of anthropogenic changes on liquefaction along the Tone River during the Tohoku earthquake in Tokyo, Japan, but no linkage between reported surface features and subsurface processes were made, nor were any subsurface liquefaction signatures documented. My results suggest that the spatial distribution and form of surface and subsurface liquefaction phenomena are significantly influenced by anthropogenic fills and other man-made features. The absence of pre-CES liquefaction supports the hypothesis that shaking intensities analogous to the 2011 Christchurch magnitude 6.0 and 6.2 earthquakes are rare and are unlikely to have occurred at the Avondale Park site for the last 700-800 years (Quigley, 2016). This study demonstrates the importance of systematically examining the impact of buried infrastructure on channelizing and influencing surface and subsurface liquefaction morphologies.

4.3 Geologic Setting

4.3.1 Christchurch

The city of Christchurch (population ~366,000) is located on the east coast of New Zealand's South Island, set upon the low-relief and low-elevation (0-20 m above sea level) eastern limit of the alluvial derived Canterbury Plains (Fig. 1a). The city and eastern suburbs are predominantly underlain by drained peat swamps, fluvial sands and silts, and estuarine, dune, and foreshore sands (Brown and Weeber, 1992) (Fig. 1b). Channelized gravels are present within the uppermost several meters and have been attributed to deposition by the braided Waimakariri River that intermittently avulsed through the city prior to European settlement (Cowie, 1957; Brown and Weeber, 1992). To the west of the central city, fluvial sands and gravels predominate. Sediments in eastern Christchurch were deposited during shoreline progradation and marine regression following the mid-Holocene highstand, with the shoreline at ~6500 yr BP recorded approximately 3 km west of the present central city (Fig. 1b; Brown and Weeber, 1992). Fluvial sand and silts were deposited by the Avon and Heathcote Rivers. The presence of underlying young unconsolidated fine sands and silts combined with high water tables (1-2 m depth) and artesian water pressures make eastern Christchurch highly susceptible to liquefaction, as confirmed by the CES (Quigley, 2013, 2016; Cubrinovski and Green, 2010).

4.3.2 Avondale Park study area

The study site at Avondale Park in eastern Christchurch experienced large spatial variations in the severity of land damage during the Canterbury earthquake sequence, and is currently designated as TC3 land (Fig. 2a-d). Avondale Park is located within an inner meander bend of the Avon River, with the closest western section of the river approximately 250 meters to the north (Fig. 3a,b). The park is essentially flat, lies at an average elevation of ~4 m above sea level, and encompasses a total area of ~38,000 m^2. The park and adjacent suburbs are underlain by alluvial sand and silt overbank deposits of the Avon River, along with sand, silt, and peat of drained lagoons and estuaries, and sand of fixed and semi-fixed dunes and beaches (Brown and Weeber, 1992) (Fig. 1b). A review of Selby (1856) indicates that swamp and grass swamp with flax rushes, fern, and tutu vegetation predominated in the Avondale Park area during the mid-19th century, prior to development of Christchurch. The position of the Avon River during this time (i.e. ~1856) is similar to present day, and it is probable that the area has fluctuated between overbank deposition during flooding events and slower rates of sedimentation in an estuarine setting. The modern coastline is located ~3 km to the east of the study site. The position of the ~5000 yr BP coastline was ~4.5 km to the west, and the ~3000 yr BP coastline was ~2.0-2.5 km east of the study site (Brown and Weeber, 1992) (Fig. 1b). The water table is located between 1-2 m depth, but may rise to ≤0.5 m depth during wet periods (Brown and Weeber, 1992).

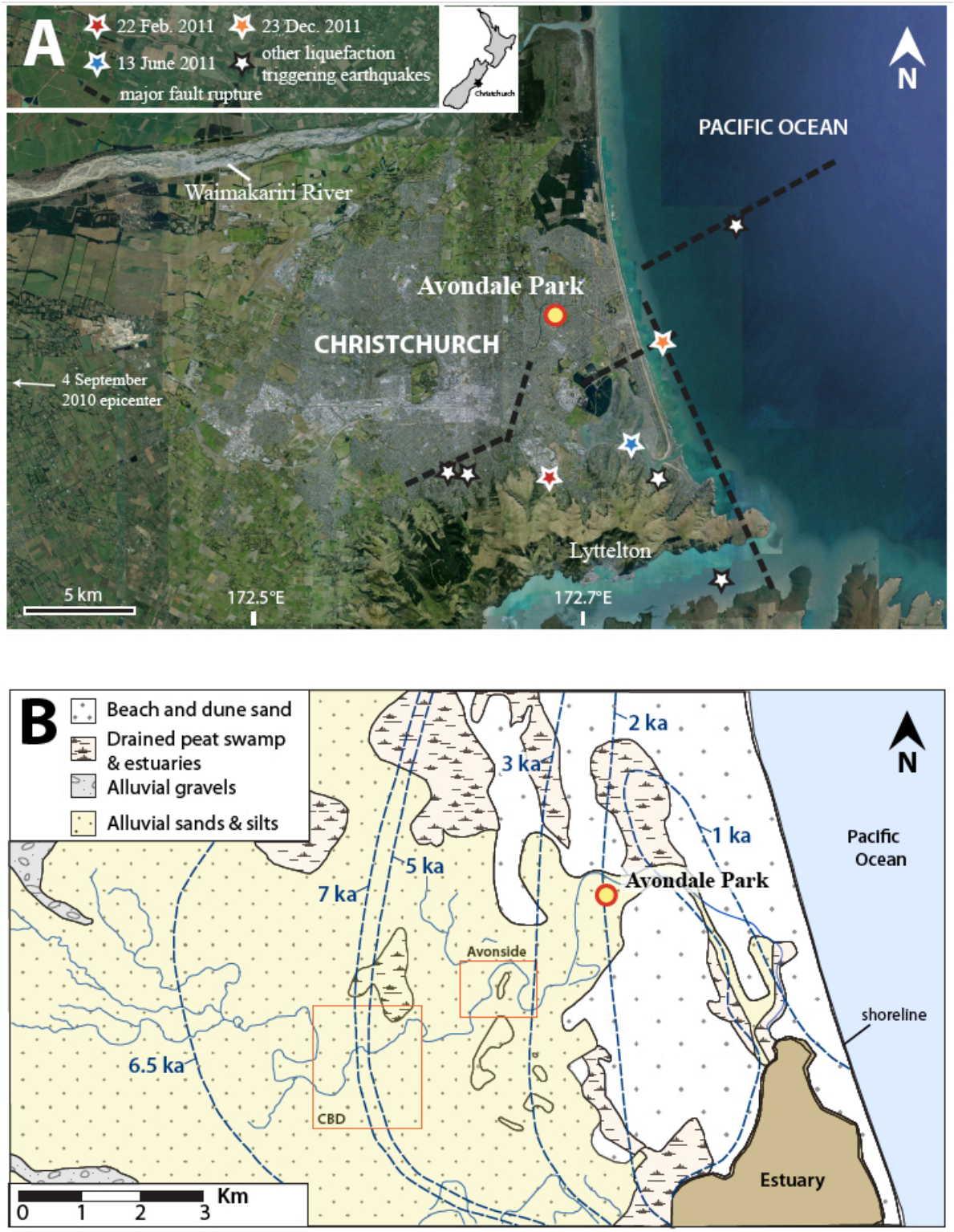

Figure 1. **(A)** Site map showing the City of Christchurch and Avondale Park study site location. Epicentral locations for the 22 February, 13 June, and 23 December 2011 earthquakes are indicated. Epicenters for other liquefaction triggering earthquakes are also displayed. The 4 September 2010 mainshock epicenter (not shown) was located approximately 40 km west of Christchurch and did not create any surface manifested liquefaction at the study site. The subsurface faults (dashed lines) that ruptured during the February, June, and December 2011 aftershocks are displayed (modified from Quigley et al., 2013). **(B)** Simplified geological map of the Christchurch area (modified from Brown and Weeber, 1992). Approximate locations of the 7-1 ka shorelines indicated with respect to the Avondale Park study site, Avonside (research area for Bastin et al., 2015), and Central Business District (CBD).

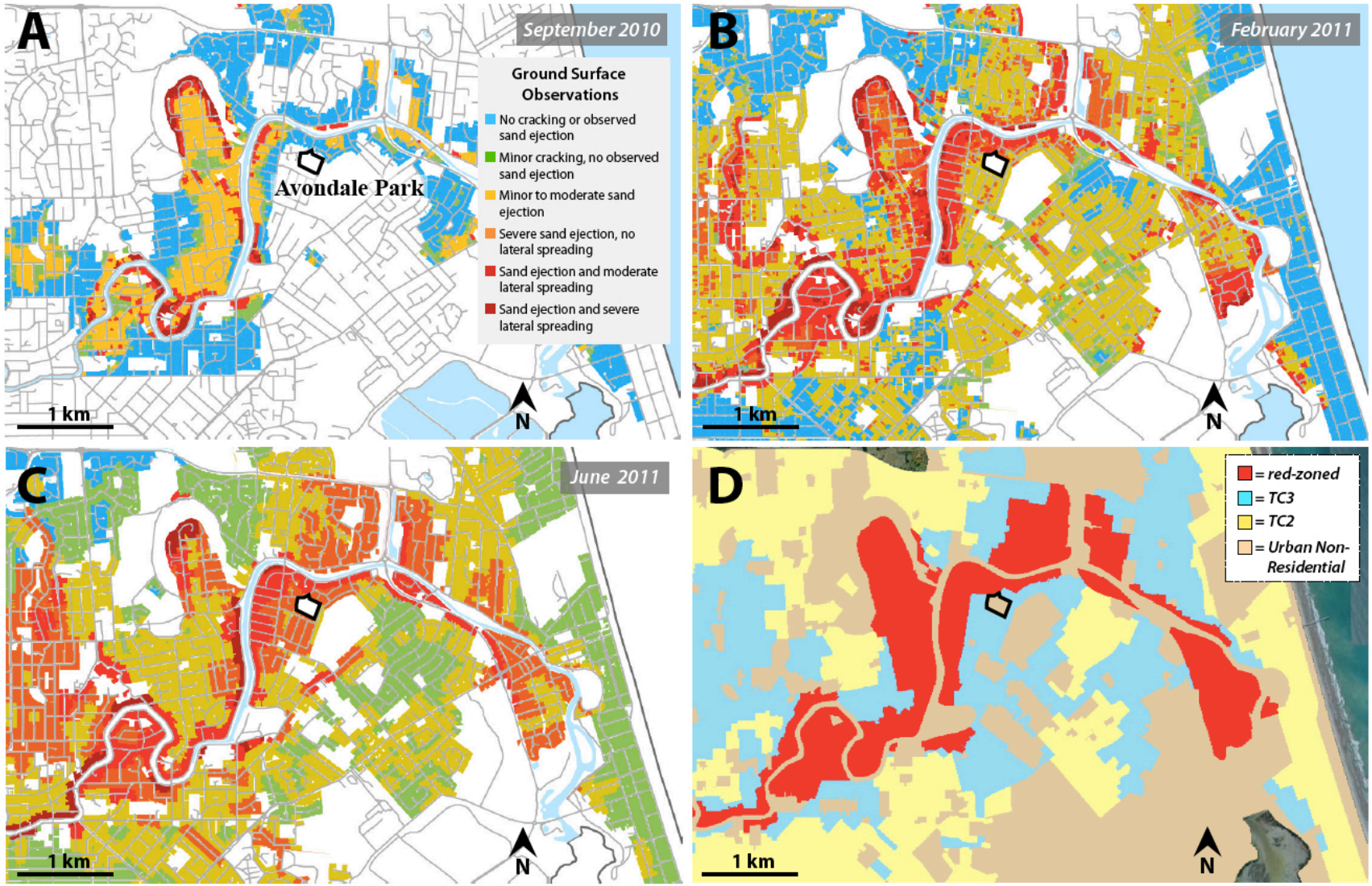

Figure 2. Liquefaction ground surface observations and residential technical categories maps for CES. **(A)** No cracking or observed sand ejection was observed near Avondale Park (including surrounding residential properties) during the 4 September 2010 mainshock earthquake. **(B)** During the 22 February 2011 earthquake moderate to severe sand ejection (with no lateral spreading) was observed at Avondale Park and surrounding residential properties. Moderate to severe lateral spreading occurred primarily at locations with a distance of less ~500 meters from the Avon River. **(C)** Severe sand ejection with no lateral spreading was observed near the Avondale Park area following the 13 June 2011 earthquake. Damage appears greater during the June event because observations are cumulative and include the effects of the previous CES earthquakes. **(D)** MBIE (Ministry of Business, Innovation and Employment) Residential Foundation Technical Categories Map, published 28 October 2011 and updated 5 December 2013. The Avondale Park study site lies within the area designated as Technical Category 3 (TC3) land, and is defined as having 'moderate to significant land damage from liquefaction possible in future large earthquakes. Foundation solutions should be based on site-specific geotechnical investigation and specific engineering foundation design.'

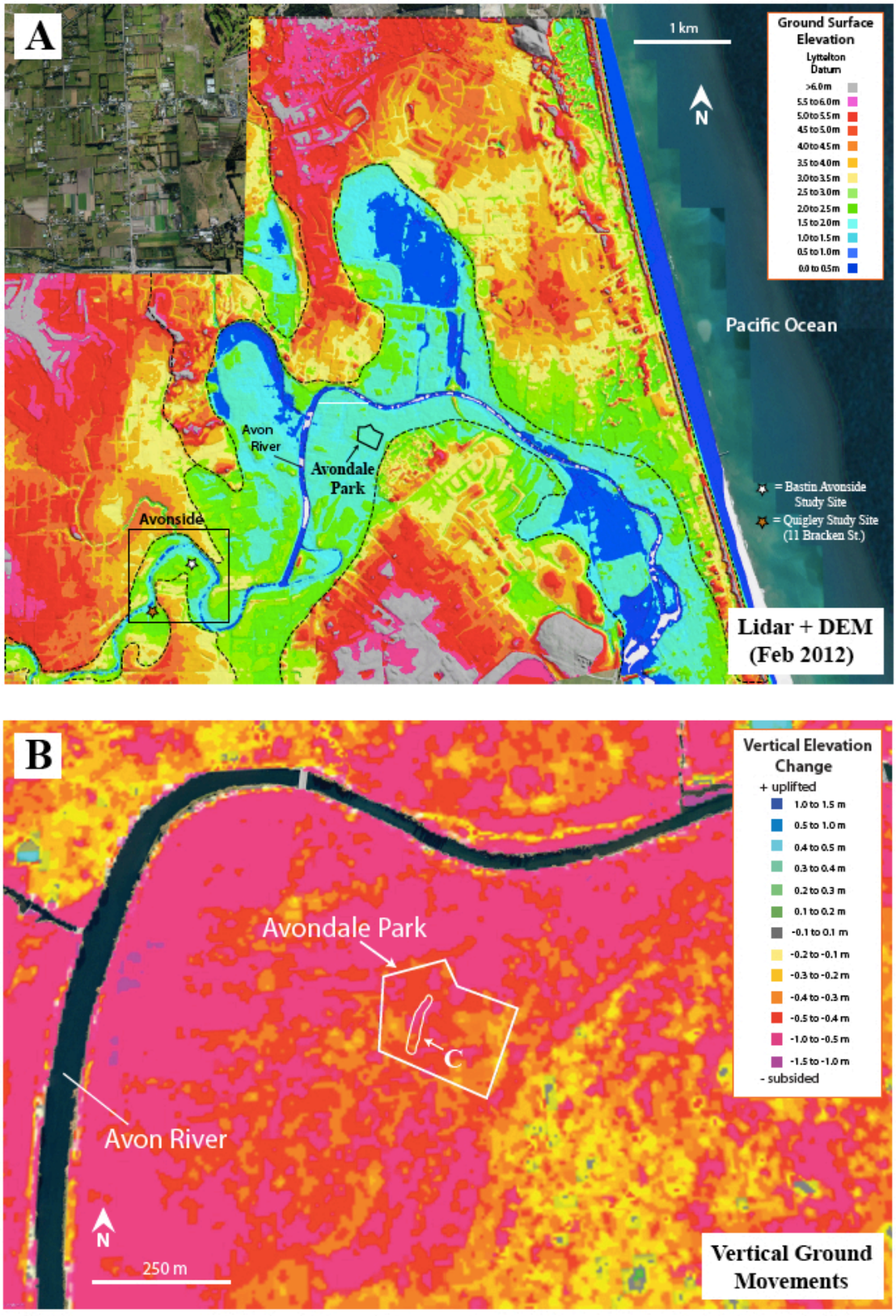

Figure 3. (A) Light detection and ranging (LiDAR) digital elevation model (DEM) for eastern Christchurch. The DEM depicts ground surface elevation for post-December 2011. The Avondale Park study site is positioned within the distal inner meander/flood plain of the Avon River. Historical aerial photographs indicate the low elevation site was occupied by swamp and marsh prior to placement of anthropogenic fill in the area. **(B)** Vertical ground movements in the area of Avondale Park from 2003 to 2012, covering the period of the 2010-2011 CES. Areas of subsidence caused by earthquake induced liquefaction are shown in yellow-pink. The outline for feature C (i.e. ~100 m long sand blow array) is shown.

A review of historical aerial photography (1940-2011) indicates there have been strong anthropogenic modifications to Avondale Park and the surrounding landscape (Fig. 4a-f). Significant modifications to the Avon River (i.e. widening and course change) and nearby landscape are evident between 1949 and 1955 (Figs 4a and 4b). Dredged material from the river was likely used to fill nearby low-lying wetland areas, including Avondale Park.

4.3.3 Liquefaction observed during the CES

Analysis of aerial photographs post-dating the 4 September 2010 Canterbury earthquake sequence mainshock indicates that sand blow development occurred at the surface during the 22 February, 13 June, and 24 December 2011 earthquakes (Figs. 5 and 6). No surface manifestation of liquefaction was evident following the 4 September earthquake. No lateral-spreading fissures were observed at Avondale Park during any of the shaking events.

Bastin et al. (2013, 2015, 2016) document paleoliquefaction features in eastern Christchurch, providing evidence that liquefaction occurred post AD 1660 and pre-AD 1905 and post-AD 1415 and pre-AD 1910, with shaking attributed to the June 1869 M_w ~4.8 Christchurch earthquake, or possibly the 1717 Alpine fault M_w ~7.9±0.3 and ca. 500-600 yr BP $M_w \geq 7.1$ Porters Pass fault earthquakes (Bastin et al., 2015; Maurer et al., 2015).

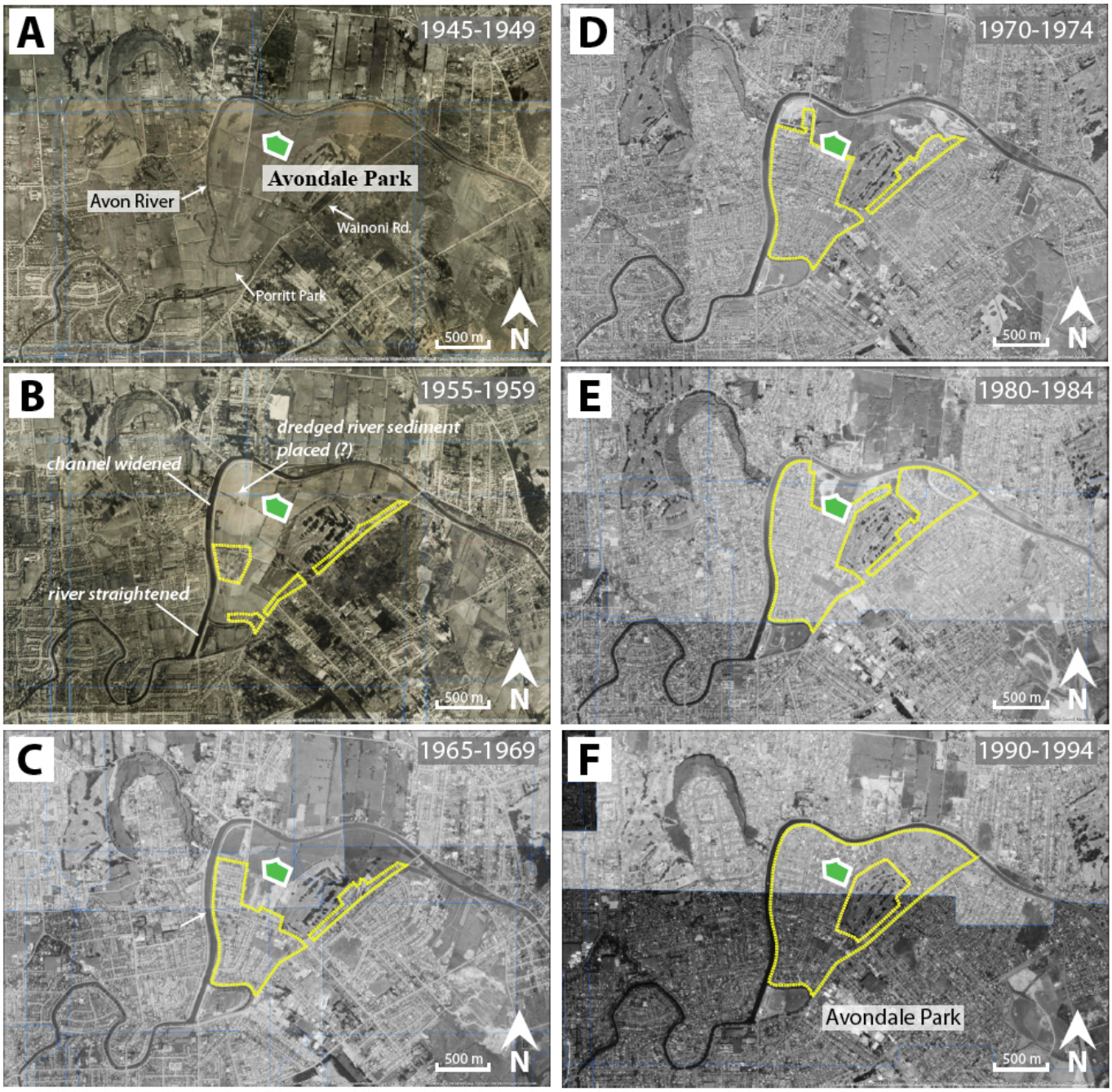

Figure 4. Historical aerial photographs highlighting the sequence (Figs. A-F) of anthropogenic modifications at Avondale Park and surrounding residential areas. Modifications to the Avon River, including straightening of the river near Porritt Park and widening of the channel began sometime after 1949 and before 1955. Sediment removed from the river during widening is a probable source for early anthropogenic fill placed in the area. Grading and development of homes progressed toward the north and east, with final placement of anthropogenic fills at Avondale Park occurring sometime around ~1990.

Figure 5. Surface liquefaction ejecta at the Avondale Park study site in eastern Christchurch. The aerial extent of surface manifested liquefaction (i.e. sand blows and sand blow arrays) is shown for the 22 February, 13 June, and 23 December Christchurch earthquakes and was mapped using high-resolution aerial photographs following each of the main shaking episodes. The June and December surface ejecta comprise ~68% and 23% of the February output, respectively. No surface liquefaction was observed at the study site during the 4 September mainshock event. Locations for T1, T2, and SCPT-1 are indicated. Surface blow arrays are conspicuously aligned with the northeastern and northwestern boundaries of the football/cricket pitch and underground utility (e.g. water) lines.

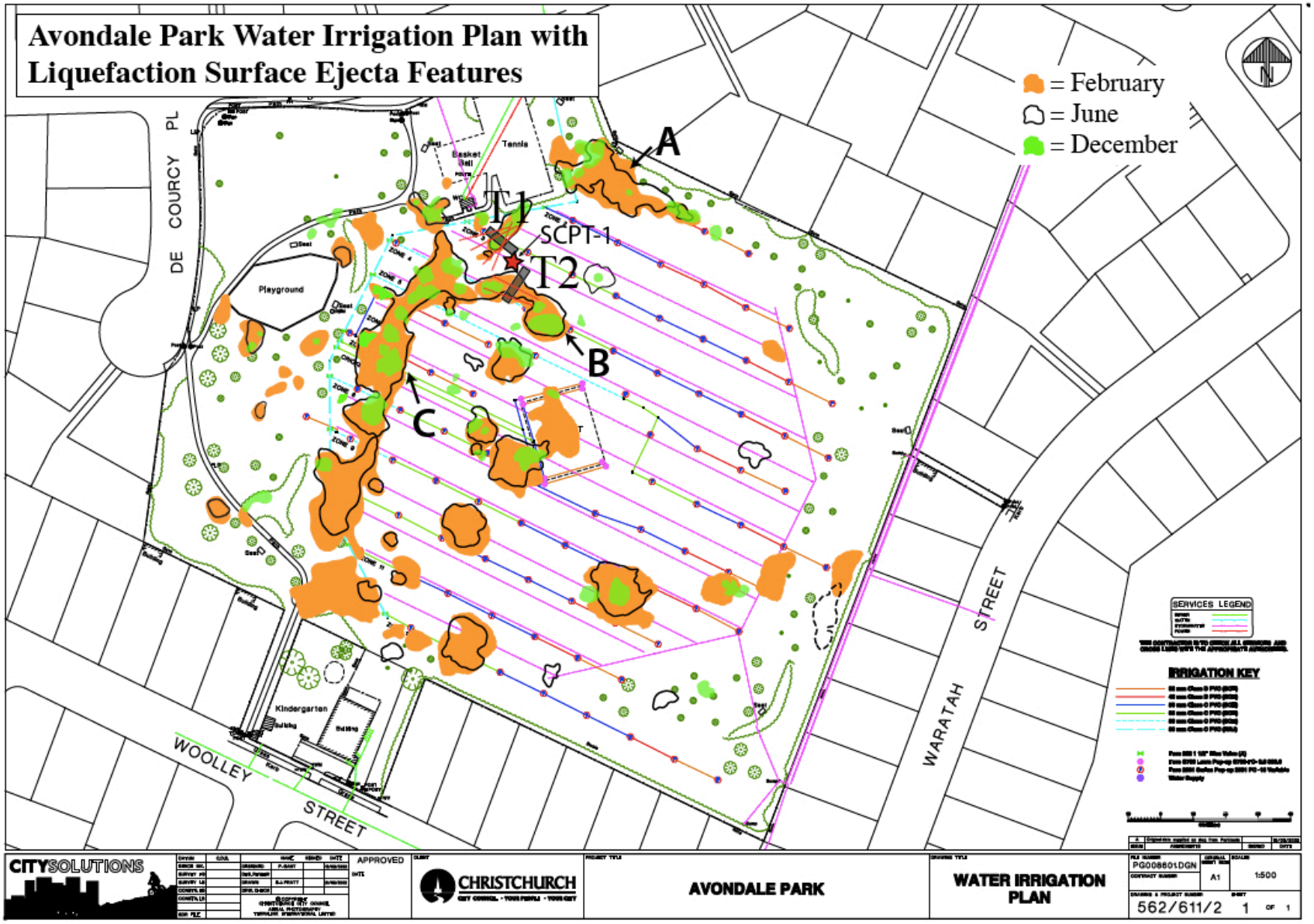

Figure 6. Surface liquefaction features superimposed on the Avondale Park water irrigation plan. Linear sand blow arrays show alignment with water irrigation lines (see A & B) and with the northeastern boundary of the cricket/football pitch (see C). A subsurface dike was observed (in T2) terminating into a gravel-filled utility trench (with perforated subdrain pipe), demonstrating the influence that anthropogenic modifications have on the subsurface and surface expression of liquefaction features.

4.4 Methods

4.4.1 Trenching

I excavated two exploratory trenches to investigate the subsurface morphology of the Canterbury earthquake sequence and search for pre-CES liquefaction features (Figs. 5-9). Avondale Park was targeted for its location in TC3 land, where moderate to significant land damage from liquefaction is possible in future large earthquakes (Fig. 2a-d). We used well-established criteria for identifying earthquake-induced liquefaction features, including analysis of aerial photography, trenching, and dating of subsurface deposits (e.g. Sims, 1975; Obermeier et al., 1991; Obermeier, 1996; Tuttle, 2001; Bastin et al., 2015). Trenches were excavated perpendicular to aligned sand blow vents (Figs. 5 and 6). Due to the presence of an extensive subsurface irrigation system and the current use of central portions of the field for cricket and football events, the trenches were positioned in the northern/northwestern corner of Avondale Park. Trench 1 had a long-axis bearing of 307° (N53°W) and a length and width of 10.0 and 2.0 meters, respectively (Fig 5, 6, and 7). Total trench depth for Trench 1 was 1.7 meters (Fig. 7). Trench 2 had a long-axis bearing of 032° (N32°E) and a length and width of 11.0 and 2.0 meters, respectively (Figs. 5, 8, and 9). Total trench depth for Trench 2 was 1.65 meters (Figs. 8 and 9). Trench walls were cleaned using handheld scrapers and then photographed and logged at centimeter scale to document small-scale changes in the morphology of the liquefaction features and the surrounding stratigraphy. The trench bottoms were also photographed at several locations of interest to highlight key liquefaction and sedimentary features. The liquefaction features and the surrounding anthropogenic and native stratigraphy were described in terms of their grain size, sorting, color (using Maunsell values), and degree of sediment mottling. Hand-auger borings were performed in Trench 1 and Trench 2 (A1 and A2, respectively) to depths of 1.20 and 1.73 meters (from trench bottom), respectively (Figs. 7, 8, and 9). Below these depths the sediment became cohesionless and failed retention within the auger head.

4.4.2 Geotechnical Testing

A single SCPTu (seismic cone penetration test with pore pressure [piezocone] measurement) was conducted between the two exploratory trenches (Figs. 5 and 10a-c; Appendix 1) to determine the (i) engineering properties of anthropogenic and native sediments and (ii) aid in quantifying the sites susceptibility to liquefaction. The SCPTu measures the resistance (e.g. tip resistance and sleeve friction) of the subsurface sediments to an instrumented cone being pushed at a constant rate, while also providing seismic shear wave and compressional velocities for the subsurface sediments. The relative resistance of the subsurface sediments acts as a proxy for the subsurface properties and for determining soil stratigraphy. The shear wave velocities are used to determine the shear modulus and Poisson's ratio

at intervals through the soil column. The shear wave velocity and shear modulus are used to determine the sediment's behavior under low-strain and vibratory loads. The tests were performed in accordance with ASTM D5778-12 "Standard Test Method for Electric Friction Cone and Piezocone Penetration Testing in Soils" and FGNZ-001 "Method Statement for Cone Penetration Testing". The SCPT penetrated to a total depth of 15.25 meters.

The liquefaction potential of the subsurface strata was evaluated from the SCPTu using the Idriss and Boulanger (2008) method as modified by van Ballegooy (2015a, b) (Fig. 10a-c). This method establishes the liquefaction potential by comparing the cyclic stress ratio (CSR), which evaluates loading induced at different depths by an earthquake, with the cyclic resistance ratio (CRR), which reflects the ability of the soil to resist liquefaction. The likelihood that a soil will liquefy is expressed as a factor of safety against liquefaction (FS), where FS<1 is considered potentially liquefiable.

4.4.3 Radiocarbon Dating

Radiocarbon dating was performed on a single charcoal sample from native sediment (silty clay) located at the bottom of Trench 1 (Table 1, Figs. 7 and 11). The ^{14}C age is used as a proxy for the age of the youngest native sediment identified at Avondale Park. The charcoal sample was dried at 40 °C for 1 week and then separated from the host sediment. A 267 mg sample was submitted to the Rafter Radiocarbon Laboratory in Wellington, New Zealand, for accelerator mass spectrometry (AMS) radiocarbon analysis. Samples were prepared for analysis by cutting and scraping of the charcoal (black with strong vascular structure) to remove attached clay. Chemical pretreatment was by acid and alkali treatment. The weight obtained after chemical pretreatment was 19.4 mg. Carbon dioxide was generated by elemental analyzer combustion and 0.5 mgC was obtained. The sample carbon dioxide was converted to graphite by reduction with hydrogen over iron catalyst. Ages were calibrated using the Southern Hemisphere calibration curve (SHCal13; Hogg et al., 2013). Conventional radiocarbon age is reported as defined by Stuiver and Polach (1977). The radiocarbon age referred to in the text is reported as a 2σ calendar calibrated age range. The uncalibrated conventional radiocarbon age and detailed age range distribution of the calendar calibrated ages are presented in Table 1.

4.5 Results

4.5.1 Trench Stratigraphy

4.5.1.1 Pre-anthropogenic stratigraphy

Native sediment (NS) is exposed within the bottom ~20-40 centimeters of Trench 1 and Trench 2 and consists of firm and dense, damp to moist, well sorted gray to bluish gray (Gley 2 5/1) silty clay with very minor sand and occasional small gravel to pebble-sized rock fragments (Figs. 7, 8, 9). We estimate sand percentage is less than ~5% and sand to pebble-sized rock fragments comprise < ~2% of the sediment volume. No internal layers or laminations are observable within NS. The upper ~10-18 cm of NS is distinct and contains dark gray bioturbation features and remnant root features (flecks, spots) that decrease in frequency and taper with depth, indicating a top-down origin (probable burrowing or old roots) and soil development (Figs. 7 and 8). Small rootlets (<1 mm diameter) are observed within NS. The bottom of the bioturbated zone is undulatory, suggesting a secondary, rather than primary depositional origin. The bioturbation zone is thickest (~8 cm greater) in Trench 1.

The contact with the overlying fill is subhorizontal with some undulation. The upper section for NS is texturally and compositionally equivalent in Trench 1 and Trench 2. Observations of cuttings from Hand-Auger A1 and A2 indicate that silty clay continues beneath the trench bottoms for a depth of 34-40 centimeters, making its total thickness ~75-80 cm. Beneath this depth NS becomes more sandy and transitions to bluish gray and dark bluish gray, well sorted, silty sand to fine and very fine sand.

Silty clay in the upper ~75-80 cm of NS suggests minimal to very low sedimentation rates, consistent with deposition in an estuary or low-lying wetland area. This is further supported by the presence of bioturbation/soil development within the upper ~10-18 cm, suggesting the presence of vegetation and pedoturbation. Silty sand and very fine to fine sand present below the silty clay is consistent within overbank deposition from the Avon River or perhaps intermittent flooding events within an estuarine setting, although the presence of thick uninterrupted clean sands (interpreted from SCPT-1; see Fig. 10) beneath the upper silty clay suggests fluvial deposition. Compiled maps by Selby (1856) show largely undeveloped land with patches of surface water (i.e. swampy terrain) at the study site location. Lidar images currently show the study site located within the inner meander bend of the Avon River (~300-500 meters from current river position) and suggests the geomorphology and depositional environment has probably fluctuated between proximal river and estuarine deposition (Fig. 3a).

Radiocarbon dating of detrital charcoal was performed on a single sample (AVP-01) collected from the bottom of Trench 1 (Table 1 and Figs. 7 and 11) to establish the depositional age of native

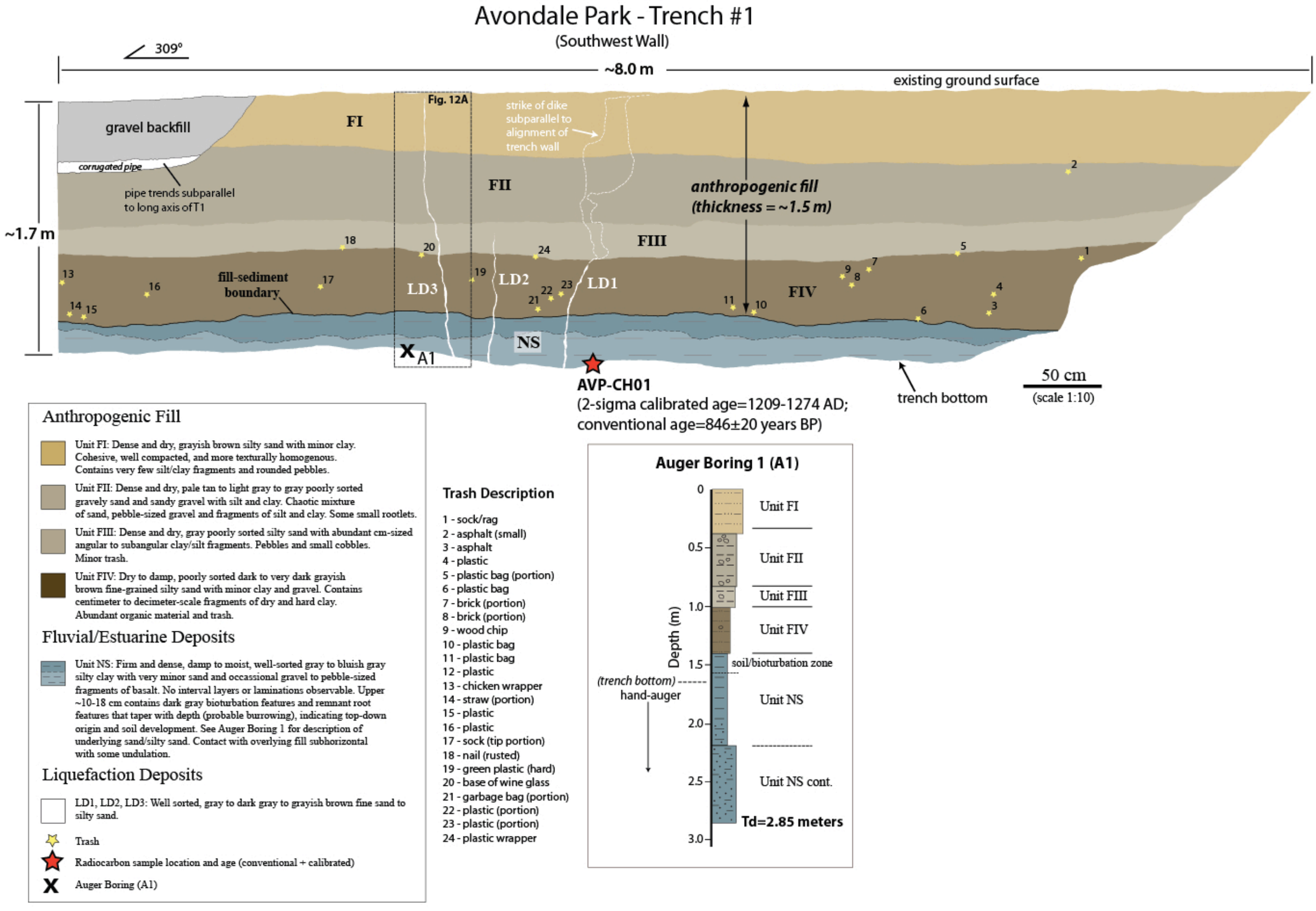

Figure 7. Detailed trench log (Scale = 1:10) of the southwest wall of T1. The Canterbury earthquake sequence (CES) liquefaction dikes (LD1-LD3) crosscut the native sediment (NS) and anthropogenic fill (FI-FIV) stratigraphy. LD1 and LD3 extend to surface, but surface sand blows are not observed at the surface, presumably as a result of post-earthquake surface reworking and grading. No sill development is evident within T1. Soil development is evident at the top of NS implying a former ground surface. Numerous trash items (n = 24) are observed within FIV, suggesting that initial placement of fill above the native sediment was uncertified and probably dumped from a nearby source (e.g. river dredgings). The location and result of the ^{14}C sample are indicated. Auger Boring 1 (~1.7-2.9 m) indicates the trench is underlain by well sorted, fine sand that contains occasional granules.

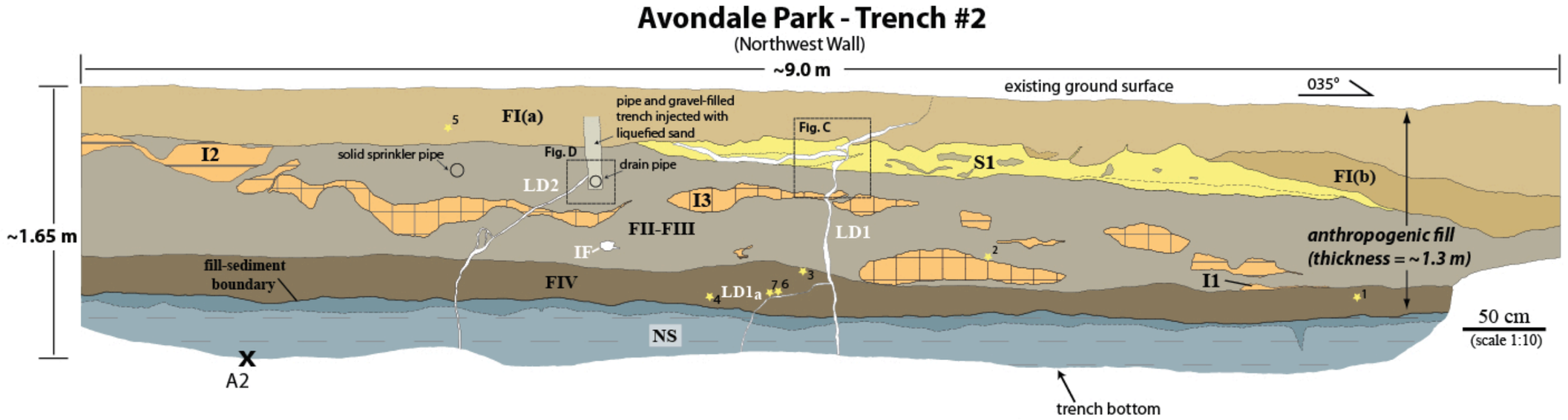

Figure 8. Detailed trench log (Scale = 1:10) of the northeast wall of T2. Liquefaction features resulting from the CES are observed crosscutting the native sediment (fluvial/estuarine deposits) and anthropogenic fill stratigraphy and injecting into fill layers. Well-defined sill morphologies occur at fill layer boundaries, while pervasive sub-horizontal to irregularly shaped injection features are contained within FII and FIII. At least two episodes of liquefaction are defined by crosscutting relationships in T2. Only the most recent liquefaction episode was able to breach the upper fill layer. LD2 terminates in a subdrain trench. Sand from the sill at the base of FI is also deposited in the subdrain trench. Auger Boring 2 (~1.6-3.4 m) indicates the trench is underlain by silty clay changing to fine sand with minor silt and occasional granules at a depth of ~2.0 m. Sediment below 2.0 meters is a possible liquefaction source.

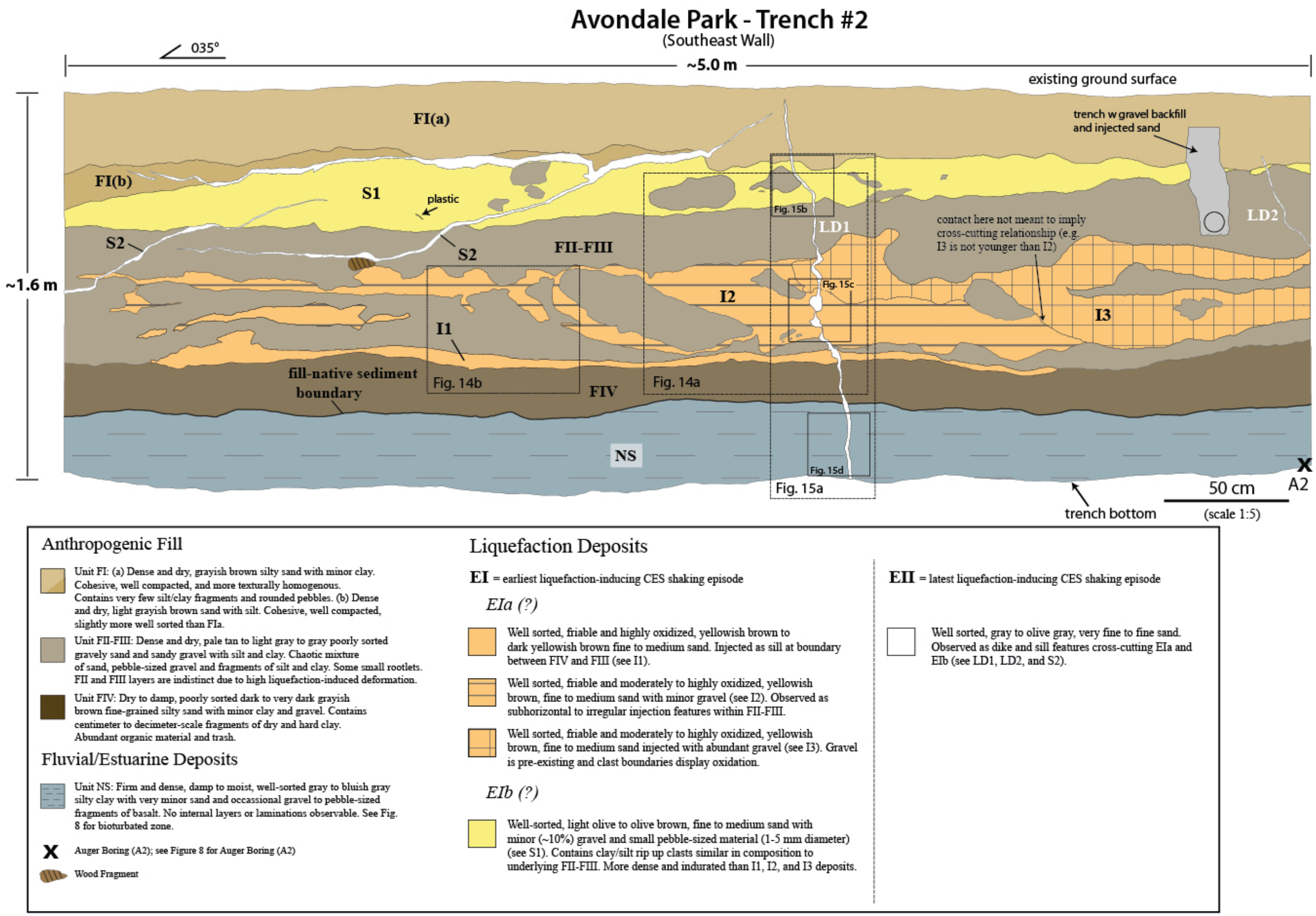

Figure 9. Detailed trench log (Scale = 1:5) of the southeast wall of T2. The southeast wall displays the highest degree of fill layer deformation from liquefaction and highlights the influence of fill on the subsurface expression of liquefaction. Well-developed sill morphologies are observed at the boundaries between NS and FIV, and FII-FIII and FI. Pervasive injection of liquefied sand into FII and FIII is observed. Liquefied sand is observed interpenetrating gravel and wrapping around large silty clay fragments. We note that no sill development is evident at the boundary between NS and FIV. Liquefied sand is injected into the gravel backfill with the subdrain trench, with the probable source being the large sill (L2) developed at the FII-FIII and FI fill boundary.

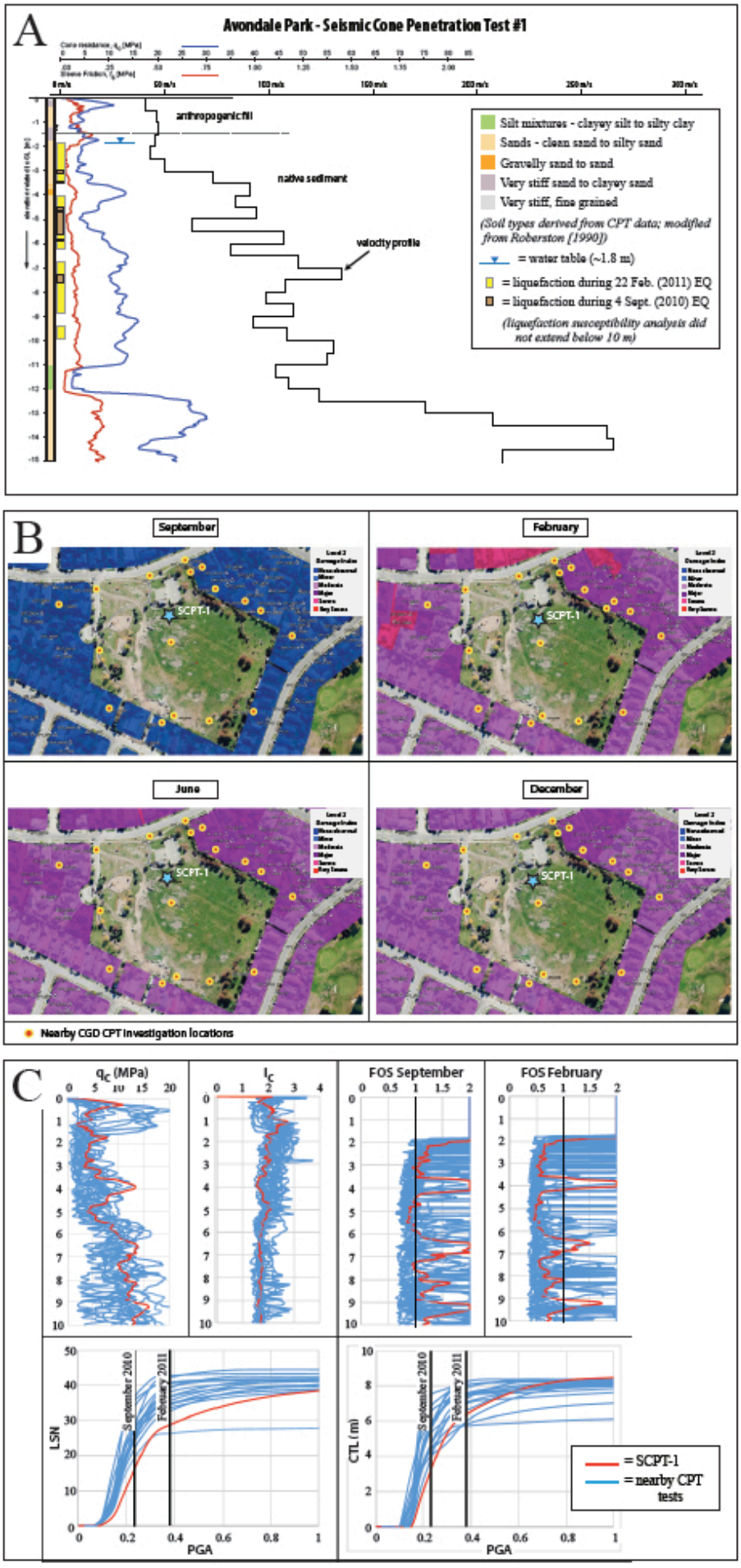

Figure 10.

(A) SCPT-1 log with seismic velocity profile. Cone resistance within the upper ~50 cm is high compared with lower section (~1 m) of the anthropogenic fill reflecting the competent nature of FI. Below ~2.0 meters the CPT indicates sand and silty sand consistently downward to a depth of ~11 meters, with no distinct gravel layers encountered. An abrupt increase in cone tip resistance and seismic velocity is indicated at a depth of ~12 m.

(B) Assessment of land damage for residential properties surrounding Avondale Park following the 4 September 2010 mainshock and 22 February, 13 June, and 23 December 2011 Christchurch aftershocks (provided by Sjoerd van Ballegooy). Location for SCPT-1 and 15 additional cone penetration tests are shown. "No to minor damage' to residential properties was observed during the September mainshock. Damage during the 22 February event ranged from 'major to severe', and 'moderate to major' during the 13 June and 23 December quakes. Major damage from the June event was greater when compared with the December shaking episode.

(C) Liquefaction susceptibility analysis (performed by Sjoerd van Ballegooy) for SCPT-1 is compared with 15 nearby cone penetration tests. The plot shows tip resistance (q_c), soil index (I_c), liquefaction susceptibility number (LSN), cumulative thickness liquefied (CTL), and factor of safety (for September and February events) for SCPT-1 (red) and adjacent CPTs (blue).

Sample ID	Sample location	Exposure unit	NZA laboratory number	$\delta^{13}C$ [‰]	Radiocarbon age (^{14}C yr B.P.)	Calibrated age 2σ (calendar yr A.D.)	Probability for each 2σ range (%)	Material
AVP-01	Avondale Park; Trench 1	Native sediment (silty clay)	60808	27.7±0.2	846±20	AD 1209 to 1274	95.2%	Charcoal

Note: NZA-Rafter Radiocarbon Laboratory; B.P. – before present

Table 1. Summary results from radiocarbon dating of charcoal within T1 native sediments at the Avondale Park study site.

Rafter Radiocarbon
Calibration Report

NZA 60808
R 40856/1
Report issued: 23 Mar 2016

CONVENTIONAL RADIOCARBON AGE 846 ± 20 years BP

Calibrated with SHCal13 (Hogg et al., Radiocarbon 55(4):1889-1902, 2013).

CALIBRATED AGE in terms of confidence intervals

1 sigma interval is	1219 AD to 1235 AD	731 BP to 715 BP (29.2% of area)
	1243 AD to 1265 AD	707 BP to 685 BP (39.4% of area)
2 sigma interval is	1209 AD to 1274 AD	741 BP to 676 BP (95.2% of area)

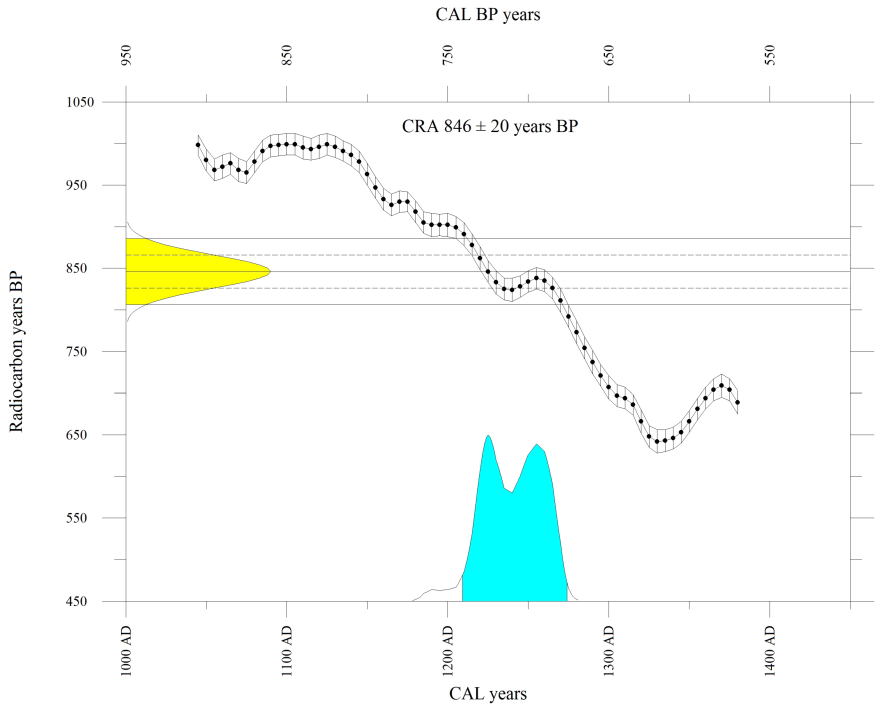

Calibration performed using Winscal v. 6.0 adapted from: Stuiver and Reimer (*Radiocarbon 35*(1): 215-230, 1993).

National Isotope Centre, GNS Science
PO Box 31-312 Lower Hutt, New Zealand Phone +64 4 570 4644
Email radiocarbon@gns.cri.nz Website www.RafterRadiocarbon.co.nz

Figure 11

Figure 11. Radiocarbon calibration report for charcoal sample AVP-01. The 2σ calibrated age (calendar yr. AD) range suggests latest deposition of native sediment at Avondale Park occurred during the time period ranging from 1209 AD to 1274 AD. A conventional radiocarbon age of 846±20 years BP was generated for AVP-01.

sediment and provide a minimum age for the last occurrence of liquefaction at the study site. We use the charcoal date as a proxy for timing of sediment deposition, assuming that erosion, transport, and deposition of the charcoal-containing sediment occurred shortly after burning (i.e. death of plant matter). The 2σ calibrated age (calendar yr. AD) range suggests latest deposition of native sediment at Avondale Park occurred during the time period ranging from 1209 AD to 1274 AD (Table 1 and Fig. 7). A conventional radiocarbon age of 846±20 years BP was generated for AVP-01 (Table 1 and Fig. 7). The radiocarbon age is consistent with other ages from this unit (Bastin et al., 2015) and, given the position of the study site with respect to paleo-shorelines (Fig. 1b) ~1 ka, estuarine deposition.

4.5.1.2 Anthropogenic fill stratigraphy

Here I summarize the anthropogenic fill layers observed within Trench 1 and Trench 2. Due to the relatively close distance between trenches (~7.5 meters), we assume the engineering characteristics of the fill layers in both trenches were roughly equivalent prior to the 2010-2011 CES, although minor variations in thickness and composition/texture are expected given the nature of importing and mixing/placing fill. Anthropogenic fill in Trench 1 was considerably less deformed/modified during the CES and therefore provides the most accurate representation of fill layers prior to the CES (Fig. 7). Four separate fill layers are delineated within Trench 1 based upon a comparison of sediment color, composition, and texture (including grain sorting) (Fig. 7). Within Trench 2, the central fill layers (i.e. FII and FIII) have been sufficiently deformed to a level where distinguishing between the two layers is difficult. Consequently, we collectively refer to these layers as FII-FIII when describing Trench 2 observations (Figs. 8 and 9). The fill layers are subhorizontal to horizontal.

4.5.1.2.1 Fill Layer IV (FIV)

FIV represents the earliest placed fill layer at Avondale Park and in Trench 1 has a thickness ranging from 34-51 cm (Fig. 7). Internal structure is chaotic to wavy, indicative of dumping and/or possibly rolling of sediment (for compaction). FIV lies directly over NS (native sediment) and consists of a dry to damp dark grayish brown to very dark grayish brown (10yr 3.5/2) fine-grained silty sand with minor clay and gravel and pebbles. Small, less abundant patches of dark brown silty clay with sand are observed. FIV contains centimeter scale fragments of clay, which appear similar in composition/texture to the underlying native sediment. Abundant organic material (e.g. wood, roots) and trash, including plastic bags, sock, wine glass handle, and asphalt are observed within FIV (Fig. 7). Twenty-four separate pieces of trash were observed during logging of Trench 1 (Fig. 7). The contact with the underlying native sediment is subhorizontal to slightly undulatory.

In Trench 2, FIV thickness is less, ranging from ~12-28 cm (Figs. 8 and 9). The fill consists of medium to dark brown to reddish brown, poorly sorted, fine to medium-grained sandy clay to silty clay with sand. The fill layer contains ~5-10% gravel (~2-7 mm diameter), distributed randomly. The increase in clay and gravel content suggests variability over a relatively small distance (<10 m). FI contains ~5 cm diameter 'lumps' of pale gray silt/clay similar to those observed in Trench 1.

4.5.1.2.2 Fill Layer III (FIII)

In Trench 1 FIII has a thickness ranging from ~16-22 cm (Fig. 7) and is comprised of dry gray (2.5y 6/1-5/1), poorly sorted, silty sand with abundant cm-sized clay/silt fragments and brownish yellow (10yr 6/6) mottling. The clay/silt fragments are pervasive (~15%) and typically angular to subangular in shape. Together with less abundant rounded pebbles and small cobbles I estimate they comprise approximately 15% of the sediment volume. Very few pieces of trash (e.g. plastic) are present within FIII, with those documented occurring near the highly oxidized contact with the underlying fill layer (F1V). FIII exhibits more cohesion than FIV, primarily as a result of the relative increase in clay/silt content.

In Trench 2, FIII thickness is ~34 cm (Figs. 8 and 9). It is difficult to distinguish between FII and FIII (see below) within Trench 2. Together, these units have been sufficiently modified by recent (2010-2011 CES) liquefaction and exhibit abundant liquefaction injection features (see liquefaction features below) (Figs. 8 and 9). Sections of the unit not disrupted by liquefaction processing consist of brown to gray silty sand with minor clay.

4.5.1.2.3 Fill Layer II (FII)

In Trench 1 FII has a layer thickness ranging from ~32-49 cm and comprises a dry, dense, and friable pale tan to light gray to gray (10yr 7/1-6/1), poorly sorted, gravely sand and sandy gravel with silt and clay (Fig. 7). FII is a chaotic mixture of sand, pebble-sized gravel (cm-scale), and fragments of silt and clay (<10 cm diameter). I estimate that FII is comprised of ~40% coarse fragments (pebbles, cobbles, silt/clay clasts) (Fig. 7). Some small rootlets (2-5 mm diameter) with mottling (10yr 6/8) are observed. With the exception of a single small piece of asphalt, FII contain no trash. The boundary with FIII is difficult to distinguish. The presence of similar silt/clay fragments within FII and FIII suggests they were likely placed around the same time and possibly sourced from the same area.

In Trench 2, FII comprises a dry, dense, friable, light to medium brown, poorly sorted silty and gravelly sand with silt and clay (Figs. 8 and 9). I estimate percent gravel to be ~30-50%. In numerous locations, the gravel has been entrained or nearly completely surrounded by injected liquefied sand.

4.5.1.2.4 Fill Layer I (FI)

In Trench 1 FI has a layer thickness ranging from ~31-47 cm (Fig. 7). It is distinct from the underlying fill layers (i.e. FII-FIV) and consists of dense and dry grayish brown (10yr 5/2) silty sand with minor clay. F1 is cohesive, well compacted, and more texturally homogenous, containing very few silt/clay fragments and rounded pebbles (Fig. 7). No trash is observed in FI. Tiny rootlets are present within the upper ~20 cm where a thin active A horizon is present. Grass comprises the upper 6-7 cm. FI represents the most recent fill layer and has been modified near the surface following the 2010-2011 CES.

In Trench 2, FI has a thickness ranging from ~28-54 cm (Figs. 8 and 9). It consists of a similar dry, grayish brown (10yr 5/2), dense, silty sand with minor clay and contains less than 5% cm-scale subangular to subrounded silt/clay clasts.

4.5.1.3 Interpretation of anthropogenic history

A review of historical aerial photography (1940-2011) indicates significant anthropogenic modifications to the Avondale Park area and the surrounding landscape (Fig. 4). The earliest historical aerial photos are consistent with observations compiled by Selby (1856) and show largely undeveloped land with patches of surface water. The entirety of Avondale Park and the surrounding area within the meander bend and west-northwest of Wainoni Road remained undeveloped until at least ~1949 (Fig. 4a). However, significant modifications to the Avon River and adjacent landscape are evident between 1949 and 1955. During this time period the north-south oriented section of the Avon River was widened and a new southern extension (near Porritt Park) was created, effectively cutting off and isolating the Porritt Park meander bend (Fig. 4b). I assume the increase in river width was facilitated by river dredging and that river sediments were either dumped in adjacent flat-lying areas and/or placed in anticipation of raising grade elevation for future residential development in the area.

The 1955-1959 aerial photo (Fig. 4b) supports the placement of sediment in the area now occupied by Avondale Park and nearby homes. The areas of moisture, evident in 1940-1949 aerial photographs (Fig. 4a), are absent and the development of homes has been initiated (Fig. 4b). It is possible that the lack of moisture apparent at the surface reflects warmer/dryer conditions and a corresponding lower water table during the time the photos were captured. However, given the apparent modifications to the landscape, including widening of the river and initiation of construction in the area, it seems more reasonable to assume that anthropogenic fills were placed in the Avondale Park area during this time. The total thickness of fills placed at this time cannot be determined from the aerial

photographs. We speculate that fill placed during this time may be represented in the exploratory trenches by FIV (thickness ~12-51 cm) (see Figs. 7, 8, and 9).

Between 1965 and 1969 development of homes in the area increased moving northwards (Fig. 4c). The suburbs north of Breezes Road and adjacent to the Avon River have been established, suggesting grade level at the time was similar to present elevation because the homes remain in the area to present day. This could suggest that the majority of the fill was placed within the Avondale Park and surrounding suburb areas prior to 1965. 1970-1974 aerial photos show the continued development and construction of homes in the area moving to the north and northwest (Fig. 4d). At this time Avondale Park had not been established but homes were constructed to its present-day southern limit. Aerial photographs indicate that the development of roads, homes, and all parks (including Avondale) was completed sometime between 1990 and 1994 (see Figs. 4e,f).

It is possible that placement of anthropogenic fills in the Avondale Park area occurred over a long time period (i.e. decades), keeping pace with road and home development in the area. Based upon personal communications with the Christchurch City Council (Kevin Williams), the Avondale Park site was 'probably filled over the years with dredged material from the Avon River'. No grading reports or records documenting fill placement at Avondale Park was available at the Christchurch City Council. The field/park was established in the late 1990's, with the first irrigation system constructed during this time. Ten centimeters of subsoil was placed beneath the field turf. From 2001-2002, a new field drainage and irrigation system was constructed at Avondale Park (Fig. 6). Some minor modifications to the surface have been performed following the 2010-2011 Canterbury earthquake sequence.

4.5.2 CES liquefaction features

4.5.2.1 Trench 1 liquefaction features

The modern liquefaction dikes (Fig. 7 – see LD1, LD2, LD3) in the Trench 1 southwest wall are oriented vertical to subvertical, have a maximum thickness of ~1.5 cm (as measured at trench bottom) and, where traceable, thin upwards to ~2-5 mm near the surface (i.e. LD1, LD3) (Fig. 7). The infilling liquefied sediment comprises dark gray to gray (10yr 4/1, 5/1) to grayish brown to dark grayish brown (10yr 5/1-5/2) well sorted, fine sand (Fig. 7). Very thin (< 0.5 mm) silt linings were observed along the dike sidewalls but seem associated only with the most recent liquefaction episode. The absence of multiple crosscutting silt linings within the modern dikes makes it impossible to determine (in the subsurface) if reactivation occurred during successive CES shaking events.

The modern dike wall boundaries range from distinct to highly oxidized depending on the surrounding sediment/fill and elevation relative to the water table. No significant mottling is observed at any of the dike wall boundaries. The highest degree of oxidation is observed within FIV (i.e. oldest anthropogenic fill layer), where the dike boundaries are difficult to identify (Fig. 12a,b). The oxidation of liquefaction features is consistently highest within FIV for both exploratory trenches. Oxidation is less pronounced within NS (although minor oxidation is observable) and generally absent to minimal within FI, FII, and FIII. Dike orientation is most irregular, particularly for LD1 (Fig. 12a) within FII and FIII, highlighting the influence that heterogeneities in anthropogenic fill (i.e. gravel and cm-scale sediment fragments) have on dike propagation and orientation. In some instances, the dike boundaries within the gravel-rich FII and FIII layers were difficult to follow and became diffuse (Fig. 12b), as the higher porosity gravels allowed for local dissipation of high fluid pressures.

The Trench 1 liquefaction dikes splay off a larger feeder dike (maximum width = 2-3 cm) observable at the trench bottom (Figs. 13a,b) and trending ~252-309° (S72°W-N51°W). LD2 and LD3 trend oblique to the main feeder dike at 222° (S42°W) and 239° (S59°W), respectively (Fig. 13a). As expected, the dike bearings correlate well with the trend of the overlying surface sand blow array (see Fig. 5), but show no obvious relationship with the trend of the nearby Avon River, suggesting that lateral spreading near the Avon River had negligible influence on dike formation at Avondale Park. We observed no modern sand blows preserved at the surface within the Trench 1. Surface sand blows have been removed or reworked as a result of natural (e.g. wind, water) and/or anthropogenic (i.e. minor grading at park) processes following the CES.

4.5.2.2 Trench 2 liquefaction features

In Trench 2, liquefaction-induced modification/deformation of the anthropogenic fill layers is significantly more pronounced (Figs. 8, 9, 14, 15). I observed a greater abundance and variety of modern liquefaction features (compared with Trench 1), including development of subvertical to oblique dikes, sills, and numerous subhorizontal to irregularly-oriented and shaped injection features (Figs. 8 and 9). For comparison, the combined area of modern liquefaction features in the Trench 2 walls is 2.0 and 2.2 m^2 (15-27% of total trench wall area) for the northwest and southeast trench walls, respectively, compared with only 0.025 m^2 (0.2% of total trench wall area) for Trench 1.

4.5.2.2.1 Dike Morphologies

The largest liquefaction dike in Trench 2 has a maximum width of ~3 cm (measured within FII-FIII layers) (see LD1 in Figs. 8 and 9). The dike width at the trench bottom is ~2.0-2.5 cm (Fig. 16). Within the northwest trench wall, LD1 continues upward vertically and then splits into a subhorizontal

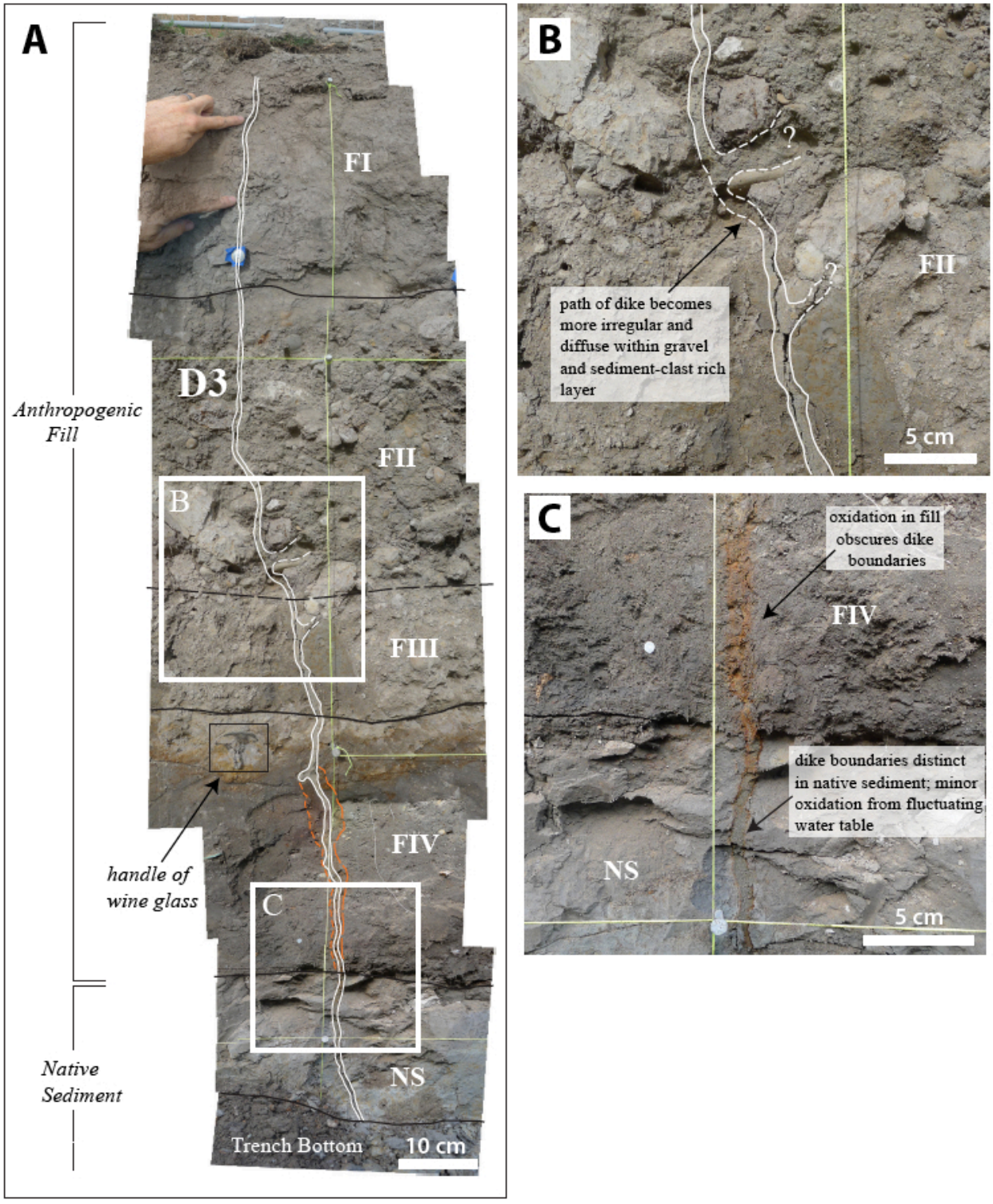

Figure 12. **(A)** CES liquefaction dike crosscuts native sediment and anthropogenic fill layers. **(B)** Dike boundaries become more diffusive within fill layers FII and FIII where gravel and randomly placed fragments of silt/clay are abundant. Sand is observed interpenetrating gravel deposits and sediment fragments. **(C)** Mottling from oxidation is greatest within FIV and highlights the potentially low preservation potential for liquefaction features within anthropogenic fill layers. The distinctive mottling in FIV also suggests that this layer has a distinct source compared with that from the overlying fill layers. For example, oxidation of the modern liquefaction dike within FIV has occurred within only the last ~5 years, implying that liquefaction dikes within this fill layer would be observable for only short time periods (e.g. 10-10^2 years).

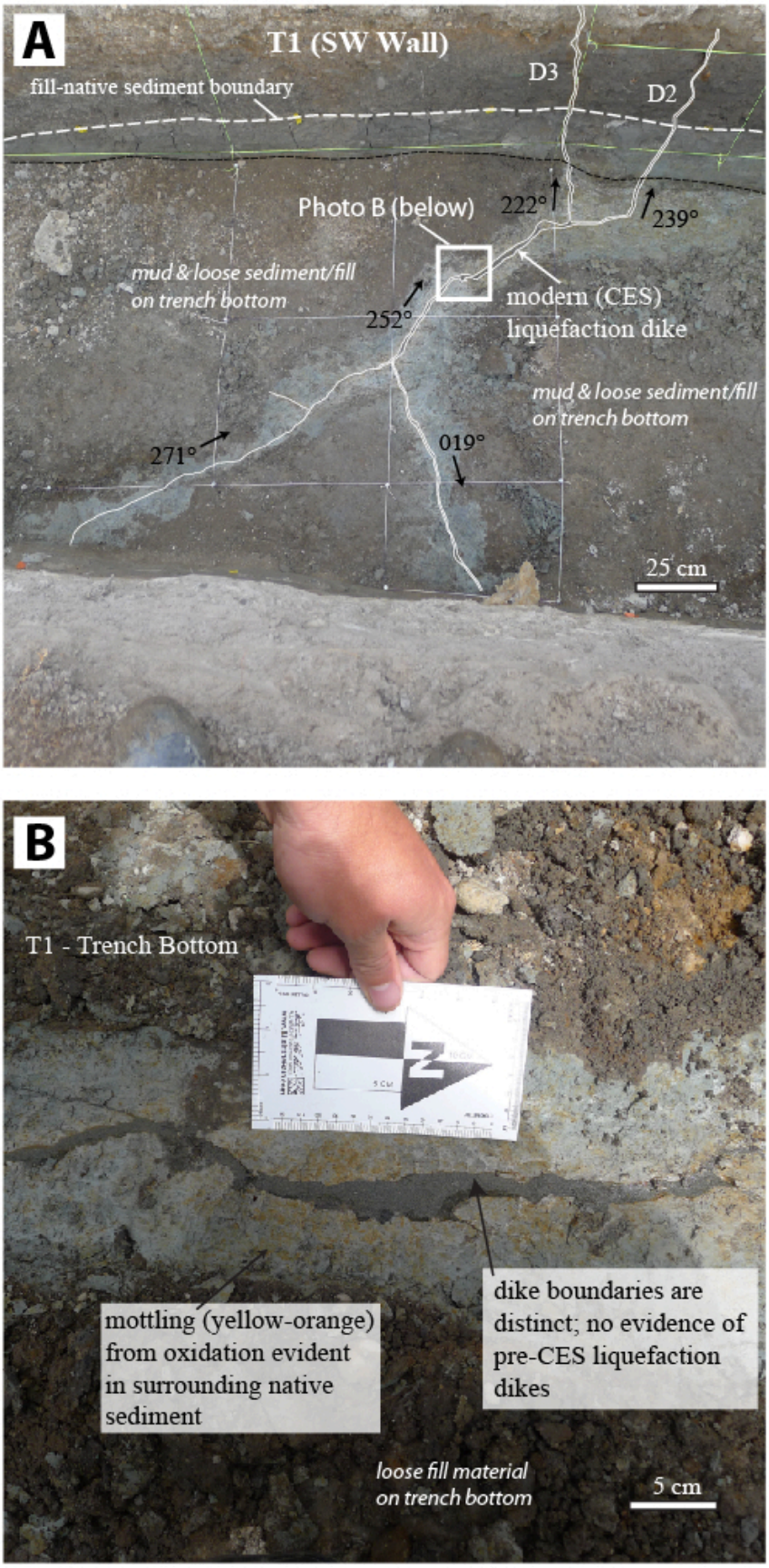

Figure 13. **(A)** Photo of modern liquefaction dike at bottom of T1. Liquefaction dikes display general NW-SE orientation, consistent with the alignment of the corresponding sand blow array at surface. Dike orientation suggests negligible influence from the Avon River, located as close as ~300 meters to the North. **(B)** Modern dike boundaries are distinct. Mottling (yellow-orange) from oxidation is evident in the surrounding native sediment but not at dike boundaries. We find no evidence of pre-CES liquefaction dikes in T1 trench bottom.

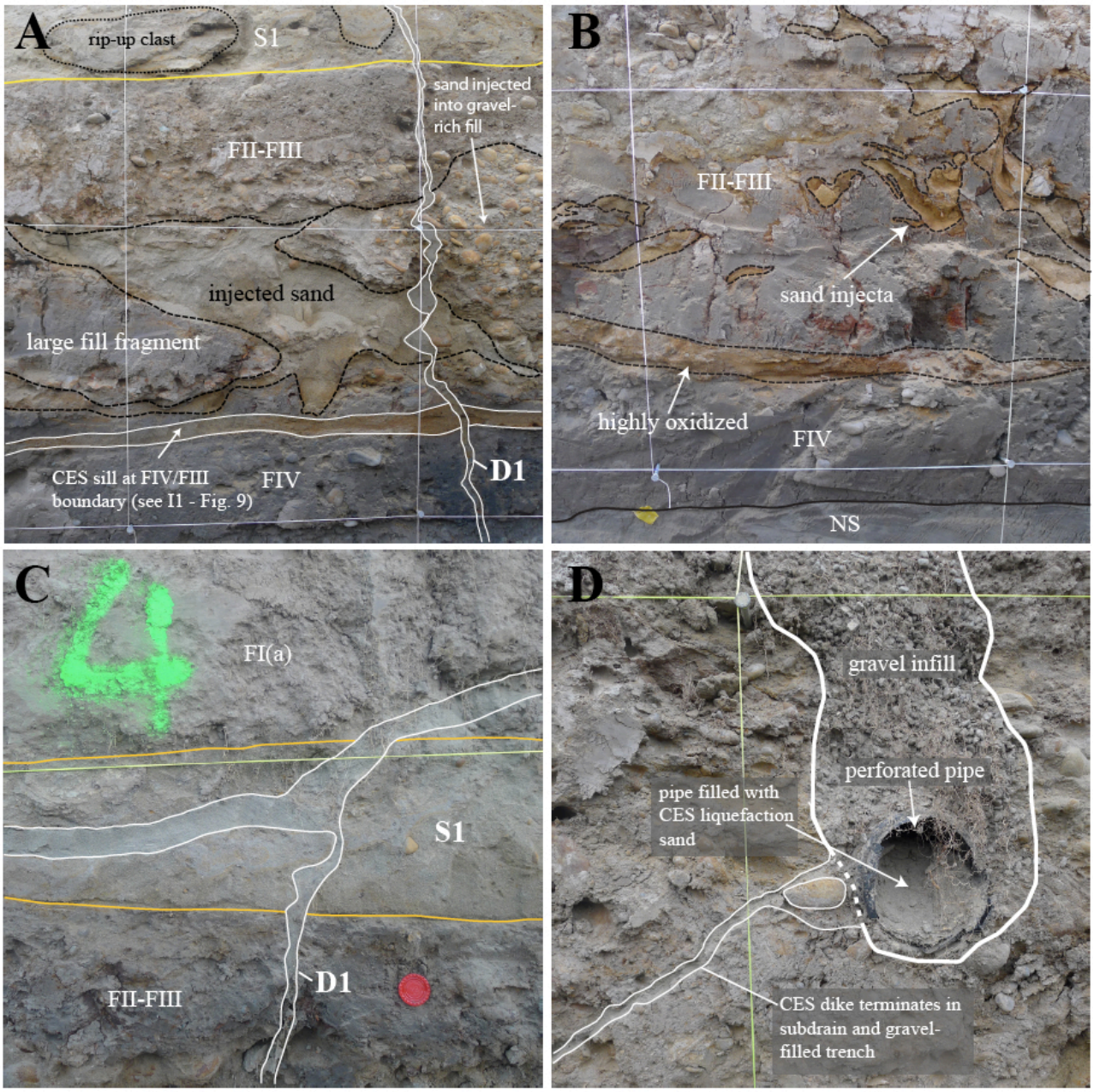

Figure 14. **(A)** Liquefied sand injecta in FII-FIII. Fine sand is observed interpenetrating and wrapping around gravel and large (cm-scale) silty-clay fragments. The injected sand in Figure A is more friable than sand found interpenetrating the gravel deposits, perhaps suggesting multiple injection events within FII and FIII. The thin sill at the FIII-FIV boundary is highly oxidized (orange-red) and could represent liquefaction during the earliest shaking episode (i.e. 4 September mainshock). **(B)** Liquefaction injecta within FII-FIII, primarily within silty-clay host fill sediment. We note that oxidation is high and probably influenced by the chemical composition of the host fill sediments. **(C)** Youngest preserved liquefaction event in T2 (northwest wall). Sill development exploited the upper boundary of pre-existing sill. **(D)** Termination of dike into existing perforated subdrain pipe, highlighting the influence of anthropogenic modifications on subsurface dike patterns. Injected sand filled the perforated pipe and interpenetrated the surrounding gravel backfill. The utility trench acted as an effective conduit for transport and deposition of liquefaction injecta.

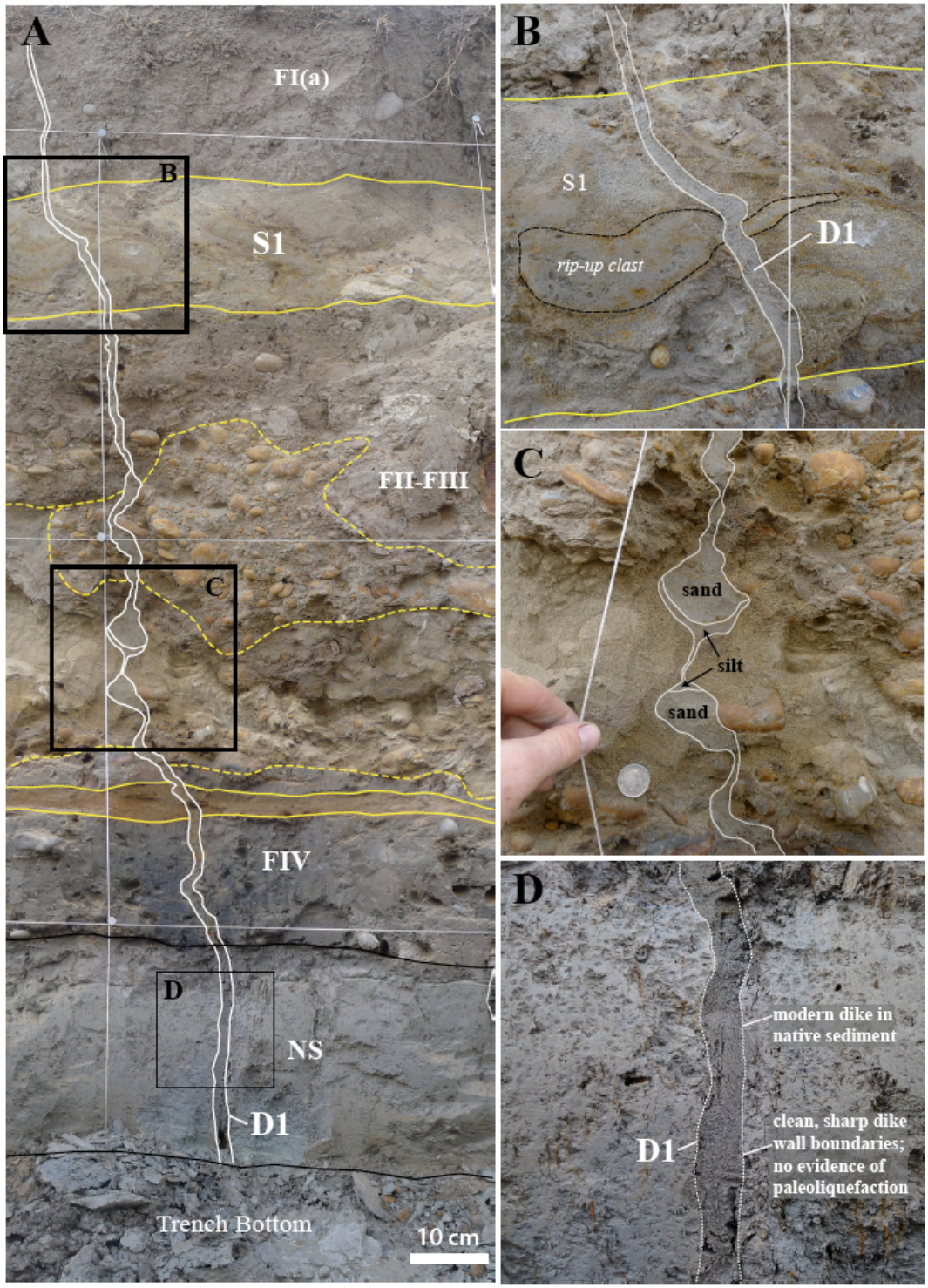

Figure 15. (A) At least two distinct episodes of modern liquefaction are evident in the southwestern wall of T2. Sill development is observed at the boundaries between F1a and FII/FIII, and between FII/FIII and FIV. Chaotic injection of liquefied sediment is focused primarily into fill layers containing abundant gravel (i.e. FII/FIII) and mm- to cm-scale sediment clasts. The gravel surfaces are oxidized, presumably from the interaction with Fe-rich fluids during shaking episodes. **(B)** D1 crosscuts the large sill (S1) present at the bottom of F1a. Sediment comprising the large sill has a higher relative density and coarser grain-size. Rip-up clasts with similar composition to underlying FII suggest fluid velocities high enough to capture fragments from host fill. **(C)** The orientation of modern liquefaction dikes is typically irregular through the gravel-rich fill layers FII and FIII and pre-existing liquefaction features. Lobate repositories for liquefied sand and silt form in the preexisting liquefaction sand. Stalling (silt drapes) of the sediment within the modern dikes is evident. **(D)** Modern liquefaction dike crosscutting native sediment (NS). The modern dikes are typically vertical to subvertical within NS and become more irregularly oriented within the anthropogenic fill layers.

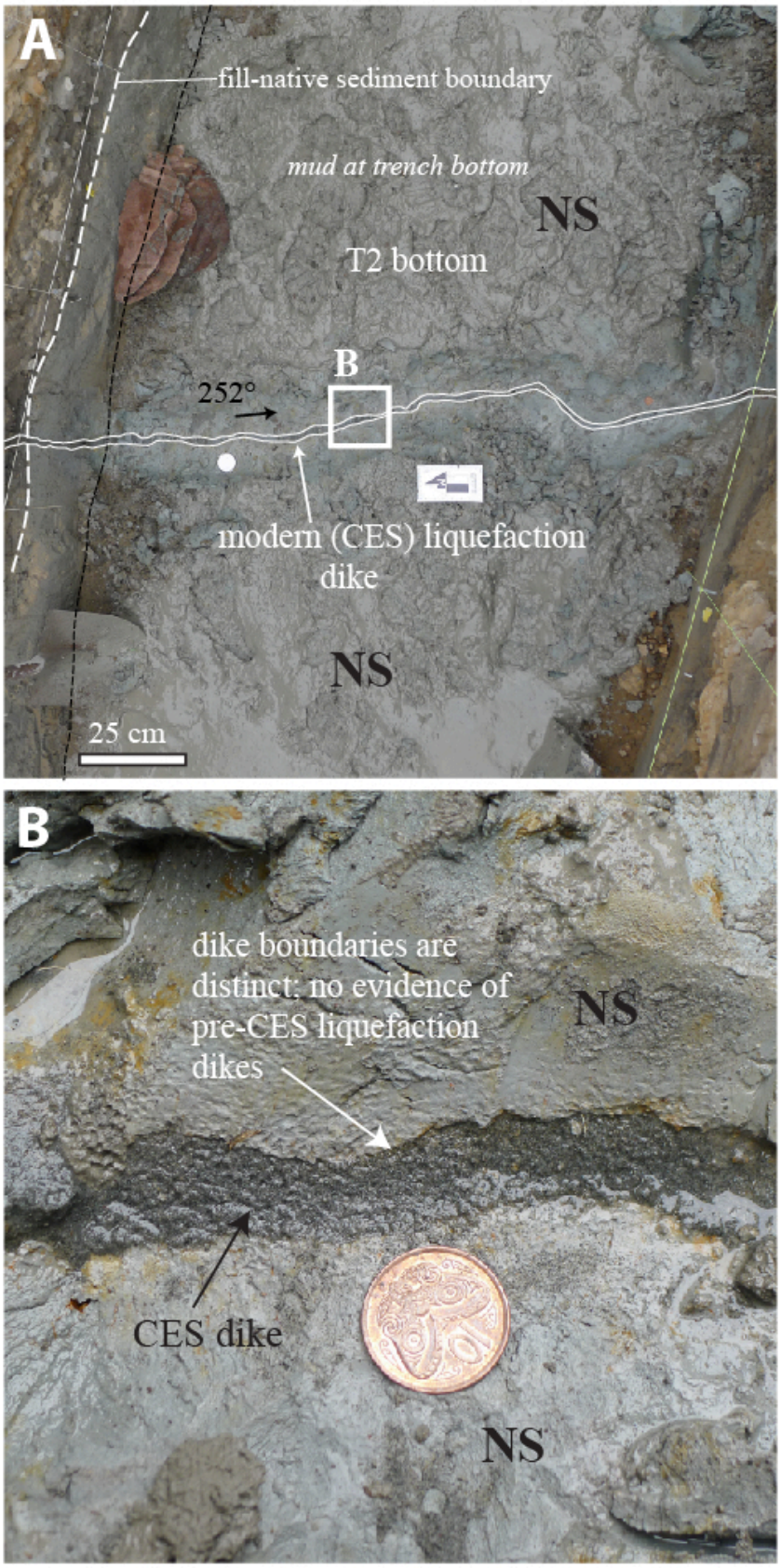

Figure 16. **(A)** Photo showing modern liquefaction dike at bottom of T2. Maximum width of dike is ~2.5 cm. The liquefaction dike has a bearing of ~110°, consistent with the strike of the surface linear sand blow array. **(B)** Modern dike boundaries are sharp/unweathered and show no oxidation and mottling indicative of pre-CES dikes. No prehistoric liquefaction dikes were observed within T2.

sill (within S1) to the left (southwest direction) and an obliquely rising continuation of LD1 to the right (northeast direction), which breaches the upper fill layer (FI) (Fig. 8). In the southeast trench wall, LD1 continues vertically to the near surface (Fig. 9). The infilling dike sediment comprises a light gray to pale grey, well sorted, fine sand and in some locations is observed fining upward into a well sorted, grey fine sand to silty sand to sandy silt before stalling (Figs. 14c and 15). I observed no distinct silt drapes at the dike wall boundaries. Oxidation along the dike boundaries is most pronounced (extends ~1/2 cm outward from wall boundaries) within FIV. LD1 strikes ~293°, a bearing consistent with the alignment of sand blows and sand blow arrays directly above Trench 2 (see Figs. 5 and 6). Surface sand blows have not been preserved above LD1. Similar to Trench 1, we assume they have been removed (during grading) or reworked (e.g. wind, water) beyond recognition subsequent to the CES.

A smaller connecting dike ($LD1_a$) (maximum width = ~1.0 cm) is observable within the northwest trench wall and is located ~60 cm to the southwest (as measured at trench bottom) (Fig. 8). It extends upward subvertically through NS before becoming subhorizontal and connecting with the LD1 within FIV (Fig. 8). The infilling sediment for $LD1_a$ comprises a slightly darker gray to bluish gray, well sorted fine sand. No oxidation is observed on the wall boundaries, and no obvious crosscutting relationship with LD1 is observed, suggesting the two were likely part of the same shaking episode but have experienced different post-formation secondary alteration.

A separate dike (LD2) is located ~2.2 meters to the south-southwest of LD1 (as measured in the NW trench wall), has a maximum width of ~2 cm, and is comprised of a light grey to pale grey fine sand (see LD2 in Figs. 8 and 9). LD2 has a similar strike (compared to LD1) of ~285°. A maximum dike width of ~2 cm is observed within the FII and FIII fill layers. LD2 extends upward vertically within the native sediment, but deflects obliquely within the fill units before terminating within a gravel filled subdrain trench (Figs. 8 and 14d). Liquefied sand (with equivalent composition/texture to that observed in LD2) has been injected into the perforated subdrain pipe and surrounding gravel backfill (Fig. 14d), and clearly indicates that gravel-filled utility excavations (and contained perforated pipes) are providing subsurface conduits for liquefaction ejecta and influencing dike development and orientation.

4.5.2.2.2 Sill Morphologies

Sill morphologies are observed in both Trench 2 walls (Figs. 8 and 9). The largest of the sills (S1) was formed at the boundary between FI and FII (Figs. 8, 9, 15a,b), highlighting the occurrence of modern liquefaction sill features at fill layer boundaries. S1 has a minimum total length of ~4.7 meters and a maximum thickness of ~28 centimeters. It is comprised of well sorted, light olive to olive brown (2.5Y 4.5/3) fine to medium sand with minor (~10%) gravel and occasional small pebble-sized material (1-5 mm diameter). The coarser grained material forms part of the overall horizontal sill layering. S1

contains large silty clay rip-up fragments, similar in composition and texture to the underlying FII-FIII unit (Figs. 8, 9, 14a, 15a,b). The rip-up clasts have diameters ranging from ~5 to ~30 centimeters, suggesting the fluidized sand had sufficient velocity to transport gravel to small pebble-sized material and also entrain large pieces of in-situ fill material. S1 is the most dense and indurated of the liquefied sand features.

Long (~3.65 m) and thin (thickness = ~1 – 12 cm) sills (see I1 in Figs. 8 and 9) are also developed at the boundary between FIV and FIII. The infilling sediment is comprised of well sorted, friable and highly oxidized yellowish-brown to dark yellowish brown (10YR 4.5/6) fine to medium sand.

Several oblique to horizontal sill splays (associated with the youngest liquefaction episode) with length ranging from ~1.0-2.3 meters and thicknesses of ~1-5 cm (see S2 in Fig. 10) are preserved in the Trench 2 walls. The infilling sediment is comprised of well sorted, gray to olive gray (5Y 5/1.5), very fine to fine sand. S2 sill features are observed at the boundaries between fill layers and pre-existing liquefaction features as well as within individual fill layers. We note that no sill development is observed at the boundary between NS and FIV (see Figs. 7, 8, 9).

4.5.2.2.3 Other liquefaction injection features

FII and FIII fill layers contain abundant horizontal to subhorizontal, elongate to irregularly shaped, liquefaction injection features (Figs. 8, 9, 14a,b, 15a). In the Trench 2 northwest wall, the liquefaction features have a 'ribbon' shape and range in length from several centimeters to ~130 cm. The total thickness for the liquefaction 'ribbons' ranges from a few centimeters to ~23 cm (Fig. 8). In Trench 2 southeast wall, the injection features are more extensive and highly connective, extending a minimum of ~4.95 meters with maximum vertical thickness attaining ~45 cm (Fig. 9).

I distinguish three primary 'types' of liquefaction injection features within FII-FIII:

(a) I1: Well sorted, friable to highly oxidized, yellowish brown to dark yellowish brown fine to medium sand, injected as sill at boundary between FIV and FIII (Figs. 8 and 9).
(b) I2: Well sorted, friable to moderately to highly oxidized, yellowish brown, fine to medium sand with minor gravel, observed as subhorizontal to irregular injection features within FII-FIII (Figs. 8 and 9).
(c) I3: Well sorted, friable and moderately to highly oxidized, yellowish brown, fine to medium sand injected into abundant gravel. The injected sand was observed penetrating and wrapping

around abundant gravel deposits and large fragments of clay/silt that were part of the *in-situ* fill. The gravel clast boundaries display oxidation (Figs. 8 and 9).

Injection features I1-I3 display the most advanced oxidation of all observed liquefaction features. I am unable to determine whether the increase in oxidation for the injection features results from a longer resident time (i.e. sourced from the earliest shaking episodes - for example, the 4 September mainshock) or is primarily influenced by the composition of the preexisting fill layer and proximity to the water table (i.e. lower elevation).

I note here a small injection feature (hereafter named 'IF', cross-sectional area = 48 cm^2) observable in the NW trench wall (beneath drain pipe) that is distinct in color (gray to olive gray) and texture (very fine to fine) from the other liquefaction injection features (i.e. I1-I3) within FII-FIII (Fig. 8 – see IF). This feature exhibits equivalent color and grain size to the youngest liquefaction dike features (i.e. LD1 and LD2 in Trench 2).

4.5.3 Timing sequence for CES liquefaction features

4.5.3.1 Trench 1

I interpret all observed liquefaction features in Trench 1 as occurring during the 2010-2011 CES because the liquefaction features crosscut anthropogenic fill that was placed sometime after ~1950 and no earthquakes of significant PGA capable of inducing liquefaction occurred post 1950 and pre-2010 (Quigley and Bradley, 2015). No paleoliquefaction features (e.g. potentially older pre-CES dike morphologies crosscutting the modern liquefaction dikes) were evident within Trench 1. The observed dike wall boundaries are distinct (see Fig. 13b), with no significant mottling evident.

The dikes in Trench 1 contain no evidence for multiple liquefaction events, although a review of aerial photographs at Avondale Park following each of the main CES earthquakes suggests at least three episodes of liquefaction occurred at the Trench 1 location (see Fig. 5). It is probable that the dike conduits were created during the 22 February earthquake and then reactivated during the 13 June, and 23 December shaking episodes. I did not observe stalling events within the modern dikes within Trench 1, nor was there any evidence of multiple liquefaction episodes (e.g. crosscutting sill drapes near the dike wall boundaries), suggesting that fluid pressures remained high enough during each of the major shaking episodes to insure complete reactivation of the dike conduits (i.e. no material deposited during previous events were left behind). It is probable that the observed infilling sediment for Trench 1 dikes preserve a record of liquefaction during the 23 December 2011 earthquake.

4.5.3.2 Trench 2

I observed evidence of two distinct CES liquefaction events within the Trench 2 trench walls, although I cannot dismiss the possibility that the I1-I3 injection features (present within FII-FIII) may record an earlier shaking episode, such as the 4 September 2010 mainshock event, which created no surface liquefaction features at the study site. Event II (i.e. EII) is the youngest of the modern liquefaction features because it is observed crosscutting Event I (i.e. EI) (see Figs. 8 and 9). EII sediment generally exhibits the lightest color, lowest degree of oxidation, has a consistently small grain size (i.e. very fine to fine sand), and is highly friable. My field observations suggest that the LD1 feeder dike reached the surface (Figs. 8 and 9) and would have created surface sand blows. The sand blows were subsequently removed by surface reworking and/or minor re-grading at the study site during the CES. Importantly, a review of aerial photography indicates that sand blow manifestation did not occur during the December event in the area of exploratory Trench 2. Consequently, I conclude that EII (in Trench 2) infilling dike and sill sediments preserve a record of liquefaction created during the 13 June 2011 earthquake, and not the 23 December event (as probably preserved within Trench 1).

EI is preserved as the largest sill feature (S1) at the FI-FII boundary (Figs. 8 and 9 – see S1 of EIb) and as numerous highly oxidized and, in some instances, highly connective, subhorizontal to irregularly shaped injection features within the FII-FIII layers (Figs. 8 and 9 – see I1-I3 of Ela). Given the large size of the S1 sill and the high volume of the EIa injection features (i.e. I1, I2, I3) within FII-FIII, it reasonable to assume that the majority of E1 liquefaction morphologies were probably created during the 22 February 2011 Christchurch earthquake, which generated the strongest ground shaking in the area during the CES and could have potentially sourced deeper sediment layers containing some percentage of gravel and coarser-grained sand (as observed in S1). However, I cannot rule out that the E1a injection features may also record liquefaction created during the 4 September 2010 mainshock, although we observed no crosscutting relationships in Trench 2 between the EIa and EIb features, and thus both may have been formed during a single shaking episode or could have been created during temporally discrete shaking episodes. The E1a injection sediment may have been unable to reach the surface due to the higher competency of the anthropogenic fill layers during the earliest stages of the CES. The highly oxidized nature of the EIa sands could suggest they have had a longer residence time and are therefore older than the other non-oxidized (or not as highly oxidized) liquefaction sands (e.g. EII and E1b morphologies).

In the NW trench wall of Trench 2 we observe a small injection feature (Fig. 8 – see small injection features ‘IF’) with sand color and grain size equivalent to EII dike sediment (i.e. youngest liquefaction sand), suggesting the two features were probably injected during the same shaking episode (i.e. 13 June 2011 event). The lack of any other irregularly shaped injection features with similar color

and texture, would suggest that the June shaking episode did not create significant injection features within the FII-FIII fill layers similar to I1-I3. The absence of oxidation within the infilling sand for IF also suggests that residence time within the FII-FIII fill layers does influence the amount of oxidation for the liquefaction features. Further, its (small injection feature) low stratigraphic position relative to other E1a injection features implies that the position of the groundwater table is not having a significant (or at least immediate) effect on oxidation of the injection features. If it did, then we would expect the small injection feature to be more oxidized, given the higher groundwater elevations during the 13 June event (compared with the 4 September, 22 February, and 23 December events).

This does not, however, help to resolve the issues of relative timing between the E1a and E1b liquefaction features. Unfortunately, the feeder dike to the S1 sill was not observable in Trench 2. If identifiable, the presence of the dike within the FII-FIII layers would quickly reveal if the episodes are synchronous (i.e. no crosscutting between E1a and E1b) or not (i.e. crosscutting evident). Based upon our trench observations and measurements, the E1b sill increases in length and thickness to the southeast and suggests the feeder dike lies further to the southwest.

4.5.4 Spatial distribution for surface liquefaction features at Avondale Park

Post-CES aerial photography was used to map spatial distribution for manifested surface liquefaction features at Avondale Park. Surface liquefaction features were mapped for the 22 February, 13 June, and 23 December earthquakes (Figs. 5 and 6). As previously noted, surface liquefaction features were not created during or shortly after the 4 September main shock earthquake. The most extensive sand blow development was experienced during the 22 February earthquake, followed by the 13 June and 23 December earthquakes (Figs. 5 and 6). The total area of surface ejecta at the Avondale Park study site was ~4190 m^2 for 22 February, ~2839 m^2 for 13 June, and ~946 m^2 for 23 December earthquakes, with June and December surface ejecta comprising ~68% and ~23% of the February surface ejecta area, respectively (see Figs. 5 and 17a,b).

Mapping of surface liquefaction features at Avondale Park indicates there was recurrent liquefaction at the site, with feeder dike reactivation common. At the Trench 1 location, surface sand blows were generated during each of the 2011 earthquakes, while at Trench 2 surface features were evident only after the February and June events (Figs. 5 and 6).

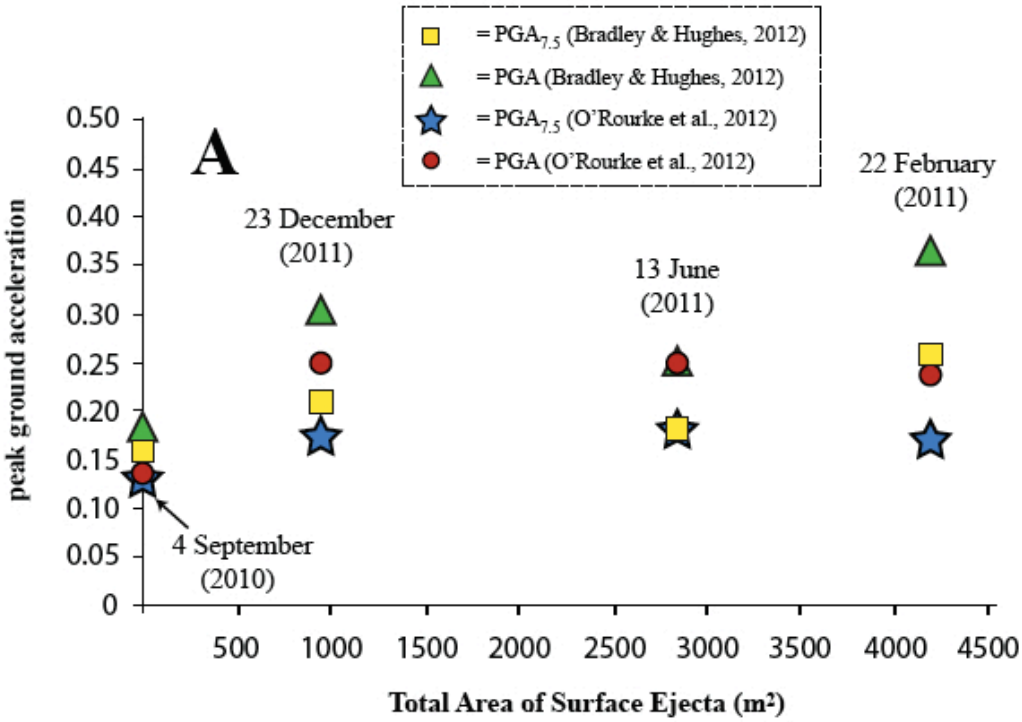

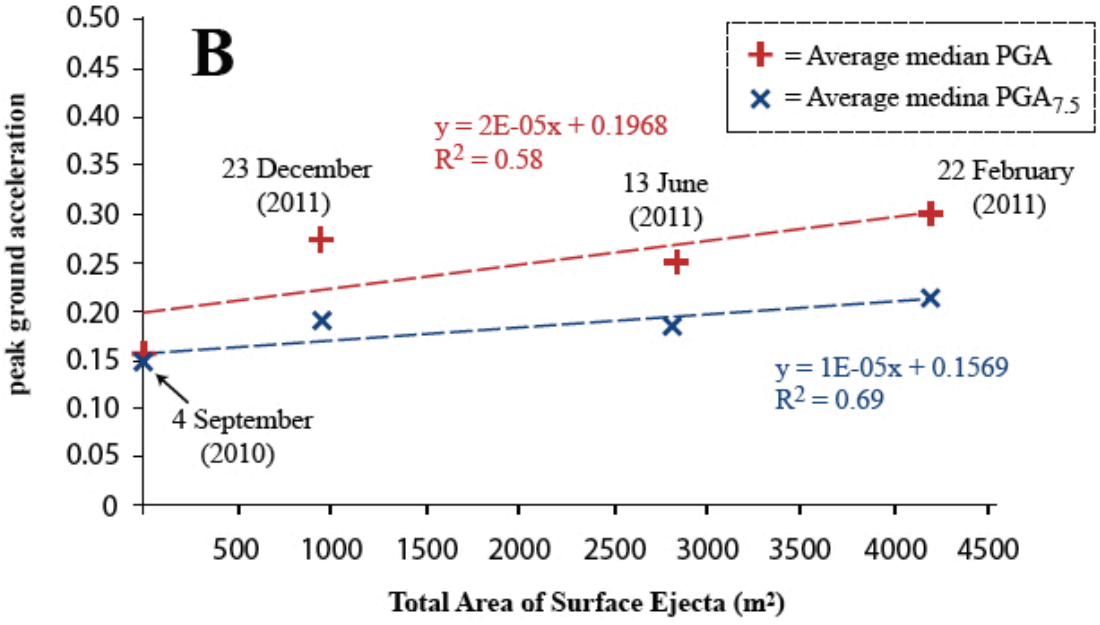

Figure 17. (A) Total area of surface ejecta as a function of PGA ad M_w 7.5-weighted PGA per Bradley and Hughes (2012) and O'Rourke et al. (2012). (B) Average median PGA and $PGA_{7.5}$ from Bradley and Hughes (2012) and O'Rourke et al. (2012) during each of the major CES events. Total area of surface ejecta shows a poor to moderate positive correlation with increasing PGA and $PGA_{7.5}$

4.5.5 Anthropogenic influences on surface and subsurface liquefaction phenomena

4.5.5.1 Surface

Figure 6 depicts the CES liquefaction surface features overlaid on the Christchurch water irrigation plan for Avondale Park. It is noted here that utility trenches or pipes in the shallow subsurface are not influencing the liquefaction source directly, but are, rather, modifying the fluidized sand/silt once the material is ascending through dike conduits within the anthropogenic fill. I used the actual (observed) locations of irrigation pipes in Trench 1 and Trench 2 to geo-rectify the alignment of the map-depicted irrigation plan at Avondale Park. The small shift (~ 1 m towards NW) creates consistency between the irrigation overlay and observed pipes (perforated and solid) in Trench 1 and Trench 2. Perforated pipes (black) were observed within the southern corner of Trench 1 and southwestern half of Trench 2 (Figs. 8 and 9). The pipes are equivalent types (diameter ~65 mm) and are parallel in orientation (see Fig. 6). The center for the Trench 1 and Trench 2 pipes are located at depths of ~50 and ~57 cm, respectively, beneath the existing ground surface. We assume the observed perforated pipes in Trench 1 and Trench 2 correlate with the 'STORMWATER' drain lines depicted (Fig. 6 - see purple dashed line) within the services legend on the water irrigation plan. Both perforated pipes are encased in gravel backfill that has been injected with liquidized sand. In Trench 2 a single solid (white) pipe (~80 mm Class C PVC) was observed that has a similar strike to the perforated pipes (Fig. 6) and is located at a depth of ~49 cm beneath the existing ground surface. The solid pipe is encased in trench fill similar in engineering characteristics to the surrounding anthropogenic fill layers and shows no infiltration by liquidized sediment.

Several sand blow linear arrays show alignment with the water irrigation lines (Fig. 6 – see 'A' and 'B'), implying the pipes and corresponding trenches influence the distribution of liquefaction injecta and surface ejecta. Further, it could be argued that the center for numerous sand blows correlate well with the position of the irrigation pipes, most notably with the perforated 'STORMWATER' pipes. I would expect that the perforated pipes and corresponding gravel-filled trenches would have a greater influence on the distribution of liquefied sediment (compared with solid pipes encased in finer-grained fills) because they would be zones of lower pressure where void space is available to capture and transport liquefaction ejecta. However, other liquefaction features such as the large linear sand blow array (Fig. 6 and 3b – see 'C') near the western-northwestern edge of the playing field do not correlate with the known locations for irrigation lines. It is possible that liquefaction feature C is sourced by a paleo-channel at depth. Although not evident at the study site (due to grading), the LiDAR (Fig. 3a) does show geomorphic features south of Avondale Park (~1 km to south/southwest near Porritt Park) that are consistent with a river trending in a similar north/northeast orientation, suggesting similar features could be present at depth (~3-10 m) beneath the study site. However, there is no distinct paleo-

channel signature (i.e. continuous zone of subsidence) evident on the differential LiDAR (Fig. 3b) in the area of liquefaction feature C. Alternatively, it is possible that feature C reflects the influence of an undocumented utility trench lying that is not depicted on Figure 6.

4.5.5.2 Subsurface

Our field observations suggest that subsurface liquefaction features are modified by three primary anthropogenic factors:

(i) Fill layer boundaries
(ii) Composition and texture (i.e. heterogeneous vs. homogeneous) of individual fill layers
(iii) Drain pipes and utility trenches

The fill layer boundaries (with the exception of FII-FIII boundary) are distinct and represent abrupt changes in texture, relative density, and in some cases (i.e. FIV-FIII boundary) relative moisture. Sill development is most prevalent at the FIV-FIII and FII-FI boundaries, where differences in composition, texture, and relative density are notable. Interestingly, I observed no sill development at the boundary between the native sediment and FI in either of the trenches (see Figs. 7, 8, and 9), suggesting perhaps a higher level of cohesion or relative compaction at this boundary. I note that the development of the sill morphologies at fill boundaries occurred primarily during the earliest stage of liquefaction (i.e. EI), and is less apparent during EII. The EII sill morphologies are observed primarily at the boundary between preexisting liquefaction features and anthropogenic fill or within preexisting liquefaction features (Figs. 8 and 9).

The occurrence of liquefaction injection features I1-I3 appears primarily controlled by the highly heterogeneous nature of FII and FIII, which comprise a chaotic mixture of gravel and small to large sediment clasts set in a silty sand matrix. The high percentage of gravel and small to large (1-10 cm diameter) sediment clasts has increased the amount of available void space (i.e. porosity) in FII and FIII, serving to release high fluid pressures and capture liquefied sand/silt. The liquefaction morphologies in FII and FIII are not observed in FIV or FI, which are more texturally homogenous (i.e. well-sorted). The engineering characteristics of FII and FIII are uniquely anthropogenic, and hence the subsurface expression of liquefaction phenomena carries a distinct human signature. Based upon our field observations, FII and FIII have a high capacity for storing liquefied sediments (see Fig. 9).

In Trench 2, I observed the influence that subdrain pipes and trenches have on the expression and orientation of liquefaction dikes. LD2 (see Fig. 8) is deflected towards and terminates in the gravel-filled utility trench. Liquefied sand has been injected into the gravel backfill and perforated subdrain

pipe (Fig. 14d), providing unequivocal evidence that utility trenches (and perforated drainpipes) offered conduits for transport and deposition of liquefaction ejecta during the CES. Given the connected and pervasive nature of the irrigation system beneath Avondale Park (Fig. 6), the influence of utility trenches on the surface and subsurface expression of liquefaction phenomena could be significant.

4.5.6 Seismic Cone Penetration Test

The SCPT-1 results (see Fig. 10a-c) indicate very stiff sand to clayey sand from ~0-0.3 m and 1.2-1.6 meters. No gravel is interpreted within the soil profile, with the exception of a ~20 cm thick layer of gravelly sand to sand at a depth of ~4 m. The lack of gravel within the upper 15 m supports our assertion that gravel observed in the anthropogenic fill layers (i.e. FII and FIII) is likely to be in-situ (i.e. part of the fill) rather than sourced from deeper native gravel-rich layers. A silty sand to sandy silt layer is interpreted from ~11-12 m depth. The remaining sections of the cone penetration test are interpreted as clean sand to silty sand.

The seismic velocity profile (Fig. 10a) shows consistency (shear wave velocity <100 m/s) downward to a depth of ~3 m. There is a sharp increase in shear wave velocity occur at ~3 m and ~12.5 m depths. From 3 m to ~12.5 m there is an overall increase in shear wave velocity (i.e. 123-174 m/s) and dynamic shear modulus (27-57 MPa). The shear wave velocity increases dramatically downward from 12.5 m and marks the occurrence of dense sand and has a maximum shear wave velocity of 315 m/s (corresponding shear modulus maximum = 198 MPa). The depth to groundwater at the time of the SCPT was 1.8 m.

4.5.7 Liquefaction susceptibility analysis

A liquefaction susceptibility analysis was performed by Sjoerd van Ballegooy on data from SCPT-1 and is compared with 15 nearby cone penetration tests within the park boundaries or adjacent residential properties (Fig. 10b,c). The results of SCPT-1 are overlaid as red traces on the summary graphs (Fig. 10c) to understand the localised soil conditions adjacent to Trench 1 and Trench 2, relative to the surrounding soil conditions. The SCPT-1 tip resistance (q_c) trace is at the upper end of the variability, relative to the surrounding CPT q_c traces, indicating that locally at the SCPT-1 location the soil is slightly denser than the surrounding soil (Fig. 10c). Additionally, the soil behaviour index (I_c) is at the lowest end of the variability relative to the surrounding CPT I_c traces, indicating the sand (in area of Trench 1 and Trench 2) is slightly cleaner and coarser than the surrounding soil (Fig. 10c). This results in a higher assessed factor of safety (FS) of predicted liquefaction triggering relative to the surrounding soil, indicating less predicted liquefaction in the soil profile at the SCPT-1 location (Fig.

10c). This in turn, results in a lower liquefaction susceptibility number (LSN) and cumulative thickness liquefied (CTL) values than any of the surrounding CPTs in the park (Fig. 10c).

At the 4 September 2010 levels of estimated ground shaking (i.e. PGA = 0.24 g), liquefaction triggering is predicted between 4m and 6m below the ground surface at the SCPT-1, whereas a much thicker layer is predicted to liquefy in the surrounding CPTs (Fig. 10c). An LSN of 16 and CTL of ~3 m is predicted (Fig. 10c). At the 22 February 2011 levels of estimated ground shaking (i.e. PGA = 0.38 g), significantly more liquefaction triggering is predicted. An LSN of 28 and CTL of ~6.5 m is generated (Fig. 10c).

The results suggest there is a high degree of soil variability occurring over short distances, implying that the soil conditions at the trench locations vary within the envelope of the conditions shown on Figure 10c. The high relative competency of the SCPT-1 soil profile (compared with other locations in the park) would help explain why no surface manifestations of liquefaction were observed after the 4 September 2010 event in the test pit locations. However, this does not explain why surface liquefaction manifestations were not observed elsewhere within the park (after the September 2010 event), where analysis of CPT profiles suggests the thickness of liquefying soil layers would have been higher. This could indicate that the overlying non-liquefiable crust is able to absorb the liquefied sediments and hence suppress the surface manifestation of liquefaction throughout the entire park area. I would expect the sediment absorption capacity of the fill layers to be greatest at the beginning of the CES (i.e. during the 4 September 2010 event) when available porosity and sediment strength are at a maximum and there is an absence of preexisting fissures or well developed dike conduits for the transmission of liquefied sediment. This combined with uncertainty in the predicted liquefaction triggering and with regards to the PGA at the study site, make it difficult to determine whether sediments were liquefied during the 4 September 2010 earthquake and subsequently suppressed by the anthropogenic fill layers, or if no liquefaction was triggered within the underlying sediments during the September mainshock event.

4.5.8 Evidence of anthropogenic influence from other published studies

At Sullivan Park in Avonside (eastern Christchurch, NZ), Bastin et al. (2015) report that fluvial stratigraphy exposed in Trench 1 and Trench 3 is crosscut by anthropogenic pits, 20-100 cm wide and 20-90 deep, with subvertical walls. The anthropogenic deposits are descried as ‘pit fill’ or ‘cesspits’ consisting of fine sand to silt with silt and soil clasts, lamb bones and fern mat. A review of the trench logs shows CES liquefaction dikes transecting pit fill but also preferentially forming at the boundary between pit fill and the adjacent native fluvial sediments (i.e. along pit walls) (Bastin et al., 2015 – see Fig. 3aA, 4a-c, Fig. 5). Small CES dikes (~10 cm long) are also observed originating within the pitfill

(see Bastin et al., 2015 – see Fig. 4a). In the Trench 2 trench floor, a ~30cm wide modern liquefaction dike is observed adjacent to the pit fill (Bastin et al., 2015 – see Figure 4c). The thick liquefaction dike is an infilled lateral spreading crack and could suggest that weaknesses or relative differences in sediment strength at the trench boundaries are zones where the non-liquefiable crust is more vulnerable to lateral spreading and/or cracking. The formation of several of the CES liquefaction dikes found adjacent to preexisting cesspits suggests that anthropogenic modifications at Sullivan Park have influenced the expression (i.e. geometry, location, size) of modern liquefaction dikes in the subsurface. The influence of the anthropogenic pits on surface patterns of liquefaction is more challenging to determine because the large lateral spreading cracks (Bastin et al., 2015 – see Fig. 2b) created during the CES are the primary control on distribution of surface sand blows and linear arrays (and subsurface liquefaction dikes) and presumably mask any subtle influences resulting from the site cesspits.

Bastin et al. (2016) explored three additional sites in Avonside but the anthropogenic fill layers do not seem to impart any significant influence on dike location and/or geometry, although the liquefaction dikes have difficulty in penetrating the uppermost fill unit comprising 'recent anthropogenic granule to pebble fill' (Bastin et al., 2016 – see Fig. 4, Trench 1). In Kaiapoi, T4 exposes ~20-30 cm of anthropogenic gravel at the trench top, but the only apparent effect on the expression of modern liquefaction is its prevention from reaching the surface in the area of the exploratory trench (Bastin et al., 2016 – see Fig. 8, Trench 4). No anthropogenic fill is reported in Quigley et al. (2013), which examines recurrent liquefaction (expressed as multiple sand blows) during the CES. Finally, Villamor et al. (2016) performed liquefaction trenching in southwest Christchurch (i.e. Lincoln) but encountered no significant fill within the exploratory trenches as part of their paleoliquefaction investigation.

4.5.9 Investigating for paleoliquefaction at Avondale Park

In addition to characterizing modern liquefaction features, Trench 1 and Trench 2 were excavated for the purpose of identifying paleoliquefaction or pre-CES features within the soil profile (i.e. anthropogenic fill and native sediment) at Avondale Park. It has been documented by Obermeier (1996) and Tuttle (2001), and locally by Quigley et al. (2013), Bastin et al. (2015), Almond et al. (2013), and Villamor et al. (2016) that the most optimal locations to search for evidence of paleoliquefaction are in areas where modern liquefaction features (i.e. surface sand blows, lateral spreading cracks, subsurface feeder dikes) have occurred, because modern features commonly utilize pre-existing liquefaction features, such as feeder dikes and lateral spreading cracks. No pre-CES liquefaction features were evident within Trench 1 and Trench 2. All liquefaction features, including dikes and sills are attributed to the 2010-2011 CES and display distinct boundaries without mottling or any significant oxidation – typical of paleoliquefaction features (Bastin et al., 2015). All observed modern liquefaction

features crosscut or are injected into anthropogenic fills which were emplaced above native sediment sometime after ~1950.

4.6 Discussion

The study of liquefaction at Avondale Park in Christchurch, NZ, has provided an opportunity to examine the influence of anthropogenic modifications on the expression of surface and subsurface liquefaction phenomena and establish (based upon our trench locations) a minimum age for the last occurrence of pre-CES (including prehistoric) liquefaction at the study site.

4.6.1 Summary of anthropogenic influences at Avondale Park

CES surface sand blows and sand blow linear arrays are conspicuously aligned with field boundaries and irrigation lines (Figs. 5 and 6), implying their probable and preferential injection into anthropogenic-created discontinuities and voids. Sill and other subsurface injection features are focused at fill layer boundaries and within heterogeneous fill layers (i.e. FII and FIII) comprised of variably sized gravels and cm to multi-centimeter scale clasts of coherent sediment (silt/clay). Modern dike orientation is clearly being influenced by the presence of shallow utility trenches. I observed a dike terminating into a gravel-filled trench in Trench 2. Taken together, this suggests that the highly variable engineering properties for discrete anthropogenic fill layers and the presence of considerable void space within connected anthropogenic subdrain and irrigation utility trenches partially controls the subsurface distribution of liquefaction features and has the capacity to absorb and suppress large volumes of liquidized sand and silt from erupting at the surface. This, in turn, limits the amount of total and differential settlement at a site and mitigates damage (e.g. to foundations, homes) by reducing (to some degree) the amount of liquidized sediment breaching the surface.

4.6.2 Influence from nearby Avon River or depositional environment

It is difficult to determine the influence that the nearby Avon River (both past and present) has had on the spatial distribution of surface and subsurface liquefaction features at Avondale Park. A review of aerial photographs dating back to 1945 indicates there are no distinct historical river/stream channels that transect the study site and lie directly beneath the anthropogenic fill at Avondale Park. Lateral spreading cracks/fissures were not evident at the study site during the CES. The strike of liquefaction dikes measured within Trench 1 and Trench 2 show some alignment with the present day Avon River, but the connection is ambiguous. Surface liquefaction features A and B (Fig. 6) are oriented subparallel to the Avon River, but their strong alignment with water irrigation lines suggests a primary anthropogenic rather than geologic influence. Surface liquefaction feature C (i.e. ~100 m linear sand blow array located along western boundary of playing field; see Figs. 5 and 6) shows SW-NE alignment with remnant (braided?) river features located to the south (see Fig. 3a) of Avondale Park, suggesting a paleo-channel (or numerous coalesced/braided paleo-channels) could be located beneath (and

sourcing) feature C. SCPT-1 indicates there is clean sand to silty sand (consistent with channel deposition) in the area of Trench 1 and Trench 2, from a depth of ~3-11 meters. However, a review of the differential LiDAR for all of the main CES events (Fig. 3b) does not indicate any localized subsidence consistent with a buried paleo-channel in the area of feature C, and thus there is no conclusive evidence to link paleo-channel features with surface and subsurface liquefaction patterns at Avondale Park. Additional trench excavations and boring/penetration tests would be required to determine the factors influencing surface liquefaction feature C. Alternatively, ground-penetrating radar (GPR) or seismic refraction could be performed to potentially reveal underlying anthropogenic or geological features.

4.6.3 Possible controls on volume of liquefaction surface ejecta

The total area for surface liquefaction ejecta at the Avondale Park study site was ~4190 m^2 for 22 February, ~2839 m^2 for 13 June, and ~946 m^2 for the 23 December 2011 shaking episodes (Figs. 5, 17 and Table 2). The June and December surface ejecta comprise ~68% and ~23% of the February output, respectively.

Figure 17a and 17b indicate a positive correlation and overall increase in total area of surface ejecta (m^2) with increasing PGA and $PGA_{7.5}$ as derived from Bradley and Hughes (2012), but suggests that peak ground accelerations were higher at the Avondale Park during the 23 December event compared with the 13 June shaking episode, although the total area of surface ejecta generated during the 23 December earthquake was ~3 times less.

PGA and $PGA_{7.5}$ derived from O'Rourke et al. (2012) (Figs. 17a,b) presents a more ambiguous relationship between peak ground acceleration and the amount of liquefaction surface ejecta during the CES at Avondale Park. Surprisingly, peak ground accelerations are predicted to have been highest during the 13 June event at the study site. This would suggest that PGA values are not resolved in high enough accuracy to demonstrate a clear positive relationship between PGA and increased aerial extent of surface liquefaction ejecta.

If PGA were the only factor influencing the total amount of liquefaction surface ejecta, then we would expect PGA during February to be the highest, followed by the June, and finally, December shaking episodes. Other factors, however, influence the amount of surface liquefaction ejecta, including the local water table elevation at the time of shaking and thickness/condition of the overlying non-liquefiable crust. I predict there was a progressive weakening of the overlying non-liquefiable crust during the CES. Water table elevations were highest during the 13 June event because it occurred during the winter. It is also important to consider that the 13 June (M_w 5.6 and M_w 5.6) and 23 December (M_w

			per Bradley and Hughes (2012)			per O'Rourke et al. (2012)		
Event	**Magnitude** (M_w)	**MSF**	[1]**PGA** (g)	**$PGA_{7.5}$** (g)	**$PGA_{7.5}$/PGA**	[2]**PGA** (g)	**$PGA_{7.5}$** (g)	**$PGA_{7.5}$/PGA**
4 September 2010	7.1	1.11	0.18	0.16	0.89	0.14	0.13	0.93
22 February 2011	6.2	1.41	0.36	0.26	0.72	0.24	0.17	0.71
13 June 2011	6.2	1.41	0.25	0.18	0.72	0.25	0.18	0.72
23 December 2011	6.1	1.44	0.30	0.21	0.70	0.25	0.17	0.68

Table 2. Summary of moment magnitude (M_w), magnitude scaling factor (MSF), peak ground acceleration (PGA), and 7.5-magnitude weighted peak ground acceleration ($PGA_{7.5}$) for 4 September 2010, and 22 February, 13 June, and 23 December 2011 earthquakes at Avondale Park study site. The 13 June and 23 December 2011 aftershocks each comprised two separate earthquakes within 80 minutes of each other. The first earthquake is inferred to have caused elevated pore water pressure in the potentially liquefiable soil, making the soil material more susceptible to liquefaction in the subsequent earthquake. Earthquake magnitudes for 13 June and 23 December 2011 earthquakes have been increased to include the effects of the initial (foreshock) smaller earthquake, in accordance with Tonkin and Taylor (2013) and van Ballegooy et al. (2014).

5.8 and M_w 5.9) 2011 aftershocks each comprised two separate earthquakes (i.e. doublets) within ~80 minutes of each other (van Ballegooy et al., 2014c). The first earthquake is inferred to have caused elevated pore water pressure in the potentially liquefiable soil, making the sediment more susceptible to liquefaction in the subsequent earthquake. We propose that the elevated water table conditions during the 13 June event could account for the increase in total surface ejecta area during the June event relative to the 23 December shaking episode.

Although many scenarios involving a variety of causal factors are possible, I favor the following explanation for the observed surface liquefaction ejecta:

(1) The 4 September 2010 mainshock had less than expected (i.e. none observed) surface ejecta because it was the first event (when the overlying non-liquefiable crust was relatively strong compared with post-September conditions), PGAs were low (see Table 2 for median PGA and $PGA_{7.5}$) compared with the other major CES events, and liquefaction dike intrusion was relatively inefficient. The liquefied sediment was effectively absorbed into the overlying anthropogenic fill layers (Figs. 8 and 9), thereby suppressing any potential surface expression.

(2) The 22 February 2011 shaking episode had the strongest PGA (Table 2 – see Bradley and Hughes [2012]) and most liquefaction. Cracking in the overlying crust occurred and liquefaction dike intrusion was efficient as evidenced by the numerous sand blows and linear sand blow arrays at the study site during the February earthquake.

(3) The 13 June 2011 event comprised two strong shaking events (separated by ~80 minutes), generated relatively high PGAs (Table 2) at the study site, and occurred during the winter when the water table was higher (compared with September, February, and December earthquake events). The higher water table would have increased water pressure and the thickness for liquefiable sediments.

(4) The 23 December 2011 event comprised two shaking episodes (separated by ~80 minutes), similar to slightly stronger (compared with the June event) at the study site (Table 2), but occurred in the summer when the water table was lower.

4.6.4 Correlation of observed subsurface liquefaction features with CES shaking episodes

A review of aerial photographs provides surface evidence for at least 3 liquefaction-inducing events at Avondale Park. I attribute them to the 2010-2011 Canterbury earthquake sequence because each event either crosscuts or intrudes into anthropogenic fills emplaced sometime after ~1950. A

review of historical seismicity suggests there have been no previous earthquakes during the past ~65 years that would have exceeded the required liquefaction triggering threshold (Bastin et al., 2015). I do note that I was unable to determine the relative contribution for each of the doublet shaking episodes during the 13 June and 23 December earthquakes, because, in each case, aerial photographs were taken only after the second shaking episode (van Ballegooy et al., 2014c). Combining an analysis of aerial photos following each of the major CES events with trenching and detailed logging of subsurface CES liquefaction features and their hosting sediments (i.e. native sediment and anthropogenic fill) enables me to cautiously correlate specific shaking episodes with the preserved subsurface liquefaction features (i.e. dikes, sills, irregular injection morphologies) observed within Trench 1 and Trench 2.

Liquefaction dikes in Trench 1 preserve only a single shaking episode, although sand blows were created at the surface above Trench 1 during each of the major 2011 events (i.e. 22 February, 13 June, 23 December earthquakes) (Figs. 5 and 6). I conclude that liquefaction dikes in Trench 1 record the final major shaking episode occurring on 23 December 2011. I found no evidence for the preservation of multiple events within the Trench 1 liquefaction dikes, suggesting reuse of the dike conduits was complete during the subsequent June and December earthquakes (assuming initial formation of the liquefaction dikes occurred during February shaking episode).

In Trench 2, surface sand blows were manifested during the 22 February and 13 June 2011 shaking events, but not during the 23 December episode (Figs. 5 and 6). My field observations suggest liquefaction dike LD1 (Figs. 8 and 9 – LD1) in Trench 1 extended to the surface and would have formed sub-aerial sand blows (see Fig. 5). The resulting sand blows have been subsequently removed or reworked by natural and man-made processes. Based upon these observations I conclude that the youngest liquefaction episode (EII – see Figs. 8 and 9) preserved in Trench 2 records the 13 June 2011 shaking episode.

EI (see Figs. 8 and 9; S1 and I1-I3) is crosscut by EII and therefore must have occurred prior to the 13 June shaking episode. Based upon the significantly greater thickness and length of the EI sill morphologies (see S1 and I2) as well as the high volume of liquefaction injecta within FII-FIII, I conclude that EI liquefaction features probably record the 22 February 2011 shaking episode, which recorded the highest ground accelerations at the Avondale Park study site during the CES. I do, however, speculate that the EI injection features (i.e. EIa; see Figs. 8 and 9) within FII-FIII may potentially record (at least partially) liquefaction during the 4 September 2010 mainshock earthquake. Surface sand blows were not created at the Avondale Park study site during the 4 September 2010 earthquake, but liquefaction susceptibility analyses on SPCT-1 and nearby CPTs (Figure 10c) suggest that liquefaction was likely to have occurred within the subsurface during the 4 September 2010 earthquake and that cumulative thickness of liquefying soils likely ranged from ~3-7.5 meters (Fig.

10c). Thus, the absence of manifested liquefaction at the ground surface at Avondale Park is somewhat surprising. If liquefaction did occur during the September mainshock then it is reasonable to assume that at least some portion of the liquefaction injection features (Figs. 8 and 9: see I1-I3) within FII-FIII were created at this time, when ground shaking intensity was not strong enough (and fluid pressures not high enough) to cause cracking in the overlying non-liquefiable crust and liquefaction dike formation was inefficient.

I recognize that the liquefaction injection features (i.e. I1-I3) within FII-FIII layers may also have been created during the June and December earthquakes. However, a comparison of liquefaction sediments created during the June and pre-June shaking episodes suggest the sediments are distinctly different, with June (and December) sediments typically finer-grained, lighter in colour, more friable, and considerably less oxidized. For instance, based upon composition, texture, and color, the small injection feature (labeled IF in Fig. 8) observed in the Trench 2 NW wall is unequivocally related to the EII liquefaction episode (including formation of LD1 and LD2) and shows significantly less oxidation compared with the highly oxidized liquefaction injection sands for I1-I3 at similar stratigraphic levels (i.e. positioned near the base of FII-FIII). The notable differences in oxidation between the EII and EI (particularly EIa) liquefaction features suggests that the degree of oxidation is, at least to some degree, time-dependent, with older sediments showing more advanced oxidation (i.e. reddish-orange colour). Consequently, if injection of sand (within FII-FIII) were to occur during the June and December events it would look similar to liquefaction sediment within LD1 and LD2 (as well IF).

The absence (with the exception of IF) of EII injection features within the Trench 2 FII-FIII layers probably reflects the reuse of pre-existing dike conduits that were initially formed during the 22 February earthquake. Once cracks/fissures were created in the non-liquefiable crust during the February event, there was no longer any need for liquefied sediment (during post-February shaking episodes) to penetrate laterally into the FII-FIII layers because preexisting dike conduits provided pathways to the surface (and the September and February events exploited the majority of any available void space).

Unfortunately, the explanation provided above does not resolve the issue of timing between EIa (Figs. 8 and 9; see I1-I3) and EIb (Figs. 8 and 9; see S1). If the feeder dike for S1 were observable then the relative timing relationship of EIa and EIb could be quickly resolved. Instead, I am left to only speculate on whether the highly oxidized injection features within FII and FIII are synchronous with the formation of EIb or preserve a record of an earlier shaking episode (i.e. September mainshock).

With regards to liquefaction during the September mainshock, it is possible that liquefaction susceptibility analyses have overpredicted potential liquefaction at Avondale Park and that none occurred during the 4 September 2010 main shock, although this is unlikely given the abundance of

CPT data and strong correlation between observed and predicted liquefaction in other sections of Christchurch (van Ballegooy, 2014c). A more plausible explanation is that the existing anthropogenic fills were able to absorb and suppress the liquefaction signature throughout the park area during the 4 September main shock earthquake. It is suggested here that prior to the CES the soil profile (including anthropogenic fill layers) at the Avondale Park study site were in an optimal condition (compared with conditions during and after the CES) for absorbing and capturing liquefied sediments. The shaking intensity during the September mainshock event was comparatively low (Table 2), and consequently it would have been difficult to generate cracks in the non-liquefiable crust and form liquefaction dikes. I envision a sequence of progressive deformation (and reduction of confining pressures) within the overlying non-liquefiable crust (including the anthropogenic fill layers) with each successive ground shaking episode during the CES.

4.6.5 Influence of anthropogenic modifications

I observed gravel-filled utility trenches (and enclosed perforated pipes) influencing the architecture of subsurface liquefaction features. Within Trench 2, a liquefaction dike was observed refracted toward (and terminating within) a nearby gravel trench, highlighting the release of fluid pressure into an anthropogenic feature. It is conceivable, and probable based upon our trench observations, that there are numerous dikes terminating into subsurface trenches beneath the surface at the Avondale Park study site. This phenomenon may be pervasive beneath the surface at Avondale Park and its impact on modifying liquefaction architecture and absorbing liquidized sediment may be considerably underestimated throughout Christchurch. This raises the important question: How much did surface (e.g. roadwork, building construction) and subsurface (e.g. trenching) anthropogenic modifications throughout the City of Christchurch influence the expression and total volume of liquefaction ejecta created during the 2010-2011 CES? Following the 2010-2011 CES, > 500,000 tonnes of liquefaction-generated sediment was cleaned-up and stored (Villemure et al., 2012). This study suggests that the volume of sediment reaching the surface at Avondale Park (and in the surrounding residential areas) would have been significantly greater if subsurface and surface anthropogenic modifications were absent. Thus, in certain cases, anthropogenic modifications may have mitigated (i.e. reduce) the overall hazard associated with liquefaction.

4.6.6 The absence of paleoliquefaction at Avondale Park study site

No paleoliquefaction is evident within the site native sediment in Trenches 1 and 2, implying that native sediments at Avondale Park have a lower susceptibility to liquefaction than the surrounding ‘red-zone’ areas closer to the Avon River. This finding is consistent with studies by Bastin et al. (2015, 2016) who find that parameters (i.e. dike width, sill length/thickness) for modern CES liquefaction

features are consistently in exceedance of those for equivalent paleoliquefaction features, suggesting that ground shaking intensities experienced during the 2011 Christchurch earthquakes (e.g. 22 February and 13 June events) are rare. Our radiocarbon age (2σ = ~1209 AD to 1274 AD) for detrital charcoal within NS (at bottom of Trench 1) implies that liquefaction has not occurred at Avondale Park (in the areas of Trench 1 and Trench 2) during the past 750-800 years, precluding regional faults such as the Alpine fault (last earthquake ~1717 AD) or Porters Pass fault (last shaking event ~500-600 yr BP) as potential liquefaction-inducing sources during that time period. Furthermore, there was no evidence that the June 1869 M_w ~4.8 Christchurch earthquake produced subsurface liquefaction at Avondale Park.

Establishing a minimum recurrence interval for liquefaction-triggering ground shaking levels at a study site is important for informing land zoning and planning strategies. Investigations in 'red-zoned' land areas (e.g. Bastin et al., 2015, 2016; Quigley et al., 2013) may be optimal for documenting and understanding liquefaction process (because preservation of liquefaction phenomena is high) but is unfavorable for informing land zoning in Christchurch, because no future building is proposed in 'red-zoned' areas. Therefore, future studies aimed at understanding the impact of liquefaction on residential and commercial structures should target land with lower liquefaction vulnerability (i.e. TC1-TC3) to examine site response over time to various shaking conditions. Trenching in TC1-TC3 land (i.e. Avondale Park) provides an important subsurface record of a site's behavior to seismic shaking and a valuable complement to the study of liquefaction-induced surface features.

Currently, shaking conditions experienced during the most severe 22 February 2011 earthquake are accepted as the standard when considering design of foundation systems (van Ballegooy, personal communication) for new residential/commercial structures and infrastructure. As a result of this, cost for new foundation systems is considerably high to the owners because only a worst-case scenario (i.e. 22 February 2011 shaking conditions) is considered and reflective of shaking intensities that are expected to recur every ~3-7 ky (Mackey and Quigley, 2014; Sohbati et al., 2016; Borella et al., 2016b). In most cases, subsurface trenching becomes the only means of understanding a site's behaviour to prehistoric shaking events because surface features (such as sand blows and sand blow arrays) are vulnerable to reworking by natural elements (e.g. water, wind) or anthropogenic influences (e.g. surface grading).

4.6.7 Potential challenges in identifying liquefaction features in anthropogenic fill

My trench observations suggest that the identification of CES liquefaction features within anthropogenic fill layers can be poor. Oxidation of liquefaction dikes is consistently highest with the oldest fill layer (i.e. FIV) and in several cases has obscured the dike wall boundaries to the degree that

it is difficult to discern the modern liquefaction feature. Figure 12c highlights the degree of oxidation typical within the FIV layer, where a reddish-orange halo extending several centimeters beyond the actual dike margins is observed. This degree of oxidation has occurred in a period of less than five years and suggests that modern liquefaction features may be rapidly obscured over annual or decadal time periods to the level that identification is challenging to impossible. Likewise, the higher porosity/permeability and heterogeneous nature of the FII and FIII fill layers enabled diffusion of the liquefaction dikes (see Fig. 12b) and consequently made tracking of the wall boundaries difficult. Future studies documenting liquefaction features in anthropogenic fill should be aware of these potential challenges.

4.7 Conclusions

This study suggests anthropogenic modifications influenced the geologic expression of surface and subsurface liquefaction phenomena during the CES. Anthropogenic fill and utility trenches are highly effective in absorbing liquefaction injecta and suppressing its surface manifestation. Liquefied sediments are captured at fill-layer boundaries and within anthropogenic layers containing the highest abundance of gravel and cm-scale sediment clasts. The utility trenches (and contained perforated pipes) act as conduits for transport and deposition of liquefaction ejecta.

Recurrent liquefaction is evident at Avondale Park where surface sand blows and linear arrays were observed during the 22 February, 13 June, and 23 December 2011 earthquake, but absent during the 4 September main shock. It is possible that the most highly oxidized injection features, contained within the lower level fill horizons, preserve a record of liquefaction during the 4 September 2010 main shock.

I did not observe any pre-CES liquefaction (including prehistoric liquefaction) features within the native soil profile at Avondale Park. Radiocarbon dating of detrital charcoal within the youngest native sediments suggests liquefaction has not occurred at the study site for at least the past 750-800 years, suggesting earthquakes generating high intensity ground shaking analogous to the 2011 Christchurch earthquakes are rare.

I present one of the first studies to systematically examine the impact of buried infrastructure on channelizing and influencing surface and subsurface liquefaction morphologies. This investigation further highlights the importance of trenching in TC3-equivalent land to refine our understanding of past ground shaking conditions at potentially buildable sites – for use in liquefaction susceptibility analyses and future land zoning decisions/policy.

4.8 Appendix 1: Supplementary Data

Factual Geotechnical Report for Seismic Cone Penetration Test (SCPT) Data - Performed by Fugro Geotechnical (NZ)

FACTUAL GEOTECHNICAL REPORT

SEISMIC CONE PENETRATION TEST (SCPT) DATA

AVONDALE PARK
CHRISTCHURCH
NEW ZEALAND

Survey Period: 26/2/2015
Fugro Geotechnical (NZ) Job No: UOC021501

Prepared For: University of Canterbury
Department of Geological Sciences
University of Canterbury
PB4800, Christchurch 8140

Client Reference No: N/A
Fugro Report No. UOC021501

0	Final	C. Cheng	A. Twiss	G. de Pascale	13/3/2015
Rev	**Description**	**Prepared**	**Checked**	**Approved**	**Date**

CONTENTS

FIGURES

TABLES

APPENDICES

ABBREVIATIONS

ASTM	American Society for Testing and Materials
BGL	Below Ground Level
CPT	Cone Penetration Test
FGNZ	Fugro Geotechnical (NZ)
GL	Ground Level
ISSMGE	International Society of Soil Mechanics and Geotechnical Engineering
PCPT	Piezocone Penetration Test
SBT	Soil Behaviour Type
SOCAR	Summary of Calculations and References

1. INTRODUCTION

1.1 Background

Fugro Geotechnical (NZ) (Fugro), a trading division of Fugro-BTW Ltd, was commissioned by University of Canterbury (Client) to undertake a geotechnical ground investigation to obtain information on ground conditions at a site, in accordance with the Scope of Works provided.

1.2 Purpose

The purpose of this report is to present the Client with certain factual geotechnical data collected on site to assist in the characterisation and interpretation of the sub surface soils at the location of a park. These include Soil Behaviour Type (SBT) and soil parameter profiles. The SBT and soil parameter profiles are to assist geotechnical interpretation and these data should only be used by a suitably qualified Geotechnical Engineer or Engineering Geologist.

Cone Penetration Testing (CPT) is a rapid and cost effective means of acquiring geotechnical and geo-environmental information. CPTs can be used to provide a continuous ground profile, infer soil stratigraphy and soil properties. CPTs provide information for foundation bearing capacity, soil liquefaction assessments and soil parameters for further engineering assessment.

All Fugro cones are developed in-house at Fugro's laboratory in Leidschendam, The Netherlands. Fugro cones are calibrated on a 12 monthly basis or when taken out of service due to the cone approaching its zero drift limits.

The measured data provided as a digital excel file include:

- Cone Resistance, q_c (MPa)
- Sleeve Friction, f_s (MPa)
- Pore Pressure, u_2 (MPa)

The derived data provided as plots in .pdf format include:

- Net Cone Resistance, q_{net} (MPa)
- Friction Ratio, R_f (%)
- Excess Pore Pressure Index, B_q
- Soil Behaviour Type (Robertson (1990) Soil Classification) – indicative only
- Undrained Shear Strength, c_u (kPa) for values of N_k = 20 and N_k = 15
- Relative Density, D_r (%) for values of K0 = 2.0 and K0 = 0.5
- Angle of Internal Friction, Φ' (degrees)
- SPT N_{60} (blows)

All of the data provided shall be used in conjunction with the Fugro Geotechnical (NZ) Summary of Calculations and References (SOCAR) presented in Appendix A.

1.3 CPT Site Location

The site is located at Avondale Park. The site is a flat area of land measuring approximately 39,630 m^2 on which is situated supporting facilities such as toilet and playground. The site is bounded by Mervyn Drive to the North, and by residential properties in the other three directions. The closest surface water feature is the Avon River which is approximately 220 m to the North of the site.

The site and CPT location map is as Figure 1.1.

Figure 1.1: Site and CPT Location Map at Avondale Park, Christchurch[1]

(NB: This plan is not drawn to scale and must not be used for future site measurements)

1.4 Limitations

Subsurface investigations are designed to obtain information that is not available from surface investigations alone. Because subsurface conditions may be variable across any given site, no single point of investigation is exhaustive to the extent that all soil conditions across the site are revealed and/or characterised. Conditions that are not present at the CPT location may therefore be present beneath the site, in particular where narrow linear features or where isolated pockets of variable ground conditions may exist.

The Fugro Service Warranty presented in Appendix B outlines the limitations of this factual geotechnical report. It should be noted that the Service Warranty does not in any way supersede the terms and conditions of the contract between Fugro and University of Canterbury.

1.5 Project Responsibilities and Use of Report

Responsibilities of the Client and Fugro regarding preparation of this report are detailed in Table 1.1.

Table 1.1: Geotechnical Project Responsibilities

Company	Status	Responsibility
University of Canterbury	Client	Project commissioning Contract holder Scope of Work Positions of required tests Locations clear of underground services or obstructions
Fugro Geotechnical (NZ)	CPT Contractor	Client liaison Project / site management Supply of geotechnical staff Supply of coordinate information of geotechnical test Geotechnical testing

The results of this Factual Geotechnical Report shall only be used for the purpose for which it was commissioned. Results however may possibly suit alternative uses. The suitability of this Factual Geotechnical Report shall be reviewed if the proposed development or activity changes.

2. PCPT GROUND INVESTIGATION

2.1 Scope of Work

The Scope of Work requested includes One (1) Seismic Piezocone Penetration Tests (SCPT) at Avondale Park, Christchurch, New Zealand at locations selected by the Client to a depth of 15 metres below existing ground level.

2.2 Ground Investigation

A geotechnical intrusive investigation was undertaken on 25th February, 2015. The investigation was undertaken using the 6x6 twenty Tonne (20 t) Fugro Geotechnical (NZ) CPT truck to push a 15 cm^2 piezocone into the ground to collect geotechnical data.

Prior to the investigation being undertaken, underground services at the site were located by the Client.

2.2.1 *In-situ* Tests

One (1) SCPT was undertaken at the location selected by University of Canterbury. Appendix A contains all of the information relevant to the SCPTs undertaken.

The tests were performed in accordance with ASTM D5778-12 "Standard Test Method for Electric Friction Cone and Piezocone Penetration Testing in Soils" and FGNZ-001 “Method Statement for Cone Penetration Testing”.

The SCPT fell within the ISSMGE Accuracy Class 1.

A summary of the SCPTs performed, with the test termination details for the SCPT, is provided in Table 2.1.

Table 2.1: SCPT Summary

CPT SUMMARY				
SCPT No.	**Target Depth [m BGL]**	**Penetration [m BGL]**	**Refusal/Stop Criteria**	**Maximum Tip Resistance [MPa]**
SCPT1	15	15.25	**D**	30.18
Refusal/Stop Criteria: **D =** Depth Achieved **E =** Excess Thrust **C =** Cone End Resistance **I** = Cone Inclination **F** = Friction **R =** Rod flex **A=** Anchor Failure **O =** Other				

2.2.2 Exploratory CPT Locations and Groundwater

The coordinates and indicative groundwater depths for the CPT test locations are presented in Table 2.2.

Groundwater depths are indicative only and cannot be used for hydrogeological interpretation. The depths presented are measured in the CPT hole on the day of the investigation and where applicable, derived from the pore pressure recorded by the cone.

Coordinates presented have been acquired using a Garmin eTrex 10 GPS device that has a horizontal accuracy of approximately +/- 3.0 m.

The geodetic datum that the coordinates are based on is the New Zealand Geodetic Datum 2000 (NZGD2000). The Map Projection for the project is New Zealand Transverse Mercator 2000 (NZTM2000), CM 173°E.

The user of the coordinate information presented in this report must consider the accuracy of the measurements. This is particularly important where the intended use may differ from the original intentions or site elevations are proposed to be changed.

Table 2.2: Exploratory CPT Coordinates and indicative groundwater depths

CPT SUMMARY						
SCPT No.	**Date**	**Time (NZDT)**	**Coordinates NZGD2000, NZTM2000 CM 173°E**		**Indicative Ground Water Level [m BGL]**	
			Easting [m]	**Northing [m]**	**Derived**	**Dipped**
SCPT1	25/2/2015	12:16a.m.	1574997	5183131	1.8	N/A

3. SEISMIC CPT INVESTIGATION

3.1 Seismic CPT Introduction

Seismic Cone Penetration Tests (SCPT) consists of a combination of ordinary Cone Penetration Tests (CPT) and Seismic Down-hole Tests. With this combi-cone the normal CPT parameters such as tip resistance, sleeve friction, slope and pore pressure can be measured.

The Seismic 'down-hole' test measures the travel time interval of body waves travelling between a wave source on the ground at the surface and an array of geophones incorporated in the seismic cone penetrometer in the ground.

The seismic cone penetrometer is a dual digital seismic cone and contains 2 three axial geophones, a half meter apart. The 3-axial geophone has one component in the x-direction, one in the y-direction and one in the z-direction. This way the horizontal as well as the vertical components of the primary pressure wave (P-wave) and the secondary shear wave (S-wave) can be measured. Wave velocities can give an indication of ground characteristics, such as low strain modulus.

3.2 Seismic CPT Procedure

A dual seismic cone is pushed into the ground. To measure the shear wave, a steel beam is coupled to the ground surface by placing it under the CPT truck (Figure 3.1). Shear waves are generated by horizontally striking the steel beam by a sledgehammer. The sledgehammer that strikes the beam acts as a trigger, initiating the recording of the seismic wave trace. Before measurements are taken, the rods are decoupled from the CPT truck to prevent energy transmission down the rods.

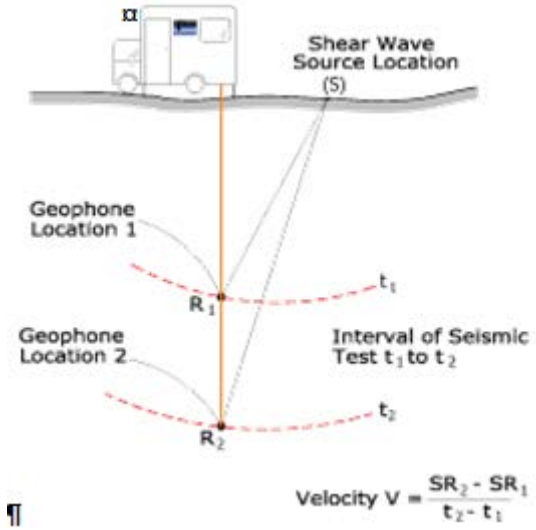

Figure 3.1: Seismic Source with Model Showing Shear Wave and Geophone Locations

At least three waves (shots) are recorded for each test depth sample interval so the operator can check consistency of the waveforms. Shear wave data is sampled at a frequency of 10kHz (10,000 samples per second) and compression wave data is sampled at 100kHz (100,000 samples per second). To maintain a desired signal resolution, the input sensitivity (gain) is increased with depth.

Offset distances of the beam from the cone and the location of the geophone are all taken into account in calculations.

The test procedure includes the following:

- Interrupting the CPT test at fixed distances for performing seismic tests

- Activating the seismic wave source and recording of the geophone signals, if necessary with re-activating to permit stacking.
- Resume CPT test

The data is recorded with a seismic data acquisition system.

3.3 Seismic CPT Test Result

Six (6) seismic CPT tests were performed: on the 25th February 2015 at locations SCPT1 as shown in Figure 1.1.

The seismic shear waves generated for each depth were polarised before analysing in order to achieve maximum accuracy.

The shear wave velocities profiles were estimated by using a combination of the VSP method, the cross correlation technique and the forward modelling and the downhill simplex method (FMDSM).

The advantage of Forward modelling and the downhill simplex method (FMDSM) compare to conventional data processing method is that it takes the refraction of shear waves into consideration during profile calculations(Baziw, 2002).

The test results include dynamic (low-strain) elastic parameters, using estimated densities. The following basic equations apply to the Shear wave velocities.

$$V_s = \sqrt{\frac{1}{2(1+\nu)} * \frac{E}{\rho}} \qquad = \sqrt{\frac{G}{\rho}}$$

Where

$\mathbf{V_s}$=	S-wave velocity	[m/s]
ρ =	density of ground	[ton/m^3]
$\dot{\mathbf{v}}$ =	dynamic Poisson ratio	[-]
E =	dynamic Young's modulus	[kPa]
G =	dynamic Shear modulus	[kPa]

The dynamic shear modulus (G) of the soil is a standard for the stiffness of the soil, and an important parameter in the dynamic analysis. The shear modulus is determined from the interval shear wave velocity (Vs) and the estimated density of the layers.

$\mathbf{G = \rho\, v_s^2}$ [kPa]

The density of the soil is estimated using the following formula.

$\mathbf{\gamma/\gamma_w = 0.27\,[\log Rf] + 0.36\,[\log(q_t/p_a)] + 1.236}$

Where

Rf =	Friction Ratio	[%]
$\mathbf{Q_t/p_a}$ =	Dimensionless Cone Resistance	[-]

Please note that the density and dynamic shear modulus provided are indicative only, it is recommend that the Client check these values before using them for geotechnical interpretation.

The results are shown in tables 3.1.

Table 3.1: SCPT11

		vs	ρ	G
depth from	depth to	velocity	density	dyn shear mod
[m] GL	[m] GL	[m/s]	[t/m3]	[MPa]
0	0.50	91	1.9	15
0.5	1.00	96	1.8	17
1	1.50	97	1.9	18
1.5	2.00	95	1.9	17
2	2.50	93	1.7	15
2.5	3.00	100	1.7	17
3	3.50	123	1.8	27
3.5	4.00	141	1.9	37
4	4.50	134	1.9	33
4.5	5.00	144	1.8	37
5	5.50	113	1.8	23
5.5	6.00	157	1.8	46
6	6.50	132	1.9	33
6.5	7.00	164	1.9	51
7	7.50	185	1.9	64
7.5	8.00	158	1.9	47
8	8.50	149	1.9	42
8.5	9.00	162	1.9	50
9	9.50	143	1.9	39
9.5	10.00	159	1.9	48
10	10.50	181	1.9	62
10.5	11.00	179	1.9	61
11	11.50	153	1.8	42
11.5	12.00	159	1.7	43
12	12.50	174	1.9	57
12.5	13.00	225	2.0	103
13	13.50	257	2.0	134
13.5	14.00	312	2.0	198
14	14.50	315	2.0	198
14.5	15.00	262	2.0	139

4. REFERENCES

ASTM D5778-12 "Standard Test Method for Electric Friction Cone and Piezocone Penetration Testing in Soils".

Robertson, P.K. (1990), “Soil Classification using the Cone Penetration Test”, Can. Geotech. Jnl., Vol. 27, No. 1, pp. 151-158.

[1] Retrieved 12/3/2015 from
http://canterburymaps.govt.nz/Viewer/#webmap=0c4c5d8e982c4704b22da9de51cd1ba3

5. DISTRIBUTION

One copy of this report has been distributed as follows:

CLIENT: University of Canterbury
Attn: Josh Borella
PB 4800, Christchurch, 8140
Jwborella@gmail.com

Appendix A
Piezocone Penetration Tests

Appendix A.1
SCPT1

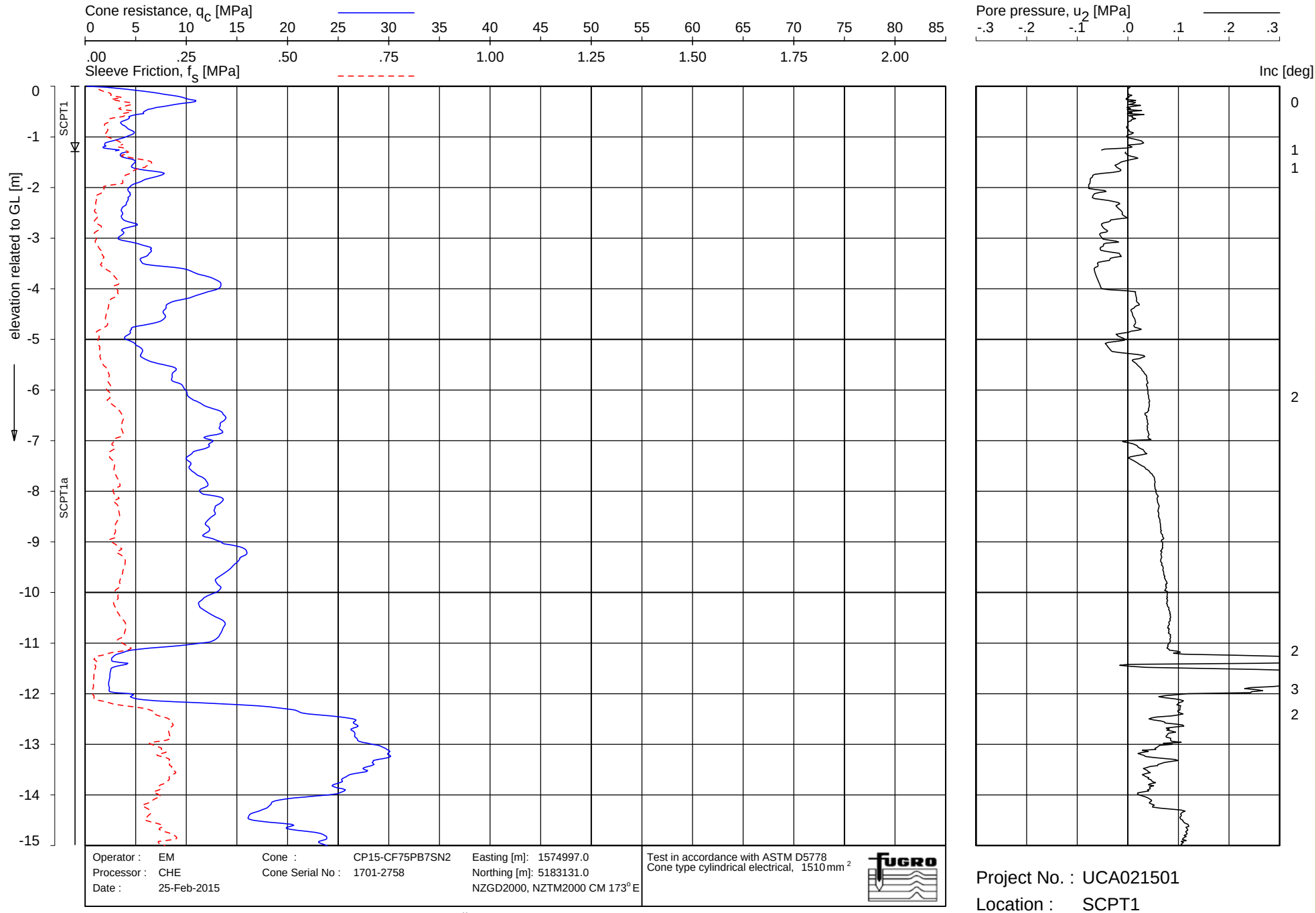

Operator :	EM	Cone :	CP15-CF75PB7SN2	Easting [m]:	1574997.0
Processor :	CHE	Cone Serial No :	1701-2758	Northing [m]:	5183131.0
Date :	25-Feb-2015			NZGD2000, NZTM2000 CM 173° E	

Test in accordance with ASTM D5778
Cone type cylindrical electrical, 1510 mm²

PIEZO CONE PENETRATION TEST

Client: UNIVERSITY OF CANTERBURY
Project: AVONDALE PARK

Project No. : UCA021501
Location : SCPT1
Equipment : REO66 20T MAN 6x6

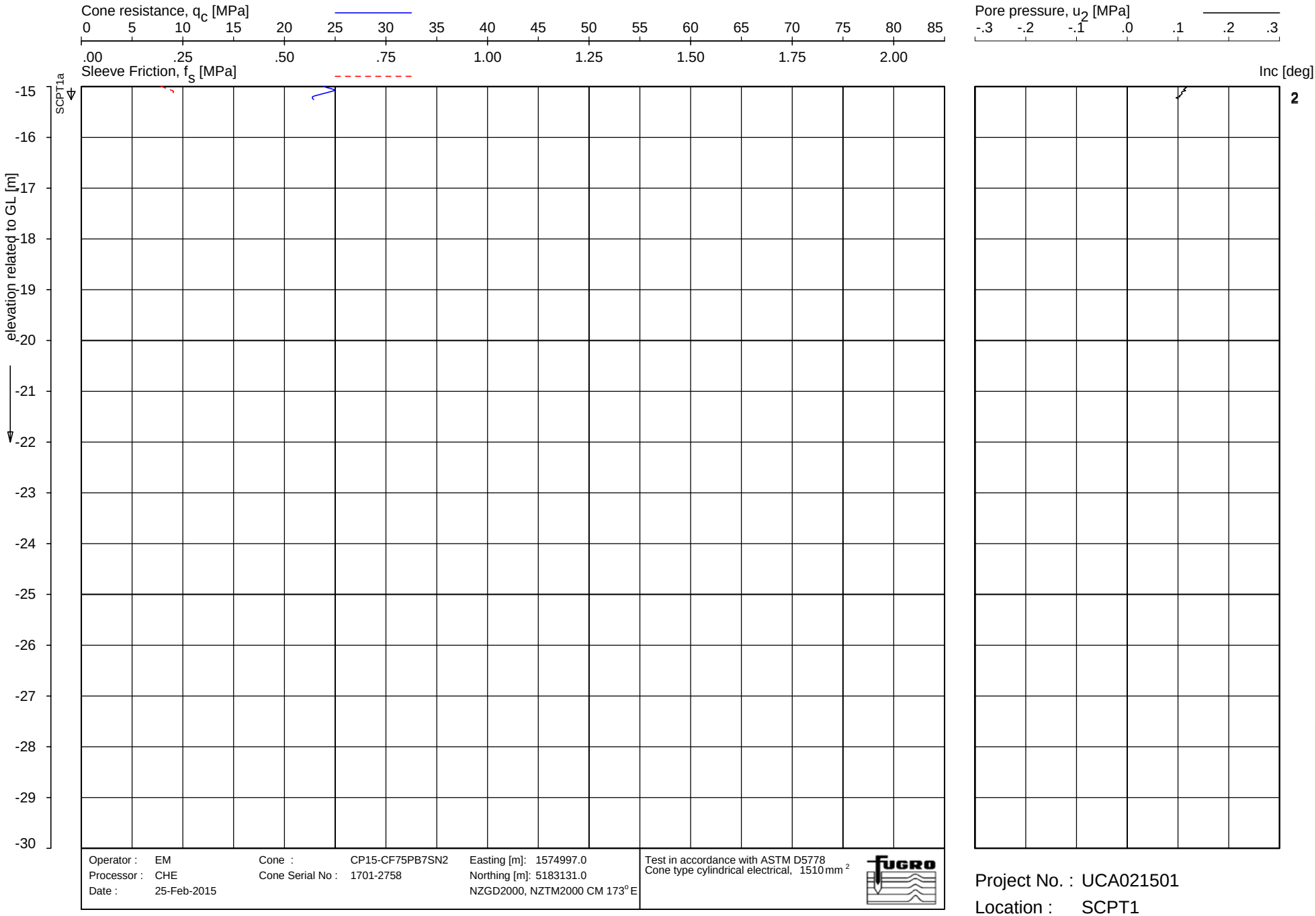

Operator :	EM	Cone :	CP15-CF75PB7SN2	Easting [m]:	1574997.0
Processor :	CHE	Cone Serial No :	1701-2758	Northing [m]:	5183131.0
Date :	25-Feb-2015			NZGD2000, NZTM2000 CM 173° E	

Test in accordance with ASTM D5778
Cone type cylindrical electrical, 1510 mm²

PIEZO CONE PENETRATION TEST

Client: UNIVERSITY OF CANTERBURY
Project: AVONDALE PARK

296

Project No. : UCA021501
Location : SCPT1
Equipment : REO66 20T MAN 6x6

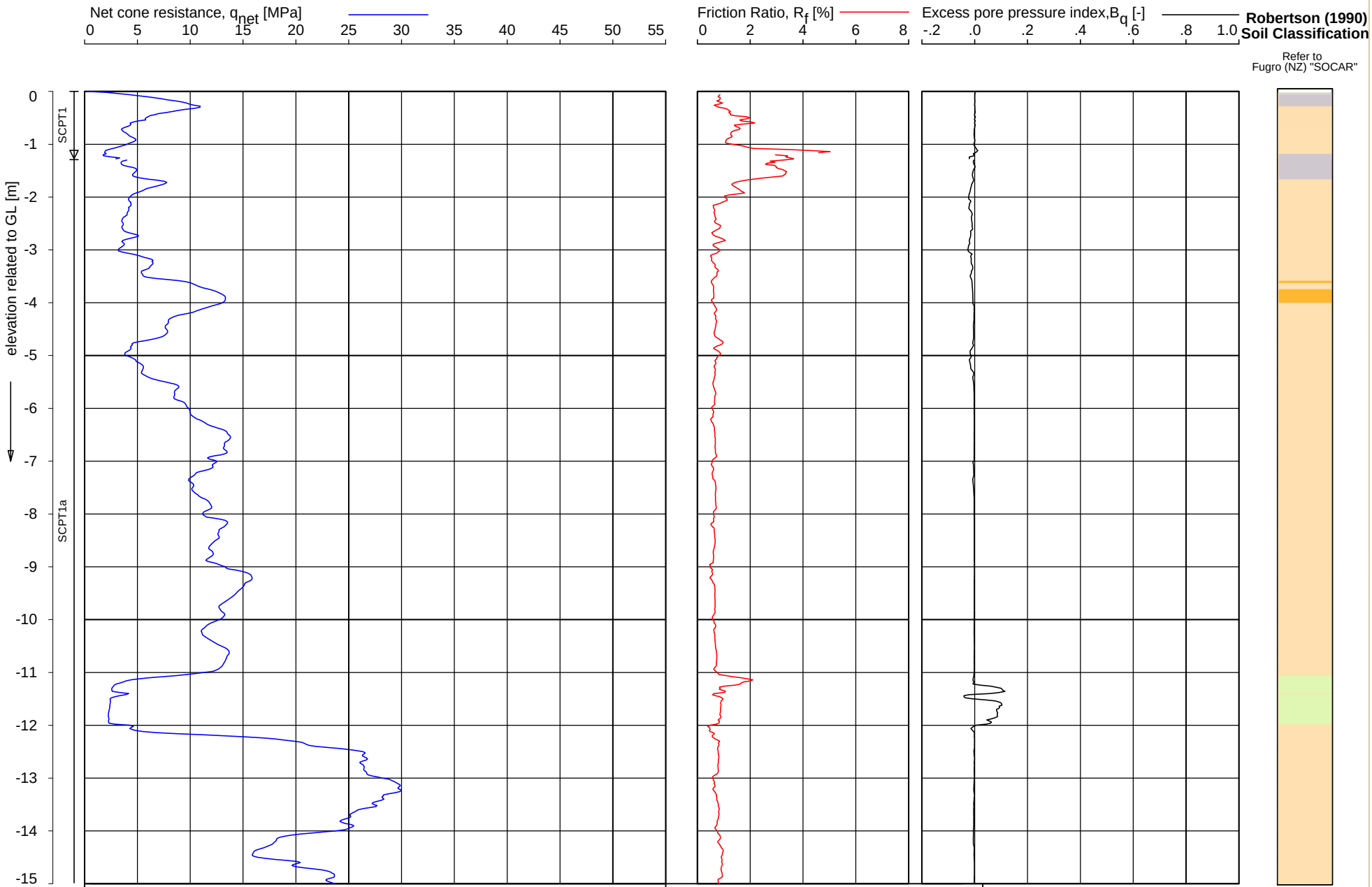

Operator :	EM	Cone :	CP15-CF75PB7SN2	Easting [m]:	1574997.0
Processor :	CHE	Cone Serial No :	1701-2758	Northing [m]:	5183131.0
Date :	25-Feb-2015			NZGD2000, NZTM2000 CM 173° E	

Test in accordance with ASTM D5778
Cone type cylindrical electrical, 1510 mm²
Note: This page **must** be read in conjunction with the Fugro (NZ) "SOCAR" Rev 01

PIEZO CONE PENETRATION TEST

Client: UNIVERSITY OF CANTERBURY
Project: AVONDALE PARK 297

Project No. : UCA021501
Location : SCPT1
Equipment : REO66 20T MAN 6x6

Net cone resistance, q_{net} [MPa]
0 5 10 15 20 25 30 35 40 45 50 55

Friction Ratio, R_f [%]
0 2 4 6 8

Excess pore pressure index, B_q [-]
-.2 .0 .2 .4 .6 .8 1.0

Robertson (1990) Soil Classification

Refer to Fugro (NZ) "SOCAR"

SCPT1a

elevation related to GL [m]

-15 -16 -17 -18 -19 -20 -21 -22 -23 -24 -25 -26 -27 -28 -29 -30

Operator :	EM	Cone :	CP15-CF75PB7SN2	Easting [m]:	1574997.0
Processor :	CHE	Cone Serial No :	1701-2758	Northing [m]:	5183131.0
Date :	25-Feb-2015			NZGD2000, NZTM2000 CM 173° E	

Test in accordance with ASTM D5778
Cone type cylindrical electrical, 1510 mm²
Note: This page **must** be read in conjunction with the Fugro (NZ) "SOCAR" Rev 01

FUGRO

Project No. : UCA021501
Location : SCPT1
Equipment : REO66 20T MAN 6x6

PIEZO CONE PENETRATION TEST

Client: UNIVERSITY OF CANTERBURY
Project: AVONDALE PARK

Appendix A.2
Summary of Calculations and References (SOCAR)

The Soil Behaviour Type (SBT) and soil parameter profiles presented in this report have been calculated using the formulae presented in this document.

Important Note – The SBT and soil parameter profiles are purely to assist rather than replace interpretation, and all data should only be used after they have been checked by a suitably qualified Geotechnical Engineer.

Formulae Used in this Report

Corrected Cone Resistance, q_t (MPa) :

$q_t = q_c + (1 - a)u_2$

q_c and u_2 in MPa

(Robertson 1990)

Normalised Cone Resistance, Q_t :

$$Q_t = \frac{q_t - \sigma_{v0}}{\sigma'_{v0}}$$

q_t, σ_{v0} and σ'_{v0} in kPa

(Robertson 1990)

Normalised Friction Ratio, F_r :

$$F_r = \frac{100 f_s}{\left(q_t - (\sigma_{v0}/1000)\right)}$$

f_s and q_t in MPa, σ_{v0} in kPa

(Robertson 1990)

Pore Pressure Ratio, B_q :

$$B_q = \frac{u - u_0}{q_t - (\sigma_{v0}/1000)}$$

u and q_t in MPa, σ_{v0} in kPa

(Robertson 1990)

SPT N_{60} (blows) :

$$N_{60} = \frac{(q_t/P_a)}{10^{(1.1268 - 0.2817 \cdot I_c)}}$$

q_t and P_a in MPa, P_a = 0.1 MPa

(Robertson 2012)

Undrained Shear Strength, c_u (kPa) :

$$c_u = \frac{q_t - \sigma_{v0}}{N_k}$$

q_t and σ_{v0} in kPa.

(Rad and Lunne 1988)

Relative Density, D_r (%) :

$$D_r\ (dry) = \frac{1}{0.0296} \ln \left[\frac{q_c}{2.494 \left(\frac{\sigma'_{v0} \left(\frac{1 + 2K_0}{3} \right)}{100} \right)^{0.46}} \right]$$

$$D_r\ (sat) = \left(\frac{-1.87 + 2.32 \ln \frac{1000 q_c}{(100 \sigma'_{v0})^{0.5}}}{100} + 1 \right) D_r\ (Dry)$$

q_c in MPa, σ'_{v0} in kPa

(Jamiolkowski et al. 2003)

Angle of Internal Friction, φ'(°) :

$$\varphi' = 17.6 + 11.0 \log_{10} \left(\frac{10 q_t}{\left(\frac{\sigma'_{v0}}{100} \right)^{0.5}} \right)$$

q_t in MPa, σ'_{v0} in kPa

(Mayne 2007)

Additional Notes

- K_0 (Coefficient of Earth Pressure) values of 0.5 and 2.0 have been used for Relative Density calculations.
- N_k factors of 15 and 20 have been used for Undrained Shear Strength calculations.
- The relative density calculation is based on clean sand.
- See overleaf for references

Soil Behaviour Type (SBT) Profiles

Soil Behaviour Type (SBT) profiles presented on report figures are automatically generated from the CPT data using the chart below (Robertson, 1990).

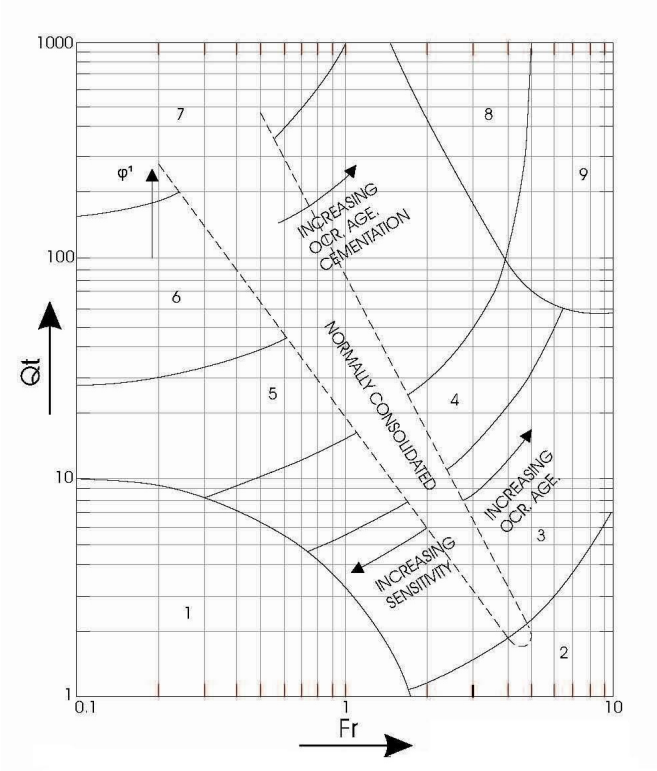

	(1)	Sensitive, fine grained		(6)	SANDS – clean sand to silty sand
	(2)	Organic soils – PEATS		(7)	Gravelly sand to sand
	(3)	CLAYS – clay to silty clay		(8)	Very stiff sand to clayey sand
	(4)	Silt mixtures – clayey SILT to silty CLAY		(9)	Very stiff, fine grained
	(5)	SAND mixtures – silty sand to sandy silt			

References

Jamiolkowski, M., Lo Presti, D.C.F. and Manassero, M. (2003), "Evaluation of Relative Density and Shear Strength of Sands from CPT and DMT", in Germaine, J.T., Sheahan, T.C. and Whitman, R.V. (Eds.), Soil Behavior and Soft Ground Construction: Proceedings of the Symposium, October 5-6, 2001, Cambridge, Massachusetts, Geotechnical Special Publication, No. 119, American Society of Civil Engineers, Reston, pp. 201-238.

Mayne, P.W. (2007), "In-Situ Test Calibrations for Evaluating Soil Parameters", in Tan, T.S., Phoon, K.K.,Hight, D.W. and Leroueil, S. (Eds.), Characterisation and Engineering Properties of Natural Soils Vol. 3", Taylor & Francis, London, pp. 1601-1652.

Rad, N.S. and Lunne, T. (1988), "Direct Correlations between Piezocone Test Results and Undrained Shear Strength of Clay", in De Ruiter, J. (Ed.), Penetration Testing 1988: Proceedings of the First International Symposium on Penetration Testing, ISOPT-1, Orlando, 20-24 March 1988, Vol. 2, A.A. Balkema, Rotterdam, pp. 911-917.

Robertson, P.K., Cabal K.L. (2012), "Guide to Cone Penetration Testing for Geotechnical Engineering", Gregg Drilling & Testing, Inc., 5th Edition, December 2012.

Robertson, P.K. (1990), "Soil Classification using the Cone Penetration Test", Canadian Geotechnical Journal, Vol. 27, No. 1, pp. 151-158.

Robertson, P.K. (2009), "Interpretation of Cone Penetration Tests – a unified approach.", Can. Geotech. J. 46(11): 1337-1355.

Appendix A.3
Practice for Cone Penetration Testing

Test Control – Penetration

General Procedure:	Refer to document titled “Cone Penetration Test” (Fugro ref. FEBV/CDE/APP/001)
Target Accuracy Class:	Class 3
Set-up Stage:	Location as directed by Client
Depth Reference Level:	Existing Ground Level
Additional Measurements:	Not applicable
Test Termination:	Refer to document titled “Cone Penetration Test” (Fugro ref. FEBV/CDE/APP/001)
Drill-Out:	Not Applicable
Test Site Restoration:	Backfill of test hole with minimum 1 m Bentonite plug and where appropriate finish with Cold Lay Tarmac

CPT Apparatus

Thrust Machine:	Truck mounted hydraulic jacking unit of nominal 200 kN thrust capacity
Mounting of Thrust Machine:	Vehicle with levelling facilities
Reaction Equipment:	Thrust machine, vehicle with combined mass of more than 20 tonnes
Push Rods:	36mm OD
Push Rod Casing:	Not applicable
Friction Reducer:	Not applicable
Penetrometer Type:	F7.5CKE2HAW2 piezocone penetrometer, 75 kN load cells (150 kN for overloading), with directional inclinometer, 1,500 mm^2 cone base area, 20,000 mm^2 sleeve area

Test Results

Data Processing and Management:	– Refer to document titled “Cone Penetration Test” (Fugro ref. FEBV/CDE/APP/001) – UNIPLOT software – Graphical scales selected to suit general presentation of data and requirements of standards, where practicable
Depth Correction for Penetrometer Inclination:	Applicable
Parameter Values for Data Processing:	– Unit Weight of Ground water 10 kN/m^3 – Average Wet Density of Soil 18 kN/m^3

References

– Computer Program UNIPLOT, Processing of CPT data

Appendix A.4
Calibration Certificates

CALIBRATION CERTIFICATE

Applicant	**FUGRO GEOTECHNICAL (NZ)**	Certificate nr.	FCL14001582
Manufacturer	Fugro Engineers B.V.	Identification	1701-2758
Instrument	**A Cone Penetrometer**		

Calibration method:
The device was calibrated according to Fugro Engineers procedures using a comparison technique against a Fugro reference standard. Fugro reference standards are periodically recertified and traceable to the National Standards and Technology (NIST) (RVA). It is derived from accepted values of natural physical constants according to the International System of units (SI). Fugro's calibration system meets or exceeds the requirements of ISO 9001:2000 and ISO/IEC 17025:2005.

This specific assembly consists of a Dual Seismic probe and a Lead Cone.
The Dual Seismic Probe governs this assembly and the Certificate nr stated on this page is of the Seismic Probe.
The Certificate nr shown on following pages is the Calibration nr of the Lead Cone.

Cone and Friction Sleeve Calibration Reference

Equipment Serial Number	6034-0001
Equipment Manufacturer	SCHENCK
Equipment Calibration Valid till	17/02/2015
Equipment Certificate	14200527.1000.1EN
Procedure used : in-house	FEBV.CAL.PRO.003

Cone and Friction Sleeve Sensor

Manufacturer	Fugro Engineers BV
Force Application Mode	Compression
Calibrated Range	0 – 75 kN
Max Load	0 – 150 kN

Pressure Calibration Reference

Equipment Serial Number	3257-0002
Equipment Manufacturer	KELLER MEETTECH
Equipment Calibration Valid till	13/11/2014
Equipment Certificate	FCLREF140027
Procedure used : in-house	FEBV.CAL.PRO.004

Pressure Sensor

Manufacturer	Kistler
Pressure Application Mode	Compression and tension
Calibrated Range	Nominal Range
Nominal Range	7 MPa

Inclinometer Calibration Reference

Equipment Serial Number	2109-0004
Equipment Manufacturer	FEBV
Equipment Calibration Valid till	14/05/2015
Procedure used : in-house	FEBV.CAL.PRO.005

Inclinometer

Manufacturer	FEBV	ADXL
Calibrated Range	0° – 15°	-10° - 10°
Max Output	0° – 30°	-15° - 15°

Environmental Conditions

Temperature during calibration	21 ± 3 °C
Pressure during calibration	1000 ± 100 mbar

Remarks.
The values given in this calibration certificate only relate to the submitted device, and to the values measured at the time of the test. Any uncertainty defined here does not include allowances for environmental changes, variation and shock during transportation, or the capability of other laboratories to repeat the measurement.

Calibration technician	Tempelaar, Rolf	Approved by :	Sinjorgo, Gerry
Calibration date:	29/07/2014	Approval date:	29/07/2014
Calibrate before:	29/07/2015		

FUGRO ENGINEERS B.V. Veerse Achterweg 10 - 2264 SG Leidschendam

Appendix B
Seismic Cone Penetration Test

Appendix B.1
SCPT1

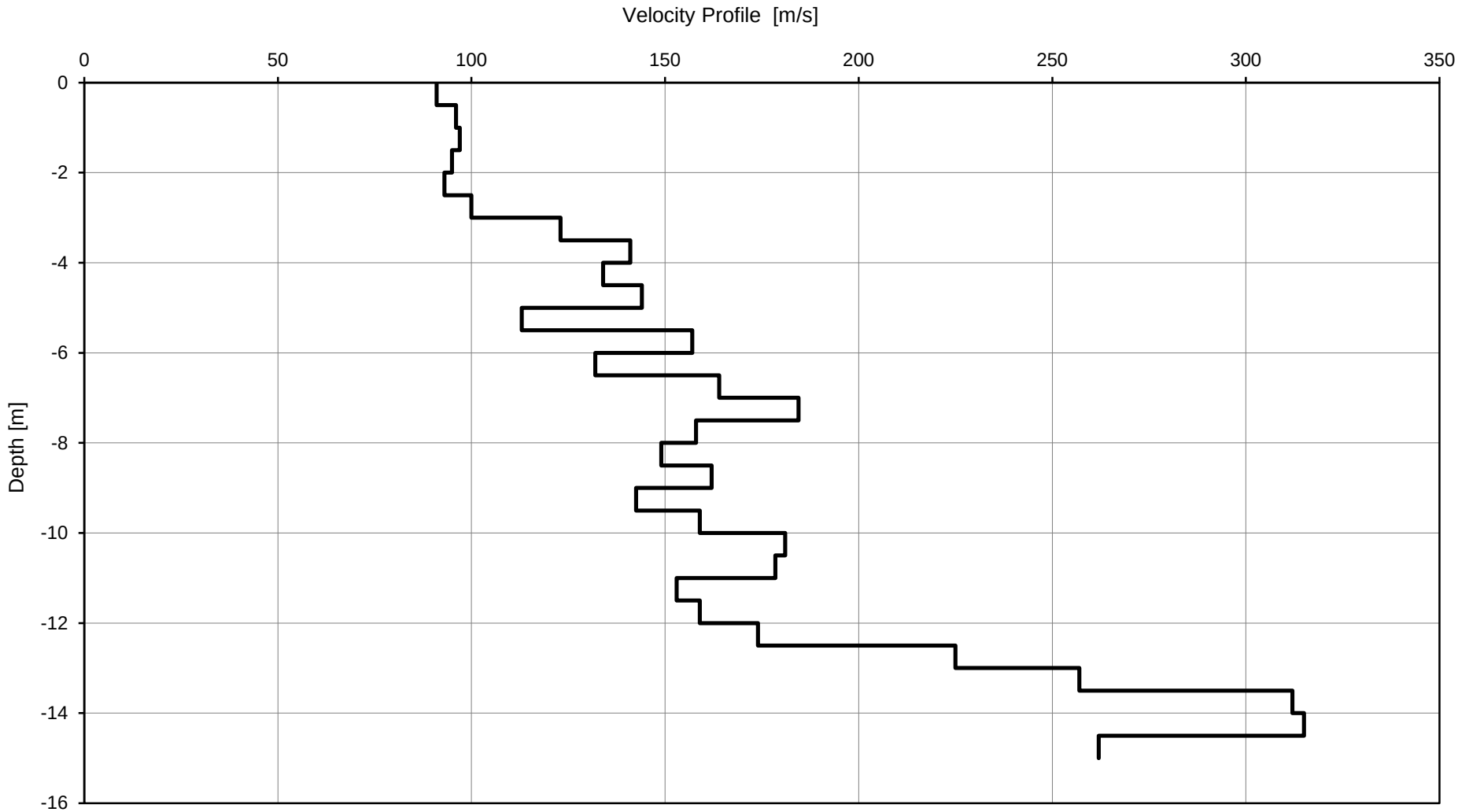

SCPT1
INTERVAL VELOCITY vs. DEPTH
Avodale Park

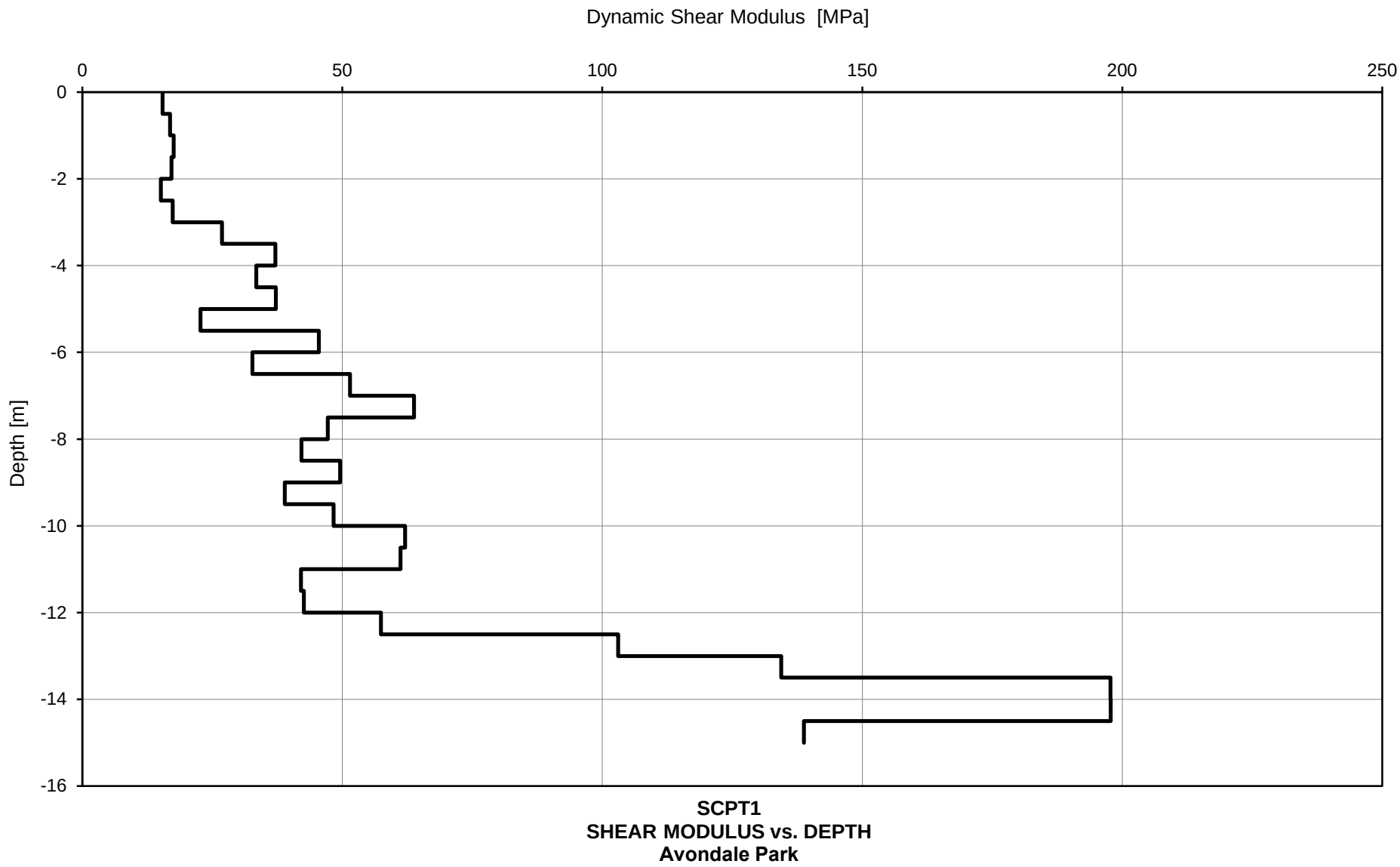

SCPT1
SHEAR MODULUS vs. DEPTH
Avondale Park

Appendix C
Service Warranty

1. This report and the assessment carried out in connection with the report (together the "Services") were compiled and carried out by Fugro Geoteochnical NZ (FGNZ) a trading division of Fugro BTW Ltd for the Client in accordance with the terms of the contract between Fugro Geotechnical NZ and the Client. The Services were performed by FGNZ with the skill and care ordinarily exercised by a competent geotechnical specialist at the time the Services were performed. Further, and in particular, the Services were performed by FGNZ taking into account the limits of the Scope of Works required by the Client, the time scale involved and the resources, including financial and manpower resources, agreed between FGNZ and the Client.

2. Other than that expressly contained in the Contract and in paragraph one above, FGNZ provides no other representation or warranty whether express or implied, in relation to the Services.

3. The Services were performed by FGNZ exclusively for the purposes of the Client. FGNZ is not aware of any interest of, or reliance by, any party other than the Client in or on the Services. Unless expressly provided in writing, FGNZ does not authorise, consent or condone any party other than the Client relying upon the Services. Should this report or any part of this report, or otherwise details of the Services or any part of the services be made known to any such party, and such party relies thereon, that party does so wholly at its own and sole risk and FGNZ disclaims any liability to such parties. Any such party would be well advised to seek independent advice from a competent geotechnical specialist and / or lawyer.

4. It is FGNZ's understanding that this report is to be used for the purpose described in Section 1 - "Introduction" of the report. That purpose was a significant factor in determining the scope and level of the Services. Should the purpose for which the report is used, or the Client's proposed development or use of the site change (including in particular any change in any design and / or specification related to the proposed use or development of the site), this report may no longer be valid or appropriate and any further use of, or reliance, upon the report in those circumstances by the Client without FGNZ's review and advice shall be at the Client's sole and own risk. Should FGNZ be requested, and FGNZ agree, to review the report after the date hereof, FGNZ shall be entitled to additional payment at the then existing rates or such other terms as may be agreed between FGNZ and the Client.

5. The passage of time may result in changes (whether man-made or otherwise) in site conditions and changes in regulatory or other legal provisions, technology, methods of analysis, or economic conditions which could render the report inaccurate or unreliable. The information, recommendations and conclusions contained in this report should not be relied upon if any such changes have taken place or after a period of two years from the date of this report or such other period as maybe expressly stated in the report, without the written agreement of FGNZ. In the absence of such written advice from FGNZ, reliance on the report after any such changes have occurred, or after the period of two years has expired, shall be at the Client's own and sole risk. Should FGNZ be asked to review the report after the period of two years has expired, FGNZ shall be entitled to additional payment at the then existing rates or such other terms as may be agreed between FGNZ and the Client.

6. The observations, recommendations and conclusions in this report are based solely upon the Services which were provided pursuant to the contract between the Client and FGNZ. FGNZ has not performed any observations, investigations, studies or testing not specifically set out or required by the contract between the Client and FGNZ. FGNZ is not liable for the existence of any condition, the discovery of which would require performance of services not otherwise contained in the Services.

7. Where the Services have involved FGNZ's interpretation and / or other use of any information (including documentation or materials, analysis, recommendations and conclusions) provided by third parties (including independent testing and / or information services or laboratories) or the Client and upon which FGNZ was reasonably entitled to rely or involved FGNZ's observations of existing physical conditions of any site involved in the Services, then the Services clearly are limited by the accuracy of such information and the observations which were reasonably possible of the said site. Unless otherwise stated, FGNZ was not authorised and did not attempt to independently verify the accuracy or completeness of such information, received from the Client or third parties during the performance of the Services. FGNZ is not liable for any inaccuracies (including any incompleteness) in the said information, the discovery of which inaccuracies required the doing of any act including the gathering of any information which was not reasonably possible for FGNZ to do including the doing of any independent investigation of the information provided to FGNZ save as otherwise provided in terms of the contract between the Client and FGNZ.

8. The soil and ground conditions information provided in the Services are based solely on evaluations of soil and ground condition samples and in situ tests at determined sample test locations and elevations. That information cannot be extrapolated to any area or elevation outside those locations and elevations unless specifically so stated in the report. In the light of the information available to FGNZ, the soil and ground conditions information are considered appropriate for use in relation to the geotechnical design and installation aspects of the structures addressed in the report, but they may not be appropriate for the design of other structures.

CHAPTER 5.

SUMMARY OF CONCLUSIONS

5.1 Key Findings

(1) Anthropocene deforestation on hillslopes in the Port Hills of southern Christchurch during the 17th to early 20th centuries enabled a subset of rockfall boulders dislodged in the 2011 Christchurch earthquakes to travel further downslope than their most travelled prehistoric predecessors. This suggests an anthropogenic influence on the geologic expression of rockfalls. Reforestation of hillslopes by mature native vegetation could help reduce future rockfall hazard by providing impediments to downslope boulder transport.

(2) Optical and radiocarbon dating of loessic hillslope sediments in New Zealand's South Island can be used to constrain the timing of prehistoric rockfalls and associated seismic events, and quantify spatial and temporal patterns of hillslope sedimentation including responses to seismic and anthropogenic forcing. Prehistoric rockfall boulders may preserve an important record of Holocene hillslope sedimentation by creating local traps (i.e. accommodation space) for sediment aggradation (i.e. colluvial wedges) and upbuilding soil formation.

(3) Prehistoric rockfalls are a ubiquitous geologic feature in the Port Hills and greater Banks Peninsula area. The probable seismogenic origin for much of the rockfall makes these deposits an important paleoseismic indicator of strong prehistoric ground shaking in the region. Mapping and characterization of contemporary and prehistoric (relatively unstudied in BP) rockfalls provide important boulder size and spatial data for use in contemporary hazard analyses and predictive modeling and reveals the impact of source rock geology and anthropogenic landscape modifications on rockfall hazard.

(4) Anthropogenic modifications have influenced the geologic expression of modern (2011) liquefaction in eastern Christchurch, New Zealand. Fill layers and irrigation utility trenches are highly effective in absorbing liquefaction injecta and suppressing its surface manifestation. Radiocarbon dating of charcoal within the youngest native sediment yields a 2σ calibrated age range of 1209 AD to1274 AD, implying that liquefaction at the study site has probably not occurred for at least the past 750-800 years and that ground shaking episodes of similar intensity to the 2011 Christchurch earthquakes are rare.

5.2 Future research

My original intention was to provide an additional thesis chapter on quantifying roughness for prehistoric boulder surfaces. The intended chapter title was "Establishing a surface roughness-age correlation for earthquake-induced prehistoric boulders in southern Christchurch, New Zealand". With the help of Frontiers Abroad students, Emmett Blau and Cameron Rossington, we have now amassed a robust set of photographs for each of the CN-dated prehistoric boulders (n=19). Using photogrammetry and Sfm software (Agisoft) we have created high-resolution point clouds for each of the prehistoric boulders. For several of the point cloud images we have calculated surface roughness using Cloud Compare software, and although highly dependent on the scale chosen, the preliminary results indicate a positive correlation between surface roughness and CN surface exposure age. To remove (or reduce) the challenges associated with determining the appropriate scale, we (being myself and Dr. Christopher Gomez) have proposed producing slope gradient maps for the individual boulder surfaces. The percent area of slopes with angle $\geq 70°$ have been targeted and provides the strongest positive correlation with the CN-surface exposure ages. Our hypothesis is that boulder surfaces which are exposed to the elements (e.g. water, wind) for longer time periods will show a higher percentage of steep micro-slope angles at the boundary between the volcanic ground mass and adjacent (and more weathering resistant) volcanic clasts. Once completed, a comparison of traditional surface roughness calculations with slope gradient maps will be conducted and conclusions presented.

The overall aim is to try and establish a correlation between surface roughness and CN surface exposure age that can be applied to other prehistoric rockfall fields. One could then target a prehistoric boulder field, such as Purau (where boulders of equivalent composition/texture exist) and take multiple photographs for numerous individual prehistoric boulders. The photographs for each boulder would then be used to generate a high-density point cloud for each of the prehistoric boulders. Once completed, surface roughness and slope angle (% above arbitrary value) would be calculated and surface exposure age estimated from the established roughness-CN age relationship at Rapaki. To validate the exposure ages, several of the boulders at Purau could be directly dated using the cosmogenic dating method established by Mackey and Quigley (2014) at Rapaki. The preliminary studies would be suitable only to the volcanic breccia boulders studied at the Rapaki location and observed at Purau. However, the methodology could be applied to any boulders with a high level of textural heterogeneity (e.g. other volcanic lithologies, conglomerates, etc.). Once a high number of CN ages have been determined, then clustering of ages could potentially reveal episodes of seismic-induced ground shaking, as we would

expect strong shaking episodes to generate a high number of similar surface exposure ages (as observed during the 2011 Christchurch earthquakes).

The techniques developed and advanced within this thesis could also be applied to the areas recently affected by the 14 November 2016 M_w 7.8 Kaikoura earthquake sequence. Early reports from GNS Science indicate there have been between 80,000 and 100,000 landslides generated during the earthquake sequence, although there have been very few specific comments on rockfalls. Given the steep terrain and exposure of bedrock in the hilly and mountainous terrain it is reasonable to assume that large amounts of rockfall have also been generated. This assumption was confirmed during our preliminary reconnaissance of the Waiau area, where we observed abundant modern and prehistoric rockfall near sections of the mapped surface rupture. The rockfalls are sourced from the Triassic Torlesse (slightly metamorphosed greywacke and argillite). In several cases colluvial wedges have developed behind (i.e. upslope) the boulders, providing an opportunity for OSL dating.

Finally, it is important that detailed mapping and characterization of prehistoric rockfalls (and volcanic source rocks) continue throughout the Port Hills and Banks Peninsula area to establish a robust data inventory for use in paleoseismic and earthquake hazard investigations. One area of particular interest is understanding the influence that volcanic lithofacies architecture (e.g. brecciated and coherent flows vs. dikes vs. lava domes) has on the size, shape, and spatial distribution of rockfalls. *How are primary emplacement and secondary cooling mechanics for each of these volcanic landforms affecting the local rockfall hazard?* Establishing this relationship will require an extensive field study of volcanic source rock terrain, but has implications for using the study of source rock geology and structure to help predict the expected magnitude of rockfall hazard at a specific location.

REFERENCES

Achard, F., Eva, H.D., Stibig, H., Mayaux, P., Gallego, J., Richards, T., Malingreau, J. (2012). Determination of deforestation rates of the world's humid tropical forests. *Science* **297**: 999-1002.

Ackerley, D., Lorrey, A., Renwick, J., Phipps, S.J., Wagner, S., Fowler, A. (2013). High-resolution modelling of mid-Holocene New Zealand climate at 6000 yr BP. *The Holocene* **23**: 1272-1285.

Aitken, M.J. (1998). An introduction to Optical Dating. Oxford University Press, USA.

Allen, S.K., Cox, S.C., Owens, I.F. (2011). Rock avalanches and other landslides in the central Southern Alps of New Zealand: a regional study considering possible climate change impacts. *Landslides* **8**: 33-48.

Almond, P., Roering, J., Hales, T.C. (2007a). Using soil residence time to delineate spatial and temporal patterns of transient landscape response. *Journal of Geophysical Research-Earth Surface* **112**: 1-19.

Almond, P.C., Roering, J.J., Hughes, M.W., Lutter, F.S., Lebouteiller, C. (2008). Climatic and anthropogenic effects on soil transport rates and hillslope evolution. *IAHS Publication* **325**: 417-424.

Almond, P.C., Shanhun, F. L., Rieser, U., & Shulmeister, J. (2007b). An OSL, radiocarbon and tephra isochron-based chronology for Birdlings Flat loess at Ahuriri Quarry, Banks Peninsula, Canterbury, New Zealand. *Quaternary Geochronology* **2**: 4–8. doi:10.1016/j.quageo.2006.06.002

Almond, P.C., Tonkin, P.J. (1999). Pedogenesis by upbuilding in an extreme leaching and weathering environment, and slow loess accretion, south Westland, New Zealand. *Geoderma* **92**: 1-36.

Almond, P., Villamor, P., Tuttle, M., Langridge, R., Clark, K., Eger, A., Bastin, S., Quigley, M., Barker, P., and Vandergoes, M. (2013). Liquefaction induced by the 2010–2011 Canterbury earthquake sequence and implications of recently discovered paleoliquefaction features: *Geological Society of America Abstracts with Programs* **44**: p. 414.

André, M. (1997). Holocene Rockwall Retreat in Svalbard: A Triple-Rate Evolution. *Earth Surface Processes and Landforms* **22**: 423–440.

Balescu, S., Ritz, J. F., Lamothe, M., Auclair, M., & Todbileg, M. (2007). Luminescence dating of a gigantic palaeolandslide in the Gobi-Altay mountains, Mongolia. *Quaternary Geochronology* **2**: 290–295.

Bannister, S.C., Gledhill, K.R. (2012). Evolution of the 2010-2012 Canterbury earthquake sequence. *New Zealand Journal of Geology and Geophysics* **55**: 295-304.

Bartelt, P., Buehler, Y., Christen, M., Deubelbeiss, Y., Graf, C., McArdell, B.W. (2013). RAMMS - rapid mass movements simulation: A numerical model for rockfall in research practice, User Manual v1.5. Davos, Switzerland.

Bastin, S.H., Quigley, M.C., Bassett, K. (2015). Paleoliquefaction in Christchurch, New Zealand. *Geological Society of America Bulletin* **127**: 1348-1365.

Bastin, S.H., Bassett, K., Quigley, M.C., Maurer, B., Green, R.A., Bradley, B., Jacobson, D. (2016). Late Holocene Liquefaction at Sites of Contemporary Liquefaction during the 2010-2011 Canterbury Earthquake Sequence, New Zealand. *Bulletin of the Seismological Society of America* **106**: 881-903.

Bastin, S.H., Quigley, M.C., Bassett, K., and Green, R.A. (2013). Characterisation of modern and paleo-liquefaction features in eastern Christchurch, NZ, following the 2010–2011 Canterbury earthquake sequence. *NZ Geomechanics News* **26**: 38–46.

Becker, A., Davenport, C.A. (2003). Rockfalls triggered by the AD 1356 Basle Earthquake. *Terra Nova* **15**: 258-264.

Bell, D.H., & Trangmar, B.B. (1987). Regolith materials and erosion processes on the Port Hills, Christchurch, New Zealand: Fifth International Symposium on Landslides. *Lausanne, A.A. Balkema* **1**: 93-105.

Berger, G.W., Tonkin, P.J., Pillans, B.J. (1996). Thermoluminescence ages of Post-Glacial loess, Rakaia River, South Island, New Zealand. *Quaternary International* **34-36**: 177-181.

Bertolini, G. (2007). Radiocarbon dating on landslides in the Northern Apennines (Italy): In *Landslides and Climate Changes*, McInnes, Jakeways, Fairbank and Mathie (eds). Taylor & Francis Group: London; 73-80.

Borella, J. Quigley, M., Vick, L. (2016). Anthropocene rockfalls travel farther than prehistoric predecessors. *Science Advances* **2**: e1600969.

Borella, J., Quigley, M., Sohbati, R., Almond, P., Gravley, D.M., Murray, A. (2016). Chronology and processes of late Quaternary hillslope sedimentation in the eastern South Island, New Zealand. *Journal of Quaternary Science* **31**: 691-712.

Bradley, B. A., Hughes, M. (2012). Conditional Peak Ground Accelerations in the Canterbury Earthquakes for Conventional Liquefaction Assessment. Technical Report Prepared for the Department of Building and Housing, 22 pp.

Brauner, B., Weinmeister, W., Agner, P., Vospernik, S., Hoesle, B. (2005). Forest management decision support for evaluating forest protection effects against rockfall. *Forest Ecology and Management* **207**, 75-85.

Brown, L.J., and Weeber, J.H. (1992). Geology of the Christchurch Urban Area: Institute of Geological and Nuclear Sciences Geological Map 1, scale 1:25,000, 1 sheet + 105 p.

Bull, W.B., and Brandon, M.T. (1998). Lichen dating of earthquake-generated regional rockfall events, Southern Alps, New Zealand. *Geological Society of America Bulletin* **110**: 60–84.

Bull, W. B., King, J., Kong, F., Moutoux, T., Phillips, W. M. (1994). Lichen dating of coseismic landslide hazards in alpine mountains. *Geomorphology* **10**: 253–264.

Burrows, C.J. (1975). A 500-year-old landslide in the Acheron River valley, Canterbury. *New Zealand Journal of Geology and Geophysics* **18**: 357-360.

Burrows, C.J. (1994). Fruit, seeds, birds and the forests of Banks Peninsula. *New Zealand Natural Sciences* **21**: 87-108.

Buylaert, J.,-P., Jain, M., Murray, A.S., Thomsen, K.J., Thiel, C., Sohbati, R. (2012). A robust feldspar luminescence dating method for Middle and Late Pleistocene sediments. *Boreas* **41**: 435-451.

Canterbury Geotechnical Database. (2013). https://canterburygeotechnicaldatabase.projectorbit.com/

Chapot, M. S., Sohbati, R., Murray, A. S., Pederson, J. L., & Rittenour, T. M. (2012). Constraining the age of rock art by dating a rockfall event using sediment and rock-surface luminescence dating techniques. *Quaternary Geochronology* **13**: 18–25.

Christen M., Bartelt P., Gruber U. (2007). RAMMS—a modeling system for snow avalanches, debris flows and rockfalls based on IDL. *PFG Photogrammetrie-Fernerkundung-Geoinformation* **4**: 289–292.

Cordes, S.E., Stock, G.M., Schwab, B.E., and Glazner, A.F. (2013). Supporting evidence for a 9.6±1 ka rock fall originating from Glacier Point in Yosemite Valley, California. *Environmental and Engineering Geoscience* **4**: 345-361.

Costa, C.H., Gonzalez Diaz, E.F. (2007). Age constraints and paleoseismic implication of rock avalanches in the northern Patagonian Andes, Argentina. *Journal of South American Earth Sciences* **24**: 48-57.

Counts, R.C., and Obermeier, S.F. (2012). Subtle seismic signatures: Using small-scale features and ground fractures as indicators of paleoseismicity, *in* Cox, R.T., Tuttle, M.P., Boyd, O., and Locat, J., eds., Recent Advances in North American Paleoseismology and Neotectonics East of the Rockies: *Geological Society of America Special Paper* **493**: 203–219.

Cowie, C.A. (1957). Floods in New Zealand 1920-1953, with Notes on Some Earlier Floods: Wellington, New Zealand, *The Soil Conservation and Rivers Control Council*, 240 p.

Crutzen, P.J. (2002). Geology of mankind. *Nature* **415**: 23.

Cubrinovski, M., and Green, R.A., eds. (2010). Geotechnical Reconnaissance of the 2010 Darfield (Canterbury) Earthquake (contributing authors: Allen, J., Ashford, S., Bowman, E., Bradley, B., Cox, B., Cubrinovski, M., Green, R., Hutchinson, T., Kavazanjian, E., Orense, R., Pender, M., Quigley, M., Wotherspoon, L.). *Bulletin of the New Zealand Society for Earthquake Engineering* **43**: 243–320.

Cubrinovski, M., Bradley, B., Wotherspoon, L., Green, R., Bray, J., Wood, C., Pender, M., Allen, J., Bradshaw, A., Rix, G., et al. (2011). Geotechnical aspects of the 22 February 2011 Christchurch earthquake. *Bulletin of the New Zealand Society for Earthquake Engineering* **44**: 205-226.

Cubrinovski, M., Bray, J.D., Taylor, M., Giorgini, S., Bradley, B.A., Wotherspoon, L., Zupan, J. (2011). Soil liquefaction effects in the central business district during the February 2011 Christchurch Earthquake. *Seismological Research Letters* **82**: 893-904.

Dorren, L.K.A., Berger, F., Imeson, A.C, Maier, B., & Rey, F. (2004). Integrity, stability and management of protection forests in the European Alps. *Forest Ecology and Management* **195**: 165-176.

Dorren, L.K.A., Berger, F., le Hir, C., Mermin, E. Tardif, P. (2005). Mechanisms, effects and management implications of rockfall in forests. *For. Ecol. Manage*. **215**: 183-195.

Evans, S.G., Hungr, O. (1993). The assessment of rockfall hazard at the base of talus slopes. *Canadian Geotechnical Journal* **30**: 620-636.

Fattahi, M.,Walker, R., Hollingsworth, J., Bahroudi, A., Nazari, H., Talebian, M., Armitage, S., Stokes, S. (2006). Holocene slip-rate on the Sabzevar thrust fault, NE Iran, determined using optically stimulated luminescence (OSL). *Earth and Planetary Science Letters* **245**: 673–684.

Forsyth P.J., Barrell D.J.A., Jongens, R. (2008). *Geology of the Christchurch Area. 1:250 000 geological map 16*. Lower Hutt, Institute of Geological & Nuclear Sciences.

Fuchs, M., Fischer, M., & Reverman, R. (2010). Colluvial and alluvial sediment archives temporally resolved by OSL dating: Implications for reconstructing soil erosion. *Quaternary Geochronology* **5**: 269–273.

Fuchs, M., & Lang, A. (2009). Luminescence dating of hillslope deposits - a review. *Geomorphology* **109**: 17–26.

Fuchs, M., Lang, A., Wagner, G.A. (2004). The history of Holocene soil erosion in the Phlious Basin, NE-Peloponnese, Greece, provided by optical dating. *The Holocene* **14**: 334–345.

Fuller, I.C., Macklin, M.G., Richardson, J.M. (2015). The Geography of the Anthropocene in New Zealand: Differential River Catchment Response to Human Impact. *Geographical Research* **53**: 255-269.

Glade, T. (2003). Landslide occurrence as a response to land use change: a review of evidence from New Zealand. *Catena* **51**: 297-314.

Goh, K.M., Molloy, B.P.J., Rafter, T.A. (1977). Radiocarbon dating of Quaternary loess deposits, Banks Peninsula, Canterbury, New Zealand. *Quaternary Research* **7**: 177-196.

Goh, K.M., Tonkin, P.J., Rafter, T.A. (1978). Implications of improved radiocarbon dates of Timaru peats on Quaternary stratigraphy. *New Zealand Journal of Geology and Geophysics* **21**: 463-466.

Goldwater, S. (1990). Slope failure in loess, a detailed investigation, Allendale, Banks Peninsula. University of Canterbury.

Grapes, R., Rieser, U., Wang, N. (2010a). Optical luminescence dating of a loess section containing a critical tephra marker horizon, SW North Island of New Zealand. *Quaternary Geochronology* **5**: 164-169.

Grapes, R., Rieser, U., Wang, N. (2010b). Reply to Lowe, D.J., Wilson, C.J.N., Newnham, R.M., Hogg, A.G. comment on Grapes, R., Rieser, U., Wang, N., 2010. Optical luminescence dating of a loess section containing a critical tephra marker horizon, SW North Island of New Zealand. *Quaternary Geochronology* **5**: 497-501.

Green, R.A., Obermeier, S.F., and Olsond, S.M. (2005). Engineering geologic and geotechnical analysis of paleoseismic shaking using liquefaction effects: Field examples. *Engineering Geology* **76**: 263-293.

Griffiths, E. (1973). Loess of Banks Peninsula. *New Zealand Journal of Geology and Geophysics* **16**: 657–675.

Guns, M. & Vanacker, V. (2014). Shifts in landslide frequency-area distribution after forest conversion in the tropical Andes. *Anthropocene* **6**, 75-85 (2014).

Guzzetti, F., Reichenbach, P., and Wieczorek, G.F. (2003). Rockfall hazard and risk assessment in the Yosemite Valley, California, USA. *Natural Hazards and Earth System Sciences* **3**: 491-503.

Hales, T.C., Roering, J.J. (2007). Climatic controls on frost cracking and implications for the evolution of bedrock landscapes. *Journal of geophysical research* **112**: F02033, doi:10.1029/2006JF000616.

Hampton, S.J., Cole, J.W. (2009). Lyttelton Volcano, Banks Peninsula, New Zealand: Primary volcanic landforms and eruptive centre identification. *Geomorphology* **104**: 284-298.

Hancox, G.T., Perrin, N.D., Dellow, G.D. (1997). Earthquake-induced landsliding in New Zealand and implications for MM intensity and seismic hazard assessment. *GNS Client Report 43601B*.

Hanson, P.R., Mason, J.A., Goble, R.J. (2004). Episodic Late Quaternary slopewash deposition as recorded in colluvial aprons, Southeastern Wyoming. *Quaternary Science Reviews* **23**: 1835–1846.

Harding, J.S. (2003). Historic deforestation and the fate of endemic invertebrate species in streams. *New Zealand Journal of Marine and Freshwater Research* **37**: 333-345.

Heimsath, A.M., Chappell, M.J., Spooner, N.A., Questiaux, D.G. (2002). Creeping soil. *Geology* **30**: 111-114.

Heimsath, A.M., Dietrich, W.E., Nishiizumi, K., Finkel, R.C. (2001). Stochastic processes of soil production and transport; erosion rates, topographic variation and cosmogenic nuclides in the Oregon Coast Range. *Earth Surface Processes and Landforms* **26**: 531-552.

Heron, D., Lukovic, B., Massey, C., Ries, W., & McSaveney, M. (2014). GIS modelling in support of earthquake-induced rockfall and cliff collapse risk assessment in the Port Hills, Christchurch. *Journal of Spatial Science* **59**: 313-332.

Heyman, J., Stroeven, A.P., Harbor, J.M., Caffee, M.W. (2011). Too young or too old: evaluating cosmogenic exposure dating based on an analysis of compiled boulder exposure ages. *Earth and Planetary Science Letters* **302**: 71-80.

Hjulström, F. (1939). Transportation of detritus by moving water: Part 1. Transportation, *in* Trask, P.D., ed., Recent Marine Sediments. *American Association of Petroleum Geologists Special Volume* **10**: 5–31.

Hogg, A., Hua, Q., Blackwell, PG et al. (2013). $SHCAL_{13}$ Southern Hemisphere Calibration, 0-50,000 years CAL B.P.. *Radiocarbon* **55**: 1889-1903.

Hughes, M. W., Almond, P. C., Roering, J. J., & Tonkin, P. J. (2010). Late Quaternary loess landscape evolution on an active tectonic margin, Charwell Basin, South Island, New Zealand. *Geomorphology* **122**: 294–308.

Hughes, M., Quigley, M., van Ballegooy, S., Deam, B., Bradley, B., Hart, D., Measures, R. (2015). The sinking city: earthquakes increase flood hazard in Christchurch, New Zealand. *GSA Today* **25**: 4-10.

Idriss, I.M., Boulanger, R.W. (2008). Soil Liquefaction during Earthquakes. Monograph Series: Oakland, California, Earthquake Research Institute, 261 p.

Ishihara, K. (1985). Stability of natural deposits during earthquakes. In: Proceedings of the 11th International Conference on Soil Mechanics and Foundation Engineering, San Francisco, CA, pp. 321-376.

Ives, D. (1973). Nature and distribution of loess in Canterbury, New Zealand. *New Zealand journal of geology and geophysics* **16**: 587-610.

Jaboyedoff, M., & Labiouse, V. (2011). Technical Note: Preliminary estimation of rockfall runout zones. *Natural Hazards and Earth System Sciences* **11**: 819-828.

Jacomb, C. (2008). The chronology of Moncks Cave, Canterbury, New Zealand. *Records of the Canterbury Museum* **22**: 45-56.

Jancke, O., Dorren, L., Berger, F., Fuhr, M., Kohl, M. (2009). Implications of coppice stand characteristics on the rockfall protection function. *For. Ecol. Manage*. **259**: 124-131.

Jibson, R.W. (1996). Use of landslides for paleoseismic analysis. *Engineering Geology* **43**: 291-323.

Johnson, D.L. (1990). Biomantle evolution and the redistribution of earth materials and artifacts. *Soil Science* **149**: 84-102.

Johnson, D.L., Domier, J.E.J., Johnson, D.N. (2005). Animating the biodynamics of soil thickness using process vector analysis: a dynamic denudation approach to soil formation. *Geomorphology* **67**: 23-46.

Johnson, D.L., Watson-stegner, D.. (1987). Evolution model of pedogenesis. *Soil Science* **143**: 349-366.

Johnson, D.L., Watson-stegner, D., Johnson, D.N., Schaetzl, R.J. (1987). Proisotropic and proanisotropic processes of pedoturbation. *Soil Science* **143**: 278-292.

Johnston, W.B. (1961). Locating the vegetation of early Canterbury: A map and the sources. *Transactions of the Royal Society of New Zealand (botany)* **1**: 5-15.

Kaczyski, R., Baranski, M. (1998). Behaviour of anthropogenic soils subjected to vibration loadings. *Journal of theoretical and applied mechanics* **2**: 241-247.

Kanari, M. (2008). Evaluation of rockfall hazard to Qiryat Shemona – Possible correlation to earthquakes. MSc Thesis, Tel Aviv University, Jerusalem.

Kasai, M., Brierley, G.J., Page, M.J., Marutani, T., Trustrum, N.A. (2005). Impacts of land use change on

patterns of sediment flux in Weraamaia catchment, New Zealand. *Catena* **64**: 27-60.

Keefer, D.K. (1984). Landslides caused by earthquakes. *Geological Society of America Bulletin* **95**: 406-421.

Keefer, D.K. (1994). The importance of earthquake-induced landslides to long-term slope erosion and slope-failure hazards in seismically active regions. *Geomporphology* **10**: 265-284.

Keefer, D.K. (2002). Investigating landslides caused by earthquakes – a historical review. *Surveys in Geophysics* **23**: 473-510.

Kettner, A.J., Gomez, B., Syvitski, J.P.M. (2007). Modeling suspended sediment discharge from the Waipaoa River system, New Zealand: The last 3000 years. *Water Resources Research* **43:** W07411.

Khajavi, N., Quigley, M., McColl, S.T., Rezanejad, A. (2012). Seismically induced boulder displacement in the Port Hills, New Zealand during the 2010 Darfield (Canterbury) earthquake. *New Zealand journal of geology and geophysics* **55**: 271-278.

Kirkman, T.W. (1996). Statistics to use. *http://www.physics.csbsju.edu/stats/* (accessed August 2015).

Lambin, E.F., Turner, B.L., Geist, H.J., Agbola, S.B., Angelsen, A., Bruce, J.W., Coomes, O.T., Dirzo, R., Fischer, G., Folke, C., George, P.S., Homewood, K., Imbernon, J., Leemans, R., Li, X., Moran, E.F., Mortimore, M., Ramakrishnan, P.S., Richards, J.F., Skanes, H., Steffen, W., Stone, G.D., Svedin, U., Veldkamp, T.A., Vogel, C., Xu, J. (2001). The causes of land-use and land-cover change: moving beyond the myths. *Global Environmental Change* **11**: 261-269.

Lang, A., Moya, J., Corominas, J., Schrott, L., & Dikau, R. (1999). Classic and new dating methods for assessing the temporal occurrence of mass movements. *Geomorphology* **30**: 33–52.

Lang, A., Wagner, G.A. (1996). Infrared stimulated luminescence dating of archaeosediments. *Archaeometry* **38**: 129–141.

Leine, R.I., Schweizer, A., Christen, M., Glover, J., Bartelt, P., Gerber, W. (2013). Simulation of rockfall trajectories with consideration of rock shape. *Multibody Systems Dynamics* **32**: 241-271.

Lewis, S.L., Maslin, M.A. (2015). Defining the Anthropocene. *Nature* **519**: 171-180.

Luckman, B.H., Fiske, C.J. (1995). Estimating long-term rockfall accretion rates by lichenometry. In *Steepland Geomorphology,* Slaymaker O (ed). Wiley and Sons: New York; 233-255.

Lundy, P.A. (1995). Engineering geological evaluation of rockfall hazards on Banks Peninsula, Canterbury. *Master's Thesis*. Department of Geological Sciences, University of Canterbury.

Mackey, B.H., Quigley, M.C. (2014). Strong proximal earthquakes revealed by cosmogenic ^{3}He dating of prehistoric rockfalls, Christchurch, New Zealand. *Geology* **42**: 975–978.

Markgraf, V., Dodson, J.R., Kershaw, A.P. et al. (1992). Evolution of late Pleistocene and Holocene climates in the circum-south pacific land areas. *Climate Dynamics* **6**: 193-211.

Massey, C.I., McSaveney, M.J., Heron, D., Lukovic, B. (2012). Canterbury Earthquakes 2010/2011 Port Hills Slope Stability: Pilot study for assessing life-safety risk from rockfalls (boulder rolls). *GNS Science Consultancy Report 2011/311.*

Massey, C.I., McSaveney, M.J., Taig, T., Richards, L., Litchfield, N.J., Rhoades, D.A., McVerry, G.H., et al. (2014). Determining rockfall risk in Christchurch using rockfalls triggered by the 2010-2011 Canterbury earthquake sequence. *Earthquake Spectra* **30**: 155-181.

Matmon, A, Shaked, Y., Porat, N., Enzel, Y., Finkel, R., Lifton, N., Agnon, A. (2005). Landscape development in an hyperarid sandstone environment along the margins of the Dead Sea fault: Implications from dated rock falls. *Earth and Planetary Science Letters* **240**: 803–817.

Maurer, B.W., Green, R.A., Quigley, M., Bastin, S. (2015). Development of magnitude-bound relations for paleoliquefaction analyses: New Zealand case study. *Engineering Geology* **197**: 253-266.

McCarroll, D., Shakesby, R.A., Matthews, J. A. (2001). Enhanced rockfall activity during the little ice age: Further lichenometric evidence from a Norwegian Talus. *Permafrost and Periglacial Processes* **12**: 157–164.

McDowell, B.J. (1989). Site investigations for residential development on the Port Hills, Christchurch. University of Canterbury.

McGlone, M.S. (1983). Polynesian deforestation of New Zealand: A Preliminary Synthesis. *Archaeology in Oceania* **18**: 11-25.

McGlone, M.S. (1989). The Polynesian settlement of New Zealand in relation to environmental and biotic changes. *New Zealand Journal of Ecology* **12**: 115–129.

McGlone, M.S. (1995). Lateglacial landscape and vegetation change and the younger dryas climatic oscillation in New Zealand. *Quaternary Science Reviews* **14**: 867-881.

McGlone, M.S., Salinger, M.J., Moar, N.T. (1993). Paleovegetation studies of New Zealand's climate since the last glacial maximum. *In Global Climates since the Last Glacial Maximum*, Wright, H.E., Kutzbach, J.D., Webb, T., Ruddiman, W.F., Street-Perrott, F.A., Bartlein, P.J. (eds). University of Minnesota Press; 294-317.

McWethy, D.B., Whitlock, C., Wilmshurst, J.M., McGlone, M.S., Fromont, M., Li, X., Dieffenbacher-Krall, A., Hobbs, W.O., Fritz, S.C., Cook, E.R. (2010). Rapid landscape transformation in South Island, New Zealand, following initial Polynesian settlement. *PNAS* **107**: 21343-21348.

Millard, A.R. (2014). Conventions for reporting radiocarbon determinations. *Radiocarbon* **56**: 555-559.

Murray, A.S., Wintle, A.G. (2003). The single aliquot regenerative dose protocol: potential for improvements in reliability. *Radiation Measurements* **37**: 377-381.

Nikonov, A.A. (1988). Reconstruction of the main parameters of old large earthquakes in Soviet Central Asia using the paleoseismogeological method. Tectonophysics **147**: 297–312.

Obermeier, S.F. (1996). Use of liquefaction-induced features for paleoseismic analysis – An overview of how seismic liquefaction features can be distinguished from other features and how their regional distribution and properties of source sediment can be used to infer the location and strength of

Holocene paleo-earthquakes. *Engineering Geology* **44**: 1-76.

Obermeier, S.F., Bleuer, N.K., Munson, C.A., Munson, P.J., Martin, W.S., McWilliams, K.M., Tabaczynski, D.A., Odum, J.K., Rubin, M., and Eggart, D.L. (1991). Evidence of strong earthquake shaking in the lower Wabash Valley from prehistoric liquefaction features: *Science* **251**: 1061-1063.

Okura, Y., Kithara, H., Samara, T., Kawasaki, A. (2000). The effects of rock fall volume on run out distance. *Engineering Geology* **58**: 109-124.

O'Rourke, T.D., Jeon, S.S., Toprak, S., Cubrinovski, M., Jung, J.K. (2012). Underground Lifeline System Performance during the Canterbury Earthquake Sequence. In *Proceedings of the 15th World Congress on Earthquake Engineering (15WCEE)*, Lisbon, Portugal, 24-28 September 2012.

Paronuzzi, P. (2008). Kinematical back-analysis of block propagations for evaluating the rockfall hazard. Abstract for 2008 Joint Meeting of The Geological Society of America.

Porter, S.C., and Orombelli, G. (1981). Alpine Rockfall Hazards: Recognition and dating of rockfall deposits in the western Italian Alps lead to an understanding of the potential hazards of giant rockfalls in mountainous regions. *American Scientist* **69**: 67-75.

Pradel, D., Wartman, J., Tiwari, B. (2014). Impact of anthropogenic changes on liquefaction along the Tone River during the 2011 Tohoku earthquake. *Natural Hazards Review* **15**: 13-26.

Price, S.J., Ford, J.R., Cooper, A.H. and Neal, C. (2011). Humans as major geological and geomorphological agents in the Anthropocene: the significance of artificial ground in Great Britain. *Philosophical Transactions of The Royal Society A* **369**: 1056-1084.

Quigley et al. (2015). Geologic expressions of contemporary and paleo-liquefaction: Insights into strong ground motion and site characteristics. *Abstract for Geologic Society of America* (2015).

Quigley et al. (2016). The 2010-2011 Canterbury Earthquake Sequence: Environmental effects, seismic triggering thresholds and geological legacy. Tectonophysics **672-673**: 228-274.

Quigley, M.C., Bastin, S., Bradley, B.A. (2013). Recurrent liquefaction in Christchurch, New Zealand, during the Canterbury earthquake sequence. *Geology* **41**: 419-422.

Quigley, M., Bradley, B. (2015). Time series of earthquake-induced ground motions at a geographic mean site for CCC assets from 1939 to 2014, University of Canterbury Consultancy Report CN4600001360-3, submission to Christchurch City Council, p. 16-22.

Ramsey, C.B. (2009). Bayesian analysis of radiocarbon dates. *Radiocarbon* **51**: 337-360.

Rinat, Y., Matmon, A., Arnold, M., Aumaître, G., Bourlès, D., Keddadouche, K., Finkel, R.C. (2014). Holocene rockfalls in the southern Negev Desert, Israel and their relation to Dead Sea fault earthquakes. *Quaternary Research* **81**: 260–273.

Ring, U., Hampton, S. (2012). Faulting in Banks Peninsula: tectonic setting and structural controls for late Miocene intraplate volcanism, New Zealand. *Journal of Geological Society, London* **169**: 773-785.

Roering, J.J., Almond, P., Tonkin, P., McKean, J. (2002). Soil transport driven by biological processes over

millennial timescales. *Geology* **30**: 1115-1118.

Roering, J.J., Almond, P., Tonkin, P., McKean, J. (2004). Constraining climatic controls on hillslope dynamics using a coupled model for the transport of soil and tracers: Application to loess-mantled hillslopes, South Island, New Zealand. Journal of *Geophysical Research* **109**: 1-19.

Rowan, A.V., Roberts, H.M., Jones, M.A., Duller, G.A.T., Covey-Crump, S.J., & Brocklehurst, S.H. (2012). Optically stimulated luminescence dating of glaciofluvial sediments on the Canterbury Plains, South Island, New Zealand. *Quaternary Geochronology* **8**: 10–22.

Runge, E.C.A., Goh, K.M., Rafter, T.A. (1973). Radiocarbon chronology and problems in the interpretation of Quaternary loess deposits, South Canterbury, New Zealand. *Soil Sci. Soc. Am. Proc.* **37**: 742-746.

Russell, J., van Ballegooy, S., Rogers, N., Lacrosse, V., Jacka, M. (2015). The effect of subsidence on liquefaction vulnerability following the 2010–2011 Canterbury Earthquake Sequence. Proceedings of the 12th Australia New Zealand Conference on Geomechanics. NZGS & AGS, Wellington, New Zealand, pp. 610–617.

Schuster, R.L., Logan, R. L., Pringle, P.T. (1992). Prehistoric Rock Avalanches in the Olympic Mountains, Washington. *Science* **258**: 1620-1621.

Selby, M.J. (1993). Hillslope materials and processes (2nd edition). Oxford University Press, New York, 451 p.

Sewell, R.J. (1988). Late Miocene volcanic stratigraphy of central Banks Peninsula, Canterbury, New Zealand. *New Zealand Journal of Geology and Geophysics* **31**: 41-64. doi: 10.1080/00288306.1988.10417809

Sewell, R.J., Weaver, S.D., Reay, M.B. (1992). Geology of Banks Peninsula. Scale 1:100 000. Institute of Geological and Nuclear Sciences map 3. Institute of Geological and Nuclear Sciences Ltd, Lower Hutt, New Zealand.

Shulmeister, J., Soons, J.M., Berger, G.W., Harper, M., Holt, S., Moar, N., Carter, J. A. (1999). Environmental and Sea-Level Changes on Banks Peninsula (Canterbury, New Zealand) through Three Glaciation–Interglaciation Cycles. *Palaeogeography, Palaeoclimatology, Palaeoecology* **152**: 101–127.

Silby, K. (*compiler)*. (1856). Christchurch Area Showing Waterways Swamps and Vegetation: Christchurch Drainage Board, available at http://resources.ccc.govt.nz/files/blackmap-environmentecology.pdf (accessed June 2013).

Sims, J.D. (1975). Determining earthquake recurrence intervals from deformational structures in young lacustrine sediments. *Tectonophysics* **29**: 141-152. doi:10.1016/0040-1951(75)90139-0.

Sohbati, R., Murray, A.S., Borella, J.W., Quigley, M.C., OSL dating of prehistoric rockfalls, Christchurch, New Zealand. Abstract and poster at UK Luminescence and ESR meeting, Scottish Universities Environmental Research Centre (SUERC), University of Glasgow, July 2015.

Sohbati, R., Borella, J., Murray, A., Quigley, M., Buylaert, J. (2016). Optical dating of loessic hillslope sediments constrains timing of prehistoric rockfalls, Christchurch, New Zealand. *Journal of Quaternary Science* **31**: 678-690.

Solonenko, V.P. (1977a). Seismogenic deformations and the paleoseismogeological method. *In Seismic Zonation of Eastern Siberia and Its Geological and Geophysical Basis (V. P. Solonenko, Ed.)*, pp. 5-47. Nauka Publishing House, Novosibirsk.

Solonenko, V.P. (1977b). Landslides and collapses in seismic zones and their prediction. *Bulletin of International Association of Engineering Geology*. **15**: 4-8.

Soons, J.M. (1979). Late Quaternary environments in the central South Island of New Zealand. *New Zealand Geographer* **35**: 16-33.

Soons, J.M., Moar, N.T., Shulmeister, J., Wilson, H.D., & Carter, J.A. (2002). Quaternary vegetation and climate changes on Banks Peninsula, South Island, New Zealand. *Global and Planetary Change* **33:** 301-314.

Speight, R. (1933). The Arthur's Pass earthquake of 9 March, 1929. *New Zealand Journal of Science and Technology* **15**: 173-182.

Steffen, W., Crutzen, P.J., McNeill, J.R. (2007). The Anthropocene: Are Humans Now Overwhelming the Great Forces of Nature? *Ambio* **36**: 614-621.

Stock, G.M., & Collins, B.D. (2014b). Reducing Rockfall Risk in Yosemite National Park. *Eos, Transactions American Geophysical Union* **95**: 261–263.

Stock, G.M., Luco, N., Collins, B.D., Harp, E.L., Reichenbach, P., Frankel, K.L. (2014a). Quantitative rock-fall hazard and risk assessment for Yosemite Valley, Yosemite National Park, California: U.S. Geological Survey Scientific Investigations Report 2014-5129, 52 p.

Stoffel, M. (2006). A Review of Studies Dealing with Tree Rings and Rockfall Activity: The Role of Dendrogeomorphology in Natural Hazard Research. *Natural Hazards* **39**: 51–70.

Stout, M., L. (1969). Radiocarbon Dating of Landslides in Southern California and Engineering Geology Implications. *Geological Society of America Special Papers* **123**: 167-180.

Stuiver, M., Polach, H.A. (1977). Discussion reporting of ^{14}C data. *Radiocarbon* **19**: 355-363.

Syvitski, J.P.M., Vorosmarty, C.J., Kettner, A.J., Green, P. (2005). Impact of Humans on the Flux of Terrestrial Sediment to the Global Coastal Ocean. *Science* **308**: 376-380.

Tatard, L. et al. (2010). Characterization and comparison of landslide triggering in different tectonic and climatic settings. *Journal of Geophysical Research* **115**, F04040, doi:10.1029/2009jf001624.

Tonkin, P.J., Runge, E.C.A., Ives, D.W. (1974). A study of late Pleistocene loess deposits, South Canterbury, New Zealand. *Quaternary Research* **4**: 217-231.

Townsend, D., Lee, J.M., Strong, D.T., Jongens, R., Smith Lyttle, B., Ashraf, S., Rosser, B., Perrin, N., Lyttle, K., Cubrinovski, M., Taylor, M.L., Hughes, M.W., Wilson, T., Almond, P., Jacka, M., McCahon, I., Christensen, S. (2016). Mapping surface liquefaction caused by the September 2010

and February 2011 Canterbury earthquakes: a digital dataset. *New Zealand Journal of Geology and Geophysics* **59**: 496-513.

Townsend, D.B., Rosser, B. (2012). Canterbury Earthquakes 2010/2011 Port Hills slope stability: Geomorphology mapping for rockfall risk assessment. *GNS Science Consultancy Report 2012/15*.

Trotter, M.M. (1975). Archaeological investigations at Redcliffs, Canterbury, New Zealand. Records of the Canterbury Museum **9**: 189-220.

Tuttle, M. (2001). The use of liquefaction features in paleo-seismology: Lessons learnt in the New Madrid seismic zone, central United States. *Journal of Seismology* **5**: 361-380.

Vacchiano, G., Motta, R., Long, J., Shaw, J. (2008). A density management diagram for Scots pine (Pinus sylvestris L.): A tool for assessing the forest's protective effect. *For. Ecol. Manage*. **255**: 2542-2554.

van Ballegooy, S., Berryman, K., Deam, B., Jacka, M. (2014a). Repeated major episodes of tectonic deformation, lateral spread and liquefaction in Christchurch during the Canterbury Earthquake Sequence of 2010–2011. *Engineering Geology for Society and Territory* **5**: 1043–1049.

van Ballegooy, S., Cox, S.C., Thurlow, C., Rutter, H.K., Reynolds, T., Harrington, G., Smith, T. (2014b). Median water elevation in Christchurch and surrounding area after the 4 September 2010 Darfield Earthquake, Version 2. *GNS Science Report 2014/18*.

van Ballegooy, S., Malan, P., Lacrosse, V., Jacka, M., Cubrinovski, M., Bray, J., O'Rourke, T., Crawford, S., Cowan, H. (2014c). Assessment of liquefaction-induced land damage for residential Christchurch. *Earthquake Spectra* **30**, 31–55.

van Ballegooy, S., Green, R., Lees, J., Wentz, R., Maurer, B. (2015a). Assessment of various CPT based liquefaction severity index frameworks relative to the Ishihara (1985) H1–H2 boundary curves. *Soil Dynamics and Earthquake Engineering* **79**: 347-364.

van Ballegooy, S., Lacrosse, V., Simpson, J., Malan, P. (2015b). Comparison of CPT based simplified liquefaction assessment methodologies based on Canterbury Geotechnical Dataset. Proceedings of the 12th Australia New Zealand Conference on Geomechanics. NZGS & AGS, Wellington, New Zealand, pp. 618–625.

Van Breemen, N., and Buurman, P. (2002). Soil Formation (2nd ed.): Dordrecht, Netherlands, Kluwer Academic Publishers, 408 p.

Vandergoes, M.J., Hogg, A.G., Lowe, D.J., Newnham, R.M., Denton, G.H., Southon, J., Barrell, D.J.A., Wilson, C.J.N., McGlone, M.S., Allan, A.S.R., Almond, P.C., Petchey, F., Dabell, K., Dieffenbacher-Krall, A.C., Blaauw, M. (2013). A revised age for the Kawakawa/Oruanui tephra, a key marker for the Last Glacial Maximum in New Zealand. *Quaternary Science Reviews* **74**: 195-201.

Varnes, D.J. (1978). Slope movement types and processes. In Landslides-Analysis and Control (R. L. Schuster and R. J. Krizek, Eds.), Special Report **176**: 11-33.

Vick, L.M. (2015). Evaluation of field data and 3D modelling for rockfall hazard assessment. *PhD Thesis*. Department of Geological Sciences, University of Canterbury.

Villamor, P., Giona-Bucci, M., Almond, P., Tuttle, M., Langridge, R.M., Clark, K.J., Ries, W., Vandergoes, M., et al. (2016). Liquefaction features produced by the 2010-2011 Canterbury earthquake sequence in southwest Christchurch, New Zealand and preliminary assessment of paleoliquefaction features. *Bulletin of the Seismological Society of America* **106.** Doi: 10.1785/0120150223

Villemure, M, Wilson, T.M., Bristow, D., Gallagher, M., Giovinazzi, S., Brown, C. (2012). Liquefaction ejecta clean-up in Christchurch during the 2010–2011 earthquake sequence. In *Proceedings of the New Zealand society for earthquake engineering annual technical conference*, Paper 131, Christchurch, New Zealand, April 13–15 2012.

Volkwein, A., Schellenberg, K., Labiouse, V., Agliardi, F., Berger, F., Bourrier, F., Dorren, L.K.A., Gerber, W., Jaboyedoff, M. (2011). Rockfall characterization and structural protection-a review. *Natural Hazards and Earth System Sciences* **11**, 2617-2651.

Waters et al. (2016). The Anthropocene is functionally and stratigraphically distinct from the Holocene. *Science* **351**.

Whitehouse, I.E. (1981). A large rock avalanche in the Craigieburn Range, Canterbury. *New Zealand Journal of Geology and Geophysics* **24**: 415-421.

Whitehouse, I.E. (1983). Distribution of large rock avalanche deposits in the central Southern Alps, New Zealand. *New Zealand Journal of Geology and Geophysics* **26**: 271-279.

Whitehouse, I.E., and Griffiths, G.A. (1983). Frequency and hazard of large rock avalanches in the central Southern Alps, New Zealand. *Geology* **11**: 331-334.

Wieczorek, G.F. (2002). Catastrophic rockfalls and rockslides in the Sierra Nevada, USA. *Geological Society of America Reviews in Engineering Geology* **15**: 1-26.

Wieczorek, G.F., and Snyder, J.B. (2004). Historical Rock Falls in Yosemite National Park, California. *U.S. Geological Survey Open-File Report 03-491*.

Wieczorek, G.F., Morrissey, M.M., Iovine, G., Godt, J. (1999). Rock-fall Potential in the Yosemite Valley, California. *U.S. Geological Survey Open-file Report 99-578*.

Wilson, H.D. (1993). Bioclimatic zones and Banks Peninsula. *Canterbury Botanical Society Journal* **27**: 22-29.

Wilson, H.D. (2008). Natural history of Banks Peninsula. Christchurch: Canterbury University Press.

Wilson, H.D. (2013). Plant life on Banks Peninsula. Cromwell, New Zealand: Manuka Press.

Woltjer, M., Rammer, W., Brauner, M., Seidl, R., Mohren, G.M.J., Lexer, M.J. (2008). Coupling a 3D patch model and a rockfall module to assess rockfall protection in mountain forests. *Journal of Environmental Management* **87**: 373-388.

Woodward, C.A., Shulmeister, J. (2005). A Holocene record of human induced and natural environmental change from Lake Forsyth (Te Wairewa), New Zealand. *Journal of Paleolimnology* **34**: 481-501.

Youd, T.L., Garris, C.T. (1995). Liquefaction-induced ground surface disruption. *ASCE Journal of Geotechnical Engineering* **121**: 805-809.

Zalasiewicz, J. (2016). What mark will we leave on the planet? A history in layers. *Scientific American* **315**: 31-37.

Zalasiewicz et al. (2015). When did the Anthropocene begin? A mid-twentieth century boundary level is stratigraphically optimal. *Quaternary International* **383**: 196-203.

Zalasiewicz, J., Williams, M., Haywood, A., and Ellis, M. (2011). The Anthropocene: a new epoch of geological time? *Philosophical Transactions of The Royal Society A* **369**: 835-841.